The Use Cardiac Magnetic Resonance Imaging Techniques in the Management of Atrial Arrhythmias

Chubb, Mark Henry

Awarding institution:
King's College London

The Use of Cardiac Magnetic Resonance Imaging Techniques in the Management of Atrial Arrhythmias

Dr M. Henry Chubb

MBBS MA MRCP MRCPCH

A dissertation submitted for the degree of

Doctor of Philosophy

Division of Imaging Sciences and Biomedical Engineering

School of Medicine

King's College London

University of London

ABSTRACT

Introduction:

The use of cardiac magnetic resonance (CMR) imaging in the performance of cardiac electrophysiological procedures has grown rapidly over the past decade. This thesis focuses on three main strands regarding the integration of CMR techniques within the management of atrial arrhythmias: prior to ablation, during ablation, and after ablation.

Methods:

Prior to catheter ablation for atrial fibrillation, 89 subjects underwent detailed CMR analysis of the AF substrate, with extended follow-up. In a first-in-man clinical trial of MR-guidance during ablation, 10 subjects underwent treatment for atrial flutter using an ablation catheter with active MR-tracking. Post AF ablation, 40 subjects were enrolled in a cross-over study, with two closely-coupled scan sessions (3 months post-ablation, 48 hour separation, total 6 LGE acquisitions per subject): scar imaging optimisation, reproducibility and thresholding were assessed. Finally, the predictive value of the VisiTag (CARTO3) objective ablation module was evaluated against optimal CMR-assessed scar.

Results:

Prior to ablation, on multi-variate Cox regression analysis only LA fibrosis was independently associated with outcome. During ablation, MR-guided therapy was performed in 9 (90%) of subjects, with two late arrhythmia recurrences. Post-ablation, it was demonstrated that optimal imaging was performed late (>30min) post-gadolinium injection. Reproducibility of scar imaging was good, and best thresholded using a blood-pool z-score method. VisiTag thresholds should be set relatively low (10g, 15seconds) to avoid a high ablation burden.

Conclusions:

CMR techniques have an important role to play in the guidance of ablation therapies for atrial arrhythmias. The implementation of these techniques, though, must be performed with a thorough understanding of the capabilities and limitations of CMR. Image acquisition, image processing, engineering constraints and subjective interpretation may lead to false findings, both positive and negative. In this cross-specialty field, cautious and informed utilisation of CMR may in time improve clinical outcomes, but further work is required to establish and confirm the precise role and benefits of the techniques.

CONTENTS

LIST OF TABLES

LIST OF FIGURES

LIST OF APPENDICES

List of Abbreviations and Acronyms

3D WH- three-dimensional whole heart
AF- atrial fibrillation
AFL- atrial flutter
AUC- area under the curve
AV- atrioventricular
BMI- body mass index
BP- blood pool
aCNR- apparent contrast-to-noise ratio
aSNR- apparent signal-to-noise ratio
b-SSFP- balanced steady-state free precession
CF- contact force
CHD – congenital heart disease
CI- confidence interval
CIED- cardiac implanted electronic device
CMR- cardiac magnetic resonance
CNR- contrast-to-noise ratio
CS- coronary sinus
CTI- cavotricuspid isthmus
DCCV- direct current cardioversion
DIR- double inversion recovery
DSC- dice similarity coefficient
EAM- electroanatomical mapping
ECG- electrocardiogram
EF- ejection fraction
EP- electrophysiology
FA- flip angle
FTI- force time integral
GBCA- gadolinium based contrast agent
GMRA- gated magnetic resonance angiogram
GRE- gradient echo
GUI- graphical user interface
ICC- intraclass correlation coefficient
IEGM- intracardiac electrogram
ICD- implantable cardioverter defibrillator
IIR- image intensity ratio
IQR- interquartile range
LA- left atrium
LAA- left atrial appendage
LAEF- left atrial ejection fraction
LAT- local activation time
LGE- late gadolinium enhancement
LIPV- left inferior pulmonary vein
LSPV- left superior pulmonary vein
LV- left ventricle
MHD- magneto-hydrodynamic
MRA- magnetic resonance angiogram
MRI- magnetic resonance imaging
MV- mitral valve
NPV- negative predictive value
PAAS- post-ablation atrial scar
PAF- paroxysmal atrial fibrillation
PersAF- persistent atrial fibrillation
PPI- post pacing interval
PPV- positive predictive value
PV- pulmonary vein
PVE- pulmonary vein encirclement
RA- right atrium
RIPV- right inferior pulmonary vein
RSPV- right superior pulmonary vein
RF- radiofrequency
RV- right ventricle
SD- standard deviation
SE- spin echo
SI- signal intensity
SNR- signal-to-noise ratio
SRM- structural remodelling
SSFP- steady-state free precession
TCL- tachycardia cycle length
TE- echo time
TOE- transoesophageal echocardiography
TR- repetition time
TSE- turbo spin echo
TV- tricuspid valve
VDT- voltage-based device tracking
VT- ventricular tachycardia
WACA- wide area circumferential ablation

EXTENDED ABSTRACT

Introduction:

The use of cardiac magnetic resonance (CMR) imaging in the performance of cardiac electrophysiological procedures has grown rapidly over the past decade. CMR is a highly attractive imaging modality, offering excellent soft tissue contrast and functional indices with no established long-term adverse effects. It has therefore been used extensively both prior to and after ablation procedures. However, many of the key advantages of CMR imaging may also be realised in real-time during the ablation procedure. This thesis focuses on three main strands regarding the integration of CMR techniques within the management of atrial arrhythmias: prior to ablation, during ablation, and after ablation.

- *Prior to ablation*. Multiple CMR indices have been developed by independent groups and have been shown to be associated with long-term outcome (arrhythmia recurrence) following catheter ablation for atrial fibrillation (AF). In this thesis, measurement techniques for the six most well-established indices, including atrial fibrosis, were developed independently and implemented. For the first time, the relative contribution and combined predictive value of the CMR-indices of AF substrate was assessed.
- *During ablation*. Real-time MR-guided electrophysiological (EP) procedures have been performed in animal models, and a very limited number of human procedures performed. Human procedures have been performed using passive tracking techniques to establish ablation catheter location, a slow and laborious process. Active tracking, whereby the catheter can signal its position in 3D space in real-time, brings MR-guided EP significantly closer to mainstream clinical implementation. This thesis documents the first-in-man study of the use of active tracking EP catheters to perform ablation of typical atrial flutter under real-time CMR guidance.
- *After ablation*. CMR has been used to assess the efficacy of ablation procedures, through the imaging of ablation lesions, and even to guide repeat catheter ablation procedures. However, the precise imaging techniques vary widely between centres, and there is a concomitant variation in imaging success. This thesis evaluates the optimal late gadolinium enhanced (LGE) imaging parameters, image interrogation techniques and reproducibility of detection of post-ablation atrial scar (PAAS), and then assesses the predictive value of a novel objective marker of ablation, the VisiTag module (CARTO3, Biosense Webster), to guide user-defined ablation thresholds.

Methods:

- *Prior to ablation*. 89 patients (53% PAF, 73% male) underwent comprehensive CMR study prior to first-time ablation (PVI +/- additional lesion sets), with median follow-up 383 days post ablation. 3D LGE acquisition (1.5T, ECG and respiratory gated, 1.3x1.3x2mm) was quantified for atrial fibrosis according to image intensity ratio. Left atrial (LA) volume and sphericity were assessed on manual segmentation at atrial diastole, and LA and left ventricular (LV) ejection fractions (EF) quantified on multi-slice cine imaging.
- *During ablation*. The setup integrated a clinical 1.5T scanner, an EP recording and ablation system, and a real-time image guidance platform with components having undergone ex vivo and in-vivo

validation. For the clinical study, 10 human subjects with typical atrial flutter (age 62± 15 years) underwent MR-guided cavotricuspid isthmus (CTI) ablation.

- *After ablation*. 40 subjects undergoing first-time radiofrequency ablation for AF (20 PAF, 31 male) underwent 3D LGE CMR imaging at 3 months in a cross-over study. Post-ablation imaging was performed on two separate occasions, separated by 3 days, with acquisitions performed at 10, 20 and 30min post-gadolinium administration (total 6 acquisitions per patient). At Scan 1, standard acquisition parameters were used (0.2mmol/kg Gadovist, 1.5T magnet strength, 4mm slice thickness). At Scan 2, patients were randomised to identical parameters (n=10), half gadolinium dose (n=10), 3T (n=10) or half slice thickness (2mm, n=10). PAAS imaging quality, reproducibility and thresholding techniques were formally assessed. For assessment of VisiTag thresholds, 24 subjects underwent standard AF ablation with VisiTag module activated. 27 export datasets were created per subject, at a pre-selected combination of thresholds of the six key parameters, based upon a UK survey of clinical practice. PAAS and VisiTag location was compared on a regional and point-by-point basis.

Results:

- *Prior to ablation*. LA EF, indexed LA volume, LA fibrosis and LV EF were all significantly correlated with long-term outcome. On multi-variate Cox regression analysis only LA fibrosis was independently associated with outcome.
- *During ablation*. Targeted radiofrequency ablation was performed in 9 (90%) subjects. Seven patients had CTI ablation completed using CMR guidance alone; 2 patients required completion under fluoroscopy, with 2 late flutter recurrences. Acute and chronic CMR imaging demonstrated efficacious lesion formation, and anatomic shape of the CTI was an independent predictor of procedural success.
- *After ablation*. Imaging of post-ablation atrial scar improves significantly with time from gadolinium administration, and a half dose of gadolinium improved contrast and total scar detected. There was good intra-scan and inter-scan reproducibility of PAAS detection, with thresholding of the scar best performed using a blood-pool z-score method. On assessment of VisiTag thresholds to predict scar formation, high force (>10g) and time (>15seconds) were associated with a lower negative predictive value, with scar frequently formed when these thresholds had not been achieved.

Conclusions:

CMR techniques have an important role to play in the guidance of ablation therapies for atrial arrhythmias. The implementation of these techniques, though, must be performed with a thorough understanding of the capabilities and limitations of CMR. Image acquisition, image processing, engineering constraints and subjective interpretation may lead to false findings, both positive and negative. In this cross-specialty field, cautious and informed utilisation of CMR may in time improve clinical outcomes, but further work is required to establish and confirm the precise role and benefits of the techniques.

THESIS OUTLINE

SECTION ONE: BACKGROUND AND LITERATURE REVIEW

Chapter 1 provides a short introduction to magnetic resonance imaging (MRI), the technique used in all the experimental chapters.

Chapter 2 contains an outline of the key electrophysiological principles relevant to the thesis. Most of the chapter addresses the two atrial arrhythmias that are the subject of the experimental chapters, atrial fibrillation (AF) and atrial flutter (AFL). There is also a review of electroanatomical mapping (EAM), as replication of the functionalities of this technique are key in the development of a clinically implementable MR-guided EP system.

Chapter 3 is a review of MR-guided electrophysiology (EP), covering technical considerations and the history of the field.

SECTION TWO: METHODS AND EXPERIMENTAL DATA

Chapter 4 details the generic methodological techniques that are relevant to all experimental data chapters. This comprises core CMR imaging techniques and parameters, CMR analysis techniques and catheter ablation techniques.

Chapter 5 presents an evaluation of six of the main CMR-derived indices of left atrial AF substrate, and compares their relative contribution in the prediction of long-term outcome following catheter ablation.

Chapter 6 documents the development, validation and first-in-man clinical study of an MR-guided EP ablation system using active catheter tracking. Using an EAM analogue on an MRI platform, ten patients underwent catheter ablation for typical AFL.

Chapter 7 provides an assessment of the optimisation of CMR late gadolinium enhanced (LGE) imaging for the detection of post-ablation atrial scar in a cross-over clinical study.

Chapter 8 reports the reproducibility of the imaging of LGE-detected post-ablation atrial scar. However, detection of scar is inseparable from the issues of signal intensity normalisation and thresholding, and therefore all three are evaluated and ablation scar is also compared to late outcome following ablation.

Chapter 9 describes the predictive value of an objective marker of ablation, the VisiTag module (CARTO3, Biosense Webster), in estimating formation of chronic atrial ablation scar. 3D LGE atrial datasets at three months post ablation are used as a marker of chronic scar following ablation, and ablation parameter thresholds are evaluated in a retrospective clinical study.

SECTION THREE: CONCLUDING REMARKS AND SUPPLEMENTARY DATA

Chapter 10 concludes the thesis by discussing original contributions and future directions.

SECTION ONE: BACKGROUND AND LITERATURE REVIEW

1 Cardiac Magnetic Resonance Imaging Principles

1.1 Basic principles of MRI

1.1.1 Nuclear spins and their properties

The principles of nuclear magnetic resonance (NMR) were proposed in the late 1940s independently by Felix Bloch and Edward Purcell and have evolved to create a powerful, varied and complex tool for medical imaging (magnetic resonance imaging, MRI).

In quantum mechanics, each particle possesses the property of spin. Particles spin about their axis, and charged particles create an associated magnetic field. Protons and neutrons each have a spin number, I, of ½, and paired protons will generally cancel out the spin state of each other. However, atomic nuclei with an odd number of protons and/or neutrons exhibit a net magnetic field, termed a magnetic dipole moment (MDM, μ). Several elements found within the human body may therefore be used for NMR assessment (^{1}H, ^{13}C, ^{19}F, ^{23}Na, ^{31}P), but ^{1}H is by far the most commonly used for medical imaging because of its abundance in biological tissues and large gyromagnetic ratio* (I= ½, γ= 42.58MHz/T).

At resting state, the MDMs of the protons are in an equilibrium state where each cancels out the other, resulting in a net magnetic field (M) of zero. When an external magnetic field, B_0, is applied, the MDMs line up with the external field, pointing parallel or antiparallel. However, there is a small net magnetisation (M_0) in the direction of B_0, representing an excess of approximately one in 1 million protons. Furthermore, in a manner somewhat analogous to a spinning top, the protons wobble or 'precess' about the B_0 axis at a frequency, ω, proportional to the gyromagnetic ratio, γ, and the B_0.

$$Larmor\ Equation: \quad \omega = \gamma B_0 \qquad Equation\ 1.1$$

1.1.2 RF pulses, excitation and relaxation

In order to interrogate the properties of a tissue within a magnetic field, the spins must be excited from their equilibrium state. This is achieved by applying radiofrequency (RF) pulses at the resonant (Larmor) frequency. These RF pulses can be seen as the application of an oscillating electromagnetic field, B_1, and the frequency of the pulse must be sufficiently close to the Larmor frequency, ω_0, in

* The gyromagnetic ratio is the ratio of a particle's (or system's) angular momentum to its magnetic momentum, and equal to half of the charge-to-mass ratio. Its SI unit is the radian per second per tesla, converted to hertz per tesla by dividing by 2π.

order to enable resonance of the torque exerted upon the baseline magnetisation. In practice, RF pulses are often labelled according to the flip angle (FA) that they produce. The longer the pulse is applied, and the greater the magnitude of B_1, the greater the angle (FA) M is moved from M_0, such that:

$$FA = \gamma \int_0^t B_1(t)dt \qquad \textit{Equation 1.2}$$

where FA= flip angle, γ= gyromagnetic ratio.

The magnitude of the net magnetisation aligned parallel to B_0 is termed the longitudinal magnetisation (M_z), whilst the net vector perpendicular to B_0 is termed transverse magnetisation, or M_{xy}. Furthermore, the RF pulse causes the spins to precess in phase, creating an oscillating magnetic field measurable at the macroscopic level.

An RF pulse that tips M fully onto the transverse plane (M_z=0, M_{xy}=M_0) is called a 90°, or 'saturation', pulse. An RF pulse that flips M all the way back to the z-axis is a 180°, or 'inversion', pulse (M_z= -M_0 and M_{xy}=0). The power of the pulse is important in terms of the total energy applied to the body within the scanner that may be deposited within tissues. This is termed the specific absorption rate (SAR), and in practice is calculated rather than measured.

1.1.2.1 T_1 relaxation

T_1 relaxation is the term applied to the return of M to M_0, the baseline equilibrium state within B_0, following excitation. It also applies in theory to the transition to M_0 when a body is first placed within an external magnetic field.

The T_1 characteristic of a tissue is determined by the efficiency of energy transfer between the protons and the surrounding tissue, 'spin-lattice' energy exchange. The most efficient, and hence swiftest, energy transfers occur when the natural motional frequencies ('tumbling rate') of a tissue (ω(tissue)) are close to the Larmor frequency (ω_0). The T_1 time is therefore dependent upon the biological tissue type (determining tumbling rate) and the strength of B_0 (determining ω_0).

The tumbling rate is influenced by the bonds between atoms and local atomic environment. For example, in water the protons have a very high degree of freedom, and therefore a high natural motional frequency ($\omega(H_2O) >> \omega_0$), in solids there is a low degree of freedom, so $\omega(\text{solids}) << \omega_0$. However, in tissues such as fat the frequency is very close to ω_0 at typical imaging field strengths ($\omega(\text{fat}) \approx \omega_0$). Therefore fat lies close to the T_1 'sweetspot' and has a shorter T_1 time than either solids or water at either end of the spectrum. Water itself, though, may be relatively constrained when in proximity to hydrophilic molecules such as some proteins, reducing the tumbling rate and therefore substantially shortening its T_1 time.

Typical T_1 relaxation time: water>solids>proteins>fat

Perhaps slightly counter-intuitively, stronger magnetic fields, B_0, tend to be associated with longer T_1 time. This is related to the increase in Larmor frequency proportional to B_0 (see Equation 1.1), and the consequent shift from the natural 'tumbling rates' of biological tissues. The tumbling rates of free water and solids remain significantly different from the Larmor frequency at all medically relevant field strengths, but those of proteins and fat progressively shift below the Larmor frequency with increasing field strength. As a result, empirical measurements suggest that biological tissue T_1 increases proportional to approximately $B_0^{1/3}$, increasing by around 25% from 1.5T to 3T (Hashemi, Bradley, and Lisanti 2010).

The return of M to M_0 is an exponential process, and the T_1 time constant is defined such that, for a flip angle of 90°:

$$M_z(t) = M_0(1 - e^{-\frac{t}{T1}}) \qquad \textit{Equation 1.3}$$

where $M_z(t)$is the magnetisation in the z-axis (in line with B_0) at time t.

Therefore, when $t=T_1$, M_z has returned to $M_0(1-1/e)$, or approximately $0.632M_0$.

1.1.2.2 T_2 and T_2* relaxation

The transverse magnetisation, M_{xy}, decays with a time constant T_2, which describes an entropic process in which there is a loss of coherence of spins rather than energy exchange. The faster the proton spins dephase following excitation, the shorter the T_2 time constant. The dephasing is largely dependent upon two main processes: the spin-spin interactions and the magnetic (B_0) inhomogeneities.

The 'spin-spin' interaction, the primary determinant of T_2 relaxation time, is dependent upon the proton density and structure of tissues. Water has minimal structure, reducing spin-spin interactions, and hence lengthening T_2 relaxation time in comparison to more organised structures such as fats, proteins or solids.

T_2 relaxation time: water>fat>protein>solids

The decay of M_{xy} is also an exponential process, and the T_2 time constant is defined such that:

$$M_{xy}(t) = M_{xyPE}e^{-t/T2} \qquad \textit{Equation 1.4}$$

where M_{xyPE} is the initial transverse magnetisation (M_{xy}) immediately post-excitation pulse.

However, magnetic inhomogeneities may exert a highly significant effect upon rapid dephasing, but are considered separately as they may be reversible if fixed (see Spin Echo Sequences below). The combined effect of spin-spin interactions and field inhomogeneities is described by decay constant T_2*, such that:

$$\frac{1}{T_2^*} = \frac{1}{T_2} + \frac{1}{T_2'} \qquad \textit{Equation 1.5}$$

where T_2' is the modelled decay constant attributable to magnetic inhomogeneities alone.

1.2 Signal detection

In performing an NMR experiment, a signal from the sample is detected following the RF excitation via a receiver coil. The small oscillating magnetic field, arising from the in-phase component of M_{xy}, will induce a current within the coil and generate a signal.

In its simplest form, the recorded signal would be that generated by free induction decay (FID). Following excitation, the spins begin to precess freely then decay dependent upon T_2* time constant. This will create a signal intensity (SI) at time t proportional to the decaying in-phase transverse magnetisation, with oscillating frequency ω_0:

$$SI(t) \propto M_{xyPE} e^{-\frac{t}{T_2^*}} (cos\ \omega_0 t) \qquad \textit{Equation 1.6}$$

where M_{xyPE} is the magnetisation in the transverse axis immediately post excitation.

However, this basic FID experiment does not allow for creation of an image, as the signal received by the coil could come from any location within the sample. Therefore, it is necessary to generate more complex excitation sequences that allow for spatial encoding (see Section 1.4).

1.2.1 Signal to Noise Ratio (SNR)

Noise arises primarily from electrical noise within the patient, due to the emission of RF secondary to thermal motion within the body. Individual voxel intensities reflect the joint contribution of RF signal from the imaged region combined with noise. Excessive noise, relative to desired signal, degrades the sharpness of imaging and the ability to distinguish different structures in the image. The relative amount of noise in an image can be quantified using the concept of signal to noise ratio (SNR). SNR is calculated as:

$$SNR = \frac{mean\ signal\ in\ ROI}{standard\ deviation\ of\ noise} \qquad Equation\ 1.7$$

where SNR = signal to noise ratio, ROI = region of interest

Signal is measured as the average signal in a small region of interest, whilst noise is typically quantified as the root mean square (RMS) amplitude of the white noise that is superimposed on the signal (Dietrich et al. 2007). Noise should be uniformly distributed across the image due to the Fourier transform reconstruction, and be of Gaussian distribution (McVeigh, Henkelman, and Bronskill 1985). The RMS amplitude of a Gaussian distribution is equal to its standard deviation, and therefore, for non-accelerated imaging sequences, the standard deviation of the signal of air outside the body is typically used as the measurement of noise. The measurement of noise in the presence of parallel processing is more complex, as noise in the MR image becomes spatially modulated, and Equation 1.7 cannot be used directly (see 1.3.3).

1.2.2 Tissue contrast

As described above, different biological tissues have different T_1 and T_2 (or T_2*) time constants, and these differences can be exploited to create contrast between tissues. This is performed primarily by varying the interval between the excitation pulse and signal sampling (echo time, TE), and the subsequent excitation pulse (repetition time, TR).

- Echo time. TE determines the time during which transverse magnetization (M_{xy}) dephasing occurs. Very early signal sampling ($TE << T_2^{(*)}$) will yield a signal almost entirely dependent upon the magnitude of M_z pre-excitation, and hence is T_1-weighted. Increasing TE increases the dependency of the image contrast on T_2 differences between tissues (T_2-weighting).
- Repetition time. TR determines the time during which longitudinal recovery takes place. A short TR generally increases the dependency of the image contrast on T_1 differences between tissues (T_1-weighting), but at the cost of progressive reduction in the overall signal as M_z has minimal time to recover. A long TR ($TR >> T_1$) will allow recovery of all M_z prior to the RF pulse, and hence will reduce the effect of the T_1 time constant on signal intensity.

A further determinant of tissue contrast is the proton density. The received signal is proportional not only to in-phase M_{xy}, but also the number of protons available for excitation (proton density). In general, proton density is more homogeneous across biological tissues than T1 or T2 and therefore proton density weighted images tend to have lower contrast.

In summary, the impact of TR, TE and proton density upon signal intensity can be expressed as follows:

$$SI \propto N(H)(e^{-\frac{TE}{T2}})(1 - e^{-\frac{TR}{T1}}) \qquad \textit{Equation 1.8}$$

where SI is signal intensity, N(H) is the proton density, TE is echo time, TR is repetition time. Assuming flip angle 90° (Hashemi, Bradley, and Lisanti 2010).

Contrast in MRI is therefore very flexible, and selection of optimal combinations of TR and TE depends upon imaging sequence and tissue T_1 and T_2 characteristics. Table 1-1 summarises the typical image weighting at combinations of TR and TE.

	Short TR	**Long TR**
Short TE	T_1 weighted Moderate SNR High contrast	"Proton Density" weighted High SNR Low contrast
Long TE	Poor SNR Poor contrast	T_2 or T_2* weighted High SNR High contrast

Table 1-1. Image weighting at combinations of repetition time (TR) and echo time (TE). (SNR = signal to noise ratio)

1.2.3 Contrast agents

When T_1-weighted sequences are used, tissues with shorter T_1 time demonstrate a higher SI. However, the difference in T_1 time of normal and pathological tissues may be insufficient to demonstrate significant imaging contrast, and therefore exogenous contrast agents may be used to alter the T_1 (and T_2) properties of tissues.

The most commonly used contrast agents are gadolinium-based contrast agents (GBCA). Gadolinium is a lanthanide metal, which with seven unpaired electrons is a strongly paramagnetic substance†.

† Substances relevant within medical MRI can be broadly divided into three groups of properties of magnetic susceptibility (Hashemi, Bradley, and Lisanti 2010).

1. Diamagnetic. Diamagnetic substances have no unpaired orbital electrons. Within an external magnetic field B_0, they produce a weak magnetic field in the opposite direction. They can be termed 'non-magnetic'.
2. Paramagnetic. Paramagentic substances have unpaired orbital electrons, and within B_0 they produce a weak magnetic field in the same direction. There is no remnant magnetic field when the external field is zero. They are weakly attracted by an external magnetic field. Gadolinium is the element with the greatest number of unpaired electrons, and with a relatively long electron spin relaxation time, and therefore causes significant T1 shortening. Substances with very large numbers of unpaired electrons, such as haemosiderin, exhibiting a very large magnetic moment in an external field are termed 'superparamagnetic'.
3. Ferromagnetic. Ferromagnetic substances become permanently magnetised, even when B_0 is removed, and are strongly attracted by a magnetic field. This group includes iron, cobalt and nickel.

The unpaired electrons interact strongly with the water proton's magnetic field. Due to thermal motion, this interaction induces significant fluctuating magnetic fields for the water protons and hence shortens T_1 (Bjørnerud 2008). The ability of a contrast agent to enhance proton relaxation is defined in terms of its relaxivity ($r_{1,2}$):

$$R_{1,2}^{C} = \frac{1}{T_{1,2}} = R_{1,2}^{0} + r_{1,2}[C] \qquad \textit{Equation 1.9}$$

where $R_{1,2}$ are the relaxation rates, the inverse of T_1 and T_2. R^C is the relaxation rate in the presence of contrast, and R^0 the rate at baseline. $r_{1,2}$ are the relaxivity constants (T_1 and T_2-relaxivity) of the agent, and C the concentration of the agent (Bjørnerud 2008)*. Note that this assumes a linear relationship between increase in relaxation rate and contrast concentration, which is an over-simplification in-vivo.*

Gadolinium has a favourable electron spin relaxation time, facilitating energy transfer, and hence a high relaxivity. It is therefore widely used for enhancing imaging contrast, but gadolinium itself is toxic in its unbound Gd^{3+} ion form. This necessitates the chelation of gadolinium within biocompatible molecules, which are generally of low molecular weight (<1000 Daltons). Despite chelation, gadolinium has been shown to cause nephrogenic systemic fibrosis (NSF) on very rare occasions, although the newer macrocyclic chelates have been demonstrated to carry an even lower risk of NSF than the linear chelates (Khawaja et al. 2015). These chelates are small enough to pass swiftly between extracellular spaces, and the agent therefore acts to enhance T_1 signal of the water of the extracellular spaces within which it may accumulate.

The impact of an administered contrast agent on MR signal is complex. Firstly, although the relaxivity values may be relatively constant, the 'dose response' is non-linear and highly dependent upon the imaging sequence and the concentration range. However, within a low concentration range, as used for the experiments detailed in this thesis, a fairly linear increase in signal intensity is observed with increasing concentration (Bjørnerud 2008). Secondly, the pharmacokinetics of contrast agent distribution are highly dependent upon tissue perfusion, extracellular volume and differential tissue permeabilities. Initially the contrast agent lies almost exclusively within the blood pool, facilitating high contrast angiography on T_1-weighted sequences. However, there is then an equilibration process as the contrast accumulates within the extracellular space, prior to physiological clearance (Knowles et al. 2008).

1.2.4 Other sources of tissue contrast

Whilst contrast agents play a key role in the imaging detailed within this thesis, there are several other relevant mechanisms through which image contrast is generated beyond T_1 and T_2 relaxation times and proton density.

1.2.4.1 Chemical shift

Protons within different molecules precess at slightly different frequencies, due to the impact on B_0 of the opposing magnetic field of the surrounding electrons. The magnetic field at the nucleus is therefore generally less than the applied B_0, thereby shifting the Larmor frequency. For example, the Larmor frequency of ^1H atoms in water molecules is typically 3.5ppm higher than those within lipid molecules. Whilst this may lead to a misregistration of several voxels (see section 1.3.1), the chemical shift may also act to accentuate soft tissue interfaces.

1.2.4.2 Magnetisation transfer

Magnetisation transfer (MT) is a technique that may be used to suppress protein-bound water. Due to the chemical shift phenomenon, protein-bound water will possess a resonant frequency 1-2kHz away from bulk water, and will have a broad peak in view of the inverse relationship between T_2 and spectral bandwidth (bulk water has a much longer T_2 than protein-bound water). Spectral pre-saturation pulses, using off-resonance MT pulses approximately 1kHz away from the centre of the peaks, will directly saturate the protein-bound spin system, but not the bulk water. However, bulk-water in communication with protein-bound water may exchange magnetisation (magnetisation transfer). Therefore, saturating the protein will lower the signal of the adjacent water, and the contrast between water compartments that may or may not be in contact with protein.

1.2.4.3 Fat suppression

For some applications, the signal from fat is undesirable, as due to its short T_1 and long T_2, it is usually much brighter than other tissues. It can be suppressed using the techniques below:

- STIR- short inversion time (TI or 'tau') inversion recovery. At 1.5T, the inversion time (see Section 1.4.4) of fat is approximately 140-160msec, and therefore the application of an inversion pulse 140msec prior to the excitation pulse will achieve nulling of the signal from fat, at the cost of some tissue signal. As it is an inversion recovery sequence, signal intensity in STIR images is, to first approximation, proportional to the magnitude of the longitudinal magnetisation at the time of excitation, and therefore tissue with the longest T_1 will generate the highest signal, in contrast to most T_1 weighted imaging.
- CHESS- chemical shift selective magnetisation preparation. As discussed previously, the resonant frequency of fat is different to other tissues, differing by around 3.5parts per million (or around 220Hz at 1.5T). A spectrally selective 90° saturation pre-pulse followed by a spoiler gradient (see Section 1.4.3.1) is applied to eliminate signal arising from fat.
- SPIR- spectral pre-saturation with inversion recovery. SPIR is a combination of STIR and CHESS. The latter will allow partial recovery of fat magnetisation prior to imaging, and SPIR instead employs a partial inversion recovery pulse, with FA between 90-180°.

1.3 Building an MR image

1.3.1 Spatial encoding

A simple echo following RF excitation contains no information on the location of the origin of the RF energy. There is therefore a requirement for further steps to encode spatial location upon a signal, and this information is imprinted in three dimensions using different adjustments of the gradient fields (see Figure 1-1). Gradient fields are transient magnetic fields that are usually induced using precisely calibrated loops of resistive wire within the scanner bore. The activation of currents within these loops creates predictable perturbations of B_0 that may be used for signal encoding.

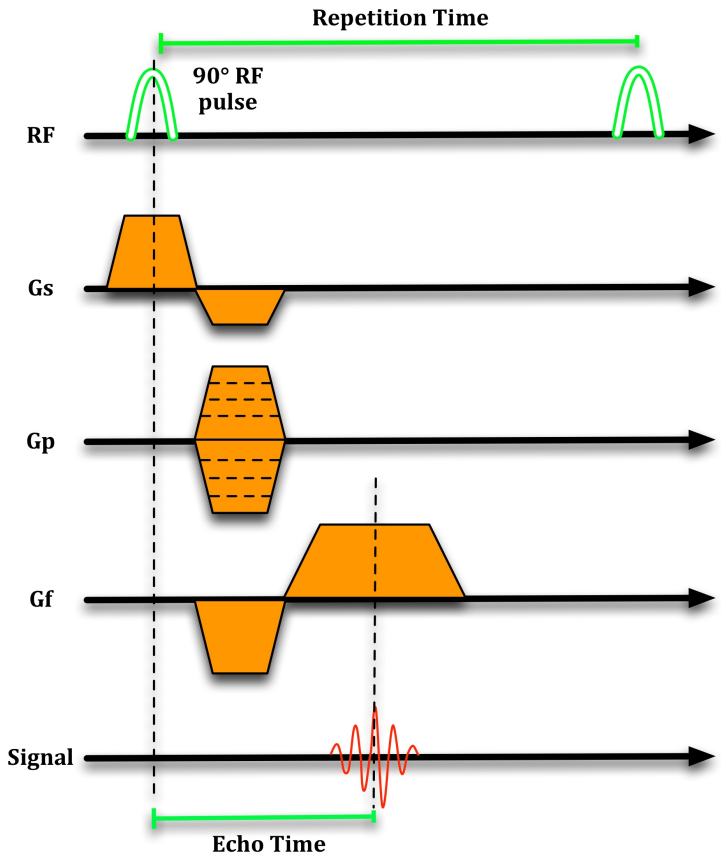

Figure 1-1. Spatial encoding.

(RF: radiofrequency, Gs: gradient in the slice selective orientation, Gp: gradient in the phase encoding direction, Gf: gradient in the frequency encoding direction.)

- Slice selection (G_s). The imaging slice is selected using the application of a gradient field during the excitation pulse. The gradient field will alter the Larmor frequency, and therefore only a selected region will be excited. The thickness of the slice will be dependent upon the bandwidth of the excitation pulse and the strength of the slice selection gradient (G_s).

- Phase encoding (G_p). Within a 2D imaging slice, two dimensions remain to be delineated. Phase encoding is performed through switching on a phase encoding gradient (G_p) for a specific time period, generating a predictable phase shift in proton spin along the Gp direction. The degree of phase encoding is limited to +180° to -180°, relative to the centre of the field. Phase encoding adds significantly to sequence acquisition time, as each phase encoding step requires a further repetition time.
- Frequency encoding (G_f). Sampling of the signal is performed during the application of a frequency encoding gradient (G_f). The frequency of the sampled signal is determined by the position of the signal origin within G_f, with a higher frequency occurring at stronger field strength.

G_s and G_f act to create unnecessary dephasing of spins, and therefore decrease the acquired signal strength. Opposite rephasing gradients are required to maximise signal at the echo time (Figure 1-1).

1.3.2 Fourier transformation and K-space

The received RF signal contains information from all the excited spins within an imaging slice. The frequency encoded components are broken down using a Fourier transformation, isolating the relative signal contribution of each frequency, and therefore the relative signal of each component in the frequency encoded direction. The analysis of relative signal contribution from each component in the phase-encoded direction requires multiple samples, each with a differing degree of dephasing, and the number of pixels in the phase encoding direction is generally equal to the number of phase encoding steps.

The use of phase and frequency encoding means that each imaging voxel is reconstructed using data from every signal sample within the slice. The sampled signals are acquired in k-space, a spatial frequency domain, where the central part of k-space contains the low spatial frequency information (contrast) and the outer parts the high spatial frequency information (detail and edges). A complete image will require the acquisition of all spatial frequencies, up to the number that define the spatial resolution of the acquisition, and the filling of k-space may theoretically be performed in any order. Conventionally, it is filled line-by-line (Cartesian data acquisition), and often this is 'linear' (with the centre of k-space and contrast acquired halfway through) or 'low-high' (with the centre outwards filled in alternating lines progressively further from the centre of k-space). Alternative techniques include radial or spiral trajectories, which entail their own advantages at the cost of increased complexity and oversampling (Plein, Greenwood, and Ridgway 2011).

The complex conjugate symmetry of k-space may be exploited to reduce acquisition times, enabling the acquisition of less than the full k-space along the phase encoding direction (partial Fourier imaging). The reduced acquisition time is achieved at the cost of reduced SNR and potentiation of

signal errors and artefacts. Once k-space is filled, a Fourier transformation converts the data to create the acquired image.

1.3.3 Parallel imaging

Signal spatial distribution information may also be derived using surface coil arrays, decreasing acquisition time. Characteristic sensitivity maps are used to provide spatial information, enabling under-sampling of k-space, usually along the phase encoding direction, and reducing acquisition time by an acceleration factor or reduction factor (R). On the Siemens systems, the reconstruction calculations are performed in k-space (GeneRalized Autocalibrating Partial Parallel Acquisition (GRAPPA)), with the reference image acquired as part of the acquisition. For Philips, the reconstruction is most often performed in the image space, with the reference image acquired prior to imaging (SENSitivity Encoding (SENSE)).

Whilst parallel imaging reduces acquisition time, it results in a reduction of SNR proportional to $\sqrt{R}$ due to decreased data sampling (Dietrich et al. 2007). Furthermore, the assessment of SNR is more complex secondary to a non-uniform distribution of noise, and this problem is particularly relevant to analyses within Chapter 7 .

Each coil element detects different noise characteristics, resulting in a heterogeneous spread of noise across the image, which is roughly described by the geometry factor (g-factor). The g-factor varies between voxels as the coil geometries and sensitivity profiles differ, and therefore measurement of the signal standard deviation in air outside the body can no longer be used as a reference measurement for noise (see Section 1.2).

The most robust method for measurement of noise is the 'multiple acquisition' method, which determines noise on a pixel-by-pixel basis. However, multiple (30-300) identical acquisitions are used to derive the noise measurement and this is clearly not practical in the clinical scenario. A second method is the 'difference' method, using only two identical acquisitions: the standard deviation in a ROI of the two subtracted images may be approximated to $\sqrt{2}$ times the standard deviation of the noise in the original images. Thirdly, an 'SNR ratio' method may be used, particularly for comparison between images with unchanged acquisition parameters. Based upon the assumption that the g-factor remains unchanged, the ratio of SNRs may be compared, providing that the ROIs relative to the coils remain unchanged as well. Background noise is typically measured in a low signal region, either air outside the body or lung. (Dietrich et al. 2007)

1.4 Basic RF pulse sequences

Thus far, only a single excitation RF pulse has been discussed. The application of precise sequences of RF pulses enables both improved signal quality and reduced acquisition times, and there is a wide array of sequences in clinical applications. However, there are two main groups of sequences used in the clinical imaging described in this thesis: spin echo and gradient echo.

1.4.1 Spin echo sequences

The spin echo sequence is used comparatively little throughout this thesis, but warrants discussion in view of its role as one of the most basic pulse sequences. The strength of the sequence lies in the rephasing 180° RF pulse that eliminates the dephasing caused by fixed magnetic field inhomogeneities. The transverse magnetization recovery is therefore dictated by T2 instead of the shorter T2*, leading to a higher SNR when compared to similar gradient-echo sequences.

A typical pulse sequence is shown in Figure 1-2. Blood is typically dark, as its motion prevent its spins from being successfully rephased, and blood signal may be further suppressed using a double inversion preparation pulse technique, where a non-slice selective 180° RF pulse is followed by a slice selective reinversion 180° RF pulse. Spin echo imaging is generally slow but may be accelerated through fast/turbo spin echo (FSE/TSE) techniques.

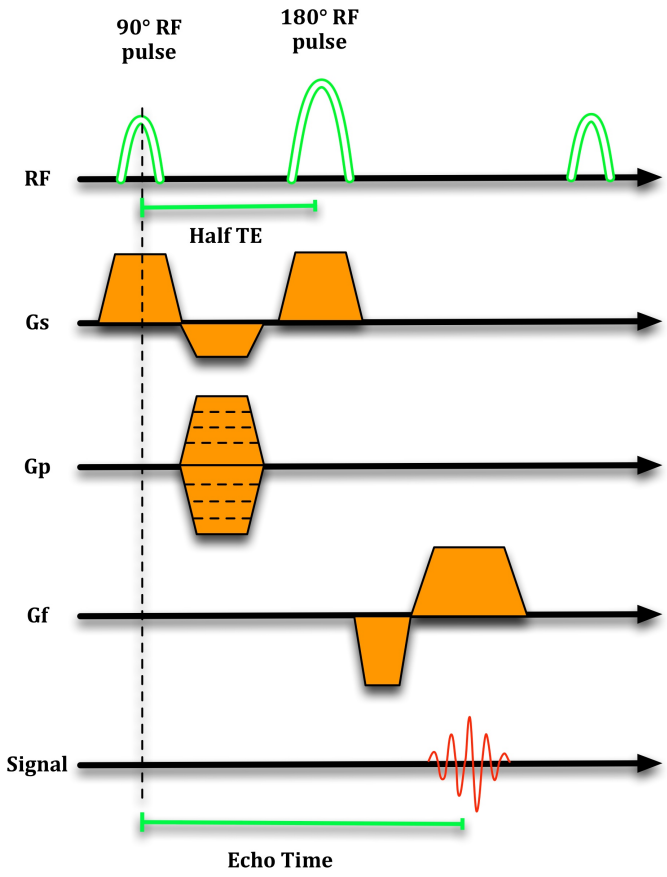

Figure 1-2. Basic spin echo sequence.

RF: radiofrequency, TE: echo time, G_s: slice selection gradient, G_p: phase encoding gradient, G_f: frequency encoding gradient.

1.4.2 Gradient echo sequences (GRE)

Gradient echo sequences are also known as gradient-recalled echo (GRE), or fast field echo (FFE-Philips systems), and they offer a substantial reduction in scan time. Using low flip angles, it is

possible to achieve acceptable degrees of M_{xy} whilst minimising loss of M_z, thereby enabling shorter TR‡. However, a 180° refocusing pulse is not used and GRE sequences are therefore significantly more susceptible than spin echo sequences to B_0 inhomogeneities and susceptibility artefacts.

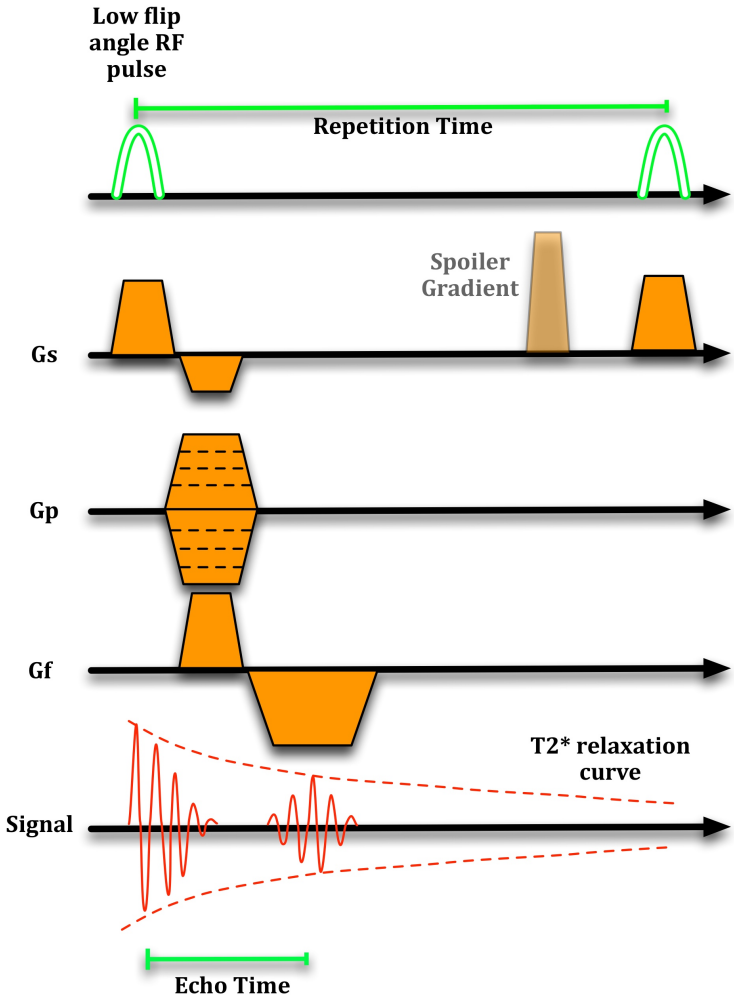

Figure 1-3. Basic Gradient Recalled Echo sequence (GRE).

A spoiler gradient may be applied prior to each excitation RF pulse (spoiled gradient recalled echo) in order to dephase any remaining transverse magnetisation. RF: radiofrequency, G_s: slice selection gradient, G_p: phase encoding gradient, G_f: frequency encoding gradient.

A basic GRE pulse sequence diagram is shown in Figure 1-3. GRE offers fast imaging, with the potential for practical 3D acquisitions. This is at the cost of decreased SNR, caused by small flip angle,

‡ For flip angle α: $M_{xy}= M_0 \sin \alpha$, and $M_z=M_0 \cos \alpha$. For example, for a flip angle of 15°, M_{xy} is approx 25.9% of M_0, whilst M_z remains 96.6% of M_0.

increased magnetic susceptibility, and signal decay at T_2* rather than T_2 rate. In addition, signal intensity depends not only upon TR and TE, but also on the flip angle. For a spoiled GRE sequence:

$$SI \propto N(H)(e^{-\frac{TE}{T2*}})(1-e^{-\frac{TR}{T1}})\left(\frac{sin\,\alpha}{1-cos\,\alpha\left(e^{-\frac{TR}{T1}}\right)}\right) \qquad \textit{Equation 1.10}$$

where SI= signal intensity, N(H)= number of excitable protons, TE=echo time, TR= repetition time, α= flip angle

When α= 90°, sin α = 1, and cos α = 0, and therefore the equation reverts to Equation 1.8. However, for very small flip angles, cos α tends to 1, and sin α to α, and Equation 1.10 tends to:

$$SI \propto N(H)(e^{-\frac{TE}{T2*}})(1-e^{-\frac{TR}{T1}})\left(\frac{\alpha}{1-\left(e^{-\frac{TR}{T1}}\right)}\right)$$

$$\Rightarrow \qquad SI \propto N(H)\alpha(e^{-\frac{TE}{T2*}}) \qquad \textit{Equation 1.11}$$

T_1 weighting is therefore significantly reduced at low flip angles, regardless of TR, and this is significant for contrast enhanced imaging. In these cases, an initial preparation pulse may be employed, which is typically a 90° saturation pulse. This establishes a more substantial effect of T_1 relaxation, effectively storing a difference in M_z available at each excitation pulse.

1.4.3 Adaptions of the GRE sequence

Fast GRE sequences, with short TR, are subject to residual transverse magnetisation that may corrupt the image. This may be dealt with in one of two ways: spoil the residual M_{xy}, or use it for further signal interrogation.

1.4.3.1 Spoiled GRE

For most GRE sequences, spoiling of the transverse magnetism is applied at each TR in order to dephase any residual transverse magnetism (see Figure 1-3). This may be applied via a spoiler gradient, or through using an RF pulse with phase offset. At short TE, the resulting image is T1 weighted, except at very small flip angles when it becomes proton density weighted, or T_2* at longer TE. It should be noted that at higher flip angles, tissue or blood that remains in-slice may rapidly become saturated, reducing SNR.

1.4.3.2 Steady-State Free Precession (SSFP)

For steady-state free precession (SSFP) imaging, additional rephasing, or 'rewinder', gradients are added prior to each RF pulse, to maintain a maximum of in-phase magnetisation (subject to T_2 decay). For short TR (less than T_2) and moderate flip angles, the contrast varies with the T_2/T_1 ratio.

1.4.3.3 Balanced-SSFP (b-SSFP)

Balanced-SSFP (b-SSFP) is similar to SSFP imaging, but the total gradient waveform area is constrained to be zero during each TR interval: balanced and symmetrical gradients are applied in all three spatial directions. For very short TR, the signal intensity is to a first approximation proportional to the T_2/T_1 ratio. Such an approach is heavily reliant on a homogenous B_0, and these images are particularly vulnerable to inhomogeneities in magnetic susceptibility, which can be caused by foreign bodies or poor shimming, b-SSFP is a fast, high SNR sequence with excellent blood/myocardium contrast and less susceptible to inflow enhancement than spoiled GRE. The T_2/T_1 ratio for blood is approximately four-fold higher than for myocardium.

	Philips		**Siemens**	
Spoiled Gradient Echo	T1 FFE	T1-weighted fast field echo	FLASH	Fast Low Angle SHot
Ultrafast spoiled gradient echo	T1 TFE	T1-weighted Turbo Field Echo	Turbo-FLASH	Turbo- Fast Low Angle SHot
SSFP	FFE	Fast Field Echo	FISP	Fast Imaging with Steady Precession
bSSFP	bFFE	Balanced Fast Field Echo	True FISP	True Fast Imaging with Steady Precession

Table 1-2. Manufacturer nomenclature for spoiled gradient echo and steady-state free precession sequences.

1.4.4 Inversion recovery pulse sequence

Following a 180° RF pulse, $M_{xy} = 0$, and $M_z = -M_0$. The recovery of M_z is dependent upon the T_1 time, as per Equation 1.3, and for each tissue will pass through $M_z=0$ at different time points. When $M_z=0$, at the null time point, an excitation RF pulse will elicit no transverse magnetisation, and hence no signal from that tissue. Solving for $M_z=0$, the inversion time to null a tissue with a given T_1 is $(\ln 2)T_1$, or approximately 0.693 (T_1).

Reconstruction of an inversion recovery image will typically be performed using magnitude images, as in other most applications of MR imaging. However, using phase information to retrieve the sign of the signal may improve contrast if the inversion time used is between the null times of the tissues of interest. A technique called phase sensitive inversion recovery (PSIR) may be used to reliably

retrieve phase information in cardiac scans (Kellman et al. 2002). In this technique, reference slices are acquired, usually on a second R-R interval, to optimise the calculation of the phase.

1.5 Principles of MR Imaging pertinent to electrophysiology

1.5.1 Electrocardiogram recording within the MR-environment

The monitoring of cardiac electrical activity within the MRI environment poses unique challenges and is significantly more complex than conventional electrocardiography (ECG). However, it is crucial for triggering of cardiac magnetic resonance (CMR) imaging acquisitions, and, in interventional electrophysiology (EP), for elucidation of timing and sequence of cardiac activation. Interference by electromagnetic fields, gradient fields and magneto-hydrodynamic (MHD) effects may cause profound corruption of the ECG, with noise one to two orders of magnitude greater than the ECG signal. MHD effects are produced when a conductive fluid travels through a magnetic field, and generates a voltage in the plane perpendicular to the magnetic field, in the direction of the fluid flow. This is therefore particularly pronounced in ventricular systole, with marked distortion of the S-T segment (Niendorf, Winter, and Frauenrath 2012).

The induced voltages may be compensated for via hardware or software approaches. Typical ECG surface electrode placement tends to be narrowly spaced, and a parallel arrangement, orthogonal to B_0, is typically used in higher magnetic field strengths, whereas at lower field strength (1.5T), alternative arrangements may derive a stronger cardiac vector with acceptable level of MR interference. Short transmission lines with high impedance (>10kΩ) and low-pass filtering (<50Hz) also act to reduce induced voltages (Schmidt, Dumoulin, and Danik 2014).

At a software level, the use of the vectorcardiogram (VCG) has been established to be more sensitive and specific for the detection of the R-wave than evaluation of a single lead (Fischer, Wickline, and Lorenz 1999). The VCG represents the electrical activity in three dimensions over time, and is therefore less affected by directional dependent artefact. Adaptive digital filters have also been used to detect and suppress the gradient induced waveforms. This works upon modelling the noise response, by reference to ECG traces acquired in the MRI environment but without gradient coil activity (Zhang et al. 2016). However, the gradient duty cycle (the proportion of the cardiac cycle occupied by gradient activity) may be up to 30%, and excessive filtering at these points risks suppression of key components of the ECG. A functional 12-lead (or equivalent) ECG remains important for the development of MR-guidance of complex EP procedures, but further work is required in order to ensure safety and adequate suppression of MR-induced electrical noise (see Section 3.5).

Alternatives for triggering of cardiac acquisitions have been widely developed, and include pulse oximetry, plethysmography and acoustic gating. However, none of these present the information required for MR-guided EP procedures.

1.5.2 Three-Dimensional Late Gadolinium Enhancement (3D-LGE)

Imaging of thin walled structures that move with the cardiac cycle, such as coronary arteries or atrial wall, is particularly challenging. A 3D fast/turbo gradient echo sequence may be used with respiratory and ECG gating to optimise resolution, combined with preparation pulses to optimise contrast. For native (without contrast enhancement) imaging, this is often a T_2 preparation scheme that allows spoiled GRE sequences to be more T2-weighted. However, for LGE imaging, an inversion recovery scheme is usually used.

3D image acquisition is performed through excitation of a thick volume of tissue, which is then encoded in one direction using frequency encoding, and the remaining two directions using phase-encoding. The advantages include that thinner slices may be achieved, with contiguous slices with no gap, whilst SNR is theoretically increased, as each echo represents data from the entire volume.

In 2D imaging:

$$SNR \propto (voxel\ volume)\sqrt{\frac{N_x N_y NEX}{BW}} \qquad \textit{Equation 1.12}$$

Whereas in 3D imaging:

$$SNR \propto (voxel\ volume)\sqrt{\frac{N_x N_y N_z NEX}{BW}} \qquad \textit{Equation 1.13}$$

> *where $N_{x,y,z}$ are the number of phase encoding steps in x,y,z directions respectively. NEX is number of excitations, and BW is bandwidth* (Hashemi, Bradley, and Lisanti 2010)

Therefore, an increase in SNR proportional to $\sqrt{N_z}$ could be anticipated, compared to a single thin 2D slice. However, this is rarely achieved: it has been demonstrated that interleaved multi-slice 2D imaging allows more time for T1 recovery than 3D imaging, which may compensate for almost all of the averaging advantage of a 3D sequence (Johnson, Wadghiri, and Turnbull 1999). None-the-less, 3D sequences remain preferable for very high resolution imaging, with sensitivity and imaging time advantages. Furthermore, the 3D acquisition prevents mismatch between slices, aiding reconstruction and homogenising artefacts across the entire acquisition.

1.5.3 Imaging in the presence of devices

Cardiac MR imaging is increasingly performed in the presence of implanted or introduced devices, and there are two main considerations: patient safety and imaging artefact.

1.5.3.1 Patient safety

Many devices are now accepted as MR conditional, and www.mrisafety.com maintains a compendium of guidelines on imaging in the presence of a wide range of devices. The most important

devices to be considered in the context of cardiac imaging are cardiac implanted electronic devices (CIEDs) such as pacemakers and implantable cardioverter defibrillators (ICDs). Potential interactions between the CIED and MR imaging include the following concerns (Ipek and Nazarian 2015):

1. Magnetic induced forces: ferromagnetic materials may experience magnetic induced attraction and torque. However, risk of device dislodgement is felt to be extremely low.
2. Gradient field induced electrical current: this could potentially cause myocardial depolarisation at the lead tip.
3. Heating and tissue damage: RF energy may induce heating, particularly at the myocardial-lead interface, with the potential for increases in pacing thresholds.
4. Reed switch activation: most devices have a 'magnet mode', which generally triggers asynchronous pacing (AOO/VOO/DOO, and therapies off for ICDs). This may be activated within the magnet.
5. Electrical reset: electromagnetic interference may lead to a "power-on-reset", which is similar to magnet mode but there is a risk of inhibition of pacing or reactivation of therapies.
6. Other inappropriate therapies and function.

Many modern CIEDs are now MR-conditional, and the frequency of complications is very low. However, even for devices without MR-conditional designs, interactions have been relatively rare. The MagnaSafe Registry was a multicentre study of non-thoracic MRI at 1.5T for patients with a "non-MRI-conditional" CIED. A total of 1500 patients were recruited (1000 pacemakers and 500 ICDs) and there were no deaths, lead failures, losses of capture or ventricular arrhythmia during MRI. There were six partial electrical resets and an increase in pacing lead threshold of 0.5V or more was observed in 0.7% of pacemaker leads and 0.8% of ICD leads (Russo et al. 2017). The Johns Hopkins team have also performed >2000 MRI scans with CIED implanted after 2001, 12% of which have been cardiac scans, reporting 9 power-on-resets but no deaths or severe adverse events. Overall, MRI in patients with CIEDs is feasible, provided the specific modality imaging benefit outweighs the low risk, and appropriate preparation measures are taken in an experienced centre.

1.5.3.2 Imaging artefact

The presence of metal typically introduces a substantial artefact, dependent upon its effect on B_0 and the sequence sensitivity to magnetic inhomogeneities. Spin echo sequences, with a refocusing 180° pulse, correct for some effects of local field inhomogeneities, whereas GRE sequences are much more susceptible. b-SSFP sequences are particularly sensitive to inhomogeneities in magnetic fields and hence spoiled GRE sequences are often preferable for cine imaging.

However, more subtle adjustments of the imaging parameters may reduce the impact of a device. Increasing the receiver bandwidth (and increased bandwidth RF pulses) should decrease the number of pixels affected by the artefact. In a similar way, fat saturation relying on spectral pre-saturation (CHESS/SPIR) will frequently fail in the presence of the perturbation in B_0, and STIR tends to be more

robust. Some manufacturers have also introduced sequences that are designed to minimise artefacts in proximity to MR conditional devices (syngo WARP, Siemens Healthcare), and these are generally spin echo sequences based on these principles. However, the overwhelming determinant of imaging quality is the size and location of the device, and these are not easily changed. Consideration for a right-sided placement of pacemaker or ICD should be made if frequent subsequent cardiac MR imaging is envisaged.

2 CARDIAC ELECTROPHYSIOLOGY PRINCIPLES

Cardiac electrophysiology (EP) is a broad field, encompassing the study of cardiac electrical activity from molecular to cellular to single chamber to whole heart scale, with a broad range of normal and pathological variants. This thesis aims to study the implementation of CMR imaging techniques in the management of a distinct subgroup of pathologies, namely atrial flutter and atrial fibrillation. This introductory chapter will discuss the relevant core concepts for these two arrhythmias, and the principles and evolution of EAM systems.

2.1 Typical atrial flutter

2.1.1 Pathophysiology

Typical atrial flutter (AFL) is a macro-re-entrant atrial tachycardia that uses the cavotricuspid isthmus (CTI) as an essential part of its circuit. The circuit is constrained in the apical direction by the tricuspid valve annulus, whilst the posterior (basal) boundaries are less well defined, occurring a variable distance from the atrioventricular (AV) ring. The posterior border is generally widest at the superior part of the right atrium (RA), and narrowest in the region of the Eustachian ridge.

The basic three criteria for re-entry were proposed by Mines in 1913 (Mines 1913). Firstly, unidirectional block is necessary for initiation. Secondly, the wave of excitation should travel in a single direction along the pathway and return to its point of origin, restarting along the same path. Thirdly, the tachycardia should terminate when one limb of the pathway is terminated or temporarily blocked. All these criteria are fulfilled in typical AFL. The substrate required to achieve re-entry includes a central area of block (functional or anatomical) with an area of slow conduction sufficient to create an excitable gap and therefore sustain a repetitive wavefront in the presence of a critical tissue mass. In AFL, the tricuspid valve annulus forms the central area of block whilst the location of zones of slow conduction may vary in position around the annulus. In younger patients, slow conduction is often at the lateral aspect of the CTI, whilst it is at the medial aspect of the CTI in older patients (Huang et al. 2008), but the mechanism of conduction slowing at the CTI is poorly understood.

Typical AFL may be observed to propagate counter clockwise or clockwise around the tricuspid valve annulus (as viewed from the ventricular side of the annulus), the commonest direction being counter clockwise in around 90% of clinical AFL cases. This preponderance is thought to be largely related to the anisotropic properties of the CTI and the provocation of unidirectional block secondary to the origin of stimulation, which may often be from pulmonary vein (PV) or left atrial (LA) discharges (Issa et al. 2012).

2.1.2 Diagnosis

The overall incidence of AFL has been quoted as 88 per 100,000 person-years in the USA, increasing with age, male sex, heart failure and lung disease (Issa et al. 2012). However, the true incidence is likely to be much higher as 25-35% of patients with AF are thought to have episodes of AFL. Patients may be asymptomatic, but frequently they present with symptoms ranging from palpitations and fatigue to dyspnoea or even acute coronary syndrome. The primary determinant of symptomology is the ventricular rate: atrial rate is typically around 300bpm (tachycardia cycle length (TCL) 200-220msec), and the ventricular rate is dependent on the conduction properties of the AV node.

Surface electrogram (ECG) diagnosis is often accurate, with characteristic 'saw-tooth' waveform of atrial activation (Figure 2-1). There is variation in surface ECG appearance for counter clockwise AFL, but some preserved features predominate. In the inferior leads, the flutter wave exhibits a slow negative deflection prior to a sharper positive deflection, with a predominantly negative polarity. V_1 is positive (or occasionally biphasic), with transition to negative flutter wave across the precordial leads. In contrast, the clockwise AFL ECG generally has broadly positive deflection in the inferior leads with characteristic notching. Lead V_1 has a broad, notched, negative component with transition to upright flutter wave in V_6. In patients with significant structural heart disease or extensive prior atrial ablation, the surface ECG appearance may be very different (Chugh et al. 2006). Furthermore, the ECG appearance of non-CTI-dependent macro re-entrant atrial tachycardias may mimic typical AFL.

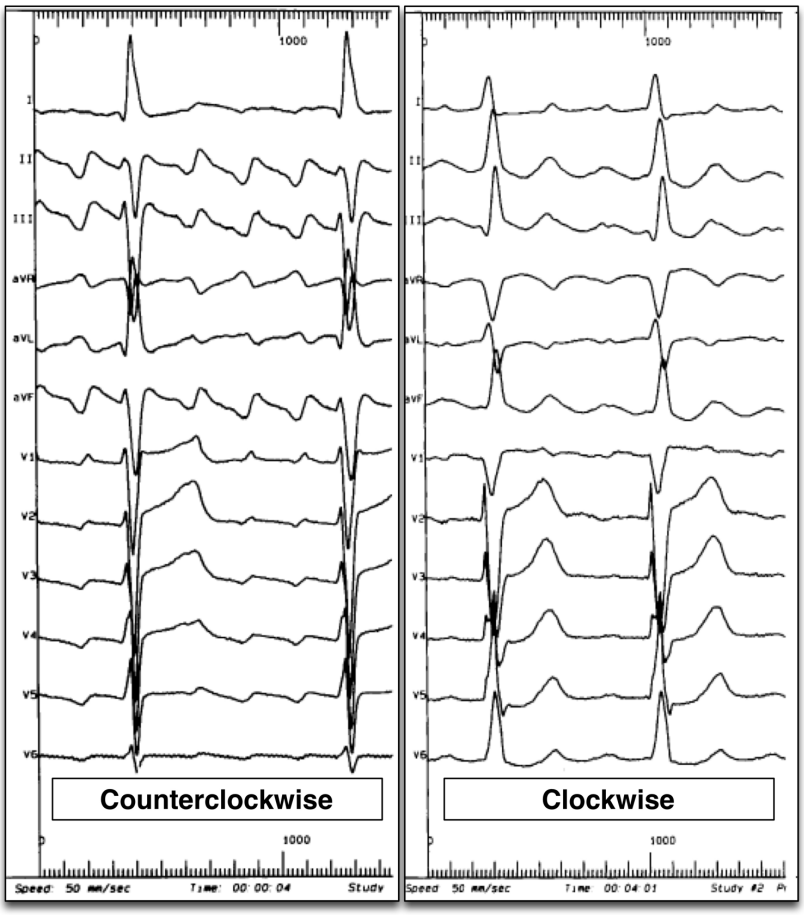

Figure 2-1. Typical atrial flutter surface ECG morphologies.

Counter clockwise (left panel) and clockwise (right panel) typical atrial flutter. Adapted with permission from Ndrepepa et al (2000).

Invasive electrophysiological testing typically employs intracardiac multielectrode catheters positioned at the tricuspid annulus and coronary sinus and may include the use of an electroanatomical mapping (EAM) system (see Section 2.3). The TCL is generally constant at around 220msec, with minimal cycle-to-cycle variation (<2%). Sequential activation mapping is used to confirm the counter-clockwise or clockwise right atrial activation pattern. Diagnostic manoeuvres are employed to confirm the diagnosis. Overdrive atrial pacing is used to achieve tachycardia entrainment[§], with manifest fusion at pacing sites distant from the circuit (CS left atrium) and concealed fusion within the circuit (any tricuspid annular site within the RA). The post pacing

[§] 'Entrainment' is defined to occur when a paced beat reaches the tachycardia circuit during the excitable gap, propagating in the orthodromic direction and colliding with the previous tachycardia cycle in the antidromic direction, 'resetting' the tachycardia with resumption of the intrinsic tachycardia rate and morphology after cessation of pacing. The presence of entrainment is verified by demonstrating (1) the presence of fixed fusion of the paced complexes at fixed pacing cycle length, (2) progressive fusion at faster pacing cycle lengths and (3) resumption of the same tachycardia morphology following cessation of pacing with a non-fused complex at a return cycle equal to the pacing cycle length (Issa, Miller, and Zipes 2012)

interval (PPI), the interval from the last pacing stimulus that entrained the tachycardia to the next recorded electrogram at the pacing site, is short (maximum TCL+20msec) on entrainment from within the AFL circuit, at the tricuspid annulus (Waldo 1997).

2.1.3 Non-ablative management

Acute treatment of AFL is like that for AF (see Section 2.2.3), and is dependent upon the clinical presentation. Initial management may involve pharmacological rate control or rhythm control using drugs or electrical cardioversion. Anticoagulation should be used with the same indications as for AF (Kirchhof et al. 2016). However, the long-term management strategy is for ablative treatment in the absence of contraindications, in view of the high procedural success rate and high rates of recurrence on medication (Level IB recommendation (Kirchhof et al. 2016))

2.1.4 Cardiac ablation

2.1.4.1 Ablation technique

The CTI is the target for AFL as it is accessible, relatively narrow and safe to ablate, and essential for the AFL circuit. The central portion of the isthmus is generally viewed as the optimal location for the ablation line: not only is it generally the narrowest part (Cabrera et al. 2005), but also the paraseptal isthmus may contain the AV nodal artery in 10% of patients, and the inferolateral isthmus contains the right coronary artery in closest proximity (Issa et al. 2012).

For an isolated AFL ablation procedure, a non-irrigated steerable RF ablation catheter is generally used and there is some evidence that a large tip (8-10mm) catheter may be more efficacious (Marrouche et al. 2003; Pérez et al. 2009). When an AFL ablation is performed in the context of an AF ablation, an irrigated catheter under EAM guidance is typically used, and results using EAM guidance alone are very similar to those achieved conventionally (Schoene et al. 2015). After positioning the catheter at the ventricular end of the isthmus, the ablation may be performed using a point-by-point or pullback technique, and more than one pass may be required to achieve block.

Conduction block can be verified using several techniques. Perhaps most simply, the transisthmus conduction interval should be prolonged, with prolongation of the interval by more than 50% (or >150msec) strongly suggesting block, but this is not fully specific with positive predictive value of <90% (Oral et al. 2001). Further confirmatory endpoints should also be used, but none can exclude very slow residual conduction across the CTI. In the presence of CTI block, an activation detour should be observed during atrial pacing (Figure 2-2A), with high to low activation of the lateral RA wall on CS pacing. On-line double potentials (Figure 2-2B), with a separation of more than 100msec, and differential pacing manoeuvres (Figure 2-2C) should also corroborate the presence of bidirectional block. Unipolar electrogram configuration, with a monophasic R wave immediately adjacent to the line of block, and detailed electroanatomical mapping have also been proposed to verify conduction block.

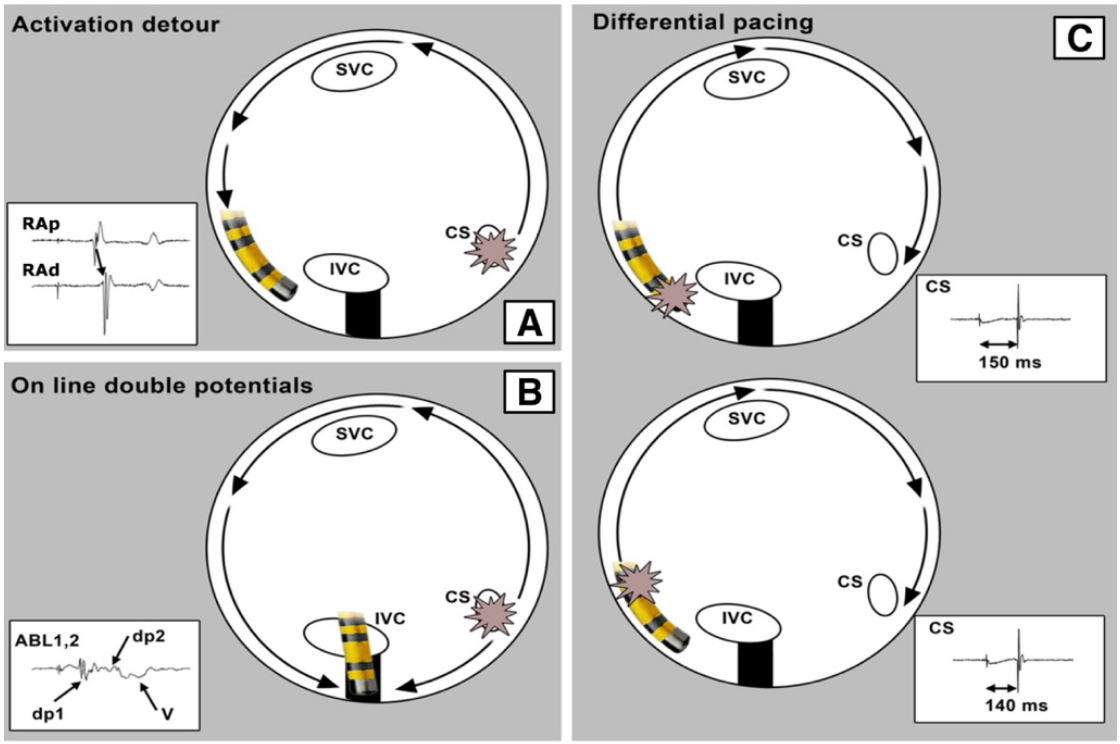

Figure 2-2. Pacing manoeuvres to confirm bidirectional cavotricuspid isthmus block post ablation.

Large black circle indicates tricuspid valve annulus, mapping catheter is yellow and pacing site indicated by pink spark. Adapted with permission from (Ganesan et al. 2012). *(CS: coronary sinus, SVC: superior vena cava, IVC: inferior vena cava)*

2.1.4.2 Ablation outcome

In contemporary practice, AFL ablation is generally safe with high procedural success rate. A recent review of a large inpatient dataset in the USA (Nationwide Inpatient Sample) found a complication rate of 3.2% and in-hospital mortality of 0.17% (89,638 procedures from 2000-2011), but data on procedural success or recurrence were not recorded (Patel et al. 2016). For assessment of procedural success, Spector et al found on meta-analysis a single-procedure success rate of 92%, rising to 97% following multiple procedures, with repeat ablation reported in 8% (Spector et al. 2009). AFL recurrence is typically early (<1month) if it is to occur, but in the longer term 35-80% of patients with AFL may represent with AF despite successful flutter ablation (Ellis et al. 2007; Pérez et al. 2009)

2.2 Atrial fibrillation

AF is the most common cardiac rhythm disturbance, with an estimated 33million individuals affected worldwide (Van Wagoner et al. 2015). Prevalence increases with age, with a lifetime risk estimated as high as 1 in 4 in developed countries, and the health impact in terms of morbidity, mortality and cost is substantial. A full and detailed evaluation of the epidemiology, pathophysiological principles

and treatment strategies for AF is beyond the scope of this thesis. However, this subsection aims to review some of the fundamental mechanisms and ablation strategies relevant to the CMR imaging evaluation of AF substrate and ablation therapy.

2.2.1 Pathophysiology

AF is a supraventricular tachyarrhythmia characterised by rapid chaotic electrical activation (fibrillation) of the atria with consequent deterioration of atrial mechanical function. Initiation and subsequent perpetuation of AF represents a synergy between focal or triggered activity that initiates AF, and the presence of a "vulnerable substrate" necessary for AF persistence (Van Wagoner et al. 2015). The atrial substrate may result from alteration of electrical properties, including shortening of atrial refractoriness and slowing of conduction, or structural changes, that include increased atrial size and the presence of scar. The principle that AF drives the evolution of AF-promoting substrate has been widely cited and reproduced (Wijffels et al. 1995; Schotten et al. 2011), and both electrical remodelling (ion channel expression and behaviour) and structural remodelling (interstitial fibrosis, apoptosis, myocyte hypertrophy) have all been shown to occur in the presence of persistent AF (Van Wagoner et al. 2015; Nattel and Dobrev 2016).

The electrophysiological mechanisms that promote and sustain AF remain controversial. Three main schools of thought are prevalent, holding AF to be caused by multiple random propagating wavefronts, rotors (localised re-entry with fibrillatory conduction) or focal electrical discharges (Figure 2-3A). These mechanisms are not mutually exclusive, and these mechanisms may act in a synergistic fashion first to initiate then to perpetuate the fibrillatory activity (Figure 2-3B).

The multiple wavelet hypothesis was proposed in 1964 by Moe and colleagues, and was widely accepted as the dominant AF mechanism until the late 80s (Moe, Rheinboldt, and Abildskov 1964; Calkins et al. 2012). Heterogeneity of atrial conduction properties lead to continuous and often chaotic interactions between multiple wavefronts, sustaining the arrhythmia. Arrhythmia stability is enhanced by decreased refractoriness, slow conduction velocities and increased tissue mass, as is frequently observed clinically (Eckstein et al. 2008).

A more organised model of re-entry is presented by the 'rotor' single circuit re-entrant hypothesis. A re-entrant mechanism of arrhythmia is classically ascribed to circus movement re-entry, characterised by a waveform that propagates around an anatomical obstacle (see section 2.1.1). However, spiral wave re-entry, or rotors, have been shown to exist in the absence of fixed anatomical obstructions. Here, an imbalance between "source" (diffusion current generated by excited myocytes available to depolarise adjacent cells) and "sink" (the adjacent cells) causes variations in conduction velocity. Regions of the activation waveform of high concavity act to increase the source: sink ratio, accelerating conduction. Conversely, high convexity promotes slow conduction, creating a spiral, or rotor, waveform that rotates upon its excitable but unexcited core, which may itself wander through the atrial myocardium (Schotten et al. 2011). Findings consistent with the presence of rotors have

been widely observed in animal studies (Guillem et al. 2016), but proof of their presence in human atria remains controversial (Walters and Kalman 2015).

The ectopic focus hypothesis is corroborated by the observation of Haïssaguerre and others that AF is initiated by focal atrial discharges and that elimination of the influence of a focal trigger may eliminate AF (Haissaguerre et al. 1994; Haïssaguerre et al. 1998). Many of the foci are identified to be within the muscular sleeves of the PVs, where electrical and geometrical properties of the myocardium differ significantly from that of the body of the atria (Schotten et al. 2011). The finding of PV foci as frequent drivers of AF are the foundation of pulmonary vein electrical isolation by catheter ablation (see below). Although PVs are the most common source of ectopy, foci have also been found in the superior vena cava, ligament of Marshall, left posterior free wall and coronary sinus.

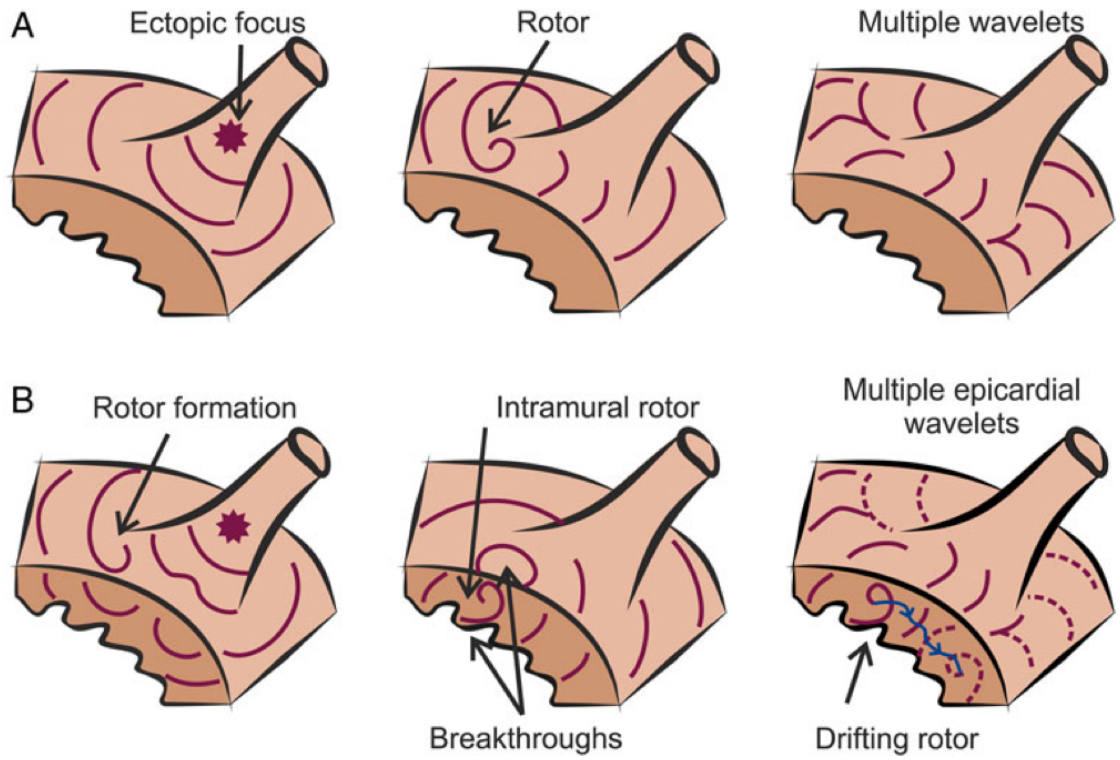

Figure 2-3. Current hypotheses for pathophysiological mechanism of AF maintenance.

(A) Diagram of AF maintenance near a PV that has been hypothesized to be driven by ectopic focus (left), rotors (middle), or multiple wavelets (right). Different wavefronts are represented in purple. (B) Representation of the compatibility of rotor maintenance with other mechanisms. Rotors can be initiated by wavebreaks near an ectopic focus (left) and underlie endocardial or epicardial breakthroughs (middle). A drifting rotor, whose trajectory is depicted in blue, can be the driver of multiple and apparently disorganized atrial wavelets (right). Reproduced and adapted with permission from (Guillem et al. 2016)

2.2.2 Diagnosis

AF may be symptomatic or asymptomatic, even in the same patient, and therefore diagnosis is frequently delayed. According to the 2012 HRS/EHRA consensus statement and 2016 ESC guidelines (Calkins et al. 2012; Kirchhof et al. 2016), AF is an ECG diagnosis confirmed by (1) "absolutely" irregular RR intervals (in the absence of complete AV block), (2) no distinct p-waves on the surface ECG and (3) an atrial cycle length (when visible) that is usually variable and less than 200msec. The arrhythmia should be documented for >30seconds, or the entire duration of a single recording if <30seconds. Onset is determined at the point of first confirmed ECG diagnosis, rather than onset of symptoms, and AF subtype is then classified according to durability of the arrhythmia (Calkins et al. 2012).

- Paroxysmal AF (PAF) is defined as recurrent AF (>/= 2 episodes) that terminates spontaneously within 7 days (or <48hours if terminated electrically or pharmacologically)
- Persistent AF (PersAF) is defined as continuous AF that is sustained beyond seven days (or >48hours if terminated electrically or pharmacologically)
- Longstanding PersAF is defined as continuous AF of greater than 12months duration
- Permanent AF is a label ascribed once a decision has been made not to restore or maintain sinus rhythm by any means.

The subtypes are broad and unspecific, and provide minimal insight into the triggers or structural remodelling underlying the disease process. There are also subtle differences between the European (Kirchhof et al. 2016) and American classifications (Calkins et al 2012), particularly in relation to timing of cardioversion. However, the classification is non-invasive, (nearly) standardised and relatively intuitive and therefore has been widely implemented in the collection and interpretation of trial data.

2.2.3 Non-ablative management of atrial fibrillation

The acute management of AF focuses upon rate or rhythm control in order to maintain haemodynamic stability, whilst considering the risk of AF-associated thrombo-embolic events, particularly stroke. Rate control may be achieved pharmacologically using agents to reduce atrioventricular conduction, with beta-blockers or calcium channel blockers found to be more effective than digoxin in the context of high sympathetic tone (Kirchhof et al. 2016). Rate control may also be used as a bridge to rhythm control and conversion to sinus rhythm, for which either drugs (particularly flecainide, propafenone or amiodarone) or electrical cardioversion may be used. Most patients with AF duration confirmed <48hours may undergo cardioversion with concomitant anticoagulation with low molecular weight heparin (Kirchhof et al. 2016). For those with AF duration >48hours, longer term anticoagulation or detailed transoesophageal echocardiographic evaluation to exclude atrial thrombus is required prior to cardioversion.

Ongoing management addresses four further domains: (1) assessment of precipitating factors and underlying cardiovascular conditions, (2) assessment of stroke risk and need for anticoagulation, (3) heart rate and requirement for rate control, and (4) symptom assessment with decision for rhythm

control (Kirchhof et al. 2016). The management of precipitating factors and modification of risk factors (including hypertension, obesity, valvular heart disease, obstructive sleep apnoea) may yield significant symptomatic and electrophysiological improvements (Pathak et al. 2015) and often requires a collaborative interdisciplinary approach. Antithrombotic management is based upon risk stratification, with most groups using the CHA_sDS_2VASC scoring system[**] as the primary guide to therapy. Oral anticoagulation therapy has historically been based upon vitamin K antagonists such as warfarin, but there is increasing evidence for the equivalency and possibly superiority of novel oral anticoagulation agents including rivaroxaban, dabigatran and apixaban (Kirchhof et al. 2016). Alternatives such as left atrial occlusion devices or surgical exclusion also exist and may be used in selected patients unsuitable for oral anticoagulants.

Long-term antiarrhythmic therapy may be based upon rate or rhythm control approaches. Whilst rhythm control may seem attractive as a more holistic approach to therapy, multiple studies have generally failed to demonstrate superiority of such an approach (Kirchhof et al. 2016; Wyse et al. 2002; Carlsson et al. 2003). Of note, the AFFIRM study randomised 4060 patients to pharmacological rhythm control or rate control and found no survival advantage in rhythm control, but an increased rate of hospitalisation and drug-related side effects (Wyse et al. 2002). There is a suggestion, though, that many of the benefits of rhythm control may be offset by the risks of the pharmacological intervention (Corley et al. 2004), and research continues to seek to delineate the optimal management strategy. Catheter ablation for AF offers a potential solution, and for selected groups of patients has been demonstrated to be superior to drug therapy (RAFFT-2 study (Morillo et al. 2014), A4 study (Jaïs et al. 2008)) .

2.2.4 Catheter ablation for AF

2.2.4.1 Indications for AF ablation

Catheter ablation for AF is accepted as an effective and potentially curative approach for appropriately selected patients with PAF, PersAF and probably longstanding PersAF, predominantly as a second line treatment following failure or intolerance of drug treatment (Class IA recommendation, ESC guidelines 2016 ((Kirchhof et al. 2016)). For those with symptomatic PAF, catheter ablation may also be considered as a first-line treatment prior to drug therapy, but incremental improvement in outcome is modest (Calkins et al. 2012; Cosedis Nielsen et al. 2012). For patients with PersAF, there is also evidence that catheter ablation may be superior to drug therapy in terms of maintaining sinus rhythm (Mont et al. 2014), but procedural success is

[**] The CHA_sDS_2VASC scoring system is based upon a point system in which 2 points are assigned for a history of stroke or TIA, or age >/=75 years. 1 point is assigned for age 65-74years, a history of hypertension, diabetes, recent cardiac failure, vascular disease and female sex. Female sex is only assigned a point in the presence of another risk factor. A score of 1 in men and 2 in women is generally accepted as an indication for consideration of oral anticoagulation, and scores of 2 or more and 3 or more respectively as an indication for oral anticoagulation (Camm et al. 2010; Kirchhof et al. 2016).

significantly lower (Ganesan et al. 2013). Nonetheless, increasing evidence for structural reverse remodelling may drive early ablative intervention (Walters et al. 2016; Liang et al. 2016).

2.2.4.2 Patient stratification

It is clear that AF ablation is more successful in some patient groups than others, but the identification of subjects most likely to benefit from a costly and potentially harmful procedure remains challenging (Link, Haïssaguerre, and Natale 2016; O'Neill and Chubb 2016). One of the few widely-accepted paradigms of AF mechanism is that development of AF requires both a trigger and a susceptible substrate, and it is within the domain of substrate susceptibility that there may be a substantial role for patient selection and tailoring of the intervention.

Patients with highest likelihood of success are generally accepted as those with PAF, no underlying cardiac disease and a non-dilated left atrium (Link, Haïssaguerre, and Natale 2016). However, the identification of further risk factors for poor procedural outcome is hampered by the necessity of trial design, dictating that subjects should undergo a relatively uniform ablation strategy: a poor outcome for a patient group may equally be ascribed to incorrect tailoring of ablation strategy as it is to patient substrate suitability for ablation in the first place.

Conventional risk factors for poorer outcome following catheter ablation include non-modifiable risk factors, including age, sex, AF type and duration of AF, and modifiable risk factors including obesity, diabetes, hypertension and sleep apnoea (Kirchhof et al. 2016). However, on meta-analysis these predictors have often been found to be unreliable (Balk et al. 2010). Imaging guided risk stratification, particularly using CMR, is explored in more detail in Chapter 5 and novel MR-derived atrial substrate parameters continue to be demonstrated. Atrial myocardial scar and fibrosis disrupt wavefront propagation, cause anisotropy and consequently promote re-entry and AF. The detection of atrial fibrosis is at the limit of CMR resolution, and therefore other parameters have also focused on substrate indices that may act as surrogates of fibrosis or alternative modes of remodelling, such as atrial shape and function.

2.2.4.3 Techniques and technologies

Ablation strategies that target the PVs and/or PV antrum remain the cornerstone for most AF ablation procedures, and complete electrical isolation of the PVs (PVI) is a core goal of ablation (Calkins et al. 2012). A wide area circumferential ablation (WACA) lesion set is typically employed to achieve this, with selective PV isolation now rarely performed. For patients with PAF, studies have failed to demonstrate significant improvement in outcome with additional lesion sets such as ablation at the intervenous ridge (McLellan et al. 2015). However, whilst an approach aiming only for PVI yields relatively good outcomes for ablation of PAF, the results for PersAF are more modest, and adjunctive lesion sets have been employed and investigated extensively in an effort to minimise recurrence (Kirchhof and Calkins 2016). Additional linear ablation lines and focal targeted ablation may also be performed.

Linear lesions between two anatomical or electrical barriers typically include mitral isthmus line (Jais et al. 2004), roof line or full posterior wall isolation. However, linear lesions may also act as an arrhythmogenic substrate if any conduction persists or recovers, and the STAR AF II study demonstrated no significant improvement in outcome with the addition of electrogram or linear ablation lesion sets (Verma et al. 2015). Linear lesions are clearly appropriate for interruption of confirmed re-entrant atrial tachycardias pathways, but their role in first-time ablation for PAF or non-PAF is tenuous (Kirchhof and Calkins 2016; Kirchhof et al. 2016).

Targeted focal ablation has also been hypothesised to improve outcome in patients with PersAF, where non-PV drivers are more common. Sanders et al found that the highest dominant frequency[††] sites for subjects with PAF were generally clustered around the PVs, whilst those in subjects with permanent (sic) AF displayed a much wider distribution (Sanders et al. 2005). Focal ablation of complex fractionated atrial electrograms[‡‡] (CFAE), highest dominant frequency regions or core regions of stable rotors have been proposed to improve long term outcome (Narayan et al. 2014). However, recent larger studies have failed to corroborate those findings (STAR AF II (Verma et al. 2015), CHASE-AF (Vogler et al. 2015) rotor ablation (Gianni et al. 2016; Buch et al. 2016)). Therefore, recent reviews suggest that PVI alone may be the most appropriate strategy for first-time ablation for PersAF (Kirchhof and Calkins 2016).

Historically, the vast majority of AF ablation procedures have been performed using radiofrequency (RF) energy. Newer RF technologies, such as contact force sensing catheters, have been demonstrated to create more consistent and reliable RF lesion formation (Kuck et al. 2012; Neuzil et al. 2013). More recently, cryoablation has been demonstrated to be non-inferior to RF in efficacy and safety, whilst potentially quicker to perform (Kuck, Brugada, et al. 2016). The implementation of cryoablation AF ablation techniques is rapidly increasing, particularly for first time PAF ablation, and laser ablation is also performed in some European centres. However, in this thesis, all ablations were performed using only RF energy.

[††] Dominant frequency is determined by Fast Fourier Transformation (see section 1.3.2) of the local recorded electrogram signal, and is the highest magnitude constituent frequency. Sites of the highest dominant frequency have been suggested to play a key role in AF maintenance (Calkins et al. 2012)

[‡‡] CFAEs are defined as low voltage (<0.15mV) multiple potential signals with one or both of the following characteristics: (1) atrial EGMs that have fractionated EGMs composed of two deflections or more, and/or have a perturbation of the baseline with continuous deflection of a prolonged activation complex; (2) atrial EGMs with a very short cycle length (<120ms), with or without multiple potential; however, when compared to the rest of the atria, this site has the shortest cycle length (Calkins et al. 2012)

2.2.4.4 Procedural endpoints

The achievement of electrical isolation of the PVs is a key goal of the vast majority of AF ablation procedures, but the technique used to verify isolation varies between operators. At a minimum, entrance block should be demonstrated, and monitoring for a further 20min should be considered (Calkins et al. 2012). However, the robustness of such an approach has been questioned, and many operators perform a more detailed assessment of electrical isolation that may include exit block and/or the use of provocative agents such as adenosine (ADVICE trial (Macle et al. 2015)). The appropriateness of aiming for electrical isolation of the PVs has been confirmed in a remarkable study by Kuck et al, in which 223 patients were randomised in a 1:1 ratio to complete PVI or to be left with an intentional gap in the WACA line. The AF recurrence rate at 3 months in the cohort with a gap was proven to be higher (79% versus 62%, $p<0.001$), albeit with conduction gaps still found in 70% of the complete PVI group at invasive reassessment at 3 months (Kuck, Hoffmann, et al. 2016).

An alternative or additional end-point is that of termination of AF through ablation, typically employing a 'step-wise' ablation approach with adjunctive focal and/or linear lesion sets in order to achieve termination (O'Neill et al. 2009). Mapping or pacing manoeuvres should be employed to demonstrate the completeness of linear block at any adjunctive ablation lines, even after the ablation-induced resumption of sinus rhythm (Kirchhof and Calkins 2016). In experienced hands, the 'step-wise' approach has yielded high long-term success rates for both PersAF (5% recurrence at 32±11months (O'Neill et al. 2009)) and PAF (26% at 12months (Faustino et al. 2015), but these findings have not been universally reproduced (Vogler et al. 2015).

2.2.4.5 Follow-up and outcomes

Follow-up and monitoring practices post-ablation vary between centres. It is generally agreed that patients should be seen at a minimum of three months post ablation, with reviews at least every six months thereafter for at least two years (Calkins et al. 2012). Intensity and duration of ECG assessment also varies, but longer-term monitoring solutions, such as event recorder or implantable loop recorder, are generally tailored to the frequency of symptoms.

Recurrence of AF is defined as the recurrence of AF more than 3months following AF ablation, and includes episodes of flutter or atrial tachycardia (Calkins et al. 2012). Early recurrence (<3 months post-ablation) of AF is common, and a blanking period is typically employed. During this period, many operators continue anti-arrhythmic drugs, with early cardioversion in the event of AF recurrence. Early AF episodes in the context of significant post-ablation inflammation may not necessarily indicate long term recurrence, but they remain a strong risk factor for later treatment failure (Liang et al. 2015; Leong-Sit et al. 2011).

Across the wide range of ablation strategies, serious complications are rare but recurrence rates remain high. Serious complications include cardiac tamponade (1-3%), PV stenosis (0-38%, highly dependent upon ablation strategy and increasingly rarely observed), atrio-oesophageal fistula (0.1-

0.25%), phrenic nerve injury (5% temporary, 0.5% permanent) and cerebral embolic events (0-7%, with a much higher incidence of silent micro emboli). Overall mortality is around 0.1% (Calkins et al. 2012). In terms of procedural success, a recent meta-analysis (Ganesan et al. 2013) found that freedom from AF at 12 months following a single procedure was 64% (67% in PAF, and 51% in non-PAF), falling to 61% for PAF and 42% for non-PAF at 3 years. With multiple procedures, the combined (PAF and non-PAF) long-term success rate was 80% at three years, but with wide variation between studies. The mechanism of AF recurrence is most commonly associated with PV electrical reconnection (Ouyang et al. 2005), and organised atrial tachycardias are found more often in the context of persistent PV isolation (Baldinger et al. 2016).

2.3 Electroanatomic mapping systems

Until the mid-1990s, electrophysiological procedures were guided almost exclusively by fluoroscopy. Procedures were long and the radiation exposure substantial. Fluoroscopy frame rates have been minimised and image contrast reduced to lower total skin doses, but the radiation exposure remains a concern. Alternative methods for assessing catheter position have therefore evolved, with electromagnetic (magnetic or electrical) positional tracking techniques first applied in the cardiac field in the mid-1990s. These tracking techniques evolved rapidly to combine with interventional workstations to form electroanatomic mapping (EAM) systems, displaying the location of multiple tracked devices in the context of acquired cardiac anatomy and electrophysiology.

Two main techniques are currently used for device tracking for EAM: transthoracic impedance fields and magnetic fields. Each of these techniques has innate advantages and disadvantages, and it is little surprise that the main manufacturers now use a combination of both technologies for their most advanced EAM systems. Biosense Webster (Diamond Bar, CA, USA) has used calibrated magnetic fields for many years, and this has generally been accepted as providing robust location information. In contrast to high frequency, low voltage, electrical fields applied across the thoracic cavity, there is minimal impact of soft tissue interfaces and impedance changes. Static accuracy has been demonstrated to be 0.2mm in-vitro, and 0.7mm in-vivo. However, magnetic field sensors within devices are costly, relatively bulky and have been limited to proprietary catheters. Typical sensor size is 1mmx4.5mm, with detection of magnetic field strength and direction arising from measurement of induced voltage on a single tip coil or three orthogonal coils. CARTO3 (Biosense Webster) therefore implemented a hybrid of magnetic and voltage based location technology, using further skin patches to detect an ultra-low current, high frequency electrical signal which is unique to each catheter electrode. This has enabled the use of non-proprietary catheters and the tracking of many more electrodes, including information on the location of device shafts, but at a lower accuracy (typically 3mm). EnSiteNavX (St Jude Medical, St Paul, MN, USA) has been long-established as a reliable EAM system using impedance field navigation alone. Device location is derived relative to a reference electrode, based on impedance gradients, and is effectively open platform allowing the use of any catheter. Concerns regarding localisation accuracy have been addressed in the recent release of EnSite Precision (St Jude Medical) which utilises a hybrid approach of both magnetic and

impedance fields, this time using the magnetic field information to provide live calibration of the impedance field.

An EAM-guided procedure can be divided into three phases- establishing cardiac anatomy, diagnostic electrophysiology, and ablation. Cardiac anatomy may be acquired through device tracking alone, or in combination with prior imaging using image fusion techniques. Using device tracking alone, the intrathoracic location of a single surface (usually endocardial) is derived by recording all locations that the tracked device has reached. This mapping technique relies upon the operator placing the device in all pertinent locations, and the EAM system interpolates those locations to generate a surface shell. Interpolation settings and compensation for respiratory motion, cardiac motion and contact force may be adjusted to optimise the fidelity of the virtual anatomy. Alternatively, prior three-dimensional imaging may be registered to EAM locations: for instance, a segmented left atrium from a contrast enhanced CT scan may be placed within the EAM field using PV and mitral valve annulus registration points. These image fusion techniques increase the likelihood that the full anatomical extent of the surface has been established, and may reduce the time taken to acquire the anatomy. However, they are reliant on accurate co-location of registration points on both imaging and EAM shells: a registration that involves not only translation or rotation, but also affine transformations that may cause inappropriate anatomical distortions.

Diagnostic electrophysiology is increasingly performed in parallel with anatomical mapping. Intracardiac electrograms may be recorded at each surface location, and metrics derived. Local activation time and peak voltage are often annotated automatically, and further characteristics may be ascribed manually to the electrogram (and therefore the corresponding cardiac location) such as fractionation or splitting of potentials. Over the past two years, increasingly automated EGM acquisition methods have reached the market, including Confidense (BiosenseWebster) and AutoMap (St Jude), which act to acquire and annotate electrogram information much faster than can be performed manually, whilst employing a sophisticated array of censoring algorithms to prevent nonsensical annotations. In this way cardiac substrate (in terms of voltage), normal sinus rhythm, paced rhythms or arrhythmias can be mapped and projected onto the cardiac chamber shell for diagnostic purposes.

Ablation is also performed in the EAM environment. The capacity to ascribe ablation parameters to cardiac locations is a highly significant step forward from fluoroscopy, without which some complex ablation procedures would be much more difficult to perform. Ablation location is technically determined within the intrathoracic cavity space, but is generally projected to an appropriate location on the cardiac chamber shell. The projection may be calibrated using respiratory or cardiac motion parameters, but it cannot currently take into account movement of the cardiac surface below the catheter tip. Ablation locations are therefore only an estimate, but increasingly sophisticated measures are being developed in order to annotate ablation parameters in an objective fashion, and even guide ablation delivery.

3 TECHNICAL CONSIDERATIONS FOR MRI-GUIDED ELECTROPHYSIOLOGY PROCEDURES

3.1 Introduction

Interventional MRI is a growing field, and the strength of MRI guidance for procedures rests fundamentally in the high contrast imaging of soft tissue structures. Coupled with the avoidance of radiation exposure, the potential for functional assessment, and the ability to exploit MR signals for calculation of the location of interventional instruments, it is clear that the implementation of interventional MRI will continue apace. For cardiac interventions, the visualisation of thin, mobile, structures presents particular challenges for MRI guidance. Cardiac electrophysiological procedures add a further dimension, as the accurate detection of intracardiac electrograms must be performed in a highly active electromagnetic environment. This chapter focuses on the technical considerations for the performance of electrophysiological procedures under MRI guidance (MR-guided EP).

3.2 The potential benefits of MR-guided EP

MRI techniques offers a high soft tissue contrast-to-noise ratio compared to x-ray, computed tomography (CT) and ultrasound. However, the environment is a challenging and expensive one, and all the benefits of MR-guided EP need to be fully realised to justify the additional difficulties and expense. Broadly speaking, these benefits can be divided into three main areas: improved precision of ablation targeting (substrate identification), improved intra-procedural guidance, and improved assessment of ablation lesion formation.

3.2.1 Substrate identification

Both ventricular and atrial arrhythmogenic substrate have been identified on CMR imaging (Ashikaga et al. 2007; Marrouche et al. 2014), and the implementation of data regarding local myocardial characterisation is increasingly used to guide procedures. However, improvements in clinical ablation outcome with the use of CMR-substrate information have been modest (Andreu et al. 2011). MR-guided EP presents a way in which CMR-derived substrate may be used more accurately and intuitively to guide procedures.

The evidence for CMR-derived arrhythmia substrate identification is strong, and ventricular substrate is generally the more amenable to evaluation by CMR. There is increased wall thickness and higher consequent contrast between healthy and pathological tissue. Ventricular tachycardia (VT) occurs due to scar related re-entry and scar can be accurately visualised using LGE techniques (Nazarian et al. 2005; Ashikaga et al. 2013). In particular, the scar border zone has been shown to be

critical in the perpetuation of the arrhythmia, and its abolition forms the basis of substrate-based VT ablation (Carbucicchio et al. 2013; Pop et al. 2013; Perez-David et al. 2011).

There is also emerging data to suggest that CMR imaging may be used to guide atrial ablation procedures. Though the atrial wall is thinner, native fibrosis and ablation scar can be identified using primarily three-dimensional LGE techniques (Marrouche et al. 2014; Khurram et al. 2014). Recent studies have been interpreted to suggest that successful ablation of fibrotic regions, distant to the PVs, may help improve AF ablation success rates (Akoum et al. 2013), and these observations have led to the instigation of the DECAAF-II trial (www.decaaf.org). Similarly, atrial re-entrant circuits can be modelled in-silico based upon atrial scar location and used to inform ablation strategies (Zahid et al. 2016), Sites of PV reconnection have been identified using CMR, with successful ablation guided by the CMR-derived substrate (Bisbal et al. 2014), but these findings have not been replicated by other groups including our own (J L Harrison, Sohns, et al. 2015).

To date, all studies that have used CMR-derived substrate identification to guide ablation have relied upon EAM image fusion techniques (see Section 2.3)(Cochet et al. 2013; Bisbal et al. 2014; V. Y. Reddy et al. 2004). Accurate, real-time, registration of EAM shell and substrate data is crucial and may be significantly affected by registration errors (including discrepancies in landmark identification on imaging and electrical criteria), cardiac chamber conformational changes (arising from differing loading conditions and tachyarrhythmias), and translational changes (due to patient movement, cardiac motion and respiratory motion). CMR-derived targets may be typically 2-4mm wide for VT ablation (Fernández-Armenta et al. 2013) and even less for atrial ablation (Bisbal et al. 2014; Ranjan et al. 2012). Small errors in registration mean that either a very broad region must be ablated or critical targets are left untouched, with consequent impact on safety, time and efficacy.

MR-guided EP can use one of two techniques in order to overcome the registration errors. The first is to use image registration within a single modality, rather than trying to match electroanatomical data to imaging data. The second is by using real-time, or near-real-time, visualisation of substrate, with the imaging performed during the same procedure. Such approaches may improve the outcome of CMR-substrate guided ablation.

3.2.2 Procedural guidance

The vast majority of complex ablation procedures are performed using EAM, and procedural guidance is largely reliant upon anatomical mapping techniques alone. Fusions with fluoroscopy, using techniques such as CARTOUNIVU™ (Biosense Webster), or intracardiac ultrasound (CARTOSOUND™ (Biosense Webster)), provide a degree of structural information in addition to that derived from solely EAM. However, the anatomical information and depth of field is inferior to that achieved with CMR imaging. Detailed information on the chamber of interest and the surrounding structures such as oesophagus, coronary arteries and adjacent chambers can assist the performance of many procedures, particularly those in patients with complex congenital heart disease (H Chubb

et al. 2014). In addition, cardiac motion derived from both respiration and the cardiac cycle can be assessed more accurately using CMR than with any other imaging modality. Accurate compensation for this motion could have significant implications for mechanisms of energy delivery.

3.2.3 Lesion evaluation

The failure to create durable and contiguous transmural lesions has been held largely responsible for the high recurrence rates following many complex ablations, particularly VT and AF (Aliot et al. 2009; Calkins et al. 2012). CMR may be used to assess acute ablation lesions (Celik et al. 2014; Ranjan et al. 2012; Dickfeld et al. 2007), and this does not necessarily mandate the performance of the procedure under MR-guidance. One approach might be to perform a conventional procedure with immediate evaluation of lesions prior to removal of sheaths. Patients would move to the MRI scanner for assessment, then return to the conventional lab for 'top-up' ablation of inadequate lesions. However, a number of factors have inhibited such an approach. First and foremost is the absence of a specific and sensitive acute CMR signature of chronic, effective, lesion formation, of sufficient precision to guide further ablation (Arujuna et al. 2012; James L Harrison et al. 2014). Ventricular lesion formation is likely to be more amenable to CMR imaging, but investigations into ventricular lesion imaging are sparse in comparison to those assessing acute atrial ablation lesions. Secondly, intra-procedural CMR imaging requires substantial disruption: all ferromagnetic material must be removed, and almost all EAM equipment is currently incompatible with CMR imaging. Patches, catheters and most long sheaths must be removed, and therefore the registration of imaging to EAM for further ablation requires the procedure to re-start almost from scratch. Thirdly, few centres have the facility to move patients easily from EP lab to MR scanner and back again with sufficient sterility and safety.

MR-guided EP has the potential to streamline the process of acute lesion imaging, and also to perform real-time imaging of lesion formation. It has been postulated that oedema may hinder radiofrequency energy delivery to the underlying viable myocardium (Arujuna et al. 2012), and immediate imaging presents the opportunity for early repeat ablation and even energy titration (Figure 3-1). Imaging techniques continue to be developed, but currently no single technique has been demonstrated to be robust enough for clinical implementation. With time, MR-guided EP may present the opportunity for accurate and tailored ablation lesions.

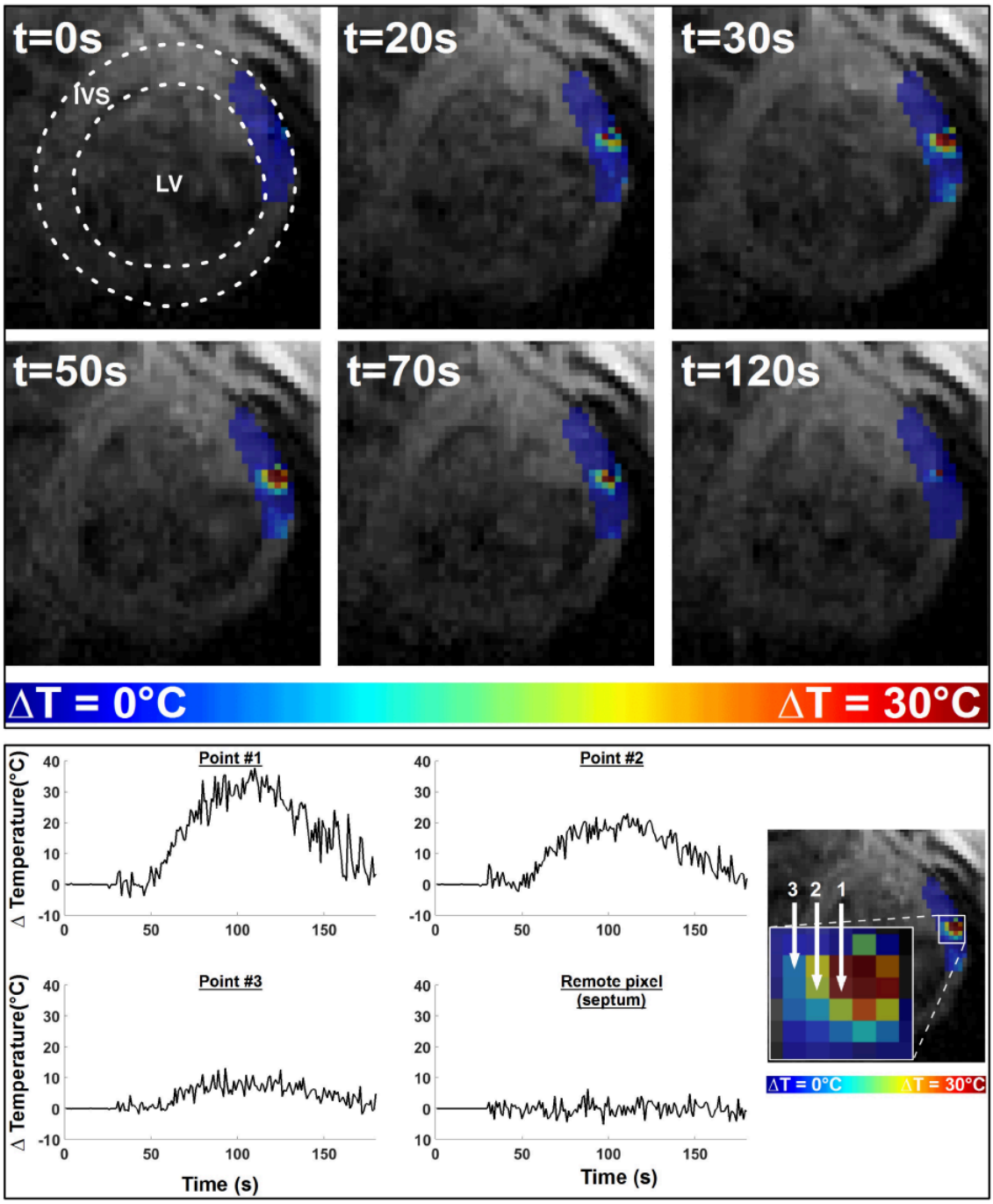

Figure 3-1. Real-time temperature mapping of left ventricular (LV) epicardial ablation lesion, using MR-thermometry (relative tissue temperature mapping).

Upper six panels show colour coded local temperature at 0 to 120 seconds post initiation of a 60second 50W radiofrequency ablation lesion, in a short-axis view (dotted lines denote limits of ventricular myocardium). Note spread of maximum temperature from epicardium to endocardium. Lower panel shows change of temperature against time at individual voxels, the locations of which are shown on the right hand side.IVS: interventricular septum. Images courtesy of Sebastien Roujol, King's College London, UK.

3.3 MR-compatibility of devices

The MR environment presents considerable challenges in terms of design and use of conventional procedural equipment. Interventional instruments, anaesthetic equipment and monitoring must all be capable of safe and effective operation in a demanding environment. Commercial ablation solutions frequently include non-compatible components, which are not limited to ferromagnetic materials, and a number of considerations must be made.

3.3.1 Constraints associated with the static field B_0

Contrary to conventional expectations, the presence of ferromagnetic materials is not absolutely contra-indicated within the MR environment. However, the use of ferromagnetic materials (see Section 1.2.3) should be carefully controlled and curtailed as far as possible. Ferromagnetic materials exhibit strong attraction along the line of the magnetic field, and torque to align the object with the field lines[§§]. Items that are fixed, such as a stent or iron doping on a catheter tip, will remain controlled within the field. However, for sensitive interventional devices such as an EP catheter the forces may be intolerable, and the susceptibility artefact tends to be very large.

The Lenz effect should also be considered for non-ferromagnetic conducting materials. Lenz's law states that if an induced current flows, its direction is always such that it will oppose the change which produced it. This produces resistance to movement of metallic materials within the magnetic field (such as old-style metallic heart valve). However, the induced electromagnetic force is unlikely to have significant effect upon the movement of catheters when close to the relatively uniform field in the centre of the bore[***]. (Graf, Lauer, and Schick 2006)

3.3.2 Constraints associated with the rapidly switching gradient fields

Rapidly switching gradient fields have important implications upon electrically conductive materials, particularly in the vicinity of highly voltage sensitive tissue such as myocardium. Modern gradient fields have a steepness of up to 100mT/m, and a slew rate of up to 200mT/m/msec (Kugel 2012). The gradient fields cause significant acoustic noise, may induce peripheral nerve stimulation, and also cause low-level heating of tissues (low in comparison to RF-induced heating- see below). However, for MR-guided EP a further consideration is induction of current and the potential for local cardiac stimulation. Individual catheter channels must be effectively isolated from all other catheter channels in order to eliminate gradient induced currents (Hilbert et al. 2015).

[§§] The force experienced by a ferromagnetic object at distance r from the scanner bore (F(r)) is proportional to $B_0(r).\partial B_0/\partial r$, where B_0 is the field strength. The torque acts to align the magnetic axis of the object parallel to the field lines, and increases with the square of the field strength ($\propto B_0^2$)

[***] $\epsilon = -\frac{\delta\phi}{\delta t}$, where ϵ is the induced voltage, and $\delta\phi$ the change in magnetic flux.

3.3.3 Constraints associated with the pulsed RF field

A high-frequency RF field is applied to tip spins to the imaging plane and refocus (see Section 1.1.2). High frequency eddy currents are also induced in soft tissue and devices, and these produce heat. Localised concentration of heating may occur in the vicinity of additional coils, cables or other conducting devices, particularly at the entry and exit points of devices where the current density is highest. However, the heating effect of both the electrical and magnetic components of the RF field is complex to simulate, and is largely dependent upon the tuning between the transmit coil and the "receiving" device (Kugel 2012). Multiple tests must be performed in order to ensure that the worst-case scenario is included, and significant constraints may be placed upon transmission lines in particular (Steffen Weiss et al. 2005).

3.4 Device tracking

Device tracking within the MR environment is of paramount importance, and there are two main methods of localisation: passive and active tracking.

3.4.1 Passive tracking sequences

Passive device tracking relies on the identification of the device on an imaging sequence. Such an approach does not require novel technology to be developed, but it suffers from poor CNR, particularly with thicker imaging slices, and is highly time-consuming.

For most passive tracking purposes, a relatively high speed imaging sequence is required in order to achieve imaging frame rates of at least 1Hz. Device identification may be based upon a device MR signature that is fundamentally reduced or enhanced for the imaging sequence. Signal reduction is generally achieved through magnetic susceptibility artefact (secondary to the presence of metals), or absence of signal (for non-metallic anhydrous devices). Enhanced signal may be achieved through the use of resonant radiofrequency devices (S Weiss, Eggers, and Schaeffter 2001) or filling a device with an enhanced signal source such as a GBCA-filled tube.

The use of passive tracking sequences generally requires significant input from a skilled MR operator in order to manipulate the imaging plane to keep the device within slice. This is relatively easily achieved in narrow tubular structures lying within a single plane, such as the aorta, but is much more difficult when there is a greater degree of varying three-dimensional movement as is the case for an EP study or ablation. Thicker imaging slices (>10mm) improve the ability to keep the device within plane, but CNR may be impaired to such a degree that the device may not be identifiable. There are also two further substantial limitations to passive tracking pertinent to MR-guided EP. The first is the difficulty in tracking more than one device at a time: EP frequently requires multiple diagnostic and ablation catheters, and the narrow MR imaging planes, in contrast to the projection view of fluoroscopy, limits the monitoring of more than one device at a time. The second limitation is the requirement to record location relative to cardiac structures. Automated image recognition techniques could theoretically be employed when the device tip is in-plane with sufficient CNR,

enabling device localisation to be referenced to pre-defined chambers. However, there is no published evidence that this capability has yet been developed.

Nevertheless, passive tracking remains a useful technique, even when actively tracked devices are used (see below). At present, the number of tracked electrodes is highly limited, and therefore there is generally no information on catheter shaft or sheath location. This mirrors the earlier iterations of EAM systems, when only the location of the catheter tip was visible. Brief runs of passive tracking sequences, preferably in imaging planes defined by the location of the actively tracked catheter tip, facilitate the determination of the shaft orientation. Such knowledge may be important in performing more complex catheter manipulations such as those required to reach within a pouch of the Eustachian ridge, or during retrograde access to the left ventricle. Furthermore, active tracking catheters are relatively bulky and expensive, and for simple diagnostic catheters a passive tracking solution may be more appropriate. Therefore passive tracking remains important even in the era of active device tracking for MR-guided EP.

3.4.2 Active tracking sequences

Active tracking of devices has been demonstrated using two main techniques. The first exploits the imaging gradient fields to derive device location. Electrical potentials may be induced by the time-variable magnetic fields in a set of miniature coils implanted in the device (Nevo 2003), and this technique has been FDA-cleared for non-cardiac MR-guided interventions (EndoScout® , Robin Medical Inc., MD, USA). However, it has not been implemented in the cardiac field. The second technique is that used in this thesis, and this employs a dedicated tracking sequence, detected by micro-coils within the catheter.

The technique was first proposed by Dumoulin et al (C L Dumoulin, Souza, and Darrow 1993). Small receive coils act to detect a highly localised spatially encoded signal from the surrounding tissue (the coils are insensitive to signal arising more than approximately 1mm away). Early versions of the tracking signal proposed a non-selective RF pulse, followed by a gradient-recalled echo with readout gradient pulse on a single axis. However, such an approach is highly susceptible to local magnetic inhomogeneities, as the location calculation is based on frequency alone. This is of particular relevance as a receive coil will create a susceptibility artefact around itself, and the orientation of the coil within B_0 will consequently shift the calculated location significantly. Therefore a more accurate approach evolved. At first, the average of two locations was calculated with opposite gradient directions, and this mitigated the errors at the cost of temporal resolution. In order to increase efficiency, a four-excitation scheme was then employed, with three gradients applied in each of four excitations, allowing a unique x-, y- and z-axis location to be calculated. In addition, multiple coils can be tracked simultaneously using the same tracking sequence, as it is limited only by the number of receivers.

This approach proved relatively robust, but there were issues that needed to be addressed even at the earliest stages.

- Signal change with receive coil orientation relative to B_0. When the receive coil lies parallel to B_0, the transverse spin magnetisation will not induce any current in the coil. Fortunately, the range of angles at which this occurs has been found to be extremely narrow (C L Dumoulin, Souza, and Darrow 1993).
- MR-signal source for micro-receive coil. The detection of a location signal is dependent upon MR-signal from MR-active material adjacent to the coil. Consideration was given to placing MR-active material within the catheter, but this was unacceptably bulky for a complex EP catheter and therefore the signal arises from material outside of the catheter itself. This severely impairs the tracking performance when the coil lies within the sheath, but this is a problem familiar to electrophysiologists used to working with impedance-based EAM systems. It is also a potential problem when the catheter is deflected 180° and the receive coil lies within the susceptibility artefact of the transmission line capacitors (see below), and care must be taken in the interpretation of tracking signal in these locations.
- Sensitivity to noise. The location accuracy is clearly impaired when SNR is low. This may occur with absence of MR-active material adjacent to the coils, but also with poor tuning of the receive coils, coupling with body coils, or resonance of the cable within the device. An approach using "phase dithering" has therefore been proposed (Charles L. Dumoulin et al. 2010). This entails the application of a dephasing gradient orthogonal to the frequency gradient, prior to echo readout. The dephasing acts to destroy signal from large regions, whilst having minimal effect upon very small volumes such as that immediately surrounding the micro-receive coil. There are an infinite number of possible dephasing directions in the two-dimensional plane defined orthogonal to the frequency encoding direction. For each given frequency encoding direction, some dephasing directions may enhance signal, whilst others may reduce it. A limited number of directions are applied for each location, typically three to six, and the highest SNR is then used for the calculation of the position of the coil.
- Double signal peak. There are in fact two signal peaks for each coil, reflecting the sensitivity at each end of the coil, rather than at the centre. The difference in frequency for these signals is dependent upon the orientation of the coil relative to the frequency encoding direction. The double peak reduces SNR and could generate location ambiguities. However, the double peak can also be exploited to improve accuracy of position calculation and orientation, using dedicated real-time evaluation of the peak locations (Figure 3-2).

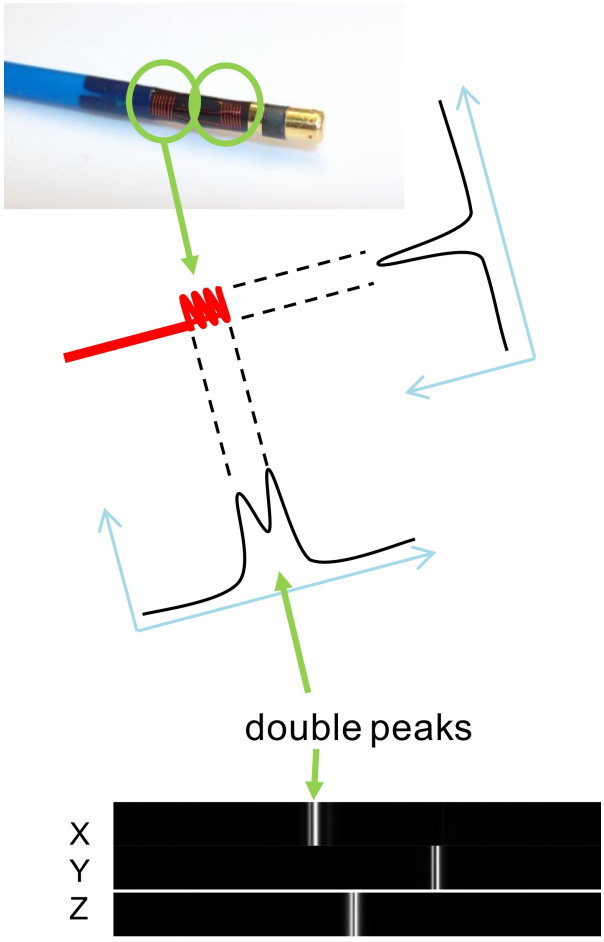

Figure 3-2. Double peak detection with active tracking sequence.

Peaks in signal are detected at each end of the micro-receive coil. Dedicated algorithms search for further signal peaks adjacent to the main peak, generally with a threshold of approximately 0.4x the height of the main peak. The central location of the coil is calculated as the mid-point of the peaks, and the distance between them also provides information on the orientation relative to the gradient field.

The signal detected by the micro-receive coils must then be passed from catheter tip to the surface coil port at the scanner itself. As discussed, there are significant concerns regarding RF safety for long transmission lines, whilst they must remain capable of conducting μV MR-receive signals. Some in-vivo studies have used thin, high resistivity 50-g coaxial cable (Dukkipati et al. 2008; Schmidt et al. 2009), but these have not been demonstrated to be safe for human interventions. Initial efforts towards lines suitable for human use aimed to replace wires with optical fibres (S Weiss et al. 1999; Steffen Weiss et al. 2004). However, this approach failed to achieve the required robustness. In parallel, other groups sought to improve RF safety by modified wires (Atalar 1999; Ladd and Quick 2000) but this and other approaches were also not developed into clinical-grade devices. Finally an approach based upon miniature transformers in the device proved to provide both the required tracking robustness and RF safety (S. Weiss et al. 2005; Vernickel et al. 2005). Further work resulted in dedicated EP catheters based on this approach (Krueger et al. 2009; Steffen Weiss et al. 2011).

3.4.3 Implementation within EAM-style interface

Whether active or passive tracking is used for MR-guided EP interventions, it is necessary to project the location within the context of the cardiac chambers. Most studies have chosen to acquire a 3D b-SSFP whole heart volume at the beginning of the procedure, and then to display the location within a segmented chamber of the volume (Figure 3-3) (Dukkipati et al. 2008; Hilbert et al. 2015; H. Chubb et al. 2014). Manual or automated (see Chapter 6) chamber segmentations have both been employed in order to provide an interface that closely mimics the strengths of a clinical EAM system. Passive and active tracking sequences may be interleafed, providing real-time location updates with visualisation of device position and surrounding anatomy, and the passive imaging slice position can be co-ordinated with catheter tip position (Koken et al. 2010). Interactive interface may also allow for the rapid switching between several MRI pulse sequences, enabling the visualisation of anatomy with different contrasts.

An alternative strategy has been proposed by the Boston group (Schmidt et al. 2013) who have modified an impedance-based tracking system, based upon Ensite Velocity (St Jude), and adapted it for use within the MRI environment. In a swine model they performed diagnostic EP procedures within the MR scanner, using the voltage-based location to guide catheter manipulation. There were considerable technical challenges in terms of optimising the location signal in the MR-environment, and tracking performance was impaired by the requirement for blanking of the tracking signal during the gradient field applications. However, the approach has been demonstrated to be feasible and may open the way for a truly hybrid approach, working in both conventional and MR EP laboratories during the same procedure, or for tracking of simpler devices within the MR-scanner itself.

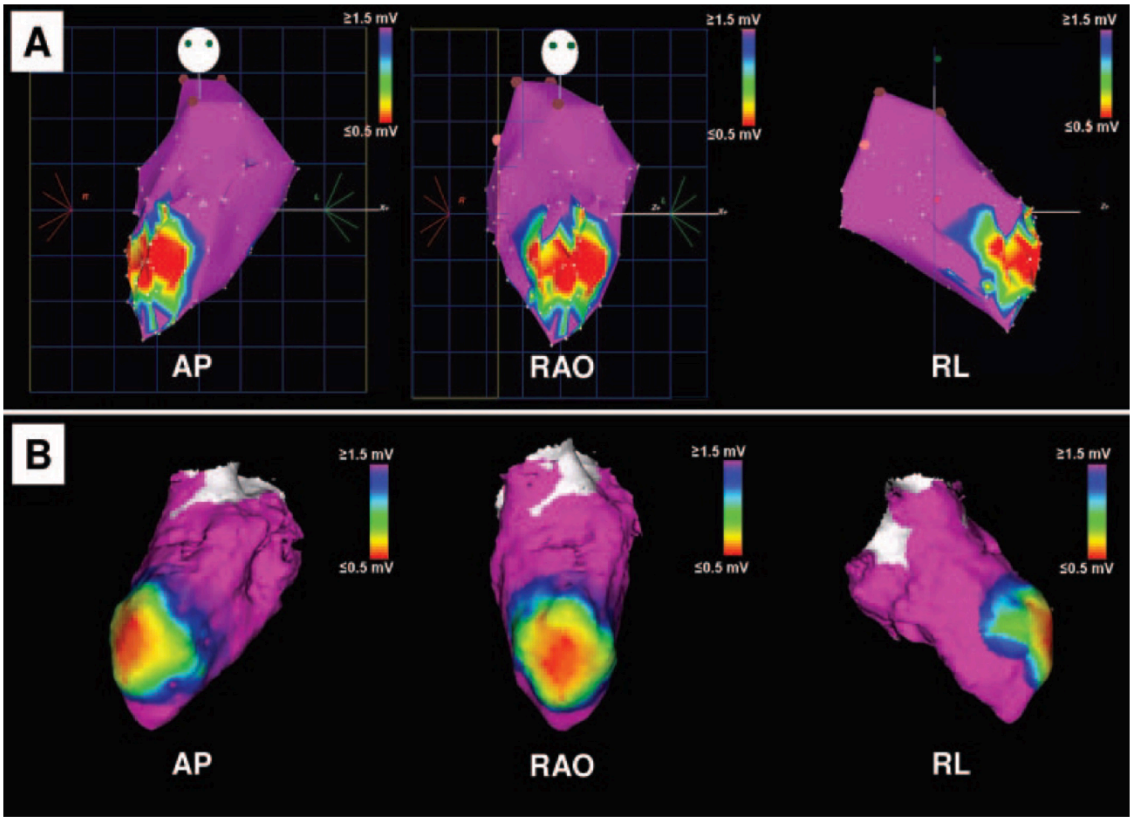

Figure 3-3. The first published example of EAM-style interface for MR-guided electrophysiological procedures.

Mapping displays the left ventricle of a swine infarct model. Three-dimensional bipolar voltage maps using standard fluoroscopy-based CARTO (A) and the MRI-guided electrophysiology system (B) in the same animal. The maps performed by both methods demonstrate the same anterior wall myocardial scar. AP: Anteroposterior; RAO: right anterior oblique; RL: right lateral. Adapted from (Dukkipati et al. 2008) *with permission.*

3.5 Electrogram fidelity

As discussed in Section 1.5.1, the detection of surface cardiac electrical activity is difficult within the MR environment, particularly in the presence of time variable gradient fields and MHD effects. MR-guided EP is currently performed with limited surface electrocardiogram data, typically restricted to four surface adhesive electrodes (Expression, Invivo Medical, Gainesville, FL, USA), with marked distortion of many components of the ECG. Identification of the ST-segment and P-wave is often obscured, and many groups are working on improving the electrogram quality (Schmidt, Dumoulin, and Danik 2014).

There are also challenges related to the detection and transmission of the intra-cardiac electrograms (IEGMs). As for a conventional EP laboratory, IEGMs must be high-pass and low-pass filtered, often with the addition of further notch filters to account for the frequency of mains electricity and other identified sources of noise. Despite filtering however, electrical noise levels remain high in the MR-

environment. MHD effects have also been shown to be dependent upon catheter orientation, and can result in detected voltages that are higher in late systole than at the R-wave (Schmidt et al. 2013). In addition, the IEGM voltage must be transmitted via a high resistivity, RF safe, transmission line, and IEGM fidelity will need to improve significantly in order to enable detection of low amplitude signals such as late diastolic potentials (Hilbert et al. 2015). There is no published example of unipolar voltage IEGM detection in the MR-environment, the measurement of which will increase the detection of environmental noise between active and indifferent electrodes. This will provide further challenges, but technical solutions are likely to evolve.

3.6 Anaesthesia and monitoring

MR-guided EP procedures are currently longer than equivalent procedures using conventional guidance, and they are performed in a noisy and potentially claustrophobic environment. Therefore, published human studies have been performed under general anaesthesia or deep sedation (Hilbert et al. 2015; H. Chubb et al. 2014; Grothoff et al. 2014; Nazarian et al. 2008). Maintaining and monitoring anaesthesia in the MR-scanner room differs from conventional anaesthesia in several ways. These include the use of MR-conditional equipment and devices within the room, interference with monitoring (including ECG- see above) and inaccessibility of the patient.

MR-conditional anaesthesia equipment is available on the commercial market, and include the Fabius® MRI from Dräger (Telford, PA, USA), which can be operated safely up to the 400 Gauss line. Alternatively, the use of a non-MR conditional anaesthetic machine has been described, with the machine chained to the wall at a distance determined safe by local physicists, usually beyond the 5 Gauss line (U. Reddy, White, and Wilson 2012). Such an approach increases the dead-space within tubing significantly, and exposes the patient to unquantified risks related to interference with machine function from the (weak) magnetic field, but it is an approach that has been employed safely over a long period of time (Razavi et al. 2003). Patient monitoring requires an MR-conditional system, and the most widely employed are those manufactured by Invivo (Expression, Gainesville, FL, USA). These are relatively expensive (>£80,000), but provide a comprehensive range of monitoring close to that achievable conventionally (CO_2, invasive blood pressure, non-invasive blood pressure, saturations, heart rate, and respiratory rate). MR-conditionality is generally restricted by power supply transformers, and in the case of the Expression is restricted to <5000 Gauss.

Effective and reliable monitoring is particularly important in the context of a patient who is largely hidden from view within the scanner bore. The airway is vulnerable with no visual confirmation of endotracheal tube position, temperature is often difficult to regulate without conventional warming, and the table is relatively hard, increasing risk to pressure areas. Furthermore, the anaesthetist generally sits within the control room to avoid scanner noise and special consideration is therefore needed for effective communication with the interventional team. All these factors need to be considered carefully in the planning of interventional procedures.

The final consideration is evacuation in the event of emergency, with particular focus on arrhythmias. There is currently no commercial MR-conditional defibrillator solution that has been released, although there is ongoing work to develop the capabilities (Schmidt et al. 2016). Therefore, robust protocols and training must be in place for evacuation of the patient to a safe zone for medical resuscitation if required.

3.7 Brief history of MR-guided EP procedures

Table 3-1 summarises the key publications from the leading groups worldwide working in MR-guided EP. Pioneering studies by the group in Johns Hopkins, led by Henry Halperin, established the benchmarks for the field in 2000 and highlighted the technical challenges that remained to be overcome (Lardo et al. 2000). Active tracking for electrophysiological procedures was established in-vivo in 2008 by the Boston group, with the creation of an early EAM-style interface that has become the standard for ongoing MR-guided EP work (Figure 3-3)(Dukkipati et al. 2008). They went on to investigate real-time visualisation of lesion formation (Schmidt et al. 2009), a challenging area that has also been investigated by the Utah group (Vergara et al. 2011).

Translation to clinical implementation has been difficult. The burden of proof of safety for human use for every item of equipment is high, and Nazarian published the first report of a diagnostic MR-guided EP study in humans in 2008 (Nazarian et al. 2008). MR-compatible catheters were created using a polyether block amide plastic body, copper wires and platinum electrodes. A susceptibility artefact approximately 1mm around the catheter was used for passive position identification on 2D fast GRE sequences, and it was possible to perform catheter mapping of a previously ablated CTI. Catheter position was confirmed through a combination of real-time MRI guidance and intracardiac electrograms. Electrical interference from gradient switching was suppressed through the use of 30-300Hz bandpass filtering, allowing even the low-voltage His bundle electrogram to be identified. However, the procedures were lengthy and the studies were discontinued.

The first human ablation procedure was performed by the group from Würzberg in 2012, completing a CTI ablation following two previous failed conventional procedures (Nordbeck et al. 2012). Given the relatively low success rates reported by subsequent investigators (Grothoff et al. 2014; Hilbert et al. 2015; H. Chubb et al. 2014), this early ablation procedure is remarkable for achieving conduction block in a difficult patient, but the case has never been published in manuscript form. The Leipzig group went on to perform further CTI ablation procedures using the Imricor Vision catheter (Imricor Inc., Minneapolis, MN, USA) under passive guidance (Grothoff et al. 2014). Ten patients underwent MR-guided ablation, but it was possible to achieve conduction block in only one of the ten patients using MR-guided ablation alone. The nine remaining patients required further ablation under conventional fluoroscopic guidance, and one of the main issues identified was the work-flow difficulty with passive tracking of the catheter. The first human study to use active catheter tracking is detailed in Chapter 6.

Group	Reference	Subjects	Procedure	Magnet and Platform	Catheter		MR Sequences			Comments
					Tracking	Manufacturer	Tracking	Real-time Imaging	Acute Imaging	
Johns Hopkins	(Lardo et al. 2000)	6 dogs	Ablation (ventricular (RV))	1.5T GE	Passive	7Fr Custom catheter (Dacron bodies and copper wires)	Fast GRE (ST 7mm, 5fps)	None	T_2W: FSE T_1W: early then late 2D post -gad	First MR-guided ablation
	(Nazarian et al. 2008)	10 dogs and 2 humans	Diagnostic (Atrial (RA) and ventricular (His bundle, RV apex))	1.5T Siemens	Passive + Enhanced Passive	Passive: 7Fr Irvine Medical Enhanced passive: 10Fr with 64MHz loop antenna	Interactive fast GRE (ST 10mm, 5fps)	N/A	N/A	First human MR-guided EP
Boston	(Dukkipati et al. 2008)	14 swine	Diagnostic (ventricular substrate- 10 chronic infarct)	1.5T GE	Active	7Fr with five receiver coils (St Jude)	Proprietary (1.4mm isotropic, 13Hz)	N/A	N/A	First using active tracking
	(Schmidt et al. 2009)	8 swine	Diagnostic (7 LA) and ablation (1 LV apex, 3 AV node)	1.5T GE	Active	8Fr with five receiver coils (St Jude)	Proprietary tracking signal (1.4mm isotropic, 13-15Hz)	Ventricle: FGRE (T_1W: 10mm ST)	AVN: early 3D LGE (ST 3.6mm) T_1W: 3D LGE 30min post gad	Torqueable sheath with 5 tracking coils also used
	(Schmidt et al. 2013)	5 swine	Diagnostic (voltage-based device tracking in MR environment)	1.5T GE	VDT	8Fr with five receiver coils (St Jude)	VDT based guidance	N/A	N/A	Modified Ensite Velocity system
Würzberg	(Nordbeck et al. 2009)	8 swine	Ablation (atrial (RA and CS) and ventricular (RV apex, His bundle))	1.5T Siemens Philips	Passive	VascoMed/Biotronik (carbon fibre conductors, 7Fr)	bSSFP, FLASH and TrueVISP (ST 8mm, 2fps)	Demonstration of RF induced noise only	None	
	(Nordbeck et al. 2011)	9 swine	Ablation (one site only: RA, RV, septum or coronary sinus)	1.5T Siemens Philips	Passive	VascoMed/Biotronik (carbon fibre conductors, 7Fr)	bSSFP and FLASH	None	T_2W: TSE T_1W: first-pass perfusion T_1W: LGE at 0-120min	Imaging also performed for 24 humans post-flutter ablation
	(Nordbeck et al. 2012) (Abstract)	1 human	Ablation (CTI- Redo after two failed conventional ablations)	1.5T	Passive	VascoMed/Biotronik (carbon fibre conductors, 7Fr)	Not detailed	None	T_2W: post ablation	First human ablation

Hamburg	(Hoffmann et al. 2010)	20 swine	Ablation (CTI)	1.5T Siemens	Passive	7Fr Custom with tuned conductor wire loop	Interactive bSSFP (ST 6mm, 5fps)	None	T_2W: TSE	
King's College, London	(Steffen Weiss et al. 2011)	8 swine	Diagnostic	1.5T Philips	Passive and Active	7Fr custom catheter, with micro-receive coils	Modified turbo GRE, 15Hz	N/A	N/A	Evaluation of RF safety
	(H. Chubb et al. 2014)	3 human (Abstract)	Ablation (CTI)	1.5T Philips	Active	Imricor Vision Catheter (9Fr)	Modified turbo gradient echo, 15Hz	None	T_2W: TSE with DIR T_1W: 3D LGE at 5,10,15,20min	First human ablation with active tracking
Utah	(Vergara et al. 2011)	6 swine	Ablation (Atrium (LA and RA))	3T Siemens	Active	SurgiVision (7Fr)	Spoiled GRE (5.5fps)	T_2W (HASTE)	T_1W: 3D LGE at 20min	
	(Ranjan et al. 2012)	12 swine	Ablation (RA- gaps filled or unfilled)	3T Siemens	Active	8Fr (MRI Interventions, Irvine), four tracking micro-coils	Spoiled GRE (5fps)	None	T_1W: 3D LGE (2.5mmST)	Gaps ablated under MR-guidance
Leipzig	(Eitel and et al 2012)	1 human (Abstract)	Diagnostic (Sinus node AV node conduction)	1.5T Philips	Passive	Imricor Vision Catheter (9Fr)	Interactive bSSFP	N/A	N/A	
	(Grothoff et al. 2014)	10 humans	Ablation (CTI)	1.5T Philips	Passive	Imricor Vision Catheter (9Fr)	Interactive bSSFP (ST 10mm, 8fps)	None	T_2W: 24 hours post ablation (3 subjects)	First human ablation series (passive tracking)
	(Hilbert et al. 2015)	6 humans	Ablation (CTI)	1.5T Philips	Active	Imricor Vision Catheter (9Fr)	Modified turbo gradient echo, 15Hz	None	Two subjects only: T_2W: TSE with DIR T_1W: 3D LGE	50% success rate (one week follow-up)
Adelaide	(Ganesan et al. 2012)	11 sheep	Ablation (PV and CTI)	1.5T Siemens	Passive	Imricor Vision Catheter (9Fr)	bSSFP (non-interactive, ST 8mm)	Nil	T_2W : TSE, T_1W: 2D LGE at 60min	
Sunnybrook	(S. Oduneye, Biswas, and Ghate 2012)	10 swine	Diagnostic (eight healthy, two infarct)	1.5T GE	Active	Imricor Vision Catheter (9Fr)	Not detailed	N/A	N/A	

	(S. O. Oduneye et al. 2015)	6 swine	Diagnostic (ventricular infarct model)	1.5T GE	Active	Imricor Vision Catheter (9Fr)	Not detailed	N/A	N/A	Detailed IEGM characterisation of scar

Table 3-1. Summary of key in-vivo MR-guided EP publications from leading centres worldwide.

GE: General Electric, (F)GRE: (fast) gradient recalled echo, ST: slice thickness, T_2W: T_2-weighted, T_1W: T_1-weighted, RA: right atrium, RV: right ventricle, CTI: cavotricuspid isthmus, VDT: voltage-based device-tracking, LGE: late gadolinium enhancement, TSE: turbo spin echo, DIR: double inversion recovery, IEGM: intracardiac electrogram

3.8 RF ablation within the MR environment

RF ablation within the MR environment has been demonstrated to be safe and feasible under the correct precautions. RF ablation of liver lesions, solid tumours in the lung, kidney and symptomatic bone tumours have all been described (Kahn and Busse 2012). The frequency of RF ablation energy is around 350kHz, significantly lower than the Larmor frequency in clinical scanners (64-138MHz). However, the rectangular-pulsed waveform of the ablation energy contains higher harmonics that have been shown to destroy imaging (Nordbeck et al. 2009; Lardo et al. 2000). Low-pass filtering is therefore required to maintain imaging quality, and this enables the potential for live imaging of lesion formation.

3.8.1 Real-time lesion imaging

There is only a small body of literature that has demonstrated real-time MR imaging of cardiac lesion formation. Clearly it can only be performed for MR-guided EP procedures, and relatively few studies have focused on this aspect of research (see Table 3-1). Real-time lesion imaging is attractive as it could provide a means to titrate energy delivery, potentially decreasing procedural time, increasing efficacy and reducing procedural risk.

Steiner et al first demonstrated the technical feasibility of real-time in-vivo MR-imaging of RF lesion formation for a swine paraspinal muscle ablation (Steiner et al. 1997). Lardo et al discussed the extent of RF-induced image artefact, and performed imaging immediately post-ablation, but did not document live visualisation of lesion formation (Lardo et al. 2000). It was not until 2009 that Schmidt et al demonstrated real-time imaging of a ventricular RF lesion, using a fast T_1-weighted gradient recalled echo sequence (ECG-gated, 10mm slice thickness, one slice per 2 second acquisition). Details regarding the results of imaging are limited to only presentation within a figure and were not quantified, but they appeared promising.

Vergara et al published a more detailed study in 2011 (Vergara et al. 2011). Using a Siemens 3T Verio scanner, they employed a respiratory-gated T_2W-HASTE (half-Fourier acquisition single-shot turbo spin echo) sequence to detect real-time lesion formation visualisation, again in a swine model. This was followed by a 3D-LGE acquisition at 20min. However, despite the increased signal-to-noise ratio offered by a 3T scanner, only 30% of lesions could be visualised during ablation. Where lesion visualisation occurred, changes were identified within 10-15second of commencement of energy delivery. Lesion size was over-estimated at later intra-ablation imaging, which is surprising for the rapidity of the changes. The number of lesions analysed was limited to only four, and this finding is in keeping with other assessments of acute T_2-weighted imaging (Arujuna et al. 2012; James L Harrison et al. 2014), but it provides an interesting insight into the temporal evolution of ablation-induced injury. However, such early distant changes means that it is unlikely that T_2-weighted imaging will prove to be specific for chronic lesion formation.

An alternative strategy for real-time imaging is to leave the catheter in place and perform 'hyper-acute' imaging of the ablation lesion, seconds after the completion of energy delivery. The susceptibility artefact of the MR-compatible catheters is generally very small, facilitating such an approach, and this would enable immediate reapplication of energy if the lesion were judged inadequate. Such an approach was taken by Schmidt et al for the imaging of atrial lesions (Schmidt et al. 2009). They felt that the spatial resolution of the T_1-weighted 2D sequence was insufficient for imaging of atrial ablation, and instead used a continuous GBCA infusion during AV node ablation. A 3D LGE sequence (3mm slice thickness, 1.3x1.3mm in plane, ECG and respiratory gated) was then performed 2 minutes post ablation, with a 2min acquisition time. Hyperenhancement was demonstrated at the AV-node in all animals, but was not quantified histologically against the extent of injury. Nordbeck et al (Nordbeck et al. 2011) employed a similar approach using a first-pass perfusion technique directly after RF ablation in the coronary sinus of a pig. The ablation lesion was marked by a profound perfusion defect, and this modality appears promising. However, the conflict in finding of hyperenhancement versus no-flow hypoenhancement needs to be resolved.

In the longer term, it is likely that real-time lesion formation imaging will rely upon more novel sequences, and exploit acute physiological changes that are currently not being assessed. Gating for cardiac and respiratory motion will remain challenging, but thermometry has proved robust in non-cardiac settings. Proton density, T_1- and T_2-relaxation times and proton resonance frequency (PRF) shift are all sensitive to temperature change, and it is the shift in PRF that is most promising for cardiac applications (Rieke 2011). Protons are surrounded by electrons which act to disturb the local magnetic field (chemical shift- see Section 1.2.4.1), reducing B_0 at a highly localised level. With increased temperature, this reduction is augmented, with breaking of inter-molecular hydrogen bonds and increased density of free electrons. The change in PRF can be exploited through spectroscopic imaging or phase mapping, and it is the latter that has been demonstrated most widely in non-cardiac ablation. PRF thermometry remains highly sensitive to motion and early work is being performed to implement this imaging modality in a cardiac model.

3.8.2 Acute lesion imaging (<4 hours)

There is a great deal more evidence for acute imaging of ablation lesions, but the sensitivity and specificity of acute lesion imaging for prediction of chronic lesion formation remains controversial. Furthermore, much of the data on human ablation relates to imaging at 24 hours post ablation, which is not a clinically useful time interval. Imaging needs to be performed at the same procedure in order to guide further ablation, and therefore a maximum time interval of around 4 hours post-ablation is considered applicable for intra-procedural acute imaging.

In animal models, it has long been established that ventricular lesions can be visualised immediately following ablation (Lardo et al. 2000). Detailed delineation of the pharmacokinetics of Gad within acute RF injury lesions (Dickfeld et al. 2007) has been performed, and has been correlated with non-enhanced sequences such as T2-weighted, turbo-spin echo techniques (Nordbeck et al. 2011). First

pass hypoenhancement and native T1 sequences have been particularly promising, and Vijayakumar et al (Vijayakumar et al. 2014) have demonstrated the utility of non-contrast T1w imaging in the acute identification of chronic lesions in a canine model of ventricular scar (see also Figure 3-4).

Non-contrast agent based imaging techniques are particularly attractive as they can be repeated multiple times. Celik at al performed a detailed study of the characterisation of acute RF lesions using native contrast, performing imaging of left ventricular lesions within 60min of ablation in 13 pigs (Celik et al. 2014). They concluded that it was the higher ferric iron concentration in lesion core that caused a shortening of T_1-relaxation time, and that this was best exploited using an inversion recovery SSFP sequence. Implementation and clinical validation in humans remains to be established.

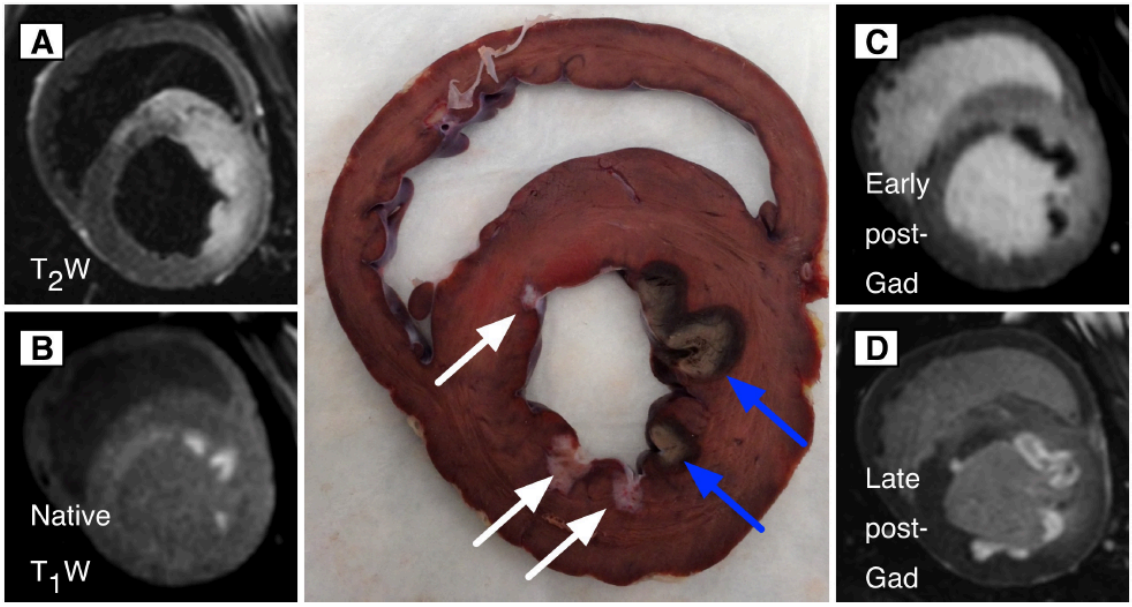

Figure 3-4. Acute imaging of canine ventricular ablation.

Central image shows a single macroscopic short-axis slice of the left ventricle. Chronic (3month) lesion locations are indicated by white arrows, and acute (<4hours) lesions by blue arrows, with a lesion core and haemorrhagic rim. A: T_2-weighted imaging. The oedema extends far beyond the ablation region and individual lesions (and gaps) cannot be discriminated. B: Native T_1-weighted imaging. Non-contrast imaging detects individual lesions and dimensions are well-correlated with lesion core. C: early (<5min) post GBCA acquisition demonstrates both no-reflow areas at the lesion core, and subtly increased signal in the regions of surrounding oedema (compare to A). D: late (45min) post GBCA acquisition, demonstrating both acute and chronic lesions. Note that the dimensions of the acute lesions appear likely to be overestimated. Images courtesy of Eugene G Kholmovski, University of Utah, by private correspondence.

3.9 Summary

MR-guided electrophysiology remains a research field in relative infancy, and advances have been slowed by the considerable technical challenges that it presents. The potential benefits, though, are substantial and research into this exciting field will accelerate greatly with the development of a robust, clinically approved, MR-guided EP system. Chapter 6 documents the first-in-man study of MR-guided catheter ablation with active catheter tracking.

SECTION TWO: METHODS AND EXPERIMENTAL DATA

4 General Methods

This chapter describes the recurring techniques and methodological principles that are relevant for all studies described in the subsequent data chapters.

4.1 Standard CMR acquisition sequences

4.1.1 3D Late Gadolinium Enhancement (LGE)

CMR imaging was performed on a 1.5T Ingenia Scanner (Philips Healthcare, Best, Netherlands), with the exception of the interventional procedural CMR studies detailed in Chapter 6. The 3D inversion recovery spoiled gradient echo acquisition was performed with coverage to include the whole of the LA in axial orientation. Repetition time was 5.5msec, echo time 3.0msec, flip angle 25° and low-high k-space ordering was employed. Further acquisition parameters were optimised as follows:

- Respiratory navigation: pencil navigator was placed upon the dome of the right hemi diaphragm. The one-dimensional slice was generally oriented with approximately 15 degrees of lateral to medial tilt from cranial to caudal, in order to minimise the volume of excited blood within the lung, and therefore the degree of respiratory navigator inflow artefact. Gating was set to 'track and gate', with a typical acceptance window of 5mm. Acquisitions for which the acceptance was >80% and <20% were terminated, in anticipation of poor respiratory selectivity or excessive acquisition time respectively.
- ECG gating. The time interval between the R-peak of the ECG and the start of data acquisition was defined using the cine images. Acquisition window was set for atrial standstill, at late ventricular systole, when the atrium is at its largest volume. A maximum acquisition window of 150msec was allowed. Across all acquisitions included in this thesis, average acquisition window onset was 301 (±41) msec post R wave, offset 412 (±44) msec post R wave, and duration 111 (±21) msec. For longer inversion times, typically encountered when scanning on 3T platform and late after GBCA administration, it was necessary to delay the start of the acquisition window. The window duration was shortened to preserve the end of the acquisition window within atrial standstill.
- Inversion time. The inversion time (TI) was selected from a Look-Locker (or TI scout) sequence performed immediately prior to every 3D acquisition. The TI was selected for optimal nulling of the myocardium of the ventricular septum, and a histogram of signal intensities within a selected region of interest was used in cases where optimal nulling time was unclear. 5msec was typically added to the assigned optimal TI, in order to compensate for myocardial T_1 drift during the acquisition.
- Spatial resolution. The spatial resolution was 1.3x1.3x4mm^3 with 2mm slice overlap, unless stated otherwise. This was reconstructed to 0.625x0.625x2mm^3. The sequence was acquired in axial orientation, and typically 50 slices were required to achieve full coverage of the LA. Further slices were added if the right atrium or left ventricle were also to be interrogated.

- Fat suppression. Spatial presaturation ('fat sat') bands were placed across the chest wall. SPIR was employed for fat suppression within the imaged region.

4.1.2 Contrast enhanced Gated Magnetic Resonance Angiogram (GMRA)

Prior to 20th August 2014, identification and segmentation of the chamber of interest (see Section 4.2) was performed directly upon the LGE imaging. However, this technique is prone to error and ambiguities in the interpretation of low contrast boundaries. Therefore all subsequent CMR scans were performed with gated magnetic resonance angiogram (GMRA) in order to assist segmentation. The technique was published by Groarke et al (Groarke et al. 2014) and acquisition settings were adjusted over the early cases, resulting in parameters that performed robustly for the vast majority of subjects. The acquisition is very similar to the conventional 3D LGE sequence above:

- Respiratory and ECG gating: identical, in order to facilitate registration
- Inversion time: on the 1.5T scanner an empirical inversion time of 200msec was selected for all cases.
- Spatial Resolution: a spatial resolution of 2x2x4mm was used for all GMRA acquisitions until 18th November 2015, at which time resolution reverted to identical to that for the LGE sequence. The rationale for the reduced resolution was rapidity of acquisition, homogeneity of image contrast and increased SNR in order to optimise semi-automated methods for identification of the blood pool / endocardium boundary. The reversion to standard resolution was driven by the technical difficulties encountered in the resampling of acquisitions to overlay upon the 3D LGE (see section 4.2.2), which were later resolved.
- Receiver bandwidth: receiver bandwidth was increased to 890Hz (fat-water ratio 0.5)
- Timing post GBCA: GBCA was given as a slow infusion (0.3ml/s) with the acquisition commenced at 90seconds from the start of the infusion, in line with the publication by Groarke et al. Similar homogeneity of blood pool signal was observed when GBCA was given as a bolus, but the standard slow infusion protocol was continued.

The GMRA sequence resulted in a high contrast acquisition with identical gating parameters to the 3D LGE acquisition, that could be used as a mask to interrogate the lower contrast LGE image (Figure 4-1). Other studies have used a non-gated conventional MRA sequence (4D Trak sequence) to achieve a high contrast mask of the blood pool (Malcolme-Lawes et al. 2013), but empirically the registration to the 3D LGE sequence appeared poor. The two sequences were formally compared at the same scan session for 20 subjects. LA volume was manually segmented from the two acquisitions, with LA appendage and PVs excluded. The GMRA sequence generated a significantly larger volume for all subjects (157±55ml versus 136±56ml, $p<0.0001$ (paired t-test)), with mean bias 21ml (95% confidence interval 2-41ml) (Figure 4-2). This volume discrepancy is a substantial mismatch in atrial size. For a theoretical sphere of the same volumes, this represents approximately a 1.5mm difference in mean radius, which is greater than half of the estimated thickness of the atrial wall (Platonov et al. 2008).

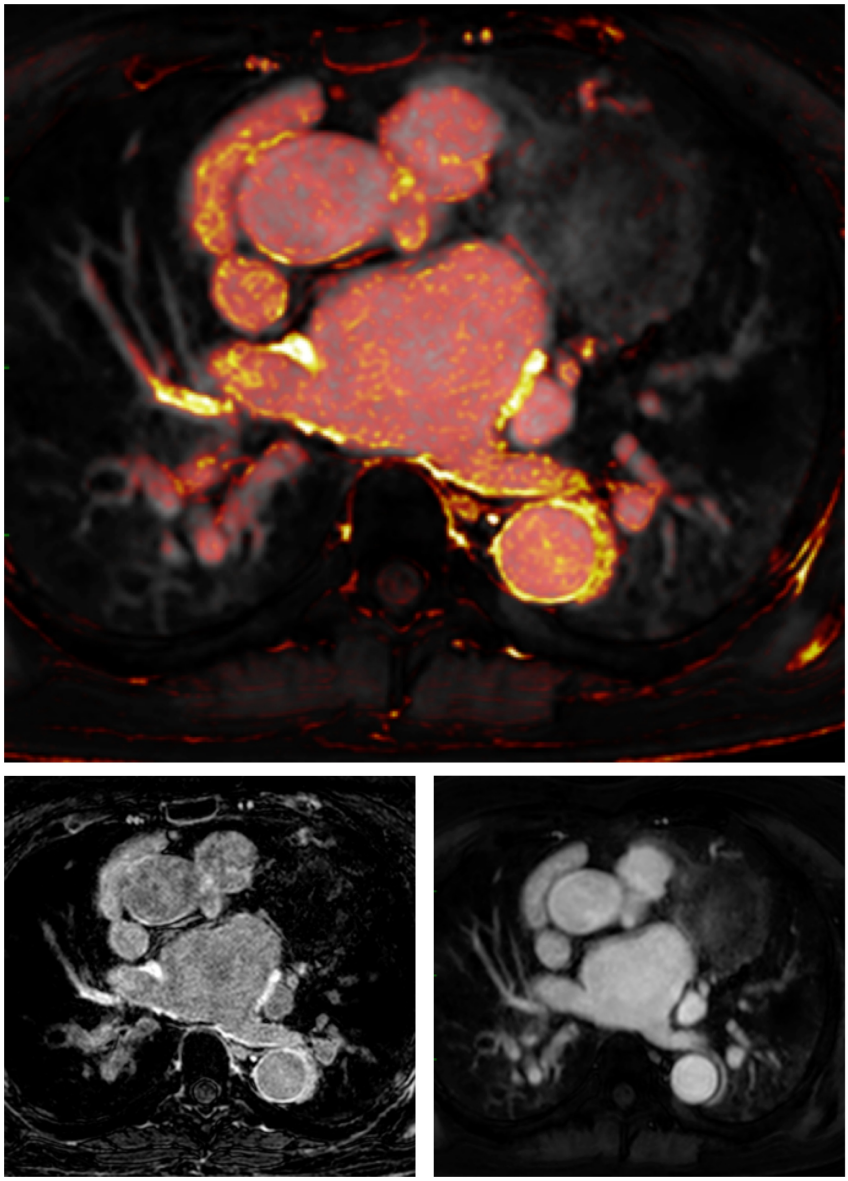

Figure 4-1 Illustration of utility of gated magnetic resonance angiogram acquisition (Subject 14- See Appendix A).

(Top panel) Image merge of LGE (bottom left, orange in overlay) and gated MRA acquisition (bottom right, white in overlay) demonstrating close alignment of acquisitions and potential value in semi-automated image intensity interrogation.

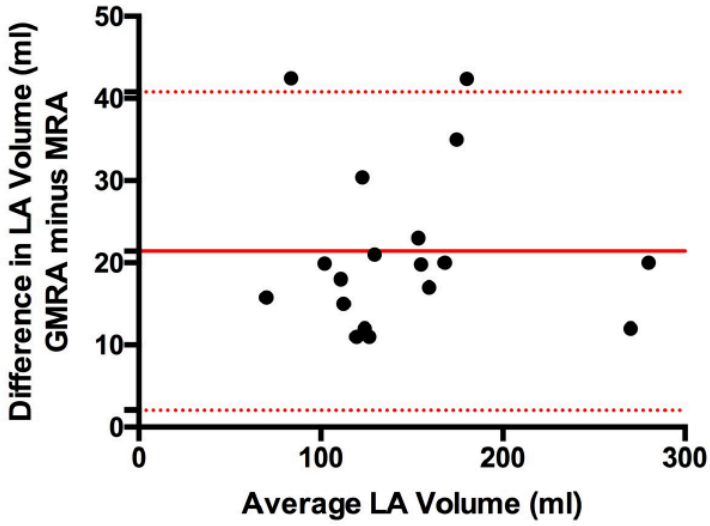

Figure 4-2. Comparison of gated and non-gated angiographic volumes of the LA.

Bland-Altman plot comparing left atrial (LA) volume, with LA appendage and PVs removed, for gated MRA and non-gated MRA sequences.

4.2 CMR analysis techniques

The quantitative assessment of a 3D CMR acquisition is dependent upon two fundamental parameters: the delineation of the region of interest and the derivation of the quantitative index from the voxel signal intensities. In the case of the assessment of atrial scar, this represents the requirement for segmentation of the chamber or wall, followed by image interrogation. These two stages of CMR analysis are discussed in sections 4.2.1 and 4.2.3, and they were combined in a single graphical user interface (GUI) called CEMRGApp that was developed with imaging and computer scientists specifically for the studies in this thesis (see section 4.2.4).

4.2.1 Segmentation techniques

Image segmentation is to divide an image into parts that have a strong correlation with objects or areas in the real world (Sonka, Hlavac, and Boyle 2008). Segmentation of a cardiac chamber or wall may be performed manually, or in an automated fashion, or in a hybrid-type approach involving both manual and automated elements, and the atria present particular challenges. These include the size of the structure of interest (atrial wall thickness <3mm) and the intensity homogeneity in comparison to neighbouring structures. Furthermore, the absence of a ground truth renders evaluation of the relative merits of different techniques more difficult.

4.2.1.1 Manual segmentation

For the atria, a manual segmentation has generally been seen as the gold standard and has been widely employed in the largest studies (Oakes et al. 2009; Marrouche et al. 2014; Khurram et al. 2014). However, the segmentation is user-dependent, suffers from degrees of subjectivity, and is highly time consuming. For an accurate, slice-by-slice segmentation of a single endocardial or

epicardial border, estimates of time taken to perform the segmentation are generally around 20-30min (Khurram et al. 2014; Oakes et al. 2009). Seg3D (NIH NCRR Centre for Integrative Biomedical Research, University of Utah, Utah, USA) and ITK-snap (University of Pennsylvania, USA) are the most widely employed software platforms for manual segmentation, but further bespoke toolkits have been used by some studies (Khurram et al. 2014).

For assessment of atrial wall signal, investigators have frequently chosen to define both the endocardial and epicardial borders (Marrouche et al. 2014; Khurram et al. 2014; Bisbal et al. 2014). Publications have not been explicit regarding the exact method used to define the second border. At a minimum, the subjectivity of border delineation in a low-contrast 3D LGE acquisition suggests that the second segmentation is performed with simultaneous display of the first segmentation, to ensure that the borders do not cross. More likely, the 'manual' definition of the second border is performed using an automated dilation or erosion technique, assuming a relatively uniform wall thickness, and then optimised manually. For example, the Johns Hopkins study by Khurram et al quotes the atrial wall thickness as 2.08±0.35mm (Khurram et al. 2014), a more uniform thickness than comparable autopsy studies (typically 2.8±1.3mm) (Platonov et al. 2008). Such an automated technique seems reasonable in the context of time constraints and limited image resolution, but the impact has not been formally reported.

Once a manual segmentation has been performed, further image processing steps are then required for visualisation. These generally include smoothing filters, and finer details in the anatomy may be lost (Karim et al. 2015)

4.2.1.2 Automated segmentation

An automated segmentation may be performed in a number of ways, with a spectrum of user input. A fully automated approach has been demonstrated on the Philips platform, using shape-constrained deformable models (SmartHeart, Philips Research Hamburg, Germany) to segment all the cardiac chambers within a high resolution 3D whole-heart b-SSFP sequence. The first clinical implementation of this technique is documented in Chapter 6, and variations of this technique have also been used by other studies using earlier versions of the software (Philips segmentation plug-in for Graphical Interface for Medical Image Analysis and Simulation (GIMIAS), Unversitat Pompeu Fabra, Barcelona) (Malcolme-Lawes et al. 2013; J L Harrison, Sohns, et al. 2015). However, it was noted that manual optimisation of the segmentation was often required, and the models struggle with LA anatomical variants (James L Harrison 2014; Karim et al. 2015). Further work has been performed on improving the automated segmentation techniques. Data and segmentations performed in the course of this thesis have be used to refine a novel deformable image registration technique for LA segmentation, using a super voxel belief propagation method (Heinrich et al. 2016), but quantification of the reliability and accuracy of this method is awaited. Following validation work, it should be feasible to implement such a technique within the graphical user interface that was developed for this study (see section 4.2.4)

Alternatively, a method employing a greater degree of user input may be performed. The most commonly used methods are region growing or K-means clustering techniques, both relying upon adequate contrast between neighbouring structures. Here, the user defines the region of interest and this region is expanded based upon defined parameters. In the course of this thesis, work was performed to enable the use of the GMRA sequence to define a LA mask (Karim et al. 2015). This uses a 'leak-sensing', threshold based, technique, exploiting Morse partitions of the image, and could be performed with <3min of user input. Results also demonstrated good similarity with manual annotations of LA anatomy, with improved smoothness, which is important for reliable image interrogation.

4.2.1.3 Semi-automated segmentation

A semi-automated segmentation technique relies upon a hybrid approach: an automated delineation of the region of interest, with manual optimisation. In reality, the reliability of all automated LA segmentation techniques is currently not sufficient to enable a blinded implementation of the automated algorithms, and a user sense-check step is necessary. At this stage, a degree of refinement of the segmentation may be performed where it is felt that there is error in the accuracy of the model. Most commonly, errors at the thin atrial septum, the interface of the descending aorta and LA, and the interface of the right pulmonary artery and LA roof are detected. In addition, the LAA and left upper PV are commonly fused due to their close apposition.

For all quantitative analyses in this thesis, a manual or semi-automated segmentation technique was employed. Where available, the GMRA was used to derive the atrial mask, and the segmentation was performed using the 'Region Growing Tool' with 3D interpolation on the MITK platform with 'Segmentation Plugin' (German Cancer Research Center, Division of Medical and Biological Informatics, Im Neuenheimer Feld 280, 69120 Heidelberg, Germany). Where a GMRA acquisition was not performed or was inadequate, manual segmentation was performed on a slice-by-slice basis on the same platform.

4.2.2 Image resampling and registration

Image resampling and registration is not necessary for single 3D LGE acquisitions that have undergone manual segmentation. However, for multiple sequential acquisitions (see Chapters 7 and 8) or where a GMRA acquisition is used for atrial segmentation, the images must be resampled to matching resolution and registered to correct for patient movement. For this thesis, the images were resampled at a 1mm isotropic resolution, which is superior to the acquired resolution for all sequences, and the images were saved as .nifti files. The registration was performed as a rigid registration (Denton et al. 1999), with six degrees of freedom (3 translations and 3 rotations). The derived transformation of the GMRA image onto the LGE image was then applied to the segmentation.

Within the graphical user interface (GUI) developed for this study (see below), the registration took 35±17 seconds for each acquisition, assessed across 255 registrations performed for Chapters 7 and 8. As a single registration the processing time required is acceptable, but for larger studies the processing time becomes substantial. It was therefore assessed whether the registration step was necessary for all acquisitions, particularly when native registration appeared good subjectively. The translation and rotation for all registrations was recorded, alongside subjective blinded assessment as to whether registration was required (Figure 4-1). Subjective grading was 'None' when there was an excellent registration, 'Minor' for <1mm subjective mismatch, and 'Major' for >1mm subjective mismatch. Results are presented in Table 4-1 and Figure 4-3, and two outliers with substantial movement (absolute translation 21mm and 24mm respectively) were excluded from the analysis. Subjective assessment was significantly associated with the magnitude of the correction required on objective rigid registration, but mismatch was generally underestimated. Furthermore, there were 26 acquisitions with an absolute translation >1mm that were judged subjectively to require no registration: in 23 (88%) of these cases the largest translation vector was in the axial (z-axis) direction, which was most difficult to assess subjectively. Given an atrial wall thickness of 2-3mm, an image mismatch of >1mm was judged as significant. Therefore image registration was performed for all acquisitions, regardless of subjective impression of image co-location.

	Subjective Registration Requirement			**p-value (Kruskal-Wallis)**
	None (n=77)	Minor (n=64)	Major (n=114)	
Absolute Translation	0.94±0.6mm	1.56±0.88mm	2.76±2.90mm	<0.0001
Absolute Rotation	0.45±0.21°	0.55±0.41°	0.78±0.48°	<0.0001

Table 4-1. Rigid registration translations and estimation of registration requirement.

Association of absolute translation and rotation required for rigid registration, and the subjective assessment as to whether registration was required, graded from None to Minor to Major registration required.

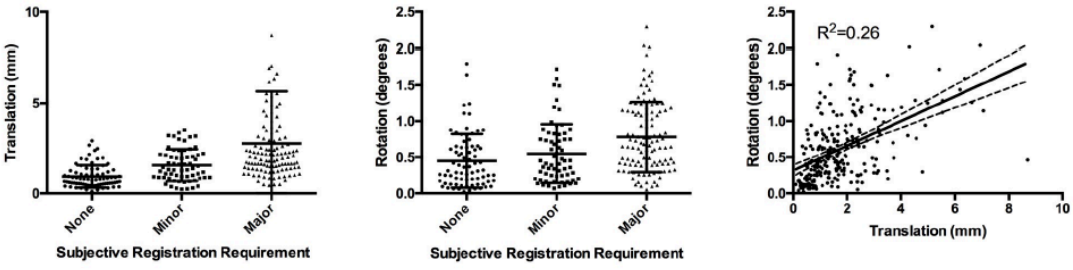

Figure 4-3. Rigid registration translations and estimation of registration requirement.

(Left) Absolute translation and (middle) absolute rotation against subjective requirement for registration. The scatter-plot on the right demonstrates the association of translation and rotation.

4.2.3 Image interrogation

Several methods have been proposed and implemented for the interrogation of image intensity following delineation of the region of interest (ROI). At its simplest, the value of every voxel with the ROI is represented, but this poses a problem for quantification and interpretation of the resulting new three-dimensional dataset (Oakes et al. 2009; Khurram et al. 2014). Each surface point on an atrial shell overlies several voxels of differing signal intensity, and investigators have generally chosen to use a highly localised (Oakes et al. 2009) or regional (Khurram et al. 2014) average to assign a single index to locations. Alternatively, multiple single lines of interrogation can be drawn between the endocardial and epicardial borders, and the signal represented by a single voxel value at each point along the line (Bisbal et al. 2014).

In recognition of this averaging process, some groups have chosen to perform a mean or maximum intensity projection interrogation of the imaging, based upon a single segmentation (Figure 4-4) (Malcolme-Lawes et al. 2013; J L Harrison, Sohns, et al. 2015; Knowles et al. 2010). For this study, the maximum and mean intensity projection interrogation algorithms integrated within the CEMRGApp were assessed and validated (Figure 4-5). To date, there is no published work that has sought to assess the correct intensity projection parameters for the assessment of atrial scar.

The impact of variations in distance of internal and external image interrogation was assessed and was found to be relatively small. Despite substantial impact upon the interrogation volume (approx 20ml with 1mm internal or external interrogation, versus 140ml with 4mm internal and external interrogation, Table 4-2 and Table 4-3), the change in percentage scar on the atrial shell was relatively small (approx 11% to 14% at minimum to maximum interrogation volume respectively, scar thresholded to 3.3 standard deviations above the blood pool mean) and almost imperceptible on visual inspection (Figure 4-7, Figure 4-8, Figure 4-9). Many studies have chosen to use a 3mm internal and 3mm external maximum intensity projection (Malcolme-Lawes et al. 2013; J L Harrison, Sohns, et al. 2015), which controls well for inaccuracies of segmentation, but risks integration of signal from distant structures. Therefore for this study an endocardial segmentation was performed and a 1mm internal and 3mm external maximum intensity projection performed for atrial post-ablation scar assessment. The smaller internal projection was performed in order to avoid detection of respiratory navigator artefact whenever possible. The 3mm external interrogation was based upon the maximum typical atrial wall thickness (Platonov et al. 2008). A more conservative 0mm internal and 2mm external mean intensity projection interrogation was used for assessment of pre-ablation atrial fibrosis, and is described in more detail in Chapter 5.

Atrial shells were exported as a .vtk file, with a raw image intensity unit recorded at each surface triangle of the shell. Atrial scar was thresholded at 3.3 standard deviations above the blood pool mean where a single validated indexing method was required (James L Harrison et al. 2014).

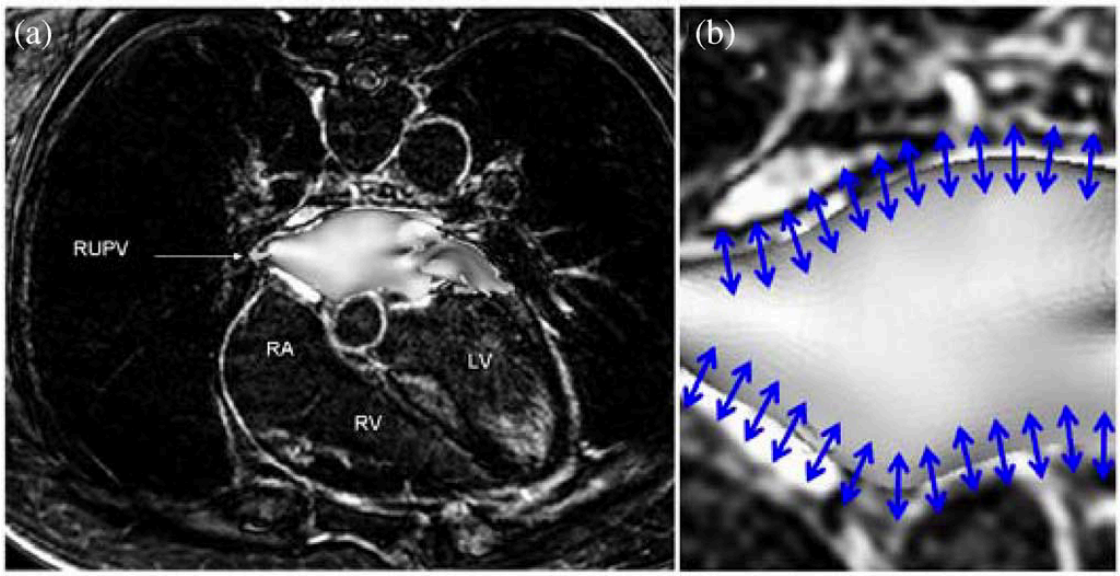

Figure 4-4 Illustration of surface fused with delayed enhancement image.

Arrows indicate the direction in which the maximum or mean intensity projection is taken.

Reproduced with permission from Knowles et al 2011 (© IEEE 2011)

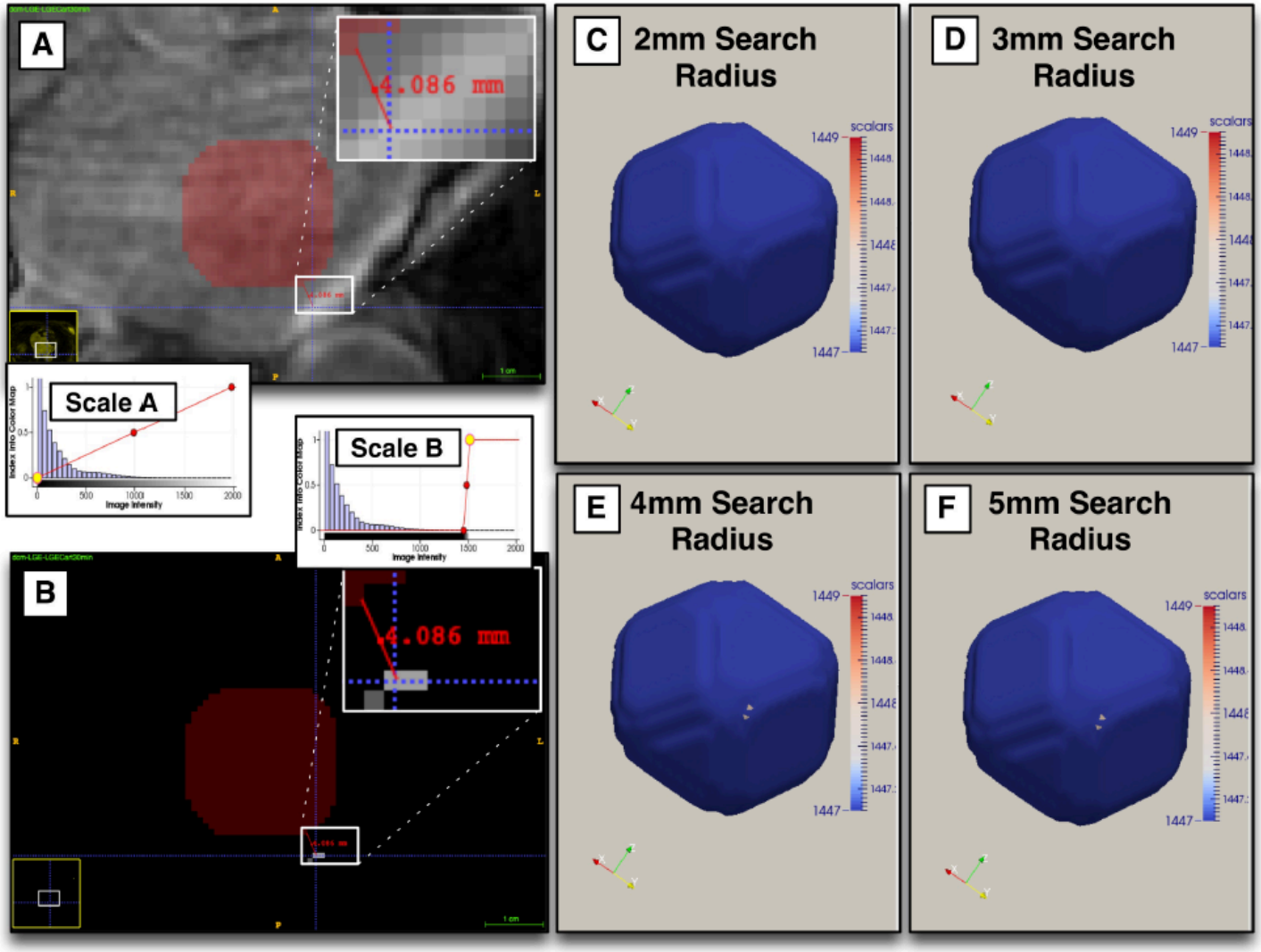

Figure 4-5. Representative validation dataset for interrogation distance and maximum intensity projection algorithm.

A standard geometry was placed within the LA, and the distance to the voxel with the highest signal intensity was measured (left hand panels, A and B). Serial maximum intensity projection interrogations of the image were performed at 2mm, 3mm, 4mm and 5mm 'Search Radius', and the generated .vtk file was thresholded at the level of the highest intensity voxel (C-E, four right hand panels). projection distances The voxel at the crosshairs is 1447 signal intensity units, and it is visualised as the bright spot on the lower two .vtk shells on the left, with accurate representation of the signal.

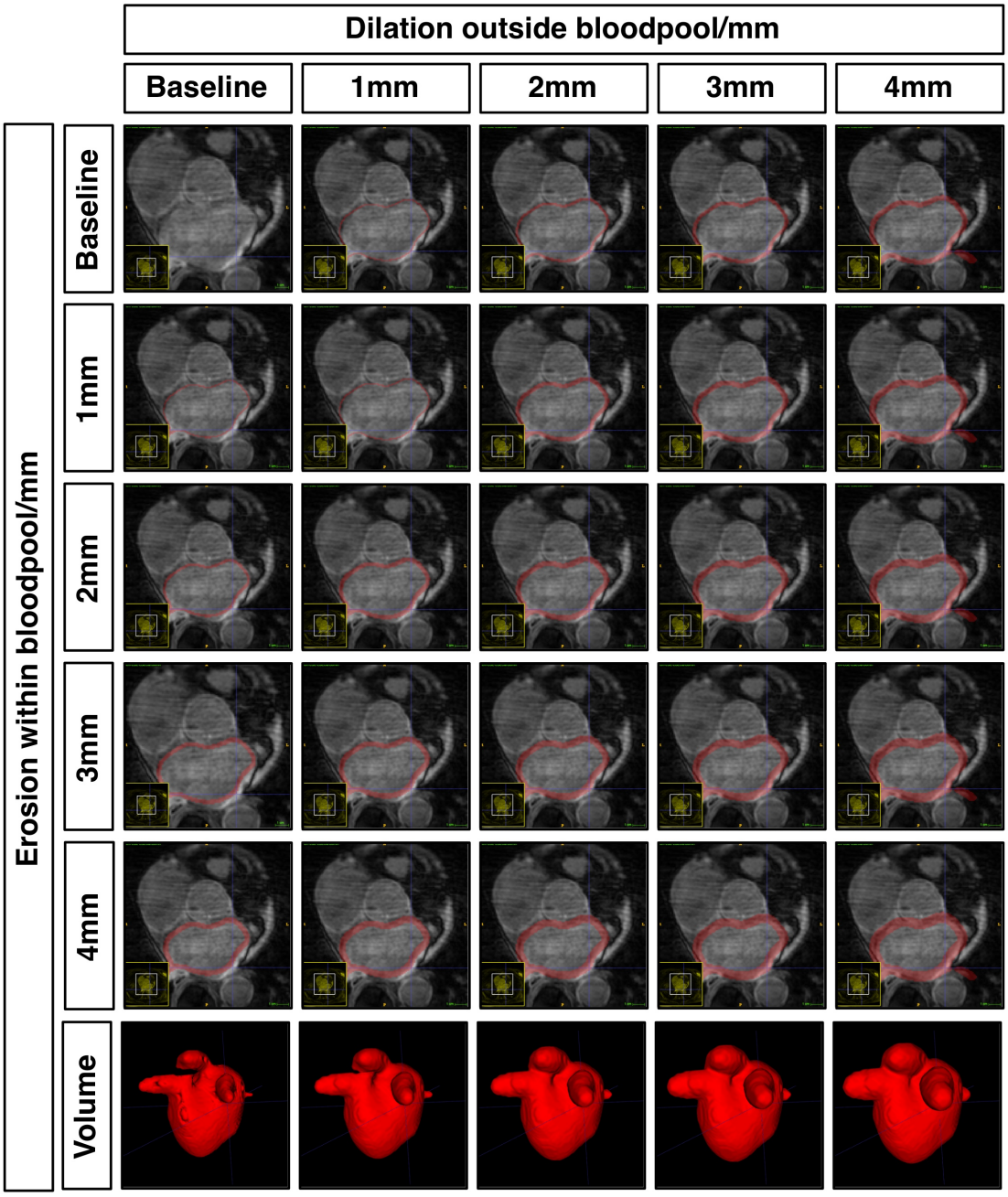

Figure 4-6. Illustration of the effect of variable erosions and dilations on the interrogation volume for scar assessment.

The external volume of the dilated segmentation is shown in the five bottom panels: note the loss of some anatomical features with increases in dilation distance. The upper 25 panels show a single representative slice for the subtracted segmentations ([dilated volume]-[eroded volume]), with segmentation shown in red.

	Baseline/ml	1mm inside/ml	2mm inside/ml	3mm inside/ml	4mm inside/ml
Baseline /ml	-	20.07	34.62	46.18	58.66
1mm outside/ml	21.5	42.22	56.77	68.33	80.8
2mm outside/ml	41.66	61.73	76.28	87.84	100.3
3mm outside/ml	59.5	79.57	94.12	105.7	118.2
4mm outside/ml	82.48	102.5	117.1	128.7	141.1

Table 4-2. Volumes of wall segmentations at variable erosion and dilation distances for single representative shell.

Total volume of interrogated voxels, calculated as the volume of a full dilation of the shell (0-4mm outside shell), minus the erosion of the shell (0-4mm inside shell). Volumes show a relatively linear response to dilation and erosion, despite irregularity of shell.

	Baseline/%	1mm inside/%	2mm inside/%	3mm inside/%	4mm inside/%
Baseline /%	-	10.98	11.53	12.12	12.58
1mm outside/%	10.70	11.51	12.06	12.64	13.11
2mm outside/%	11.39	12.21	12.72	13.28	13.73
3mm outside/%	11.80	12.59	13.10	13.65	14.08
4mm outside/%	12.12	12.90	13.41	13.94	14.36

Table 4-3. Scar burden at variable maximum intensity projection distance for single representative shell.

% is the percentage of the total surface area of the LA containing scar. thresholded at 3.3standard deviations above the blood pool mean.

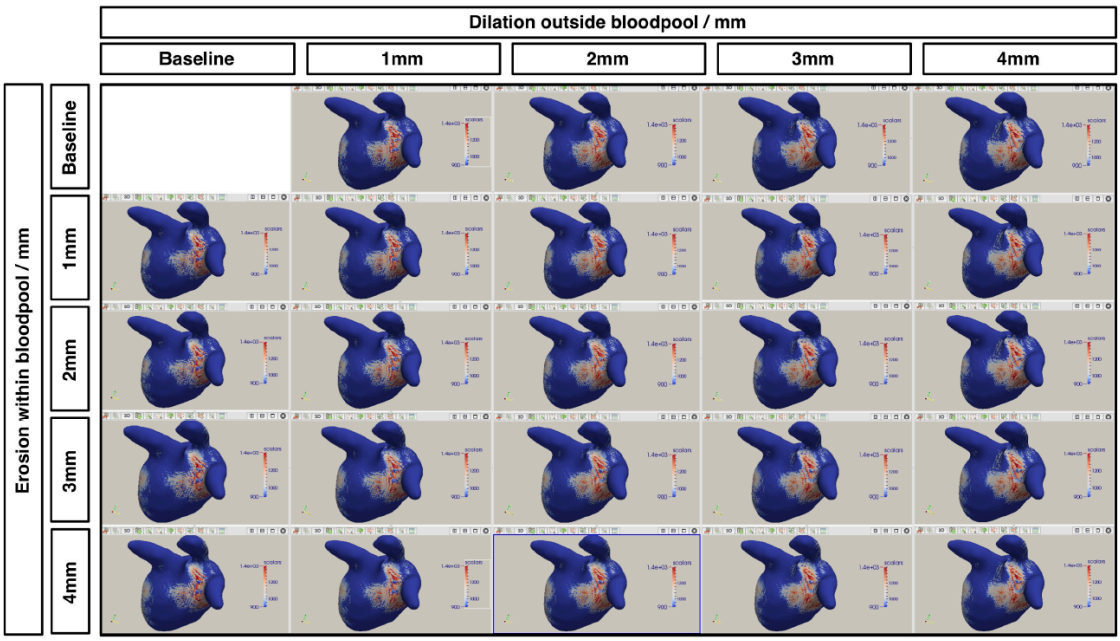

Figure 4-7. Left lateral view of representative LA shell at variable maximum intensity projection distances.

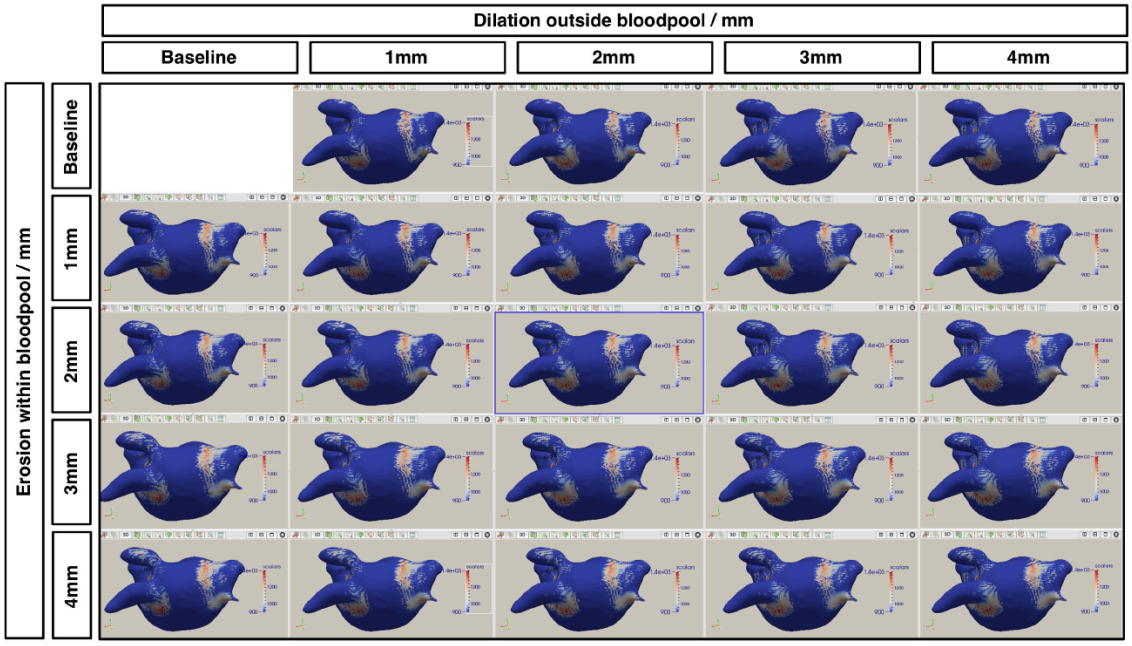

Figure 4-8. Posterior view of representative LA shell at variable maximum intensity projection distances.

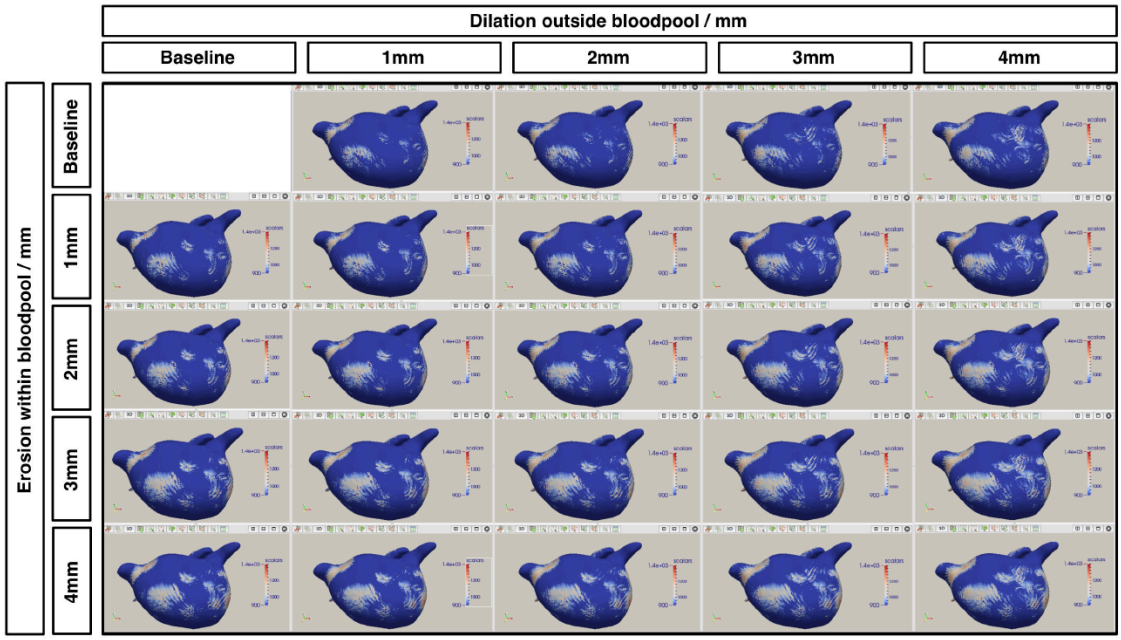

Figure 4-9. Anterior view of representative LA shell at variable maximum intensity projection distances.

4.2.4 GUI development

The CEMRGApp GUI was developed in order to facilitate, visualise and validate the multiple CMR analysis steps required for assessment of atrial scar. I developed the GUI in collaboration with imaging and computer scientists (Dr Rashed Karim, Dr Orod Razeghi, Dr Steven Niederer and Prof Kawal Rhode), with a view to creating a user-friendly interface that could be shared with other groups. Several solutions were investigated, and assessed for cross-platform compatibility, ease of software distribution, long-term maintenance, and scope of pre-developed tools. The platform that was settled upon is one developed by researchers and engineers of Mint Medical and the German Cancer Research Centre (DKFZ) in Heidelberg. The Medical Imaging Interaction Toolkit (MITK) is a free open-source software system suitable for development of interactive medical image processing tools, combining the Insight Toolkit (ITK) and the Visualisation Toolkit (VTK). MITK also offers features relevant to medical imaging but covered neither by ITK nor VTK.

MITK can be used at three distinctive levels. At the application level MITK Workbench enables end-users to perform regular image processing tasks, at the toolkit level MITK supplements the standard ITK and VTK with concepts for interactive applications, and at the framework level MITK offers an infrastructure for end-user applications. CEMRGAPP was developed as an MITK based framework extended with ready to use plugins. It was made available as source code on Bitbucket and in binaries for Linux and Mac OSX, and the interface is demonstrated in Figure 4-10.

Plugins were constructed that performed the resampling, facilitated segmentation, performed rigid registration of images, applied the derived rigid registration algorithm to specific segmentations,

enabled bespoke smoothing of manual segmentations, performed image interrogation (mean intensity projection and maximum intensity projection) and enabled quantification of scar and sphericity (see section 5.3.7).

4.2.5 Image interpretation

The analysis techniques detailed in this section (segmentation, image resampling and registration, image interrogation) are all necessary to obtain as faithful a representation as possible of the signal intensity of the original raw CMR imaging. This signal intensity, on LGE imaging, is interpreted to be proportional to the extracellular volume, itself related to fibrosis (see Section 1.2.3), but the relationship is not well understood in the atrial wall. It is therefore important for the analysis techniques to be compared to those of other established groups, which themselves have been validated to fibrosis to a varying degree.

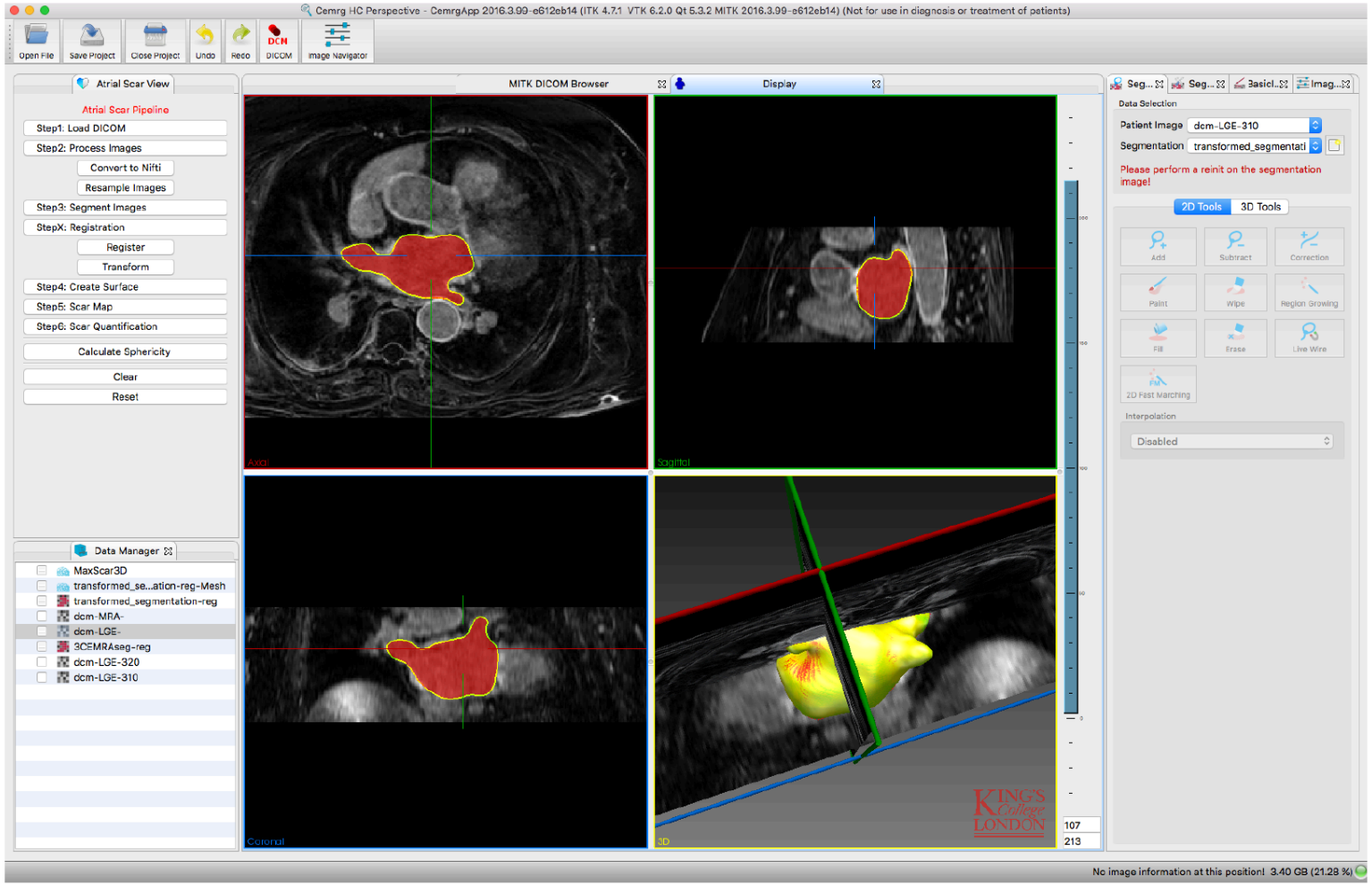

Figure 4-10. CEMRGApp interface.

On the left side the bespoke tools for atrial scar assessment are shown, with Data Manager lying beneath. A multiplanar reconstruction is shown in the middle panels, with segmentation in red. The 3D reconstruction of the scar shell (.vtk) is shown on the bottom right, with normal atrial tissue in yellow and scar in red. Standard segmentation and morphological tools are shown on the right

4.3 Comparison to published CMR analysis techniques

The image analysis technique described in the previous section was developed de novo in view of the absence of openly available solutions from other centres. Two main groups have published multiple studies assessing pre-ablation atrial fibrosis (Utah and Johns Hopkins), but the imaging processing platforms are not released in their full forms. Both these groups have also assessed post-ablation atrial scar, using the same image interrogation techniques, and there are several further groups that have participated more actively in this field, including Boston (Taclas et al. 2010), Imperial College London (Hunter et al. 2013), Barcelona (Bisbal et al. 2014) and King's College London (Knowles et al. 2010; Arujuna et al. 2012; J L Harrison, Sohns, et al. 2015). This section aims to summarise the key features of the techniques of the two main centres (Utah and Johns Hopkins), for comparison to those used in this study. The methods of the Boston, Imperial College London, Barcelona and KCL groups are discussed further specifically in relation to post-atrial scar assessment in Chapters 7 and 8.

4.3.1 Utah method- slice-by-slice thresholding

The Utah method has been summarised and implemented in multiple publications (see Table 4-4), but the most detailed breakdown of their technique was included as a supplement in the Oakes et al paper, published in 2009 (Oakes et al. 2009). The same software and techniques have also been used by the Bordeaux group (Cochet et al. 2015; Jadidi et al. 2013). In brief, the scar quantification is based upon an endocardial and epicardial segmentation of the LA, and a threshold is then assigned on a slice-by-slice basis. "Normal" tissue is defined as the lower region of a pixel intensity histogram, between 2% and 40% of the maximum intensity within the LA wall. The fibrosis threshold is defined as voxels 'two to four standard deviations above the mean of "normal"', and can vary between slices (Figure 4-11)

There is no doubt that the technique has enabled an assessment of LA SRM that has correlated strongly with real outcomes and other independent cardiac and non-cardiac parameters. However, there are concerns that remain unresolved:

- Reproducibility.

  Inter and intra-observer reproducibility has been assessed in several of the publications, notably in 2009 and 2014 (Oakes et al. 2009; C. McGann et al. 2014). However, there are no published reproducibility studies documenting the reproducibility of findings between different scans for the same patient. The recent DECAFF study (Marrouche et al. 2014) has investigated the issue of inter-centre reproducibility, in terms of whether the CMR sequences can be reproduced in other centres, but has not resolved the question of reproducibility of the analysis technique itself.
- Subjectivity

The slice-by slice analysis of the segmented atrial wall requires a subjective assessment of the threshold for assignation of signal intensity to fibrosis, and the criteria that the operator uses to select the threshold are not defined.

- Physiological correlates

  A small subgroup (10 patients undergoing cardiac surgery (C. McGann et al. 2014)) have had their local LGE-defined fibrosis compared to histological findings, and there has been a strong correlation, despite concerns that registration issues might make such a comparison difficult to perform. Further robust assessment of the association between LGE-defined fibrosis, histology and other surrogate markers of fibrosis such as intracardiac electrogram fractionation and voltage is required.

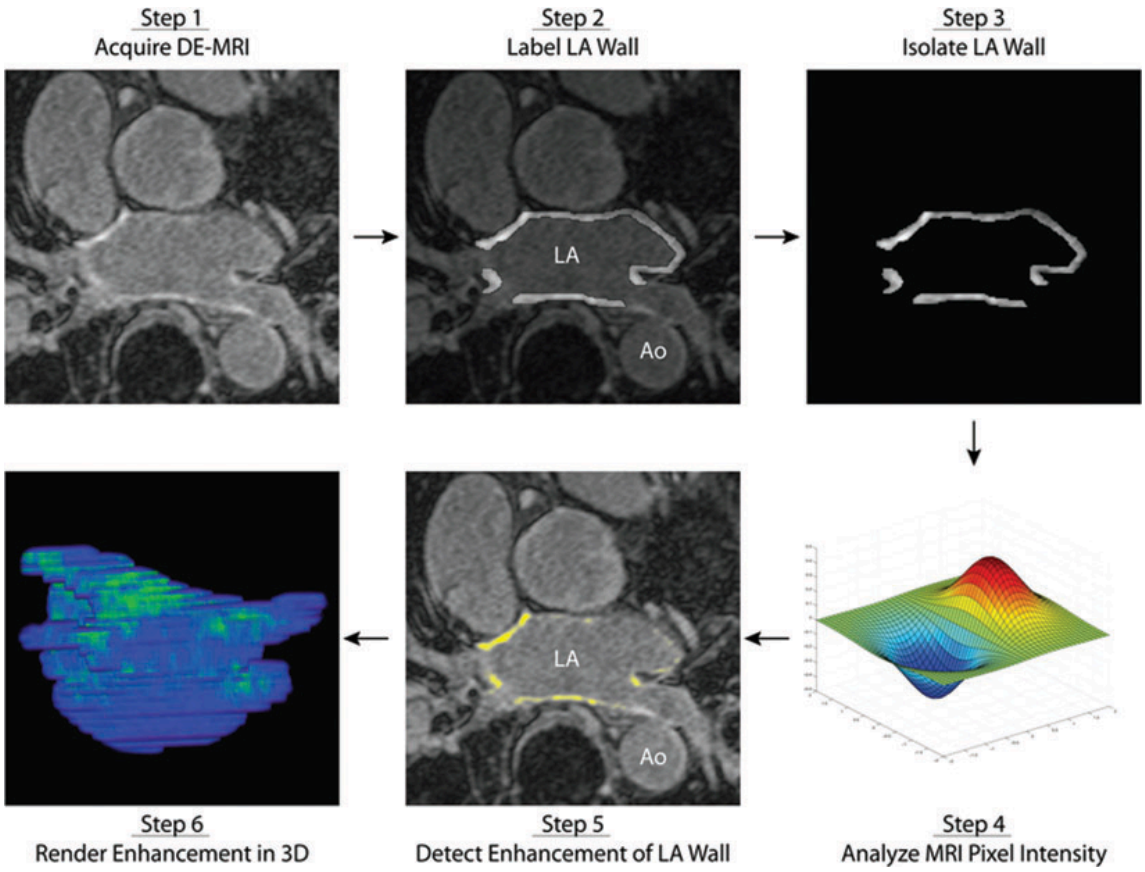

Figure 4-11. The Utah method of atrial fibrosis quantification.

After LGE images are obtained (Step 1), the endocardial and epicardial borders are manually contoured and isolated (Steps 2 and 3), and the extent of LGE is then quantified using the pixel intensity distribution (Step 4), qualitative confirmation is then performed, a colour lookup table mask is then applied to better differentiate enhanced and nonenhanced tissue (Step 5), and finally a 3-dimensional rendering of the LA is generated allowing for better visualization and spatial localization of the LGE (Step 6). Reproduced with permission from Vergara et al (2011) (Vergara and Marrouche 2011).

Publication	Patients	Outcome measure	Conclusion
Oakes et al 2009	81 patients, 6 volunteers	AF recurrence at 6-19 months	Degree of SRM may predict responders to AF ablation
Kuppahally et al 2010	68 patients 31 mild SRM (<10%) 37 severe SRM (>10%)	Echocardiographic LA strain post ablation	Severe SRM group had no improvement in LA strain post ablation
Mahnkopf et al 2010	40 patients with lone AF 293 patients with AF and comorbidities	SRM quantification and comorbidities	SRM is independent of comorbidities and is a predictor of AF recurrence
Daccarett et al 2011	387 patients with AF	Correlation of SRM with stroke and $CHADS_2$ score	SRM is independently associated with prior stroke
Akoum et al 2012	344 patients with AF (LA fibrosis) 134 patients (RA fibrosis)	Pacemaker implantation at 329 ±245 days	SRM is associated with clinically significant sinus nodal disease
Akoum et al 2013	178 patients with AF undergoing TOE and CMR imaging prior to ablation	Spontaneous echo contrast (SEC) or LAA thrombus	SRM is independently associated with SEC/thrombus
Akkaya, et al 2013	384 patients (105 with LVEF <50%, 279 with LVEF >50%)	LVEF prior to and after ablation	Increased SRM is associated with reduced LVEF and less recovery of LVEF post ablation
Akkaya et al 2013	404 patients (122 with LV mass index >116g/m^2)	Pre-ablation LV mass	Increased SRM is associated with increased LV mass index
Marrouche et al 2014	DECAAF study SRM quantified in 272 of 329 patients (15 centres)	Hazard ratio of recurrence	Increased SRM is independently associated with AF recurrence
C. McGann et al 2014	426 patients with AF, 21 controls	AF recurrence and histological correlation of SRM with biopsy (10 patients only)	SRM correlates with histological findings
Akoum et al 2015	DECAAF study 177 patients with CMR imaging at 3 months post ablation	Recurrence at 325 days	Residual (non-ablated) atrial fibrosis is associated with recurrence
Rizvi et al 2016	145 patients (all underwent exercise test prior to ablation)	Exercise capacity (EC) Recurrence at 1 year	Weak correlation (R^2=0.071) between SRM and EC. EC is not an independent predictor of outcome

Table 4-4 Summary of the major publications from the Utah group regarding pre-ablation atrial fibrosis.

SRM: structural remodelling (LA structural remodelling as assessed by late–gadolinium MRI detection of fibrosis), TOE: transoesophageal echocardiogram, LAA: left atrial

appendage. (Oakes et al. 2009; Kuppahally et al. 2010; Mahnkopf et al. 2010; Daccarett et al. 2011; Akoum et al. 2012; Akoum et al. 2013; Akkaya, Higuchi, Koopmann, Damal, et al. 2013; Akkaya, Higuchi, Koopmann, Burgon, et al. 2013; Marrouche et al. 2014; C. McGann et al. 2014; Akoum et al. 2015; Rizvi et al. 2016)

4.3.2 Johns Hopkins technique: image intensity ratio (IIR)

Whilst the Utah group has looked to compare the LGE signal intensity of pathological, fibrotic LA wall to "normal" LA myocardium, the Johns Hopkin's group have chosen to compare voxel signal intensity to that of the blood pool (Khurram et al. 2014). In the creation of a normalised image intensity ratio (IIR), some of the concerns of partial voluming of the atrial blood pool are overcome. The signal intensity of the LA wall is evaluated within each sector (20 per slice, 3.5mm slice thickness), and divided by the blood pool mean to generate a ratio. Thresholds for assignation as fibrosis were derived via comparison to local voltage on electroanatomical mapping (Figure 4-12). It was noted that the IIR closely correlated with local intracardiac bipolar LA voltage measurements, but some of that correlation may be augmented by the fact that 32 of the 75 patients had had a prior ablation.

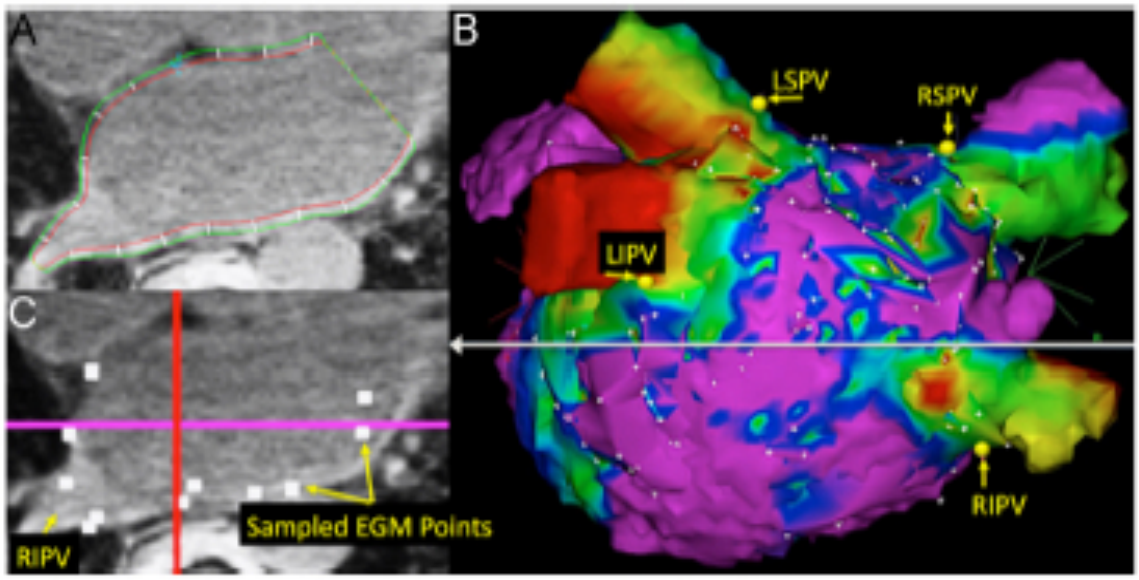

Figure 4-12 Example of LGE 3D LA dataset and EAM registration.

A: Manually drawn endo- and epicardial contours on LGE axial planes. Each plane is divided into 20 sectors within the contours, and the mean pixel intensity of each sector is calculated. B: Registration of EAM points to LA angiogram by using standard techniques. Anterosuperior ostial left superior pulmonary vein (LSPV) and right superior PV (RSPV) as well as anteroinferior ostial left inferior PV (LIPV) and right inferior PV (RIPV) points (yellow balls) were used to merge the MR angiogram with the EAM by using standard EAM system tools, thus minimizing rotational errors. Multiple posterior wall and anterior wall points (white dots) were then used for surface registration. C: Multiplanar reformatted panel corresponding to the grey line in panel B is visualized. The merged coordinates from panel B were then used within the Volley software to merge the EAM with the LGE planes.

Image sectors from axial planes corresponding to each EAM point (white boxes) on that plane were identified. Image intensities of each sector corresponding to EAM point voltages were recorded. EAM: electroanatomical map; LA: left atrial; LGE: late gadolinium enhancement. Reproduced with permission from Khurram et al 2014 (Khurram et al. 2014).

4.4 Atrial fibrillation ablation strategy

Catheter ablation procedures for all subjects with AF (Chapters 5, 7, 8, and 9) were performed by two operators at St Thomas' Hospital London. Class I and III antiarrhythmic medications, with the exception of amiodarone, were discontinued at least five half-lives prior to the procedure. Patients taking warfarin underwent ablation on uninterrupted warfarin so long as the INR was less than 3.5. Patients on novel oral anti-coagulants discontinued medication the day before the procedure and restarted 6 hours after the procedure.

Ablation procedures were performed under general anaesthesia with transoesophageal echo to exclude intracardiac thrombus and to guide transseptal puncture. Three 8Fr short sheaths were inserted at the femoral vein, with two upsized to two 8.5Fr SR0 long sheaths under fluoroscopic guidance. A 6Fr decapole catheter was placed in the coronary sinus to provide an electrophysiological and electroanatomical reference. Following transseptal puncture, intravenous heparin was administered to maintain activated clotting time >300seconds.

The majority of procedures were performed using CARTO3 (Biosense Webster/Johnson&Johnson, New Jersey, USA), with 8 procedures in total (data included in Chapters 5, 7 and 8) performed using EnSite Velocity (St Jude Medical, St Paul, Minnesota, USA). Detailed three-dimensional LA anatomy was acquired on EAM without image integration, typically using 20 electrode Lasso catheter (Biosense Webster) or 21 electrode Pentaray catheter (Biosense Webster), with mitral valve annulus identified electrically using the ablation catheter.

For patients with a diagnosis of PAF and in sinus rhythm, a point-by-point wide area circumferential ablation (WACA) achieving PVI was typically performed using an 8Fr irrigated SmartTouch catheter (Biosense Webster), or 8Fr irrigated TactiCath catheter (St Jude). Target ablation parameters were >5g for at least 15seconds per RF delivery location. Power was 30W throughout the LA except on the posterior wall where it was limited to 25W. Procedural endpoint was defined as PV isolation as confirmed on entry block (and exit block if PV capture could be achieved). For patients presenting with PersAF, a WACA was performed followed by additional ablation lesion sets (mitral line, roof line, inferior posterior line, complex fractionated electrogram ablation) as indicated.

A waiting time of 30 minutes following the last RF delivery was observed to permit assessment of linear and circumferential conduction block. Once sheaths were removed from the LA, protamine

100mg was administered and on-table echocardiography used to confirm the absence of pericardial effusion. Anti-arrhythmic medication was not uniformly discontinued in all patients following ablation.

Patients were typically discharged home the day after the ablation procedure.

5 Cardiac Magnetic Resonance Imaging of the Arrhythmia Substrate: Atrial Fibrillation

5.1 Aims

To assess the ability of CMR-derived indices of cardiac structure and function to predict response to ablation for AF.

5.2 Introduction

Catheter ablation is an effective treatment for appropriately selected patients with AF (Calkins et al. 2012). What constitutes appropriate selection, however, remains poorly understood and vigorously debated. In the emerging era of "mechanism-directed therapy", one perspective might be that any patient with AF is a potential candidate for ablation when an electrophysiological target can be identified and therefore eliminated. An alternative perspective considers catheter ablation as a precious resource, to be offered only when there is a high likelihood of a safe, clinically successful and relevant outcome for the patient. An understanding of the complex interplay of mechanisms in their structural context represents a major goal of patient-tailored AF therapy (O'Neill and Chubb 2016). CMR represents a widely acceptable technique for the assessment of atrial structural remodelling (SRM), which may be linked to likelihood of procedural success.

The LA and PVs may be visualised on CMR imaging, and the imaging technique therefore plays a core role in many centres prior to ablation procedures. It is a reasonable step to use the same imaging modality to determine markers of atrial SRM. The most widely published CMR-derived index that has been shown to be associated with outcome is that of atrial wall LGE quantification. However, several other MR derived indices of LA SRM have also been proposed and validated in single-centre studies, and the complex interaction of these indices has not been established. This study aims to evaluate the following indices:

5.2.1 Pre-ablation LA fibrosis quantification

LGE imaging has long been used for the assessment of ventricular myocardium. More recently, successful LGE characterisation of the atrial wall has been demonstrated, and was first used to visualise the formation of scar post-ablation using a three-dimensional LGE sequence (Peters et al. 2007). The Utah group have used the same imaging principles to assess the extent of pre-ablation fibrosis, and have demonstrated a robust correlation with long-term outcome, in terms of recurrence of arrhythmia following ablation procedure (Oakes et al. 2009; Marrouche et al. 2014). However, the technique is labour-intensive, highly sensitive to imaging quality, subject to some degrees of subjectivity, and requires bespoke image processing software, and therefore pre-ablation fibrosis

assessment is not widely employed (Calkins et al. 2012). Some groups have chosen to employ the Utah image interrogation techniques (Jadidi et al. 2013), whilst other groups have developed their own (Khurram et al. 2014; Malcolme-Lawes et al. 2013). Image acquisition parameters remain broadly similar, but there are significant differences in the quantification of scar, leading to widely differing normal ranges (O'Neill and Chubb 2016).

5.2.2 Left atrial size

LA diameter is established as a marker of atrial SRM and a predictor of AF recurrence (Vaziri et al. 1994; Psaty et al. 1997; Berruezo et al. 2007; Dodson et al. 2014). CMR imaging may be used to assess atrial volume, which may be calculated from multi-slice imaging techniques (typically cine imaging), or from segmentation of a 3D volumetric dataset. Maximum LA size is measured at end atrial diastole (end ventricular systole), and has been shown to be associated with long-term AF recurrence (Dodson et al. 2014; Costa et al. 2015)

5.2.3 Left atrial function

LA systolic function is difficult to quantify on echocardiographic imaging, but is relatively easily assessed on CMR imaging. Function may be evaluated on volumetric analysis of multi-slice cine imaging, or on extrapolation from cine two-chamber and four-chamber slices. However, the phases of atrial contraction are more complex than ventricular contraction, and therefore there are several indices of atrial function. In a large cohort of 346 patients, Dodson et al demonstrated that the risk of recurrence is associated with LA passive ejection fraction (Dodson et al. 2014). Habibi et al went on to review both LA passive ejection fraction and LA total ejection fraction (LAEF). On multivariable analysis, LAEF was found to be the only index of LA function that was independently associated with arrhythmia recurrence, and LAEF has therefore been included as the index of LA function. (Habibi et al. 2016).

5.2.4 Left ventricular function

AF may be both a cause and effect of left ventricular (LV) systolic dysfunction. It is well-established that pre-existing LV systolic dysfunction is associated with up to 6-fold increase in risk of developing AF (Benjamin et al. 1994). LV dysfunction has also been shown to be associated with an increased risk of AF recurrence post-ablation in some, but not all, studies (Balk et al. 2010; Dodson et al. 2014). However, LV function in many studies has been assessed using echocardiography, rather than the gold standard of CMR imaging, and therefore CMR derived LV function was included in the analysis.

5.2.5 Left atrial shape

LA shape, in addition to atrial size, has been demonstrated to be correlated with AF recurrence. One group (Bisbal et al. 2013) has described the segmentation of the body of the LA from a non-gated magnetic resonance angiogram (MRA). The resulting 'sphericity index', derived through quantitative comparison to a sphere, was found to be strongly predictive of AF recurrence.

5.2.6 Pulmonary venous anatomy

Pulmonary venous anatomy, as assessed by cross-sectional imaging, has also been shown to be related to long-term outcome, with a reduced risk of recurrence in those with a single left sided PV (13% versus 34%) (McLellan, Ling, Ruggiero, et al. 2014).

5.3 Methods

5.3.1 Patients

Patients planned for first-time AF ablation procedure were referred for routine pre-procedural clinical CMR scan, from January 2014 to October 2015. Patient demographics and comorbidities were documented at the time of the scan and paroxysmal and persistent AF were defined as per HRS/EHRA guidelines (Calkins et al. 2012). Patients who underwent subsequent cryoablation (n=1) or did not receive GBCA (n=2, one previous allergic reaction, one patient choice) were excluded. Patients were included regardless of rhythm at the time of scan.

5.3.2 CMR imaging acquisition

See Section 4.1 for full details of CMR imaging protocols. Cine imaging was performed using a standard multislice bSSFP technique (typical parameters: effective TR 2.7msec, TE 1.3msec, 1.25x1.25mm^2 in-plane, slice thickness 10mm, 50 phases).

5.3.3 Fibrosis assessment

Analysis was performed on an MITK-based platform (German Cancer Research Centre, Heidelberg, Germany), with custom-build modifications to enable the quantification of atrial fibrosis. The LA endocardial surface was defined via manual segmentation within the 3D LGE volume on a slice by slice basis, using 3D interpolation to minimise slice-by-slice discontinuities. A 2mm surface dilation was used to define the epicardial border, in keeping with established methods (Khurram et al. 2014), and a mean intensity projection technique through the defined atrial wall was used to ascribe a single signal intensity value to each point on the LA endocardial surface model (vtk shell, typically 20,000 polygons per shell). The mitral valve, distal PVs (>approx 2mm distal to antrum) and LAA were removed using the Clip filter in Paraview (Kitware, New York, NY, USA) and the surface was re-extracted as a binary file.

Scar quantification was performed through measurement of the proportion of the surface area above a defined threshold. Three different methods were used to define threshold values, corresponding to established publications. The first was an image intensity ratio (IIR), derived from the Johns Hopkins quantification technique (Khurram et al. 2014), with a threshold equivalent to 0.97 times the mean of the blood pool (BP) signal intensity. This quantification method was used as the primary fibrosis score, in view of the close replication of published technique, strong published association with outcome and avoidance of user selected thresholds. The second was an atrial BP z-score, derived

from the Imperial College London quantification technique (Malcolme-Lawes et al. 2013), with a threshold equivalent to 3 (BP) standard deviations (SD) above the BP mean. The third was an atrial wall z-score, derived from the Utah quantification technique (Oakes et al. 2009), with thresholds at 2, 3 and 4 (atrial wall) SDs above the atrial wall mean. It should be noted that for the final technique a universal threshold was applied, and there was no slice-by-slice tailoring of the threshold. BP signal mean and SD were measured for a 4ml spherical volume placed in the centre of the LA blood pool, distant from artefact including respiratory navigator signal. Atrial wall signal mean and SD were measured across the whole, clipped, atrial shell. For reproducibility assessment, 43 LGE volumes were re-segmented independently by a separate observer (WS). The same image interrogation technique was employed.

5.3.4 Left atrial size

LA size was assessed in atrial diastole at maximum volume. The left atrium was manually segmented from the 3D LGE volume, excluding the atrial appendage and pulmonary veins. The volume of the segmentation was assessed using ITK-snap (Version 3.4.0, University of Pennsylvania, USA). For reproducibility assessment, 45 LGE volumes were re-segmented independently by a separate observer (WS).

5.3.5 Left atrial function

LA function was assessed on multi-slice short-axis cine imaging stack. The LA was manually contoured at maximum volume (LAV_{max}- end atrial diastole), and minimum volume (LAV_{min}- end atrial systole), with the appendage and veins excluded. LAEF was defined as total LA emptying fraction ((LAV_{max}-LAV_{min})/LAV_{max}). For reproducibility assessment, 45 patients underwent independent measurement by a separate observer (JG).

5.3.6 Left ventricular function

LV function was also assessed on the same multi-slice short-axis imaging stack, using a conventional manual chamber contouring technique. Volumes were assessed using ViewForum (Philips Healthcare, Best, Netherlands). Reproducibility was not assessed for this well-established technique.

5.3.7 Atrial sphericity

LA sphericity was calculated according to the methods of Bisbal and co-workers (Bisbal et al. 2013). The LA body was segmented on the 3D LGE acquisition on a slice by slice basis on the MITK platform. The segmentation was performed separately to that defined for the atrial fibrosis analysis, and excluded the LAA and PVs. A VTK shell was created from the segmentation and the centre of mass and best fit sphere for the shell atrium was calculated per the published technique (see Figure 5-1C). The coefficient of variation of the sphere (CVS) was defined as σ_{AR}/AR, where σ_{AR} is calculated as:

$$\sigma_{AR} = \sqrt{\frac{1}{LACA} \sum_{i=1}^{i=num\_triangles} ((Ti_a)(\| (LAC_{mc} - Ti_{mc}) \| - AR)^2)}$$

where LACA is LA cavity area (2d surface area), Ti_a is the area of each triangle of the mesh, LAC_{mc} is the centre of mass of the whole LA cavity, Ti_{mc} is the centre of mass of each triangle, and AR is the average radius of the best fit sphere. LA sphericity was then defined as (1-CVS)*100. For reproducibility assessment, 45 LGE datasets were re-segmented by an independent observer (KL).

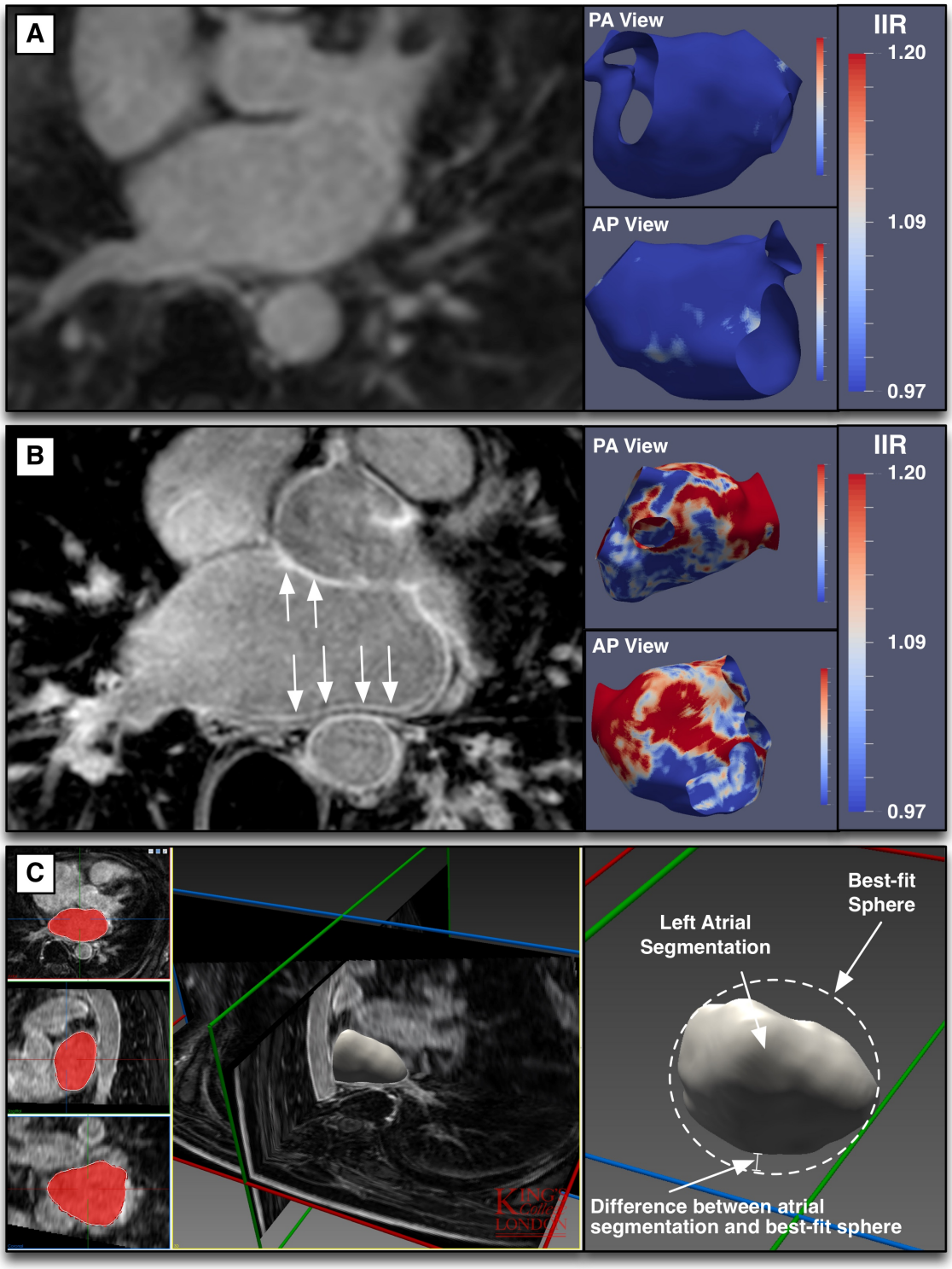

Figure 5-1. Illustration of left atrial fibrosis quantification and sphericity assessment.

(A) Low fibrosis left atrium (LGE CMR- 5% (left)), with atrial shell thresholded at image intensity ratio (IIR) 0.97. (B) High fibrosis left atrium (65%), white arrows indicating regions of LA wall enhancement (C) (Left) multiplanar reconstruction of 3D LGE dataset, with LA body-only segmentation, and (right) demonstration of sphericity calculation. For this subject, sphericity was 88.6%.

5.3.8 Pulmonary venous anatomy

Pulmonary venous anatomy was assessed on the 3D LGE dataset. They were classified as normal (2 left and 2 right veins), single left (with any combination of right sided veins), isolated three right sided veins (with 2 left sided veins), or any other pulmonary venous arrangement.

5.3.9 Atrial fibrillation ablation procedure

The atrial ablation procedure strategy is detailed in Section 4.4.

5.3.10 Subject follow-up

Recurrence of AF post-ablation was defined as a recurrence of AF (>30seconds), or episodes of atrial tachycardia or atrial flutter, in line with HRS/EHRA guidelines (Calkins et al. 2012), and confirmed on ECG or Holter/event monitoring. There were no episodes of AV nodal re-entrant tachycardia, AV re-entrant tachycardia or ventricular tachycardia documented following ablation. Follow-up was at 3months post-ablation, with symptom review, 24 hour tape and 12 lead ECG performed. Subsequently, patients were typically reviewed at 6 and 12months after the index procedure, and yearly thereafter. A 12 lead ECG ± Holter monitor was performed at each clinical review, in the absence of reported symptoms. If symptoms were reported, patients underwent 12 lead ECG, 24 (or 48/72) hour Holter monitor, cardiac implantable device interrogation or assessment using implantable loop recorder, according to symptom frequency and clinical suspicion.

Patients without recurrence were censored at the time of the last available follow-up. A blanking period of three months was employed post ablation. However, in the presence of continued arrhythmia recurrence outside of the blanking period, the timing of recurrence was dated to the earliest documented arrhythmia post-ablation.

5.3.11 Statistics

Normally distributed continuous variables are presented as mean ± standard deviation, and median with interquartile range (IQR) for non-normal distribution or non-continuous ordinal data. Statistics were analysed using SPSS Statistics (Version 22, Armonk, NY). Baseline characteristics and CMR indices were compared using χ^2 test or Student t-test as appropriate. Kaplan-Meier survival curves were compared using Log-rank (Mantel-Cox) test. Multivariable Cox proportional-hazards models were used to assess the association of pre-determined indices against arrhythmia recurrence, and results are presented as hazard ratio (HR) with 95% confidence interval. For Model 1, the analysis was adjusted for age and sex only. For Model 2, in addition, the analysis was adjusted for hypertension, body mass index, diabetes mellitus, type of AF and AF duration. For Model 3, all adjustment factors were retained, but all CMR indices were assessed in a single model. Receiver operator characteristic curves and outcomes for binomial logistic regression were censored at 150 days.

5.3.12 Ethics

All pre-ablation CMR studies were clinically indicated, and subjects provided written consent for retrospective analysis (REC reference 09-H0802-78).

5.4 Results

5.4.1 Patients

In total, 89 subjects underwent full CMR prior to routine first-time ablation, and baseline demographics and findings are detailed in Table 5-1. Median total follow-up time was 383 days (IQR 204-613days), and there were 30 recurrences, at median 92 days (IQR 30-118days). Kaplan-Meier survival curves for baseline parameters are shown in Figure 5-2. In assessment of recurrence, all subjects had at least one 24 hour tape performed, with 50 (56%) subjects undergoing ECG Holter monitoring on ≥1 occasion for at least 48hours, and a further 3 subjects had an implantable loop recorder or device. There was no significant difference in intensity of monitoring between recurrence and non-recurrence groups. CMR imaging was completed for all subjects for all indices, with the exception of three subjects for whom atrial fibrosis could not be assessed (poor myocardial nulling in two, and unacceptable artefact in one).

		All Subjects (n=89)	No Recurrence (n=59)	Recurrence (n=30)	p-value
Male		65 (73%)	38 (64%)	27 (90%)	0.010
Paroxysmal AF		48 (53%)	37 (63%)	11 (37%)	0.11
CHA_2DS_2VASC Score		1 (IQR 0-2)	1 (IQR 0-2)	0 (IQR 0-1)	0.004
AF duration (years)		3.9 (IQR 2.0-5.0)	3.6 (IQR 2.0-4.5)	4.3 (IQR 2.0-5.0)	0.41
Significant Comorbidities		26 (29%)	30 (51%)	16 (53%)	0.82
Hypertension		23 (26%)	17 (29%)	6 (20%)	0.37
Ischaemic Heart Disease		7 (8%)	3 (5%)	4 (13%)	0.17
Age (years)		59.6 ±11.0	60.6±11.6	57.3±9.7	0.22
Weight (kg)		88.4±15.9	87.0±16.2	91.3±15.0	0.21
Height (cm)		175.4±8.1	173.9±8.2	178.4±7.0	0.009
BMI (kg/m^2)		28.7±4.8	28.7±5.1	28.7±4.4	0.94
LA size on echo (LAPx (mm))		48.4 ± 8.4	47.6 ±7.7	49.6 ± 9.5	0.34
Heart Rate at scan (bpm)		71±15	68±14	77±16	0.011
SR at baseline scan		53 (60%)	39 (66%)	14 (47%)	0.077
Follow-up duration (days)		383 (IQR 204-613)	334 (IQR 191-516)	463 (IQR 252-676)	0.147
Longest duration of rhythm monitoring	**24 hour ECG**	36	21	15	0.19
	48 hour ECG	40	27	13	0.82
	72 hour ECG	4	4	0	0.14
	7 day ECG	6	4	2	0.93
	Device interrogation or ILR	3	3	0	0.20

Table 5-1. Baseline demographics and findings.

AF: atrial fibrillation, BMI: body mass index, LA: left atrium, SR: sinus rhythm, LAPx: long axis parasternal. Significant comorbidity was defined as Charlson comorbidity index >/= 1 (Charlson et al. 1987)

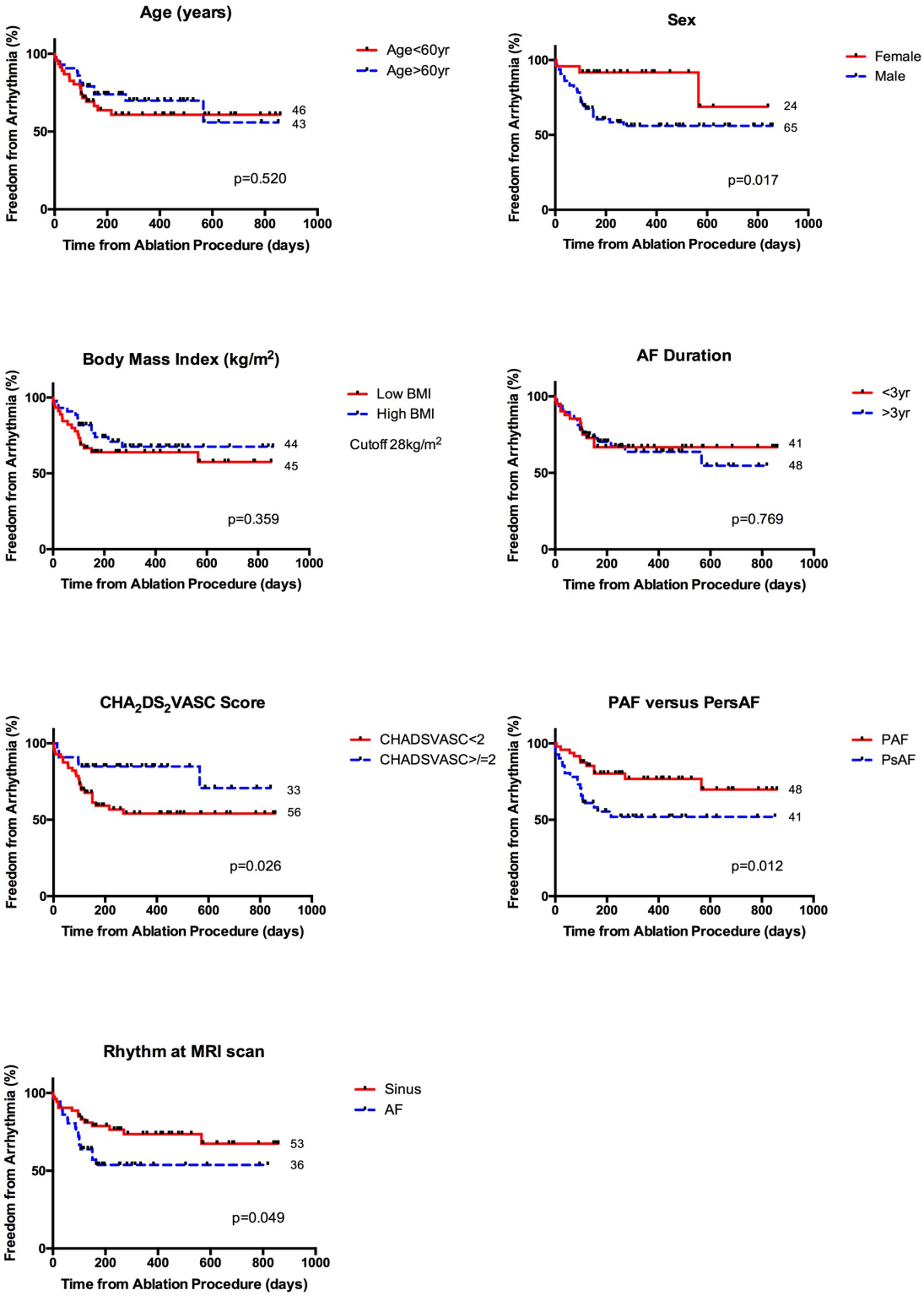

Figure 5-2. Kaplan Meier survival curves for baseline indices.

Each parameter has been dichotomised, and the number of subjects in each group at time=0 is shown at the end of each curve (total =89 in all plots). Where there is no established cut-off value for high and low risk, a cut-off value as close the 50th centile as possible has been used, and the values are indicated to the right of associated plots.

5.4.2 CMR indices

CMR-derived indices are summarised in Table 5-2, and associated Kaplan-Meier plots in Figure 5-3. LV native T1 time and LV mass were also assessed for association with outcome, with no difference between no-recurrence and recurrence groups (LV mass: 111±32g and 111±25g (p=0.96); LV native T1 time 992±42msec versus 979±34msec (p=0.15) respectively). A single left-sided PV occurred with similar frequency in recurrence and non-recurrence groups (p=0.81) and therefore was not included in further evaluations.

On separate multivariable analysis adjusting for age and sex (Model 1), only atrial fibrosis (p=0.002) and LA EF (p=0.018) were independently associated with recurrence (Table 5-3). In Models 2 and 3, with adjustment for multiple risk factors, atrial fibrosis was the only factor independently associated with recurrence. LA EF demonstrated significant collinearity with AF type (mean 40±14% in PAF, versus 21±13% in non-PAF, p<0.001), and therefore was not independently associated with outcome in Model 2 (HR for non-PAF 2.0, p=0.03).

	All Subjects (n=89)	**No Recurrence (n=59)**	**Recurrence (n=30)**	**p-value**
LA fibrosis (%)	33.5±18.8	28.9±16.7	42.6±19.4	0.002
Indexed LA Volume (ml/m^2)	61.6±18.8	60.9±17.8	63.3±21	0.59
LA ejection fraction (%)	30.9±16.5	34.3±15.8	24.1±16.1	0.006
LV ejection fraction (%)	60.7±10.3	62.7±10.5	57.0±8.9	0.009
LA sphericity	82.1±3.4	82.3±3.4	81.7±3.5	0.42
Single left sided pulmonary vein	8 (9%)	5 (6%)	3 (10%)	0.81

Table 5-2. CMR-derived indices by recurrence group.

Normal pulmonary venous anatomy was classified as 2 left and 2 right pulmonary veins. LA: left atrium, LV: left ventricle.

	Model 1			**Model 2**			**Model 3**		
	HR	95% CI	P-value	HR	95% CI	P-value	HR	95% CI	P-value
Fibrosis (%)	1.031	1.011-1.051	0.002	1.035	1.013-1.058	0.002	1.032	1.008-1.056	0.007
Indexed LA Volume (ml/m^2)	1.003	0.995-1.012	0.435	0.997	0.976-1.019	0.804	0.998	0.974-1.023	0.883
LA EF	0.064	0.007-0.622	0.018	0.178	0.013-2.501	0.200	0.645	0.012-34.83	0.830
LV EF	0.038	0.001-1.209	0.064	0.056	0.001-2.596	0.141	0.059	0.000-9.725	0.277
Sphericity	0.965	0.872-1.067	0.487	0.939	0.843-1.042	0.258	0.923	0.810-1.023	0.229

Table 5-3. Multivariable Cox regression analysis of the association of established CMR indices with arrhythmia recurrence.

For Model 1 and 2, each row represents a separate multi-variable analysis. Model 1 is adjusted for age and sex alone, Model 2 additionally for hypertension, body mass index, diabetes mellitus, type of AF and AF duration. Model 3 contains all factors of Model 2, and all CMR derived indices, in a single multivariable analysis. LA: left atrium, LV: left ventricle, EF: ejection fraction, HR: Hazard Ratio, CI: confidence interval.

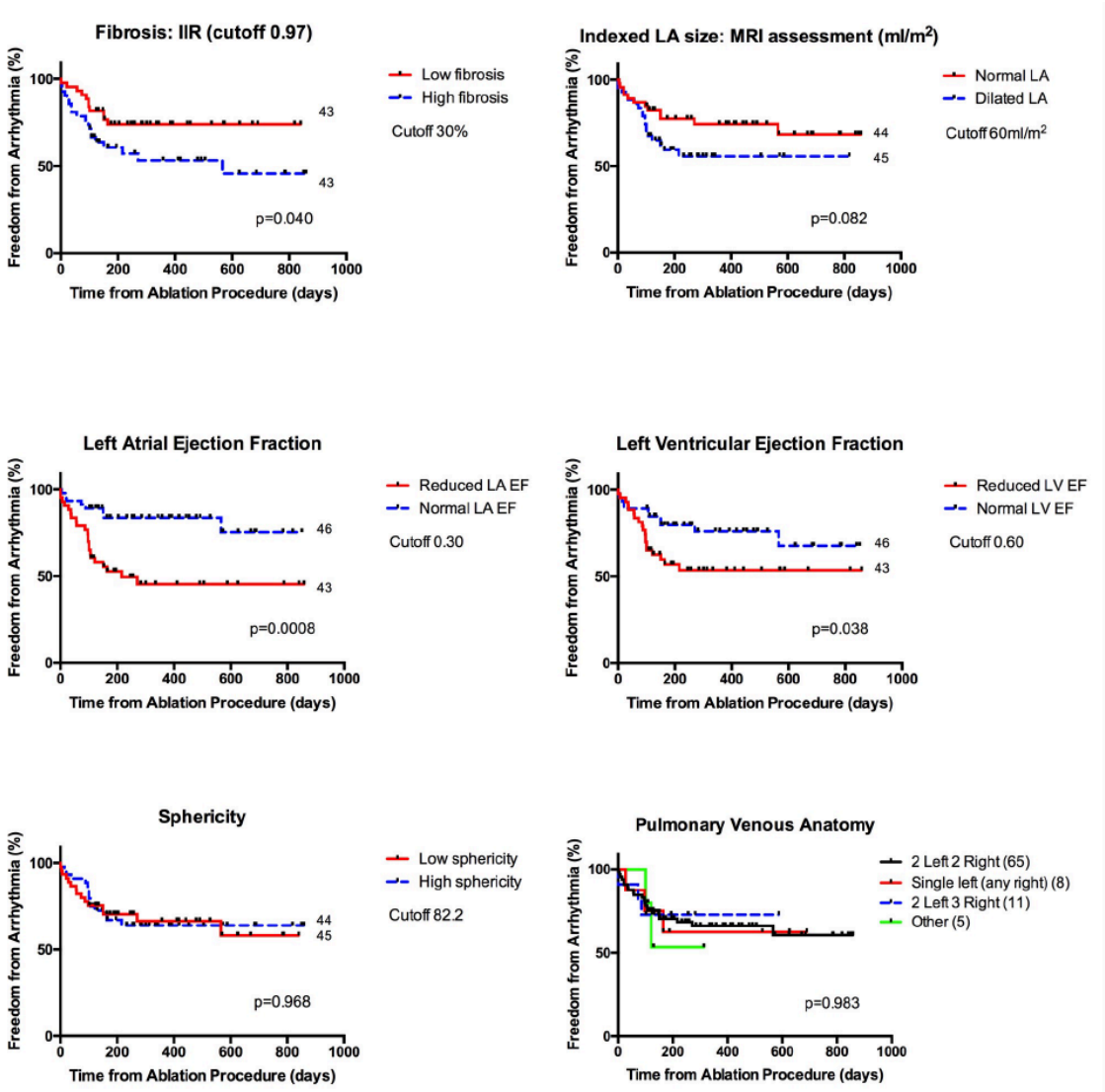

Figure 5-3. Kaplan Meier survival curves for CMR indices.

Each parameter has been dichotomised, except for PV anatomy, and the number of subjects in each group at the start of the follow-up is shown at the end of the curve (total =89 in all plots except fibrosis, where n=86). Where there is no established cut-off value for high and low risk, a cut-off value as close the 50th centile as possible has been used, and the cut-off values are indicated to the right of associated plots.

5.4.3 Atrial fibrosis burden

Atrial fibrosis burden was associated with arrhythmia recurrence on univariable and multivariable analysis. The relationship of the three atrial fibrosis quantification methods was also assessed and is summarised in Figure 5-4. There is minimal correlation between the fibrosis score assessed as an IIR, and the two alternative methods (blood-pool z-score and shell z-score thresholds). Fibrosis scores derived at thresholds of 2 and 3 standard deviations above the shell mean designated only very small portions of the shell as scar, and many shells had no surface points that achieved the thresholds. However, there remained a significant association between BP derived z-scores and

outcome, and 3SD above shell mean threshold and outcome, as shown in the associated Kaplan-Meier plots.

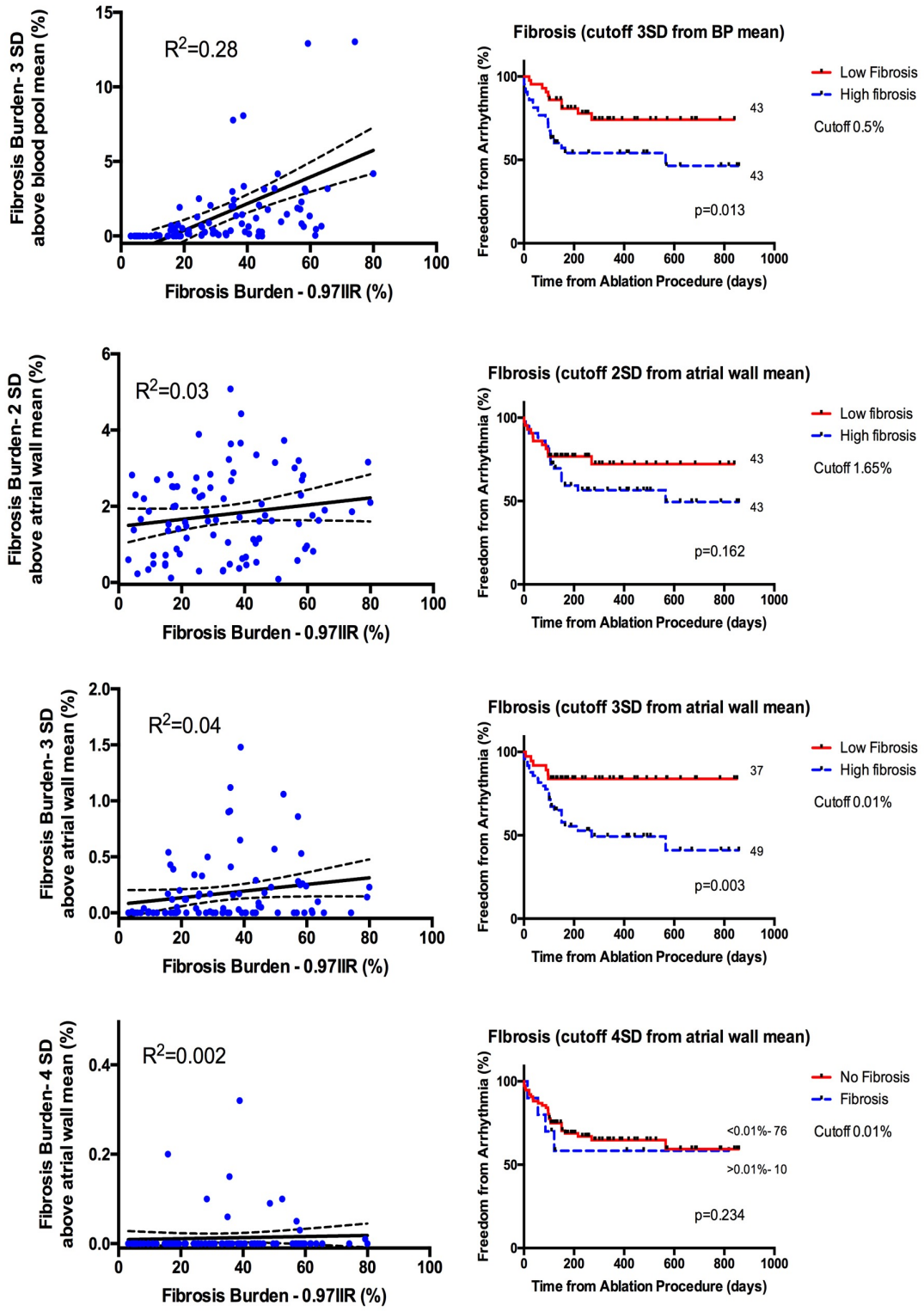

Figure 5-4. Co-dependence of the cut-off values for quantification of atrial fibrosis.

The left hand scatter plots show the fibrosis burden against image intensity ratio (IIR)-derived index, with regression line (±95% confidence interval). R^2 correlation coefficient for linear regression is shown for each plot. Right hand Kaplan Meier plots show

corresponding survival curves for each fibrosis quantification methods. Note that the lower three pairs of plots all correspond to the Utah method (Oakes et al. 2009)*, but do not include a slice-by-slice variation of the cut-off value, and for many shells there were no scalars that were above the defined threshold.*

5.4.4 Confounding variables and collinearity

Analyses have been performed including all eligible patients, regardless of underlying arrhythmia type (paroxysmal or persistent) and the rhythm at scan. The heart rhythm at the time of CMR assessment is a clear confounding factor, with particular impact on LAEF (Figure 5-5), as is the type of AF, which was significantly associated with outcome on assessment of survival curves (Figure 5-2). On exclusion of subjects in AF, there was no significant increase in recurrence rate in those with lower ejection fraction (p=0.09).

The collinearity of the CMR indices is quantified in Table 5-4. The regression coefficients were generally weak, demonstrating relative independence. There was a significant association with AF type for all indices (see Figure 5-6), but there was substantial overlap throughout with a clear absence of dichotomisation.

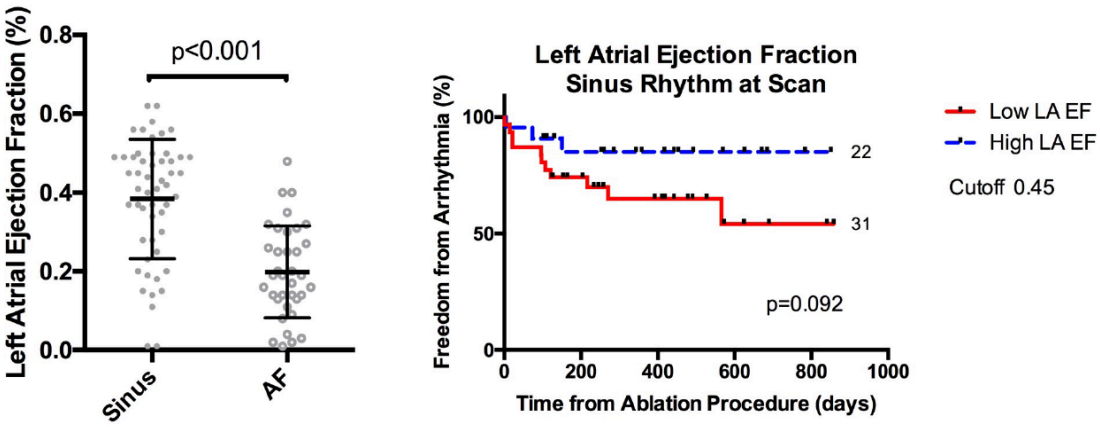

Figure 5-5. Association of rhythm at scan and LA ejection fraction

(Left panel) The association of LA ejection fraction with rhythm at the time of scan. (right panel) Kaplan Meier plot showing a non-significantly increased recurrence rate for those with a reduced LA ejection fraction. The cut-off value is derived from Habibi and co-workers (Habibi et al. 2016)*.*

	LA fibrosis (%)	Indexed LA Volume (ml/m²)	LA ejection fraction (%)	LV ejection fraction (%)	LA sphericity
LA fibrosis (%)	N/A	R^2= 0.001 p=0.72	R^2=0.12 P<0.001	R^2=0.06 p=0.03	R^2<0.001 p=0.82
Indexed LA Volume (ml/m²)	-	N/A	**R^2=0.20** **P<0.001**	R^2=0.09 p=0.005	R^2=0.19 P<0.001
LA ejection fraction (%)	-	-	N/A	**R^2=0.29** **P<0.001**	R^2=0.04 p=0.06
LV ejection fraction (%)	-	-	-	N/A	R^2=0.003 p=0.59

Table 5-4. Quantification of collinearity of CMR-derived indices.

Values shown are the linear regression correlation coefficient and p-values for each pair of CMR indices.

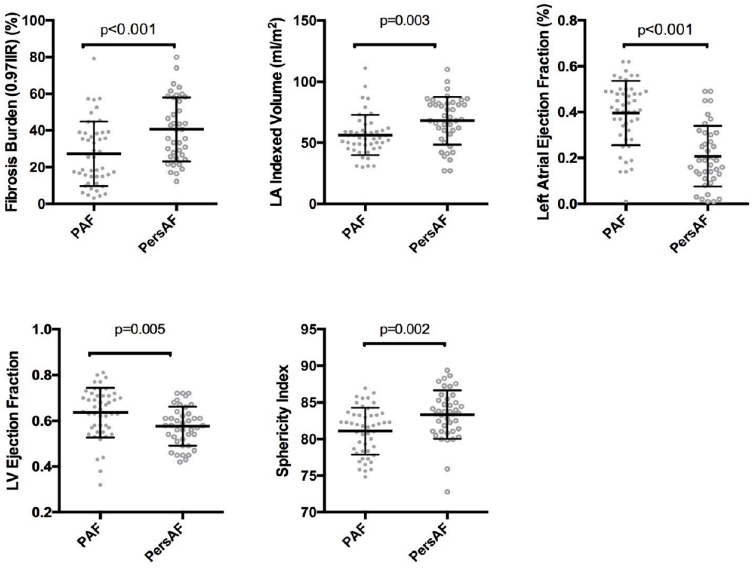

Figure 5-6. Plots demonstrating the segregation of each CMR index according to AF type.

5.4.5 Reliability of parameter assessment

The assessment of each CMR index is complex, and the reliability of all CMR index derivations was assessed. Interobserver Bland-Altman plots are shown in Figure 5-7. Interobserver differences should be interpreted in the context of the dynamic range of the index observed across the subject cohort, and agreement was generally good with minimal impact of the measurement error upon the derived CMR index-outcome association. Interobserver Lin's concordance correlation coefficients

were 0.866 (95% CI 0.787-0.917) for LA fibrosis, 0.923 (95% CI 0.873-0.954) for indexed LA volume, 0.860 (95% CI 0.779-0.912) for LAEF and 0.906 (95% CI 0.842-0.945) for sphericity.

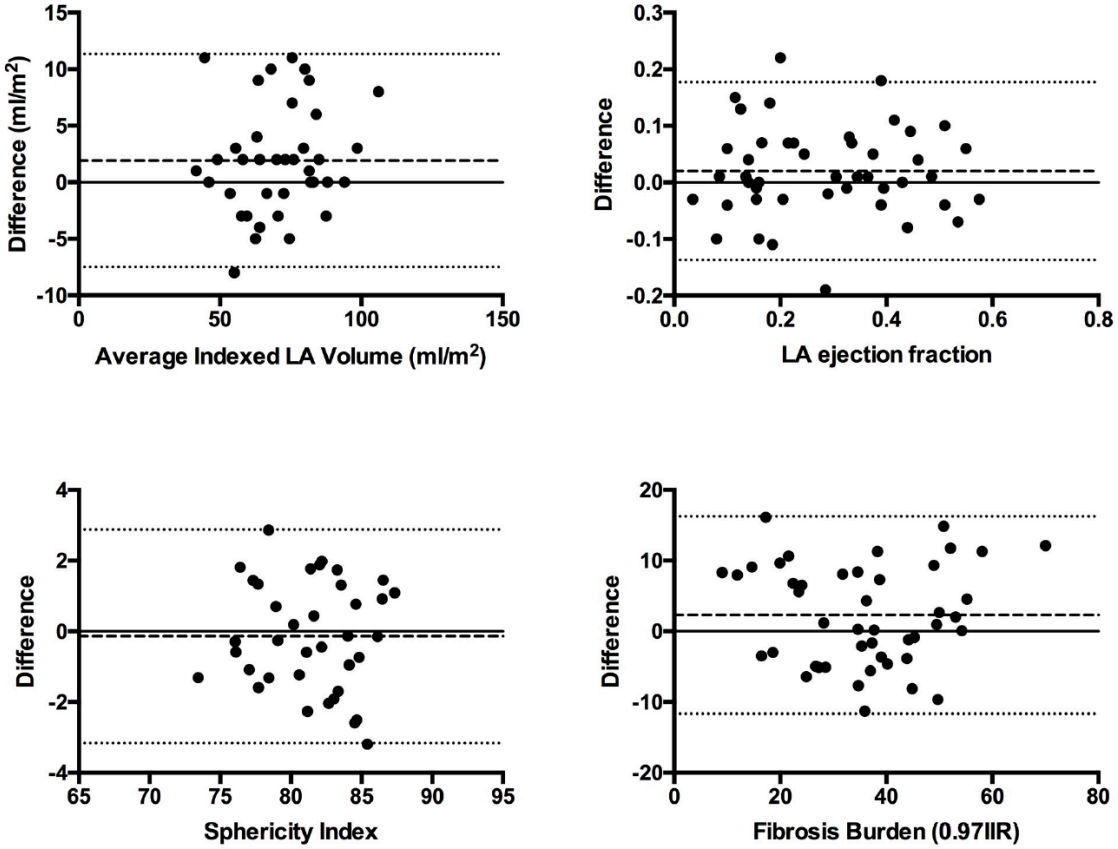

Figure 5-7. Bland Altman plots demonstrating the interobserver differences in measurement for each CMR index.

The reliability of left ventricular ejection fraction has been widely reported and was not-reassessed.

5.4.6 Predictive value

Figure 5-8 shows receiver operator characteristic curves for the five CMR indices, with outcomes dichotomised (recurrence/no-recurrence) at 150 days. There were 26 recurrences by 150 days. For the index with the greatest area under curve, fibrosis index, the sensitivity (proportion of recurrences correctly identified) and specificity (proportion of non-recurrences correctly identified) at an index value of 35% were 63% and 64% respectively. 90% of recurrences were predicted at a threshold of 15%, but with a specificity of only 23%. Conversely, at a fibrosis cut-off value of 50%, specificity for recurrence was 95% with sensitivity 44%. At the observed overall recurrence rate, this represents a positive predictive value of 80% at the 50% fibrosis threshold, with a negative predictive value of 79%.

A binomial logistic regression was performed to ascertain the combined effects of the CMR parameters (atrial fibrosis, LAEF, LVEF, indexed LA volume, sphericity) on the likelihood of

arrhythmia recurrence. The logistic regression model was statistically significant, $\chi^2(5)= 21.47$ ($p=0.001$). The model explained 32.6% (NagelKerke R^2) of the variance in arrhythmia recurrence and correctly classified 77.8% of cases. Sensitivity was 53.8%, and specificity 89.1% (Table 5-5). Of the five CMR parameters, only fibrosis was statistically significant (Table 5-6).

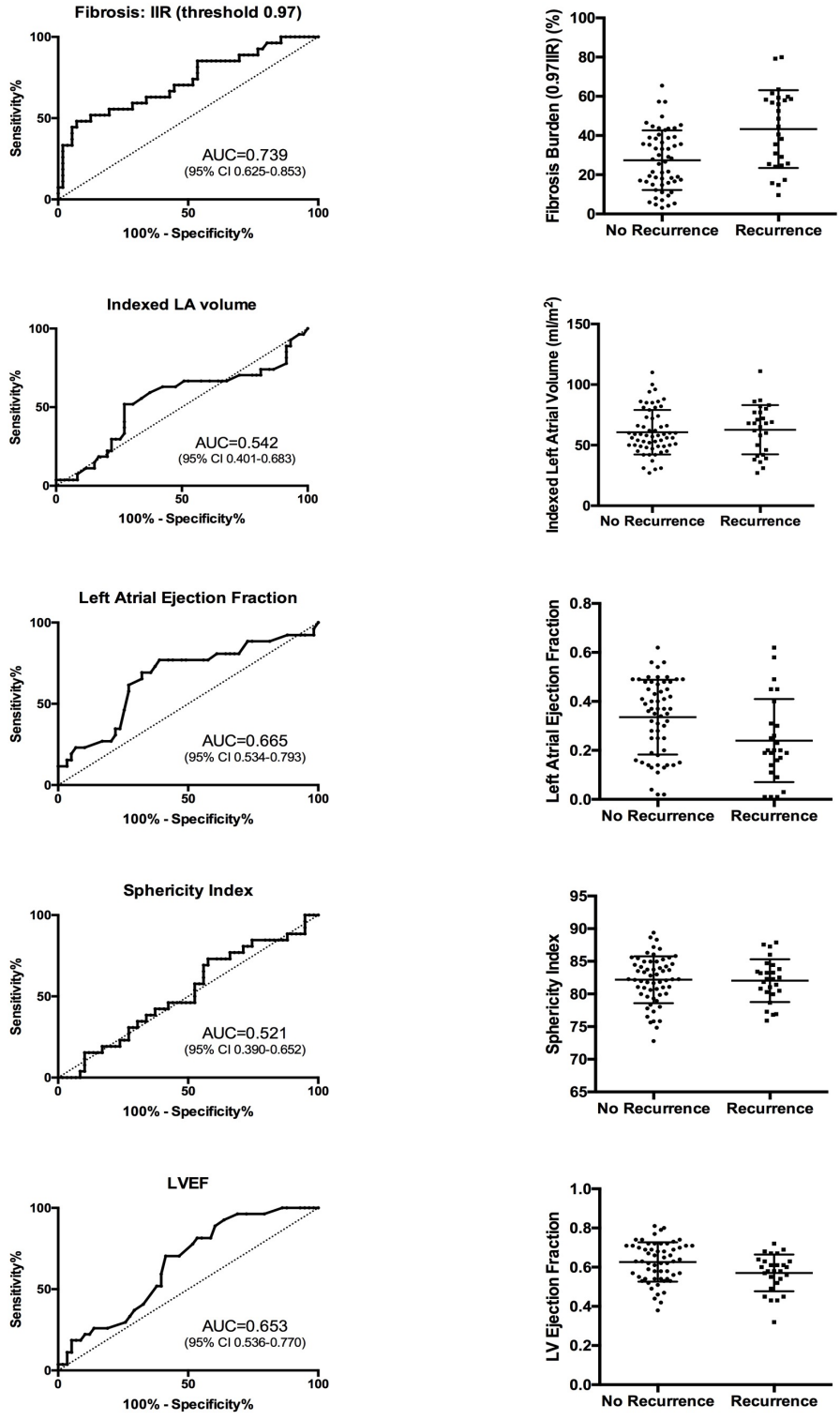

Figure 5-8. Receiver operator characteristic curves (left sided panels) and index distribution between subjects with recurrence and no recurrence (right sided panels) at 150days post procedure.

AUC: Area under curve. CI: confidence interval

		Predicted		
		No Recurrence	Recurrence	Percentage Correct
Outcome	No Recurrence	49	6	Specificity 89.1%
	Recurrence	12	14	Sensitivity 53.8%
		NPV 80.3%	PPV 70.0%	Accuracy 77.8%

Table 5-5. Classification table for binomial logistic regression analysis of arrhythmia recurrence.

PPV: positive predictive value, NPV: negative predictive value

	Odds Ratio	**95% CI**		**Significance**
		Lower	Upper	
Fibrosis (%)	1.072	1.025	1.122	0.002
LA Max Volume (ml/m^2)	1.002	0.969	1.037	0.896
LAEF (%)	0.263	0.003	22.73	0.558
LVEF (%)	0.024	0.000	18.70	0.272
Sphericity	0.995	0.842	1.177	0.955
Constant	0.606			0.945

Table 5-6. Binomial logistic regression model: AF recurrence and CMR indices.

CI: confidence interval.

5.5 Discussion

The long-term outcome following AF ablation is excellent in selected patients but for others the outcome remains suboptimal. In parallel with technical and methodological developments in ablation procedures, improved patient selection has the potential to impact on success rates for intervention. Multiple CMR indices have been shown to be associated with long-term outcome, but their implementation in parallel has never been demonstrated. Moreover, many studies have excluded patients in AF, and it is this group that stands to benefit the most from accurate stratification. This study has taken a real-world cohort of first-time AF ablation patients, and the key findings are as follows:

1. LA fibrosis is independently associated with long-term outcome, as assessed by arrhythmia recurrence

2. LAEF, LVEF and indexed LA volume are significantly associated with outcome, but the association is not independent of other established baseline indices
3. LA sphericity, using the assessment methods of this study, is not associated with outcome.

5.5.1 Comparison with prior studies

LA fibrosis has been proposed as a powerful risk stratification modality for patients being considered for AF ablation. However, the implementation of the technique outside of two core centres in Utah and Johns Hopkins (Oakes et al. 2009; Khurram et al. 2015) has been limited. Teams in Bordeaux and London have validated fibrosis scores, using the Utah method and an automated maximum intensity projection technique respectively (Malcolme-Lawes et al. 2013; Jadidi et al. 2013). However, widespread adoption of the technique has been limited by the requirement for CMR imaging specialists and image processing teams using bespoke software and considerable experience.

This study has implemented a relatively streamlined approach in the generation of a fibrosis index, and has replicated the mainstream image thresholding techniques. The study did not set out to replicate the exact image processing techniques (see below), but instead aimed to produce a technique that could be made freely available to other centres and would eliminate as much of the subjectivity and time consuming segmentation as possible. Consequently, LA fibrosis scores are different for this study, as they are between previous studies. The hazard ratio per % increase in fibrosis in this study (1.035, 95% CI 1.013-1.058) was comparable to the DECAAF study (HR 1.06) and the IIR study (approximate HR 1.05). However, it is important to note that the mean fibrosis score was lower for DECAAF (18.1±8.7%) than this study and that for IIR (33.5±18.8% and 35.9±14.8% respectively), with a commensurate reduction in range. This infers a significantly weaker association of LA fibrosis and outcome than that found in DECAAF, but the superiority of one technique over another is difficult to explain in the context of low dice scores for overlapping scar on objective quantification (Karim et al. 2013).

LAEF, LVEF and indexed LA volume have been shown to be independently associated with outcome in other studies (Habibi et al. 2015; Dodson et al. 2014). In this combined assessment, the association was replicated, but was not shown to be independent of established risk factors. This may reflect the broad inclusion criteria, which are likely to weaken associations that are stronger in a more homogenous cohort. For instance, it is clear that LAEF may be associated with the rhythm at the baseline scan. However, a risk stratification method needs to be as inclusive as possible, and elimination of subjects in AF is not generally feasible. DC cardioversion can clearly be co-ordinated with MR assessment, but the time-dependent impact of cardioversion on LV and LA function has not been detailed sufficiently, and the longer the MR scan is delayed post-cardioversion, the more likely the arrhythmia is to recur. Larger, inclusive studies are required for the effective implementation of these measures in the PersAF population.

Somewhat surprisingly, LA sphericity demonstrated no association with AF ablation outcome, in contrast to the findings of other groups (Bisbal et al. 2013). It is an attractive index: reproducible and relatively intuitive to understand, as there is a clear variation in shape even to the naked eye. However, in this study there was no association with outcome, and this may be related at least in part to the method of assessment. Bisbal and co-workers assessed sphericity using a non-ECG gated magnetic resonance angiogram acquisition, which may acquire in atrial systole or diastole, whereas in this study the sphericity was assessed at a uniform point in the cardiac cycle, in atrial diastole. However, derived sphericity scores for this study and the Bisbal study were very similar (PAF: 81.1±3.2 versus 81.4±2.95 and PersAF: 83.3±3.3 and 82.8±3.4 respectively), as was the reliability of the measure (this study interobserver Lin's concordance correlation coefficient ICC 0.91, versus 0.94). The sphericity index may be more important when assessed in atrial systole, but this is dependent upon imaging in sinus rhythm. For the study described by Bisbal et al, there may also have been some degree of confounding of rhythm at scan (AF versus sinus) and sphericity, but in the current study the association between rhythm at scan and outcome was relatively weak, and further investigation is required.

5.5.2 Image interrogation

A mean intensity projection technique was used in this study, rather than a voxel by voxel (Khurram et al. 2014; Oakes et al. 2009) or maximum intensity projection (Malcolme-Lawes et al. 2013) technique. A voxel-by-voxel technique was avoided for two reasons. Firstly, delineation of the epicardial surface of the LA wall is difficult and subjective in many locations: the roof, floor and septal surfaces pose particular difficulties, and publications appear to include non-myocardial regions such as the interatrial fold in quantification methods of atrial fibrosis (Khurram et al. 2014). The delineation of the margins of the blood pool is generally less subjective, and there are data to suggest that the atrial wall thickness is relatively uniform in most regions (Hall et al. 2006). The degree of uniformity between subjects and locations requires further investigation and an atlas-based wall expansion index may improve image interrogation accuracy (Whitaker et al. 2016). Secondly, a voxel-by-voxel interrogation adds a further dimension to the image interrogation, increasing complexity where each location of the atrial surface represents a variable number of signal intensity values. An averaging process is inevitable in order to present a readily interpretable representation of fibrosis. A maximum intensity projection technique was avoided as it has been demonstrated that areas of fibrosis are detectable at below the blood pool intensity (Khurram et al. 2014): a maximum value, particularly if interrogation is performed inside as well as outside the endocardial border, will fail to detect any myocardial signal enhancement below the threshold of the blood pool.

However, there is an impact of the mean intensity projection technique on the application of thresholds. In this study, each surface point signal intensity value was derived as the average of multiple voxels (median n=2), and the standard error of the mean is reduced in proportion to $\sqrt{n}$. Consequently, the blood pool and shell standard deviations should be increased by $\sqrt{n}$, in order to account for averaging process. The change in fibrosis value from two to three to four SD above the

shell mean (see Figure 5-4) demonstrates the shift that occurs with such a change in threshold values, and further correction would be required to allow comparison of absolute values between techniques. Such a correction was not felt to be necessary at the outset as the absolute fibrosis percentages vary widely between studies. The crossover point for hazard ratio (from below- to above-average cohort risk) was approximately 35% for Khurram et al. (Khurram et al. 2015) and 18% for DECAAF (Marrouche et al. 2014): and the discrepancy does not invalidate the index itself. Indeed, the weakness of the correlation observed in Figure 5-4 and the preservation of association with outcome presents the interesting potential for the synergistic implementation of multi-level fibrosis thresholds for the same subject. Binarisation of fibrosis into scar and healthy based on a single threshold is clearly not physiological. The degree of fibrosis heterogeneity and ratio of dense versus low-grade scar merits further investigation in terms of improving predictive value of fibrosis assessment.

5.5.3 Clinical implementation

The aim of the study was to implement multiple CMR indices for AF recurrence post-ablation, with a view to generating a weighted risk score for future validation, based on all parameters and derived from a single imaging procedure. Such a risk score would be extremely valuable clinically. However, in this patient cohort only LA fibrosis was independently associated with outcome. The study may have been underpowered to detect the impact of LAEF, LVEF and indexed LA volume, especially in the context of minimal patient exclusion criteria. LA sphericity, as evaluated using this method, was not associated with outcome.

The most useful outcome would be a reliable predictor for patients highly unlikely to benefit from a standard ablation procedure. In this study, a fibrosis cut-off of 50% had a positive predictive value for recurrence of 80%. However, excluding this cohort would risk 20% of those patients not having a procedure from which they might otherwise derive substantial benefit. Furthermore, only 17/86 (20%) of patients fell into this high fibrosis group.

Larger studies may show that combining LA fibrosis with other CMR-derived indices improves predictive value further. Combination with other CMR indices such as atrial T1 mapping (Beinart et al. 2013; Ling et al. 2014), LV scar (Neilan et al. 2013; Suksaranjit et al. 2015), ventricular post-contrast T1-mapping (McLellan, Ling, Azzopardi, et al. 2014), and PV size (Hauser et al. 2015) may improve overall performance, but were not investigated in this study. However, a multimodality score is most likely to achieve the highest precision, and other non-invasive non-CMR indices including surface ECG dominant frequency (Lankveld et al. 2016), CHA_2DS_2Vasc score (Jacobs et al. 2015) and LA deformation patterns on echocardiography (Montserrat et al. 2015) may be combined with invasive characterisation such as voltage mapping (Masuda et al. 2016) (Kosiuk et al. 2015) in order to optimise ablation strategies through the identification of a high-performance biomarker.

5.5.4 Limitations

This study aimed to implement a 'real-world' assessment of CMR-derived indices, and it is important that limitations should be acknowledged. Firstly, the cohort size, and in particular the number of recurrences (30), is small for the evaluation of so many indices. However, the use of a single centre and two operators was important to minimise inter-procedural variations. Here, 96% of patients underwent ablation using contact force data, and criteria for progressing from PVI alone to more extensive ablation strategies were dependent upon patient and electrophysiological findings, and were not determined by CMR indices.

The use of arrhythmia recurrence as an outcome measure is imperfect on a number of counts. Firstly, arrhythmia episodes may be missed without continuous, uninterrupted, monitoring techniques. Even then, the algorithms for recognition of AF may fail to recognise some episodes. Secondly, death, stroke, symptoms or quality of life are more relevant outcome measures, but they are either thankfully rare or difficult to measure. Thirdly, even when arrhythmic episodes are captured, there is a lack of consensus on the definition of recurrence: typical atrial flutter is frequently defined not to constitute a recurrence. This study has used the most widely employed recurrence definitions, in the context of thorough clinical follow-up, but there exists the possibility that brief recurrences are likely to have been missed that may have been captured by more comprehensive monitoring strategies.

It is also important to consider whether patients should only be scanned in sinus rhythm. Imaging quality is generally inferior in AF, and indices vary between sinus rhythm and AF. However, as discussed, imaging immediately post cardioversion is unlikely to be the most robust solution, or straightforward to implement in all clinical environments. Correction of CMR indices for heart rhythm will be required if they are to achieve wider implementation.

5.6 Conclusion

In this study, the individual and combined predictive value of CMR-derived indices for AF recurrence post-ablation were evaluated. In this real-world cohort, only LA fibrosis was found to be independently associated with outcome. An effective biomarker for AF ablation stratification and tailoring of treatment is required, but it seems likely that CMR can perform only a partial evaluation of the atrial substrate. Combinations of multimodality indices or more sophisticated tissue characterisation techniques are required in order to further improve pre-ablation assessment.

5.7 Acknowledgements

I would like to thank Dr Orod Razeghi and Dr Rashed Karim for their work in helping to create a robust image processing platform and sphericity index derivation, Dr John Whitaker for performing some of the more recent CMR scans, Dr Rahul Mukherjee for assisting in the tracing of long-term outcomes, Kulvinder Lal for performing the inter-observer reproducibility assessments of sphericity, Dr Wieland Staab for performing the inter-observer reproducibility assessments of fibrosis, and

Jaspal Gill for performing the inter-observer reproducibility assessments of LA ejection fraction and LA volume. I would also like to thank all the KCL radiographers, including Leia Mazur, David Snell, Anita Kingston, Carl Evans, Cristelle Botha, Louise McGrath, and Stephen Sinclair for their patience, help and understanding in optimising the atrial imaging.

6 Intra-Procedural Imaging: Magnetic Resonance Guided Ablation of Typical Right Atrial Flutter

6.1 Contributions

All data (ex-vivo, pre-clinical and clinical) were published for the first time in a single manuscript (Henry Chubb et al. 2017), with the intention that the MR-EP system was presented as a single narrative. The narrative has been maintained for this chapter, but it is important to be clear regarding my contribution to the work detailed below.

The ex-vivo technical validation work was performed in Germany by Dr Steffen Weiss and Dr Sascha Krueger, who also performed the analyses. I have presented these results in my own words and with my own interpretation. The in-vivo technical validation work, porcine thigh muscle ablation, was performed in the USA by the Imricor team. For this work, I obtained the raw data and performed my own analyses, on account of the critical relevance of lesion formation in the light of atrial flutter recurrence. I have presented the results in my own words. The pre-clinical data was collected prior to the start of my PhD, co-ordinated by Dr James Harrison and performed in Aarhus in Denmark. Initial analysis was performed by James Harrison, and the text has been written by me based upon his detailed accounts. I co-ordinated and ran the clinical study, including MHRA and ethical approval, recruitment of all patients, management of the system set-up throughout the procedures, follow-up and scan at 3months and all data analysis.

6.2 Aims

To document the pre-clinical development and clinical implementation of an MR-guided ablation system with active catheter tracking.

6.3 Introduction

Over the last decade, centres worldwide have sought to establish the core technologies and techniques for MR-guided electrophysiological procedures (MR-EP). Building upon the principles of interventional MR procedures (Razavi et al. 2003), platforms have been developed that are capable of performing diagnostic and interventional electrophysiological (EP) procedures in an MR environment in animals (Lardo et al. 2000; Nazarian et al. 2008; Dukkipati et al. 2008; Schmidt et al. 2009; Hoffmann et al. 2010; Nordbeck et al. 2012; Ganesan et al. 2012; Ranjan et al. 2012; S. O. Oduneye et al. 2015) and humans (H. Chubb et al. 2014; Nazarian et al. 2008; Sommer et al. 2012; Grothoff et al. 2014; Hilbert et al. 2015). Whilst relatively simple in concept, MR-EP presents a range

of complex technical challenges. Most obviously, the operating environment is within a strong magnetic field, and therefore the use of magnetic material is severely curtailed. Other important challenges include radiofrequency (RF) safety, gradient field safety, and minimisation of mutual electromagnetic interference between MRI and EP components. All this must be achieved whilst maintaining the multiple functions of the ablation catheter (manoeuvrability, position tracking, measurement of low amplitude intracardiac potentials, pacing, temperature sensing, RF ablation energy delivery). Equally importantly, MR imaging with various suitable contrasts and MR device tracking must be developed and combined into a clinically viable workflow that replaces conventional fluoroscopy and exploits the unique capabilities of MR for imaging of cardiac anatomy and arrhythmia substrate.

On account of these challenges, overall progress in the field of MR-EP has been relatively slow. It has been possible to demonstrate use of ablation catheters within MR-scanners (Lardo et al. 2000; Nazarian et al. 2008; S. O. Oduneye et al. 2015), performance of ablation in animals (Schmidt et al. 2009; Hoffmann et al. 2010; Nordbeck et al. 2011; Ganesan et al. 2012; Ranjan et al. 2012) and of MR-guided ablation of atrial flutter in humans (Grothoff et al. 2014; Hilbert et al. 2015; Nordbeck et al. 2012). However, in order to make the leap from research to viable clinical tool, the realisation of RF-safe active tracking in a clinical-grade catheter is paramount. Passive tracking relies upon MR visualisation of the ablation catheter and is therefore slow and prone to localisation errors. Active tracking enables automation of the tracking of the catheter, freeing the operator to work in real-time throughout the cardiac target field.

The achievement of active tracking opens up all the strengths of fast electroanatomic mapping (EAM), including local activation time (LAT) mapping and voltage mapping, which may then be combined synergistically with real-time imaging of cardiac anatomy, arrhythmia substrate and surrounding structures. This study documents the development of the first MR-guided electrophysiology platform using active catheter tracking for ablation of arrhythmias from development to pre-clinical validation to clinical translation.

6.4 Methods

The technical development of the underlying technologies for the MR-EP catheter and guidance platform was performed between 2004 and 2010. This study details the pre-clinical optimisation, testing and system validation (2010-2013) and clinical studies with medium term follow-up (2014-2015). Approximately 9 months after the start of the clinical study, the system that was developed and validated was made available to a second group, who started clinical studies in 2015 and have recently published acute results of their first six cases (Hilbert et al. 2015). However, this paper describes the technical developments, their integration into a clinical system, as well as the pre-clinical validation and acute and medium term results in patients.

6.4.1 MR-EP setup

The working MR-EP setup combined a standard clinical 1.5 Tesla MR scanner (Achieva, Philips Healthcare, Best, Netherlands), a clinical patient monitoring system suitable for MR use (Expression, Invivo, Gainsville, FL, USA), a standard clinical RF generator (IBI 1500, St. Jude Medical, St. Paul, MN) with an investigational EP recording system specifically designed for MR use (Horizon, Imricor Medical Systems, Burnsville, MN, USA), investigational MR electrophysiology and ablation catheters (Vision Ablation Catheter, Imricor Medical Systems, Figure) and a novel MR-EP guidance platform for mapping and ablation of cardiac arrhythmias (Interventional MRI Suite (iSuite), Philips Research, Hamburg, Germany) (Figure 6-2).

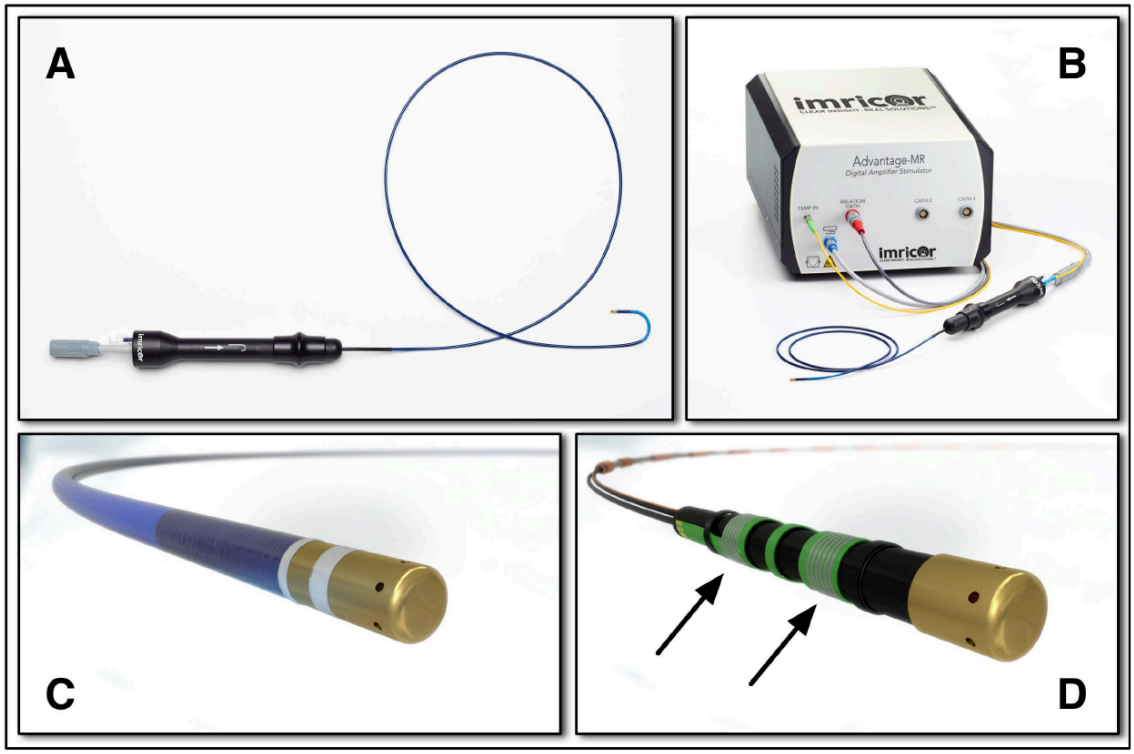

Figure 6-1. MR-EP Imricor investigational devices

(A) Investigational ablation catheter (Vision Catheter, Imricor) and (B) Horizon Digital Amplifier Stimulator (DAS) connected to ablation catheter. (C) Detailed view of ablation tip with (D) stripped back view. Arrows indicate location of two miniature solenoid receiver coils.

6.4.2 MR-compatible ablation catheter

An irrigated 9F deflectable MR-EP mapping and ablation catheter (Vision, Imricor Medical Systems) was designed for this study, equipped with a unidirectional deflectable tip (D-curve) utilizing a polymer pull cable. The electrodes were gold, rather than platinum, in order to reduce the MR-artifact (3.5mm tip electrode and ring electrode), and the catheter shaft was reinforced with polymer

braiding providing torque response. Ferromagnetic materials were virtually eliminated except for the miniature tuning capacitors used to tune the tracking coils to the scanner frequency. MR RF safety was ensured through multiple engineering solutions for cable and device configurations. Tracking coils (see 6.4.3) were connected via transformer cables with transformers deliberately located to minimize coil heating, (Steffen Weiss et al. 2005; Steffen Weiss et al. 2011). For the catheter electrode wires, an RF winding structure was used that passes small intracardiac electrogram (IEGM) potentials, larger pacing stimuli, and high power RF ablation energy, whilst simultaneously presenting a high impedance around the Larmor frequency at 1.5T (64MHz). Temperature sensing was facilitated by a fibre-optic cable utilizing a fibre Bragg grating at its tip. Gradient field safety was provided by a combination of the high resistivities and the Horizon MR-EP Digital Amplifier Stimulator (DAS- Figure 6-1B)

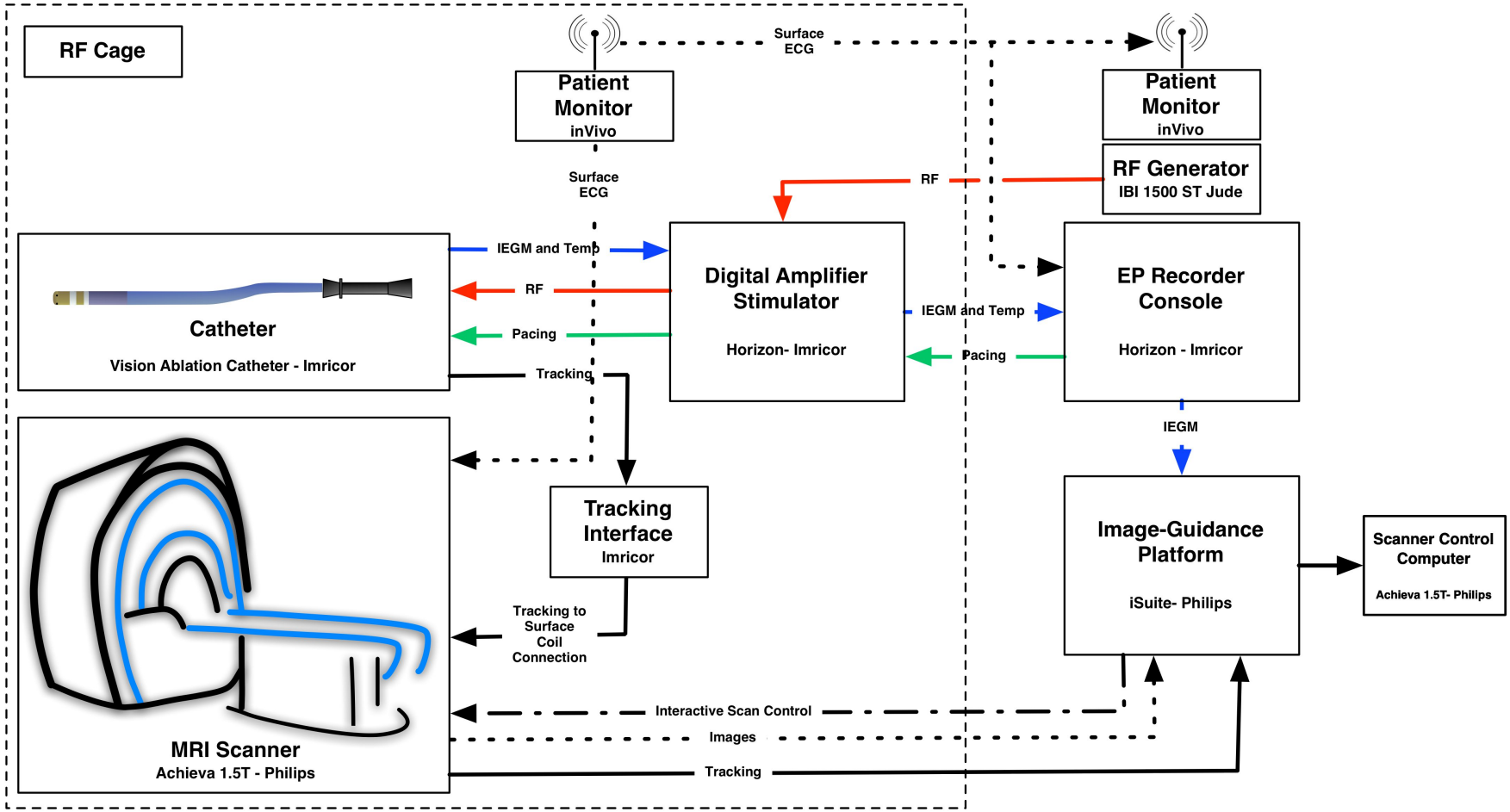

Figure 6-2. MR-EP setup.

IEGM: intracardiac electrogram.

6.4.3 Active catheter tracking

The investigational catheter was equipped with two miniature 2.5mm solenoid MR receive coils, positioned 2mm and 11mm proximal to the ring electrode (Figure S1(D)), and 7.75mm and 15.5mm proximal to the ablation tip. The receive coils were permanently tuned to the scanner frequency of 63.87MHz. The tracking sequence was a modified Fast Field Echo (FFE) sequence (10Hz tracking rate), acquiring signal from the blood around the coils and the system was capable of tracking up to three catheters simultaneously (TR 5.1msec, TE 2.6msec, in-plane resolution 0.83mm, flip angle 10degrees, acquiring three mutually orthogonal k-space lines through k_0, along the system main axes). A relaxation pause was added following the three readouts, giving a tracking frequency of 10Hz.

The catheter was connected to a catheter interface module (Horizon Tracking Interface, Imricor Medical Systems), comprising pre-amplifiers for the MR tracking signal and RF safety circuitry, which in turn was connected to a coil connector of the Achieva MR scanner. Robustness and accuracy of tracking was improved using orthogonal dephasing gradients in the MR tracking sequence, for background signal suppression (Charles L. Dumoulin et al. 2010), and a dedicated evaluation of the spatial projections of the micro coil signal for increased accuracy (see 3.4.2).

The tracking signal enabled the localization of the two tip coils in three dimensions. Using this information, the location of a 3D model of the catheter tip was displayed on the image guidance platform and overlaid on a pre-acquired balanced steady state free precession 3D whole heart (bSSFP-3DWH) dataset.

6.4.4 Electrophysiology recording system

The Horizon system (Imricor Medical Systems, Burnsville, MN) is an MR-Conditional EP recording system with an integrated stimulator that monitored, amplified, filtered and digitized the IEGM signals from the investigational catheters, and the ECG signals from the Invivo patient monitor. Horizon was also used to generate pacing stimuli and calculated the temperature measured at the fibre Bragg grating embedded in the tip of the ablation catheter. The system acted as an interface for RF energy delivery (including ablation return electrode) and to the iSuite image guidance system for electroanatomical mapping. The DAS was located within the scanner room, and the Horizon host computer and display module were located in the control room.

RF energy from a commercial RF generator (IBI 1500, St Jude Medical) was filtered in order to reduce imaging artifact and interference. Digitized IEGM and ECG data were transmitted to the Horizon host computer in the scanner control room via fiber optic cable, where IEGM, ECG, temperature, impedance, pacing parameters and status, RF power, and ablation duration data were displayed in real time on the Horizon display module (Figure 6-4). Pacing stimuli could be delivered to any

connected electrode pair. IEGM timing measurements were made manually and were transmitted via a dedicated Ethernet cable to the iSuite host computer.

6.4.5 iSuite image guidance platform

The iSuite (Philips Research, Hamburg, Germany) image guidance platform included a computer located in the MR control room with a custom software application, a software patch for the MR scanner, and an MR-conditional foot pedal located next to the scanner. The iSuite computer was connected to the MR scanner and the screen output of the computer was repeated on a monitor next to the scanner. A foot pedal was connected to the computer via a cable equipped with filters to remove RF noise and maintain MR image quality. All functions of the iSuite could be controlled from the computer, with simultaneous control of the imaging mode (real-time imaging or active catheter tracking) via the foot pedal. The iSuite provided visualisation of 3D datasets by multi-planar reformatting (MPR) of 2D slices in user-defined orientations, or by surface models created by segmentation of anatomical structures. The positions of the tips of the EP catheters were projected onto the surface model view and the MPR slice position automatically updated to show relevant views (Figure 6-3A).

There was also the facility to interleave real-time and cine MR image slices, with slice orientation calculated automatically to include the catheter shaft and demonstrate the catheter- myocardium interface. The scan plane was automatically modified to ensure it was perpendicular to the wall of the heart to give an accurate representation of the underlying morphology (Steffen Weiss et al. 2013; Voigt et al. 2013) (Figure 6-3B). Cine imaging parameters were TR 3.8ms, TE 1.9ms, flip angle 45 degrees, in-plane resolution 1.4x1.4mm2, slice thickness 8mm, 30 cardiac phases. Real time imaging was performed using a balanced fast field echo sequence (bFFE). Acquisition parameters were typically TR 3.0ms, TE 1.5ms, flip angle 45degrees, slice thickness 8mm, in plane resolution 2.3x2.3mm^2, SENSE factor 2, frame rate 8/s.

All electrical activation data was acquired during CS pacing. For each sampling point, the time delay from the pacing artifact to the local RA electrogram was measured on the EP recording system and automatically transmitted to the image guidance platform to produce a conventional color-coded LAT map on the RA shell (Figure 6-3A).

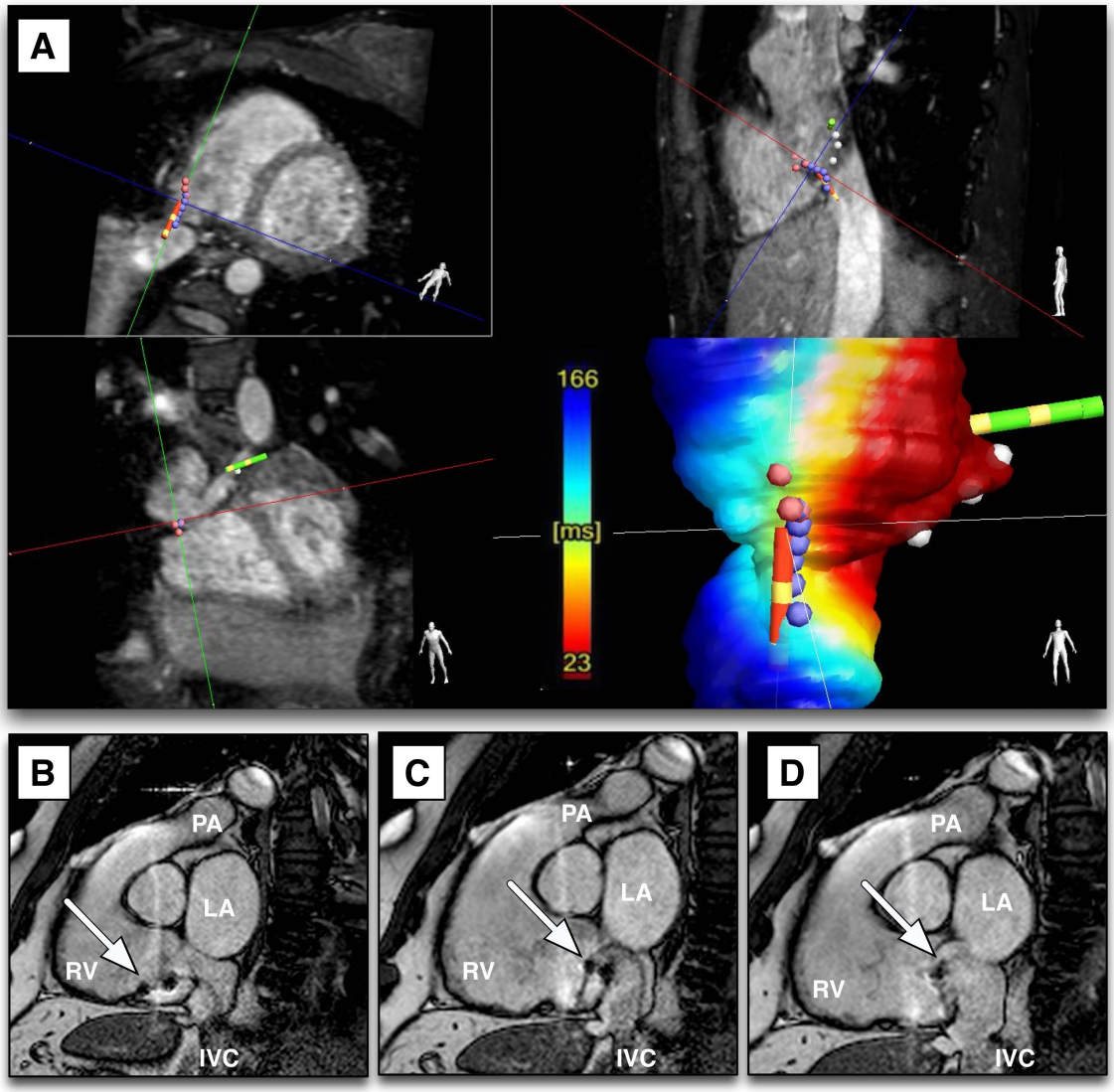

Figure 6-3. iSuite Visualisation.

A: Screenshot demonstrating three multiplanar reconstruction views, with projected ablation catheter (red) and coronary sinus catheter (green) positions. The 3D mesh shows local activation time map for right atrium. Red dots: ablation lesions delivered. Purple dots: planned ablation sites. B-D: Still frames from cine MR acquisitions during an ablation procedure. The minimal impact of catheter related artefact on the catheter-myocardium interface should be noted. Ablation catheter (white arrow) at tricuspid valve annulus (B), midway along cavotricuspid isthmus (C) and at the prominent Eustachian ridge (D).

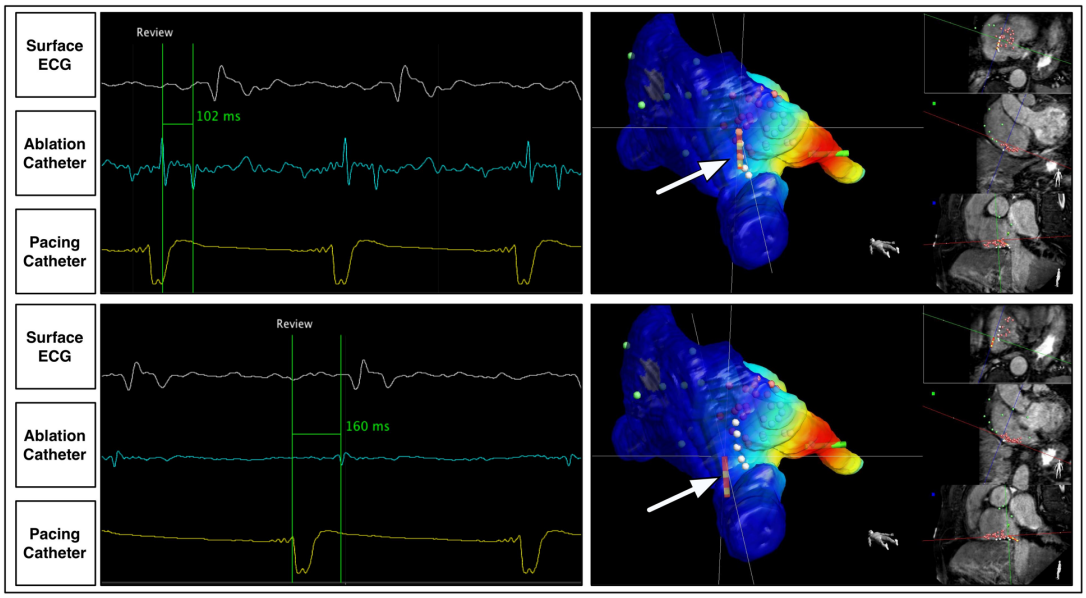

Figure 6-4. Intracardiac electrograms recorded during ablation procedure.

Top left: double potential on the ablation line (102msec), with corresponding catheter position shown top right (white arrow, ablation points in red). Bottom left: septal to lateral conduction delay (160msec) at end ablation, corresponding catheter position shown bottom right.

6.4.6 Ex-vivo technical development

6.4.6.1 Magnetically induced torque

The study was performed at MR:comp GmbH (Gelsenkirchen, Germany), according to ASTM F2213-06. The torque was measured by using a torsional spring, with the investigational catheter placed centrally on a holder, connected rigidly to the torsional spring. The apparatus was placed in the center of the magnet of the MR bore ((1.5T Intera, Philips Medical Systems) where the magnetic field was uniform. The torque was determined from the measurement of the deflection angle of the holder from its equilibrium position, and was measured at 36 angular positions, with maximum $\Delta\theta$ 17 degrees.

6.4.6.2 Magnetically induced force

The study was performed at MR:comp GmbH, according to ASTM F2052-06e1. The investigational catheter was suspended by a string at the point in the MR bore that produced the greatest magnetically induced deflection (1.5T Intera, Philips Medical Systems). Measurements were made at two locations: maximum technically accessible spatial gradient ($|\Delta B|$) (5.68T/m), and static spatial magnetic field gradient product ($|B|.|\Delta B|$) (7.76 T^2/m). The angular deflection of the string from the vertical was measured, and the force calculated..

6.4.6.3 RF heating

The study was performed in a Philips Intera 1.5T scanner in a mobile MRI unit leased from DMS Health Technologies (Maple Grove, Minnesota), using a phantom that met the specification of ASTM F2182-02. A balanced turbo field echo scan was selected on account of high reported SAR (TR 4.8ms, TE 2.4 ms, Whole body/level 4.0W/kg), with scan duration 800seconds. Temperature was assessed using Neoptix (Québec, Canada) T1 fibre optic temperature sensors, and Neoptic Reflex signal conditioner for receiving and recording temperature measurements.

In stage 1, saline was used to determine the insertion length resulting in maximum temperature rise, with temperature measurements taken at 5cm intervals along a curved trajectory. Once this was ascertained (40-45cm insertion depth), the test media was changed to gelled saline, in order to eliminate thermal convection (conductivity 0.48S/cm), and temperature rise assessed with the investigational catheter placed at the assigned location for maximum temperature rise.

6.4.6.4 Active catheter tracking

The study was performed in Hamburg, Germany using 1.5T Achieva MR Scanner (Philips). The investigational catheter was suspended by a dedicated device holder and positioned in a bowl phantom filled with standard phantom liquid. Subsequently, the catheter was fixed in different orientations to assess the influence of read-out and B_0 direction. For each orientation, MR imaging and active tracking measurements were used to estimate the tip position and direction independently. The difference in catheter position as derived from imaging and tracking measurements was evaluated as tracking accuracy. The standard deviation of repeated active tracking measurements was evaluated as tracking precision. Imaging was performed using a turbo spin echo (TSE) single slice protocol (TR 158ms, TE 5.8ms, TSE factor 11, T_{shot} 64ms, in-plane resolution 0.6x0.6mm, slice thickness 1.5mm), and taken to be gold standard of tip position. True tip position on MR imaging was degraded by metal artefact related to the gold catheter tip, and therefore a wooden pin was aligned parallel to the catheter, with identical tip position in a direction parallel to catheter axis, and was used to calculate exact tip location.

6.4.7 RF lesion formation- porcine thigh model

Procedures were performed at the Animal Preclinical Services Laboratory, Minneapolis, MN, USA, registered with the United States Department of Agriculture to conduct research in laboratory animals. The studies were reviewed and approved by the institutional Animal Care and Use Committee. Five Yorkshire Cross pigs were used. Under anaesthesia, a cut-down of the lateral thigh muscle was performed. The skin was tented to create a cradle to pool blood or saline during testing, and circulating blood was added to the cradle during the application of RF energy.

The study was performed as an open, unmasked study. Each animal received standardised irrigated (17ml/min) RF ablation with either the control catheter (Biosense Webster Thermocool, Diamond Bar, CA, USA) or the investigational catheter (Vision Catheter), using IBI T1500 RF generator (St Jude). A total of 76 ablation lesions were performed for each catheter, with each thigh receiving

lesions solely from control or test catheter. The following ablation parameters were selected to cover the range of settings that may be used for clinical electrophysiology studies (Table 6-1).

	Duration			
	30 seconds	60 seconds	90 seconds	120 seconds
Power (W)	20	20	20	20
	25	25	25	25
	30	30	30	30
	35	35	35	35
	40	40	40	40
	45	45	45	45
	50	50	50	50

Table 6-1. Duration and power settings evaluated for the Vision ablation catheter and Thermocool catheter.

Following all treatment, femoral arterial sheaths were placed to administer TTC (2,3,5-Triphenyl-2H-tetrazolium chloride) to the lesion sites, and euthanasia was performed following adequate circulation. The thigh was then isolated and immersed in 10% NBF. Measurements were made of lesion surface length, surface width and depth following incision along the lesion axis.

6.4.8 Subjects

6.4.8.1 Pre-clinical study

The complete MR-EP ablation system was tested prospectively in five Danish Landrace pigs (Aarhus University Hospital, Skejby, Denmark, approximately 40kg). Studies complied with institutional and national guidelines for the care and use of animals.

6.4.8.2 Clinical study

Ten patients with typical atrial flutter were consented for ablation of isthmus dependent atrial flutter under MR guidance. Inclusion criteria were age 18-80 years undergoing first time clinically indicated ablation therapy of documented paroxysmal or persistent counter-clockwise (typical) right atrial flutter. Procedures were performed on uninterrupted warfarin or interrupted rivaroxaban. Exclusion criteria included any contraindication to MR imaging or GBCA, previous ablation, previous cardiac surgery and any intracardiac mass including thrombus or myxoma. Patient characteristics are summarised in Table 6-2.

	Value
Age/ years	62.1 (±14.5)
Weight/ kg	82.7 (±13.6)
BMI/ kg/m²	26.8 (±3.9)
Male Gender	8 (80%)
Significant Comorbidities	7 (70%)
Flutter at Procedure	7 (70%)
Structural Heart Disease	0
Left atrial volume/ml	121 (±48)
Right atrial volume/ml	131 (±72)
LV ejection fraction	64% (±5.2%)

Table 6-2. Baseline patient characteristics.

BMI: body mass index.

One further subject was accepted for the study, but did not undergo an interventional procedure. The subject met all inclusion criteria, met no exclusion criteria and was fully informed and consented. However, relative contra-indications were present, with a raised body mass index, borderline low left ventricular function and previous right hip replacement. The patient was aware that it might not be possible to proceed to ablation on the day of the procedure, and following careful discussion it was felt that if there were any instability under anaesthesia, the risks of performing the procedure in an MRI environment were likely to outweigh any potential benefits. On clinical grounds a transesophageal echocardiogram was performed under general anaesthetic, with detailed CMR imaging to review coronary arteries, ventricular function and ventricular scar. However, cardiovascular stability under anaesthesia was poor and LV function was worse than on pre-procedural assessment, and therefore the interventional procedure was not performed. The subject has subsequently had a standard CTI ablation. This subject has not been included in further analysis and the local monitoring team was informed of the decision not to proceed to ablation under MR-guidance.

The clinical study was performed at the interventional MR suite, St Thomas' Hospital (London, UK), approved by the UK Health Research Authority (NRES Committee East of England, reference 14/EE/0031, UKCRN Study ID 14226), and informed consent was obtained from all patients.

6.4.9 Pre-clinical system evaluation

The procedure was performed in the MR scanner without fluoroscopy. Animals were pre-sedated using azaperone (4 mg/kg) and midazolam (0.5 mg/kg). General anaesthesia was induced using intravenous ketamine (5 mg/kg) and midazolam (0.5 mg/kg), and maintained with propofol (3mg/kg/hr) and fentanyl (15mcg/kg/hr). Animals were intubated and mechanically ventilated. Two 9F sheaths were placed percutaneously in the right femoral vein, followed by a bolus intravenous injection of 100 IU/kg heparin.

6.4.9.1 Pre-clinical: Pre-ablation Imaging

A bSSFP-3DWH dataset was acquired without contrast in order to provide a 'road-map' for the procedure. An acquisition window in ventricular diastole was selected, with maximum window 180msec (sagittal orientation, 2x2x2mm resolution, (reconstructed 1.3x1.3x1.3mm), T_2 preparation, pencil respiratory navigation, five-channel phased array coil). The RA was manually segmented from the bSSFP-3DWH using freely available 3D medical image segmentation software (itk-SNAP Version 2.2.0) and the shell imported into iSuite to act as a roadmap for mapping and ablation.

As a baseline for post-ablation imaging, T2-weighted (T_2W) images were also acquired prior to ablation (multi-slice Turbo Spin Echo (TSE), double inversion recovery (DIR) pre-pulse, SPIR fat suppression, echo time (TE) 45ms, repetition time (TR) twice the cardiac cycle length, 1.5x1.5 mm (reconstructed 1.0x1.0 mm), slice thickness 3mm).

6.4.9.2 Pre-clinical: electro-anatomical mapping and ablation

Active catheter tracking was used to place investigational catheters in the coronary sinus (CS) and RA, using the segmented roadmap. Activation data was acquired during CS pacing. For each sampling point, the time delay (LAT) from the pacing artifact to the local RA electrogram was measured on the EP recording system and automatically transmitted to the image guidance platform to produce a color-coded activation map on the RA shell.

Point-by-point RF ablation (35W, 48^{o}C, 60s per lesion, 17 ml/min irrigation) was then performed from the superior vena cava (SVC) to the inferior vena cava (IVC) along the posterior wall of the RA and the location of each ablation point recorded on the RA shell. A linear set of RA ablation lesions, rather than CTI line, was chosen due to the propensity of swine to develop VF in response to RV ablation. The foot pedal was used to allow rapid switching from active catheter tracking (for catheter navigation) to real-time imaging (to confirm the tracked catheter position before each RF delivery).

Following completion of the intercaval ablation lesion and post-ablation MR, the activation map was repeated according to the same protocol.

6.4.9.3 Pre-clinical: post-ablation imaging and histology

T_2W imaging was repeated immediately post-ablation with identical parameters. 3D LGE imaging was then performed approximately 20minutes after administration of 0.2ml/kg Gadovist (Bayer HealthCare Pharmaceuticals, Berlin, Germany). (Respiratory-navigated, ECG-triggered inversion recovery turbo field echo acquisition, 1.3x1.3x4 mm, reconstructed to 0.6x0.6x2 mm (TE 3.0ms TR 6.2 ms, flip angle 25°)).

Following procedure completion, euthanasia was performed using an intravenous bolus of phenobarbital (80 mg/kg) and the porcine hearts were explanted and the RA was opened and photographed. The hearts were then fixed in formaldehyde. The ablation line and surrounding tissue were excised *en bloc* and cut into 4mm sections perpendicular to the ablation line. Each cross section was photographed and then dehydrated, embedded in paraffin, sectioned (3μm sections) and stained with haematoxylin and eosin for microscopic examination.

6.4.10 Clinical study

For the clinical study, procedures were performed under general anaesthesia. Beyond the five Gauss (500μTesla) line, two 10F long venous sheaths were placed percutaneously in the right femoral vein and the patient was then moved to the MR scanner bore.

6.4.10.1 Clinical study: pre-ablation imaging

bSSFP-3DWH imaging was performed without contrast as above (32-channel phased-array coil). Patients in atrial flutter (7/10 subjects) at the start of procedure underwent DC cardioversion (50-100J) prior to entry to the scanner in order to facilitate cardiac gating. An automated segmentation technique, using a shape-constrained deformable-model, was used to derive the RA contour (SmartHeart, Philips Research, Hamburg, Germany). CS and IVC were delineated manually (itk-SNAP) and added to the cardiac model to assist the procedure.

The length and morphology of the CTI were measured on bSSFP-3DWH using the technique detailed by Kirchhof et al (Kirchhof et al. 2009). IVC/CTI angle was measured as the angle between two tangential lines placed parallel to the CTI floor and the adjacent wall of the IVC. Measurements were performed twice by a single observer (HC, one month between measurements) and once by a second observer (JH) to assess reproducibility.

6.4.10.2 Clinical study: electro-anatomical mapping and ablation

Activation mapping was performed as above prior to ablation. A point-by-point RF ablation (35-45W, 60s per lesion, 17 ml/min irrigation) was performed along a pre-planned CTI line during coronary sinus pacing. CTI conduction block was confirmed by a superior to inferior activation pattern at the lateral wall on CS pacing, with LAT mapping repeated following completion of ablation. Bidirectional block was confirmed by differential pacing from two sites lateral to the CTI line.

The protocol allowed a maximum of two hours (from first ablation lesion) to obtain bidirectional CTI block. For patients in whom this was not achieved, the subject was moved to a conventional fluoroscopy suite and ablation completed using a conventional non-irrigated ablation catheter (Large Curve Blazer II, 8mm tip (Boston Scientific, Mass., USA)) under fluoroscopic guidance.

6.4.10.3 Clinical study: post-ablation imaging

All clinical subjects underwent acute T_2W imaging immediately after ablation (parameters as above). 3D LGE imaging was performed acutely post-ablation for all but two human subjects that underwent MR-guided ablation: the time required for procedure completion precluded late acute imaging in these two subjects. LGE acquisition parameters were identical to those for the pre-clinical study, but performed in a slice orientation parallel to the CTI. Multiple time-separated LGE acquisitions were performed, and the dataset commenced at 20minutes post-contrast was used for RF lesion analysis. T_2W enhancement was quantified using a threshold of 3.3 standard deviations (SD) above the adjacent right ventricular myocardial signal, and ablation volume was assessed within the pseudo-3D dataset using Seg3D (University of Utah, Utah, USA).

Chronic lesion imaging was performed at 3 months post ablation. An ECG and respiratory gated Magnetic Resonance Angiogram (MRA) was performed using a previously described technique (Groarke et al. 2014). This high contrast sequence was used to derive a mask of the RA for interrogation of the 3D LGE sequence imaging the CTI, acquired along the axis of the CTI ablation line (acquisition parameters as for acute LGE post-ablation imaging, commenced at 20minutes post contrast injection). MR derived scar was interrogated using a maximum intensity projection (MIP) technique (2mm inside and outside RA shell), and thresholded on the 3D scar mesh to a signal intensity of 3.3SD above the blood pool mean (James L Harrison et al. 2014). The ablated area of the RA floor was assessed defining the superior margin of the RA floor as the most inferior axial slice lying above the CS os, and inferior margin as the most superior axial slice below the RA floor. Measurements were performed using Paraview (Kitware, New York, NY, USA) (Figure 6-5).

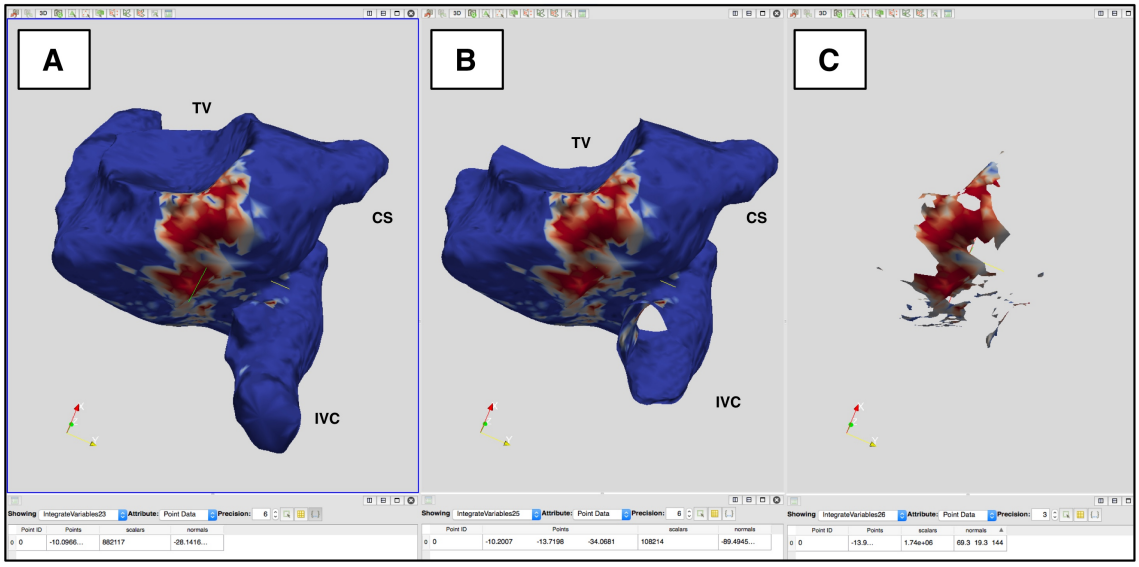

Figure 6-5. Assessment of cavotricuspid isthmus scar.

A: the maximum intensity projection mesh was thresholded at 3.3 standard deviations above the blood pool mean, and the region of the floor of the right atrium defined as described in the text (B). The total scarred area was then measured (C). TV: tricuspid valve, CS: coronary sinus, IVC: inferior vena cava.

Lesion specific scar was also assessed using a point-specific technique. The catheter tip site during RF delivery was recorded relative to the bSSFP-3DWH sequence, and then referenced to the chronic imaging using an affine registration technique (Rueckert et al. 1999). The registration technique was used to define the matrix for the transformation of the bSSFP-3DWH during ablation to the 3D MRA sequence at chronic imaging, and the same matrix was applied to the RF delivery sites. The derived RF lesion sites were then projected to the closest surface on the 3D scar mesh and the projection distance and associated scar were recorded. The scar value was recorded as the maximum signal intensity within a 3mm radius of the projected lesion site (Figure 6-6).

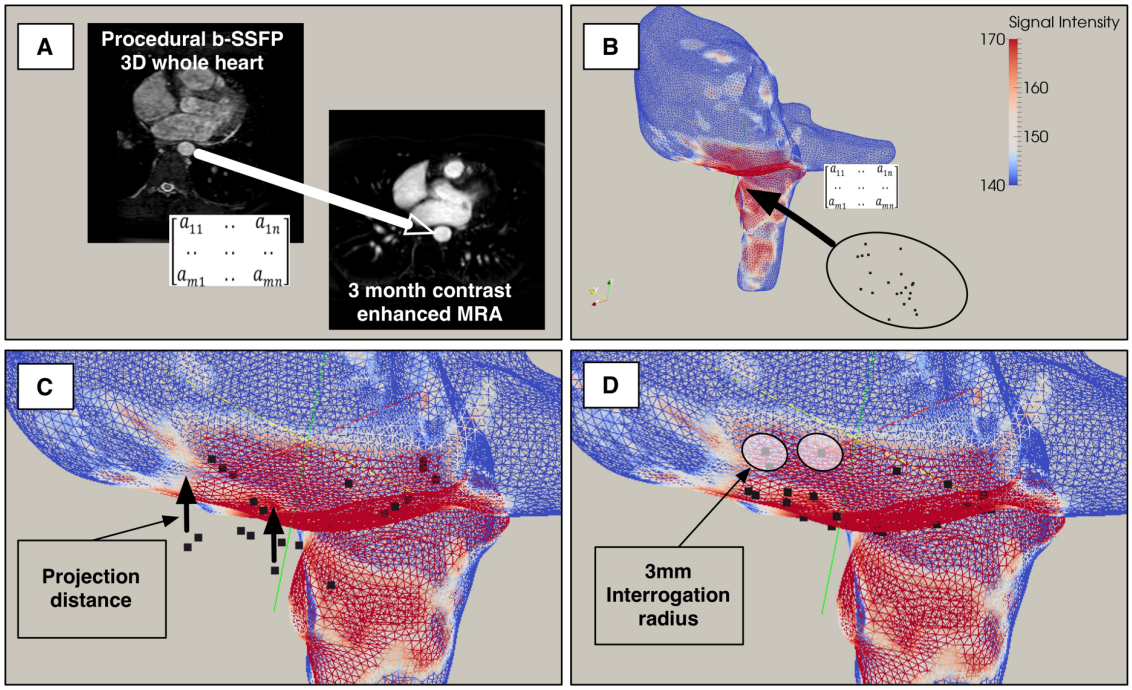

Figure 6-6. Method for evaluation of scar formation at lesion sites.

A: derivation of rigid registration transformation. B: typical right atrial mesh, with ablation lesion sites shown as black dots within the same Cartesian co-ordinate system (black circle). The matrix represents the transformation derived from the rigid registration (A), which is applied to the lesions in order to move to the same patient space. C: ablation lesions are then projected to the nearest mesh position, and the projection distance recorder. D: the scar around each ablation lesion site was then interrogated, using a 3mm radius.

6.4.10.4 Clinical study: hepatic injury

Hepatic injury was assessed acutely and at three months post ablation. T_2-weighted imaging and gadolinium enhanced imaging were visually assessed, and graded according to a four-level grading system. Imaging was thresholded at 3.3 standard deviations above RV myocardium for T_2-weighted imaging, and 3.3 standard deviations above blood pool for LGE. Nil: no enhancement; mild: hepatic capsule only; moderate: hepatic capsule and liver <5mm depth; severe: hepatic capsule and liver >5mm depth. Chronic scar was assessed on LGE imaging as described above. The liver was manually segmented and a maximum intensity projection technique used to interrogate enhancement. Projection distance was 1mm outside of liver, and 3mm within liver, in order minimise interrogation of diaphragm, pericardium and adjacent myocardium.

6.4.11 Statistics

Continuous variables are expressed as mean ±standard deviation. Statistical analysis was performed using IBM SPSS Statistics (Version 22, Armonk, NY). ANCOVA (full factorial model) was used to

determine difference of regression lines, and intra-class correlation coefficient was calculated using a two-way mixed model.

6.5 Results

6.5.1 Ex-vivo technical validation

The maximum magnetically induced torque and force on the investigational catheter at 1.5T were <2.2mNm and <7.7mN respectively, well below regulatory thresholds (351mNm and 79.5mN). The maximum temperature rise on any portion of the investigational catheter due to RF induced heating was observed at the tracking coil locations at a catheter insertion depth of 45cm, and was measured to be 2.1°C above background heating.

Average tip displacement, the discrepancy between actively tracked and gold-standard TSE-derived positions, along the axis of the catheter, was 0.90±0.58mm. The angular deviation of catheter orientation from its true direction was 8.5 ±3.6degrees.

6.5.2 In-vivo technical validation

In the assessment of system RF ablation energy delivery, the porcine thigh lesion formation using the control catheter (Thermocool) was greater per energy delivered than that for the Vision catheter 0.057 mm^3/J (95% CI 0.041 to 0.072) versus 0.036 mm^3/J (95% CI 0.029 to 0.044), p=0.02). The coefficient of determination (R^2) for lesion formation was lower for the control catheter (0.424 versus 0.544) (Figure 6-7).

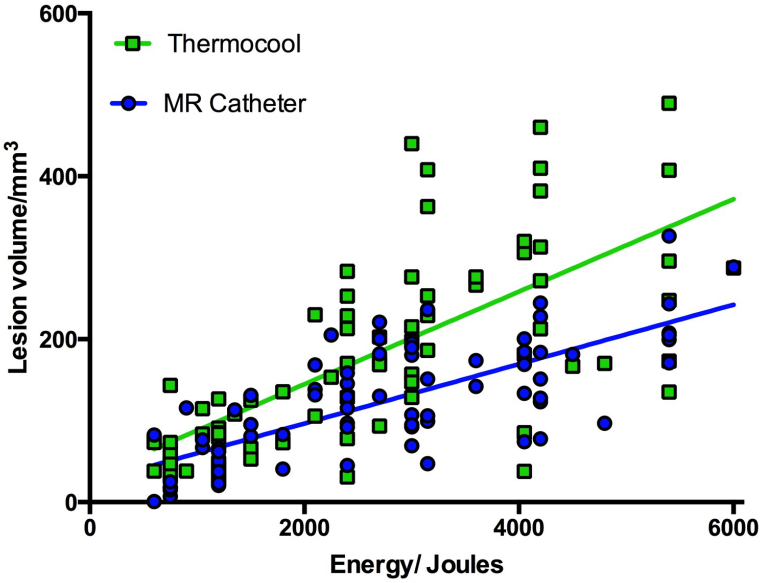

Figure 6-7. Ablation lesion formation in a porcine thigh model.

Lesion volume is plotted against total delivery energy.

6.5.3 System performance

6.5.3.1 Pre-clinical study

Active catheter tracking was achieved in all animals, and the two investigational MR catheters were positioned in the CS and RA without the requirement for fluoroscopy. Bipolar IEGMs were recorded with minimal MR interference and a LAT map was created during CS pacing in all animals. Using active tracking, activation maps during CS pacing were created in all animals (mean number of points 34 ± 5, mean acquisition time 20 ± 8 minutes) prior to ablation. Irrigated RF ablation was successfully performed from the SVC to IVC in all five animals. Activation maps following ablation demonstrated a change in the pattern of activation of the RA, with activation detour secondary to the linear ablation lesion.

All five animals survived until the end of the procedure and there was no evidence of cardiac perforation, pericardial effusion or cardiac tamponade.

6.5.3.2 Clinical study

Active catheter tracking, appropriate catheter manipulation and activation mapping were achieved in all 10 subjects. SmartHeart was capable of creating a 3D roadmap automatically in all subjects, and LAT map (28±7 points) created in 24± 11minutes. Cine MR imaging was used to confirm catheter position and there was no detected discrepancy in projected and imaged positions (Figure 6-3B-D), including during RF delivery. Bipolar EGMs of sufficient quality for local activation annotation were recorded (Figure 6-4).

MR-guided RF ablation was performed in nine of the 10 subjects. Ablation was not possible for one subject due to a persistent impedance error detected by the non-investigational RF generator, later attributed to an error in generator setup. The procedure was therefore performed in a conventional EP laboratory. For the nine remaining subjects, seven (78%) had an acutely successful procedure under MR guidance alone with a post-procedural transisthmus conduction time ranging from 124msec to 180msec (mean 160msec). Two subjects (22%) required completion of the CTI line under fluoroscopic guidance, using a conventional non-irrigated ablation catheter (post-MR guided ablation transisthmus conduction times 73 and 95 msec respectively). Radiation exposure in patients who underwent solely MR-guided ablation was zero, and was mean 90 (range 64-106) $cGy.cm^2$ for those three patients who required conventional fluoroscopically guided ablation.

Total procedure time was 314±54 minutes, including the additional time for conventional fluoroscopically guided ablation (286±29min excluding fluoroscopy). Time from first to last ablation lesion under MR guidance was 78±40 min, with an average of 24±9 lesions required under MR guidance (total ablation time 18.3±9.1 min) (Figure 6-8). There were no significant safety concerns and all patients were discharged within 24 hours of the procedure.

Final ablation outcome is summarised in Figure 6-9. Two subjects had a late recurrence of atrial flutter. One returned asymptomatic at three months and the second presented symptomatic to the emergency department. Both patients underwent a second ablation procedure under conventional EAM guidance (CARTO 3, Biosense Webster/Johnson&Johnson, USA) with evidence of low voltage IEGMs in the region of prior ablation (Figure 6-10). In all other patients there were no further arrhythmias detected on 24-hour tape or 12-lead ECG at 3 months follow-up.

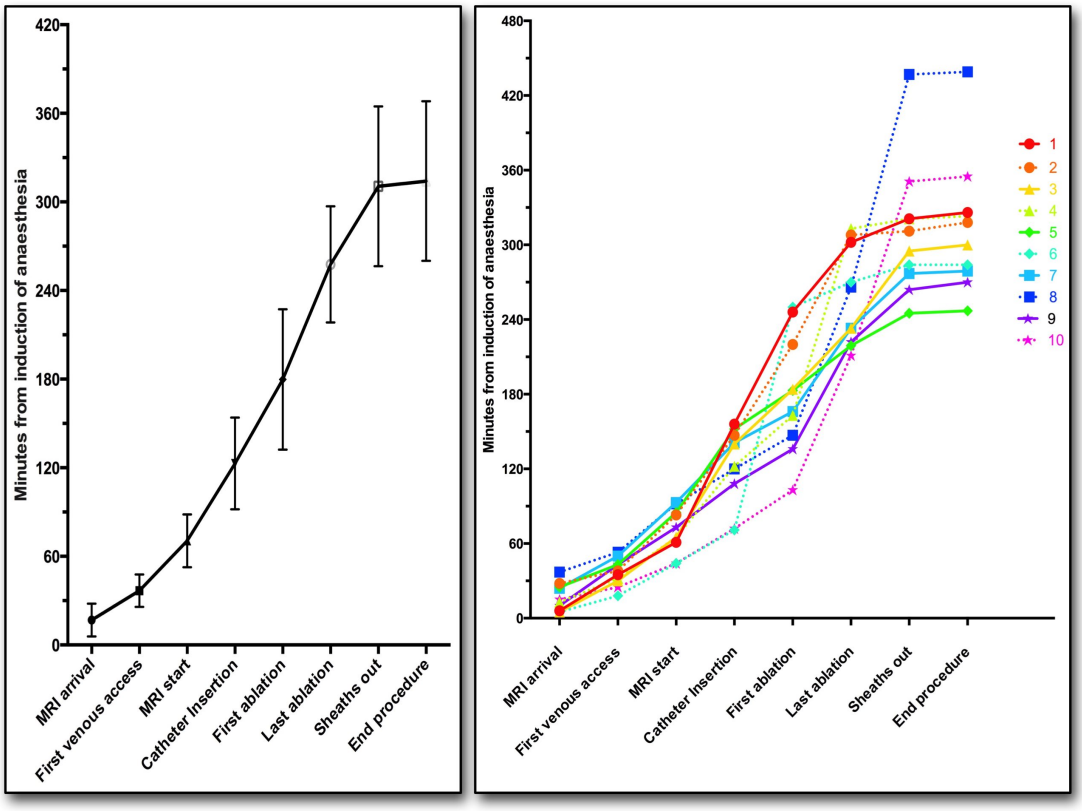

Figure 6-8 Clinical study procedural time breakdown.

(Left) Aggregate timeline for human flutter ablation procedures. (Right) Breakdown for individual subjects. Subjects 8 and 10 required completion of MR-guided ablation under fluoroscopic guidance. Subject 6 had ablation performed under fluoroscopic guidance following non-investigational equipment error.

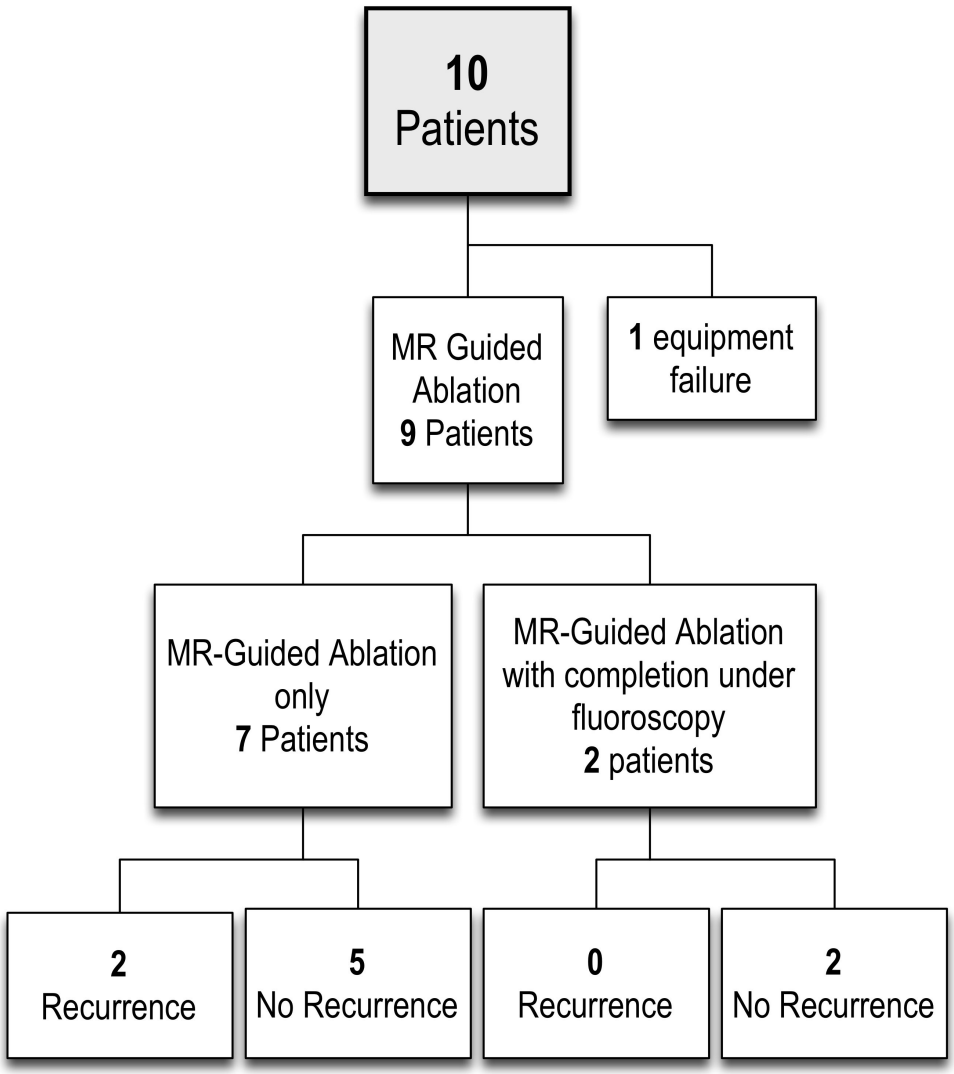

Figure 6-9. Flowchart outlining study outcome for human subjects

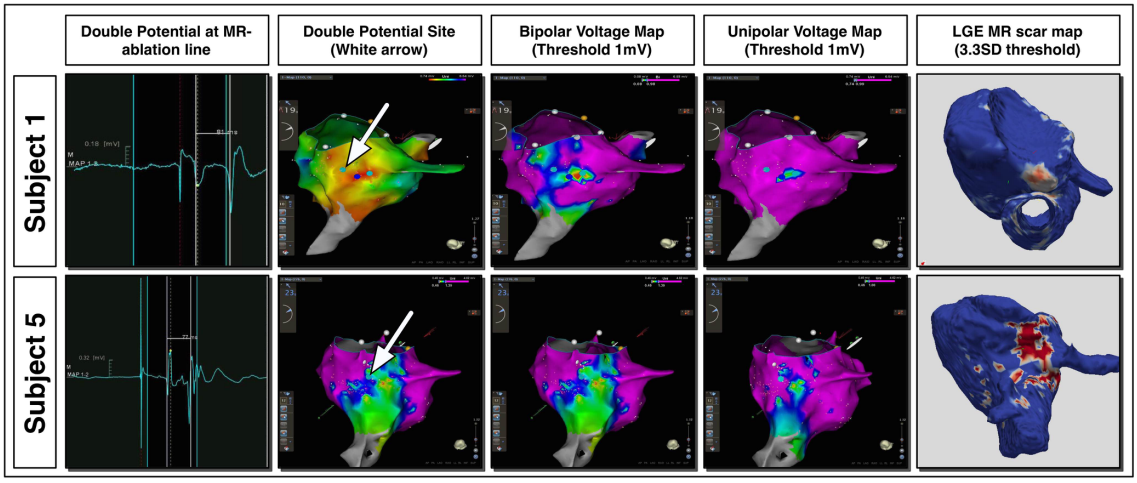

Figure 6-10. CARTO3 assessment of the intracardiac electrical characteristics following MR guided ablation, for the two subjects with atrial flutter recurrence.

Double potentials were recorded on the MR-guided ablation line, with reduced bipolar and unipolar voltage at the site of prior ablation and scar as assessed on late (3month) CMR imaging (far right panel).

6.5.4 Intra-procedural ablation assessment

6.5.4.1 Pre-clinical study

Pre-ablation, no appreciable T_2W enhancement was seen in any of the animals. Post-ablation, there was increased T_2W enhancement and atrial wall thickness between the SVC and IVC in all animals.

6.5.4.2 Clinical study

Post-ablation T_2W imaging was performed at a mean of 27±17 min after the final ablation lesion. Mean volume of CTI T_2W enhancement was 6.4 (±4.0) ml and there was no significant correlation with total ablation time (R^2=0.009). Gaps in T_2W enhancement along the ablation line could not be discerned in any patient, and enhancement position closely overlaid ablation lesion sites (Figure 6-11). Gadolinium-enhanced imaging was performed in 7 out of 9 human subjects who underwent MR-guided ablation. Early no-reflow in the CTI region was seen in all 7 cases, with subsequent LGE (Figure 6-11). Again, there were no discernible gaps in the ablation line.

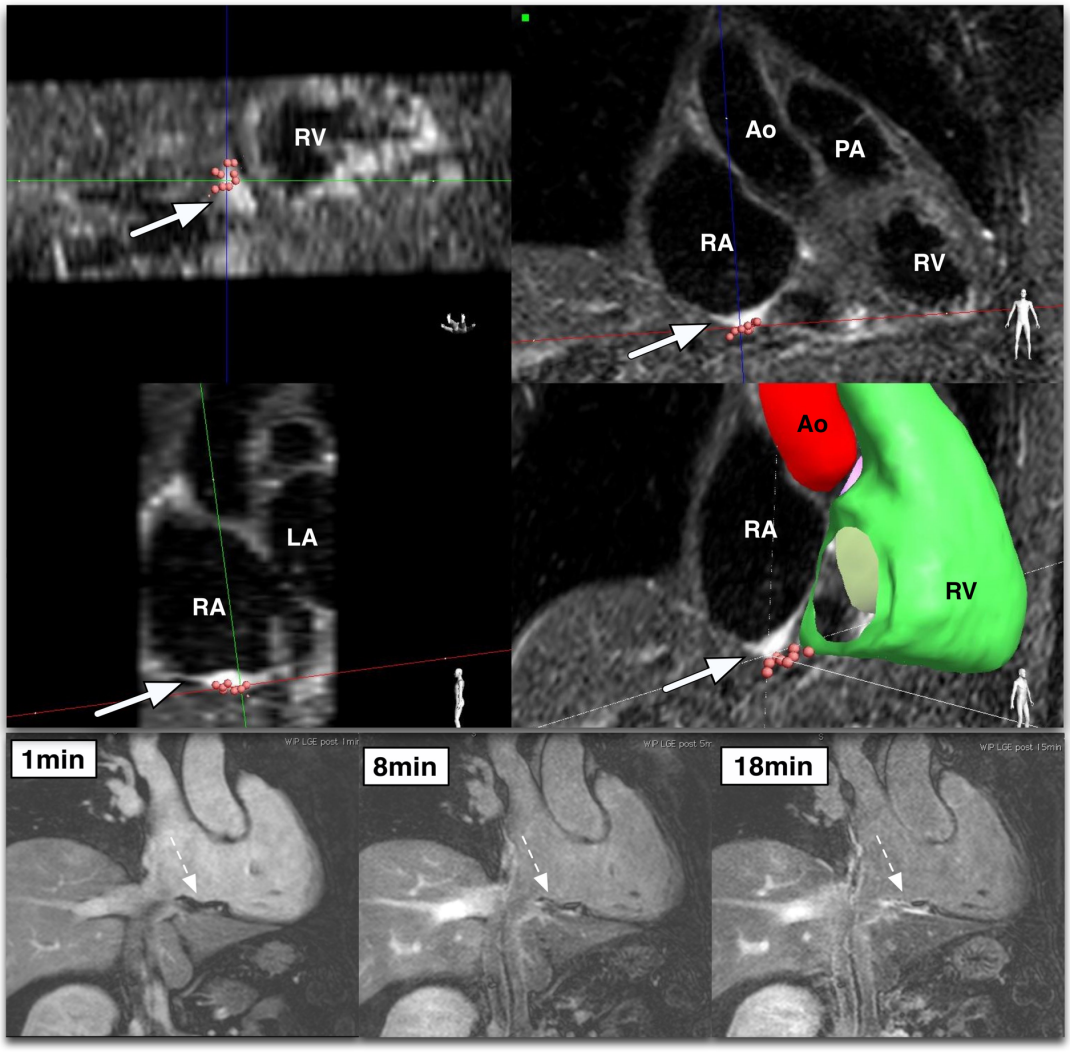

Figure 6-11. Acute post-ablation imaging.

(Top four panels) Multiplanar reconstruction of pseudo-3D T2 weighted MR acquisition, demonstrating location of oedema (white arrows) at cavotricuspid isthmus following ablation. Red dots indicate location of radiofrequency energy delivery calculated using active tracking. (Bottom three panels) gadolinium enhanced imaging for a single human subject following successful ablation. Dashed white arrow indicates cavotricuspid isthmus location, and time in minutes is following GBCA administration. Dark regions of early non-enhancement ('no reflow', indicating poor tissue perfusion of gadolinium contrast following ablation) at 1min become progressively more enhanced over the subsequent 18minutes with slow uptake of GBCA then sequestration within the increased extracellular space related to radiofrequency lesions. (RA: right atrium, LA: left atrium, PA: pulmonary artery)

6.5.5 Final lesion assessment

6.5.5.1 Pre-clinical study

The linear ablation lesion was inspected macroscopically, both immediately after heart explantation and following fixation in formaldehyde. There was close correspondence between the iSuite 3D RA shell, showing the intended location of ablation, and the sites directly visualised (Figure 6-12A and B). A macroscopic cross-section through the ablation line (showing the typical features of RF injury – a central zone of pallor and a surrounding haemorrhagic border zone) and microscopic sections (stained with haematoxylin and eosin) are shown in Figure 6-12D and E. Microscopic examination demonstrated histological findings consistent with RF ablation.

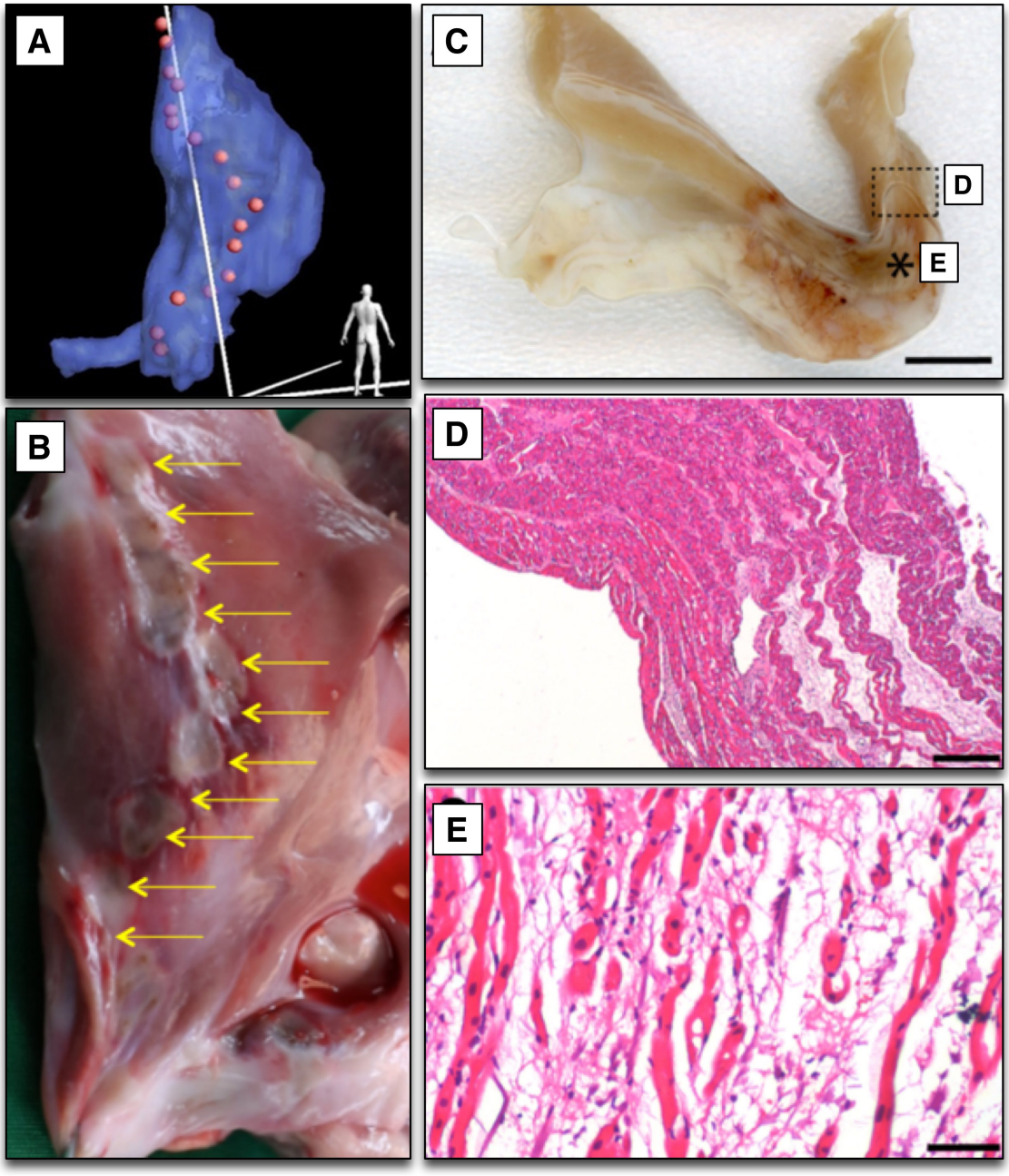

Figure 6-12. Histological validation of ablation in pre-clinical study.

*Macroscopic examination. A: 3D anatomical shell from iSuite in a corresponding view showing the position of ablation lesions (red circles). B: macroscopic view of the opened RA, with the SVC at the top of the image and the IVC at the bottom of the image. The ablation line is seen on the posterior wall of the RA (arrows). Microscopic examination. C: tissue slice cut perpendicular to the ablation line shows transmural injury. Scale bar 5 mm. D: border zone between ablated and spared atrial wall (marked with dashed box in C). Haematoxylin-eosin stain. Scale bar 250 μm. E: higher magnification of ablated tissue (marked with * in C). Scale bar 50 μm.*

6.5.5.2 Clinical study

Ablation scar at the CTI was found in all patients at 3 months on LGE imaging (Figure 6-13). There was no relationship between total ablation time and total scarred area (R^2=0.003) or proportion of the floor of the right atrium occupied by scar (R^2=0.02). For ablations performed using the investigational catheter versus conventional non-irrigated catheter (alone or in combination), there was no detected difference in surface area of scar (11.3 (±11.7) cm^2 versus 13.8 (±6.4) cm^2).

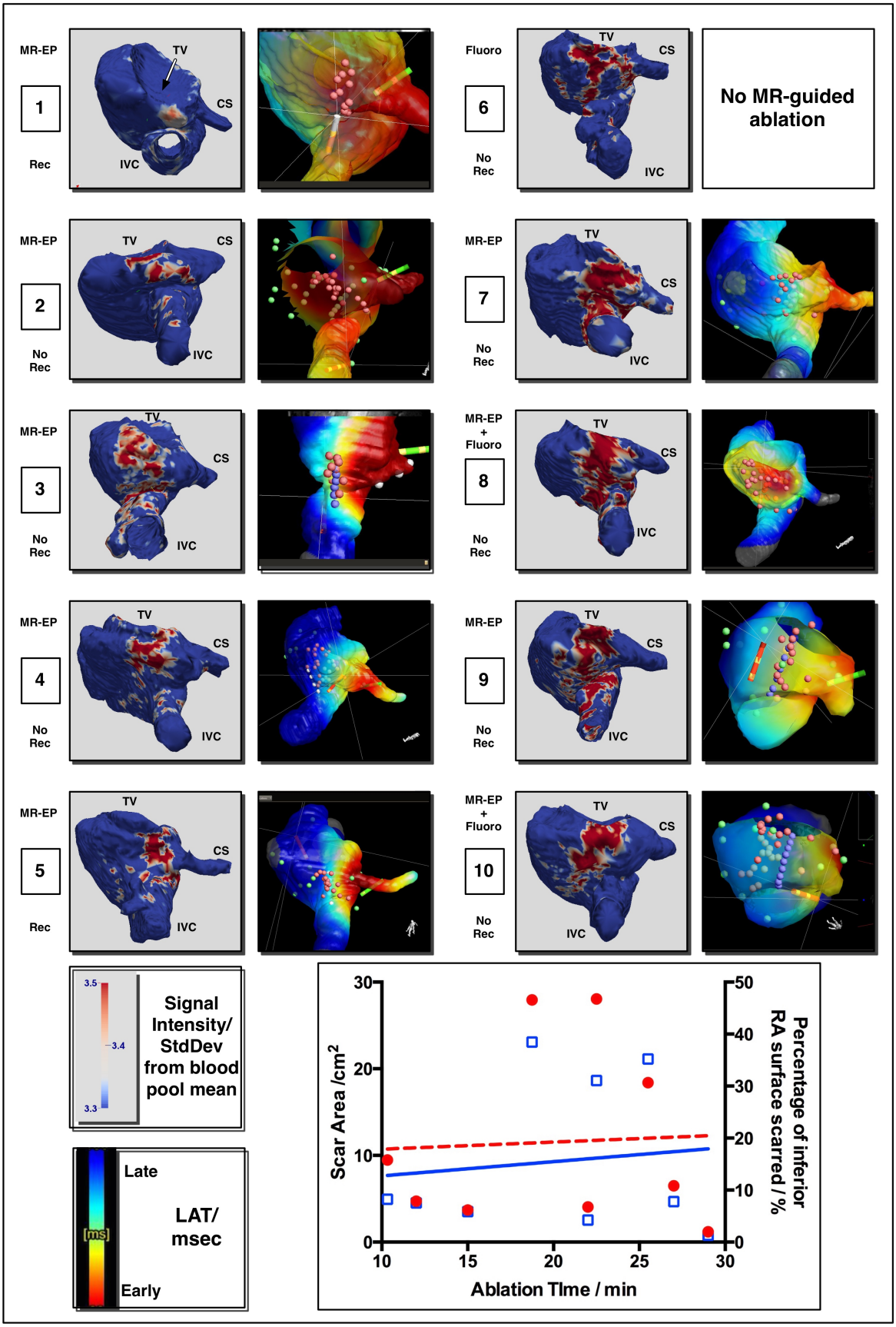

Figure 6-13. LGE CMR imaging of the right atrium at post ablation.

For each subject, on the left panel an inferior view of a maximum intensity projection of the right atrium (RA) shell is shown, atrial scar thresholded at 3.3 standard deviations above the blood pool mean. Right panel shows final ablation lesion set for each patient (iSuite screenshot, red dots show ablation lesion sites, purple dots planned ablation sites and green dots locations for local activation time assessment). Ablation modality is detailed above the subject number (MR-EP: MR guided ablation only; Fluoro: fluoroscopy only; MR-EP + Fluoro: fluoroscopy guided completion of ablation following MR-guided ablation). Final outcome is detailed below the subject number (No Rec: no recurrence of flutter; Rec: recurrence). Graph (bottom right) shows total scar area (red circles, left axis, dashed regression line) and percentage of the inferior right atrium scarred (blue squares, right axis, solid regression line) at 3 month CMR imaging, against total ablation time under MR guidance. RA: right atrium, CS: coronary sinus, IVC: inferior vena cava, TV: tricuspid valve, BP: blood pool, LAT: local activation time.

For lesion specific scar assessment, patients who underwent fluoroscopically guided ablation (either alone or in combination) were excluded (n=3), leaving a total of 151 ablation lesions assessed (Table 6-3). 108 lesions (72%) were associated with scar on the 3D mesh, and projection distance to mesh was mean 6.2mm (±4.1mm). MR-assessed scar was significantly greater when the RF energy was delivered inside the mesh or < 10mm outside of the right atrial mesh (signal intensity 6.2 ±4.1 and 5.0±2.8 standard deviations (SD) above blood pool mean respectively, versus 1.43±2.9 SD at >10mm ($p<0.001$)). In predicting effective ablation, the area under receiver operator characteristic curve for distance from mesh was 0.68.

	All Lesions	**Inside mesh**	**Outside mesh <10mm**	**Outside mesh >10mm**	
Total	151	19	110	23	N/A
Projection Distance/ mm	6.2 ± 4.1	4.4 ±3.2 (Range 0.4-11)	5.0 ± 2.8	13.0 ± 2.4 (Range 10-21)	N/A
Scar present at ablation point	108 (72%)	16 (84%)	90 (82%)	4 (17%)	P<0.001
Mean Scar Signal (SD from Mean)	4.7 ± 3.9	6.2 ±4.1	5.0 ±2.8	1.43 ±2.9	P<0.001

Table 6-3. Lesion specific scar formation.

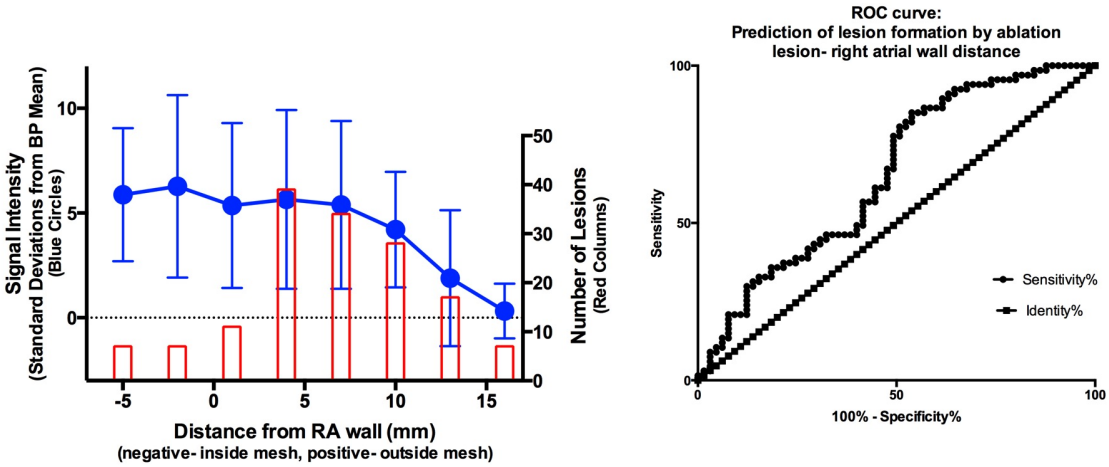

Figure 6-14. Ablation lesion specific scar formation.

(Left) Left-sided axis (blue circles)- scar signal intensity against distance of ablation lesion from right atrial wall. Right-sided axis (red bars)- number of lesions at each distance from RA wall. (Right). Receiver operator characteristic curve (ROC) for prediction of lesion formation by distance from the right atrial wall. Area under the curve 0.68.

6.5.6 Determinants of successful ablation

Table 6-4 details the relationship of CTI anatomy and acute ablation imaging parameters to the outcome of an acutely successful ablation procedure under MR-guided ablation alone. The subject who underwent entirely fluoroscopically guided ablation (see above) is excluded from the analysis. The IVC/CTI angle showed minimal overlap between successful/unsuccessful groups, but the small sample sizes preclude meaningful statistical analysis. Intraobserver and interobserver intraclass correlation coefficients for IVC/CTI angle measurement were 0.90 (95% CI 0.53-0.97) and 0.89 (95% CI 0.54-0.98) respectively.

	All subjects	Acutely Successful (n=5)	Unsuccessful (n=4)
CTI Length/mm	34 (±12)	30 (±13)	37 (±10)
CTI Depth/mm	2.9(±1.0)	2.6 (±0.7)	3.2 (±1.4)
Eustachian Ridge/mm	6.2 (±4.2)	3.6 (±2.7)	8.0 (±4.1)
IVC/CTI angle/degrees	117 (±19)	127 (±12)	99 (±13)
T_2W volume/ml	6.4 (±4.0)	6.9 (±5.2)	5.8 (±3.2)
T_2W mean thickness/ mm	4.6 (±1.9)	5.2 (±2.4)	3.7 (±0.8)
T_2W minimum thickness/ mm	2.1(±1.7)	2.6 (±2.0)	1.4 (±1.1)

Table 6-4. Determinants of acutely successful MR-guided ablation.

Unsuccessful includes both acutely unsuccessful (with subsequent fluoroscopically guided completion of procedure, n=2) and late recurrence (n=2). CTI: cavotricuspid isthmus; IVC: inferior vena cava; T_2W: T_2-weighted.

6.5.7 Hepatic injury

The incidence of hepatic injury is summarised in Table 6-5. There was a wide variation in size and location of the left hepatic vein , with a median distance to CTI 6mm (range 3-18mm), and median calibre 4mm (range 1.4-9mm). No enhancement was detected within 4mm of the hepatic vein.

Subject	Ablation modality	MR-guided RF energy/kJ	Acute: T_2W enhancement	Acute: Early no reflow	Acute: LGE	Chronic: Residual LGE
1	MR	21.7	Mild	Nil	Mild	Mild
2	MR	52.8	Mild	Nil	Nil	Mild
3	MR	32.4	Mild	Mod	Mild	Nil
4	MR	81	Severe	*	*	Mild
5	MR	40.5	Mod	*	*	Mild
6	Fluoro	N/A	N/A	N/A	N/A	Nil
7	MR	50.6	Mild	Mild	Mod	Mild
8	MR + fluoro	68.8	Mod	Mild	Mod	Mild
9	MR	60.7	Mild	Mild	Mild	Mild
10	MR + fluoro	72.9	Nil	Mod	Mod	Mild

Table 6-5. Hepatic enhancement following atrial flutter ablation.

Note that two subjects did not undergo gadolinium enhanced imaging following ablation (*), and one subject did not have MR-guided ablation.

6.6 Discussion

These studies have demonstrated the development, feasibility and safety of an actively-tracked MR-guided electrophysiology set-up, capable of robust performance in the demanding MR-environment in both animals and humans. Many of the key attributes of conventional EAM systems, such as operator ease of use and intuitive data representation, have also been established. The clinical study has identified limitations in efficacy and highlighted discrete areas for further development, but demonstrates significant progress of MR-EP towards clinical utility.

6.6.1 MR-EP system evaluation

Using this MR-EP set-up, active catheter tracking for ablation was achieved for the first time in humans (H. Chubb et al. 2014). This is in contrast to passive tracking techniques that rely on detection of magnetic susceptibility artefacts or signal voids to locate the catheter tip, necessitating constant communication between the electrophysiologist and a skilled manipulator of the imaging planes. With passive tracking, complex movements of a curved catheter almost inevitably cause the catheter to leave the imaging plane, and in human studies skilled operators have struggled considerably to perform many relatively routine aspects of EP ablation procedures, such as selective intubation of the coronary sinus or completion of CTI block (Grothoff et al. 2014). All these factors impact upon procedural success rate, safety and time.

With active catheter tracking, accurate and fast EAM was enabled with generation of activation time maps by the image guidance platform. In both humans and animals up to 40 mapping points were

recorded in less than 20 minutes, whereas passive tracking requires 2-5 minutes for each MR-acquired mapping point (Nordbeck et al. 2009). Furthermore, automatic tip alignment algorithms enabled rapid slice determination for optimal imaging of the ablation catheter within the soft tissue environment (Voigt et al. 2013), a unique capability that may be invaluable for more complex ablation procedures and for imaging of real-time lesion formation during ablation. Imaging could be performed during energy delivery, and the impact of the 500kHz RF energy source on MR-imaging, based around the 64MHz proton precession frequency at 1.5T, was minimal.

6.6.2 Clinical study- procedural outcome

The overall time for the human procedures was long, averaging over five hours for a procedure that rarely exceeds one hour under conventional fluoroscopic guidance. It should be noted that imaging and mapping protocols were performed that would not typically be required for a simple ablation, but even accounting for these phases the duration remains substantially longer than conventional methods.

Furthermore, the overall medium-term success rate for flutter ablation was low (72% for MR-guided ablation alone, 56% overall) compared to 85-92% for conventional flutter ablation techniques. In all subjects who underwent MR-guided ablation there was significant scar at 3 months at the site of ablation. However, in four patients there was either a need for further lesions under fluoroscopy, or recurrence at medium-term follow-up of three months. The cause of failure in this subset of patients required detailed assessment, and is likely to be related to three factors: failure to recognise the correct target for ablation, failure to reach the correct location, or failure to form effective ablation lesions.

6.6.2.1 Ablation target recognition

Diagnosis of the arrhythmia mechanism and selection of the CTI as the ablation target was based upon the 12 lead ECG P wave morphology during atrial flutter in patients with normal echocardiography. The two recurrences were of confirmed typical atrial flutter, successfully treated with completion of a CTI line. The absence of activation mapping or entrainment to confirm the diagnosis is unlikely to have impacted upon procedural outcome.

At the end of the MR guided ablation, the assessment of the adequacy of the ablation line was performed both electrically and through MR imaging. The acquired IEGMs were acceptable and could demonstrate double potentials and local timings (Figure 6-4). Electrical assessment of bidirectional block was performed to an acceptable standard however electrogram fidelity was insufficient for demonstration of low amplitude, fractionated electrograms which might indicate a zone of slow conduction. Imaging could not identify gaps in the cavotricuspid isthmus ablation lines and therefore locations for targeting for further MR-guided ablation could not be delineated.

6.6.2.2 Catheter reach to ablation target

The reach of the current MR-compatible catheter, which was designed to mimic a D curve profile and to function as an all-purpose EP catheter, may have been insufficient in patients with an acute IVC/CTI angle (Table 6-4 and Figure 6-15). There was substantial difficulty in catheter manipulation to the IVC end of the CTI during procedures, which is reflected in the Eustachian ridge as the site of highest voltage (least scar) for the two patients who returned for re-do ablation procedure (Figure 6-10).

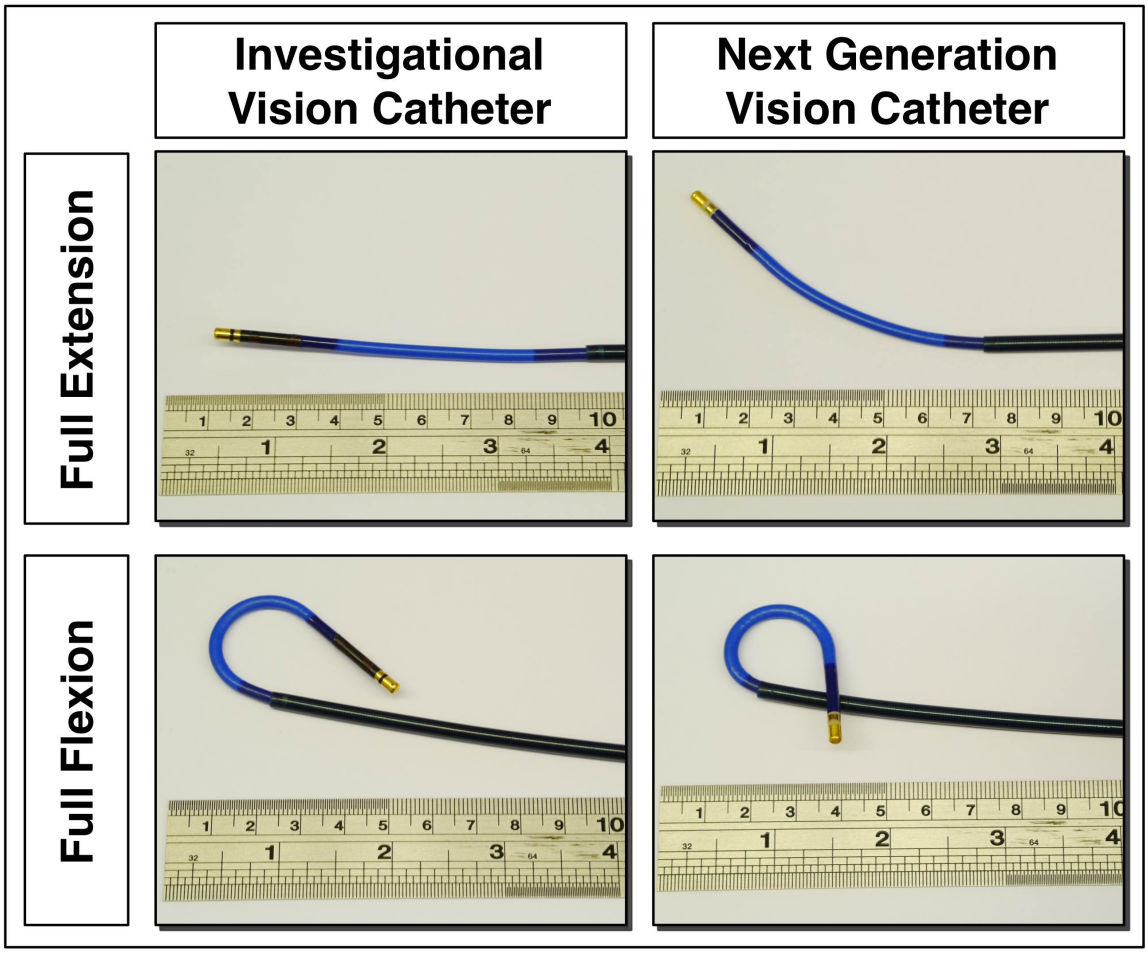

Figure 6-15. Investigational catheter reach.

Reach characteristics of investigational Vision catheter (left) and second generation catheter (right). Support is provided by 10Fr long Mullins sheath, and note reduced maximum angulation of the investigational catheter.

6.6.2.3 Ablation lesion formation

The pre-clinical study clearly demonstrated efficacious lesion formation (Figure 6-12). This was confirmed on late assessment of ablation lesions in the clinical study, and both electrical (CARTO) and MR assessment demonstrated effective chronic scar formation. Lesion-by-lesion analysis for the clinical study found that 72% of lesions were associated with scar, although transmurality remains challenging to assess. Comparison with conventional ablation is difficult as MR-guided ablation is

uniquely suited for lesion formation assessment, with virtual elimination of registration issues: the registration of EAM-guided ablation to imaging is subject to imperfect comparisons of variable landmarks. However, a 72% lesion formation rate at 3 months is comparable to conventional ablation studies (Bisbal et al. 2014) where up to 25% of an ablation line may not be associated with chronic scar.

Contrary to expectation, greater wall deformation was associated with less efficacious chronic lesion formation. The lesion-by-lesion evaluation was conceived as a contact-force surrogate, and it was hypothesised that lesions performed deeper within the mesh would be more likely to cause the creation of a chronic lesion. Several explanations may be postulated for this finding. Firstly, the further the projection distance, the more likely that the lesion will be projected to an inappropriate location, not reflecting true catheter-myocardial contact location. Secondly, substantial catheter pressure may cause tissue compression and increased energy delivery to adjacent structures (F. H. M. Wittkampf and Nakagawa 2006). Thirdly, the tracking signal may suffer from increased interference once the catheter doubles back on the shaft, placing the receiver coils in closer proximity to the capacitors, and therefore corrupting the location calculation. The final issue was noted ex-vivo, and requires further investigation.

6.6.3 Hepatic injury

RF ablation for atrial flutter is frequently associated with pain, typically experienced at the chest and shoulder tip. The mechanism has not been determined definitively, but has been postulated to be related to pericardial irritation, cardiac sensory nerve stimulation or hepatic irritation (Timmermans 2003). The pain can be severe, in some cases necessitating procedural termination without achievement of the ablation endpoint. In prospective studies of flutter ablation it has been graded at mean 4.6 (±2)/10, with average peak pain 6.8 (±2.4) /10, despite 2.5mg morphine and 2.5mg diazepam pre-procedure (Bastani et al. 2013).

Real-time MR guided procedures provide a unique insight into the mechanism of pain, and in this study it was clear that there was frequently both early and late enhancement of the liver adjacent to the CTI. Furthermore, it is interesting that the one ablation performed without an irrigated catheter (subject 6) had no late enhancement of the liver, perhaps reflecting shallower lesions with the non-irrigated Blazer catheter. Differentiation of diaphragm from hepatic capsule was difficult in some cases, and prospective evaluation with conscious patients, contemporaneous pain scores, liver enzyme measurements and imaging immediately post ablation may be warranted to investigate this hypothesis further. Correlation with size and position of the left hepatic vein would also be helpful, and it may be found that those without the protective effect of a large blood vessel in proximity are more likely to suffer procedural pain and can be managed appropriately.

6.6.4 Future developments and clinical implications

6.6.4.1 MR-Guided ablation system

MR-EP provides a platform for anatomically-guided ablation procedures, informed by cardiac structure and arrhythmia substrate amenable to imaging, such as scar, with the tantalising possibility of visualization of acute lesion formation during the procedure. The implications for ablation procedures for AF (Bisbal et al. 2014; Marrouche et al. 2014) and ventricular tachycardia (Nazarian et al. 2005) are substantial, and the most complex ablation procedures are likely to reap the greatest benefit from the additional capabilities of CMR imaging. However, further complementary developments are also required.

A number of commercial and academic institutions are working on technologies responding to challenges such as communication in the noisy MR environment, MR-compatible 12-lead ECG, MR-compatible defibrillation, rapid and automated MR-scar segmentation, and transseptal puncture equipment. These are at varying stages of commercial development (Rogers and Lederman 2015; Bhagirath et al. 2015), and their realisation will bring MR-EP ever closer.

6.6.4.2 Imaging

The complex structural and physiological responses to ablation, including interstitial oedema, hyperaemia, tissue coagulation and microvascular obstruction can be visualized using CMR imaging. Acute lesion imaging techniques may rely on native intrinsic contrast (T_1 and/or T_2 weighted (Arujuna et al. 2012; Celik et al. 2014; Lardo et al. 2000; Vergara et al. 2011; Dickfeld et al. 2007)) or contrast agent enhancement (LGE (Celik et al. 2014; Lardo et al. 2000; Ranjan et al. 2012)), but acute imaging of lesions within the thin atrial myocardium remains particularly challenging (Williams et al. 2015; J L Harrison, Whitaker, et al. 2015). Purely T_2-weighted imaging is a blunt tool. No gaps in ablation line were identified acutely with T2 or LGE imaging, and this was despite a 56% clinical success rate. This finding of low sensitivity of acute atrial lesion imaging for gaps is in keeping with that of other groups and further developments in acute post ablation MR imaging techniques are necessary (Ranjan et al. 2012; Williams et al. 2015; James L Harrison et al. 2014; J L Harrison, Sohns, et al. 2015). Identifying gaps within the ventricle is likely to be more easily achievable in the first instance. Lesion imaging in the future is likely to rely on the intrinsic T_1–time shortening that occurs swiftly with effective lesion formation (Celik et al. 2014), and non-enhanced visualisation techniques are particularly attractive for repeated imaging.

6.6.5 Limitations

The studies were designed to take the new MR-EP platform from development to pre-clinical to first-in-man feasibility trials. As such, there are limitations that should be acknowledged. Using the methodology of this study, the ablation procedure for atrial flutter does not constitute a comprehensive assessment of the capability of surface ECG and IEGM fidelity to guide more complex electrophysiological procedures. Local activation times were mapped only on pacing, and not in

arrhythmia. However, ablation location relative to the TV annulus was guided by IEGMs, and sites for further ablation were also identified based upon electrophysiological features. IEGM fidelity will continue to improve towards that achievable for conventional EAM, but will require further engineering and time to match it.

In addition, the arrhythmia was not mapped, following the decision to cardiovert at the start of the procedure on account of the impact of arrhythmia on acquisition of ECG-gated MR-imaging. The primary concern was for the timely acquisition of the 3D whole-heart, and this was adversely affected by the clinical arrhythmia. However, active tracking technology is independent of heart rhythm and arrhythmia mapping should not be limited in further studies. Technical solutions for the swift acquisition of a high resolution 3D road map in arrhythmia will require further development.

Finally, ablation procedures in both animals and humans were weighted towards achievement of effective and targeted RF lesions, and imaging protocols were relatively focused on more conventional imaging sequences that demonstrated feasibility rather than long-term durability of acute lesions.

6.7 Conclusions

Real-time MRI guidance of EP procedures is feasible, and active tracking technologies enable an approach and workflow that closely mimics conventional EAM. MR-compatible catheters can be used to create effective ablation lesions, including for the treatment of atrial flutter in humans. The MR-EP system is currently slower and less effective than conventional ablation and this appears to be related primarily to the reach of the investigational catheter. However, MR-EP provides contemporaneous, high fidelity imaging of cardiac anatomy, fibrotic arrhythmia substrate and ablation lesions. Further innovation of these new tools may lead to fundamental changes in the way in which both simple and complex ablation procedures are performed.

6.8 Acknowledgements

In addition to those detailed at the start of the chapter, I would also like to thank all the other people who helped make this feasibility study possible. In particular, I would like to thank the anaesthetists (Dr Shyamala Moganasundram and Dr Daniel Taylor), radiographers (Stephen Sinclair and Tracy Moon), and physiologists (Dr Julian Bostock and Ms. Shahada Begum) for their hard work in making sure that the procedures ran safely and smoothly. I would also like to thank Dr Rashed Karim for his work writing the software script for the projection of ablation locations onto the MRI scar shell.

7 Atrial Imaging Post Radiofrequency Ablation: Optimisation of Lesion Imaging

7.1 Aims

To establish the optimal imaging parameters to detect post ablation atrial scar (PAAS).

7.2 Introduction

Over the last two decades there has been a substantial increase in the implementation of catheter ablation for the treatment of AF. Concurrently, advances in CMR imaging have enabled clinically useful visualisation of the LA wall and ablation lesions (Akoum et al. 2015; Badger et al. 2010; Fukumoto et al. 2015; Peters et al. 2007; C. J. McGann et al. 2008; Bisbal et al. 2014; Hunter et al. 2013; J L Harrison, Sohns, et al. 2015; Malcolme-Lawes et al. 2013; Taclas et al. 2010). However, arrhythmia recurrence rates post-ablation remain high, and there is evidence that many of these recurrences are secondary to pulmonary venous reconnection or linear lesion discontinuities following ineffective lesion formation. Effective and reliable non-invasive assessment of PAAS provides a unique insight into lesion formation, and may help guide further ablation procedures.

LGE acquisition techniques have been shown to be the most sensitive to detect PAAS (James L Harrison et al. 2014) and can identify gaps in ablation lesion sets (Ranjan et al. 2012). In 2009, Peters et al demonstrated that AF recurrence post-ablation correlates with the extent of PAAS (Peters et al. 2009). This finding was corroborated by Badger et al in 2010, who found that complete encirclement of a PV by CMR-defined PAAS had a 100% positive predictive value in identifying electrical isolation (Badger et al. 2010). However, the clinical implementation of these findings is controversial. In patients requiring repeat AF ablation procedure, some groups have shown good correlation between CMR-derived lesion gaps and sites of successful re-isolation (Bisbal et al. 2014; Taclas et al. 2010), whilst others have shown the opposite (J L Harrison, Sohns, et al. 2015; Spragg et al. 2012).

Consistent between all studies is the finding that complete encirclement of PVs by PAAS is a rare occurrence. 90-100% of patients do not have complete encirclement of all PVs by CMR-detected PAAS (Badger et al. 2010; Akoum et al. 2015; Spragg et al. 2012; Taclas et al. 2010; Bisbal et al. 2014). This is in the context of a recurrence rate in these studies of 30-50%. In many cases, electrical reconnection will not result in AF recurrence (Cappato et al. 2003; Kuck, Hoffmann, et al. 2016), but on invasive assessment many of the veins remain isolated, despite detection of gaps (Bisbal et al. 2014). The specificity of PAAS gaps for electrical reconnection is low. Imaging techniques need to be optimised in order to maximise detection of effective ablation injury.

The core imaging sequences have remained relatively unchanged from those first proposed and evaluated by the Boston and Utah groups (Peters et al. 2007; C. J. McGann et al. 2008). The T1-weighted ECG- and respiratory-navigated 3D turbo gradient echo sequence is now widely available on most imaging platforms and moderately robust (Marrouche et al. 2014). Novel sequences will continue to be developed and employed, but mainstream use of PAAS imaging in the medium term is highly likely to rely upon these conventional imaging techniques. However, the acquisition parameters vary widely between leading groups (see Table 7-1). Timing post- GBCA administration, scanner field strength, slice thickness and even GBCA dose differ and this chapter evaluates the relative contribution of these imaging parameters to PAAS quantification.

The measurement of improvement in imaging should ideally be referenced to a gold standard or hard clinical endpoint. For assessment of PAAS, there is no gold standard readily available. Comparison to invasive voltage mapping is prone to registration errors (See Chapter 9). Furthermore, voltage does not entirely reflect scar formation (Kowalski et al. 2012) and varies according to the electrode characteristics used to perform voltage mapping (Josephson and Anter 2015; Tung et al. 2016). Furthermore, the clinical end-point of arrhythmia recurrence does not necessarily reflect a lack of PAAS in any given location (J L Harrison, Sohns, et al. 2015). This study, therefore, has sought to measure the improvement in imaging parameters through the assessment of conventional subjective and objective imaging quality markers, including post-processed atrial scar quantification.

	Centre	Subjects	Timing post-gadolinium	GBCA Dose	Scanner Strength	Slice thickness
Badger et al (2010)	Utah, USA	144	15min (repeated if 'suboptimal')	0.1mmol/kg (Multihance)	1.5T	2.5mm
Taclas et al (2010)	Boston, USA	19	15-20min	0.2mmol/kg (Magnevist)	1.5T	4mm
Hunter et al (2013)	Imperial/Barts, London, UK	50	20min	0.4mmol/kg (Magnevist)	1.5T	4mm
Bisbal et al (2014)	Barcelona, Spain	15	25-30min	0.2mmol/kg (Gadovist)	3T	2.5mm
Fukumoto et al (2015)	Johns Hopkins, USA	20	10-32min	0.2mmol/kg (Magnevist)	1.5T	2mm
Harrison et al (2015)	King's College London, UK	20	20min	0.2mmol/kg (Gadovist)	1.5T	4mm
Akoum et al (2015)	DECAAF, Multicentre	177	15min	0.1-0.2mmol/kg (Multiple agents)	1.5T (9 centres) 3T (5 centres)	2.5mm

Table 7-1. Post-ablation atrial scar imaging techniques utilised in leading centres worldwide.

In-plane resolution is 1.25x1.25mm or 1.3x1.3mm for all centres. GBCA: gadolinium based contrast agent†††

7.3 Methods

7.3.1 Study population

Between January 2014 and September 2015, all patients undergoing routine MR imaging prior to a first-time AF ablation procedure were approached to join the study. 40 subjects provided written and informed consent and the study was approved by the National Research Ethics Service (South London Research Ethics Committee reference 08/H0802/68). Exclusion criteria included

††† Note relaxivities vary significantly between GBCAs: Multihance r_1=6.3 L mmol^{-1} s^{-1} (1.5 T) r_1= 5.5 L mmol^{-1} s^{-1} 1 (3T), Magnevist r_1=4.1 L mmol^{-1} s^{-1} (1.5 T) r_1= 3.7 L mmol^{-1} s^{-1} 1 (3T), Gadovist r_1=5.2 L mmol^{-1} s^{-1} (1.5 T) r_1= 5.0 L mmol^{-1} s^{-1} (3T) (Rohrer et al. 2005)

contraindication to MR imaging or prior allergic reaction to contrast agent. Baseline demographics were documented at the initial scan, including age, weight, height, body mass index (BMI), duration of AF, type of AF, and rhythm at scan. . Comorbidities including ischaemic heart disease and diabetes mellitus were recorded.

All patients underwent CMR imaging once before and twice following clinically indicated catheter ablation for AF (Figure 7-1). The first post-ablation CMR scan (Scan 1) was performed at approximately three months after the ablation procedure, regardless of rhythm or arrhythmia recurrence (median 94 days, (interquartile range (IQR) 89-101 days)), and was performed using standard acquisition parameters (see below). A second scan session (Scan 2) was performed approximately 2 days later (median 48.1 hours, IQR 47.9-49.1hours). Subjects were allocated to scan 2 in 3T scanner or the same 1.5T scanner. 3T scanner availability was limited, and therefore it was not possible to randomise the allocation, but the allocation was performed blinded to patient outcome and demographics. The remaining patients were randomised in equal ratios to one of three different imaging parameter groups for scan 2: repeat scan with identical acquisition parameters, repeat with half dose of GBCA, or repeat with half-slice thickness.

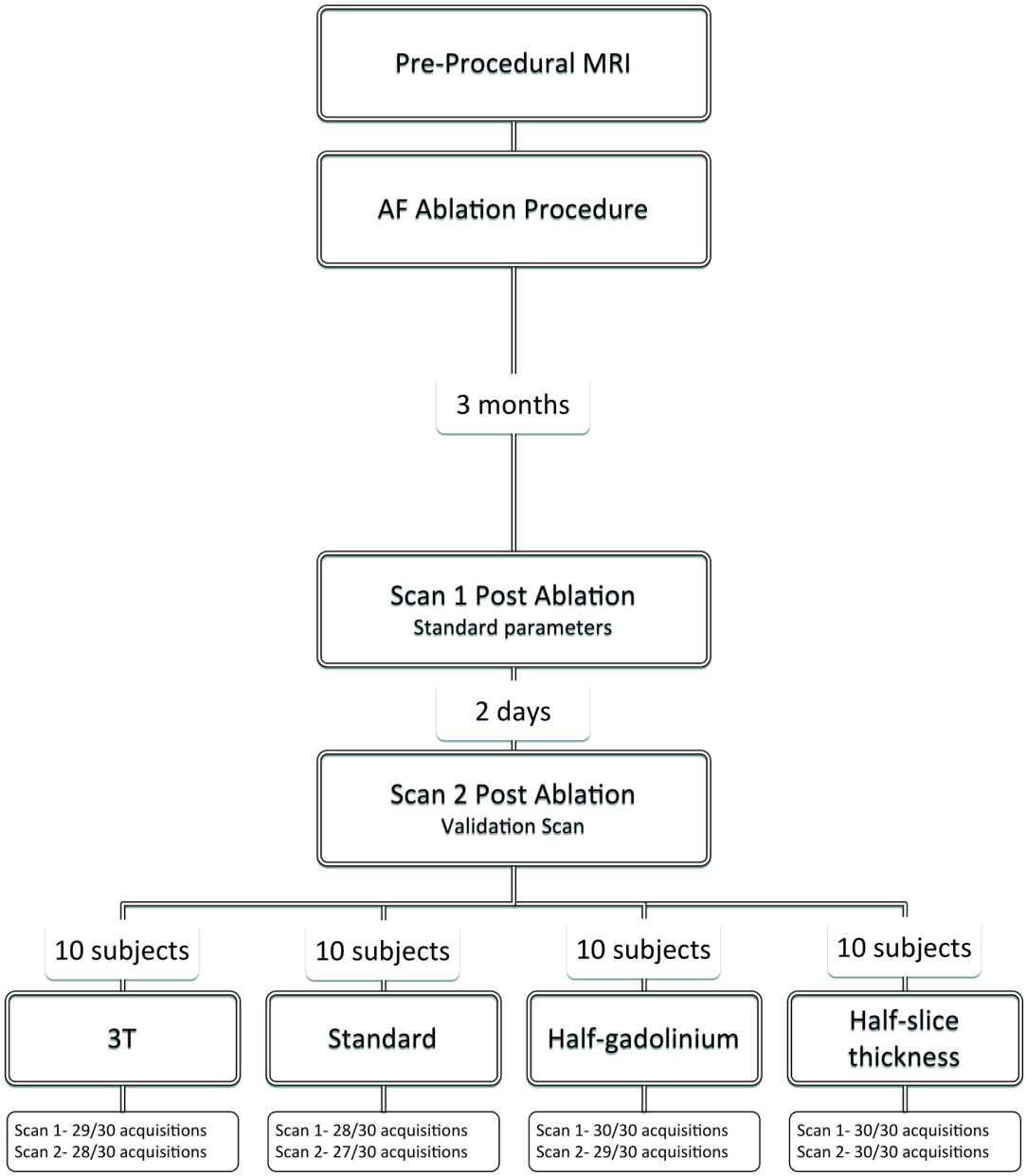

Figure 7-1. Flowchart demonstrating subject allocation and number of scan acquisitions achieved.

7.3.2 CMR protocol

All patients underwent detailed assessment at baseline prior to ablation, including left ventricular (LV) and right ventricular (RV) volumes and function, LA volumes and function, LA sphericity assessment, LA fibrosis assessment and documentation of baseline demographic. A single, standard LA 3D LGE dataset was acquired. The standard 3D LGE acquisition parameters are detailed in 4.1.1.

Scan 1 (post-procedure) was performed using the same 3D LGE acquisition parameters as the baseline scan, and a total of three LA 3D LGE datasets were acquired. The start of the dataset acquisitions were at 10minutes, 20minutes and 30minutes after GBCA administration. In cases

where the acquisitions took longer than 10minutes, the subsequent acquisition was started immediately.

Scan 2 (post-procedure) was performed with allocated modifications of the baseline scan.

1. Half-gadolinium dose. 0.1mmol/kg of gadobutrol (Gadovist) was injected at the same rate (0.3ml/s), with identical scanning parameters thereafter.
2. Half-slice thickness. The acquired voxel size was reduced to 1.3x1.3x2mm (reconstructed 0.625x0.625x1mm). Field of view remained unchanged to cover the whole of the left atrium, and therefore approximately 90-100 slices were acquired.
3. 3T scanner. Scans were performed on Philips Achieva 3T scanner with 32-channel coil. Parameters were matched to those for 1.5T scanning as closely as possible (TR 4.4msec, TE 2.1msec, flip angle 35°, slice thickness 4mm, acquired voxel size 1.3x1.3x4mm).

Native T_1-time constant assessment was performed prior to GBCA administration at each scan session in order to confirm myocardial washout. This was assessed using a balanced steady state free precession single breath-hold modified inversion recovery look-locker (MOLLI) sequence, in a single mid-ventricular short axis slice (TE: 1.64ms, TR 3.3ms, flip angle 50°, voxel size 1.8x1.8x8mm, phase encoding steps n =166, 11 images from three inversions (3 +3 + 5) with three heartbeat pauses prior to the second and third inversions and an adiabatic prepulse). Myocardial T_1 relaxation was measured at the septal myocardium, avoiding contamination from the blood pool, and also at the centre of the blood pool, with T_1 time constant extrapolated from the exponential model fitted using ViewForum workstation (Philips Healthcare) (Dabir et al. 2014).

7.3.3 Atrial fibrillation ablation protocol

The details of the ablation procedure are documented in Chapter 4.4

7.3.4 Imaging assessment

7.3.4.1 Qualitative assessment

Qualitative assessment of all acquisitions was performed independently by three experienced observers (HC, JH, SA). Observers were presented with a single representative transverse slice at the level of the aortic root in random order, with 10 initial training sets, and 20 random acquisitions repeated in order to assess intra-observer reproducibility. Likert Scale assessment was performed, with acquisitions graded across four criteria: image sharpness, scar contrast, freedom from artefact and quality of myocardial nulling. All criteria were scored from 1-5, with a score of 5 indicating optimal imaging.

7.3.4.2 Signal-to-Noise and Contrast-to-Noise ratios

All acquisitions were analysed for signal-to-noise (SNR) and contrast-to-noise (CNR) ratios. In the presence of parallel imaging, noise is spatially heterogeneous throughout the imaging field, and

should ideally be quantified through the assessment of multiple (>10) identical acquisitions. However, this is not feasible on account of the highly significant additional imaging time, and the shifting tissue signal intensities during the acquisition following GBCA administration.

Apparent SNR (aSNR) and apparent CNR (aCNR) were therefore calculated as the relationship between the mean signal intensity within a circular region of interest (ROI) within the blood (SI_{Blood}), the mean of a ROI within scar (SI_{Scar}), and the standard deviation of the background signal within the lungs (SD_L) (Kolbitsch et al. 2011).

$$aSNR_{Scar} = \frac{SI_{Scar}}{SD_L} \quad \text{Equation 8.1}$$

$$aSNR_{Blood} = \frac{SI_{Blood}}{SD_L} \quad \text{Equation 8.2}$$

$$aCNR = aSNR_{Scar} - aSNR_{Blood} \quad \text{Equation 8.3}$$

ROIs were all selected within the same transverse slice, at the level of the origin of the left main coronary artery. For SI_{Blood}, a 200mm^2 circular ROI was placed in the LA blood pool, distant from potential artefact due to inflow enhanced by respiratory navigator signal; for SI_{Scar}, a 5mm^2 ROI within the most intense region of PAAS within slice, and for SD_L a 200mm^2 ROI within the lung, distant from any apparent large blood vessels at the same distance from the surface coils as the blood pool ROI.

7.3.5 Scar quantification

The methods for quantification of atrial scar are documented in Chapter 4.2. Scar was thresholded at 3.3 standard deviations above the blood pool mean (James L Harrison et al. 2014).

7.3.6 Statistical analysis

Data are expressed as mean (± standard deviation) for normally distributed data, and median (with interquartile range (IQR)) for non-normally distributed data. Statistical analysis was performed using IBM SPSS Statistics (Version 22, Armonk, NY). Baseline parameters were compared using unpaired t-test for normally distributed continuous variables, Mann-Whitney U test for non-parametric variables and X^2-test for categorical data. Intraclass correlation coefficient (ICC) was assessed using a two-way mixed effects model (average measures, alpha model). Assessment was for consistency for interobserver, and absolute agreement for intra-observer, and are quoted with 95% confidence interval (CI) (McGraw and Wong 1996). Two-way ANOVA (repeated measures) was used to assess scan parameters and acquisition time. For acquisition time, Wilcoxon matched-pairs signed rank test was used to compare side-by-side time points, and Friedman test for overall effect of acquisition time, in view of significant deviation from normal distribution.

7.4 Results

The MR imaging sets for 40 subjects were evaluated. In total, there were 40 datasets (one per subject) acquired prior to ablation and 231 datasets post-acquisition (271 out of maximum possible 280, 96.7%). Of the nine 3D LGE acquisitions not performed, three were at Scan 1 (patient tolerance), three at the standard scan 2 (single patient with viral illness), one from half gadolinium scan 2 (patient tolerance) and two from 3T scan 2 (patient tolerance) (Figure 7-1). Myocardial T1 time at scan 1 was 989±21msec, and at scan 2 was 987±22msec (paired t-test p=0.34, subjects allocated to 3T excluded).

Subject baseline demographics are summarised in Table 7-2. There were no significant differences between patients allocated to 1.5T versus 3T scanner.

	All Subjects (n=40)	**Scan 2 1.5T (n=30)**	**Scan 2 3T (n=10)**	**p-value**
Male	31 (78%)	22 (73%)	9 (90%)	0.27
Paroxysmal AF	20 (50%)	17 (56%)	3 (30%)	0.14
CHA_2DS_2VASC Score	1 (IQR 0-2)	1 (IQR 0-2)	0 (IQR 0-1.5)	0.28
AF duration (years)	3.0 (IQR 2.1-5.3)	2.5 (IQR 1.9-5.0)	5.5 (IQR 2.6-12.5)	0.19
Significant Comorbidities	22 (56%)	16 (53%)	6 (60%)	0.71
Age (years)	61 ±10	61±8	61±13	0.99
Weight (kg)	88 ±17	88±18	87±12	0.77
Height (cm)	176 ±7.1	176±6.4	177±9.3	0.60
BMI (kg/m^2)	28.4±5.3	28.7±5.9	27.6±3.1	0.48
HR at baseline scan (bpm)	61 ±10	61±8	61±13	0.99
Sinus rhythm at baseline scan	25 (62.5%)	19 (63%)	7 (70%)	0.70
LV ejection fraction (%)	60 ±10	62±10	58±11	0.41
LA size (ml)	121 ±32	122±37	119±19	0.75
LA sphericity	82.6 ±3.8	82.7±3.9	82.2±3.6	0.72
LA fibrosis at baseline (%)	36.0 ±13.9	36.7±15.1	33.9±9.3	0.49
LA ejection fraction (%)	30 ±18	29±19	34±12	0.41
LV native T_1 time (msec)	988 ±22	991±24	985±21	0.33

Table 7-2. Baseline demographics, as assessed at the initial scan prior to ablation procedure.

LA sphericity and LA fibrosis were analysed according to methods detailed in Chapter 5, with the Johns Hopkins threshold (image intensity ratio 0.97) used to quantify fibrosis. P-value is for comparison between patients that underwent scan 2 in 1.5T versus 3T

scanners. LA: left atrium, LV: left ventricle, BMI: body mass index, HR:heart rate, bpm: beats per minute.

7.4.1 Scar imaging

A single representative transverse slice for every acquisition volume, at the level of the aortic root, is included in Appendix A.

7.4.2 Likert scale assessment of imaging quality

Imaging quality in terms of sharpness, scar contrast and overall score improved with time from GBCA administration across all imaging parameter sets ($p<0.0001$), whilst freedom from artefact and quality of myocardial nulling remained unchanged (Figure 7-2). Between imaging parameter sets, imaging at 3T had a lower overall imaging score, primarily driven by inferior sharpness and increased artefact. Imaging quality for the other imaging parameter sets demonstrated minimal significant differences, with the exception of the improved scar contrast at 10min for the half gadolinium dose scans ($p=0.03$). Likert score assessment was evaluated for reliability, and there was generally good interobserver consistency (ICC=0.888 (95% CI 0.862-0.910)) and excellent intraobserver agreement (ICC=0.964 (95% CI (0.939-0.979)) (Table 7-3). Imaging acquisitions where myocardial nulling did not receive at least a score of 3 ('Good') from all three observers were excluded from further analysis (n=7 out of 231, 3%).

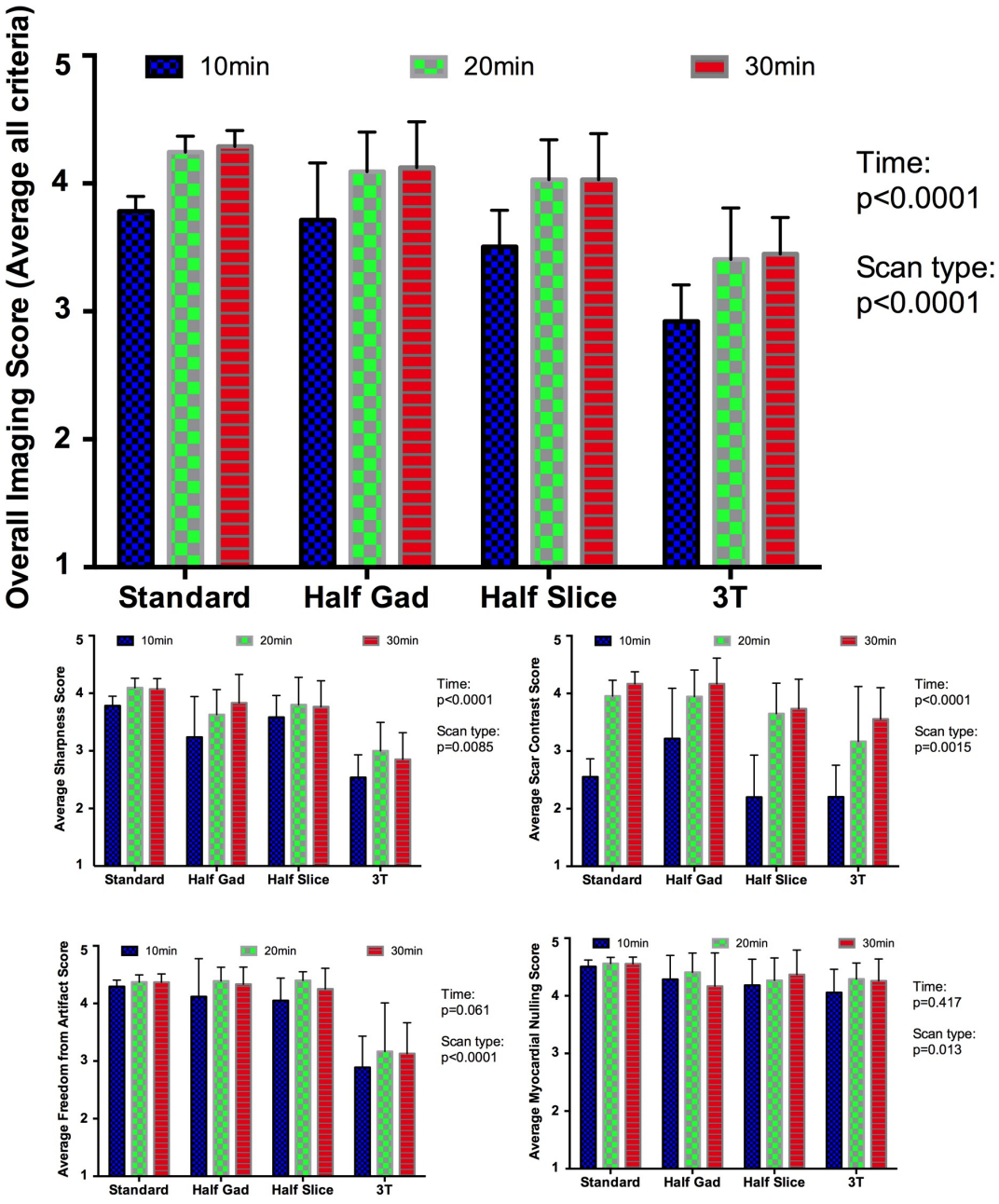

Figure 7-2. Summary of Likert Scores for each set of imaging acquisition parameters

See above for full details of imaging parameters. The blue, green and red columns indicate imaging performed at 10min, 20min and 30min post GBCA injection respectively. P-values for two-way ANOVA.

Intraclass Correlation Coefficient	Sharpness	Scar Contrast	Freedom from Artefact	Myocardial Nulling	Total
Interobserver	0.763 (0.707-0.809)	0.892 (0.866-0.913)	0.789 (0.739-0.830)	0.824 (0.783-0.859)	0.888 (0.862-0.910)
Intraobserver	0.924 (0.872-0.954)	0.965 (0.942-0.979)	0.853 (0.755-0.912)	0.876 (0.786-0.927)	0.964 (0.939-0.979)

Table 7-3. Inter- and intraobserver intraclass correlation coefficients.

Brackets indicate 95% confidence intervals.

7.4.3 Timing of LGE acquisition

Following GBCA administration, 3D LGE acquisitions were targeted to be commenced at 10, 20 and 30min (performed at 10.7±2.6min, 22.6±3.6min and 33.6±5.0min respectively). The small drift in true rather than intended acquisition time reflects acquisition times >10min, and also operator time taken to compensate for inadequate respiratory navigator signal, ECG noise, patient movement and patient-related delays such as anxiety. Total acquisition time for the sequence was broadly similar at all time intervals (6.4±3.1min at 10min, 6.7±2.5min at 20min and 7.3±3.5min at 30min (p=0.06), across all imaging parameters). Average acquisition time varied between imaging parameter sets (6.4±2.7min control, 7.2±2.4 half gadolinium, 8.4±2.7min half slice thickness, 6.2±2.4min 3T, p=0.002)

Figure 7-3 shows the effect of acquisition timing on blood pool aSNR, scar aSNR, aCNR and overall scar area, for standard acquisitions only (n=49 at each time point, total 147 3D datasets). For all parameters there was a significant change with time: blood pool aSNR fell (p=0.009), as scar aSNR, aCNR and scar area all increased (p=0.0016, p<0.0001 and p<0.0001 respectively). For blood pool and scar aSNR, there was no significant change with Bonferroni correction between 20 and 30min (p=0.03 and p=0.30 respectively). However, post-processing of atrial scar is heavily reliant on the interaction of these two factors, and both aCNR (p=0.0009) and total atrial scar (p<0.0001) continued to rise.

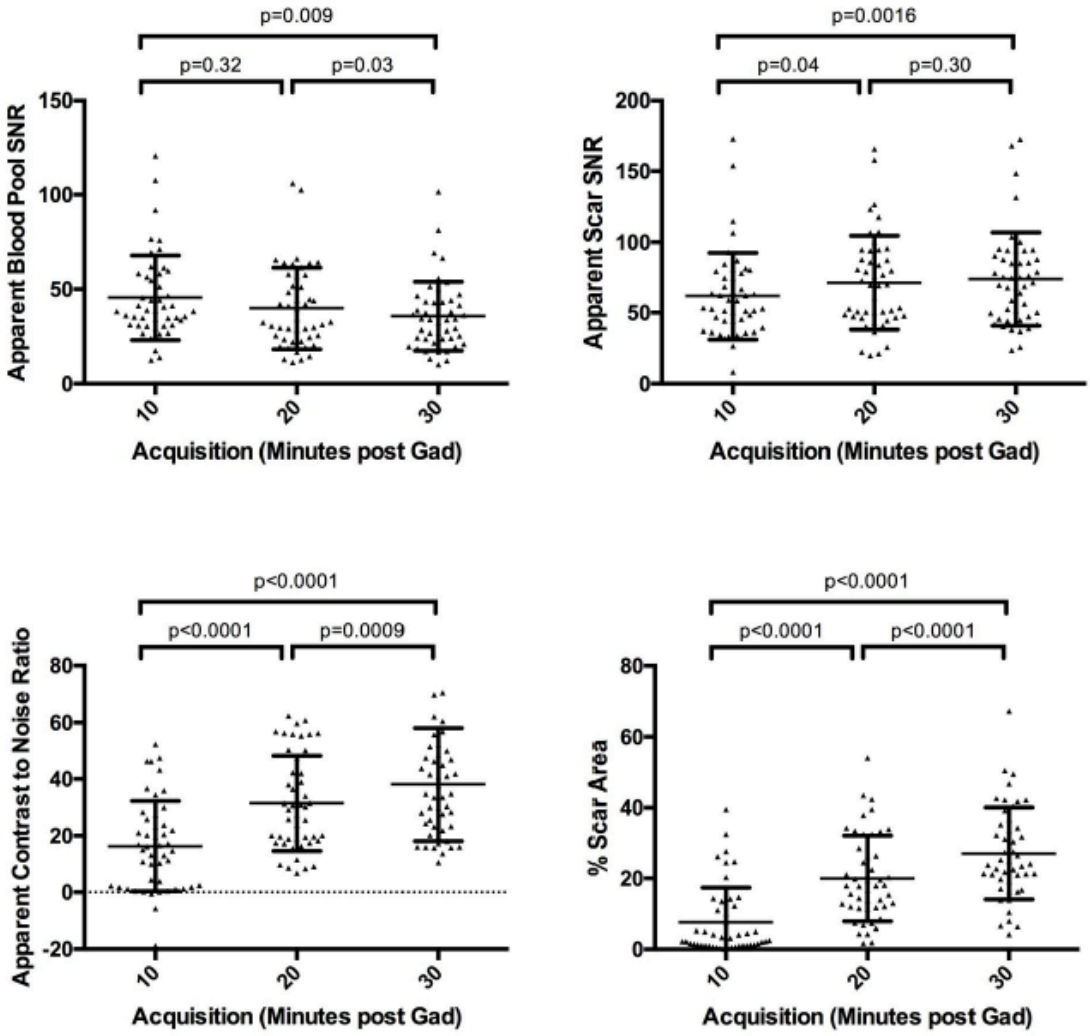

Figure 7-3. Relationship of acquisition timing post GBCA administration and signal/contrast-to-noise ratios.

(Top left) apparent blood pool signal-to-noise ratio (SNR), (top right) apparent scar SNR, (bottom left) apparent scar to blood pool contrast-to-noise ratio, and (bottom right) LA scar area as a percentage of left atrium, thresholded at 3.3 standard deviations above blood pool mean. Values presented are for standard acquisition parameters only (n=49 at each time point). For each plot, three p-values are presented: the top is p-value for Friedman test, assessing overall impact of time, and the bottom two are the p-values for Wilcoxon matched-pairs signed rank test.

7.4.4 Scan parameters

The effect of scan parameters on aCNR and scar area are shown in Figure 7-4 and Figure 7-5 respectively. Timing of the acquisition post GBCA administration remained an important determinant of aCNR and scar area across all imaging parameters ($p<0.0001$ to $p=0.023$), except for aCNR in the cohort randomised to half GBCA dose, where the impact of scan parameter dominated (time: $p=0.529$, scan parameters: $p<0.0001$).

For the control group, with identical scanning parameters in scan sessions 1 and 2, there was no significant difference between scan sessions. Half GBCA dose increased the aCNR ($p<0.0001$) and the detected scar area ($p=0.0039$). At half slice thickness, there was no significant change in aCNR ($p=0.77$) but scar area was lower ($p=0.004$). One potential factor to account for the absence of decrease in aCNR could have been the timing of the acquisitions, if half-slice acquisitions were significantly later due to over-run of the longer acquisition. However, there was no significant difference at any time point for scan 1 versus scan 2 acquisition commencement times (10min: 11.6±4min versus 10.3±1.4min ($p=0.31$), 20min: 23.2±5.4min versus 23.3±3.3min ($p=0.95$), 30min 35.5±6.8min versus 34.1±4.6min ($p=0.51$) respectively). For 3T bore strength there was no significant overall decrease in aCNR ($p=0.12$) but there was an overall decrease in scar area ($p=0.019$).

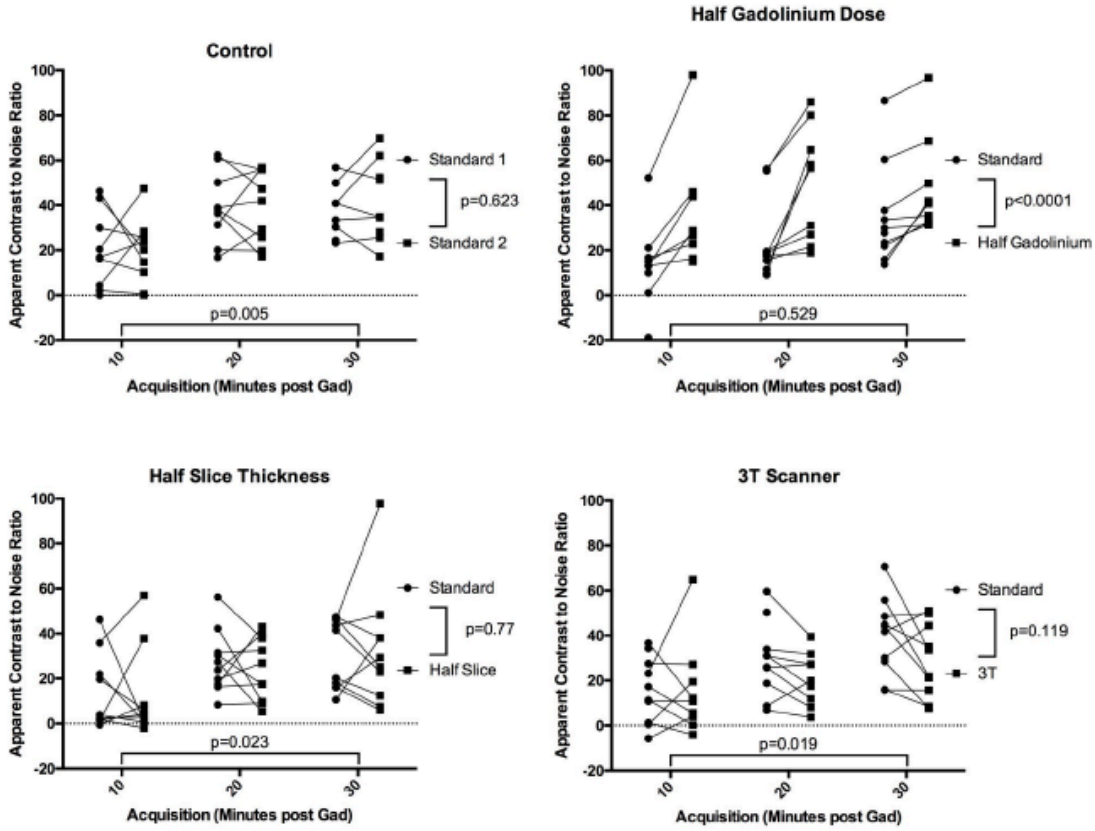

Figure 7-4. Impact of scan parameters on apparent scar to blood pool contrast-to-noise ratio.

Paired acquisitions at 10, 20 and 30min post GBCA injection, for control subjects (top left), half GBCA dose (top right), half slice thickness (bottom left) and 3T scanner (bottom right). Scan 1 (standard acquisition, circle) and scan 2 (experimental acquisition, square) are linked for each subject. P-values are for two-way repeated measures ANOVA: at the bottom of each plot is the p-value for variance with time, and to the right is the p-value

for variance with acquisition parameter. Unpaired acquisitions are shown as unlinked circle or square, and were not included in statistical analyses.

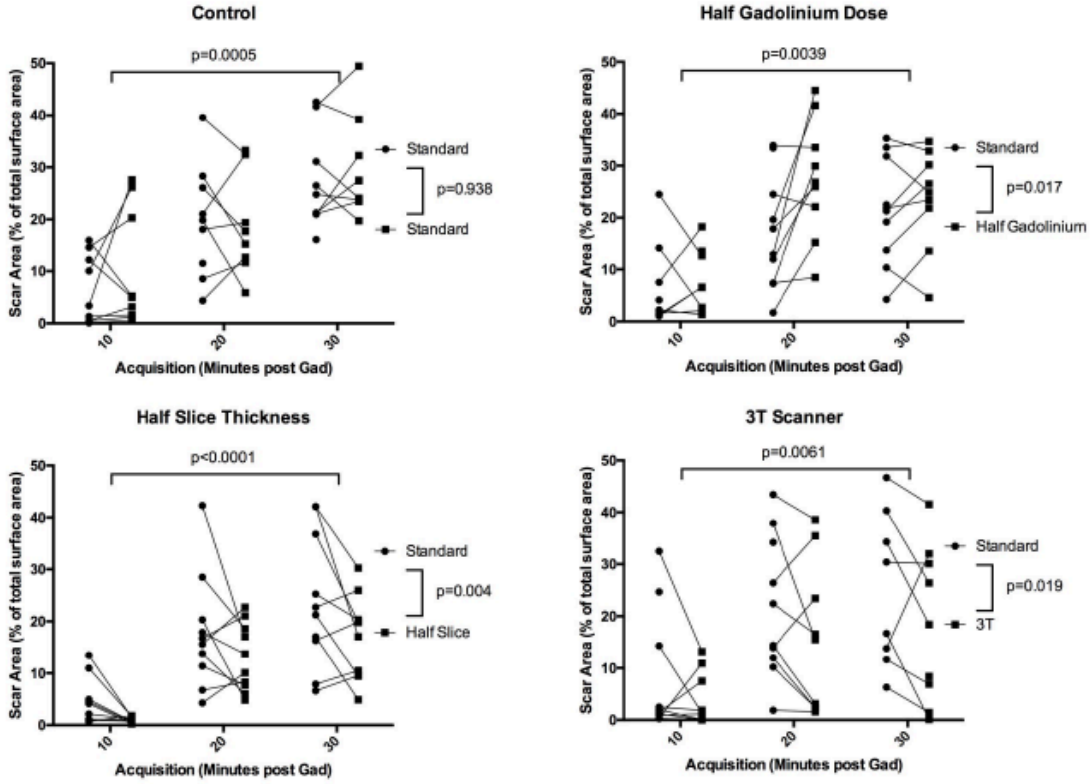

Figure 7-5. Impact of scan parameters on LA scar area, as a percentage of total LA surface area.

Paired acquisitions at 10, 20 and 30min post GBCA injection, for control subjects (top left), half GBCA dose (top right), half slice thickness (bottom left) and 3T scanner (bottom right). Scan 1 (standard acquisition, circle) and scan 2 (experimental acquisition, square) are linked for each subject. P-values are for two-way repeated measures ANOVA: at the top of each plot is the p-value for variance with time, and to the right is the p-value for variance with acquisition parameter. Unpaired acquisitions are shown as unlinked circle or square, and were not included in statistical analyses.

7.5 Discussion

The quality of 3D LGE imaging of PAAS varies widely between different scanning parameters. This has important implications for the routine performance of these scans and, in particular, clinical decision making on the basis of MR-defined metrics. The findings are summarised as follows:

1. Imaging quality improves with time from GBCA administration and LGE imaging is best performed at least 30min after injection of contrast

2. Half dose of GBCA (0.1mmol/kg) improved aCNR and the amount of PAAS detected, without significant detrimental effect upon imaging quality
3. Halving slice thickness reduced the amount of PAAS detected
4. Imaging at 3T magnet strength did not improve aCNR in this patient cohort, and was associated with a reduction in imaging quality and amount of scar detected

7.5.1 Timing of acquisition

The finding that aCNR and scar detection improved with time is not surprising. In an informative study by Goldfarb et al (Goldfarb, Arnold, and Roth 2009), they documented the T_1 values for left ventricular myocardial scar, viable myocardium and blood pool at two minute intervals following GBCA administration. Assessment was continued for up to one hour, and it was found that discrimination between scar and viable myocardium was significant even at very early acquisitions (<10min). However, the discrimination between blood pool and scar was only significant at >10min, and continued to improve with time, such that imaging at >30min was recommended for blood pool to scar differentiation.

For PAAS imaging, it is the blood pool to scar differentiation that is crucial, not viable myocardium to scar. All centres currently acquire 3D LGE imaging with in-plane resolution around 1.3x1.3mm (Table 7-1), and therefore blood pool partial voluming effects are inevitable for most voxels within an atrial wall of thickness 2-4mm (Platonov et al. 2008; Khurram et al. 2014). PAAS detection will be improved as the blood pool signal falls, regardless of the image interrogation technique. This is most critical when the maximum intensity projection technique is used to interrogate scar (Badger et al. 2010; J L Harrison, Sohns, et al. 2015; Hunter et al. 2013; Malcolme-Lawes et al. 2013), but the principle also applies for a voxel-by-voxel interrogation of the atrial wall (Bisbal et al. 2014; Akoum et al. 2015; Fukumoto et al. 2016; Taclas et al. 2010).

The timing of 3D LGE acquisition varies widely in published studies, with no centre routinely imaging at >30min (Table 7-1). There have been two large non-selective studies of PAAS imaging, where CMR imaging was performed regardless of recurrence status. Both acquired 3D LGE sequences at around 15min post-GBCA administration. Badger et al detected gaps in PV scar at 405/576 veins (70%) and in 93% of patients overall (Badger et al. 2010). Akoum et al, on assessment of a subset of the DECAAF study, detected circumferential scar at 1.26 veins per patient (gaps estimated at 67% of veins) and in 93% of patients overall (Akoum et al. 2015). The findings of the present study suggest that the incidence of gaps may have been substantially lower if image acquisition had been delayed until later after GBCA administration.

7.5.2 Scan parameters

The improvement in PAAS imaging with half GBCA dose relates largely to the increase in blood pool to scar contrast, and the superiority is most marked at early acquisitions. The persistence of the improved aCNR at 20 and 30min is an interesting illustration of the aphorism that ‘less is more’. The

highly significant improvement in imaging with reduced GBCA dose is not necessarily apparent from first principles, and this is an important finding of the study. From equation 1.9 in 1.2.3, and equation 1.10 in 1.4.2, it is clear that the relationship between contrast concentration and signal intensity is not a linear one. A halving of contrast concentration in any given compartment will not result in a halving of relaxation rate (the inverse of the relaxation time constant), and in turn the increase in signal resulting from a shortened T_1 time-constant is a relationship that is also dependent on inversion time and repetition time (Knowles et al. 2008). Furthermore, the time dependent concentrations of GBCA within the blood pool and atrial myocardial scar compartments have not been ascertained (Knowles et al. 2008).

The lack of improvement in imaging at 3T may be explained at least in part by challenges in image acquisition that are more frequently encountered in this environment. ECG interference is higher, leading to triggering errors, and the respiratory navigator is less reliable, although once successfully commenced overall acquisition time was unchanged from controls. Contrast behaviour is also relatively unchanged, with minimal reduction in relaxivity of GBCAs at higher field strengths ($5.0 mmol^{-1}s^{-1}$, (range $4.7\text{-}5.3 mmol^{-1}s^{-1}$) at 3T in plasma, versus $5.2 mmol^{-1}s^{-1}$ (range $4.9\text{-}5.5 mmol^{-1}s^{-1}$) at 1.5T) (Rohrer et al. 2005). However, the acquisition window was late atrial diastole (onset 296±40msec, end 398±39msec post R-wave), which was more frequently impinged upon at the longer inversion times necessary for imaging at 3T, requiring compromise in terms of acquisition window.

There was a general decline in imaging quality with half-slice thickness, which is not surprising. The reduced voxel size will decrease the voxel SNR, but on direct image assessment the blood pool and scar aSNR remained relatively preserved (Supplementary Figure 7-6 and Supplementary Figure 7-7) as was aCNR. However, there was a significant decrease in PAAS area overall. This has implications for the detection of small gaps. In the recent study by Bisbal et al, they found median gap size of 13mm, but the smallest was 1.6mm (Bisbal et al. 2014), and Ranjan et al detected deliberate gaps as small as 1.4mm, using a 1.0x1.0x1.5mm resolution 3D LGE acquisition in an animal model (Ranjan et al. 2012). Small gaps will only be detectable within plane for thicker slice 3D acquisitions, and not if it lies between slices. Two consecutive orthogonal acquisitions may represent the best compromise for accurate gap detection whilst maintaining scar sensitivity, but would require more complex registration and co-processing for gap detection.

7.5.3 Clinical implications

PAAS imaging in the immediate term presents opportunities for non-invasive evaluation of conventional and novel therapies. This includes assessment of the impact of contact force (Sohns et al. 2013), evaluation of ablation extent by cryoballoon (Halbfass et al. 2015), and even ablation-induced modification of fat pads containing ganglionated plexi (Higuchi et al. 2013). Optimal, and ideally uniform, imaging acquisition parameters would increase precision and facilitate comparison of studies.

The use of PAAS imaging to guide ablation procedures is more controversial. Inter-scan reproducibility needs to be demonstrated, and sensitivity needs to improve. However, if the findings of Bisbal et al can be replicated then there is opportunity for swifter and more efficacious re-do procedures (Bisbal et al. 2014). This may become even more relevant in the light of the recent PRESSURE trial (Gupta et al, presented Late Breaking Clinical Trials, HRS 2016, http://ondemand-qc.hrsonline.org/common/media-player.aspx/26/23/1866/14988). In this study, 80 patients underwent routine paroxysmal AF ablation prior to randomisation to routine follow-up or repeat PVI isolation procedure at 2 months, regardless of symptoms. For those that underwent prophylactic repeat procedure, 12 month arrhythmia-free survival was increased from 58% to 83% (p=0.03). Non-invasive CMR correlates that identify subjects who would benefit from pre-emptive repeat procedures could be extremely valuable.

For post-ablation macro re-entry arrhythmias, identification of PAAS may also assist in the pre-procedural prediction of the arrhythmia mechanism. This in turn may inform activation mapping strategy, diagnostic manoeuvres and possibly lesion delivery. Zahid et al used atrial LGE datasets to derive patient specific models of LA tachycardia pathways, in combination with fibre orientation atlas. In 7 out of 10 patients (all post–PVI) it was possible to model a LA macro-reentrant circuit, and the ablation trajectory that was successful clinically was predicted in-silico in all 7 patients (Zahid et al. 2016).

This study has clear implications for modification of PAAS imaging practices: delaying LGE acquisition to at least 30minutes post administration of contrast increases visualisation of PAAS. However, the optimal timing for PAAS detection was not identified as the imaging quality continued to improve at 30min (with true acquisition commencement in this study closer to 35min). Further studies are required to assess imaging at >35min, but the effect of time was significantly diminished at 20 versus 30min, compared to 10 versus 20min, suggesting that improvement was beginning to plateau. Practical considerations also have to be made, and scan durations of >60min will be more costly, less efficient for managing a CMR service and may compromise patient compliance. GBCAs could be administered prior to commencement of the scan, but this would preclude early gadolinium enhanced imaging or angiography. Alternatively, a split imaging session, with offline image registration and interleaving of subjects, could be considered but would require a repetition of patient set-up and surveys. It is likely that a suitable compromise would include administration of GBCA and early post-gadolinium imaging at the earliest possible opportunity, with all functional and ventricular scar imaging performed during a minimum 30min waiting time.

7.5.4 Limitations

This study was performed at 3 months post ablation, and is an evaluation of chronic scar formation. As such, the results are not directly applicable to the assessment of acute lesion formation, and could not be used to guide acute repeat ablation during the index procedure in a hybrid-type environment.

Likewise, there is evidence that there is a slow fading of scar with time (Badger et al. 2009), and the application of these results to imaging >3months post-ablation should be performed with caution.

There is no gold standard for validation of PAAS detection, in the absence of histological assessment. Voltage mapping has been only weakly correlated with PAAS, and it is likely that registration errors, bipolar sampling considerations and electrode size confer upon voltage mapping a similar level of error as CMR assessment of scar. Furthermore, there is evidence that voltage and true scar are only moderately well-correlated (Kowalski et al. 2012). Therefore the study has focused on optimising sensitivity, rather than evaluations of specificity of scar detection.

In terms of the study design, the acquisitions could not be performed at identical timepoints post-GBCA administration, which may introduce a bias for late acquisition for patients that experienced more difficult and prolonged imaging acquisitions. In addition, on account of technical considerations it was not possible to randomise patients to the 3T scanner. The interval between scan sessions was minimised in order to control for time dependent scar maturation (Badger et al. 2009), but there was a possibility of residual GBCA accumulation between scans. T1 relaxation times for the myocardium were unchanged between scan sessions, and there was no systematic difference between scans in any parameter for control patients. However, recent studies have suggested that very low concentrations may persist beyond 48 hours (Lancelot 2016), despite the interval being >20 half-lives, but the impact on the results is likely to be minimal.

7.6 Conclusions

Imaging of post-ablation atrial scar improves with greater delay from GBCA administration, with imaging recommended at least 30min post-contrast. A half dose of GBCA is superior in terms of contrast-to-noise ratio and area of scar detected, whilst reduced slice thickness and imaging at 3T tend to result in inferior imaging quality.

7.7 Acknowledgements and Contributions

I recruited all subjects and performed all of the baseline, pre-ablation scans. The measurement of signal intensities within every region of interest was performed in collaboration with an MSc student whom I supervised, Shadman Aziz, who won the prize for best undergraduate project in 2015 on an analysis of the first half of the data cohort. He performed approximately half of the ROI measurements. Of those that I did not perform myself, I re-verified a random selection of 20 acquisitions. I am also grateful to Prof Rene Botnar and Dr Marcus Henningsson for their guidance in the estimation of noise in the presence of parallel processing. I performed all the statistical analyses myself.

7.8 Supplementary Figures

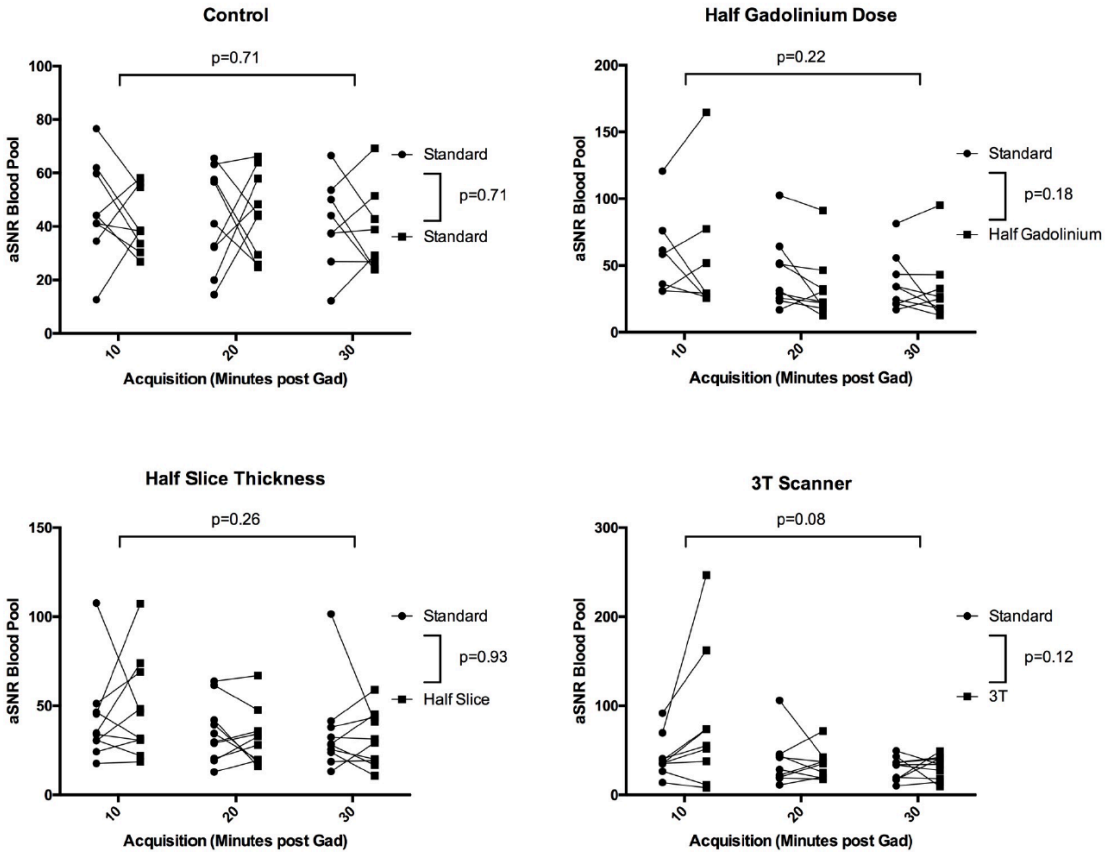

Figure 7-6. Impact of scan parameters on blood pool apparent signal to noise ratio.

Paired acquisitions at 10, 20 and 30min post GBCA injection, for control subjects (top left), half GBCA dose (top right), half slice thickness (bottom left) and 3T scanner (bottom right). Scan 1 (standard acquisition, circle) and scan 2 (experimental acquisition, square) are linked for each subject. P-values are for two-way repeated measures ANOVA: at the top of each plot is the p-value for variance with time, and to the right is the p-value for variance with acquisition parameter. Unpaired acquisitions are shown as unlinked circle or square, and were not included in statistical analyses.

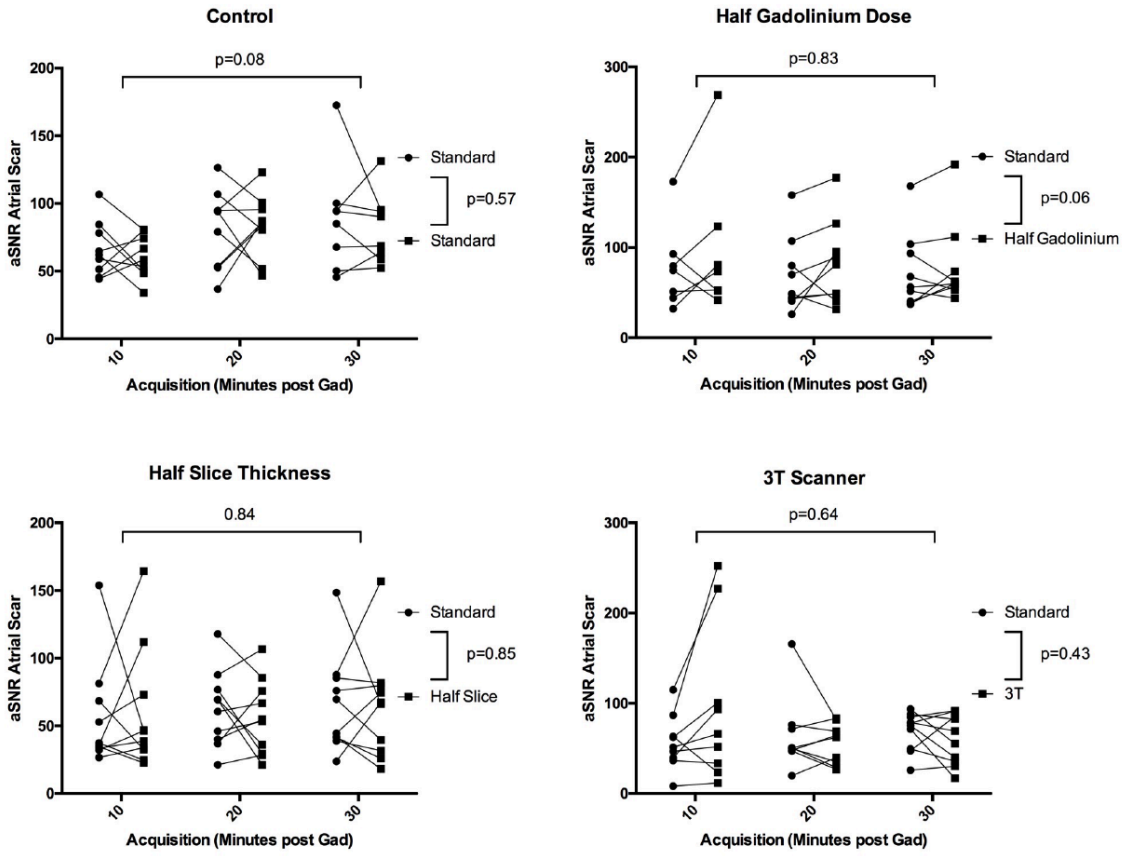

Figure 7-7. Impact of scan parameters on scar apparent signal to noise ratio.

Paired acquisitions at 10, 20 and 30min post GBCA injection, for control subjects (top left), half GBCA dose (top right), half slice thickness (bottom left) and 3T scanner (bottom right). Scan 1 (standard acquisition, circle) and scan 2 (experimental acquisition, square) are linked for each subject. P-values are for two-way repeated measures ANOVA: at the top of each plot is the p-value for variance with time, and to the right is the p-value for variance with acquisition parameter. Unpaired acquisitions are shown as unlinked circle or square, and were not included in statistical analyses.

8 The Reproducibility and Thresholding of Cardiac Magnetic Resonance Imaging of the Left Atrium Following Radiofrequency Ablation

8.1 Aims

To assess the reproducibility of the 3D LGE CMR technique to determine locations of PAAS.

To determine the optimal normalisation technique for the scaling of arbitrary signal intensity scalars, and hence

To establish the optimal thresholding technique for delineation of PAAS, and to re-assess the impact of thresholding upon reproducibility of PAAS detection.

To evaluate the predictive value of PAAS imaging for late arrhythmia recurrence

8.2 Introduction

The technique of 3D LGE imaging for the assessment of PAAS has been used for almost a decade but its reproducibility has never been formally quantified. This step is crucial from both a clinical and research perspective as the use of the technique becomes increasingly mainstream. From a clinical perspective, confidence in the technique should be founded upon the knowledge that the location of PAAS remains fixed between scanning sessions. At a research level, the reproducibility of an imaging technique has a profound impact upon the design and scaling of research studies (Bellenger et al. 2000) and the interpretation of its results. Quantification of the reproducibility of PAAS imaging, between multiple acquisitions, scanning sessions and established variations in imaging protocols, was the first objective of this study.

However, there is no single metric of PAAS imaging that has been established. Whilst some have looked to determine scar burden and location (Badger et al. 2010; Hunter et al. 2013), others have sought to determine the presence of gaps in the ablation line (Bisbal et al. 2014; J L Harrison, Sohns, et al. 2015), each using a bespoke thresholding and image interrogation technique (Table 8-1). Therefore, techniques to assess point-by-point scar location, to measure global scar burden, and to

establish ablation gaps objectively need to be developed in order to establish quantitative measures of PAAS for reproducibility assessment.

All measures of PAAS are closely entwined with the SI threshold by which they are identified. Similar to assessment of ventricular myocardial scar (Flett et al. 2011), the selection of an appropriate threshold is complicated by the requirement for a normalisation method of SIs. CMR-derived image SI is expressed in arbitrary units, and absolute threshold values may be expressed as a raw SI value, but indexing to acquisition specific reference SIs is almost always required. This is generally performed using a direct ratio to a single acquisition specific metric, such as blood pool or scar SI, or alternatively using a two-metric normalisation method where both a mean and standard deviation are defined. For instance, PAAS may be thresholded at a set number of (blood pool) standard deviations from the blood pool mean, creating effectively a Z-score. Therefore the two-metric normalisation technique may be interpreted as a surrogate for confidence in the differentiation of one voxel population from another, but it is highly sensitive to the measurement of the index of variance. The relative strengths of the two groups of normalisation techniques has not been established, and formed the second objective of this study.

Once a normalisation technique has been selected, an appropriate threshold is also required. The thresholding of PAAS on LGE imaging is challenging and there is no consensus in the literature regarding the best method for establishing an image intensity threshold. Table 8-1 summarises levels that have been used by established groups for delineation of PAAS: it is clear that different methods will derive different patterns of PAAS for the same acquisition, which may lead to very different scar quantification measures. Ideally, image intensity threshold would be validated from a gold standard, such as histology, and recent studies have sought to do so (James L Harrison et al. 2014). However, a number of factors lead to the introduction of measurement error, and hence to wide ranges for confidence intervals. Post-mortem topographical and scaling changes, registration of histological section to imaging section and accurate histological identification of scar all lead to challenges in establishing a clear relationship between histological findings and local imaging intensity. Alternatively, scar may be compared to invasive voltage mapping. However, not-withstanding reservations in using voltage as an accurate surrogate of scar (Kowalski et al. 2012), there are significant technical challenges related to registration of EAM and post-ablation CMR scar imaging, and the correlation coefficients of the relationship between the two are generally poor (R^2=0.57 (Badger et al. 2010), R^2=0.04 (J L Harrison, Sohns, et al. 2015). Derivation of an evidence-based threshold for PAAS in humans was therefore the third objective of this study.

Finally, the association of PAAS and AF recurrence remains controversial (Taclas et al. 2010; Spragg et al. 2012; Bisbal et al. 2013; J L Harrison, Sohns, et al. 2015). The fourth objective of this study was to assess the association of the derived indices of PAAS with long-term AF recurrence.

Study	Centre	Number of patients	Thresholding Reference	Thresholding Level	Validation
(Badger et al. 2010)	Utah, USA	144	Atrial wall z-score	3 SD above normal atrial wall tissue	EAM voltage comparison (R^2=0.57)
(Bisbal et al. 2014)	Barcelona, Spain	15	Scar IIR	40% or 60% of maximum scar	EAM voltage and repeat ablation
(J L Harrison, Sohns, et al. 2015)	King's College, London	20	Blood pool z-score	Nil (minimum point on PV antrum)	EAM voltage (R^2=0.04) and repeat ablation
(Fukumoto et al. 2015)	Johns Hopkins	20	Blood pool IIR	LGE: >0.97 Dense LGE: >1.61	EAM voltage
(Malcolme-Lawes et al. 2013)	Imperial College, London	11	Blood pool z-score	3SD above BP	EAM voltage
(Hunter et al. 2013)	Barts and Imperial College, London	50	Myocardial z-score	5 SD above vent myocardium	Ablation type (WACA versus cryo)
Taclas et al (2010)	Boston, USA	19	Blood pool z-score	'average 3.6SD above BP'	

Table 8-1. Thresholding techniques for establishing post-ablation atrial scar.

8.3 Methods

8.3.1 Subjects, imaging protocol and ablation protocol

Study population and imaging protocol are described in Sections 7.3.1 and 7.3.2 respectively. Further details of imaging acquisition parameters are provided in Section 4.1. The ablation protocol is detailed in Section 4.4.

8.3.2 Imaging interrogation and comparison technique

Imaging interrogation techniques are described in detail in Section 4.2. For all acquisitions a semi-automated segmentation of the gated magnetic resonance angiogram (GMRA) acquisition was performed where possible, which was then registered (rigid registration) independently to each LGE acquisition of the same imaging session (Acq_1, Acq_2, Acq_3, see Table 8-2 for nomenclature). For the

subsequent imaging session at 48-72 hours, the GMRA acquisition at post-ablation scan 1 ($GMRA_1$) was registered to the GMRA acquisition of post-ablation scan 2 ($GMRA_2$), which was itself then registered to each subsequent LGE acquisition (Acq_4, Acq_5, Acq_6). Through this method, an identical atrial shell could be used for all six acquisitions for most subjects. The GMRA was inadequate for semi-automated segmentation in six subjects, for whom a manual segmentation of Acq_1 was performed, and registered to all subsequent acquisitions.

Adequacy of fit of the registered segmentation was visually assessed for every acquisition, and was rejected if the LA segmentation to LA wall distance was >1mm in the majority of slices. In these cases, a new LA segmentation was performed. For all acquisitions, the registration within scan session (Acq_1 to Acq_2 and Acq_3, or Acq_4 to Acq_5 and Acq_6) was good, and re-segmentation within scan session was never required. However, for two subjects, in whom there was a change in heart rhythm between scans, the registration between scan sessions was inadequate and therefore a new segmentation was performed for each scan session.

LA scar was interrogated using a maximum intensity projection (MIP) technique, 1mm inside endocardial shell and 3mm beyond endocardial shell, and a single SI value was assigned to each triangular face of the generated .vtk shell (typically 40,000 faces per LA shell). For all reproducibility measures, Acq_1 and Acq_4 (acquisitions performed at 10min post GBCA administration) were not assessed on account of the poor imaging quality and low scar: blood pool CNR (see Chapter 7). Comparison between two acquisitions *i* and *j* is termed $C_{i,j}$, and multiway comparisons between acquisitions *i, j,... j+1* termed $C_{i,j...,j+1}$.

3D Late Gadolinium Enhanced Acquisition			**Scan Session 1**			**Scan Session 2**		
			10min	20min	30min	10min	20min	30min
			Acq_1	**Acq_2**	**Acq_3**	**Acq_4**	**Acq_5**	**Acq_6**
Scan Session 1	10min	**Acq_1**	-	$C_{1,2}$	$C_{1,3}$	$C_{1,4}$	$C_{1,5}$	$C_{1,6}$
	20min	**Acq_2**	-	-	$C_{2,3}$	$C_{2,4}$	$C_{2,5}$	$C_{2,6}$
	30min	**Acq_3**	-	-	-	$C_{3,4}$	$C_{3,5}$	$C_{3,6}$
Scan Session 2	10min	**Acq_4**	-	-	-	-	$C_{4,5}$	$C_{4,6}$
	20min	**Acq_5**	-	-	-	-	-	$C_{5,6}$
	30min	**Acq_6**	-	-	-	-	-	-

Table 8-2. Image acquisition and comparison nomenclature.

Acq_i is the i^{th} post-ablation LGE acquistion for each subject, $C_{i,j}$ is the comparison between Acq_i and Acq_j.

8.3.3 Left atrial volumes and cardiac function

LA size and function were evaluated on CMR imaging prior to ablation, and then again at post-ablation scan 1 and 2. LA volume was assessed based upon the segmentation of the LA. PVs and LA appendage were manually removed, and volume was indexed to body surface area (BSA- calculated according to the method of Du Bois and Du Bois (Du Bois and Du Bois 1916)). LA and LV function were assessed on multi-slice short-axis cine imaging, as detailed in Section 5.3.5. LA function was assessed on both post-ablation scan 1 and 2, whilst LV function was assessed on only one post-ablation scan.

8.3.4 Reproducibility of thresholded PAAS

Research groups have almost universally chosen to threshold PAAS, and a variety of normalisation methods and absolute thresholds have been implemented (Badger et al. 2010; Bisbal et al. 2014; J L Harrison, Sohns, et al. 2015; Fukumoto et al. 2015; Malcolme-Lawes et al. 2013; Hunter et al. 2013; Taclas et al. 2010). However, evidence for identification of thresholds has frequently relied upon correlation with voltage mapping techniques, which are prone to registration and voltage sampling errors, or extrapolation from ventricular scar studies. A histologically validated value of 3.3 standard deviations above the blood pool mean was therefore used for all indices where a single threshold value was required (James L Harrison et al. 2014).

Three measures of reproducibility of thresholded PAAS were used. The first measure was that of total scar burden, expressed as a proportion of the surface area of the LA shell occupied by PAAS. The second measure exploited the identical morphologies of the shells to calculate a Sorensen Dice Similarity Coefficient (DSC), assessing the co-location of CMR-derived scar on a face-by-face basis on the atrial shell (Crum, Camara, and Hill 2006) . The DSC was calculated according to Equation 9.1, assessing both healthy and scar regions. Intra-scan DSC was calculated for pooled analysis of $C_{2,3}$ and $C_{5,6}$, whilst inter-scan DSC was calculated for pooled analysis of $C_{2,5}$ and $C_{3,6}$.

$$DSC_{i,j}(Threshold(T)) = \frac{2(Scar_i \cap Scar_j)+2(Healthy_i \cap Healthy_j)}{All\ Tissue_i + All\ Tissue_j} \quad \text{Equation 9.1}$$

where $DSC_{i,j}(Threshold(T))$ is the DSC for the comparison of Acq_i with Acq_j, at the same signal intensity threshold T. $Scar_i$ and $Healthy_i$ are the faces designated as scar and healthy tissue respectively at threshold T.

The third measure of scar was a gap quantification method, developed in collaboration with Marta Núñez and Constantine Butakoff at Universitat Pompeu Fabra, Barcelona, Spain. In brief, the technique aimed to perform an objective measurement of the proportion of the wide area circumferential ablation line that is occupied by uninterrupted scar on LGE CMR, a percentage PV encirclement (PVE) (Figure 8-1). Scar was again thresholded at 3.3 standard deviations above the blood pool mean, and the full method of the derivation of PVE is detailed in Appendix B.

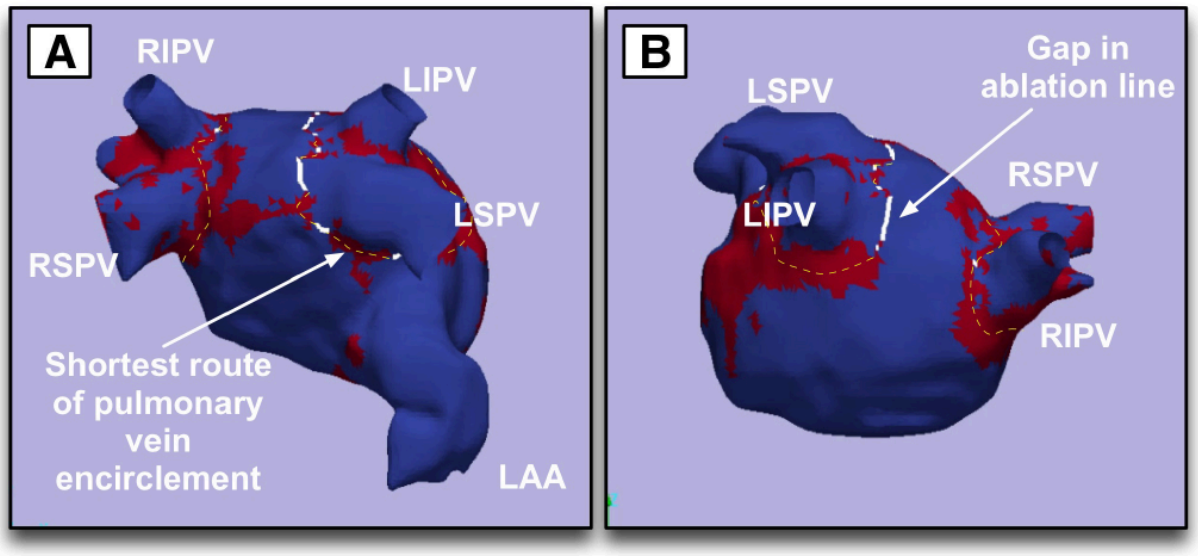

Figure 8-1. Illustration of derivation of pulmonary vein encirclement (PVE) measurement.

Atrial shell (16M, Acq_2) is thresholded at 3.3 standard deviations above the blood pool mean, with scar shown in red and healthy atrial myocardium in blue. The computed route of the PV encirclement is shown in yellow dashed line, whilst detected gaps in the ablation line are shown in white. For this acquisition, the PVE for the right sided veins was 98.5%, and for the left was 81.5%. (LSPV: left superior PV, LIPV: left inferior PV, RSPV: right superior PV, RIPV: right inferior PV)

8.3.5 Reproducibility of PAAS imaging without thresholding

These three measures are all highly dependent upon the scar threshold, and therefore the imaging reproducibility was also assessed point-by-point using a method that was not dependent upon thresholding. However, signal intensity is expressed in arbitrary units, and therefore normalisation methods were required to enable inter-scan comparisons.

8.3.5.1 Signal intensity normalisation methods

Shell surface SI units were normalised using four different acquisition specific reference methods, based upon established image analysis techniques (Table 8-1). Two of the methods are direct ratios, indexing by a single acquisition specific metric: blood pool image intensity ratio (BP-IIR- ratio of SI to blood pool mean)(Fukumoto et al. 2015) and scar image intensity ratio (Scar-IIR- ratio of SI to best scar in reference slice)(Bisbal et al. 2014). The other two methods index by both a mean and a variance: nulled myocardium z-score (V-Myo-Z: number of (ventricular myocardial) standard deviations (SD) from healthy ventricular septal myocardium mean)(Hunter et al. 2013), and blood pool z-score (BP-Z: number of (blood pool) SDs from the blood pool mean)(Taclas et al. 2010; J L Harrison, Sohns, et al. 2015; Malcolme-Lawes et al. 2013). Blood pool and scar reference values were obtained in a single standard slice at the level of the aortic root (see Section 7.3.4.2 and Appendix A).

Ventricular myocardial mean and SD were obtained in the mid-septum in a region of homogenous signal intensity (50mm^2) without blood pool contamination. Kurtosis and skew were not controlled for in any of the indexing systems.

The referencing method employed by Utah, i.e. SDs from the mean atrial wall intensity within slice, was not formally assessed for two main reasons. Firstly, the thresholding is on a slice by slice basis, and is allowed to vary between slices. It is technically possible to assess each transverse slice for mean and standard deviation, but it was not feasible to assign a subjective threshold at each slice on every acquisition. Secondly, the threshold technique is likely to represent a hybrid of the V-Myo-Z and BP-Z indexing methods . Partial voluming effects at the atrial myocardium to blood pool interface mean that the voxels designated as the thin atrial wall are highly likely to contain signal from both blood pool and myocardium. The inversion time aims to null atrial myocardium, but most centres use ventricular myocardium as a surrogate for atrial myocardium (Badger et al. 2010; Bisbal et al. 2014; Taclas et al. 2010; J L Harrison, Sohns, et al. 2015), based upon the assumption that atrial myocardial signal should closely mimic that of ventricular myocardium.

8.3.5.2 Shell comparisons

Following normalisation, intraclass correlation coefficients (ICCs) for both consistency and absolute agreement were calculated on a face-by-face basis (typically 40,000 triangular faces per shell), exploiting the identical morphology of the atrial shells.

8.3.6 Derivation of a gold standard for thresholding of PAAS

Two methods were assessed for determination of a gold standard for thresholding of PAAS. Firstly, an expert-derived gold standard for PAAS threshold was assigned based upon comparison to the sites of energy delivery at the time of ablation. For twenty subjects, the locations of objective markers of ablation (VisiTag markers (Biosense Webster)) were projected upon the EAM-derived LA shell (see Chapter 9 for details of technique). The presence of an objective ablation marker (at any VisiTag parameter setting) was used to define all potential ablation locations. Each CMR LGE shell ($Acq_{1\text{-}6}$) was then compared side by side to the ablation shell, and the CMR SIs binarised to scar and no scar at user-defined values, using Paraview (Kitware, New York, NY, USA). An optimal threshold value was selected that was judged to balance sensitivity for scar, without unacceptable loss of specificity, blinded to derived conventional threshold values (Figure 8-2).

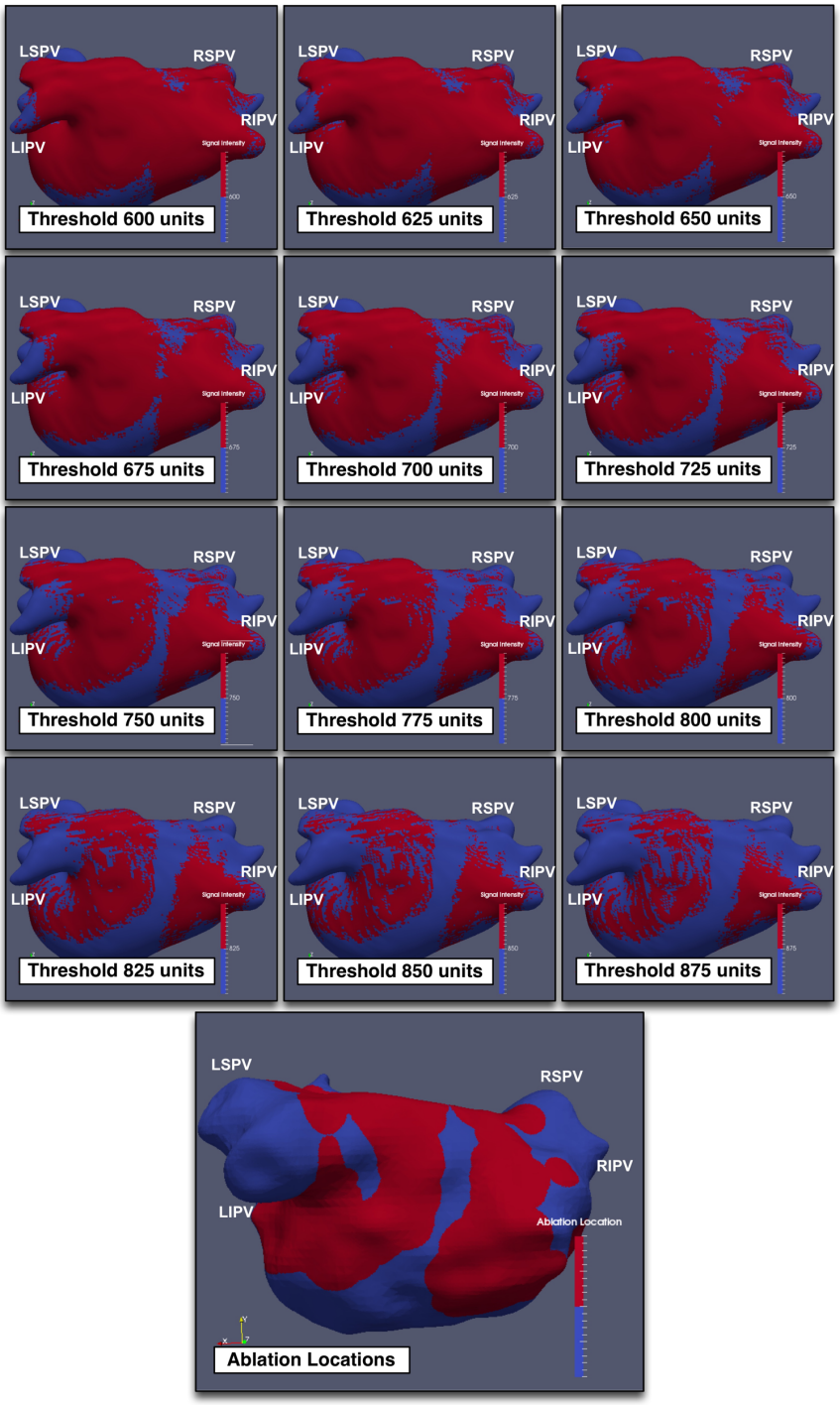

Figure 8-2. Example of subjective selection of threshold for scar delineation (subject 40T, Acq_6).

Upper twelve panels show the CMR imaging shell with binary threshold level defined in arbitrary signal intensity units. The bottom panel shows the ablation locations, as defined by location of objective ablation markers (VisiTag markers- see Chapter 9 for further details). Note the lack of specifity of CMR imaging-defined scar at low threshold, and lack of sensitivity at high thresholds: here, 750 SI units was selected as an appropriate threshold, where there is adequate separation between ablation regions, but minimal scar

drop-out within ablation regions. For this acquisition, 600 SI units is 0.2 standard deviations above blood pool mean, and 875 SI units is 4.4SD above BP mean. LSPV: left superior PV, LIPV: left inferior PV, RSPV: right superior PV, RIPV: right inferior PV.

The second method, an objective comparison of CMR scar to ablation locations was performed on a point-by-point basis. For each of the twenty subjects, a single representative CMR LA shell was fused to the EAM LA shell, using an iterative closest point registration technique, detailed in Section 9.3.8.2. Similar to above, a DSC was then calculated to assess the co-location of CMR-derived scar and ablation locations (Equation 9.2).

$$DSC_i(Threshold(T))) = \frac{2(Scar_{CMR} \cap Lesion_{EAM})}{Scar_{CMR} + Lesion_{EAM}} \qquad \text{Equation 9.2}$$

where DSC_i(Threshold(T)) is the DSC for the comparison of the fused CMR shell Acq_i with the ablation location EAM shell, at signal intensity threshold T. $Scar_{CMR}$ are the faces designated as scar on the CMR shell, at Threshold(T), and $Lesion_{EAM}$ are the faces associated with an objective ablation marker (VisiTag)

On account of the identical morphology of the CMR shells for each subject, the same single image fusion could be used for each acquisition ($Acq_{1\text{-}6}$) for a single subject. A DSC was derived for every SI threshold for each acquisition, and the SI value for the highest DSC recorded as the DSC-derived threshold. Acquisitions for which the highest DSC was below the BP mean, representing cases where optimal DSC was achieved when the vast majority of the shell was assigned as scar, were excluded.

A final threshold method was also evaluated, using an Otsu thresholding technique. Otsu's method is a clustering-based image thresholding technique that aims to derive a 'least-cost' threshold through assessment of all potential thresholds values, aiming to minimise the within-class variance (Otsu 1975). Whilst the technique may be extended to multiple thresholds, in this case it was used only for dichotomisation of the shell signal intensities, based upon the hypothesis that there are only two signal intensity groups: scar and healthy tissue. Otsu thresholding was performed on the population of signal intensities upon the LA shell, not the whole image, and therefore a signal threshold value was derived for every shell.

8.3.7 Association of scar with arrhythmia recurrence

Arrhythmia recurrence was assessed as detailed in Section 5.3.10, and the scar burden and %PVE were assessed against the binary outcome of recurrence of atrial arrhythmia. Where a repeat LA ablation procedure was performed, the presence or absence of electrical reconnection of each PV pair was recorded and corresponding PVE assessed.

8.3.8 Statistics

Normally distributed continuous variables are presented as mean ± standard deviation, and median with interquartile range (IQR) for non-normal distribution or non-continuous ordinal data. Baseline characteristics and CMR indices were compared using χ^2 test or Student t-test as appropriate. Statistics were analysed using SPSS Statistics (Version 22, Armonk, NY) unless otherwise stated. For ICC, a two-way mixed effects model was selected, on the assumption that the measurement technique (sequence timing, acquisition parameters and indexing technique) was a systematic source of variance (McGraw and Wong 1996). ICC was generated for both consistency and absolute agreement using Matlab (Version R2015a, The Mathworks, Inc.), and the ICC plugin (Arash Salarian, Version 1.2), C-1 and A-1 type analysis for consistency and absolute agreement respectively. Inter-scan ICC was calculated for $C_{2,3,5,6}$ (four-way comparison between $Acq_{2,3,5,6}$). ICC of 0.41 to 0.60 was interpreted to represent "moderate" agreement, 0.61 to 0.80 "good" agreement, and >0.81 "excellent" agreement (Landis and Koch 1977). Repeated measures one-way ANOVA was used to assess differences in ICC between normalisation methods, with Tukey's range test used to correct for multiple comparisons.

8.4 Results

The subject characteristics and acquisitions achieved are summarised in Section 7.4 and Table 7-2, with representative imaging for each acquisition included in Appendix A. There were a total of 231 out of maximum possible 240 acquisitions completed (96.2%). 40 acquisitions were completed at 10min on scan 1 (Acq_1), 40 Acq_2, 37 Acq_3, 39 Acq_4, 39 Acq_5 and 36 Acq_6.

8.4.1 Left atrial volumes and cardiac function post-ablation

Findings are shown in Figure 8-3. There was no significant change in LA indexed volume pre- and post-ablation (57.8±16.5ml/m^2 versus 53.9±15.3ml/m^2, p=0.08 (paired t-test)). On subgroup analysis of subjects in AF at the time of the baseline scan, there was a significant reduction in LA volume post-ablation (69.7±16.2ml/m^2 versus 60.5±18.0ml/m^2, p=0.03). For LA ejection fraction (LAEF), there was no significant change pre- and post ablation (0.317±0.172 versus 0.331±0.114, p=0.52). On subgroup analysis of those in AF at the time of the baseline scan, there remained no significant change in LAEF (0.189±0.112 versus 0.237±0.098, p= 0.29). Left ventricular ejection fraction improved from pre- to post-ablation (0.608±0.099 versus 0.64±0.074, p=0.04), and this improved was most marked in the group in AF at the time of the baseline scan (0.549±0.087 versus 0.645±0.066, p=0.023).

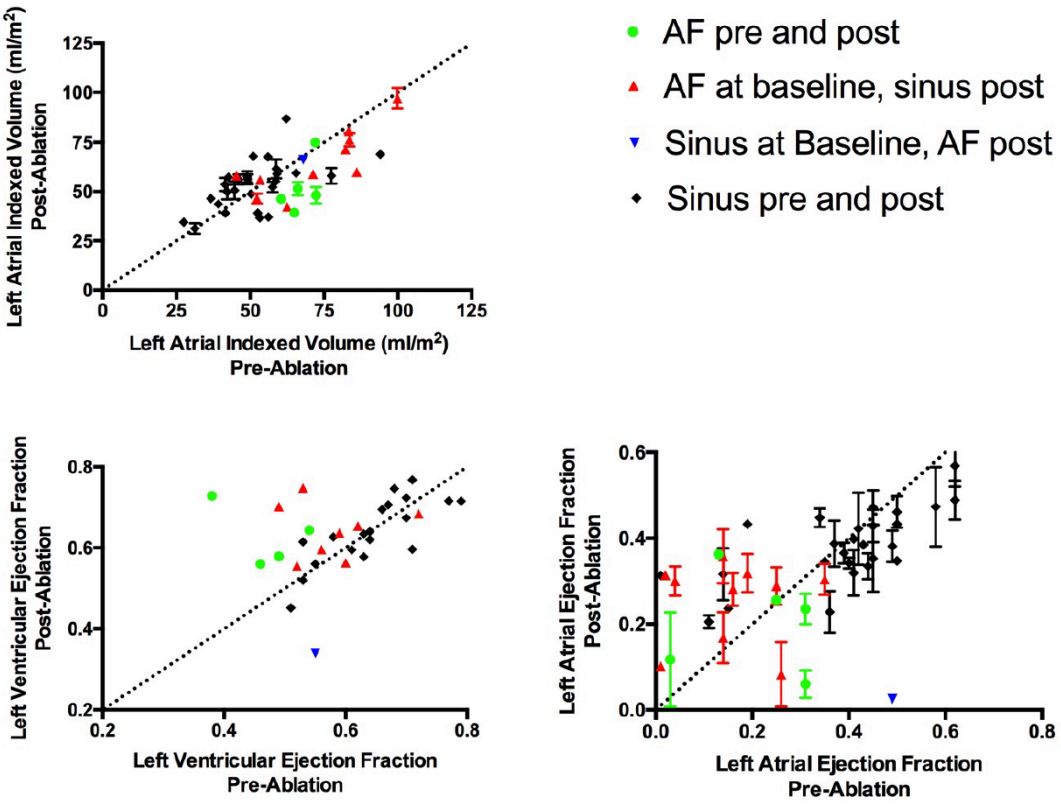

Figure 8-3. Post-ablation volumetric and functional comparisons.

Relationship of pre- and post-ablation LA indexed volume (top left), left ventricular ejection fraction (LVEF) (bottom left) and LA ejection fraction (bottom right). Dotted straight line is line of equality (x=y). Error bars represent standard deviation of the two sets of measurements, performed at each of the two post-ablation scans. LVEF was measured at only one of the two post-ablation scans, and therefore there are no error bars.

Agreement in post-ablation measurement of LA ejection fraction and LA indexed volumes was generally good, particularly in the measurement of LA indexed volume. Bland-Altman plots are shown in Figure 8-4.

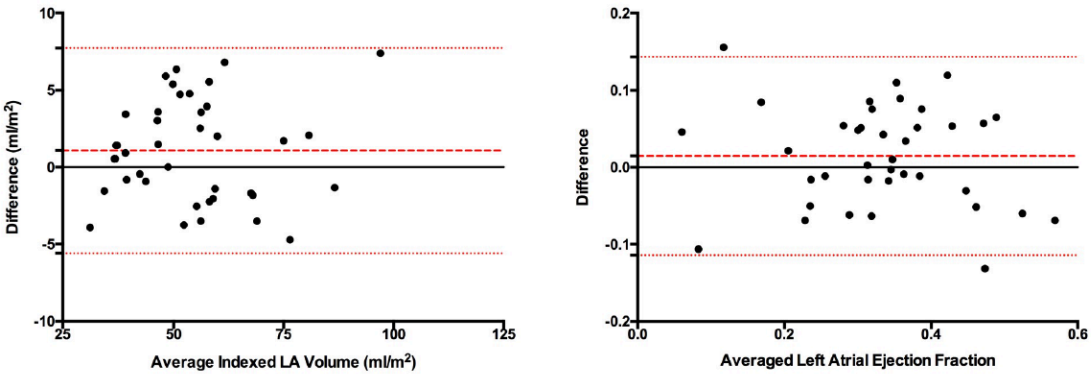

Figure 8-4. Bland Altman plots demonstrating agreement between the measurements of Indexed LA volume (left) and LAEF (right)

Measurements are assessed at each of the two post-ablation scans. Heavy dashed red line shows mean bias (scan 1 measurement minus scan 2 measurement), with light dashed lines illustrating 95% confidence interval.

8.4.2 Reproducibility of PAAS imaging

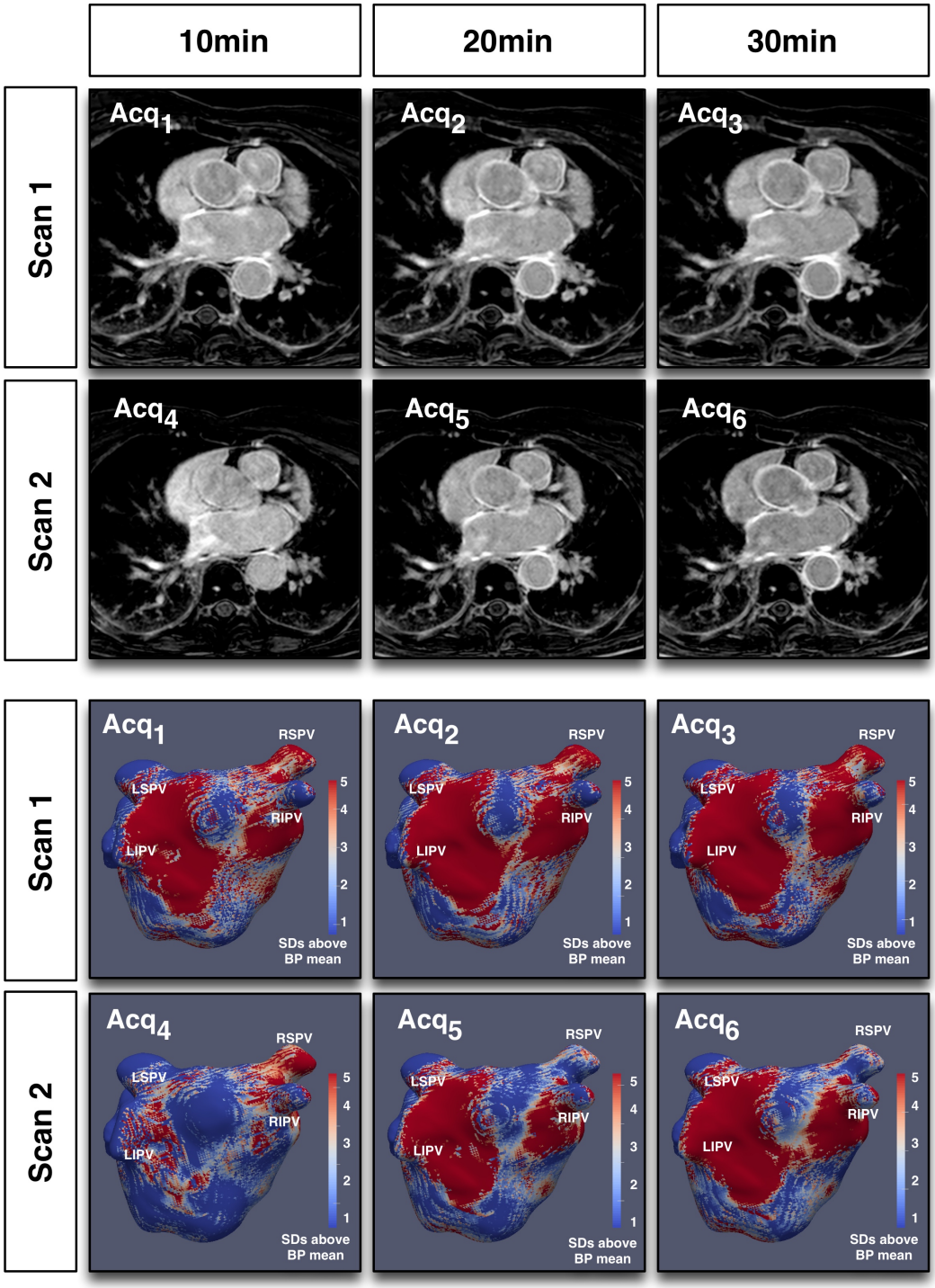

Figure 8-5. Examples of raw images and corresponding scar shells for a single subject (ID:30)

Scans 1 and 2 were performed using identical (standard) acquisition parameters, with acquisitions performed at 10min, 20min and 30min post injection of gadolinium. Upper six panels show single representative slices of the 3D LGE dataset, at the level of the aortic root. Lower six panels show corresponding scar shells, normalised according to blood pool

z-score. Note the relatively poor reproducibility for acquisitions at 10min. Acq: acquisition. LSPV: left superior pulmonary vein, LIPV: left inferior pulmonary vein, RSPV: right superior pulmonary vein, RIPV: right inferior pulmonary vein, SD: standard deviation, BP: blood pool.

8.4.2.1 Total scar burden

ICC for scar burden for acquisitions performed at 10min post gadolinium ($C_{1,4}$) was very poor at 0.070 (95% CI -0.249 – 0.373). This correlated with poor imaging quality at this time point. Scar to blood pool contrast was significantly lower at 10min versus 20min ($Acq_{1 \text{ and } 4}$ (10min post gad) 16.3±15.9 versus $Acq_{2 \text{ and } 5}$ (20min) 31.4 ± 16.8, p<0.0001), as was scar burden ($Acq_{1 \text{ and } 4}$ 7.1% ± 6.8% versus $Acq_{2 \text{ and } 5}$ 21.7% ± 15.6%, p<0.0001) (Figure 8-5). Acquisitions performed at 10min post gadolinium (Acq_1 and Acq_4) were therefore removed from further analyses.

At 20 and 30min post gadolinium, reproducibility of total scar burden was good for intra-scan comparisons ($C_{2,3}$ and $C_{5,6}$ pooled analysis), with an ICC 0.752 (95% CI 0.481-0.869). Scar burden was also significantly higher for acquisitions performed at 30min (20min: 21.7±15.6%, 30min: 28.0±16.1%, p<0.0001). Inter-scan ICC improved with time from acquisition (Figure 8-6), with ICC 0.556 (95% CI 0.280 – 0.747) at 20min ($C_{2,5}$) and 0.702 (95% CI 0.482 to 0.839, p<0.0001 between groups) at 30min ($C_{3,6}$). On assessment of only those subjects that underwent identical scan protocol at Scan 1 and Scan 2, the ICCs at 10min ($C_{1,4}$), 20min ($C_{2,5}$) and 30min ($C_{3,6}$) were 0.237 (95% CI -0.544- 0.765), 0.678 (95% CI 0.119-0.916) and 0.723 (95% CI 0.083-0.938), respectively.

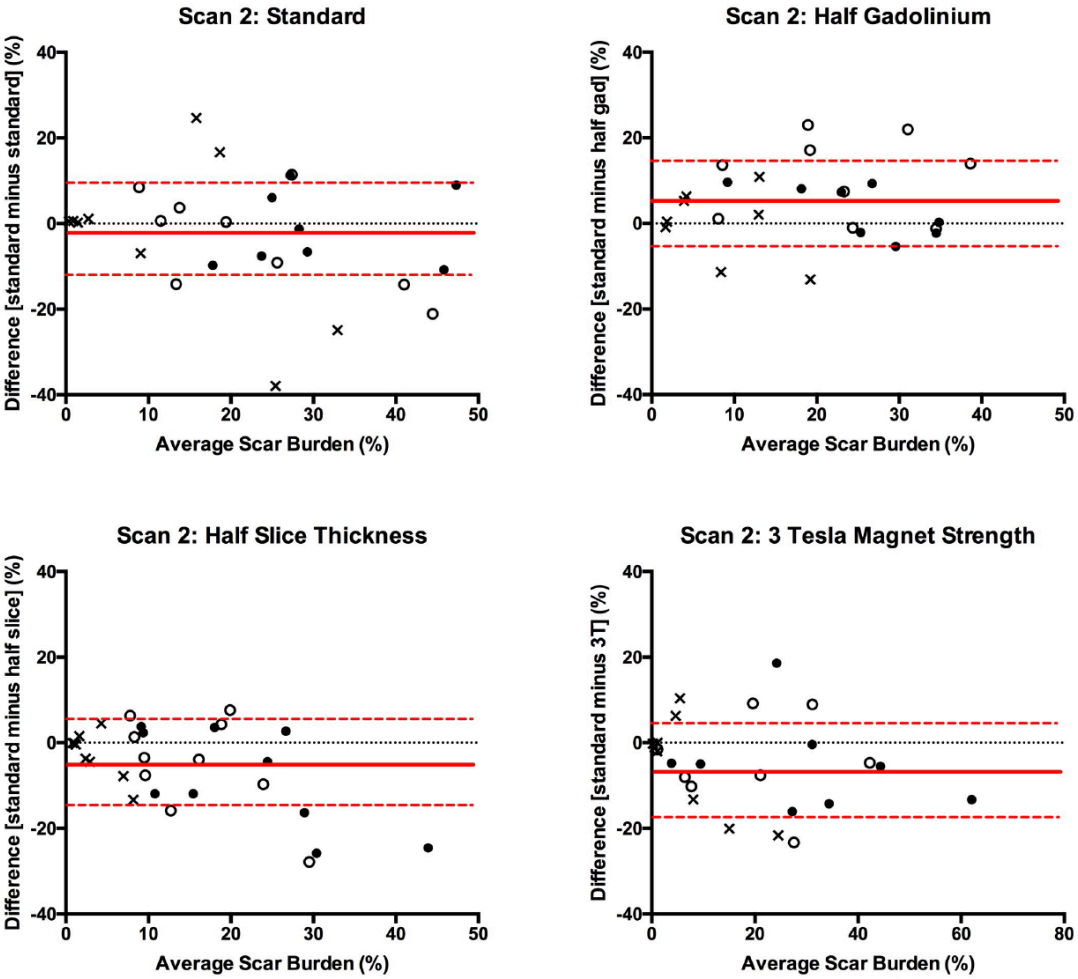

Figure 8-6. Bland Altman plots demonstrating the reproducibility of LA shell scar burden between scan acquisitions.

The top left chart shows the comparison for acquisitions performed with identical imaging paramters. The other three charts show the reproducibility for those performed with differing imaging protocols, as previously detailed. Crosses show data points for comparison of acquisitions at 10min post gadolinium ($C_{1,4}$), open circles for comparison of acquisitions at 20min post gadolinium ($C_{2,5}$), and closed circles for comparison of acquisitions at 30min post gadolinium ($C_{3,6}$).

8.4.2.2 Dice similarity coefficient for co-location of PAAS

The DSCs at the threshold of 3.3SD above BP mean are shown in Table 8-3. There was generally good overlap of scar and healthy tissues respectively, with overall DSC 0.849 ± 0.069 for intra-scan comparisons ($C_{2,3}$ and $C_{5,6}$ pooled analysis), and 0.821 ±0.042 for inter-scan comparisons ($C_{2,5}$ and $C_{3,6}$ pooled analysis).

Acquisition parameters	Intra-scan Dice Similarity Coefficient			Inter-scan Dice Similarity Coefficient		
	$C_{2,3}$	$C_{5,6}$	All	$C_{2,5}$	$C_{3,6}$	All
Standard	0.843 ±0.073	0.863 ±0.047	0.847 ±0.069	0.835 ±0.045	0.807 ±0.038	0.821 ±0.042
Half gadolinium	NA	0.805 ±0.073	0.805 ±0.073	0.801 ±0.064	0.821 ±0.041	0.811 ±0.052
Half slice thickness	NA	0.879 ±0.043	0.879 ±0.043	0.845 ±0.080	0.823 ±0.080	0.834 ±0.080
3T	NA	0.876 ±0.067	0.876 ±0.067	0.822 ±0.086	0.811 ±0.086	0.817 ±0.086
All	0.843 ±0.073	0.855 ±0.061	0.849 ±0.069	0.827 ±0.069	0.816 ±0.062	0.821 ±0.065

Table 8-3. Dice similarity coefficient (DSC) for co-location of post ablation atrial scar and healthy tissue.

Scans thresholded at 3.3 standard deviations above the blood pool mean. $C_{i,j}$ is a comparison between acquisitions i and j: refer to methods for details. All acquisitions on Scan 1 ($Acq_{1,2,3}$) were performed with standard parameters, and therefore $C_{2,3}$ is only expressed for standard parameters.

8.4.2.3 Reproducibility of pulmonary vein encirclement

PVE was significantly lower at 20min than 30min (76.4±21.9% versus 82.3±18.1%, p<0.0001), but despite this there remained a good intra-scan reproducibility ($C_{2,3}$ and $C_{5,6}$ pooled analysis) with ICC 0.784 (95% CI 0.633-0.865). Mean bias (20min minus 30min) was -5.9% (95% confidence interval -29.8% to +18.0%)(Figure 8-7).

For inter-scan comparisons ($C_{2,5}$ and $C_{3,6}$ pooled analysis), the ICC was 0.694 (95% CI 0.567-0.798). There was better reproducibility at later acquisitions: the ICC at 20min alone ($C_{2,5}$) was 0.675 (0.95% CI 0.511-0.792) versus 0.744 (95% CI 0.601-0.842) at 30min alone ($C_{3,6}$) (p=0.02). PVE was significantly higher at each time point when a half dose of GBCA was used (standard: 70.7±26.0% versus half gad: 84.7±15.6%, p<0.001, denoted by closed circles in Figure 8-7). When scan sessions with identical imaging parameters and timing ($C_{2,5}$ and $C_{3,6}$ standard acquisition only) were considered in isolation, there was an excellent degree of reproducibility between scans, with ICC 0.892 (95% CI 0.784-0.947). Mean bias ($C_{2,5}$ and $C_{3,6}$) was +1.2% (95% confidence interval -10.6% to +13.0%, standard deviation of bias 6.0%) (Figure 8-7, bottom right panel).

An analysis of the additional determinants of PVE (scar burden and scan quality) is presented in the Chapter Appendix A (Section 8.8).

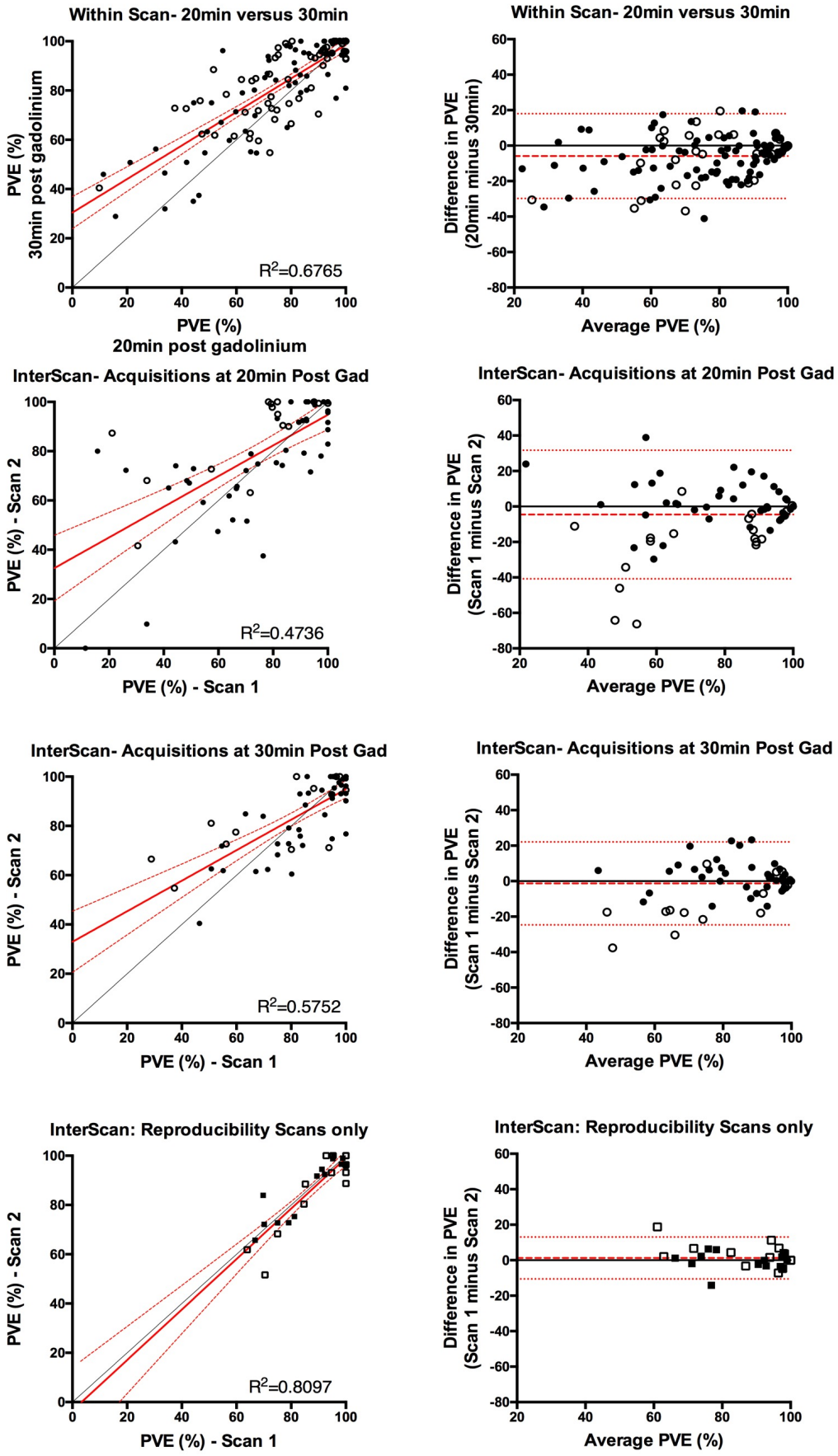

Figure 8-7. Reproducibility of pulmonary vein encirclement (PVE) measurements.

Scatter plots (left column- with black unbroken line showing line of equality, and red line linear regression line ± 95% confidence interval) and Bland-Altman plots (right column- red lines show mean bias ± 95% confidence interval) demonstrating reproducibility of assessment of PVE by CMR LGE. Each point represents PVE score for a single vein pair (left-sided or right-sided). The top row shows intra-scan reproducibility: ($C_{2,3}$ (closed circles) and $C_{5,6}$ (open circles)). Note the higher PVE at 30min versus 20min. Rows two to four show inter-scan reproducibility. Second row shows reproducibility for acquisitions at 20minutes post gadolinium ($C_{2,5}$). Open circles represent comparisons where the second scan was performed with half gadolinium dose. Third row shows reproducibility for acquisitions at 30minutes post gadolinium ($C_{3,6}$). Again, open circles represent comparisons where the second scan was performed with half gadolinium dose. Fourth row shows reproducibility between scans when identical imaging parameters were employed. Open squares denote comparison between acquisitions at 20min only ($C_{2,5}$), and closed squares comparison between acquisitions at 30min ($C_{3.6}$).

8.4.3 Impact of normalisation method upon reproducibility

For all normalisation methods, the pooled intra-scan ICCs for consistency and agreement are shown in Table 8-4. There was high consistency between acquisitions at the same imaging session (intra-scan ICC 0.754-0.804 across all normalisation measures), and fair to good consistency between scan sessions (inter-scan, ICC 0.677-0.721 across all normalisation measures). The highest ICC for consistency intra-scan was with no normalisation, but for inter-scan it was with normalisation by scar intensity (scar IIR).

Absolute agreement between scanning sessions (inter-scan) was much more heavily dependent upon the normalisation method used. Without normalisation, absolute agreement was very poor (ICC 0.243), and remained poor even for the 10 subjects for whom the scans were performed with identical acquisition parameters (reproducibility subjects: ICC 0.568). However, with appropriate normalisation, the inter-scan ICC rose to 0.670 (IQR 0.589-0.720), and to 0.759 (IQR 0.739-0.768) for the subject who underwent identical protocols at Scans 1 and 2. The highest ICC for absolute agreement was consistently with BP z-score normalisation. Both the scar IIR and BP z-score techniques consistently outperformed BP IIR and myocardial z-score techniques (Figure 8-8 and Figure 8-9) across most measures, and BP z-score normalisation significantly outperformed all other normalisation methods for inter-scan absolute agreement.

		Intra-scan ($C_{2,3}$ and $C_{5,6}$)		**Inter-scan ($C_{2,3,5,6}$)**		**Inter-scan (standard parameters only)**	
		Consistency	Absolute Agreement	Consistency	Absolute Agreement	Consistency	Absolute Agreement
Normalisation Technique	Nil	**0.804** (IQR 0.756-0.860)	0.708 (IQR 0.580-0.799)	0.677 (IQR 0.568-0.742)	0.243 (IQR 0.088-0.443)	0.791 (IQR 0.769-0.833)	0.568 (IQR 0.356-0.707)
	BP Z-score	0.796 (IQR 0.729-0.848)	0.750 (IQR 0.667-0.827)	0.713 (IQR 0.659-0.764)	**0.670** (IQR 0.589-0.720)	0.790 (IQR 0.767-0.799)	**0.759** (IQR 0.739-0.768)
	V-Myo Z-score	0.754 (IQR 0.688-0.815)	0.499 (IQR 0.355-0.702)	0.677 (IQR 0.622-0.742)	0.363 (IQR 0.258-0.458)	0.748 (IQR 0.744-0.788)	0.436 (IQR 0.339-0.549)
	BP IIR	0.788 (IQR 0.723-0.837)	0.743 (IQR 0.644-0.805)	0.691 (IQR 0.655-0.722)	0.628 (IQR 0.530-0.677)	0.770 (IQR 0.664-0.799)	0.679 (IQR 0.622-0.744)
	Scar IIR	0.801 (IQR 0.752-0.852)	**0.772** (IQR 0.647-0.813)	**0.721** (IQR 0.682-0.774)	0.618 (IQR 0.491-0.694)	**0.809** (IQR 0.773-0.828)	0.691 (IQR 0.576-0.744)

Table 8-4. Median (with interquartile range (IQR)) intraclass correlation coefficients (ICCs) for point-by-point comparison, using each normalisation technique.

"standard parameters only" are those subjects that underwent identical scan protocol at post ablation scans 1 and 2. Highest ICC in each column is highlighted in bold. IIR: image intensity ratio, BP: blood pool, V-Myo: ventricular myocardium.

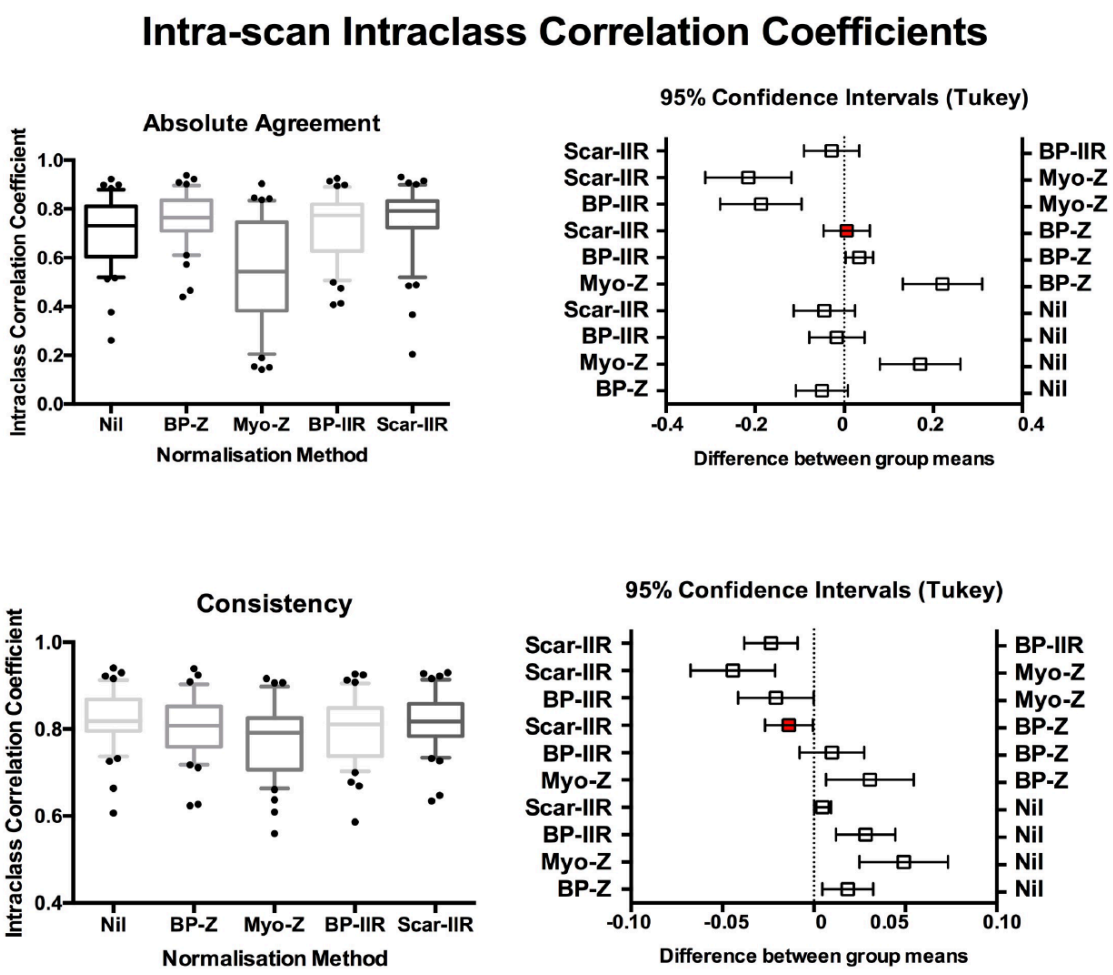

Figure 8-8. Intra-scan Intraclass Correlation Coefficients (ICCs)

An assessment of all paired scans performed under the same standard imaging conditions. Left hand graphs (box and whiskers) show median, with box at interquartile range and whiskers at 10th and 90th percentiles, with each point showing the ICC for a single shell comparison. Right hand graphs show the group by group comparisons for each pair of normalisation techniques, with the symbol (and 95% confidence interval (Tukey)) placed on the side of the equivalence line that favours the normalisation technique. The comparison between the two best-performing normalisation measures (Scar IIR and BP Z-score) is highlighted in red. Upper two graphs show ICC for absolute agreement, lower two graphs for consistency (Scar-IIR: scar image intensity ratio, BP-IIR: blood pool image intensity ratio, Myo-Z: nulled myocardium z-score, BP-Z: blood pool z-score, nil: no normalisation.)

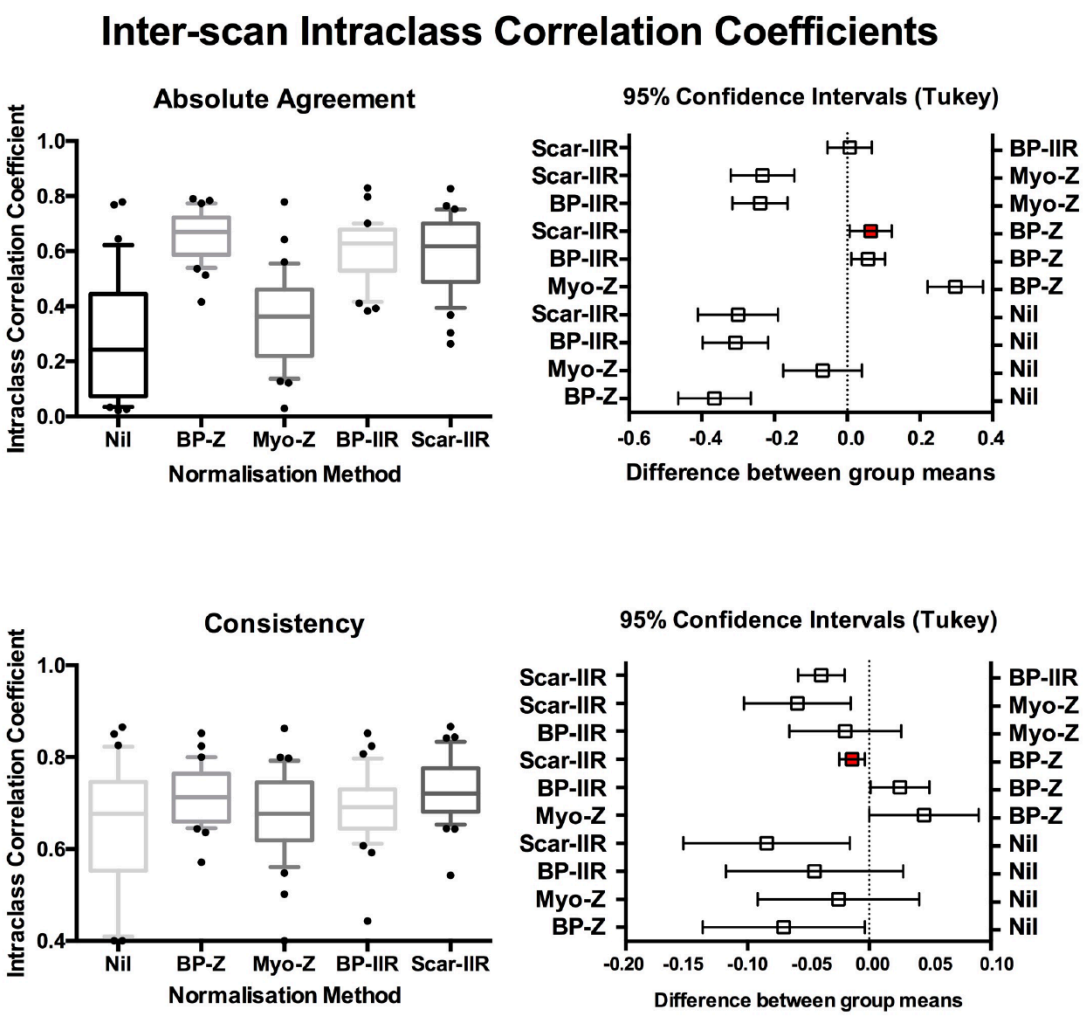

Figure 8-9. Inter-scan Intraclass Correlation Coefficients(ICCs)

An assessment of all four scans performed at two separate imaging sessions. See Figure 8-8 legend for details.

8.4.4 Thresholding of PAAS imaging

8.4.4.1 Normalisation of signal intensities

Across all 228 acquisitions, BP SD was on average 9.4±3.9% of the mean BP SI, and for ventricular myocardium (V-Myo) it was 45.6±18.6% of mean V-Myo SI. Otsu threshold represented a BP z-score of 1.37±2.54, V-Myo z-score of 16.4±14.6, BP IIR of 1.17±0.26 and scar IIR of 0.66±0.13. On exclusion of the 10 minute acquisitions, which often had very poor contrast, the Otsu threshold was at BP z-score of 2.33±1.95, V-Myo z-score of 17.3±16.9, BP IIR of 1.25±0.25 and scar IIR of 0.63±0.08. A comparison of standard threshold values for all acquisitions are shown in Figure 8-10, plotted against a BP z-score threshold of 3.3. There is a significant correlation between all normalisation techniques ($p<0.0001$ for all comparisons), but it is clear that there is a wide variation in the stringency of thresholds employed in published studies. The thresholds of V-Myo at 6 and scar IIR at 0.5 are much lower than the more stringent typical BP z-score threshold (3.3), BP IIR (1.1) and Otsu thresholds.

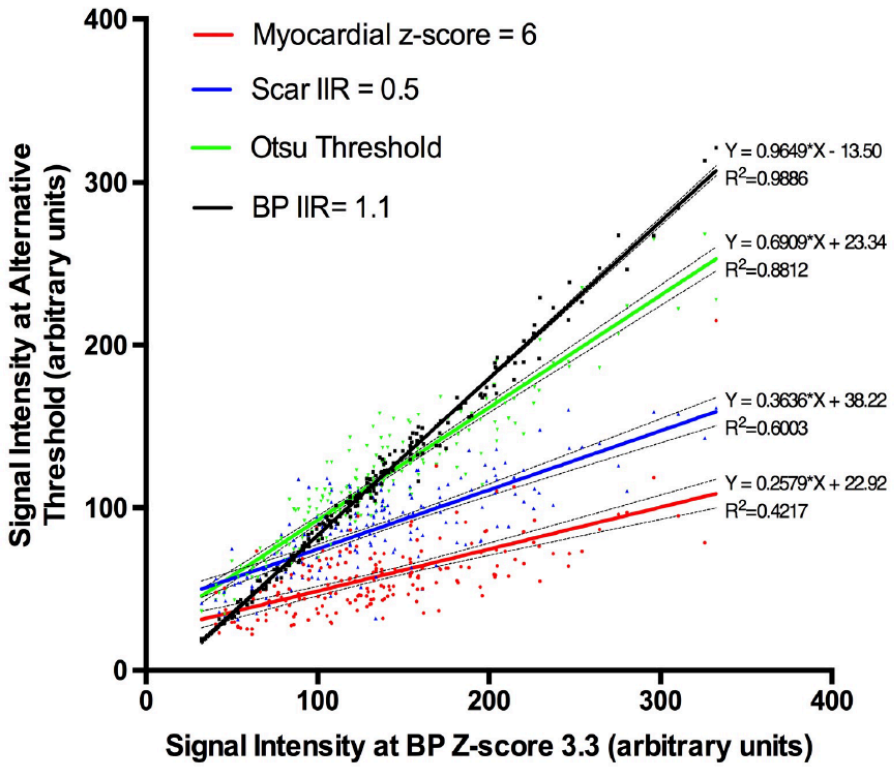

Figure 8-10. Relationship of threshold levels.

Graph demonstrating relationship between the most commonly used thresholding technique (blood pool (BP) z-score, with threshold at 3.3 standard deviations from the BP mean) and and other standard threshold values. IIR: image intensity ratio, V-Myo: ventricular myocardium.

8.4.4.2 Derivation of a gold-standard threshold value

The median expert-derived SI threshold was assessed only for the 20min and 30min acquisitions, as the contrast was generally poor for acquisitions at 10min. A total of 79 acquisitions were assessed. Median threshold was 109 SI units (IQR 92-144), and they are expressed in terms of normalised values in Table 8-5. A BP z-score threshold at 3.3 appears to be over-stringent, whilst all other conventional threshold values are too permissive except for Otsu threshold at 30min ($p<0.0001$ for all comparisons to established thresholds, except Otsu at 30min ($p=0.18$)). In addition, there is a significant change over time for all normalisation methods with the exception of ventricular myocardial z-score.

The objective DSC-derived thresholds demonstrated a similar pattern. Again, acquisitions at 10min were excluded, and a further 35 shells were excluded as derived DSC threshold was at a value below the BP mean. Thresholds were lower than those for expert derived thresholds (median 96 (IQR 75-120), $p<0.001$), but the correlation was strong (R^2 linear regression 0.93). DSC thresholds are expressed in terms of normalised values in Table 8-5. There was no significant difference in values for 20min and 30min scans.

	Conventional Threshold	Expert-derived				Objective DSC-derived			
		Mean Value (All)	Mean Value (20min)	Mean Value (30min)	p-value (20 vs 30 min)	Mean Value (All)	Mean Value (20min)	Mean Value (30min)	p-value (20 vs 30 min)
BP Z-score	3 to 3.6 (James L Harrison et al. 2014; Malcolme-Lawes et al. 2013; Taclas et al. 2010)	2.22 ±1.26	1.96 ±1.31	2.47 ±1.16	<0.001	1.69 ±1.06	1.44 ±0.85	1.92 ±1.18	0.15
V-Myo Z-score	5 (Hunter et al. 2013)	15.3 ± 5.7	15.1 ±4.9	14.8 ±5.2	0.70	12.1 ±4.2	12.1 ±4.8	12.1 ±3.6	0.87
BP IIR	0.97-1.6 (Fukumoto et al. 2015)	1.24 ±0.30	1.21 ±0.24	1.27 ±0.23	0.002	1.18 ±0.11	1.16 ±0.11	1.20 ±0.11	0.22
Scar IIR	0.4-0.6 (Bisbal et al. 2014)	0.676 ±0.131	0.670 ±0.107	0.628 ±0.097	0.001	0.577 ±0.099	0.594 ±0.093	0.564 ±0.104	0.45
Ratio to Otsu Threshold	N/A	1.06 ±0.12	1.05 ±0.10	1.02 ±0.10	0.002	0.938 ±0.103	0.944 ±0.097	0.933 ±0.110	0.20

Table 8-5. Gold-standard threshold levels.

Gold standard expert-derived thresholds and DSC-derived thresholds expressed in units of standard normalisation methods (blood pool (BP) z-score, ventricular myocardium (v-myo) z-score, BP image intensity ratio (IIR) and scar IIR). Ratio to Otsu threshold is also shown (gold standard/Otsu threshold). Units are expressed for all scans, scans performed at 20min after GBCA administration only, and at 30min only. P-value is paired t-test within scan session ($C_{2,3}$ and $C_{5,6}$)

8.4.5 Recurrence of atrial arrhythmia

Total follow-up post ablation was for a median 417 days (IQR 285-628 days), and in total there were 13 patients (33%) with a recurrence of AF or tachycardia, at median 88 days (IQR 57-100days) post ablation. 11 patients elected to undergo a further ablation procedure, with two patients undergoing conservative management (one with a single episode of AF successfully treated with IV flecainide at 566 days post ablation, and the second with a single DC cardioversion at 98 days, just outside of the blanking period, both with no subsequent recurrence).

Overall scar burden was 23.3±14.2% in the no recurrence group, and 28.3±20.2% in the recurrence group (p=0.32). There was also no significant difference in average PVE between groups (no recurrence: 81.7% (IQR 63.2-96.3%), recurrence: 86.1% (IQR 73.2-95.4%), p=0.10). Electrical reconnection of at least one PV pair was confirmed in 10 of the 11 subjects that underwent repeat ablation, and sites of reconnection versus respective PVE are shown in Figure 8-11. There was no significant relationship between PVE and likelihood of electrical isolation of the vein pair: subjects could demonstrate very high or even complete PVE on CMR imaging, but still have electrical reconnection of the vein pair.

Complete PVE (>99%) of both vein pairs was observed in a total of 11 acquisitions (out of total 152 'late' acquisitions performed at 20 or 30min post GBCA administration, 7%). Of these, a recurrence was observed on 3 occasions (27%, chi-square p=0.94). One subject had >99% PVE of both veins on both acquisitions within a single scan session (subject had recurrence of AF), and no subject had >99% PVE on all four 'late' acquisitions. Near-complete PVE (>95%) of both vein pairs was observed on 25 acquisitions (16%, 9 with recurrence), 7 times on both acquisitions within a scan session (2 with recurrence), and once on all four late acquisitions (none with recurrence). Again, there was no significant association with recurrence (p= 0.23, p=0.85, p=0.55, respectively).

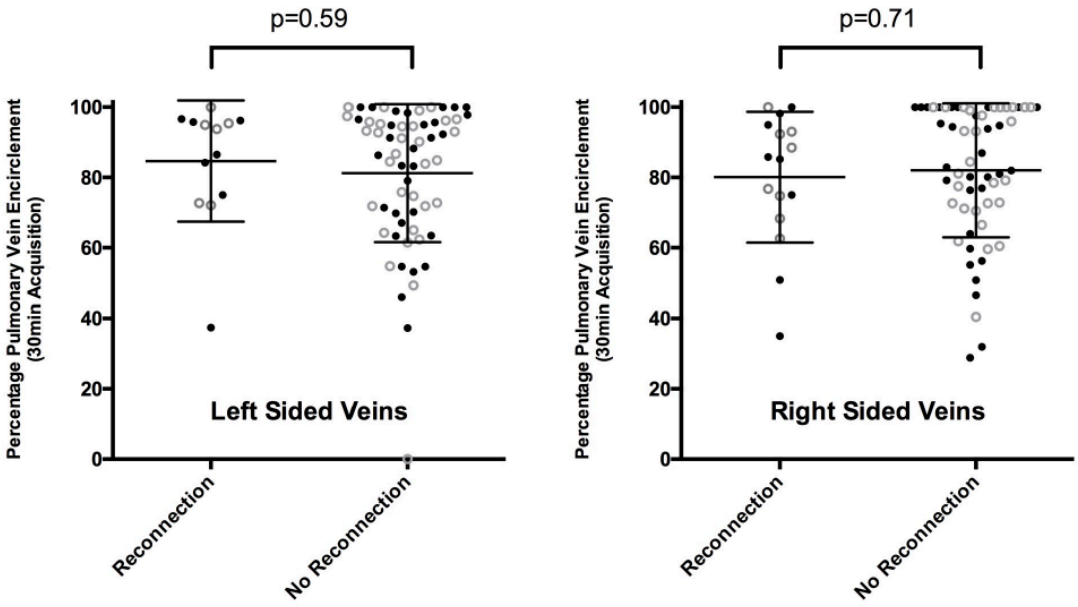

Figure 8-11. Relationship between percentage PVE and electrical reconnection.

Electrical reconnection was assessed at repeat procedure in patients who had a sustained recurrence of arrhythmia (n=11), and analysed as vein pairs (left and right, as indicated on charts). Closed circles indicate PVE at scan 1, open circles PVE at scan 2, and PVE scores are shown only for acquisitions at 20min (Acq_2 and Acq_5) and 30min (Acq_3 and Acq_6) post gadolinium.

8.5 Discussion

The key findings of this study can be summarised as follows:

1. There is good intra-scan reproducibility of thresholded PAAS imaging (between acquisitions at 20min and 30min post-GBCA administration)
2. There is good to excellent inter-scan reproducibility of PAAS imaging when identical imaging parameters are used
3. There is good inter-scan reproducibility of non-thresholded PAAS, provided that the signal intensities are normalised using appropriate methods
4. Normalisation of SIs is best performed using a BP z-score, or a scar IIR
5. The thresholds for identification of PAAS used by established studies vary very widely
6. Threshold for identification of PAAS is likely to lie between 2 and 3 SD from the BP mean, and the Otsu thresholding technique is a reliable and objective alternative
7. There was no significant relationship between PAAS summary indices and AF recurrence

8.5.1 Reproducibility

The reproducibility of the global summary indices of thresholded PAAS (total scar burden, DSC and PVE) was good to excellent for optimal imaging acquisitions. Imaging quality was found to be poorer when the 3D LGE sequence was acquired at less than 20min after GBCA administration, and this was reflected in very low ICCs for comparisons involving acquisitions at 10min post-GBCA administration. For intra-scan comparisons, there was generally good reproducibility for the comparison of acquisitions at 20min and 30min post GBCA administrations (ICC for absolute agreement 0.752 - 0.784), with more scar consistently identified on scans acquired at 30min. For inter-scan comparisons, the ICC was as high as 0.892, with a 95% confidence interval of agreement of 12%, on assessment of PVE with identical imaging parameters. The clinical implications of these small differences in measurements of PAAS remain to be established. However, the measures of reproducibility are of a similar magnitude to those of ventricular scar imaging (Mahrholdt et al. 2002; Vermes et al. 2013), a very widely accepted clinical imaging modality, and are superior to those of myocardial perfusion imaging (Morton et al. 2012).

The use of a single threshold (3.3 standard deviations above the blood pool mean) could have inappropriately strengthened or weakened the measures of reproducibility, depending upon the clinical accuracy of the threshold selected. It was therefore necessary to employ a measure of reproducibility that was independent of thresholding, and the intra-scan and inter-scan variability remained good. The ICC for inter-scan absolute agreement was as high as 0.759 on a point-by-point analysis when only the reproducibility group was assessed. This fell to 0.67 when all scanning parameter groups were assessed, but this still represents moderate to good reproducibility in the context of very different imaging parameters. These ICCs are for absolute agreement, which are

important for comparison between scans, enabling the designation of a fixed threshold. This study suggests that it is valid to compare scans between patients and scanning sessions, even with different acquisition parameters, provided that the imaging is normalised or thresholded appropriately.

The demonstration and quantification of the reproducibility of the imaging technique will facilitate the design and evaluation of further studies. Knowledge of the inter-scan variability assists in the determination of the sample size required to demonstrate a statistically significant alteration in the parameter assessed. In this study, for therapies evaluated with identical scanning protocols, the standard deviation of the measurement error of PVE between scans was only 6%. Furthermore, this study suggests that sample size could also be reduced through ensuring that acquisitions are performed later (>20min) post GBCA administration.

The reproducibility of assessment of indexed LA volume and LA ejection fraction was within acceptable limits. In accordance with a recent study by Kowallick et al, 95% CI of difference in measurement of LA volume was <10ml/m^2, but the difference in LAEF was higher (95% CI 12%), which may reflect the impact of atrial rhythm on image acquisition and processing (Kowallick et al. 2015).

8.5.2 Normalisation methods

In the absence of a gold standard for assessment of PAAS, a reproducibility study serves as a useful surrogate for imaging validation. The close coupling of the two scan sessions (approximately 48hours) makes reasonable the assumption that the true location and extent of PAAS should be virtually unchanged (Badger et al. 2009), and therefore optimal imaging processing techniques should improve the reproducibility of indices of scar delineation.

The referencing or normalisation of arbitrary signal intensity units remains challenging, but it is essential in order to facilitate comparison of scans and thresholding of key features. In this study, it was clear that the use of some normalisation methods was actually worse than processing raw signal intensities alone. The V-Myo z-score performed particularly poorly, and caused a deterioration in intra-scan ICC and inter-scan ICC for the reproducibility group compared to no normalisation. In contrast, the three other normalisation methods significantly improved absolute agreement. This finding is similar to that for normalisation of ventricular LGE scar. Flett et al evaluated seven threshold levels (two normalisation techniques and one manual method), and found that a full width at half maximum (FWHM) threshold, essentially a scar IIR of 0.5, was the most reproducible whilst a V-myo z-score score was consistently worse (Flett et al. 2011).

Overall the BP z-score method was superior in terms of reproducibility for most measures of absolute agreement, although scar IIR was marginally superior for assessment of intra-scan reproducibility. This has important implications for the interpretation of results that have used a ventricular

myocardial z-score for referencing of atrial scar, such as a relatively recent study that found that LGE imaging was not sufficiently accurate to reliably identify ablation lesions (Hunter et al. 2013).

8.5.3 Derivation of thresholds for PAAS identification

An approach to imaging validation via reproducibility optimisation does not assist in the selection of an appropriate threshold, and therefore an alternative approach was required. Manual delineation of scar has been performed for ventricular scar on LGE imaging, but was found to be poor in terms of inter and intraobserver variability (Flett et al. 2011) and therefore was not performed for the more challenging atrial scar delineation. The alternative that was used in this study, a comparison against sites of intended ablation, aimed to minimise visually the enhancement of regions of the atrial shell that had not been ablated at any point during the procedure, whilst maintaining scar coverage in areas that had received RF energy. The CMR shell was compared to an EAM that documented even minimal ablation energy at each location, and was deliberately blinded to contact force and ablation time parameters. The impact of these parameters is explored in detail in Chapter 9: the unquantified effect on scar formation may have caused subconscious bias in the selection of imaging thresholds, and was therefore avoided. The close correlation of the objective DSC-derived threshold and manual threshold (R^2=0.93) largely reflects the similarity in the two processes of optimising fit, one automated and one manual.

Both threshold derivation techniques generated normalised thresholds that differ slightly from those used previously, which is perhaps not surprising. BP z-score threshold of 3.3 appeared overly stringent, risking the mis-assignment of scar regions as healthy, whilst most other established thresholds may be too permissive. In particular, the variation in applied BP IIR thresholds is striking, with a recent study by the Johns Hopkins group using a threshold of 0.97 to delineate LGE, and 1.6 for dense LGE (Fukumoto et al. 2015). Based upon data in this study, a BP IIR of 1.6 would typically represent a BP z-score of >6SD. However, on assessment of ablation induced LGE, they found that sites of LGE had a BP IIR of 1.25±0.25, very similar to the derived threshold in this study (1.24±0.30). Simulations by another group using Bloch equations to model SI of BP and PAAS have been also been performed, suggesting that a BP IIR (which they termed 'enhancement ratio') of 1.4 is sufficient for identification of atrial scar (Peters and Bertelsen 2015).

The wide confidence intervals for thresholds is consistent with previous studies. A histological validation of LGE imaging of PAAS identified a BP z-score of 3.3 to represent a 1:1 ratio of CMR: histological scar volumes (James L Harrison et al. 2014). However, alternative thresholds of +1.5 to +5 SDs were within a single standard deviation of the measured ratio, with the 95% confidence interval spreading correspondingly further. In this context, the confidence intervals for thresholding are comparatively tight. However, it is important to consider the fallacy of thresholding and the false assumption of dichotomisation of scar and healthy myocardium. Scar borderzone, with an altered ratio of connective tissue (collagen, fibroblasts) to healthy myocytes, and partial thickness lesions are both well established to exist post-ablation (Kowalski et al. 2012). The identification of these

borderzones is more important than dense scar in the understanding of arrhythmogenesis in the ventricle (Fernández-Armenta et al. 2013) and a similar principle is likely to apply in the atrium. However, the thin atrial wall (2-4mm typically) greatly limits the identification of partial thickness lesions at current imaging resolutions, and also the differentiation of scar borderzone due to partial voluming effects. Therefore, dichotomisation of atrial scar remains the most approachable option at the current limits of resolution, and it must be accepted that the precise threshold will allocate varying proportions of the borderzone to scar or healthy myocardium populations.

Otsu thresholding was also explored as it has previously been advocated for the delineation of ventricular LGE scar (Vermes et al. 2013). In this study it was found to correlate closely with BP z-score, the optimal normalisation method, and is relatively reliable in terms of consistency versus derived thresholds. The simplicity of the computation and its objectivity is attractive, and it warrants further assessment of its use in routine practice.

8.5.4 Association of PAAS imaging and outcome

The absence of a significant relationship in this study between detection of gaps in the CMR-derived ablation line and recurrence questions the immediate relevance of PAAS imaging. This finding is in keeping with some recent studies (J L Harrison, Sohns, et al. 2015; Spragg et al. 2012), but at odds with others which have demonstrated a relationship (Bisbal et al. 2014; Taclas et al. 2010). In one of the first and largest studies of PAAS, Badger et al found that only 10 out of 144 (7%) of patients had complete PVE of all PVs, but that there were no recurrences in this group. The metrics used to assess gaps in this study are arguably more rigorous, but the overall proportion without a gap in both vein pairs' encirclement is similar (7% of acquisitions had >99% PVE of both veins), and was not associated with recurrence.

However, the interplay of interruption of the continuity of the PVI lesion set and AF recurrence is a complex one: many gaps will not necessarily lead to recurrence of arrhythmia, whilst very small gaps may be sufficient for electrical reconnection. In a recent meta-analysis of the relationship of PV reconnection and AF recurrence, Nery et al reviewed 11 studies totalling 683 subjects (Nery et al. 2016). Amongst those with AF recurrence, only 86% had at least one PV reconnected. Conversely, overall 59% of patients who were free of AF had at least one PV reconnection, and Jiang et al (Jiang et al. 2014) demonstrated that there was a 90% rate of reconnection at 12months in the absence of recurrence. This is corroborated by a recent remarkable randomised controlled study published by Kuck et al (Kuck, Hoffmann, et al. 2016) which directly investigated the impact of a small deliberate gap in the PVI lesion set. The AF recurrence rate at 3 months in the cohort with a gap was slightly higher (79% versus 62%, $p<0.001$), but conduction gaps were still found in 70% of the complete PVI group at invasive reassessment at 3 months.

The results of this study suggest that detection of PAAS is a reproducible finding, but the clinical implications for guidance of repeat procedures are unclear and warrants further investigation.

8.5.5 Limitations

The limitations discussed in Chapter 7 remain relevant. However, there are additional limitations that should also be reviewed on the assessment of reproducibility. The first is the method of image interrogation, and whether the technique introduces bias towards improved reproducibility. The technique involved a rigid image registration step, in order to maintain morphologically identical LA shells which were important for subsequent assessments. The endocardial mask (GMRA acquisition) was generally registered to the subsequent LGE acquisitions, with a translation of mean magnitude 1.9±1.6mm, and rotation 0.62±0.41° (see 4.2.2). For the majority of the subjects this was performed blinded to scar, using the GMRA sequence only. However, in five subjects the registration was of a 10min acquisition to subsequent LGE acquisitions. The re-registration goodness of fit is evaluated across all high contrast features within the dataset, including bone and soft tissue, and therefore the effect of LA scar (approx 6ml within 6,000ml dataset, <0.1%) was felt to be negligible, particularly given the poor PAAS enhancement on the 10min acquisitions.

The summary indices of PAAS were all developed specifically for this study and further validation of their robustness is warranted. In particular, the implementation of semi-automated steps in image interrogation has meant that inter- and intra-observer variability has not been explored in this study. Further evaluation of the variation in summary indices warrants the re-segmentation of the LA endocardium, with subsequent image processing steps repeated.

8.6 Conclusions

CMR imaging of PAAS is a reproducible finding, particularly when the 3D LGE dataset is acquired at least 30min after the administration of GBCA. Intra-scan and inter-scan reproducibility is good to excellent. Normalisation of signal intensities is required in order to facilitate the use of a consistent threshold, and in most cases is best referenced to the blood pool signal as a z-score including SD of blood pool signal. The threshold for PAAS lies between 2 and 3SD from the blood pool mean, and the use of an objective Otsu threshold should be considered.

8.7 Acknowledgements and Contributions

This study has only been possible with the contributions of a number of colleagues and collaborators, some of which have already been outlined in Chapter 7.

The image interrogation technique is discussed in detail in the Methods section, and was developed in collaboration with primarily Dr Rashed Karim and Dr Orod Razeghi. Segmentation and registration of every shell was performed by myself, as was assessment of LA volumes and function. The three indices of PAAS for reproducibility assessment were developed separately. The total scar burden and dice similarity coefficient measures were conceived by myself and coded by Dr Rashed Karim. The PVE measure was originally conceived by myself and proposed to Catalina Tobon-Gomez. Following

her departure to work in industry, the project was taken forward by Marta Núñez and Constantine Butakoff at Universitat Pompeu Fabra, Barcelona, Spain. They have developed multiple iterations of the image processing platform, and I have helped to guide the development from a clinical perspective. All PAAS indices were provided by collaborators as raw values for each shell, and I performed all subsequent analyses.

The use of ICCs to compare signal normalisation measures was performed in collaboration with Dr Sebastien Roujol. I sourced and tested the Matlab code to derive ICCs, and Dr Roujol wrote the Matlab script to integrate this code in order to interrogate all shell comparisons following normalisation of SI values on each shell.

For manual thresholding, I used the EAM shells that were extracted and processed in collaboration with Kulvinder Lal and Dr Steven Williams (see Chapter 9). Manual selection of thresholds was performed by myself, and the code for the DSC generation was developed in collaboration with Dr Rashed Karim. Again, raw values were generated for each comparison and subsequently analysed by myself. I proposed the Otsu thresholding of the LA shells to Dr Rashed Karim, and he also wrote that code, generating a single value for each shell.

Arrhythmia recurrence data was collected with the assistance of Dr Rahul Mukherjee: we jointly shared the task of full and detailed follow-up of every patient, and I verified every outcome.

All statistical calculations, with the exception of the ICC calculation above, were performed by myself.

8.8 Chapter Appendix A- Pulmonary Vein Encirclement

Figure 8-12 shows the relationship between total scar burden, scan quality and PVE. It is clear that there is a significant relationship between PVE and scar burden (R^2 for both vein pairs 0.632 (linear regression) and 0.818 (one phase decay regression)), but that scar burden is not the only determinant of PVE. Likewise, there is a significant relationship between PVE and overall scan quality (R^2 for both vein pairs 0.302), but a high degree of PVE can still be detected on relatively poor quality scans (see Section 7.3.4.1. for details of derivation of Likert score)

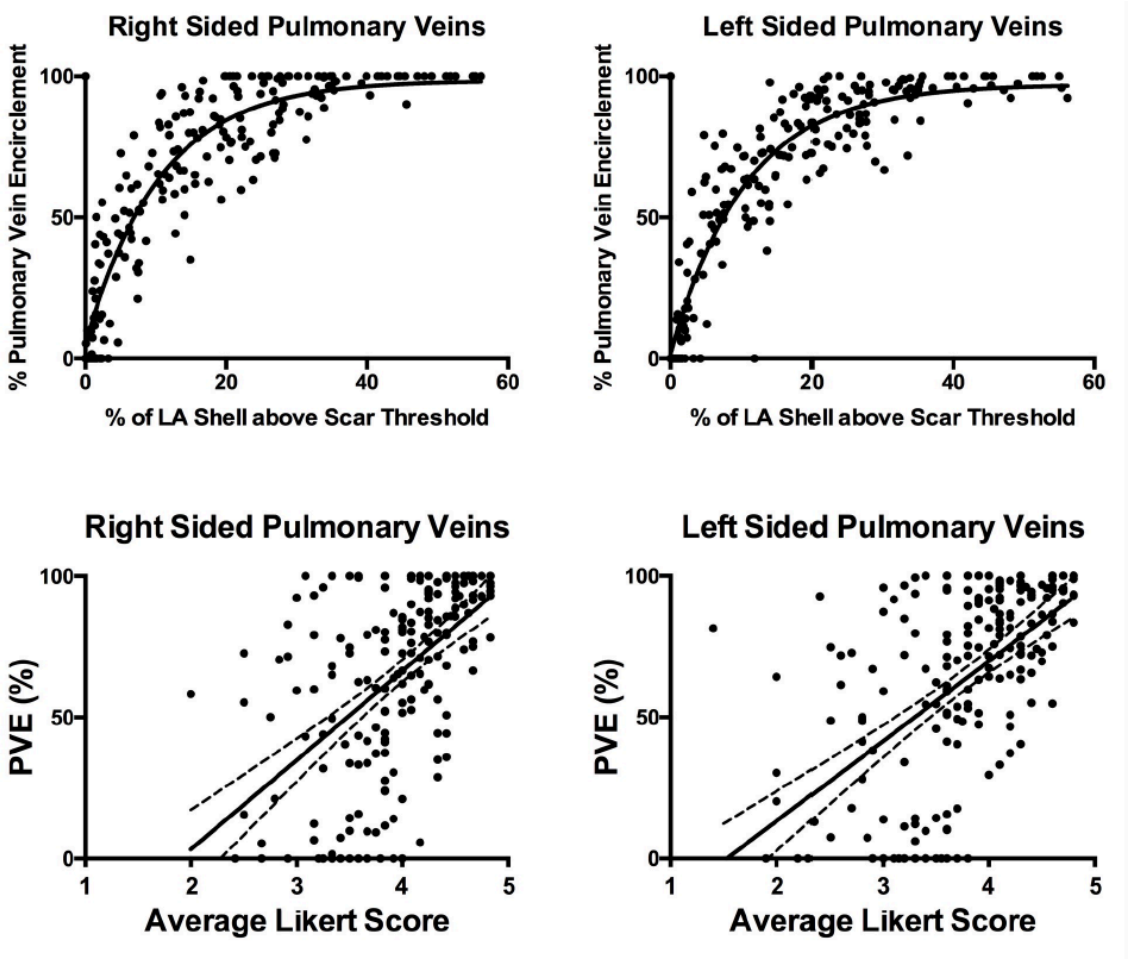

Figure 8-12. The dependence of pulmonary vein encirclement (PVE) upon scan parameters.

(Top row) Percentage PVE against the proportion of the whole LA scar that is above the threshold of 3.3 standard deviations above the blood pool mean. Note the increase in PVE with increase in total scar burden, but that in some cases complete PVE may be observed in the presence of low (<20%) total scar burden, whilst in others a much larger proportion of the shell may be ascribed to scar status without complete PVE. (Bottom row) Percentage PVE against scan quality, expressed in terms of overall average Likert Score across all four criteria (see Chapter 7). Again, there is a general increase in % PVE with improved scan quality, but a wide range of degree of PVE is observed with both high and low quality scans.

9 Imaging Post Ablation: Predictive Value of Objective Markers of Radiofrequency Ablation Efficacy for Chronic Atrial Lesion Formation on Late Gadolinium Enhanced CMR Imaging

9.1 Aims

To determine the VisiTag thresholds that best correlate with chronic atrial ablation lesion formation, as assessed by LGE CMR.

9.2 Introduction

Catheter-myocardial contact is a key determinant of ablation lesion formation, with many studies demonstrating the importance of contact force (CF) technology in the determination of ablation lesion quality and size (Haldar et al. 2013; Kuck et al. 2012; Neuzil et al. 2013; Yokoyama et al. 2008; Shurrab et al. 2015) . Real-time CF measurement and display using CF-sensing catheters provides immediate feedback to the operator, improving catheter positioning (Okumura et al. 2008) and estimation of radiofrequency (RF) energy delivery (Neuzil et al. 2013).

However, it has been recognised from the outset of clinical implementation of CF technology that absolute CF is only one of several factors contributing to RF lesion formation (F. H. M. Wittkampf and Nakagawa 2006). In tandem with electroanatomical mapping (EAM) systems, multiple parameters can be assessed simultaneously, including ablation time, catheter stability, impedance drop, and catheter tip temperature. Simple summative indices such as force time integral (FTI) have been shown to be associated with lesion formation (Sohns et al. 2013), but there has been a drive towards more objective and inclusive markers of predicted tissue injury. VisiTag (Biosense Webster, Diamond Bar, CA, USA) is a software module within the CARTO EAM system that was introduced in 2014 to permit quantification and display of RF-induced injury. It enables operators to specify the values of a specific selection of parameters (including minimum CF, time at location, stability indices, impedance drop and temperature) that must be met in order for a VisiTag marker to be placed at the ablation location. As such, it is an objective binary marker of ablation that is highly dependent upon the thresholds selected by the operator.

Ex-vivo (F. H. Wittkampf, Hauer, and Robles de Medina 1989) and pre-clinical work (Williams et al. 2015) has contributed to informed selection of VisiTag thresholds, but there remains a wide variation between clinical operators (Fujiwara et al. 2016; Lin et al. 2013; Okumura et al. 2016). Human atria, particularly in those with severe atrial remodelling, are likely to respond to RF energy in a manner that differs from standard animal models. However, histological assessment is clearly not feasible. CMR imaging is the most promising and reliable modality for non-invasive ablation lesion assessment, using LGE as a marker of extracellular space, and therefore fibrosis secondary to tissue injury. Animal and human studies have demonstrated a strong correlation between ablation lesions and LGE signal intensity, as assessed histologically (James L Harrison et al. 2014; Williams et al. 2015) and by voltage mapping (Badger et al. 2010; Bisbal et al. 2014; Malcolme-Lawes et al. 2013).

9.3 Methods

9.3.1 Study population

Between March 2014 and September 2015, patients with pre-procedural baseline CMR scan undergoing first-time ablation procedure for AF were approached to join the study. Inclusion criteria included ablation performed using SmartTouch ablation catheter (Biosense Webster) and that VisiTag module was activated for the entire ablation procedure. Exclusion criteria included contraindication to further CMR imaging or prior allergic reaction to contrast agent. 24 patients in total were recruited. Subjects provided written and informed consent and returned for CMR scan assessment of atrial scar at 3months. Baseline demographics were documented at the initial scan, including age, weight, height, body mass index (BMI), ischaemic heart disease, diabetes mellitus, duration of AF, type of AF, and rhythm at scan. Comorbidities were recorded.

The study was performed at St Thomas' Hospital, London, UK and was approved by the UK Health Research Authority (NRES Committee for South London, reference 08/H0802/68).

9.3.2 Ablation procedure

The details of the ablation procedure are documented in Chapter 4.4

9.3.3 CMR imaging acquisition and image interrogation

The details of the 3D LGE acquisition are documented in Chapter 4.1.1. Only the acquisition performed at 30minutes post-GBCA, under standard acquisition parameters, was analysed for each patient. Image interrogation was performed as documented in Chapter 4.2, and shells were exported with CMR LGE signal intensity assigned at each triangular face. Binarisation to scar and no scar was required for some assessments, and in these cases the threshold was assigned at 3.3 standard deviations (SD) above the blood pool (BP) mean (James L Harrison et al. 2014).

9.3.4 VisiTag parameter survey

A questionnaire regarding prevailing practice in the use of contact force settings was sent in September 2015 to all UK centres performing AF ablation. The full set of questions with potential responses is shown in Table 9-1, and was circulated via SurveyMonkey (Palo Alto, CA, USA). The responses were used to determine median ranges for the default VisiTag parameter settings (see below).

1. How many AF ablations does your institution perform each year?									
<50	*51-150*	*151-250*	*251-350*	*351-500*	*501-700*	*701-1000*	*>1000*		
2. At your Institution, how often do you:									
A. Use CARTO for AF ablation procedures									
B. Use a contact force sensing catheter when using CARTO for AF ablations ?									
C. Activate the VisiTag module when using CARTO with a force sensing catheter									
Never (<1% of ablations)	*Rarely (1-20% of ablations)*	*Sometimes (20-50% of ablations)*		*Often (50-80% of ablations)*		*Almost always (80-99% of ablations)*		*Always (>99% of ablations)*	
3. Catheter Position stability: 'Minimum Time' What setting do you usually use for 'Minimum Time' at your institution?									
*Nil**	*5-9sec*	*10-14sec*	*15-19sec*	*20-24sec*	*25-29sec*	*30-34sec*	*>34sec*	*Varies§*	
4. Catheter Position Stability: 'Max Range'. What setting do you usually use for 'Max Range' at your institution?									
*Nil**	*<2mm*	*2mm*	*3mm*	*4mm*	*5mm*	*6mm*	*7mm*	*>7mm*	*Varies§*
5. Force over Time: 'Time Percentage' What setting do you usually use for 'Time Percentage' at your institution?									
*Nil**	*<40%*	*40-49%*	*50-59%*	*60-69%*	*70-79%*	*80-89%*	*>89%*	*Varies§*	
6. Force over Time: 'Minimum Force' What setting do you usually use for 'Minimum Force' at your institution?									
*Nil**	*<4g*	*5-8g*	*9-12g*	*13-16g*	*17-20g*	*21-24g*	*>24g*	*Varies§*	
7. Impedance Drop What setting do you usually use for 'Impedance Drop' at your institution?									
*Nil**	*<4ohms*	*5-8ohms*	*9-12ohms*	*13-16ohms*	*17-20ohms*	*>20ohms*	*Varies§*		
8. Target Temperature What setting do you usually use for 'Target Temp' at your institution?									
*Nil**	*<38 ˚C*	*39-40 ˚C*	*41-42 ˚C*	*43-44 ˚C*	*45-46 ˚C*	*>46 ˚C*	*Varies§*		
9. Please rank the following factors in the order that you feel are most important in determining the formation of an effective ablation lesion (1= most important, 6= least important)									
Catheter position stability: time		*Catheter position stability: range*		*Force over time: time percentage*		*Force over time: minimum force*		*Impedance drop*	*Target Temperature*

Table 9-1. Contact force parameter settings survey.

Questions in bold, with permitted responses in italics below. Nil: option in full read "Filter not activated routinely". Varies§: option in full read "Varies widely between operators.*

9.3.5 VisiTag data export

CARTO3 (Biosense Webster) has a comprehensive 'Export Data' tool, enabling operators to review and analyse retrospectively most elements of an interventional procedure. The reconstruction of the ablation procedure off-line is well established, and the data export includes all information required to reconstruct the mesh of the cardiac chamber, all catheter movements, intracardiac and surface electrograms, and ablation information recorded during RF sessions (including power, impedance and temperature). Where the SmartTouch™ module has been activated, all contact force information is also recorded at a sampling rate of 20Hz. The data is referenced to manual ablation location annotations (9.5sec prior and 0.5sec after), and includes the force in grams and the axial and lateral contact angles. This ablation data may be supplemented and cross-referenced with an additional export file which contains contact force and angles for all timepoints when RF is activated (again, at 20Hz sampling rate), increasing reliability distant from manual ablation markers. With the implementation of the VisiTag module, further ablation details are recorded broken down into the 'Grid' points, containing a millimetre by millimetre breakdown of time, temperature, power and force achieved at each location in 3D space.

In theory, the information contained within these files may be used to reconstruct the timeline and ablation parameters for the ablation procedure, and a VisiTag surrogate can be estimated. However, the algorithms used to determine the placement of the objective VisiTag marker are not published, and therefore any surrogate is prone to error. For example, "Stability Maximum Range" (hereafter called "Range"- see Figure 9-1) is defined as the maximum distance that the calculated catheter tip position may move before ablation parameters are allocated to a different location. However, the mechanism by which the central locations of adjacent lesions are identified is not clear, and is related to a moving average of the cluster of ablation points. Likewise, "Force over Time-Time (%)" (hereafter called "Percentage Time") reflects a rolling average of the amount of time that the CF has been greater than the minimum stipulated force, but the start and finish of the analysis window has not been stipulated. "Force over Time- Minimum Force" (hereafter called "Force"), "Stability Minimum Time" (hereafter called "Time"), "Impedance Drop" and "Target Temperature" are clearer, but again there are ambiguities that preclude the creation of an exact replica of VisiTag markers.

Therefore, in order to assess the predictive value of VisiTag markers, the data was exported with VisiTag status ascribed directly by the CARTO3 system. The default settings were selected based upon the median values of the UK survey (force 8g, time 10seconds, range 3mm, percentage time 50%, impedance drop filter 'off', target temperature filter 'off'). Each parameter was then adjusted maintaining all other parameters constant at default values, and a new export dataset created. The number of settings exported for each parameter were weighted according to the subjective impression of relative importance of the parameter in the survey:

- 'Force' (g)- ten setting levels- 2, 4, 6, (8-default), 10, 12, 14, 16, 18, 20

- 'Time' (seconds)- six setting levels- 5, (10-default), 15, 20, 25, 30
- 'Percentage time' (%)- six setting levels- 30, 40, (50- default), 60, 70, 80
- 'Range' (mm)- six setting levels- 2,(3-default), 4, 5, 6, 7
- 'Impedance drop' – two setting levels – on (10 Ω), (off- default)
- 'Target temperature'- two setting levels – on (42°C), (off- default)

In total, 27 export datasets were created for each subject. Examples of VisiTag density across all parameter thresholds, for a single subject (39F) is shown in Chapter Appendix A.

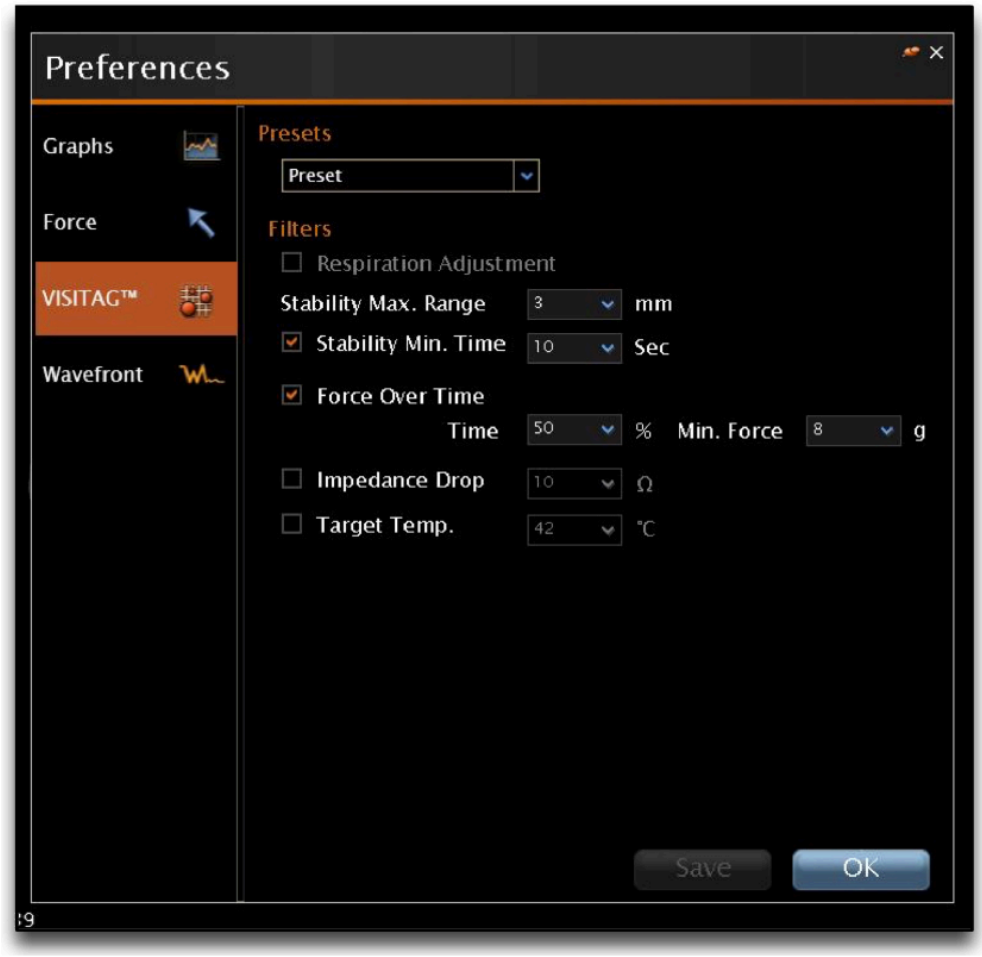

Figure 9-1. VisiTag preference window, with default settings applied

9.3.6 Comparison of ablation and CMR shells

The CARTO3 export datasets were processed using custom written Matlab software (MathWorks, MA, USA), and the scripts are documented in Chapter Appendix B. I was responsible for the design and logic of the programming, and a colleague familiar with the syntax of Matlab (Steven Williams) implemented the design. For each subject, the mesh was extracted, remeshed (see below) and the 27 sets of VisiTag locations extracted. A 7.5mm search radius was defined for each triangle of the remeshed shell, and the surface triangles were binarised to those associated with a VisiTag marker, and those that were not . The 7.5mm search radius was defined based upon anticipated maximum

lesion radius width of 4.5mm at 30W (Thiagalingam et al. 2010), with the addition of a default "Range" threshold of 3mm. The surface mesh was created with 27 layers, each containing the binary data for a defined VisiTag setting in an identical anatomical orientation.

9.3.7 Lesion continuity assessment

The presence of continuous CMR LGE scar was assessed at each of 18 regions for each patient shell (Figure 9-2), thresholded at 3.3 SD above the BP mean. Continuous VisiTag marker presence was assessed for the same regions at each of the 27 parameter setting groups. Lesion continuity on CMR LGE and VisiTag markers was assessed in Paraview (Kitware, New York, NY, USA), and the ablation line was considered continuous in the absence of any gap >1mm. Distances were measured as a straight line between closest points of lesion apposition, using the 'Ruler' source tool.

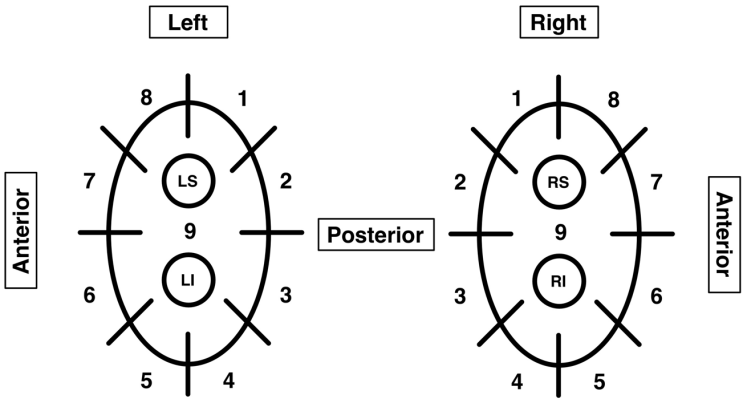

Figure 9-2. Regions for assessment of CMR LGE scar and VisiTag presence.

LS: left superior PV, LI: left inferior, RS: right superior, RI: right inferior.

9.3.8 Point-by-point assessment

9.3.8.1 Re-meshing of left atrium

The core model for the surface mesh was created from the CARTO mesh dataset. However, these surface meshes lack ideal characteristics for further analysis: they are anisotropic, with a widely varying inter-vertex distance, and there are frequent misshapen regions on closer examination, such as 'kites'. Any analysis based on a triangle-by-triangle technique is prone to systematic inaccuracies, especially in regions of extreme curvature. The surfaces were therefore remeshed to create a smooth, isotropic, surface domain for analysis. vmtk (Orobix, Bergamo, Italy) was used to remove surface kites and Meshlab (ISTI, Pisa, Italy) to preform Poisson smoothing and mesh regularisation with a uniform edge length of 0.4mm (Figure 9-3).

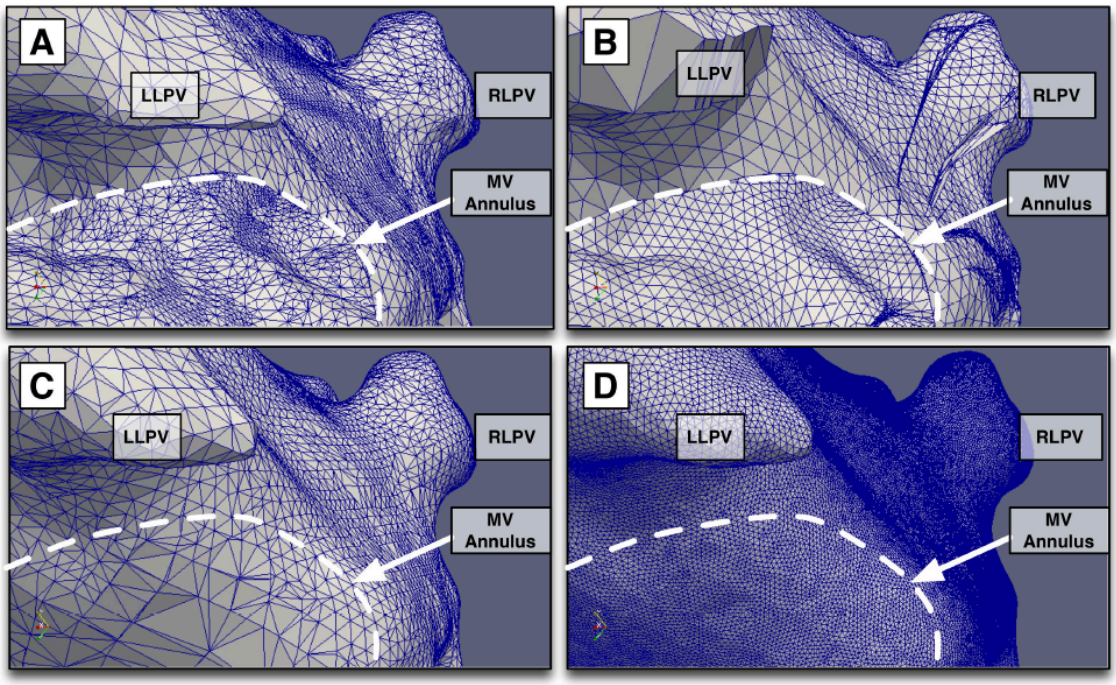

Figure 9-3. Left atrial re-meshing technique.

The original CARTO mesh export dataset is a surface with a wide variation in surface triangulation size (A), with size largely determined by local curvature. Initial attempts at simple remeshing caused significant artefacts (B), secondary to small shell imperfections (not shown). The surfaces were therefore Poisson smoothed (C) and remeshed at high resolution (D).

9.3.8.2 Fusion of CMR data to CARTO3 shell

Fusion of CMR shell to CARTO3 shell was performed using an iterative closest point (ICP) technique. Anatomical landmarks were ascribed to both the CMR imaging shell and CARTO mesh, and the two shells fused, blinded to VisiTag thresholds. CMR data was placed on the high resolution CARTO3 mesh. Mis-registration resulted in a varying degree of matching of scar to ablation location, despite excellent visual correlation of ablation scar (Figure 9-4). A strong qualitative relationship between ablation and atrial scar was apparent, but in some locations a direct point-by-point assessment led to a falsely poor correlation. All registrations were therefore performed twice, and Sorensen dice similarity coefficient (DSC) used to analyse co-location of thresholded CMR LGE scar and VisiTag status (at "default" threshold settings)(Crum, Camara, and Hill 2006).

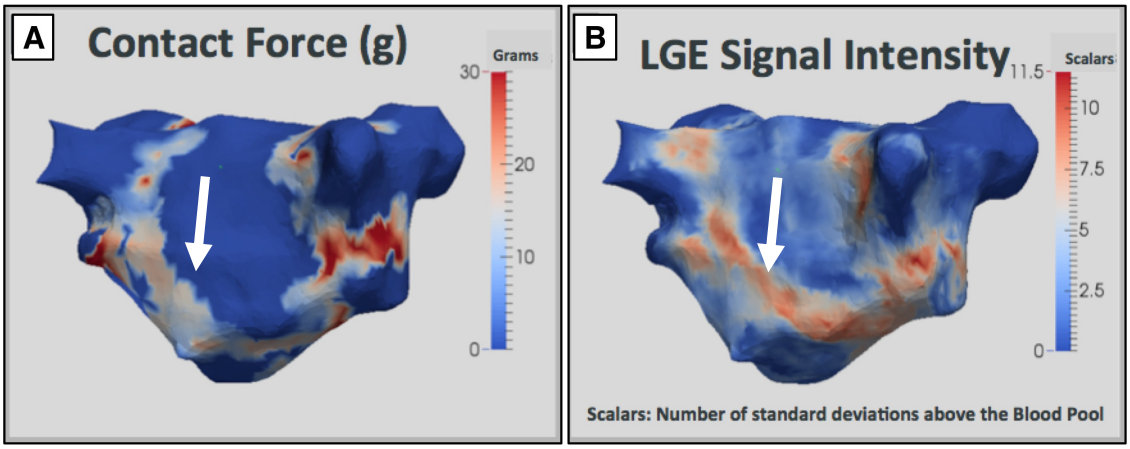

Figure 9-4 Illustration of the subtle mismatch of EAM and CMR LA shells.

(A) 3D rendering derived from CARTO3 shell demonstrating contact force. (B) Maximum intensity projection of CMR LGE signal, fused to the CARTO3 shell. Note the strong qualitative correlation of contact force and signal intensity, but the relatively poor point-by-point correspondence in some locations (white arrow)

9.3.8.3 Data analysis

For every surface triangle on the CMR and ablation meshes, there were 27 VisiTag values (binary data) and one CMR LGE scar value (signal intensity), with typically 200,000 to 400,000 triangular surfaces per shell. This resolution is far in excess of the source data (1.3x1.3x2mm for CMR scar and 7.5mm search radius for ablation shell), and the uniform triangle size across subjects inferred that a greater proportion of the data points arose from the subjects with the largest LA surface area. Therefore, the surface was resampled at 5000 points per patient, corresponding to an inter-vertex distance of approximately 3mm and weighting the data equally for each patient.

9.3.9 Electrical reconnection of pulmonary veins

Both VisiTag-derived and CMR-derived lesion continuity were assessed against the site of electrical reconnection, which was assessed as detailed in Section 8.3.7.

9.3.10 Statistical methods

Normally distributed continuous variables are presented as mean ± standard deviation, and median with interquartile range (IQR) for non-normal distribution or non-continuous ordinal data. Statistics were analysed using SPSS Statistics (Version 22, Armonk, NY). For assessment of VisiTag accuracy for scar prediction, the locations of CMR-derived chronic scar were taken as the indication of effective lesion formation. Sensitivity and specificity of VisiTag prediction of lesion formation were assessed on a regional or point-by-point basis, using standard methods (outlined in Table 9-2). Within-patient differences for binary thresholding (impedance on/off, temp on/off) were compared using Wilcoxon

matched-pairs signed rank test, and the non-parametric Friedman test was used for multi-setting parameters (force, time, range, percentage time).

	Condition Positive (CMR-Scar Positive)	**Condition Negative** (CMR-Scar Negative)	
Predicted Condition Positive (VisiTag Positive)	True Positive (TP)	False Positive (FP)	**Positive Predictive Value** *(nTP)/(nVisiTag +ve)*
Predicted condition Negative (VisiTag Negative)	False Negative (FN)	True Negative (TN)	**Negative Predictive Value** *(nTN)/(nVisiTag –ve)*
	Sensitivity *(nTP)/(nCMRscar +ve)*	**Specificity** *(nTN)/(nCMRscar -ve)*	**Accuracy** *(nTP+nTN)/(nAll Points)*

Table 9-2. Methods for determination of key indices of VisiTag performance.

n(group) indicates the number of points within each subgroup.

9.4 Results

9.4.1 Subjects

24 subjects were included in the study, and demographics are summarised in Table 9-3. On assessment of DSC, 6 shell pairs (VisiTag and CMR scar) had a DSC<0.3, with significant scar mis-registration confirmed on visual assessment. These 6 subjects were excluded from point-by-point analysis, and a breakdown of the characteristics of the two subgroups is also detailed in Table 9-3. Of note, the LA volume on pre-ablation assessment was significantly smaller for patients with poor DSC (99±15ml versus 141±44ml, p=0.002), and the 3D LGE acquisition contrast-to-noise ratio (scar: blood pool) was significantly poorer (26±12 versus 44±24, p=0.04).

	All Subjects (n=24)	Good Dice Coefficient (n=18)	Poor Dice Coefficient (n=6)	p-value
Male	18 (75%)	15 (83%)	3 (50%)	0.10
Paroxysmal AF	11 (61%)	8 (44%)	3 (50%)	0.81
CHA_2DS_2VASC Score	1 (IQR 0-2)	1 (IQR 0-2)	2 (IQR 1-3)	0.11
AF duration (years)	3.0 (IQR 1.75-5.5)	2.0 (IQR 1.5-5.0)	4.0 (IQR 2.2-5.7)	0.99
Significant Comorbidities	14 (58%)	10 (56%)	4 (67%)	0.63
Age (years)	62 ±11	61±12	65±10	0.40
Weight (kg)	88 ±20	89±20	84±23	0.50
Height (cm)	175 ±8	176±7	171±8	0.20
BMI (kg/m^2)	28.9±6.7	28.9±6.7	28.7±7.3	0.94
Heart Rate at scan	76±26	76±29	75±14	0.84
Sinus rhythm at scan	19 (79%)	14 (78%)	5 (83%)	0.77
Max LA volume pre-ablation (ml)	130±42	141±44	99±15	**0.002**
Max LA volume at post-ablation scan (ml)	124±40	129±45	108±14	0.11
Change in LA Volume (ml)	-1±46	-11±28	+9±13	**0.03**
LA sphericity pre-ablation	82.9±3.6	82.8±3.7	83.1±3.7	0.89
LA fibrosis pre-ablation (%)	37.4±12.8	37.3±11.1	37.8±18.2	0.95
Scan quality (Likert scale, %)	85±7	87±4	79±9	0.09
CMR Scan CNR	39±23	44±24	26±12	**0.04**
Dice Similarity Coefficient (Point-by-Point)	0.38±0.11	0.44±0.06	0.21±0.05	**<0.001**
Dice Similarity Coefficient (Regional)	0.87±0.08	0.88±0.08	0.85±0.07	0.55

Table 9-3. Summary of baseline demographics and scan characteristics.

DSC is the Dice Similarity Coefficient, assessing co-location of CMR-derived scar and VisiTag. Poor DSC was defined as DSC<0.3 on point-by-point assessment. AF: atrial fibrillation, BMI: body mass index, LA: left atrium, CNR: contrast-to-noise ratio (scar to blood pool).

9.4.2 VisiTag settings survey

The survey was completed by a total of 14 centres, representing approximately 7000 AF ablation cases per year. CARTO3 was used for a median "50-80%" of ablations (IQR "50-80%" to "80-99%"),

and of these cases CF information and VisiTag module were used a median ">99%" (IQR "80-99%" to ">99%") and ">99%" (IQR "80-99%" to ">99%") of the time respectively. On a centre by centre estimation, CARTO3, CF information and VisiTag module were therefore used for approximately 5200, 5000 and 4600 cases per year respectively. The VisiTag™ thresholds and subjective ranking of importance in lesion formation are shown in Table 9-4. 'Force' was generally judged to be the most important VisiTag-assessed parameter in terms of lesion formation, but it was ranked as low as 5th by some institutions. 'Target Temperature' and Impedance Drop' filters were generally not activated. 'Target Temperature' was generally viewed as of lowest importance, but 'Impedance Drop' was ranked first by one institution and second by two institutions. Interestingly, both the centres that placed 'Impedance Drop' second in ranking of importance chose not to activate the filter routinely.

	Median Threshold (IQR)	**Median Ranking (IQR)**	**Filter not activated routinely**	**Varies widely between operators**
'Force' (grams)	"5-8" (IQR "5-8" to "5-8")	1 (IQR 1-3)	0	1 (7%)
'Time' (seconds)	"10-14" (IQR "5-9" to "10-14")	3 (IQR 2-4)	0	1 (7%)
'Range' (mm)	3 (IQR 2-4)	3 (IQR 2-4)	0	1 (7%)
'Percentage Time' (%)	"50-59" (IQR "50-59" to "50-59")	3 (IQR 2-4)	2 (14%)	4 (29%)
'Impedance Drop'	None stipulated	5 (IQR 4-5)	12 (86%)	2 (14%)
'Target Temperature' (°C)	"41-42" (IQR "39-40"to"41-42")	6 (IQR 6-6)	8 (57%)	1 (7%)

Table 9-4. Results of UK survey of VisiTag parameter settings.

IQR: interquartile range.

9.4.3 VisiTag density

The proportion of the left atrium (LA) associated with VisiTag markers was assessed at each parameter threshold (Figure 9-5). With increasingly stringent thresholds, the number of VisiTag markers falls, and hence the proportion of the atrium associated with a marker also falls. The impact of 'Force' and 'Time' is profound ($p<0.0001$, Friedman statistic 207 and 120 respectively), with less than half the atrial coverage at highest VisiTag thresholds compared to lowest (Force: 0.29±0.07 at 2g, 0.14±0.06 at 20g, Time: 0.30±0.06 at 5 sec versus 0.13±0.05 at 30sec). The impact of 'Percentage

Time' is less marked (0.28±0.06 at 30%, 0.26±0.06 at 80%), but remains significant. There is a 56% and 74% fall in marker extent with activation of 'Impedance Drop' filter and 'Target Temperature' filter respectively.

The relationship of VisiTag extent with alteration in 'Range' is more complex. The number of markers increases from 2mm to 3mm threshold, but then decrease as the markers agglomerate at larger 'Range' sizes. On a point-by-point basis, there are locations that may be associated with only one or two Range thresholds, and these may be at any size (Table 9-5).

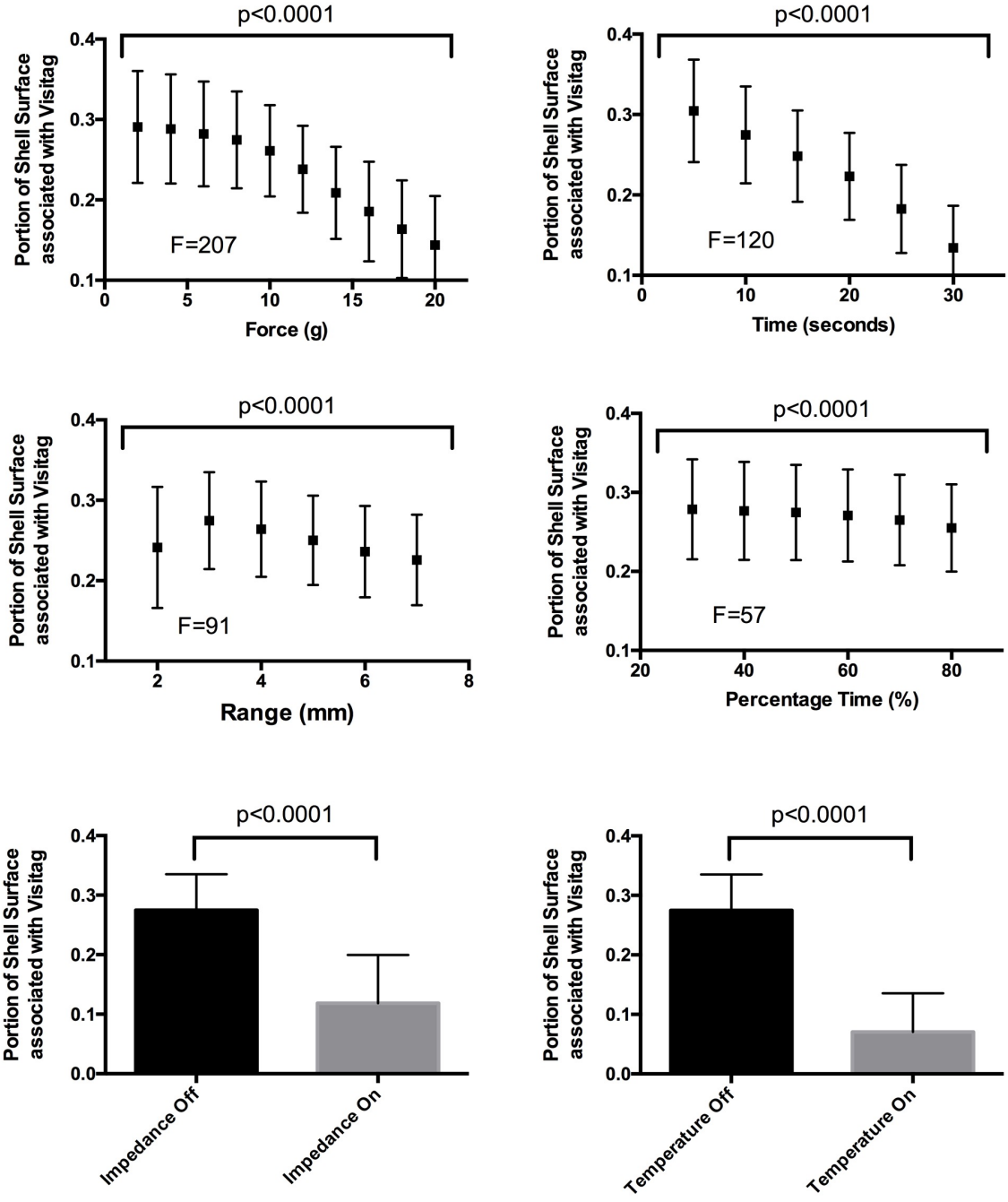

Figure 9-5. The proportion of the left atrium (LA) associated with VisiTag marker, with variation in thresholds.

F: Friedman statistic, generated from the Friedman test, a non-parametric statistical test similar to repeated measures ANOVA.

Number of Contiguous VisiTag 'Ranges' →	1 e.g. 2mm only	2 e.g. 2 and 3mm	3 e.g. 2,3, 4mm	4 e.g. 2,3,4 ,5mm	5 e.g. 2,3,4 ,5,6mm	6 (all 'Ranges' positive)	Any other combination
Min 2mm (%)	3.1	3.5	3.4	3.7	3.4	60.6	4.8
Min 3mm (%)	1.6	1.1	0.8	0.8	8.1	-	-
Min 4mm (%)	0.7	0.3	0.2	1.3	-	-	-
Min 5mm (%)	0.5	0.2	0.5	-	-	-	-
Min 6mm (%)	0.3	0.5	-	-	-	-	-
Min 7mm (%)	0.6	-	-	-	-	-	-
Total	6.8	5.6	4.9	5.8	11.5	60.6	4.8

Table 9-5. VisiTag distribution at varying 'Range' thresholds.

Values within table are the percentage of VisiTag positive shell surface covered by each VisiTag "Range" combination. A high "range' value does not necessarily mean that VisiTag confirmation is less stringent. At any given shell location, VisiTag confirmation may be achieved at an assortment of VisiTag 'Range' thresholds. The rows are sorted according to the smallest 'Range' threshold achieved, and the columns are sorted according to the number of contiguous 'Range' thresholds at which a VisiTag was achieved. The final column shows the proportion of Shell covered by a non-contiguous set of 'Ranges'.

9.4.4 Lesion continuity assessment

The results of the regional assessment are shown in Figure 9-6. Continuous, uninterrupted, scar on thresholded CMR LGE was present at 67% of regions in total, with significant regional variation ($p<0.001$). The inter-ostial region was ablated on the right in 13 patients (54%), and on the left in 9 patients (37%), and of these continuous scar was present in 6 patients (47%) on right and 7 patients (78%) on the left. 'Force' thresholds were generally highest at the right anterior region and left posterior regions. A slightly different pattern was observed for 'Time' thresholds: on the right they remained highest anteriorly, but on the left were highest infero-anterior. Median 'Percentage Time' was 80% in all regions. As shown in Table 9-5, 'Range' is not an ordinal scale variable. A median number of 6 (all) VisiTag 'Range' settings were positive at all regions.

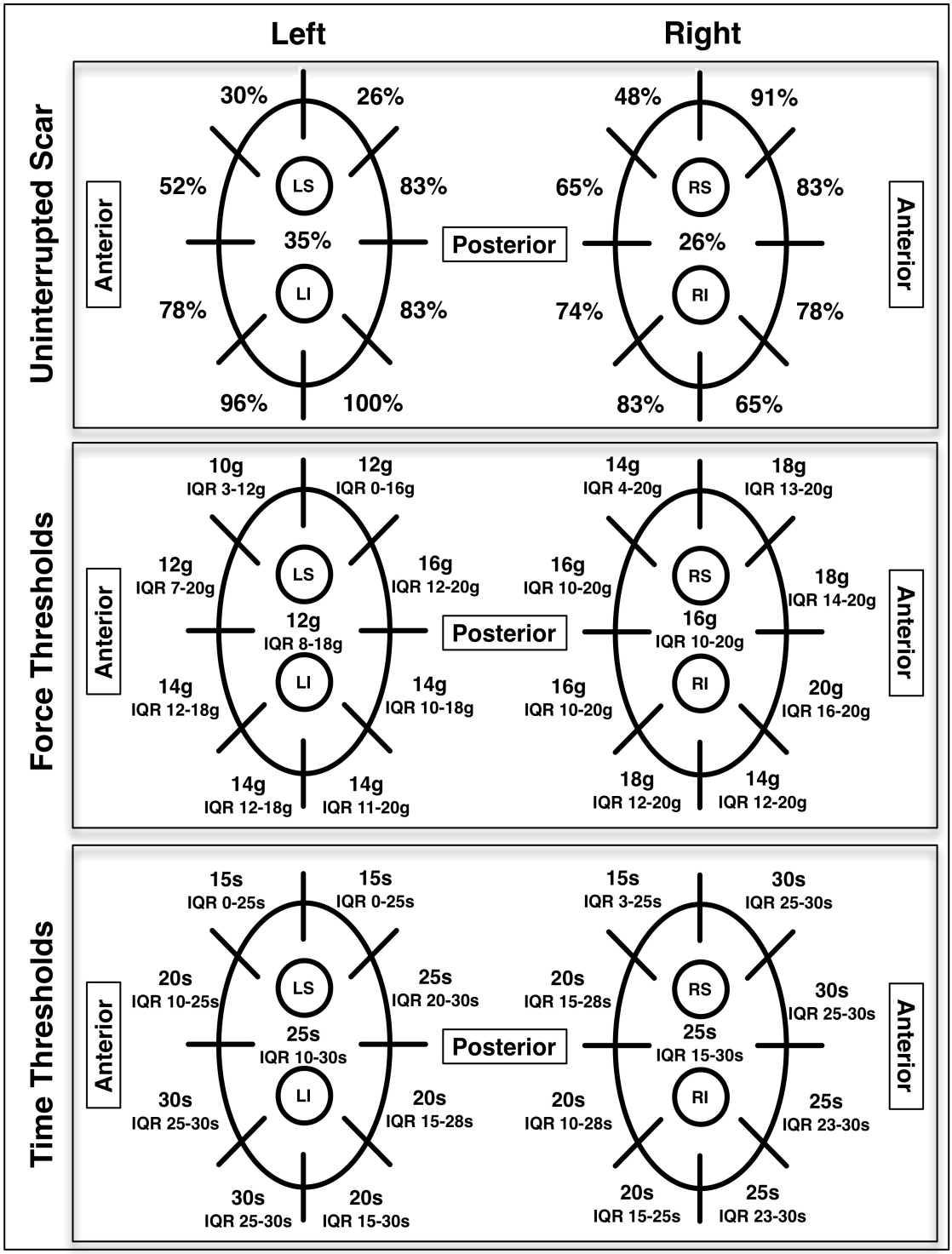

Figure 9-6.Presence of continuous LGE scar or VisiTag markers by ablation region.

(Top) Regional distribution of continuous scar on CMR LGE, expressed as percentage of all subjects. (Middle) median 'Force' threshold (in grams, with interquartile range (IQR)). (Lower) median 'Time' threshold (in seconds, with IQR). For region 9 (inter-ostial) bilaterally in middle and lower plots, values reflect only subjects in whom inter-ostial ablation was performed. LS: left superior PV, LI: left inferior, RS: right superior, RI: right inferior.

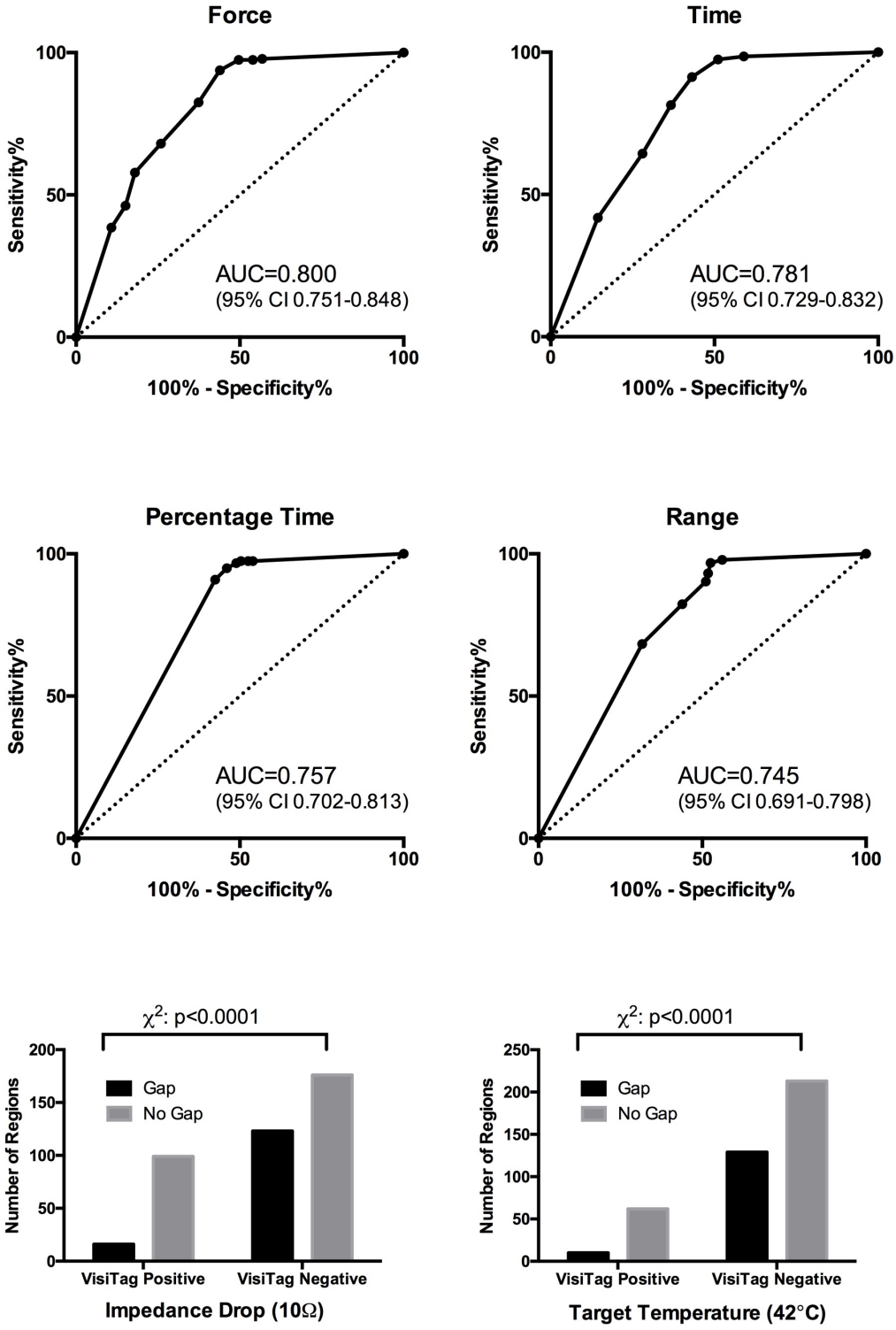

Figure 9-7. Predictive value of continuous VisiTag markers for uninterrupted scar.

(Top four panels). Receiver operator characteristic (ROC) curves for prediction of continuous CMR LGE scar within each region by presence of VisiTag markers, varied over multiple thresholds. For 'Range' threshold, which is not an ordinate variable, the summative statistic is number of 'Range' thresholds for which the region demonstrated no gaps. The bottom two panels are frequency histograms, demonstrating the proportion of

regions with and without CMR LGE gaps, according to the presence or absence of VisiTag markers once the threshold was imposed. AUC: area under curve.

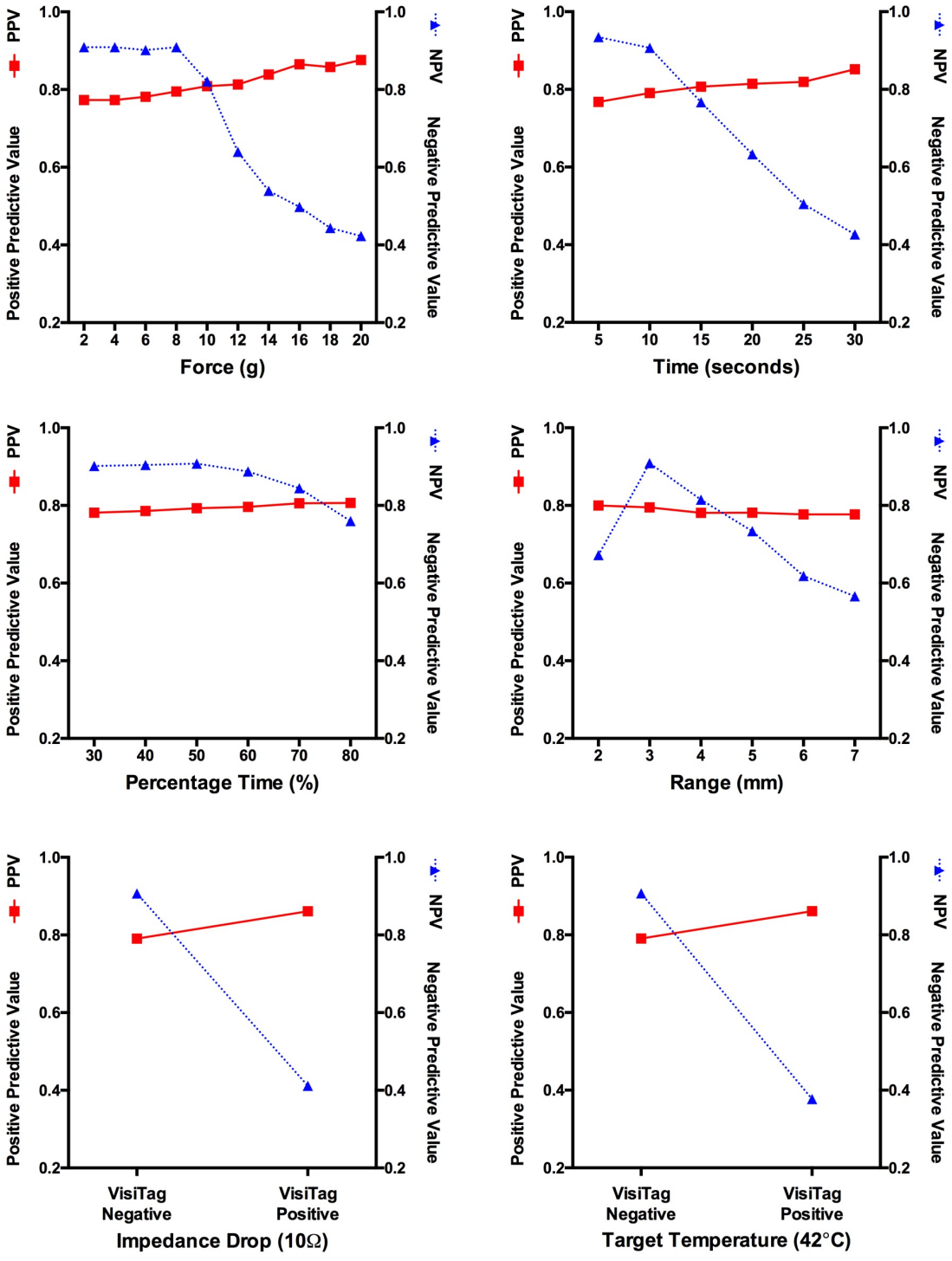

Figure 9-8. Positive predictive value (PPV) and negative predictive value (NPV) of VisiTag predicting continuous scar on CMR LGE, across thresholds.

Figure 9-7 shows ROC curves for the prediction of continuous CMR LGE scar within a region by presence or absence of a gap in VisiTag markers. There was a significant relationship ($p<0.0001$) between a gap in markers and gap in CMR LGE for all four parameters. For 'Force', the sensitivity and specificity were 0.975 and 0.504 respectively at 8g, shifting to 0.822 and 0.626 at 12g, 0.582 and 0.820 at 16g and 0.385 and 0.892 at 20g. Positive predictive value (PPV) and negative predictive value (NPV) for prediction of uninterrupted scar are shown in Figure 9-8. The PPV improves steadily with increasing 'Force' threshold, but there is a step in the progression of NPV. NPV is static between 2g and 8g (0.909 and 0.909 respectively) then drops rapidly to 0.539 at 14g: the false negative rate increases significantly once the 'Force' threshold is set above 8g.

'Time' demonstrates a more linear response to changes in thresholds, with sensitivity and specificity 0.975 and 0.489 respectively at 10 seconds, and 0.418 and 0.856 respectively at 30 seconds. 'Percentage Time' changes the presence of markers little across the thresholds: the AUC represents the sensitivity and specificity of the default VisiTag parameters. 'Range' demonstrates a peak in sensitivity at 3mm (0.975), with relatively stable specificity throughout (maximum 0.576 at 2mm, minimum 0.475 at 4mm). The implementation of the 'Target Temperature' and 'Impedance Drop' filters greatly improves the specificity (from 0.489 to 0.928 and 0.489 to 0.885 respectively), but at the cost of a much higher false negative rate and consequently lower NPV.

A binomial logistic regression was performed to ascertain the effects of the 'Force', 'Time', 'Target Temperature' and 'Impedance Drop' thresholds on the likelihood of continuous CMR LGE scar. "Percentage Time' and 'Range' were excluded due to significant collinearity with default values, and complex distribution of non-ordinate values respectively. The logistic regression model was statistically significant, $\chi^2(4)=148$, $p<0.0001$. The model explained 41.7% (Nagelkerke R^2) of the variance in scar formation and correctly classified 82% of cases. Sensitivity was 94.9% and specificity 56.8% at a cut-off value of 0.5 (see Table 9-6). Of the four predictor variables, only 'Force' and 'Time' were statistically significant (Table 9-7).

		LGE CMR Assessment		
		Uninterrupted Scar	Gap	
VisiTag prediction	Uninterrupted scar	261	60	PPV: 81.3
	Gap	14	79	NPV: 84.9
	Percentage Correct	Sensitivity 94.9	Specificity 56.8	Accuracy 82.1

Table 9-6. Classification table for binomial logistic regression analysis of gap assessment.

PPV: positive predictive value, NPV: negative predictive value

	Odds Ratio	**95% CI**		**Significance**
		Lower	Upper	
'Force' (per gram)	1.14	1.075	1.208	<0.0001
'Time' (per second)	1.054	1.016	1.093	0.005
'Target Temperature'	0.973	0.443	2.137	0.946
'Impedance Drop'	0.659	0.341	1.273	0.214
Constant	0.215			0.009

Table 9-7. Variables in equation: binomial logistic regression.

CI: confidence interval.

9.4.5 Point-by-point assessment

9.4.5.1 Quality of shell registration

DSC was assessed for each ablation and CMR shell pair, thresholded at default VisiTag parameters and 3.3 SD above BP mean respectively. The average difference in DSC between the shell pairs at each of two fusion processes was 0.003±0.002, indicating a highly reproducible fusion (Figure 9-9). However, there was a wide range in accuracy of registration, with DSC ranging from 0.13 to 0.54. The six shells with severe mis-registration were excluded from further analysis, and the characteristics of the subgroups have been reviewed above. An example of good scar: ablation lesion registration is shown in Figure 9-10 and Figure 9-11.

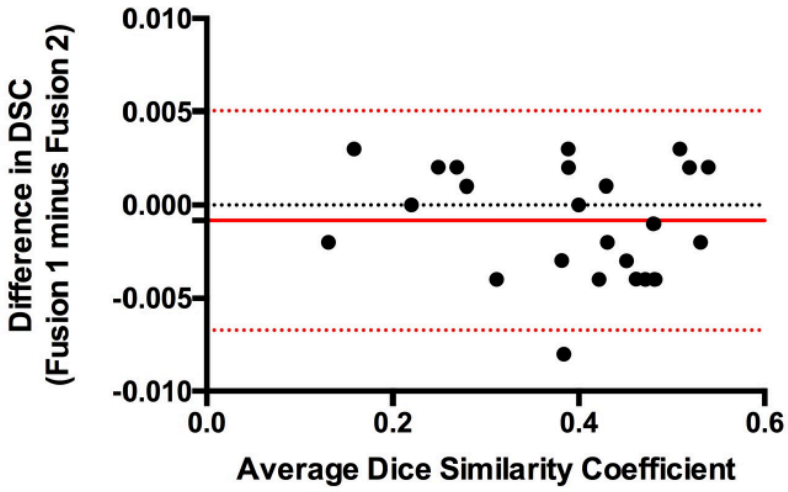

Figure 9-9. Bland Altman plot demonstrating reproducibility of dice similarity coefficient (DSC) following two independent shell fusions.

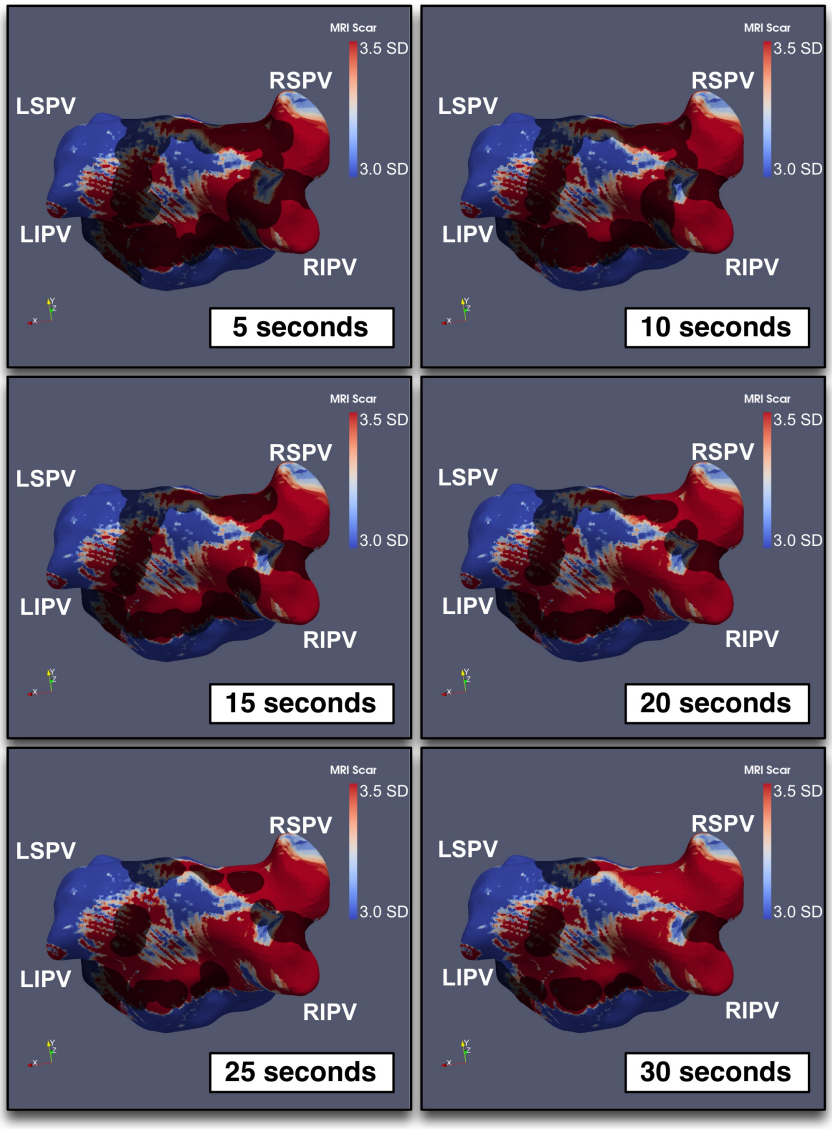

Figure 9-10. Example of 'Time' threshold alteration.

CMR signal intensity (blue-red shell, scar in red) with VisiTag locations overlaid in grey at varying thesholds (5-30seconds). Note over-estimation of lesion formation (low specificity) compared to chronic scar at low threshold, and underestimation (low sensitivity) at high threshold.

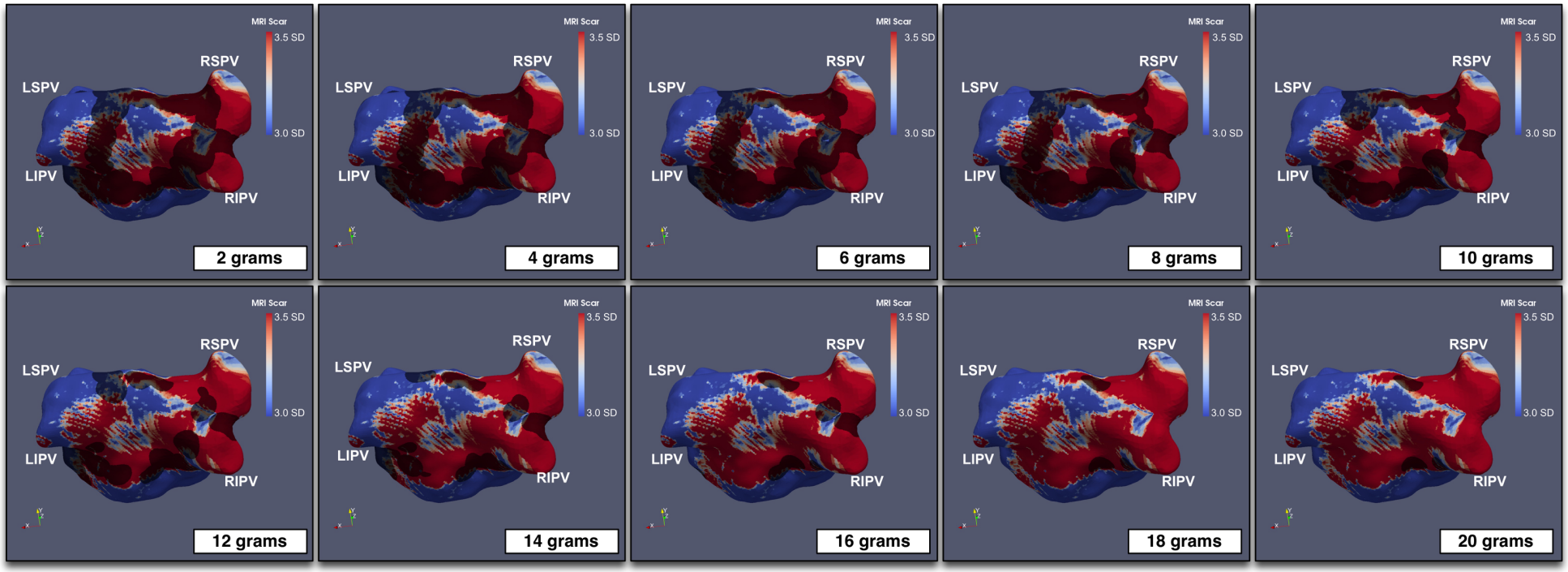

Figure 9-11. Example of 'Force' threshold alteration.

CMR signal intensity (blue-red shell, scar in red) with VisiTag locations overlaid in grey at varying thresholds (2-20grams). Again, note over-estimation of lesion formation (low specificity) compared to chronic scar at low threshold, and underestimation (low sensitivity) at high thresholds.

9.4.5.2 Quantification of predictive value of VisiTag markers

The relationship between CMR imaging scar and local VisiTag parameters were assessed on a point-by-point basis across the whole left atrium, and the results are shown in Figure 9-12. There was a general increase in CMR signal intensity with increased VisiTag thresholds, and the change was most marked for the alterations in 'Force' and 'Time' . NPV for CMR LGE scar was altered minimally by changes in threshold, with a clinically irrelevant (but significant) fall in NPV at higher thresholds ($p<0.001$ for all parameters). Positive predictive value (PPV) rose more markedly ($p<0.001$ for all parameters except 'Percentage Time' where $p=0.04$), with improved PPV for scar formation at higher thresholds.

ROC curves were generated for 'Force', 'Time', 'Percentage Time' and 'Range' parameters for assessment of the whole left atrium, and also for assessment of VisiTag positive regions only (Figure 9-13). AUC was generally low across all parameters and both assessment methods. On assessment of the whole LA, there was generally high specificity but low sensitivity, reflecting a high true negative rate (with the assessment of large regions of unablated LA) but also a high false positive rate. On assessment only of regions covered by at least one VisiTag a different pattern was observed. Sensitivity was generally high for low stringency thresholds (for example, average 0.903 for 'Force' 2g, 0.941 for 'Time' 5seconds), but at the cost of very low specificity (0.145 and 0.102 respectively). Conversely, at high stringency thresholds sensitivity was low (0.467 for 'Force' 20g, 0.423 for 'Time' 30seconds), but with improved specificity (0.598 and 0.612 respectively).

The VisiTag positive region was also assessed for the impact of VisiTag thresholds on sensitivity for chronic lesion formation and DSC (Figure 9-14). Sensitivity fell overall with increased stringency of all parameters, but was most marked for 'Force' and 'Time'. The fall in sensitivity with increasing 'Force' threshold demonstrated a step pattern. The decrease in sensitivity was non-significant for each 2g increase from 2g to 8g ($p= 0.02$ to 0.03, with threshold $p=0.006$ with Bonferroni correction), but was significant thereafter (8 versus 10g $p=0.002$, further increments $p<0.0001$). For 'time', no step was observed ($p<0.0001$ for all inter-threshold comparisons). 'Range' had a significant increase in sensitivity from 2 to 3mm ($p=0.001$), followed by significant falls at each further threshold increment ($p<0.001$ throughout). Changes in 'Percentage Time' thresholds had the smallest impact on sensitivity ($p=0.002$ to $p=0.3$).

There was a similar overall pattern for fall in DSC with increasing threshold, which was significant for all parameters except 'Percentage Time'. Interthreshold comparisons for 'Force' were non-significant below 8g, borderline for 8-10g ($p=0.02$), and significant for 10-12g comparison and all comparisons at higher threshold ($p<0.0001$). For 'Time', all inter-threshold comparisons were significant ($p<0.003$ throughout), and for 'Range' only the comparisons between 5-6mm and 6-7mm were significant ($p<0.001$).

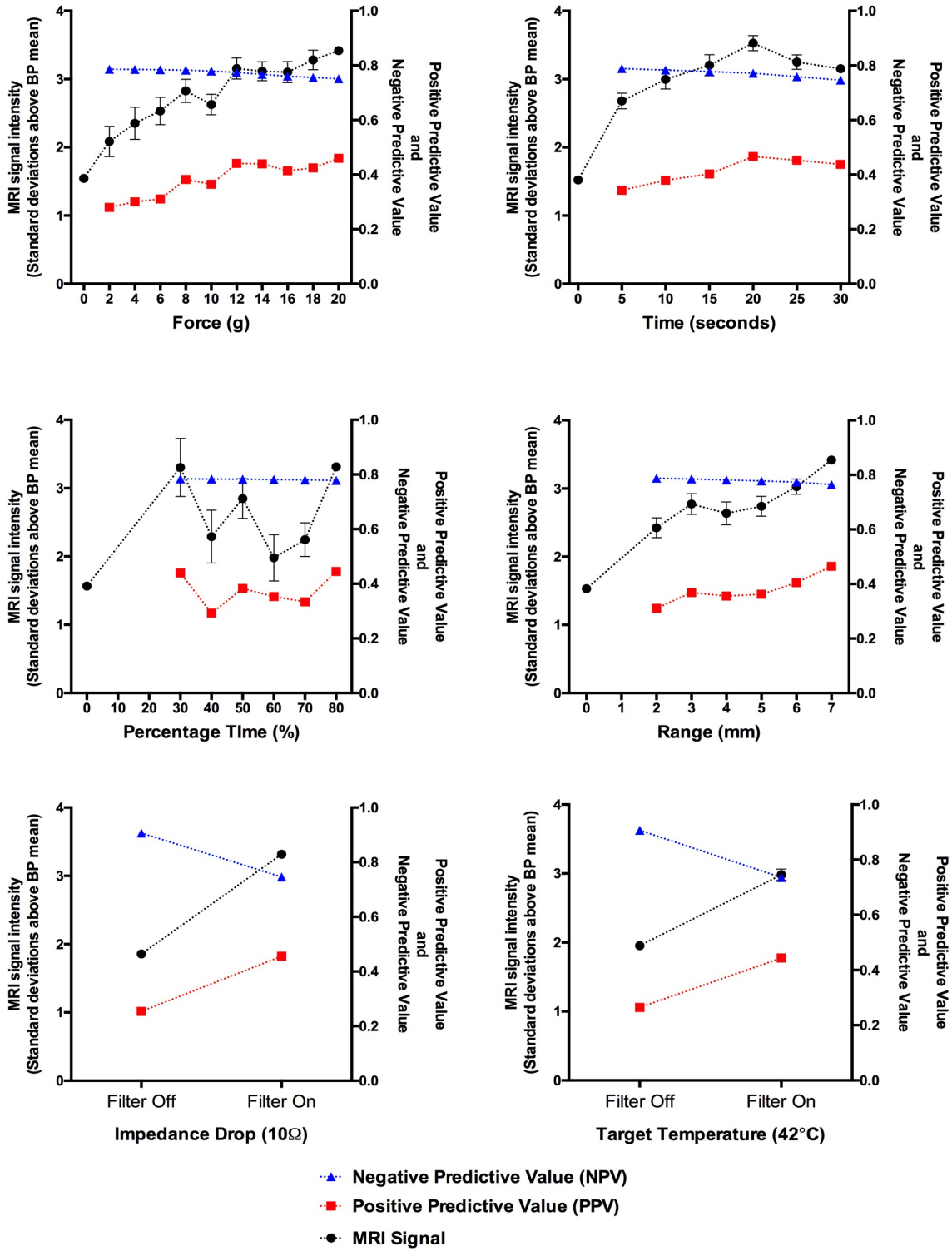

Figure 9-12. Predictive value of VisiTag marker for LGE scar (point-by-point)

Positive predictive value (PPV), negative predictive value (NPV) and CMR LGE signal intensity (SI) assessed on a point-by-point basis at each VisiTag threshold. CMR SI is expressed as number of standard deviations above the blood pool (BP) mean, error bars show 95% confidence interval of the mean.

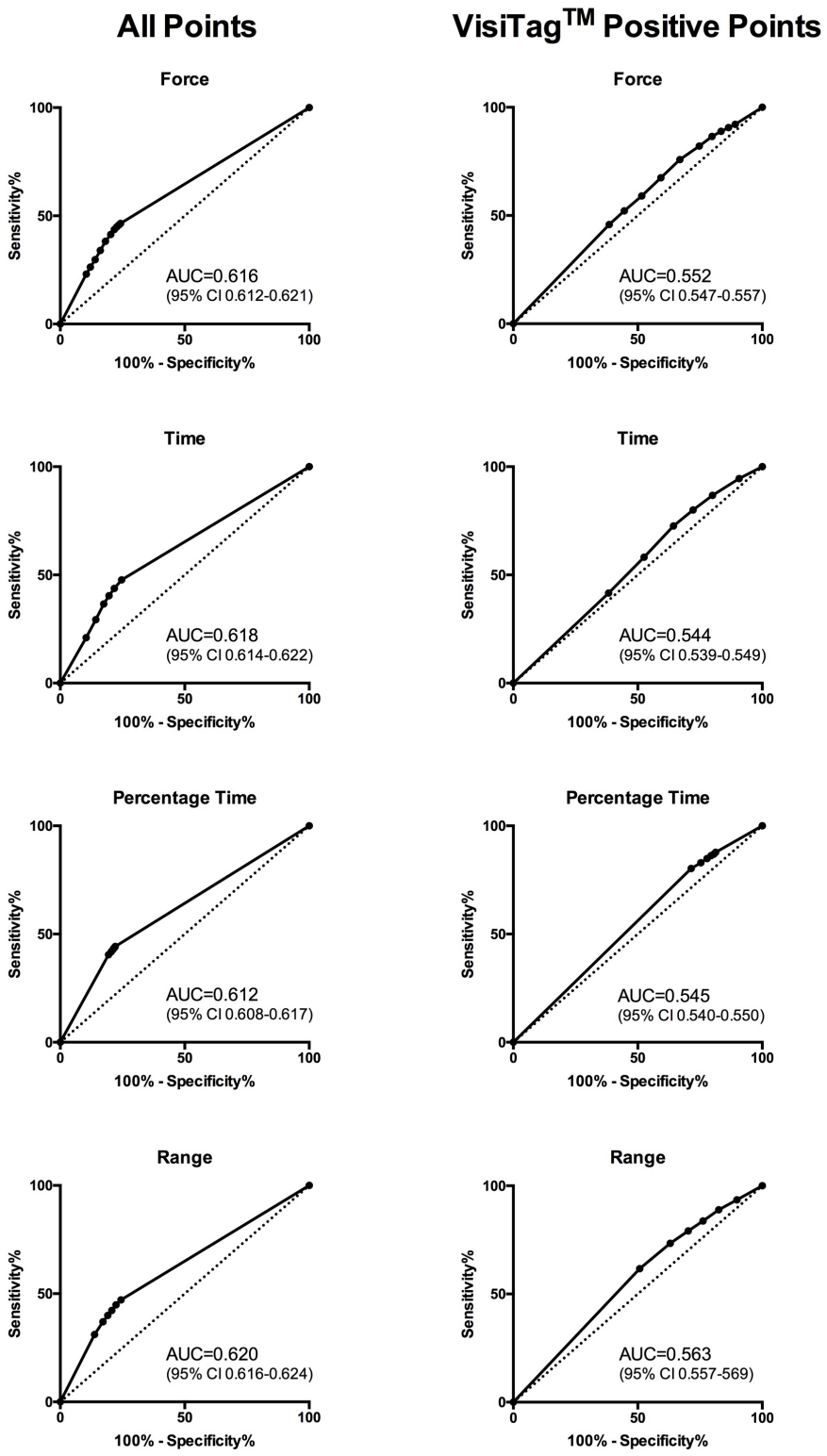

Figure 9-13. Receiver operator characteristic (ROC) curves for prediction of CMR LGE scar by VisiTag marker, on a point-by-point assessment.

Left column shows ROC curves for assessment of whole of LA, and right column only for assessment of points that are associated with a VisiTag marker at a minimum of one threshold setting.

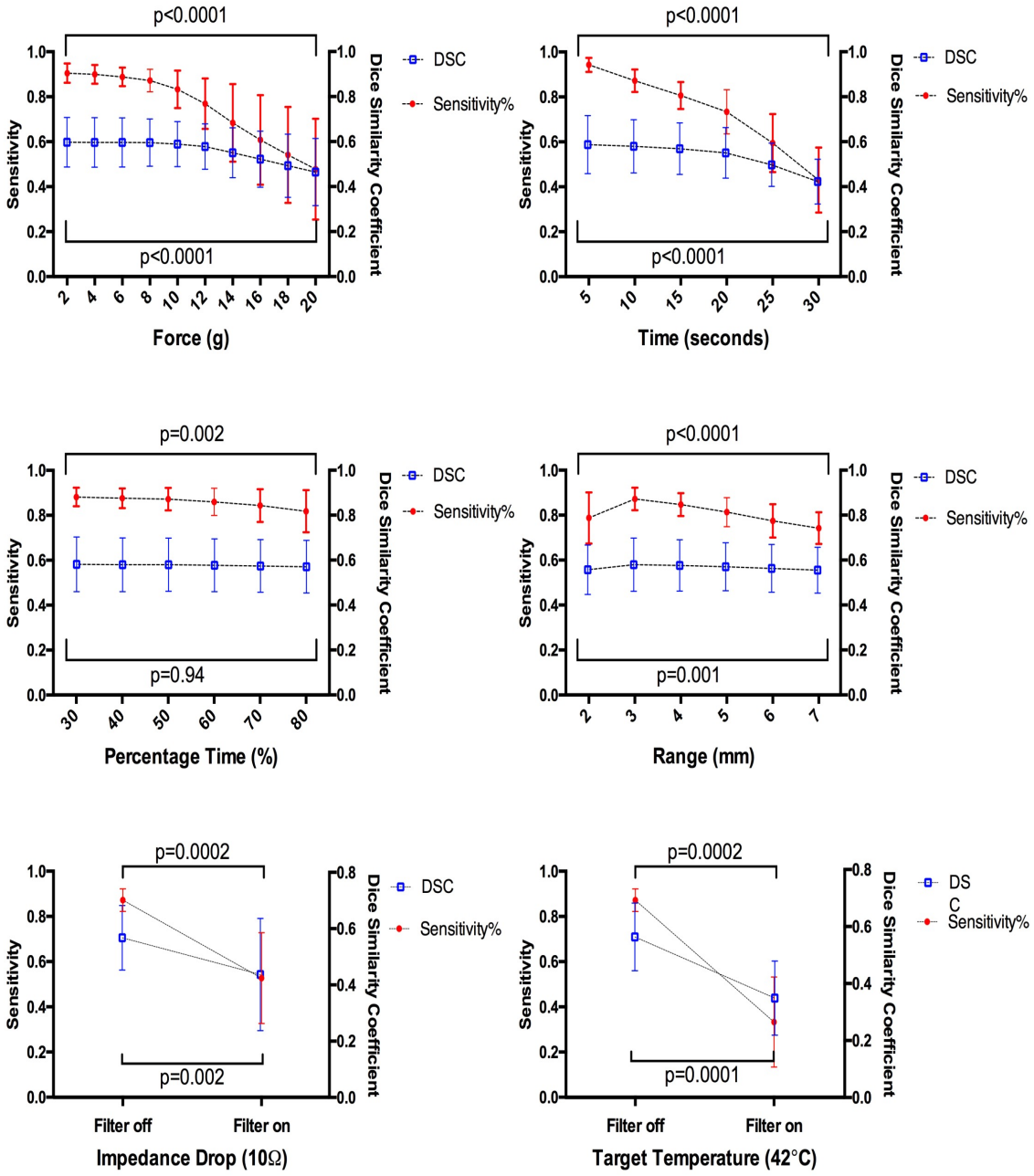

Figure 9-14. Impact of VisiTag threshold settings on sensitivity for prediction of scar.

Sensitivity analysis was performed for VisiTag regions only, and is the proportion of CMR imaging-derived scar associated with VisiTag at that threshold: as thresholds become more stringent, scar is formed without the placement of a VisiTag. Dice similarity coefficient (DSC) was assessed for the whole shell. P-values shown are for overall trend in sensitivity (upper value) and DSC (lower value) (Friedman test).

9.4.6 Predictive value of CMR and Visitag lesion continuity in the prediction of electrical reconnection

8 patients (33%) had a recurrence of arrhythmia, all of whom went on to have a repeat ablation procedure. 17 of the 32 (53%) individual veins were found to be electrically reconnected. The

sensitivity and specificity of contiguous VisiTags (at default settings) in predicting electrical isolation were 46% and 29% respectively (accuracy 38%). The sensitivity and specificity of uninterrupted CMR scar in predicting electrical isolation were 80% and 35% respectively (accuracy 56%) Sensitivity and specificity of contiguous VisiTags were both improved when the least stringent settings were used ('Force' 2g or 'Time' "5sec"), at 60% and 41% respectively for both settings (accuracy 44%).

9.5 Discussion

This study was designed to assess the value of VisiTag markers in the prediction of chronic scar following AF ablation, and to examine the impact of variations in thresholds for each parameter. The principal findings can be summarised as follows:

1. 'Force': Higher VisiTag thresholds are associated with low sensitivity and poor NPV: scar is frequently created at lower CF
2. 'Time': there is an increased likelihood of scar formation with all incremental increases in time thresholds
3. 'Range': the interaction of the 'Range' threshold and location of VisiTag placement is complex, however, the changes in threshold are associated with only a minor change in scar formation
4. 'Percentage Time': there is minimal change in scar formation with increased stringency of the 'Percentage Time' threshold.
5. 'Target Temperature' and 'Impedance Drop': the implementation of these filters at these settings (42°C and 10 Ω respectively) increases the PPV for scar, but at the cost of a much higher false negative rate.

9.5.1 Contact force

There is increasingly compelling evidence for the improvement in clinical outcomes with the use of contact force technologies. Leading on from the early benchmark clinical studies (TOCCATA study (Kuck et al. 2012) and EFFICAS I (Neuzil et al. 2013)), meta-analysis has demonstrated the benefit of operator feedback of real-time CF. Use of CF technology is associated with a reduced risk of recurrence following AF ablation, reduced ablation time, and may reduce total procedural time (Afzal et al. 2015; Shurrab et al. 2015), but the findings have not been reproduced universally in carefully designed randomised studies (W. Ullah et al. 2016).

Furthermore, the target CF for creation of permanent, transmural lesions remains unclear. The EFFICAS I study was the first to propose firm recommendations, suggesting that a target CF of >20g and FTI >400gs was associated with a reduced risk of electrical reconnection at 3 months on invasive testing. These targets were used in the subsequent EFFICAS II study, which reported a consequentially improved durability of PV isolation at three months (98%, compared to 81% in

EFFICAS I) (Kautzner et al. 2015). Most other studies, though, have been reluctant to stipulate a target CF, in the context of increased risk of complications with high CF (Yokoyama et al. 2008). The SMART-AF study, using CF information for ablation of drug-refractory paroxysmal AF (PAF) in 172 patients, deliberately did not define a target CF (Natale et al. 2014). Likewise, the more recent TOCCASTAR study (V. Y. Reddy et al. 2015), in which 300 patients were randomised to treatment of PAF with or without CF sensing catheter, did not define a target CF. Both SMART-AF and TOCCASTAR did look at CF retrospectively. SMART-AF found that clinical outcome was improved when ≥80% of ablation lesions were performed within 'user-defined' target ranges (overall average CF 17.9±9.4g), whilst TOCCASTAR noted that ablation effectiveness improved from 58% to 76% with the use of 'optimal CF', defined as ≥90% of lesions created with CF ≥10g. Such findings are difficult to implement clinically, and seem to suggest that perhaps consistent catheter control, rather than CF alone, is a strong determinant of effective lesion formation.

More recently, studies have suggested that more conservative CF levels may be safer and equally efficacious. Pre-clinical work by Williams et al (Williams et al. 2015) found no difference in chronic atrial lesion formation using high CF (22.6±11.4g) versus low CF (7.8±4.0g), validated on LGE imaging, chronic voltage mapping and histology. In humans, SMART-AF found no evidence of increased ablation effectiveness at higher CF, but there was an increased rate of procedural major adverse events with CF ≥ 14g. Kimura et al (Kimura et al. 2014) found no improvement in ablation, in terms of residual acute electrical connection, for CFs ≥10g, and Andreu et al (Andreu et al. 2016) found that a CF threshold of >12g predicts a complete lesion within a PV antral segment with high specificity.

In this context, the findings of this study are interesting. The fixing of 'Time', 'Range' and "Percentage Time' VisiTag thresholds controls for the first time the potential confounder of variation in catheter stability. Here, the sensitivity for VisiTag prediction of scar was flat for 2-8g, but then fell markedly at higher CF, suggesting that chronic scar was frequently formed at lower CF, and more stringent thresholds may to lead to excessive ablation. However, the specificity and positive predictive value of VisiTag placement continued to improve with increasing CF ≥10g. This implies that CF ≥10g is required in order to be confident of lesion formation, even though a large proportion of chronic scar is formed at lower CF. The selection of a CF threshold is, unsurprisingly, a trade-off between confidence in efficacy and safety. However, this study quantifies the decreasing benefit of increasing thresholds above 14g.

9.5.2 Ablation time

Increased total ablation time and FTI have been shown to be associated with improved ablation efficacy (Waqas Ullah et al. 2014; Neuzil et al. 2013), and increased chronic scar formation on CMR imaging (Sohns et al. 2013). To my knowledge, no clinical studies have sought to dissociate the effect of time from force, either applying constant force or constant FTI over varying time periods. However, there is a suggestion that the effect of RF energy on chronic lesion formation may begin to

plateau above 500gs (Waqas Ullah et al. 2014) or total 20seconds of effective ablation (F. H. Wittkampf, Hauer, and Robles de Medina 1989). It has also been shown that it takes around 10seconds for full power to be achieved when ablating in temperature control mode (Waqas Ullah et al. 2014). In this study there was improved specificity for lesion formation with increasing time up to 30 seconds, and there was no significant plateau of sensitivity, in contrast to 'Force' thresholds. The FTI was not formally assessed in this study, but a minimum FTI can be estimated from VisiTag thresholds. At the highest 'Force' and 'Time' thresholds, minimum FTIs were approximately 200gs and 300gs respectively, and FTI exceeded 1000gs at <1% of VisiTags at default settings (note that FTI is highly dependent upon 'Range' setting (Figure 9-18)). Any improvement in efficacy at higher FTI was not assessed in view of the interaction of 'Force', 'Time' and 'Range' in the generation of the metric, and the limitation of point-by-point analysis by misregistration issues.

9.5.3 Other parameters

Alteration of 'Range' and 'Percentage Time' thresholds appeared to have only a minor impact upon VisiTag performance. 'Range' reflects the distance the catheter is allowed to travel before ablation indices are allocated to a separate VisiTag marker. The decrease in number of markers at higher 'Range' thresholds reflects the increased area that the marker represents, despite the increased leniency of the marker threshold. The peak number of markers at 3mm suggests that this is a suitable setting to capture both catheter stability and ablation location, but it should be noted that 2.5mm was not assessed. The significant reduction in proportion of shell associated with VisiTag marker at high 'Range' threshold reflects the fixed search radius: consideration should be given to increasing the size of the marker on visualisation in CARTO3 if a large range is stipulated, but there is a risk that the majority of ablation energy will be delivered in only a select proportion of the marker.

'Percentage Time' reflects a rolling average of the amount of time that the CF has been greater than the minimum stipulated force, and as such it would be anticipated to be a strong marker of catheter stability. However, on assessment of the data in this study the 'Percentage Time' was found to be >80% for the vast majority of lesions, and therefore it has proved an ineffective filter at minimum force 8g. At higher target CF it may become a more critical index of catheter stability.

'Target Temperature' and 'Impedance Drop' filters are used by few operators (Table 9-4 and Table 9-8), but they clearly improve discrimination in terms of positive predictive value. The manufacturers themselves recommend that the filters are not used during ablation, but only for retrospective review of ablation parameters. In view of the limited implementation of the filters, only a single filter setting was assessed. They may warrant further assessment in the future.

	Force	Time	Range	Percent Time	Imp Drop	Target Temp	Comments
(Fujiwara et al. 2016)	5g	5sec	1mm	25%	Off	Off	Assessment of acute reconnection (37 patients). Difference only in 'Time' and FTI between conducting and non-conducting lesions
(Lin et al. 2013)	6g	15sec	4mm	60%	Off	Off	Review publication-institutional preference reported
(Okumura et al. 2016)	10g[a] 8g[b]	10s[a] 5s[b]	3mm[a,b]	50%[a] 25%[b]	Off[a,b]	Off[a,b]	Stricter settings ([a]) resulted in non-significant (p=0.1) reduction in dormant conduction (54 patients)

Table 9-8. VisiTag thresholds used in published studies or reviews.

9.5.4 CMR imaging assessment of chronic scar

LGE CMR techniques have been shown to be a valid assessment of chronic ablation scar injury, associated with clinical outcome measures (Badger et al. 2010; Peters et al. 2007; Bisbal et al. 2014; Fukumoto et al. 2015; James L Harrison et al. 2014; Akoum et al. 2015). In this thesis, I have demonstrated methods for optimisation of imaging of atrial ablation, and the reproducibility of the technique, and therefore it is appropriate to use LGE CMR as a non-invasive assessment of PAAS formation. However, it is also important to bear in mind the limitation of PAAS assessment in the direct prediction of electrical reconnection ((J L Harrison, Sohns, et al. 2015) and Section 8.4.5). The poor accuracy of both VisiTag lesions and CMR-derived scar in predicting PV reconnection in this study is likely to reflect the complex relationship between recurrence, electrical reconnection, and objective measures of post-ablation scar. There is also corroborative evidence that the qualitative correlation between ablation and CMR-derived scar is strong. Andreu et al (Andreu et al. 2016) recently demonstrated a strong relationship between minimum CF and visual assessment of location of gaps in CMR-derived scar. At a CF of >12g there was >94% specificity in prediction of an uninterrupted ablation line in one of the 18 PV segments, but there was no control for the impact of time or catheter stability. In this study, on similar regional qualitative assessment, the sensitivity is generally higher and specificity lower at similar CF thresholds, with comparable AUC for CF (0.800 versus 0.834 for Andreu et al). This is likely to be due to the difference in CF quantification using manual versus objective (VisiTag) annotation, with variable versus fixed time integration. Incidence of gaps on LGE were very similar (33% versus 39% for Andreu et al), despite different image

interrogation and thresholding methods, but differing CF interpolation methods between ablation points may also play a role in the difference between the two studies.

Quantitative point-by-point assessment requires further registration of the two datasets, with an inevitable degree of misregistration of the two anatomies. Techniques such as CARTOMerge™ were considered at the outset of the study, but the technique cements the subtle misregistration errors without any opportunity to quantify or rectify the mismatch. Therefore the registration was performed independent to the procedure, and it has proven a robust process, as demonstrated by the high reproducibility of DSC between independent fusion episodes. However, registration errors remain inevitable, and Taclas et al, using a similar registration technique to fuse EAM and CMR anatomies, found a mean registration error of 3.6±1.3mm (Taclas et al. 2010).

Alternative fusion techniques, using location of scar and ablation to inform the fusion process have been demonstrated (Roujol et al. 2013), and may reduce the degree of mismatch but with innate biasing of the results. The contrast in sensitivity and specificity between the regional assessment and point-by-point assessment is stark, and is likely to reflect the homogeneity of the ablation. Subtle variations in ablation parameters on a mm-by-mm basis have proven difficult to detect, but the broad changes in sensitivity across 'Force' and 'Time' threshold ranges have remained clear. This is reflected in the relatively flat PPV, where a large proportion of the shift in sensitivity is confounded by the change in VisiTag density. Furthermore, NPV is difficult to assess on a point-by-point basis: the absence of CMR imaging-derived scar at marker location may be related to mis-registration, rather than ineffective lesion formation.

9.5.5 Limitations

This study was a retrospective analysis of standard PV isolation procedures for both persistent and paroxysmal AF. All ablations were performed by two experienced operators, using a similar point-by-point ablation technique and reflect real-world practice. However, the target CF and ablation strategy were not formally controlled. The use of the LGE scar as the gold standard for scar formation is a technique that has been shown to be sensitive to the presence of scar, but not highly specific (Bisbal et al. 2014; J L Harrison, Sohns, et al. 2015). Despite the implementation of the findings of earlier chapters within this thesis, LGE may have missed scar where it was in fact present, and this would imply that lower thresholds than those identified may be effective. Some of the statistical analyses did not take into account clustering by patients, and a hierarchical analysis may be preferable. In addition, a quantitative step analysis of the change in gradients with thresholds (looking for plateau) was not performed on account of the large standard deviations at relatively few measurement intervals. Finally, VisiTag annotation does not take into account power delivery, and this is almost certainly another important factor in lesion formation. New objective lesion annotation indices that have been introduced after this study was performed, such as "Ablation Index" (Carto3, Biosense Webster), integrate this parameter (Das et al. 2016), and further evaluation of outcome is

required. However, the algorithms used to derive the "Ablation Index" are not published and therefore it was not possible to assess the predictive value of the index itself retrospectively.

9.6 Conclusion

Markers created on objective assessment of ablation parameters are highly predictive of chronic lesion formation on regional assessment. On point-by-point assessment, the relationship is much weaker and is likely to represent subtle mis-registrations. Scar formation increases in a non-linear fashion with increased contact force, and in a linear fashion with increased ablation time. The relationship with stability indices, 'Percentage Time' and 'Range' is more complex, with 'Percentage Time' having minimal impact on predictive value. This study provides the first detailed clinical assessment of the impact of ablation parameter thresholds on scar formation. It quantifies the relationship between sensitivity and specificity at each threshold, assisting informed clinician selection of threshold values.

9.7 Acknowledgements

I would like to thank Kulvinder Lal for her dedicated assistance in downloading the majority of the VisiTag export files, Dr Rashed Karim for writing the software to perform the shell fusions, Dr Steven Williams for writing the scripts for the export of the VisiTag shell data, Dr Radoslaw Kiedrowicz for his help obtaining the CARTO3 studies and early analysis, and Dr Matthew Wright and Prof Mark O'Neill for performing the procedures and providing feedback on the chapter.

9.8 Chapter appendix A- VisiTag review

This appendix documents the change in VisiTag density and labelling across the thresholds examined in this study, for a single subject (39F). For each parameter, all other settings are fixed at default values (see above).

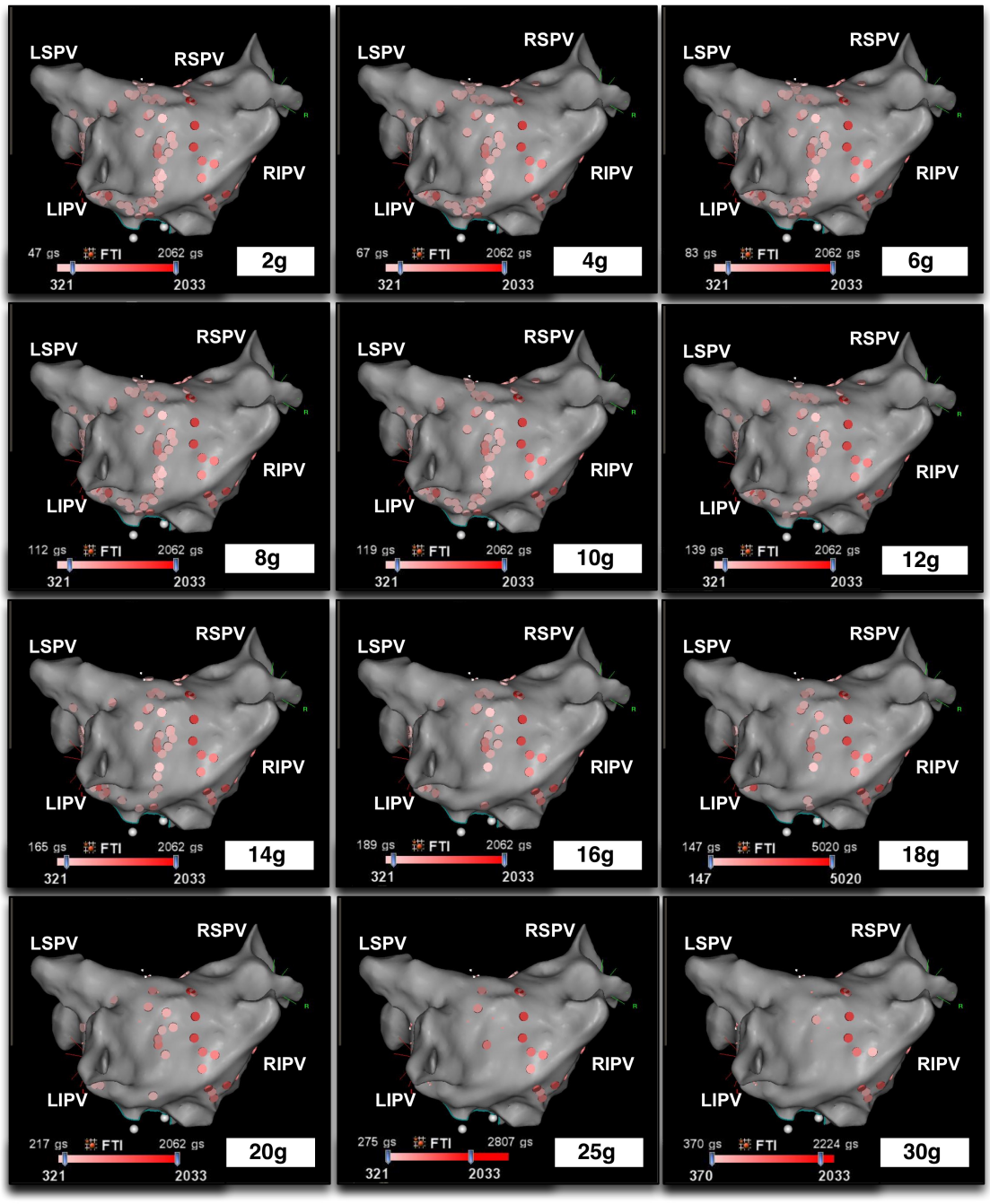

Figure 9-15. VisiTag locations with variation of 'Force' (grams).

Colouring of tags is according to FTI (force time interval) in gram.seconds. LIPV: left inferior pulmonary vein (PV), RIPV: right inferior PV, RSPV: right superior PV, LIPV: left inferior PV.

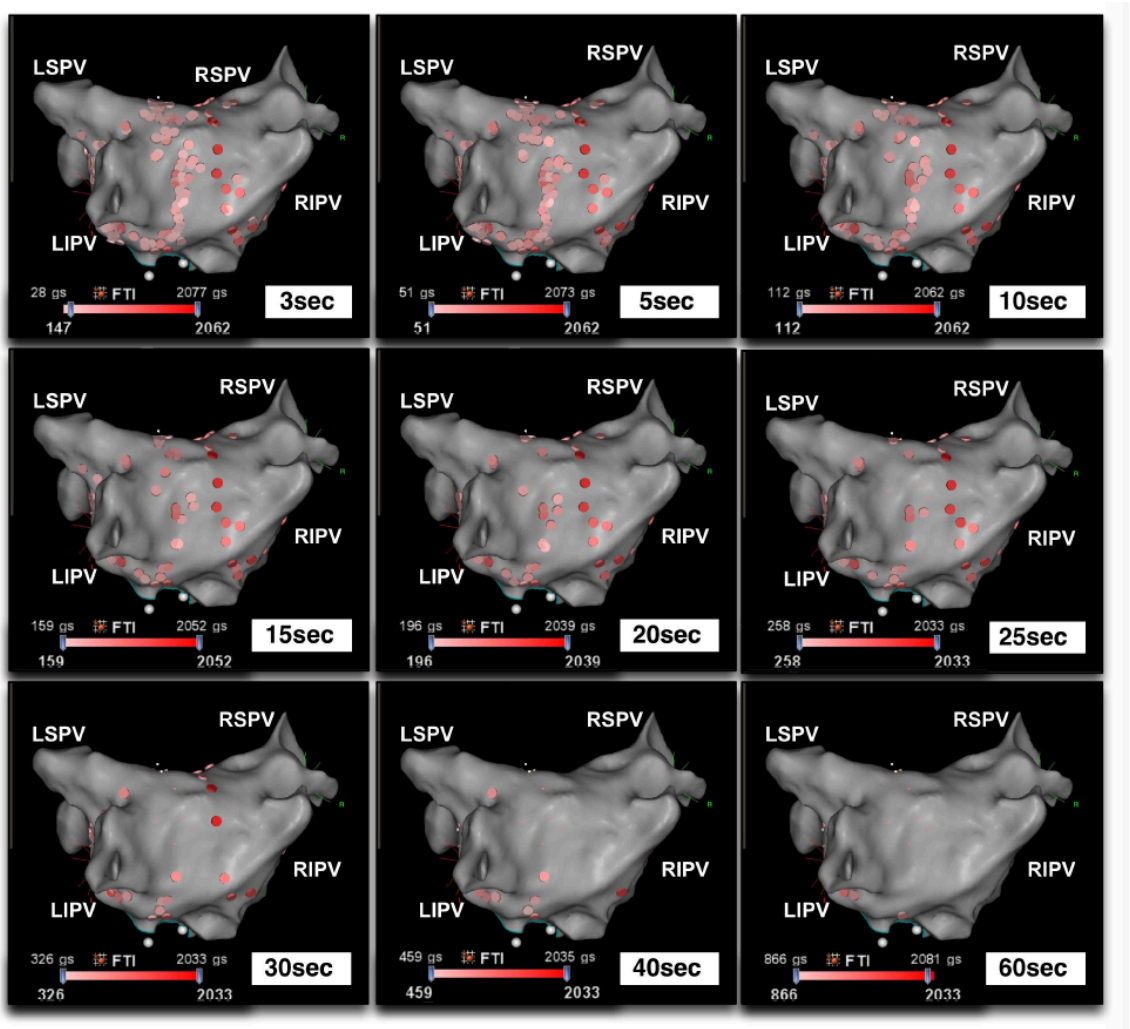

Figure 9-16. VisiTag locations with variation of 'Time' (seconds).

Colouring of tags is according to FTI (force time interval) in gram.seconds. LIPV: left inferior pulmonary vein (PV), RIPV: right inferior PV, RSPV: right superior PV, LIPV: left inferior PV.

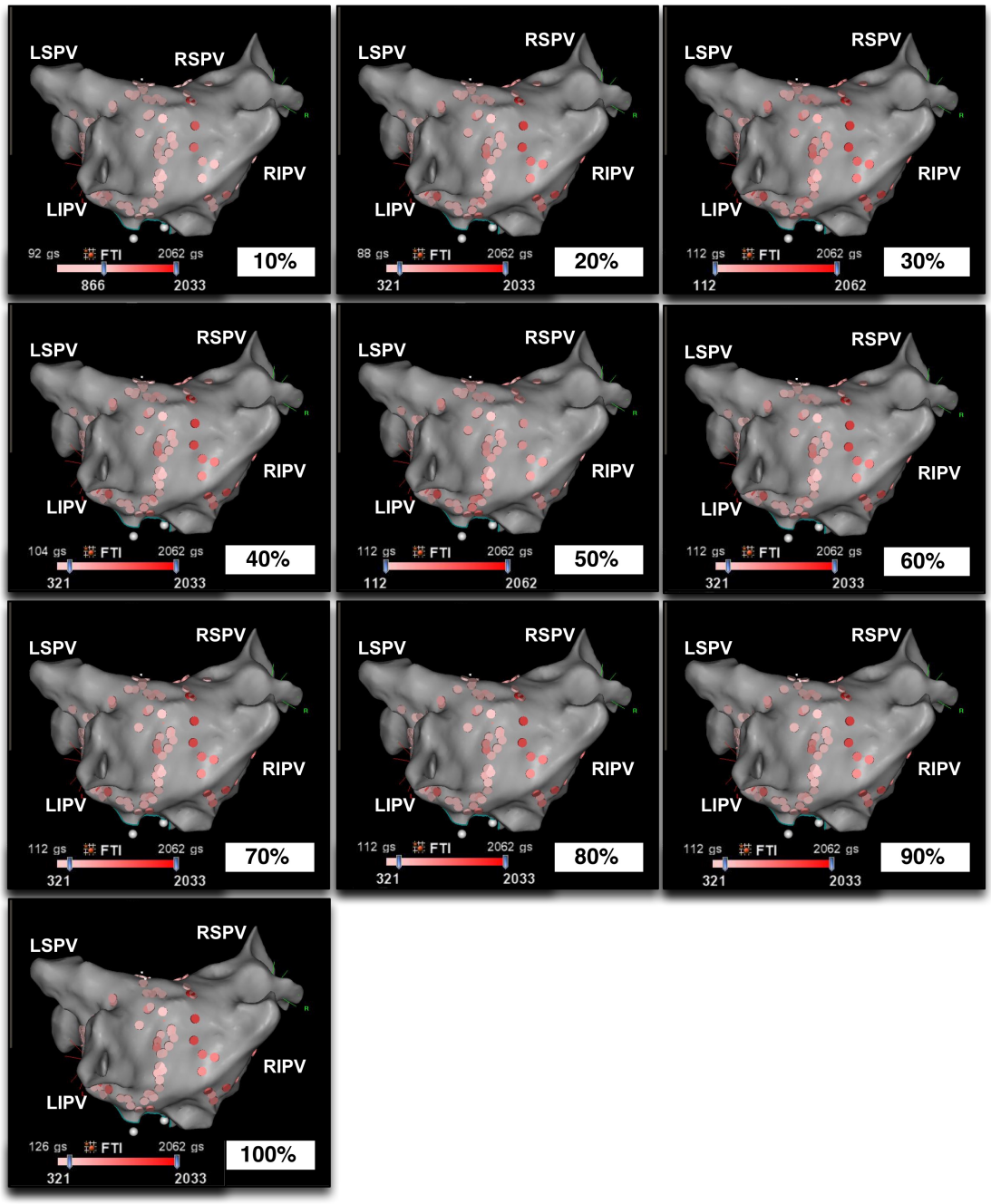

Figure 9-17. VisiTag locations with variation of 'Percentage Time'.

Colouring of tags is according to FTI (force time interval) in gram.seconds. LIPV: left inferior pulmonary vein (PV), RIPV: right inferior PV, RSPV: right superior PV, LIPV: left inferior PV.

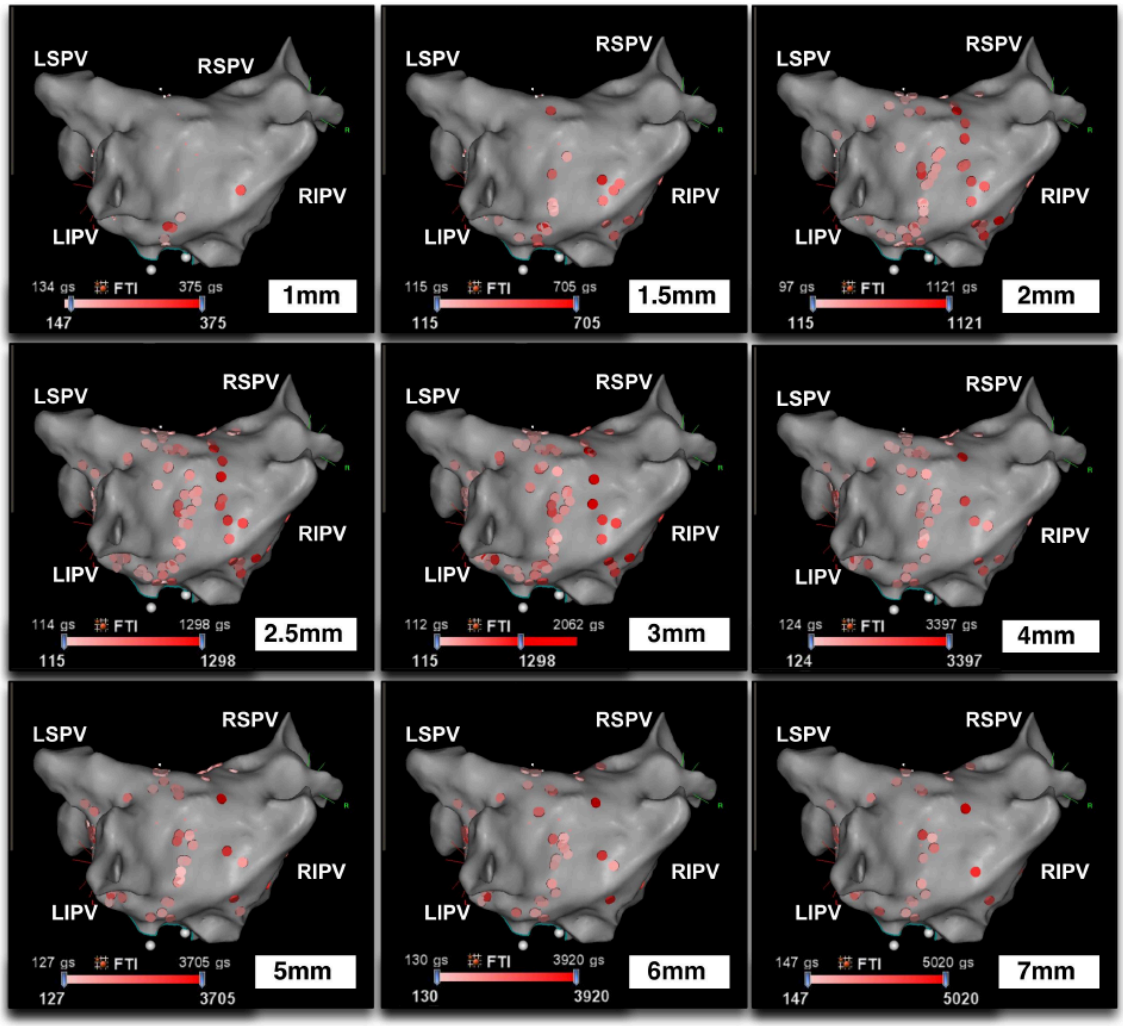

Figure 9-18. VisiTag locations with variation of ''Range' (in mm).

Colouring of tags is according to FTI (force time interval) in gram.seconds. LIPV: left inferior pulmonary vein (PV), RIPV: right inferior PV, RSPV: right superior PV, LIPV: left inferior PV.

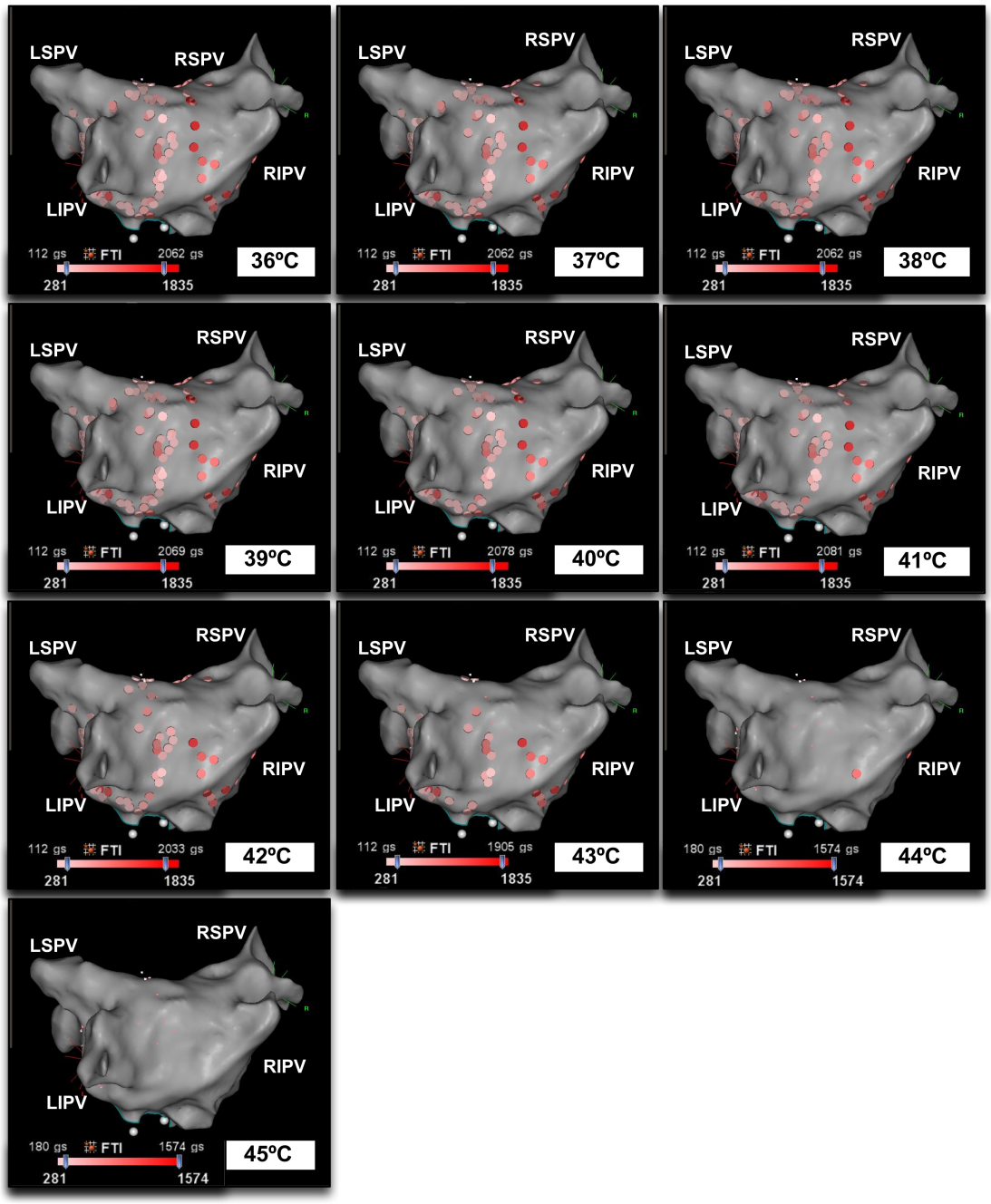

Figure 9-19. VisiTag locations with variation of 'Target Temperature' (in °C).

Colouring of tags is according to FTI (force time interval) in gram.seconds. LIPV: left inferior pulmonary vein (PV), RIPV: right inferior PV, RSPV: right superior PV, LIPV: left inferior PV.

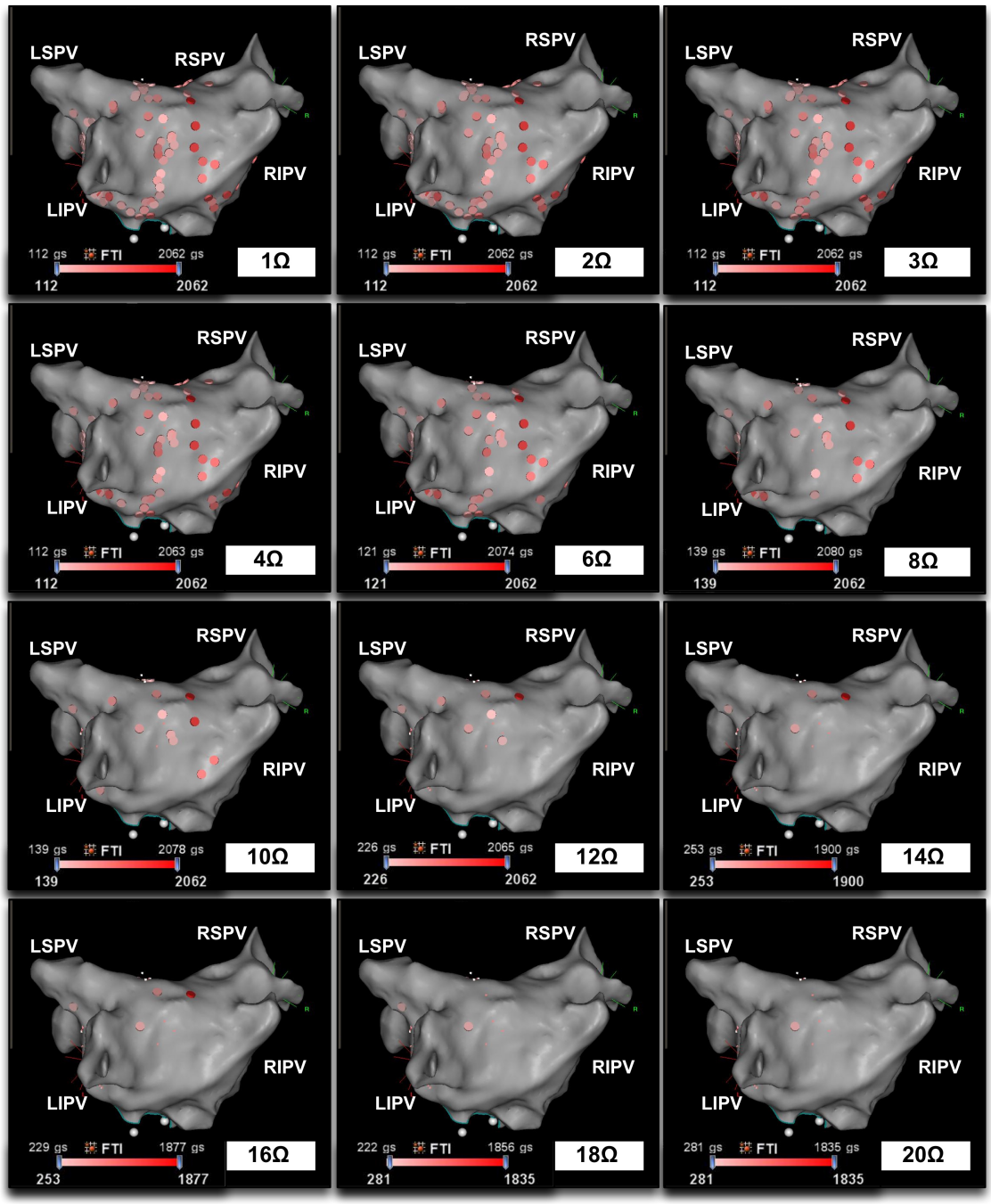

Figure 9-20. VisiTag locations with variation of 'Impedance Drop' (in ohms (Ω)).

Colouring of tags is according to FTI (force time interval) in gram.seconds. LIPV: left inferior pulmonary vein (PV), RIPV: right inferior PV, RSPV: right superior PV, LIPV: left inferior PV.

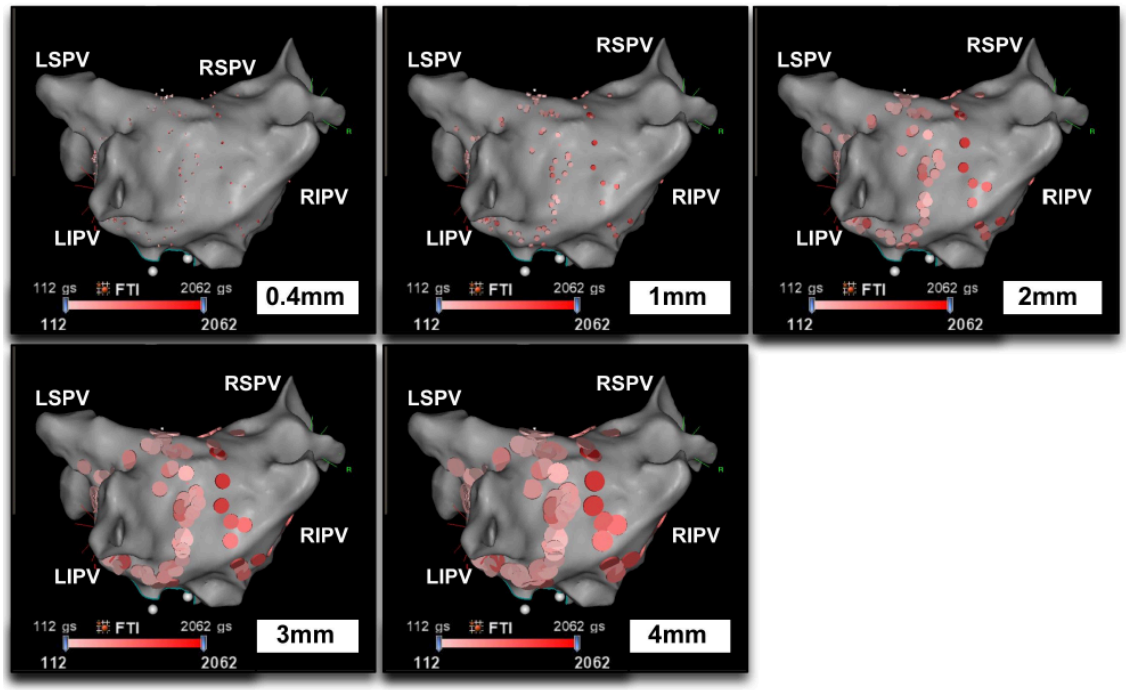

Figure 9-21. VisiTag visualisation with variation of tag size (mm).

VisiTag settings are kept at default, with only the projected size of the tag altered.

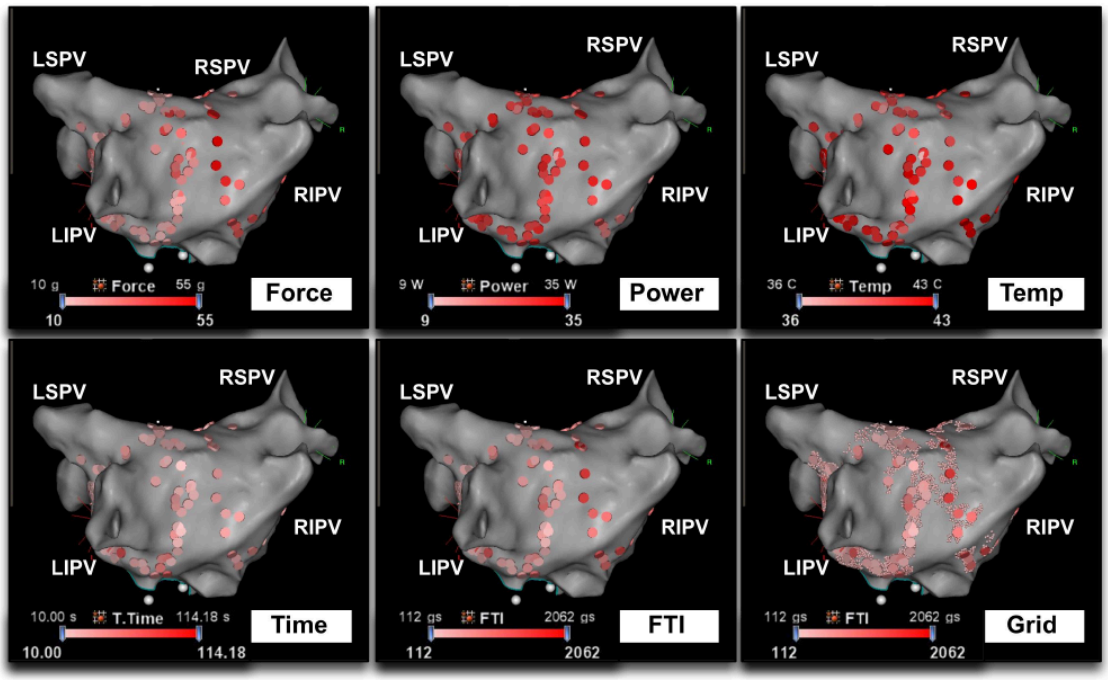

Figure 9-22. VisiTag visualisation set up.

The colouring of tags is varied according to force (in grams (G), power (in Watts (W). temperature (in °C), total time (in seconds), and force time integral (FTI, in gram.seconds). The bottom right panel demonstrates the visualisation of VisiTags alongside Grid tags.

9.9 Chapter appendix B- Matlab scripts


```
function henry_combineVisitagMRIData2
% HENRY_COMBINEVISITAGMRIDATA takes the visitag data (0/1 for each triangle
% in the shell and combines it with the MRI scar data (0/1 for each
% triangle in the shell) and outputs CSV files.
%
% Usage:
%   henry_combineVisitagMRIData
% Where:
%   There are no input or output arguments
%   Cases to be included in the programme run are hard-coded at line 40.
%   Output is to CSV files for post-processing.
%
% HENRY_COMBINEVISITAGMRIDATA completes the following actions:
%   1. Load MRI and Visitag VTK files
%   2. Locates the range, time, percent and force data in the Visitag VTK file
%   3. Locates the column of 'Any_Visitags' in the Visitag VTK file
%   4. Thresholds the MRI at 40% of SI maximum
%   5. Writes the Visitag/MRI data for individual cases to CSV files (e.g. 33SP.vtk)
%   6. Writes all the Visitag/MRI data concatenated to a single file (called rawdata.vtk)
%   7. Counts the number of visitag+/visitag-/scar+/scar- cells in the whole population
%   8. Calculates TP/FP/TN/FN values based on the above
%   9. Writes four CSV files (one for range, percent, force and time) containing:
%       [Visitag+ Visitag- MRI+ MRI- TP FN TN FP]
%       (with columns representing different values for range, percent force or time)
%
% Author: Designed by Henry Chubb, implemented by Steven Williams (2015)
% Modifications -
%   1. Threshold changed to import from "thesholds.csv": 3.3 sd from mean
%   (July 2016)
%
% Info on Code Testing:
% ------------------------------------------------------------------
% test code
% ------------------------------------------------------------------
%
% ------------------------------------------------------------------
% code
% ------------------------------------------------------------------

% define MRI data paths
baseDir = '/Volumes/Data1/Henry/ROMPA SmartTouch';

% define Visitag data paths
baseDir_visitag = [baseDir '/VisitagShells/minDist_7.5/'];

% define CMR data paths
baseDir_cmr = [baseDir '/CMRonCarto'];

meshesVisitag = nameFiles(baseDir_visitag);
meshesCmr = nameFiles(baseDir_cmr);

if numel(meshesVisitag) ~= numel(meshesCmr)
    error('HENRY_COMBINEVISITAGMRIDATA\The number of files in the MRI directory is not the same as the number of files in the Visitag directory');
end

% load the thresholds
thresholdFile = [baseDir '/Thresholds.csv'];
M = csv2cell(thresholdFile);


outputData = [];

rangeValue = [2 3 4 5 6 7]';
timeValue = [5 10 15 20 25 30]';
percentValue = [30 40 50 60 70 80]';
forceValue = [2 4 6 8 10 12 14 16 18 20]';

rangeData = zeros(numel(rangeValue), 8);
timeData = zeros(numel(timeValue), 8);
percentData = zeros(numel(percentValue), 8);
forceData = zeros(numel(forceValue), 8);

% step through each case
for iCase = 1:numel(meshesVisitag);

        % load the VTK files
        hVtk_MRI = VTKReader([baseDir_cmr '/' meshesCmr{iCase}]);
        hVtk_Visitag = VTKReader([baseDir_visitag '/' meshesVisitag{iCase}]);
        hVtk_MRI.readAllData();
        hVtk_Visitag.readAllData();

        % load the thresholds
        ind = findStr(M(:,1), meshesCmr{iCase}(1:4));
        thresh = M{ind,2};

        % perform thresholding on the MRI data
        mriFaceData = trVertToFaceData(hVtk_MRI.getTriRep, hVtk_MRI.PointData);
        mri = mriFaceData;
        mri(mriFaceData<thresh) = 0;
        mri(mriFaceData>=thresh) = 1;

        % Find the location of all the data
        fieldName = hVtk_Visitag.CellDataNames;

        range(1) = find(strcmpi(fieldName, 'range2'));
        range(2) = find(strcmpi(fieldName, 'default'));
```

```
        range(3) = find(strcmpi(fieldName, 'range4'));
        range(4) = find(strcmpi(fieldName, 'range5'));
        range(5) = find(strcmpi(fieldName, 'range6'));
        range(6) = find(strcmpi(fieldName, 'range7'));

        time(1) = find(strcmpi(fieldName, 'time5'));
        time(2) = find(strcmpi(fieldName, 'default'));
        time(3) = find(strcmpi(fieldName, 'time15'));
        time(4) = find(strcmpi(fieldName, 'time20'));
        time(5) = find(strcmpi(fieldName, 'time25'));
        time(6) = find(strcmpi(fieldName, 'time30'));

        percent(1) = find(strcmpi(fieldName, 'percent30'));
        percent(2) = find(strcmpi(fieldName, 'percent40'));
        percent(3) = find(strcmpi(fieldName, 'default'));
        percent(4) = find(strcmpi(fieldName, 'percent60'));
        percent(5) = find(strcmpi(fieldName, 'percent70'));
        percent(6) = find(strcmpi(fieldName, 'percent80'));

        force(1) = find(strcmpi(fieldName, 'force2'));
        force(2) = find(strcmpi(fieldName, 'force4'));
        force(3) = find(strcmpi(fieldName, 'force6'));
        force(4) = find(strcmpi(fieldName, 'default'));
        force(5) = find(strcmpi(fieldName, 'force10'));
        force(6) = find(strcmpi(fieldName, 'force12'));
        force(7) = find(strcmpi(fieldName, 'force14'));
        force(8) = find(strcmpi(fieldName, 'force16'));
        force(9) = find(strcmpi(fieldName, 'force18'));
        force(10) = find(strcmpi(fieldName, 'force20'));

        any_visitag = find(strcmpi(fieldName, 'ANY_VISITAGS'));
        %atRisk = numel(find(hVtk_Visitag.CellData{any_visitag})); %#ok<FNDSB>

        % Write a spreadsheet for an individual case; and concatenate with
        % the previous cases into the outputData matrix
        filename = [meshesCmr{iCase}(1:4) '.csv'];
        matVisitags = cell2mat(hVtk_Visitag.CellData);
        tempData = [matVisitags mriFaceData mri];
        caseNumber = str2double(meshesCmr{iCase}(1:2));
        caseNumbers = repmat(caseNumber, length(tempData), 1);
        outputData = [outputData; [caseNumbers tempData]];

        csvwrite(filename, tempData);
        txt = [strjoin(hVtk_Visitag.CellDataNames, ',') ',MRI,MRI-thresh'];
        inserttextintotextfile(filename, 1, txt);


end

% Write a spreadsheet of the outputData matrix
csvwrite('rawdata.csv',outputData);
txt = ['CaseNumber,' strjoin(hVtk_Visitag.CellDataNames, ',') ',MRI,MRI-thresh'];
inserttextintotextfile('rawdata.csv', 1, txt);


    function data = local_Intersection(dataset, celldata, M, colAnyVisitag)
        % dataset is the indexes into celldata
        % atrisk are the number of triangles with any visitags
        % M is the MRI data
        % colAnyVisitag indexes into celldata

        % remove any MRI data that is not within any_visitag zone
        M(colAnyVisitag==0) = [];

        for iData = 1:numel(dataset)
            V = celldata{dataset(iData)};

            % remove any Visitag data that is not within any_visitag zone
            V(colAnyVisitag==0) = [];

            %T = V & mri;
            %intersection(iData) = numel(find(T)) / atRisk; %#ok<AGROW>

            % rowData1 is [Visitag+ Visitag- MRI+ MRI-]
            rowData1 = [numel(V(V==1)) numel(V(V==0)) numel(M(M==1)) numel(M(M==0))];
            % rowData2 is [TP FN TN FP]
            rowData2 = [sum(M&V) sum(M&~V) sum(~M&~V) sum(~M&V)];

            data(iData, 1:8) = [rowData1 rowData2];
        end
    end
end
```

Published with MATLAB® R2015a

```
% HENRY_PROCESSVISITAGDATA reads all Carto3 export files, verifying
% correct labelling of the export dataset, then interrogating sites.txt to
% define VisiTag locations. A multi-dimensional vtk file is created, with
% 27 layers, each corresponding to a specific permutation of VisiTag
% threshold settings.
%
% Usage:
%   henry_processVisitagData
%
% HENRY_PROCESSVISITAGDATA completes the following actions:
%   1. Gets the full list of cases
%   2. Defines the default export settings for verification step
%   3. Loads each subject's Carto3 export datasets
%   4. Stepwise, verifies the correct labelling of the export datafile, referenced to
%   'VisiTagSettings.txt'
%   5. For each VisiTag "sites.txt", labels all triangles within the remeshed shell (MeshRM) according to
%   distance from VisiTag (minDist defined)
%   6. Creates a final dataset of "any_visitag", which is positive (1) if
%   any threshold setting is positive
%   7. Writes and labels a multidimensional .vtk file
%
% Author: Designed by Henry Chubb, implemented by Steven Williams (2016)
% Modifications -
%
% Info on Code Testing:
% ------------------------------------------------------------------
% test code
% ------------------------------------------------------------------
%
% ------------------------------------------------------------------
% code
% ------------------------------------------------------------------


% Get the list of cases
baseDir = '/Volumes/Data1/Henry/ROMPA SmartTouch'; % Henry's Hard Drive
meshesRM = nameFiles([baseDir filesep 'MeshesRM']);
numCases = numel(meshesRM);

% Define the median values
medianValues.useRespirationCompensation = 0;
medianValues.isLocationStabilityFilterEnabled = 1;
medianValues.locationStabilityThreshold = 3;
medianValues.minimalAblationTimeThreshold = 10;
medianValues.isImpedanceDropFilterEnabled = 0;
medianValues.impedanceDropThreshold = 10; %irrelevant unless ImpON
medianValues.isContactForceFilterEnabled = 1;
medianValues.contactForcePercentThreshold = 50;
medianValues.contactForceValueForPercentThreshold = 8;
medianValues.isTemperatureFilterEnabled = 0;
medianValues.temperatureThreshold = 43; %irrelevant unless TempON

% Preinitialise some variables
dataRange = [];
dataTime = [];
dataPercent = [];
dataForce = [];

% The distance between triangles and visitags
minDist = 7.5;

% Step through each case
invalidCases = false(numCases);
for iCase = 24:24%numCases
    % Check if Visitag data exists
    subFolders = nameFolds([baseDir filesep meshesRM{iCase}(1:4)]);
    initials = meshesRM{iCase}(3:4);
    tfDataExists = any(strcmpi(subFolders, initials));
    if ~tfDataExists
        continue
    else
        casePath{iCase} = [baseDir filesep meshesRM{iCase}(1:4) filesep initials]; %#ok<*SAGROW>
        expFolders = nameFolds(casePath{iCase});

        % Get a list of all data directories for a case
        for iExp = 1:numel(expFolders)
            % Go two folders further down ...
            firstSubFolder = nameFolds([baseDir filesep meshesRM{iCase}(1:4) filesep initials filesep expFolders{iExp}]); % Study 1
            secondSubFolder = nameFolds([baseDir filesep meshesRM{iCase}(1:4) filesep initials filesep expFolders{iExp} filesep firstSubFolder{1}
            dataDirectory{iExp} = [baseDir filesep meshesRM{iCase}(1:4) filesep initials filesep expFolders{iExp} filesep firstSubFolder{1}]; % Ac
            visiTagDirectory{iExp} = [baseDir filesep meshesRM{iCase}(1:4) filesep initials filesep expFolders{iExp} filesep firstSubFolder{1} fil
        end %iExp

        % Confirm all visitag settings are correct
        for iExp = 1:numel(expFolders)
            disp(['----- Checking data: ' expFolders{iExp} '-----'])
            % Load VisiTagSettings.txt
            visitagSettings = read_visitagsettings([visiTagDirectory{iExp} filesep 'VisiTagSettings.txt']);
            medianValuesTemp = medianValues;
            switch lower(expFolders{iExp}(1:3))
                case 'def'
                    % do nothing
                case 'for'
                    medianValuesTemp.contactForceValueForPercentThreshold = str2double(expFolders{iExp}(regexp(expFolders{iExp}, '\d')));
                case 'imp'
                    medianValuesTemp.isImpedanceDropFilterEnabled = 1;
```

```
            case 'per'
                medianValuesTemp.contactForcePercentThreshold = str2double(expFolders{iExp}(regexp(expFolders{iExp}, '\d')));
            case 'ran'
                medianValuesTemp.locationStabilityThreshold = str2double(expFolders{iExp}(regexp(expFolders{iExp}, '\d')));
            case 'tem'
                medianValuesTemp.isTemperatureFilterEnabled = 1;
            case 'tim'
                medianValuesTemp.minimalAblationTimeThreshold = str2double(expFolders{iExp}(regexp(expFolders{iExp}, '\d')));
            otherwise
                error('HENRY_PROCESSVISITAGDATA: Unrecognised folder name')
        end
        if visitagSettings.useRespirationCompensation ~= medianValuesTemp.useRespirationCompensation
            disp('Error: useRespirationCompensation set incorrectly');
            %invalidCases(iCase) = true;
        else
            disp(['useRespirationCompensation set to ' num2str(visitagSettings.useRespirationCompensation) ' ............. OK']);
        end
        if visitagSettings.isLocationStabilityFilterEnabled ~= medianValuesTemp.isLocationStabilityFilterEnabled
            disp('Error: isLocationStabilityFilterEnabled set incorrectly');
            invalidCases(iCase) = true;
        else
            disp(['isLocationStabilityFilterEnabled set to ' num2str(visitagSettings.isLocationStabilityFilterEnabled) ' ....... OK']);
        end
        if visitagSettings.locationStabilityThreshold ~= medianValuesTemp.locationStabilityThreshold
            disp('Error: locationStabilityThreshold set incorrectly');
            invalidCases(iCase) = true;
        else
            disp(['locationStabilityThreshold set to ' num2str(visitagSettings.locationStabilityThreshold) ' ............. OK']);
        end
        if visitagSettings.minimalAblationTimeThreshold ~= medianValuesTemp.minimalAblationTimeThreshold
            disp('Error: minimalAblationTimeThreshold set incorrectly');
            invalidCases(iCase) = true;
        else
            disp(['minimalAblationTimeThreshold set to ' num2str(visitagSettings.minimalAblationTimeThreshold) ' .......... OK']);
        end
        if visitagSettings.isImpedanceDropFilterEnabled ~= medianValuesTemp.isImpedanceDropFilterEnabled
            disp('Error: isImpedanceDropFilterEnabled set incorrectly');
            invalidCases(iCase) = true;
        else
            disp(['isImpedanceDropFilterEnabled set to ' num2str(visitagSettings.isImpedanceDropFilterEnabled) ' ........... OK']);
        end
        if visitagSettings.isImpedanceDropFilterEnabled == 1 % ImpOn, so check impedanceDropThreshold
            if visitagSettings.impedanceDropThreshold ~= medianValuesTemp.impedanceDropThreshold
                disp('Error: impedanceDropThreshold set incorrectly');
                invalidCases(iCase) = true;
            else
                disp(['... with impedanceDropThreshold set to ' num2str(visitagSettings.impedanceDropThreshold) ' ... OK']);
            end
        end
        if visitagSettings.isContactForceFilterEnabled ~= medianValuesTemp.isContactForceFilterEnabled
            disp('Error: isContactForceFilterEnabled set incorrectly');
            invalidCases(iCase) = true;
        else
            disp(['isContactForceFilterEnabled set to ' num2str(visitagSettings.isContactForceFilterEnabled) ' ............ OK']);
        end
        if visitagSettings.contactForcePercentThreshold ~= medianValuesTemp.contactForcePercentThreshold
            disp('Error: contactForcePercentThreshold set incorrectly');
            invalidCases(iCase) = true;
        else
            disp(['contactForcePercentThreshold set to ' num2str(visitagSettings.contactForcePercentThreshold) ' .......... OK']);
        end
        if visitagSettings.contactForceValueForPercentThreshold ~= medianValuesTemp.contactForceValueForPercentThreshold
            disp('Error: contactForceValueForPercentThreshold set incorrectly');
            invalidCases(iCase) = true;
        else
            disp(['contactForceValueForPercentThreshold set to ' num2str(visitagSettings.contactForceValueForPercentThreshold) ' ... OK']);
        end
        if visitagSettings.isTemperatureFilterEnabled ~= medianValuesTemp.isTemperatureFilterEnabled
            disp('Error: isTemperatureFilterEnabled set incorrectly');
            invalidCases(iCase) = true;
        else
            disp(['isTemperatureFilterEnabled set to ' num2str(visitagSettings.isTemperatureFilterEnabled) ' ............. OK']);
        end
        if visitagSettings.temperatureThreshold == 1 % TempON, so check temperatureThreshold
            if visitagSettings.temperatureThreshold ~= medianValuesTemp.temperatureThreshold
                disp('Error: temperatureThreshold set incorrectly');
                invalidCases(iCase) = true;
            else
                disp(['... with temperatureThreshold set to ' num2str(visitagSettings.useRespirationCompensation) ' ... OK']);
            end
        end
    end %iExp

    if invalidCases(iCase)
        disp(['***' casePath{iCase}(end-6:end-3) ': INVALID DATA, see above ***']);
        continue % on to the next case
    else % process this case
        % Import all data folders for a case
        hVtk = VTKReader([baseDir filesep 'meshesRM' filesep meshesRM{iCase}]);
        shell = hVtk.readAllData().getTriRep();
        textprogressbar('importing data: ');
        for iExp = 1:numel(expFolders)
            visitag{iExp} = read_visitag_sites([visiTagDirectory{iExp} filesep 'Sites.txt']);
            fieldName{iExp} = expFolders{iExp}(regexp(expFolders{iExp},'\w'));
            textprogressbar((iExp/numel(expFolders))*100);
        end %iExp
        textprogressbar(' done');
```

```
            % Label triangles within minDist of a visitag
            textprogressbar('calculating distances: ');
            cellData = zeros(length(shell.Triangulation),iExp);
            for iExp = 1:numel(expFolders)
                [~, allCentroids] = tricentroid(shell);
                dist = distBetweenPointClouds(allCentroids, visitag{iExp}(:,4:6));
                cellData(dist<minDist,iExp)=1;
                textprogressbar((iExp/numel(expFolders))*100);
            end
            textprogressbar(' done');

            % Create a dataset "any(visitag)"
            cellData(:,end+1) = any(cellData,2);
            fieldName{end+1} = 'ANY_VISITAGS';

            % Write a multidimensional VTK
            outputFileName = [casePath{iCase}(end-6:end-3) '_visitags_minDist' num2str(minDist) '.vtk'];
            op = writeTriRep2VTK(shell, [], 'outputfile', outputFileName, 'scalarnames', fieldName, 'type', 'binary', 'celldata', cellData);

            % Save the data for use in Matlab
            allData{iCase} = cellData;
            allDataNames{iCase} = fieldName;
            allDataCaseNames{iCase} = casePath{iCase}(end-6:end-3);

            % Find the location of all the data
            range2 = find(strcmpi(fieldName, 'range2'));
            range3 = find(strcmpi(fieldName, 'default'));
            range4 = find(strcmpi(fieldName, 'range4'));
            range5 = find(strcmpi(fieldName, 'range5'));
            range6 = find(strcmpi(fieldName, 'range6'));
            range7 = find(strcmpi(fieldName, 'range7'));

            time5 = find(strcmpi(fieldName, 'time5'));
            time10 = find(strcmpi(fieldName, 'default'));
            time15 = find(strcmpi(fieldName, 'time15'));
            time20 = find(strcmpi(fieldName, 'time20'));
            time25 = find(strcmpi(fieldName, 'time25'));
            time30 = find(strcmpi(fieldName, 'time30'));

            percent30 = find(strcmpi(fieldName, 'percent30'));
            percent40 = find(strcmpi(fieldName, 'percent40'));
            percent50 = find(strcmpi(fieldName, 'default'));
            percent60 = find(strcmpi(fieldName, 'percent60'));
            percent70 = find(strcmpi(fieldName, 'percent70'));
            percent80 = find(strcmpi(fieldName, 'percent80'));

            force2 = find(strcmpi(fieldName, 'force2'));
            force4 = find(strcmpi(fieldName, 'force4'));
            force6 = find(strcmpi(fieldName, 'force6'));
            force8 = find(strcmpi(fieldName, 'default'));
            force10 = find(strcmpi(fieldName, 'force10'));
            force12 = find(strcmpi(fieldName, 'force12'));
            force14 = find(strcmpi(fieldName, 'force14'));
            force16 = find(strcmpi(fieldName, 'force16'));
            force18 = find(strcmpi(fieldName, 'force18'));

            temp_dataRange = [size(visitag{range2},1); size(visitag{range3},1); size(visitag{range4},1); size(visitag{range5},1); size(visitag{ra
            temp_dataTime = [size(visitag{time5},1); size(visitag{time10},1); size(visitag{time15},1); size(visitag{time20},1); size(visitag{time
            temp_dataPercent = [size(visitag{percent30},1); size(visitag{percent40},1); size(visitag{percent50},1); size(visitag{percent60},1); s
            temp_dataForce = [size(visitag{force2},1); size(visitag{force4},1); size(visitag{force6},1); size(visitag{force8},1); size(visitag{fo

            dataRange = [dataRange temp_dataRange];
            dataTime = [dataTime temp_dataTime];
            dataPercent = [dataPercent temp_dataPercent];
            dataForce = [dataForce temp_dataForce];
        end
    end %~tfDataExists
end %iCase

dataRangeX = [2 3 4 5 6 7]';
dataTimeX = [5 10 15 20 25 30]';
dataPercentX = [30 40 50 60 70 80]';
dataForceX = [2 4 6 8 10 12 14 16 18]';
```

Published with MATLAB® R2015a

SECTION THREE: CONCLUDING REMARKS

10 CONCLUSIONS

10.1 Original Contributions

The aim of this thesis was to explore the application of CMR imaging techniques to the management of atrial arrhythmias, at three main timepoints with reference to the ablation procedure.

- **Prior to ablation**- assessment of the AF substrate
    - There are a large number of CMR-derived indices that have been proposed to be predictive of long-term outcome following catheter ablation. Most of these are likely to represent markers of LA remodelling, but some may also impact upon the procedure itself, such as pulmonary venous anatomy. However, the indices are generally time-consuming to generate, and an integrated approach has been required in order to help guide clinicians and patients in their selection of AF management strategy.
    - This thesis has independently demonstrated the utility of the assessment of LA fibrosis. LA ejection fraction and left ventricular ejection fraction trend towards significance, and in larger studies may have an additive effect in terms of improving prediction of long-term outcome. However, the impact of sphericity, LA volume and pulmonary venous anatomy could not be replicated, and these findings have important implications for centres looking to set up CMR-derived AF pre-assessment services.
- **During ablation**- first-in-man study of MR-guided ablation
    - Establishing feasibility and safety of a highly novel procedure is challenging, and the work performed in the course of this thesis has created a platform for further development of the technique. The outcome of the procedure was not compared formally to a control cohort undergoing conventionally guided AFL ablation, but the clinical outcome was clearly inferior both in terms procedural time and outcome at 3 months. However, many of the issues were demonstrated to be related to catheter reach and handling characteristics, rather than the core technology itself.
    - Clearly the field of MR-EP requires substantial time and resources to develop to the level of conventional EAM systems. Much more work is also required to maximise the benefits of working in the challenging environment, particularly substrate assessment and real-time lesion evaluation, but the study was highly informative in guiding further grant applications and development of completely new imaging platform.
- **After ablation**- cross-over study of imaging of post-ablation atrial lesions and application to the assessment of a novel objective marker of ablation energy delivery

- The reproducibility and optimisation study of post-ablation atrial scar imaging has generated a huge amount of data, and there are several key, new, messages to be drawn from the study
- Firstly, in terms of optimisation of imaging, it is clear that imaging late after gadolinium administration improves the contrast-to-noise ratio of scar to blood pool, and consequently the reproducibility of scar imaging. A half-dose of gadolinium based contrast agent should also be considered.
- The normalisation method for referencing of signal intensity has also varied widely between centres, but it is clear that some methods are superior to others. Referencing to ventricular myocardial signal intensity risks significant mis-allocation of scar and healthy myocardial populations, whilst a blood pool z-score has been demonstrated for the first time to be the superior normalisation method in terms of reproducibility of scar locations and overall distribution
- The demonstrable reproducibility of post-ablation scar imaging justifies the use of the technique in the assessment of the objective marker of ablation energy delivery, the VisiTag module. In this way it has been possible to provide for the first time an evidence base to help guide the selection of appropriate VisiTag thresholds.

10.2 Future Directions

10.2.1 Prior to ablation: MR assessment of the arrhythmia substrate

As was alluded to in the discussion of Chapter 5, the synergistic use of multiple atrial fibrosis interrogation techniques is intriguing. In this thesis, a surrogate of the different image processing techniques was used, and the main difference between the techniques is in fact the threshold level. Despite using very different SI thresholds to detect scar, and a very poor correlation in fibrosis level was observed between techniques, a significant association with late outcome was maintained. Focal and diffuse fibrosis within the atrium has been demonstrated (Dzeshka et al. 2015). It seems highly plausible that these represent different pathologies along a fibrosis spectrum, detectable at different SI thresholds, and that they may be relatively independent predictors of successful outcome following catheter ablation.

10.2.2 During ablation: MR-guided ablation procedures

In Chapter 6 it was demonstrated for the first time that it is feasible to perform a clinical ablation procedure under MR guidance, using active tracking of the ablation catheter. However, MR-guidance for relatively simple, and conventionally highly successful, ablation procedures is unlikely to yield significant improvements in terms of patient outcome or health economics. On the other hand, complex procedures for which conventional ablation methods have resulted in relatively modest success rates may be improved by the application of direct MR guidance and image. One area that is amenable to study is ventricular tachycardia, where arrhythmia substrate and lesion imaging will be much improved with a greater myocardial mass.

Figure 10-1, Figure 10-3, and Figure 10-2 demonstrate the early results of an MR-guided ablation system for the treatment of ventricular tachycardia, developed in collaboration with Imricor and Siemens Healthcare GmBH (Siemens Healthineers, Erlangen, Germany). This project is supported by a substantial grant from the Wellcome Trust and NIHR and aims to develop a platform for clinical ablation of ventricular tachycardia over the next 10 years.

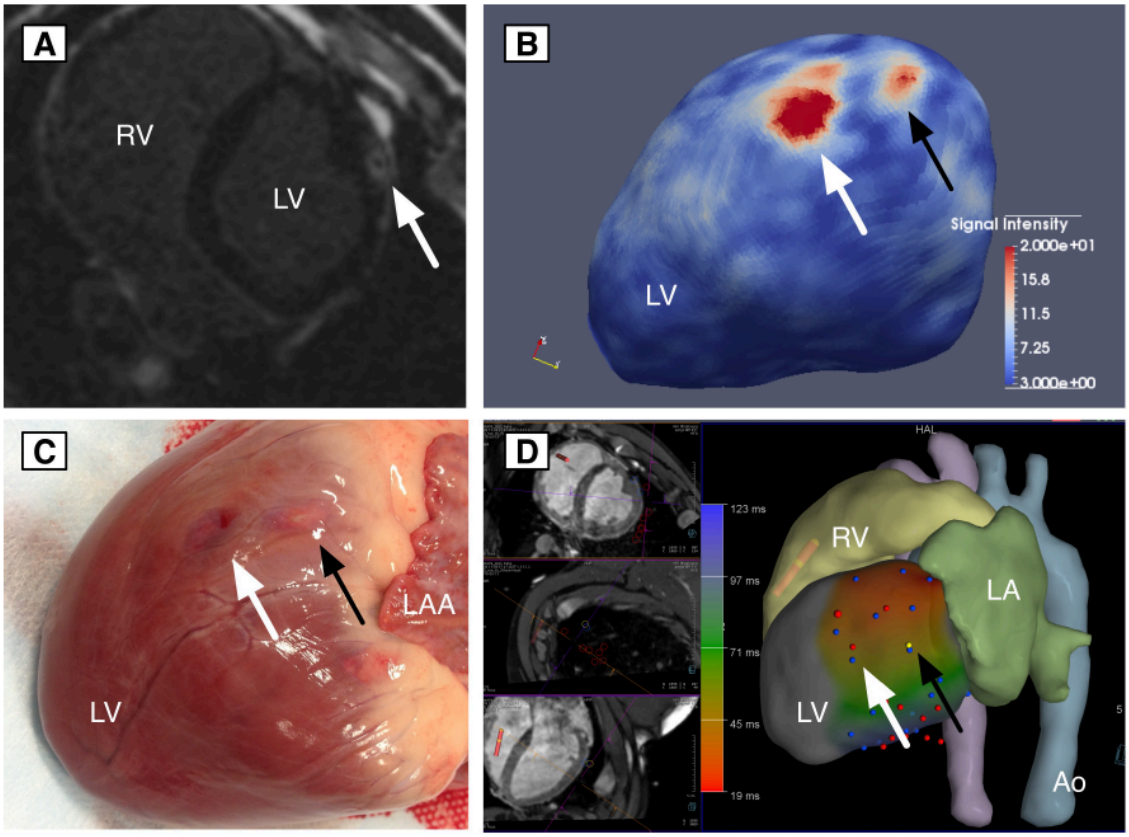

Figure 10-1. Early results of MR-guided ventricular epicardial ablation.

A: Single slice of 3D LGE acquisitions, performed at 30min post gadolinium based contrast agent administration, and approximately 1 hour post ablation. Site of ablation is indicated by arrow. Note rim of enhancement with central core of no-reflow B: Left ventricular shell (maximum intensity projection) interrogating the acquisition shown in A. Large lesion (white arrow) was formed with 60W energy for 60s, and the smaller lesion (black arrow) with 50W. C: macroscopic findings at 2 hours post ablation. D: ablation lesion locations (arrows) shown on the MR-EP guidance platform, developed in collaboration with Siemens.

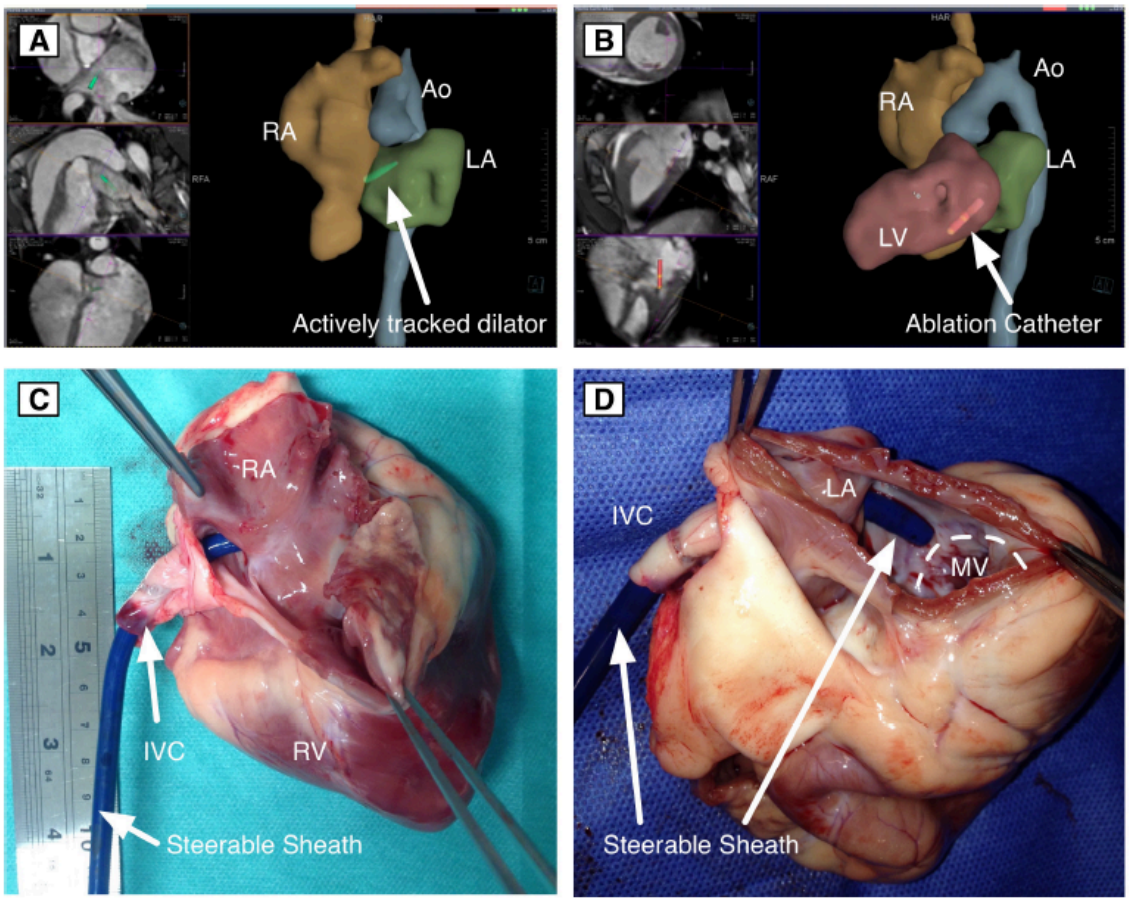

Figure 10-2. First successful MR-guided actively-tracked trans-septal puncture, in a swine model.

A: Position of actively-tracked dilator shown on multiplanar imaging and chamber shells, immediately post puncture of the atrial septum. B: anterograde access of ablation catheter to the LV immediately following trans-septal puncture. C and D: position of the steerable sheath across the atrial septum at post-mortem evaluation.

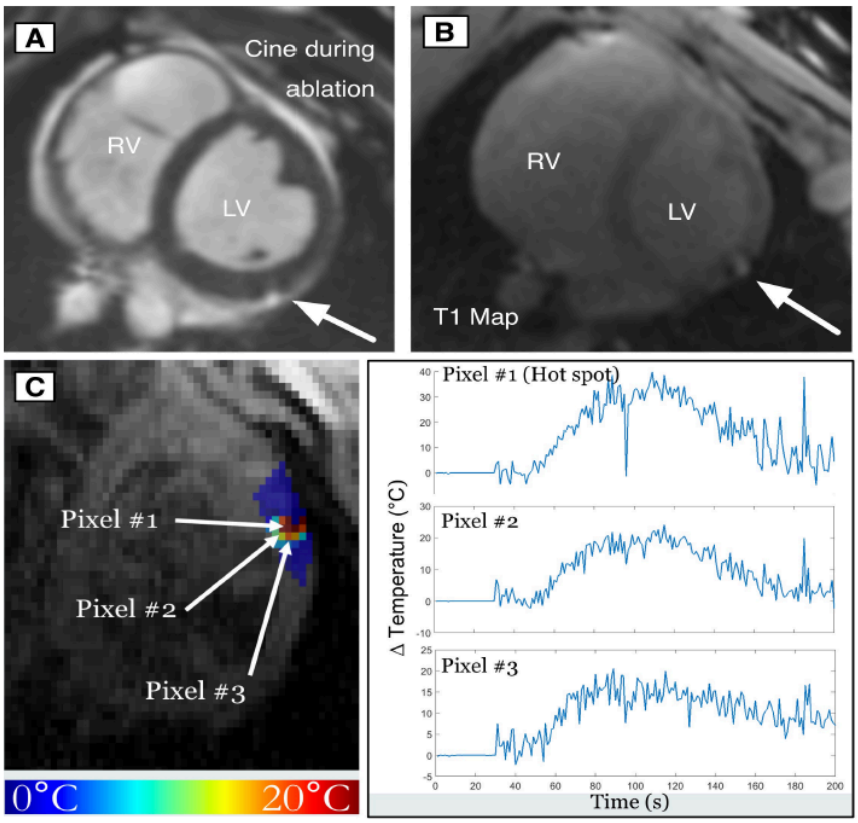

Figure 10-3. Acute and real-time MR imaging of lesion formation.

A: conventional cine imaging during RF energy delivery. Arrow indicates location of the ablation catheter, confirmed on active tracking. Note the absence of any significant interference by the RF energy source upon image acquisition. B: T1 mapping performed at seven minutes post ablation: note significant lengthening of the T_1 relaxation time at ablation location (arrow). C: Real-time MR thermometry during RF energy delivery, with highly significant temperature rise at ablation core, and much lower rises for pixels adjacent to the ablation region.

10.2.3 Post ablation: MR assessment of ablation

In Chapter 8 it was demonstrated that MR-imaging of ablation lesions in the atrium is a reproducible technique. However, the issue of thresholding of ablation lesions within the atrium remains challenging, with a broad range of signal intensities likely to represent a spectrum of scar, from dense core scar to scar borderzone. LGE imaging remains, at present, the most sensitive technique for detecting these changes in the thin-walled atrium, but an objective thresholding method would be highly desirable in order to help establish clinical and research protocols to guide the implementation of imaging of ablation lesions.

As an alternative to conventional thresholding by signal intensity cut-off, an image subtraction technique was developed in the course of this thesis. It was established in Chapter 7 that the scar: blood pool SI ratio typically rises with time following gadolinium administration (Figure 7-4), in the context of almost identical imaging parameters (only the inversion time was altered between

acquisitions in order to maintain optimal ventricular nulling). There was no observed significant trend in blood pool SI (Figure 7-6) or PAAS SI (Figure 7-7) but within patients the trend was towards a divergence of these two SIs. Therefore a technique was developed that aimed to exploit the time derivative of the signals of these structures (Figure 10-4).

The morphologically identical LGE shells were compared on a face-by-face basis. In total, three new shells per patient imaging session were derived by subtracting the local SIs: 20min minus 10min ($C_{1,2}$, and $C_{4,5}$), 30min minus 10min ($C_{1,3}$ and $C_{4,6}$), and 30min minus 20min ($C_{2,3}$ and $C_{5,6}$). It was hypothesised that a negative derived SI would be an objective indication of healthy tissue, and a positive derived SI an indication of scar tissue (Figure 10-4). However, as discussed previously, the SD of the SIs of atrial scar is proportionally large at baseline. The result of the summation (or subtraction) of two populations with means μ_1 and μ_2 and standard deviations SD_1 and SD_2 respectively is to create a scar voxel population that may have a mean (μ_1 minus μ_2) further from the mean of healthy tissue, but a larger derived standard deviation (SD_1 plus SD_2) (Figure 10-5). Consequently the technique in its simplest form does not help to inform the selection of scar.

However, the implementation of multiple acquisitions and more sophisticated image processing techniques, such as the time derivative of local signal intensity, has promise to act as a gold standard for scar detection.

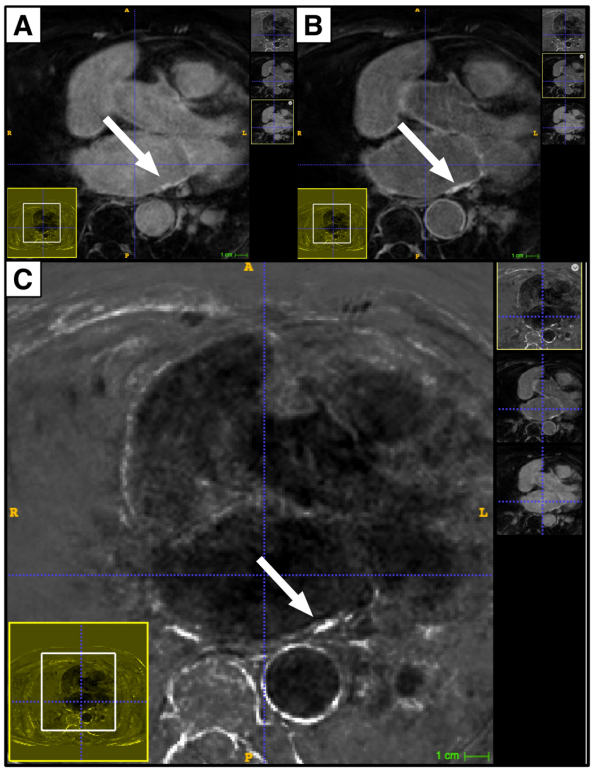

Figure 10-4 Principles of image subtraction technique.

Single representative slice of acquisition (subject 27, post-ablation scan 1) performed under standard parameters at 10min post gadolinium (A- Acq_1) and 30min post

gadolinium (B- Acq$_3$), with subtraction image ([B-A], C$_{1,3}$) shown in C. Note enhanced contrast at the core of scar in the subtraction image (white arrow), in comparison to B.

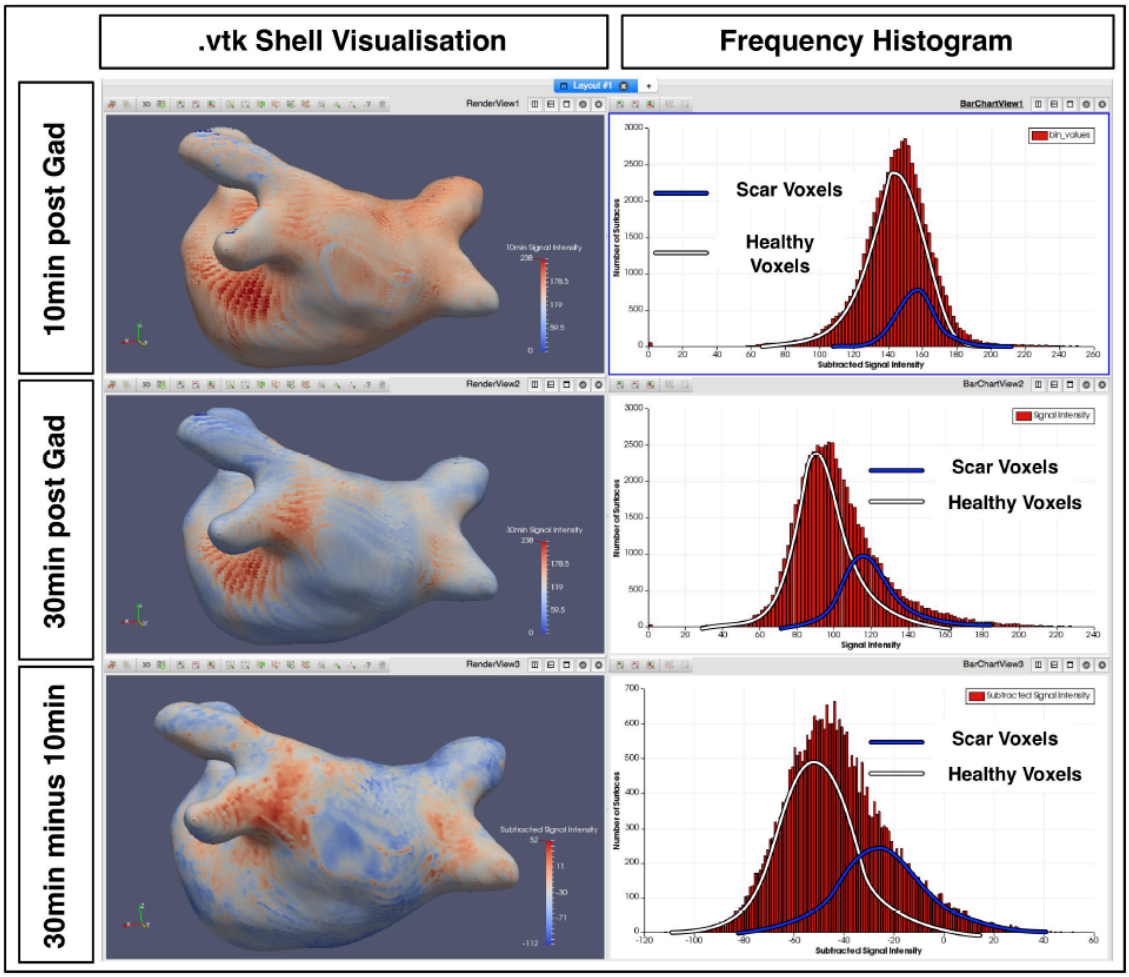

Figure 10-5. Visualisation of LA shells and subtraction shell, with associated pixel intensity frequency histograms (subject 27, scan 1).

Note in the top two rows the shift of the putative scar population (blue line) away from the healthy myocardial population (white line) with time from gadolinium administration. The subtraction shell and associated pixel intensity frequency histogram is shown in the third column. The means of the two populations (scar and healthy) are likely to have separated to a greater degree, but in the process of population subtraction, the standard deviation has increased, making thresholding of the two populations more challenging.

ACKNOWLEDGEMENTS

"*You're quite right, Mr. Hatter. I do live in a topsy-turvy world. It seems like I have to do something wrong first, in order to learn from what not to do. And then, by not doing what I'm not supposed to do, perhaps I'll be right. But I'd rather be right the first time, wouldn't you?*"
Alice, Alice's Adventures in Wonderland, Charles Lutwidge Dodgson, 1885

Throughout the course of this thesis I have been extremely grateful for the support, advice, time, dedication and wisdom of many people across the academic and clinical fields that the studies have encompassed.

Firstly, I would like to thank my supervisors, Professor Reza Razavi and Professor Mark O'Neill, without whom this would not have been possible. Professor Razavi has been steadfastly encouraging and supportive, opening avenues and new ideas, facilitating collaborations and introductions, helping to overcome hurdles when they appeared insurmountable, and unfailingly optimistic. Professor O'Neill has been indispensable for his experience and sage guidance, always available no matter how busy, helping me to say "no" on occasions, and working tirelessly to support the clinical sides of the studies.

Secondly, there is also a huge number of people who have been involved in all the projects, and particular thanks go to those who have helped me with computing and image processing problems. Dr Rashed Karim, Dr Orod Razeghi, Dr Steven Niederer, Dr Thomas Fastl, Dr Sebastien Roujol and Dr Steven Williams have all helped me on many occasions, patiently coding the many dead-ends that I have explored, as well as the work that is included in this thesis. Dr Steven Williams is also one of my research colleagues, and I would like to thank him for his guidance, as well as Dr John Whitaker, Dr James Harrison, Dr Rahul Mukherjee and many more. I have also greatly enjoyed working with several medical students and visiting clinicians and I am thankful to Shadman Aziz, Kulvinder Lal, Dr Wieland Staab and Dr Radoslaw Kiedrowicz in particular. There are many more that I should mention, some of whom are acknowledged at the end of individual chapters. However, particular mention should go to all the radiographers who were indispensable companions, not only on days when the MRI scanner was misbehaving, but also when it was not!

Finally, I would like to thank my family, including both my wife's and my parents, for their tireless support and patience, particularly towards the end of the write-up of this thesis once I had returned to full-time clinical work. My wife, Gemma, and our two children have been enormously understanding of my distractions, travels, frustrations, revisions and procrastinations and I will be forever grateful.

GRANTS, PUBLICATIONS AND PRESENTATIONS

Grants

Personalised thermal-fluid models for planning catheter ablation therapy for atrial arrhythmia". Named co-applicant. Principal Investigator (PI) Adelaide de Vecchi
EPSRC, UK (EP/P013228/1) Awarded January 2017. **£115,814**

"Pathway to the clinical acceptance of KCL catheter robot for cardiac ablation". Named co-applicant. PI Hongbin Liu.
Informatics Operations Committee, King's College London. Awarded March 2016. **£5,900**

"Magnetic Resonance Guided Ablation System for Treatment of Ventricular Tachycardia (MR-GAST-VT)". Named co-applicant, primary author of grant application. PI Prof R Razavi
Wellcome Trust and Department of Health. Awarded Oct 2015. **£1,744,455**

"Development of imaging and computational tools for improving catheter ablation treatments of atrial fibrillation". Named co-applicant, PI Oleg Aslanidi.
Cardiovascular Healthcare Technology Co-operative, National Institute for Health Research. Awarded Sept 2015. **£20,000**

Publications related to thesis

C Corrado J Whitaker, H Chubb, SE Williams, M Wright, J Gill, M O'Neill, SA Niederer. **"Predicting spiral wave stability by personalised electrophysiology models."** *Computing in Cardiology Conference (CinC), 2016 (pp229-232). IEEE*

H Chubb, SE Williams, J Whitaker, J Harrison, R Razavi, M O'Neill. **"Cardiac Electrophysiology under MRI Guidance: an emerging technology"** *Arrhythmia & Electrophysiology Review, 2017 DOI 10.15420/aer.2017:1:2*

AE Campbell-Washburn, MA Tavallaei, M Pop, EK Grant, H Chubb, K Rhode, GA Wright. **"Real-time MRI guidance of cardiac interventions"** *Journal of Magnetic Resonance Imaging 2017 May 11. DOI 10.1002/jmri.25749*

SE Williams, JL Harrison, H Chubb, J Whitaker, R Kiedrowicz, CA Rinaldi, M Cooklin, M Wright, S Niederer, M O'Neill. **"Local activation time sampling density for atrial tachycardia contact mapping: how much is enough?"** *Europace 2017. Epublished. DOI 10.1093/europace/eux037*

M Varela, R Morgan, A Theron, D Dillon-Murphy, H Chubb, J Whitaker, M Hennningsson, T Schaeffter, C Kolbitsch, O V Aslandi. "**Novel MRI Technique Enables Non-Invasive Measurement of Atrial Wall Thickness"** *IEEE Transactions on Medical Imaging 2017 (in press)*

L O'Neill, H Chubb, M O'Neill. **"Arrhythmia in Congenital Heart Disease – A Current Perspective".** *European Journal of Arrhythmia and Electrophysiology 2017. DOI 10.17925/EIAE.2016.02.01.22*

R Morgan, M Colman, H Chubb, G Seemann, O Aslanidi. **"Slow conduction in the border zones of patchy fibrosis stabilises the drivers for atrial fibrillation: Insights from multi-scale human atrial modelling"** *Frontiers in Physiology (in Press- accepted October 2016)*

H Chubb, J L Harrison, S Weiss, S Krueger, P Koken, L Ø Bloch, W Yong, G S Stenzel, S R Wedan, J L Weisz, J Gill, T Schaeffter, M D O'Neill, R Razavi. **"Development, Pre-Clinical Validation and Clinical Translation of a Cardiac Magnetic Resonance-Electrophysiology System with Active Catheter Tracking for Ablation of Cardiac Arrhythmia".** *JACC EP, 2017, 3(2) 89-103; DOI:10.1016/j.jacep.2016.07.005*

H Chubb, E Rosenthal. **"Implantable cardioverter-defibrillators in congenital heart disease".** *Herzchrittmachertherapie + Elektrophysiologie, German Journal of Cardiac Pacing and Electrophysiology, 2016;27:95-103. DOI 10.1007/s00399-016-0437-3*

C Corrado J Whitaker, H Chubb, S A Niederer**. "Personalized models of human atrial elctrophysiology derived from endocardial electrograms".** *IEEE Transactions on Biomedical Engineering, ePublished May 2016. DOI 10.1109/TBE.2016.2574619*

H Chubb, M O'Neill, E Rosenthal*.* ***"*Pacing and Defibrillators in Complex Congenital Heart Disease".** *Arrhythmia & Electrophysiology Review, 2016;5(1):57-64 DOI:10.15420/AER.2016.2.3*

J Whitaker, R Rajani, H Chubb, M Gabrawi, M Verela, M Wright, S A Niederer, M O'Neill. **"The role of myocardial wall thickness in atrial arrhythmogenesis"** *Europace. 2016 ePublished Jan 2016. Doi:10.1093/europace/euw014*

M O'Neill, H Chubb. **"Look Before You Leap: Optimizing Outcomes of Atrial Fibrillation Ablation."** *JACC Cardiovasc Imaging. 2015 9(2):149-51. PMID 26777219*

SE Williams, J Harrison, H Chubb, LO Bloch, NP Andersen, H Dam, R Karim, J Whitaker, J Gill, M Cooklin, CA Rinaldi, K Rhode, M Wright, T Schaeffter, WY Kim, H Jensen, R Razavi, MD O'Neill "**The Effect of Contact Force in Atrial Radiofrequency Ablation: Electroanatomical, CMR and Histological Assessment in a Chronic Porcine Model"** *JACC Clin. Electrophysiol. 2015;1:421–431*.

R Karim, H Chubb, W Staab, S Aziz, R J Housden, M O'Neill, R Razavi, K Rhode. **"Left Atrial Segmentation from 3D Respiratory and ECG-gated Magnetic Resonance Angiography"** *Functional Imaging and Modeling of the Heart, Lecture Notes in Computer Science, 2015;9126:155-163*

C Corrado, SE Williams, H Chubb, M O'Neill, SA Niederer. **"Personalisation of Atrial Electrophysiology Models from Decapolar Catheter Measurements."** *Functional Imaging and Modeling of the Heart, Lecture Notes in Computer Science, 2015;9126:21-28*

JL Harrison, J Whitaker, H Chubb, M O'Neill. **"Advances in CMR of Post-Ablation Atrial Injury"** *Current Cardiovascular Imaging Reports 06/2015; 8(6)*

H Chubb, J Whitaker, SE Williams, CE Head, NAY Chung, M Wright, M O'Neill . **"Pathophysiology and Management of Arrhythmias Associated with Atrial Septal Defect and Patent Foramen Ovale"** *Arrhythmia and Electrophysiology Review, 2014;3(3):168-72. PMID 26835086*

H Chubb, SE Williams, M Wright, E Rosenthal, M O'Neill. **"Tachyarrhythmias and catheter ablation in adult congenital heart disease"** *Expert Rev Cardiovasc Ther. 2014 Jun;12(6):751-70. PMID 24783943*

Oral presentations related to thesis (first author only)

H Chubb. **"How to set-up an MR-guided electrophysiology laboratory".** *Invited speaker at SCMR, Washington DC, USA, 02/02/2017*

H Chubb, J Harrison, S Williams, J Whitaker, M Wright, T Schaeffter, M Cooklin, R Razavi, M O'Neill. **"Hepatic capsule enhancement is commonly seen during MR-guided ablation of atrial flutter: a mechanistic insight into procedural pain."** *Cardiostim, Nice, France, 10/06/2016*

H Chubb, S Aziz, J Harrison, S Williams, J Whitaker, M Wright, T Schaeffter, R Razavi, M O'Neill. **"Optimisation of Late Gadolinium Enhanced (LGE) Imaging of Atrial Ablation Scar"** *Heart Rhythm UK Congress, Birmingham, 6/10/2015*

H Chubb, J Harrison, S Williams, J Whitaker, S Weiss, S Krueger, G Stenzel, T Schaeffter, R Razavi, M O'Neill. **"Feasibility of fully MR-guided ablation with active tracking: from pre-clinical to clinical application"** *Heart Rhythm UK Congress, Birmingham, 5/10/2015*

- *Shortlisted for Young Investigators Award.*

H Chubb, J Harrison, S Williams, J Whitaker, S Weiss, S Krueger, G Stenzel, T Schaeffter, R Razavi, M O'Neill. **"Feasibility of fully MR-guided ablation with active tracking: from pre-clinical to clinical application"** *EHRA Europace, Milan, Italy, 22/06/2015*

H Chubb, J Harrison, S Williams, J Whitaker, S Weiss, S Krueger, G Stenzel, T Schaeffter, R Razavi, M O'Neill. **"Pre-clinical validation and clinical translation of MR-guided ablation system with active tracking"** *Heart Rhythm Society, Boston, USA, 13-16th May 2015*

H Chubb. **" MR-Guided treatment of Arrhythmias".** Invited speaker at SCMR, 5th February 2015, Nice, France

H Chubb, J Harrison, S Williams, S Weiss, S Krueger, J Weisz, G Stenzel, M O'Neill, T Scaeffter, R Razavi. **" The feasibility of MR-guided ablation of atrial flutter using active catheter tracking".** *iMRI, Leipzig, Germany, 10/10/2014*

H Chubb, SE Williams, N Linton, J Harrison, K Rhode, J Gill, A Rinaldi, M Cooklin, MJ Wright, R Razavi, E Rosenthal, M O'Neill **"Dot Mapping: a Novel Technique for Dual Electrophysiological Dataset Representation Facilitates Recognition of Complex Intra-Atrial Re-Entrant Tachycardia Substrate in Repaired Adult Congenital Heart Disease"** *Heart Rhythm UK Congress, Birmingham, 8/10/2014*

H Chubb, SE Williams, J Harrison, C Sohns, J Gill, A Rinaldi, M Cooklin, T Schaeffter, MJ Wright, R Razavi, M O'Neill **"Does a Greater Contact Force Create More Scar? A Quantification of the Relationship between Late Gadolinium Enhancement on Cardiac MR Imaging and Catheter Contact on AF Ablation"** *Heart Rhythm UK Congress, Birmingham, 6/10/2014*

H Chubb, J Harrison, S Williams, S Weiss, S Krueger, J Weisz, G Stenzel, M O'Neill, T Schaeffter, R Razavi. **"First in Man: Real-time magnetic resonance-guided ablation of typical right atrial flutter using active catheter tracking".** *Medical Engineering Centres Annual Meeting and Bioengineering14, Imperial College, London, 11/09/2014*

Poster presentations (first author only)

H Chubb, R Karim, SE Williams, J Harrison, J Whitaker, M Wright, T Schaeffter, R Razavi, M O'Neill. **"Does higher contact force impair lesion formation at the cavotricuspid isthmus? Insights from MR-guided ablation of atrial flutter"** *Cardiostim, Nice, France, 8th-10th June 2016*

H Chubb, R Karim, SE Williams, J Harrison, J Whitaker, M Wright, T Schaeffter, R Razavi, M O'Neill. **"Does higher contact force impair lesion formation at the cavotricuspid isthmus? Insights from MR-guided ablation of atrial flutter"** *Heart Rhythm Society, Boston, USA, 3rd-7th May 2016*

H Chubb, SE Williams, J Harrison, J Whitaker, M Wright, T Schaeffter, R Razavi, M O'Neill. **"Hepatic capsule enhancement is commonly seen during MR-guided ablation of atrial flutter: a mechanistic insight into procedural pain."** *Heart Rhythm Society, Boston, USA, 3rd-7th May 2016*

H Chubb, K Lal, K Kouranloo, J Whitaker, M Wright, R Kiedrowicz, R Razavi, R Karim, M O'Neill**. "Atrial sphericity and left atrial fibrosis are independent tools for characterisation of atrial structural remodelling"** *EHRA Europace, Milan, Italy, 21st-24th June, 2015*

H Chubb, R Karim, J Harrison, S Aziz, J Whitaker, SE Williams, M Wright, R Kiedrowicz, R Razavi, M O'Neill. **"MRI-assessed scar following atrial ablation is a reproducible finding between repeat scans"** *EHRA Europace, Milan, Italy, 21st-24th June, 2015*

H Chubb, K Lal, J Whitaker, M Henningsson, M Wright, R Kiedrowicz, R Razavi, R Karim, M O'Neill. "**Left atrial segmentation may be automated using a novel ECG and respiratory gated magnetic resonance angiography (gMRA) technique"** *EHRA Europace, Milan, Italy, 21st-24th June, 2015*

H Chubb, SE Williams, J Whitaker, S Aziz, J Harrison, M Wright, R Kiedrowicz, T Schaeffter, R Razavi, M O'Neill. **"Optimisation of late gadolinium enhanced (LGE) MR imaging of atrial ablation scar: contrast-to-noise ratio improves with time"** *EHRA Europace, Milan, Italy, 21st-24th June, 2015*

H Chubb, J Harrison, S Williams, S Weiss, S Krueger, J Weisz, G Stenzel, M O'Neill, T Scaeffter, R Razavi**. "First in Man: Real-time magnetic resonance-guided ablation of typical right atrial flutter using active catheter tracking"**
Heart Rhythm UK Congress, Birmingham, 8/10/2014

H Chubb, SE Williams, N Linton, J Harrison, K Rhode, J Gill, A Rinaldi, M Cooklin, MJ Wright, R Razavi, E Rosenthal, M O'Neill **"The use of a simultaneous multi-modality representation of complex arrhythmias in congenital heart disease"** *Medical Engineering Centres Annual Meeting and Bioengineering14, Imperial College, London, 10/09/2014*

H Chubb, SE Williams, J Harrison, C Sohns, J Gill, A Rinaldi, M Cooklin, T Schaeffter, MJ Wright, R Razavi, M O'Neill **"The correlation of late gadolinium enhancement with contact force: what is the effect of contact force on late scar formation?"** *Medical Engineering Centres Annual Meeting and Bioengineering14, Imperial College, London, 10/09/2014*

H Chubb, SE Williams, N Linton, J Harrison, K Rhode, J Gill, A Rinaldi, M Cooklin, MJ Wright, R Razavi, E Rosenthal, M O'Neill **"Dot Mapping: a Novel Technique for Dual Electrophysiological Dataset Representation Facilitates Recognition of Complex Intra-Atrial Re-Entrant Tachycardia Substrate in Repaired Adult Congenital Heart Disease"** *Cardiostim, Nice, France, 17-20th June 2014*

H Chubb, SE Williams, J Harrison, C Sohns, J Gill, A Rinaldi, M Cooklin, T Schaeffter, MJ Wright, R Razavi, M O'Neill **"Does a Greater Contact Force Create More Scar? A Quantification of the Relationship between Late Gadolinium Enhancement on Cardiac MR Imaging and Catheter Contact on AF Ablation."** *Cardiostim, Nice, France, 17-20th June 2014*

H Chubb, SE Williams, N Linton, J Harrison, K Rhode, J Gill, A Rinaldi, M Cooklin, MJ Wright, R Razavi, E Rosenthal, M O'Neill **"A Novel Technique for Dual Electrophysiological Dataset Representation: Dot Mapping Facilitates Recognition of Complex Intra-Atrial Re-entrant Tachycardia substrate in repaired Adult Congenital Heart Disease"** *Heart Rhythm Society, San Francisco, USA, 7th-10th May 2014*

H Chubb, SE Williams, J Harrison, L Bloch, H Dam, R Karim, T Schaeffter, MJ Wright, R Razavi, M **O'Neill "Use of Pace-Capture to assess a linear lesion: a CMR-Voltage analysis in a pig recovery model of Chronic Ablation Injury"** *Heart Rhythm Society, San Francisco, USA, 7th-10th May 2014*

H Chubb, SE Williams, J Harrison, C Sohns, J Gill, A Rinaldi, M Cooklin, T Schaeffter, MJ Wright, R Razavi, M O'Neill **"Quantitative Cardiac Magnetic Resonance analysis of the Relationship between Contact Force and Scar Formation after catheter ablation of Atrial Fibrillation"** *Heart Rhythm Society, San Francisco, USA, 7th-10th May 2014*

REFERENCES

Afzal, Muhammad R, Jawaria Chatta, Anweshan Samanta, Salman Waheed, Morteza Mahmoudi, Rachel Vukas, Sampath Gunda, Madhu Reddy, Buddhadeb Dawn, and Dhanunjaya Lakkireddy. 2015. "Use of Contact Force Sensing Technology During Radiofrequency Ablation Reduces Recurrence of Atrial Fibrillation: A Systematic Review and Meta-Analysis." *Heart Rhythm* 12 (9): 1990–96. doi:10.1016/j.hrthm.2015.06.026.

Akkaya, Mehmet, Koji Higuchi, Matthias Koopmann, Nathan Burgon, Ercan Erdogan, Kavitha Damal, Eugene Kholmovski, Chris McGann, and Nassir F Marrouche. 2013. "Relationship between Left Atrial Tissue Structural Remodelling Detected Using Late Gadolinium Enhancement MRI and Left Ventricular Hypertrophy in Patients with Atrial Fibrillation." *Europace* 15 (12): 1725–32. doi:10.1093/europace/eut147.

Akkaya, Mehmet, Koji Higuchi, Matthias Koopmann, Kavitha Damal, Nathan S Burgon, Eugene Kholmovski, Chris McGann, and Nassir Marrouche. 2013. "Higher Degree of Left Atrial Structural Remodeling in Patients with Atrial Fibrillation and Left Ventricular Systolic Dysfunction." *Journal of Cardiovascular Electrophysiology* 24 (5): 485–91. doi:10.1111/jce.12090.

Akoum, Nazem, Genaro Fernandez, Brent Wilson, Christopher Mcgann, Eugene Kholmovski, and Nassir Marrouche. 2013. "Association of Atrial Fibrosis Quantified Using LGE-MRI with Atrial Appendage Thrombus and Spontaneous Contrast on Transesophageal Echocardiography in Patients with Atrial Fibrillation." *Journal of Cardiovascular Electrophysiology* 24 (10): 1104–9. doi:10.1111/jce.12199.

Akoum, Nazem, Christopher McGann, Gaston Vergara, Troy Badger, Ravi Ranjan, Christian Mahnkopf, Eugene Kholmovski, Rob Macleod, and Nassir Marrouche. 2012. "Atrial Fibrosis Quantified Using Late Gadolinium Enhancement MRI Is Associated with Sinus Node Dysfunction Requiring Pacemaker Implant." *Journal of Cardiovascular Electrophysiology* 23 (1): 44–50. doi:10.1111/j.1540-8167.2011.02140.x.

Akoum, Nazem, David Wilber, Gerhard Hindricks, Pierre Jais, Josh Cates, Francis Marchlinski, Eugene Kholmovski, et al. 2015. "MRI Assessment of Ablation-Induced Scarring in Atrial Fibrillation: Analysis from the DECAAF Study." *Journal of Cardiovascular Electrophysiology* 26: 473–80. doi:10.1111/jce.12650.

Aliot, Etienne M., William G. Stevenson, Jesus M. Ma Almendral-Garrote, Frank Bogun, C. Hugh Calkins, Etienne Delacretaz, Paolo Della Bella, et al. 2009. "EHRA/HRS Expert Consensus on Catheter Ablation of Ventricular Arrhythmias: Developed in a Partnership with the European Heart Rhythm Association (EHRA), a Registered Branch of the European Society of Cardiology (ESC), and the Heart Rhythm Society (HRS); I." *Europace* 11 (6): 771–817. doi:10.1093/europace/eup098.

Andreu, David, Antonio Berruezo, José T Ortiz-Pérez, Etelvino Silva, Lluis Mont, Roger Borràs, Teresa María de Caralt, et al. 2011. "Integration of 3D Electroanatomic Maps and Magnetic Resonance

Scar Characterization into the Navigation System to Guide Ventricular Tachycardia Ablation." *Circulation. Arrhythmia and Electrophysiology* 4 (5): 674–83. doi:10.1161/CIRCEP.111.961946.

Andreu, David, Federico Gomez-Pulido, Mireia Calvo, Alicia Carlosena-Remírez, Felipe Bisbal, Roger Borras, Eva Benito, et al. 2016. "Contact Force Threshold for Permanent Lesion Formation in Atrial Fibrillation Ablation: A Cardiac Magnetic Resonance-Based Study to Detect Ablation Gaps." *Heart Rhythm* 13 (1): 37–45. doi:10.1016/j.hrthm.2015.08.010.

Arujuna, Aruna, Rashed Karim, Dennis Caulfield, Benjamin Knowles, Kawal Rhode, Tobias Schaeffter, Bernet Kato, et al. 2012. "Acute Pulmonary Vein Isolation Is Achieved by a Combination of Reversible and Irreversible Atrial Injury After Catheter Ablation: Evidence From Magnetic Resonance Imaging." *Circulation: Arrhythmia and Electrophysiology* 5 (4): 691–700. doi:10.1161/CIRCEP.111.966523.

Ashikaga, Hiroshi, Hermenegild Arevalo, Fijoy Vadakkumpadan, Robert C. Blake, Jason D. Bayer, Saman Nazarian, M. Muz Zviman, et al. 2013. "Feasibility of Image-Based Simulation to Estimate Ablation Target in Human Ventricular Arrhythmia." *Heart Rhythm* 10 (8): 1109–16. doi:10.1016/j.hrthm.2013.04.015.

Ashikaga, Hiroshi, Tetsuo Sasano, Jun Dong, M Muz Zviman, Robert Evers, Bruce Hopenfeld, Valeria Castro, et al. 2007. "Magnetic Resonance-Based Anatomical Analysis of Scar-Related Ventricular Tachycardia: Implications for Catheter Ablation." *Circulation Research* 101 (9): 939–47. doi:10.1161/CIRCRESAHA.107.158980.

Atalar, Ergin. 1999. "Safe Coaxial Cables." *Proceedings of the 7th Annual Meeting of ISMRM, Philadelphia.*, 1006.

Badger, Troy J, Marcos Daccarett, Nazem W Akoum, Yaw a Adjei-Poku, Nathan S Burgon, Thomas S Haslam, Saul Kalvaitis, et al. 2010. "Evaluation of Left Atrial Lesions after Initial and Repeat Atrial Fibrillation Ablation: Lessons Learned from Delayed-Enhancement MRI in Repeat Ablation Procedures." *Circulation. Arrhythmia and Electrophysiology* 3 (3): 249–59. doi:10.1161/CIRCEP.109.868356.

Badger, Troy J, Robert S Oakes, Marcos Daccarett, Nathan S Burgon, Nazem Akoum, Eric N Fish, Joshua J E Blauer, et al. 2009. "Temporal Left Atrial Lesion Formation after Ablation of Atrial Fibrillation." *Heart Rhythm* 6 (2): 161–68. doi:10.1016/j.hrthm.2008.10.042.

Baldinger, Samuel H., Jason S. Chinitz, Sunil Kapur, Saurabh Kumar, Chirag R. Barbhaiya, Akira Fujii, Jorge Romero, et al. 2016. "Recurrence of Atrial Arrhythmias Despite Persistent Pulmonary Vein Isolation After Catheter Ablation for Atrial Fibrillation." *JACC: Clinical Electrophysiology* 2 (6). Journal of the American College of Cardiology: 723–31. doi:10.1016/j.jacep.2016.05.013.

Balk, Ethan M, Ann C Garlitski, Alawi a Alsheikh-Ali, Teruhiko Terasawa, Mei Chung, and Stanley Ip. 2010. "Predictors of Atrial Fibrillation Recurrence after Radiofrequency Catheter Ablation: A Systematic Review." *Journal of Cardiovascular Electrophysiology* 21 (11): 1208–16. doi:10.1111/j.1540-8167.2010.01798.x.

Bastani, Hamid, Nikola Drca, Per Insulander, Jonas Schwieler, Frieder Braunschweig, Göran Kennebäck, Bita Sadigh, Jari Tapanainen, and Mats Jensen-Urstad. 2013. "Cryothermal vs. Radiofrequency Ablation as Atrial Flutter Therapy: A Randomized Comparison." *Europace* 15 (3): 420–28. doi:10.1093/europace/eus261.

Beinart, Roy, Irfan M. Khurram, Songtao Liu, Hirad Yarmohammadi, Henry R. Halperin, David A. Bluemke, Neville Gai, et al. 2013. "Cardiac Magnetic Resonance T1 Mapping of Left Atrial Myocardium." *Heart Rhythm* 10 (9): 1325–31. doi:10.1016/j.hrthm.2013.05.003.

Bellenger, N G, L C Davies, J M Francis, a J Coats, and D J Pennell. 2000. "Reduction in Sample Size for Studies of Remodeling in Heart Failure by the Use of Cardiovascular Magnetic Resonance." *Journal of Cardiovascular Magnetic Resonance* 2 (4): 271–78. doi:10.3109/10976640009148691.

Benjamin, Emelia J., Daniel Levy, Sonya M. Vaziri, Ralph B. D'Agostino, Albert J. Belanger, and Philip A. Wolf. 1994. "Independent Risk Factors for Atrial Fibrillation in a Population-Based Cohort The Framingham Heart Study." *JAMA : The Journal of the American Medical Association* 271 (11): 840–44. doi:10.1001/jama.1994.03510350050036.

Berruezo, Antonio, David Tamborero, Lluis Mont, Begona Benito, Jose Maria Tolosana, Marta Sitges, Barbara Vidal, et al. 2007. "Pre-Procedural Predictors of Atrial Fibrillation Recurrence after Circumferential Pulmonary Vein Ablation." *European Heart Journal* 28 (7): 836–41. doi:10.1093/eurheartj/ehm027.

Bhagirath, P., M. van der Graaf, R. Karim, K. Rhode, C. Piorkowski, R. Razavi, J. Schwitter, and M. Gotte. 2015. "Interventional Cardiac Magnetic Resonance Imaging in Electrophysiology: Advances Toward Clinical Translation." *Circulation: Arrhythmia and Electrophysiology* 8: 203–11. doi:10.1161/CIRCEP.114.002371.

Bisbal, Felipe, Esther Guiu, Pilar Cabanas-Grandío, Antonio Berruezo, Susana Prat-Gonzalez, Bárbara Vidal, Cesar Garrido, et al. 2014. "CMR-Guided Approach to Localize and Ablate Gaps in Repeat AF Ablation Procedure." *JACC. Cardiovascular Imaging* 7 (7): 653–63. doi:10.1016/j.jcmg.2014.01.014.

Bisbal, Felipe, Esther Guiu, Naiara Calvo, David Marin, Antonio Berruezo, Elena Arbelo, José Ortiz-Pérez, et al. 2013. "Left Atrial Sphericity: A New Method to Assess Atrial Remodeling. Impact on the Outcome of Atrial Fibrillation Ablation." *Journal of Cardiovascular Electrophysiology* 24 (7): 752–59. doi:10.1111/jce.12116.

Bjørnerud, Atle. 2008. *The Physics of Magnetic Resonance Imaging FYS-KJM 4740*. Oslo: University of Oslo.

Bois, Delafield Du, and Eugene F Du Bois. 1916. "Clinical Calorimetry: Tenth Paper a Formula to Estimate the Approximate Surface Area If Height and Weight Be Known." *Archives of Internal Medicine* 17 (6): 863–71.

Buch, Eric, Michael Share, Roderick Tung, Peyman Benharash, Parikshit Sharma, Jayanthi Koneru, Ravi Mandapati, Kenneth A. Ellenbogen, and Kalyanam Shivkumar. 2016. "Long-Term Clinical Outcomes of Focal Impulse and Rotor Modulation for Treatment of Atrial Fibrillation: A Multicenter Experience." *Heart Rhythm* 13 (3): 636–41. doi:10.1016/j.hrthm.2015.10.031.

Cabrera, José Angel, Damian Sánchez-Quintana, Jerónimo Farré, José Manuel Rubio, and Yen Ho Siew. 2005. "The Inferior Right Atrial Isthmus: Further Architectural Insights for Current and Coming Ablation Technologies." *Journal of Cardiovascular Electrophysiology* 16 (4): 402–8. doi:10.1046/j.1540-8167.2005.40709.x.

Calkins, H., K. H. Kuck, R. Cappato, J. Brugada, A. J. Camm, S.-A. Chen, H. J. G. Crijns, et al. 2012. "2012

HRS/EHRA/ECAS Expert Consensus Statement on Catheter and Surgical Ablation of Atrial Fibrillation: Recommendations for Patient Selection, Procedural Techniques, Patient Management and Follow-Up, Definitions, Endpoints, and Research Trial Design." *Europace* 14 (4): 528–606. doi:10.1093/europace/eus027.

Camm, John, Paulus Kirchhof, Gregory Y H Lip, Ulrich Schotten, Irene Savelieva, Sabine Ernst, Isabelle C Van Gelder, et al. 2010. "Guidelines for the Management of Atrial Fibrillation: The Task Force for the Management of Atrial Fibrillation of the European Society of Cardiology (ESC)." *European Heart Journal* 31 (19): 2369–2429. doi:10.1093/eurheartj/ehq278.

Cappato, Riccardo, Silvia Negroni, Domenico Pecora, Stefano Bentivegna, Pier Paolo Lupo, Adriana Carolei, Cristina Esposito, Francesco Furlanello, and Luigi De Ambroggi. 2003. "Prospective Assessment of Late Conduction Recurrence across Radiofrequency Lesions Producing Electrical Disconnection at the Pulmonary Vein Ostium in Patients with Atrial Fibrillation." *Circulation* 108 (13): 1599–1604. doi:10.1161/01.CIR.0000091081.19465.F1.

Carbucicchio, Corrado, Nadeem Ahmad Raja, Luigi Di Biase, Valeria Volpe, Antonio Dello Russo, Chintan Trivedi, Stefano Bartoletti, et al. 2013. "High-Density Substrate-Guided Ventricular Tachycardia Ablation: Role of Activation Mapping in an Attempt to Improve Procedural Effectiveness." *Heart Rhythm* 10 (12): 1850–58. doi:10.1016/j.hrthm.2013.09.059.

Carlsson, Jörg, Sinisa Miketic, Jürgen Windeler, Alessandro Cuneo, Sebastian Haun, Stefan Micus, Sabine Walter, and Ulrich Tebbe. 2003. "Randomized Trial of Rate-Control versus Rhythm-Control in Persistent Atrial Fibrillation." *Journal of the American College of Cardiology* 41 (10): 1690–96. doi:10.1016/S0735-1097(03)00332-2.

Celik, Haydar, Venkat Ramanan, Jennifer Barry, Sudip Ghate, Vivian Leber, Samuel Oduneye, Yiping Gu, et al. 2014. "Intrinsic Contrast for Characterization of Acute Radiofrequency Ablation Lesions." *Circulation. Arrhythmia and Electrophysiology* 7 (4): 718–27. doi:10.1161/CIRCEP.113.001163.

Charlson, Mary E., Peter Pompei, Kathy L. Ales, and C. Ronald MacKenzie. 1987. "A New Method of Classifying Prognostic Comorbidity in Longitudinal Studies: Development and Validation." *Journal of Chronic Diseases* 40 (5): 373–83. doi:10.1016/0021-9681(87)90171-8.

Chubb, H., J. Harrison, S. E. Williams, S. Weiss, S. Krueger, K. Rhode, M. O'Neill, T. Schaeffter, and R. Razavi. 2014. "First in Man: Real-Time Magnetic Resonance-Guided Ablation of Typical Right Atrial Flutter Using Active Catheter Tracking [Abstr]." *Europace* 16 (suppl 3): iii25-iii25. doi:10.1093/europace/euu242.7.

Chubb, H, S E Williams, M Wright, E Rosenthal, and M O'Neill. 2014. "Tachyarrhythmias and Catheter Ablation in Adult Congenital Heart Disease." *Expert Review of Cardiovascular Therapy* 12 (6). Informa UK, Ltd. London: 751–70. doi:10.1586/14779072.2014.914434.

Chubb, Henry, James L. Harrison, Steffen Weiss, Sascha Krueger, Peter Koken, Lars Ø Bloch, Won Yong Kim, et al. 2017. "Development, Pre-Clinical Validation, and Clinical Translation of a Cardiac Magnetic Resonance–Electrophysiology System With Active Catheter Tracking for Ablation of Cardiac Arrhythmia." *JACC: Clinical Electrophysiology* 3 (2): 89–103. doi:10.1016/j.jacep.2016.07.005.

Chugh, Aman, Rakesh Latchamsetty, Hakan Oral, Darryl Elmouchi, David Tschopp, Scott Reich, Petar

Igic, et al. 2006. “Characteristics of Cavotricuspid Isthmus-Dependent Atrial Flutter after Left Atrial Ablation of Atrial Fibrillation.” *Circulation* 113 (5): 609–15. doi:10.1161/CIRCULATIONAHA.105.580936.

Cochet, Hubert, Yuki Komatsu, Frederic Sacher, Amir Sherwan Jadidi, Daniel Scherr, Matthieu Riffaud, Nicolas Derval, et al. 2013. “Integration of Merged Delayed-Enhanced Magnetic Resonance Imaging and Multidetector Computed Tomography for the Guidance of Ventricular Tachycardia Ablation: A Pilot Study.” *Journal of Cardiovascular Electrophysiology* 24 (4): 419–26. doi:10.1111/jce.12052.

Cochet, Hubert, Amaury Mouries, Hubert Nivet, Frederic Sacher, Nicolas Derval, Arnaud Denis, Mathilde Merle, et al. 2015. “Age, Atrial Fibrillation, and Structural Heart Disease Are the Main Determinants of Left Atrial Fibrosis Detected by Delayed-Enhanced Magnetic Resonance Imaging in a General Cardiology Population.” *Journal of Cardiovascular Electrophysiology* 26 (5): 484–92. doi:10.1111/jce.12651.

Corley, Scott D, Andrew E Epstein, John P DiMarco, Michael J Domanski, Nancy Geller, H Leon Greene, Richard a Josephson, et al. 2004. “Relationships between Sinus Rhythm, Treatment, and Survival in the Atrial Fibrillation Follow-Up Investigation of Rhythm Management (AFFIRM) Study.” *Circulation* 109 (12): 1509–13. doi:10.1161/01.CIR.0000121736.16643.11.

Cosedis Nielsen, Jens, Arne Johannessen, Pekka Raatikainen, Gerhard Hindricks, Håkan Walfridsson, Ole Kongstad, Steen Pehrson, et al. 2012. “Radiofrequency Ablation as Initial Therapy in Paroxysmal Atrial Fibrillation.” *The New England Journal of Medicine* 367 (17): 1587–95. doi:10.1056/NEJMoa1113566.

Costa, Francisco Moscoso, Antonio Miguel Ferreira, Silvia Oliveira, Pedro Galvao Santos, Anai Durazzo, Pedro Carmo, Katya Reis Santos, et al. 2015. “Left Atrial Volume Is More Important than the Type of Atrial Fibrillation in Predicting the Long-Term Success of Catheter Ablation.” *International Journal of Cardiology* 184 (1): 56–61. doi:10.1016/j.ijcard.2015.01.060.

Crum, William R., Oscar Camara, and Derek L G Hill. 2006. “Generalized Overlap Measures for Evaluation and Validation in Medical Image Analysis.” *IEEE Transactions on Medical Imaging* 25 (11): 1451–61. doi:10.1109/TMI.2006.880587.

Dabir, Darius, Nicholas Child, Ashwin Kalra, Islam Z Mahmoud, Toby Rogers, Rolf Gebker, Ananth Kidambi, et al. 2014. “Age-Gender Normal Values of Native and Post-Contrast Myocardial T1 Relaxation Times (Lambda) on 1.5T and 3T Using MOLLI: A Multicenter, Single Vendor Cardiovascular Magnetic Resonance Study.” *Journal of Cardiovascular Magnetic Resonance* 16 (Suppl 1): P23. doi:10.1186/1532-429X-16-S1-P23.

Daccarett, Marcos, Chris J McGann, Nazem W Akoum, Rob S MacLeod, and Nassir F Marrouche. 2011. “MRI of the Left Atrium: Predicting Clinical Outcomes in Patients with Atrial Fibrillation.” *Expert Review of Cardiovascular Therapy* 9 (1): 105–11. doi:10.1586/erc.10.177.

Das, Moloy, Jonathan J. Loveday, Gareth J. Wynn, Sean Gomes, Yawer Saeed, Laura J. Bonnett, Johan E.P. Waktare, et al. 2016. “Ablation Index, a Novel Marker of Ablation Lesion Quality: Prediction of Pulmonary Vein Reconnection at Repeat Electrophysiology Study and Regional Differences in Target Values.” *Europace*, no. September: euw105. doi:10.1093/europace/euw105.

Denton, E R, L I Sonoda, D Rueckert, S C Rankin, C Hayes, M O Leach, D L Hill, and D J Hawkes. 1999.

"Comparison and Evaluation of Rigid, Affine, and Nonrigid Registration of Breast MR Images." *Journal of Computer Assisted Tomography* 23 (5): 800–805.

Dickfeld, Timm, Ritsushi Kato, Menekem Zviman, Saman Nazarian, Jun Dong, Hiroshi Ashikaga, Albert C Lardo, Ronald D Berger, Hugh Calkins, and Henry Halperin. 2007. "Characterization of Acute and Subacute Radiofrequency Ablation Lesions with Nonenhanced Magnetic Resonance Imaging." *Heart Rhythm* 4 (2): 208–14. doi:10.1016/j.hrthm.2006.10.019.

Dietrich, Olaf, José G Raya, Scott B Reeder, Maximilian F Reiser, and Stefan O Schoenberg. 2007. "Measurement of Signal-to-Noise Ratios in MR Images: Influence of Multichannel Coils, Parallel Imaging, and Reconstruction Filters." *Journal of Magnetic Resonance Imaging : JMRI* 26 (2): 375–85. doi:10.1002/jmri.20969.

Dodson, John A., Tomas G. Neilan, Ravi V. Shah, Hoshang Farhad, Ron Blankstein, Michael Steigner, Gregory F. Michaud, et al. 2014. "Left Atrial Passive Emptying Function Determined by Cardiac Magnetic Resonance Predicts Atrial Fibrillation Recurrence after Pulmonary Vein Isolation." *Circulation: Cardiovascular Imaging* 7 (4): 586–92. doi:10.1161/CIRCIMAGING.113.001472.

Dukkipati, Srinivas R., Richard Mallozzi, Ehud J. Schmidt, Godtfred Holmvang, Andre D'Avila, Renee Guhde, Robert D. Darrow, et al. 2008. "Electroanatomic Mapping of the Left Ventricle in a Porcine Model of Chronic Myocardial Infarction With Magnetic Resonance-Based Catheter Tracking." *Circulation* 118 (8): 853–62. doi:10.1161/CIRCULATIONAHA.107.738229.

Dumoulin, C L, S P Souza, and R D Darrow. 1993. "Real-Time Position Monitoring of Invasive Devices Using Magnetic Resonance." *Magnetic Resonance in Medicine* 29 (3): 411–15. doi:10.1002/mrm.1910290322.

Dumoulin, Charles L., Richard P. Mallozzi, Robert D. Darrow, and Ehud J. Schmidt. 2010. "Phase-Field Dithering for Active Catheter Tracking." *Magnetic Resonance in Medicine* 63 (5): 1398–1403. doi:10.1002/mrm.22297.

Dzeshka, Mikhail S., Gregory Y H Lip, Viktor Snezhitskiy, and Eduard Shantsila. 2015. "Cardiac Fibrosis in Patients With Atrial Fibrillation: Mechanisms and Clinical Implications." *Journal of the American College of Cardiology* 66 (8). Journal of the American College of Cardiology: 943–59. doi:10.1016/j.jacc.2015.06.1313.

Eckstein, Jens, Sander Verheule, Natasja M de Groot, Natasja de Groot, Maurits Allessie, and Ulrich Schotten. 2008. "Mechanisms of Perpetuation of Atrial Fibrillation in Chronically Dilated Atria." *Progress in Biophysics and Molecular Biology* 97 (2–3): 435–51. doi:10.1016/j.pbiomolbio.2008.02.019.

Eitel, Charlotte, and et al. 2012. "Electrophysiology Study Guided by Real-Time Magnetic Resonance Imaging." *European Heart Journal* 33 (15): 1975. doi:10.1093/eurheartj/ehr414.

Ellis, Keith, Oussama Wazni, Nassir Marrouche, David Martin, Marc Gillinov, Patrick McCarthy, Eduardo B. Saad, et al. 2007. "Incidence of Atrial Fibrillation Post-Cavotricuspid Isthmus Ablation in Patients with Typical Atrial Flutter: Left-Atrial Size as an Independent Predictor of Atrial Fibrillation Recurrence." *Journal of Cardiovascular Electrophysiology* 18 (8). Blackwell Publishing Inc: 799–802. doi:10.1111/j.1540-8167.2007.00885.x.

Faustino, Massimiliano, Carmine Pizzi, Tullio Agricola, Borejda Xhyheri, Grazia Maria Costa, Maria Elena Flacco, Lorenzo Capasso, et al. 2015. "Stepwise Ablation Approach versus Pulmonary

Vein Isolation in Patients with Paroxysmal Atrial Fibrillation: Randomized Controlled Trial." *Heart Rhythm* 12 (9): 1907–15. doi:10.1016/j.hrthm.2015.06.009.

Fernández-Armenta, Juan, Antonio Berruezo, David Andreu, Oscar Camara, Etelvino Silva, Luis Serra, Valeria Barbarito, et al. 2013. "Three-Dimensional Architecture of Scar and Conducting Channels Based on High Resolution Ce-CMR Insights for Ventricular Tachycardia Ablation." *Circulation. Arrhythmia and Electrophysiology* 6 (3): 528–37. doi:10.1103/PhysRevLett.110.233602.

Fischer, Stefan E., Samuel A. Wickline, and Christine H. Lorenz. 1999. "Novel Real-Time R-Wave Detection Algorithm Based on the Vectorcardiogram for Accurate Gated Magnetic Resonance Acquisitions." *Magnetic Resonance in Medicine* 42 (2): 361–70. doi:10.1002/(SICI)1522-2594(199908)42:2<361::AID-MRM18>3.0.CO;2-9.

Flett, Andrew S., Jonathan Hasleton, Christopher Cook, Derek Hausenloy, Giovanni Quarta, Cono Ariti, Vivek Muthurangu, and James C. Moon. 2011. "Evaluation of Techniques for the Quantification of Myocardial Scar of Differing Etiology Using Cardiac Magnetic Resonance." *JACC: Cardiovascular Imaging* 4 (2). Elsevier Inc.: 150–56. doi:10.1016/j.jcmg.2010.11.015.

Fujiwara, Ryudo, Kimitake Imamura, Yoichi Kijima, Tomoya Masano, Ryoji Nagoshi, Amane Kohzuki, Hiroyuki Shibata, et al. 2016. "The Importance of Catheter Stability Evaluated by VisitagTM during Pulmonary Vein Isolation." *Journal of Interventional Cardiac Electrophysiology* 46 (2). Journal of Interventional Cardiac Electrophysiology: 161–66. doi:10.1007/s10840-016-0103-z.

Fukumoto, Kotaro, Mohammadali Habibi, Esra Gucuk Ipek, Irfan M Khurram, Stefan L Zimmerman, Vadim Zipunnikov, David D Spragg, et al. 2015. "Comparison of Preexisting and Ablation-Induced Late Gadolinium Enhancement on Left Atrial Magnetic Resonance Imaging." *Heart Rhythm* 12 (4): 668–72. doi:10.1016/j.hrthm.2014.12.021.

Fukumoto, Kotaro, Mohammadali Habibi, Esra Gucuk Ipek, Sohail Zahid, Irfan M. Khurram, Stefan L. Zimmerman, Vadim Zipunnikov, et al. 2016. "Association of Left Atrial Local Conduction Velocity with Late Gadolinium Enhancement on Cardiac Magnetic Resonance in Patients with Atrial Fibrillation." *Circulation: Arrhythmia and Electrophysiology* 9 (3): 1–7. doi:10.1161/CIRCEP.115.002897.

Ganesan, Anand N., Joseph B. Selvanayagam, Rajiv Mahajan, Suchi Grover, Sachin Nayyar, Anthony G. Brooks, John Finnie, et al. 2012. "Mapping and Ablation of the Pulmonary Veins and Cavo-Tricuspid Isthmus with a Magnetic Resonance Imaging-Compatible Externally Irrigated Ablation Catheter and Integrated Electrophysiology System." *Circulation: Arrhythmia and Electrophysiology* 5 (6): 1136–42. doi:10.1161/CIRCEP.112.974436.

Ganesan, Anand N, Nicholas J Shipp, Anthony G Brooks, Pawel Kuklik, Dennis H Lau, Han S Lim, Thomas Sullivan, Kurt C Roberts-Thomson, and Prashanthan Sanders. 2013. "Long-Term Outcomes of Catheter Ablation of Atrial Fibrillation: A Systematic Review and Meta-Analysis." *Journal of the American Heart Association* 2 (2): e004549. doi:10.1161/JAHA.112.004549.

Gianni, Carola, Sanghamitra Mohanty, Luigi Di Biase, Tamara Metz, Chintan Trivedi, Yalcin Gokoglan, Mahmut F. Gunes, et al. 2016. "Acute and Early Outcomes of Focal Impulse and Rotor Modulation (FIRM)-Guided Rotors-Only Ablation in Patients with Nonparoxysmal Atrial

Fibrillation." *Heart Rhythm* 13 (4): 830–35. doi:10.1016/j.hrthm.2015.12.028.

Goldfarb, James W., Sheeba Arnold, and Marguerite Roth. 2009. "Gadolinium Pharmacokinetics of Chronic Myocardial Infarcts: Implications for Late Gadolinium-Enhanced Infarct Imaging." *Journal of Magnetic Resonance Imaging* 30 (4): 763–70. doi:10.1002/jmri.21901.

Graf, Hansjörg, Ulrike A Lauer, and Fritz Schick. 2006. "Eddy-Current Induction in Extended Metallic Parts as a Source of Considerable Torsional Moment." *Journal of Magnetic Resonance Imaging : JMRI* 23 (4): 585–90. doi:10.1002/jmri.20539.

Groarke, John D, Alfonso H Waller, Tomas S Vita, Gregory F Michaud, Marcelo F Di Carli, Ron Blankstein, Raymond Y Kwong, and Michael Steigner. 2014. "Feasibility Study of Electrocardiographic and Respiratory Gated, Gadolinium Enhanced Magnetic Resonance Angiography of Pulmonary Veins and the Impact of Heart Rate and Rhythm on Study Quality." *Journal of Cardiovascular Magnetic Resonance* 16 (1): 43. doi:10.1186/1532-429X-16-43.

Grothoff, Matthias, Christopher Piorkowski, Charlotte Eitel, Thomas Gaspar, Lukas Lehmkuhl, Christian Lücke, Janine Hoffmann, et al. 2014. "MR Imaging-Guided Electrophysiological Ablation Studies in Humans with Passive Catheter Tracking: Initial Results." *Radiology* 271 (3): 695–702. doi:10.1148/radiol.13122671.

Guillem, Mariá S., Andreu M. Climent, Miguel Rodrigo, Francisco Fernández-Aviles, Felipe Atienza, and Omer Berenfeld. 2016. "Presence and Stability of Rotors in Atrial Fibrillation: Evidence and Therapeutic Implications." *Cardiovascular Research* 109 (4): 480–92. doi:10.1093/cvr/cvw011.

Habibi, Mohammadali, Joao A C Lima, Esra Gucuk Ipek, Stefan L Zimmerman, Vadim Zipunnikov, David Spragg, Hiroshi Ashikaga, et al. 2016. "The Association of Baseline Left Atrial Structure and Function Measured with Cardiac Magnetic Resonance and Pulmonary Vein Isolation Outcome in Patients with Drug-Refractory Atrial Fibrillation." *Heart Rhythm*. doi:10.1016/j.hrthm.2016.01.016.

Habibi, Mohammadali, Joao A C Lima, Irfan M. Khurram, Stefan L. Zimmerman, Vadim Zipunnikov, Kotaro Fukumoto, David Spragg, et al. 2015. "Association of Left Atrial Function and Left Atrial Enhancement in Patients with Atrial Fibrillation Cardiac Magnetic Resonance Study." *Circulation: Cardiovascular Imaging* 8 (2). doi:10.1161/CIRCIMAGING.114.002769.

Haïssaguerre, Michel, Pierre Jaïs, Dipen C. Shah, Atsushi Takahashi, Mélèze Hocini, Gilles Quiniou, Stéphane Garrigue, Alain Le Mouroux, Philippe Le Métayer, and Jacques Clémenty. 1998. "Spontaneous Initiation of Atrial Fibrillation by Ectopic Beats Originating in the Pulmonary Veins." *New England Journal of Medicine* 339 (10): 659–66. doi:10.1056/NEJM199809033391003.

Haissaguerre, Michel, Frank I Marcus, Bruno Fischer, and Jacques Clémenty. 1994. "Radiofrequency Catheter Ablation in Unusual Mechanisms of Atrial Fibrillation:." *Journal of Cardiovascular Electrophysiology* 5 (9). Blackwell Publishing Ltd: 743–51. doi:10.1111/j.1540-8167.1994.tb01197.x.

Halbfass, P. M., M. Mitlacher, O. Turschner, J. Brachmann, and C. Mahnkopf. 2015. "Lesion Formation after Pulmonary Vein Isolation Using the Advance Cryoballoon and the Standard Cryoballoon: Lessons Learned from Late Gadolinium Enhancement Magnetic Resonance Imaging." *Europace*

17 (4): 566–73. doi:10.1093/europace/euu260.

Haldar, Shouvik, Julian W E Jarman, Sandeep Panikker, David G Jones, Tushar Salukhe, Dhiraj Gupta, Gareth Wynn, Wajid Hussain, Vias Markides, and Tom Wong. 2013. "Contact Force Sensing Technology Identifies Sites of Inadequate Contact and Reduces Acute Pulmonary Vein Reconnection: A Prospective Case Control Study." *International Journal of Cardiology* 168 (2). Elsevier Ireland Ltd: 1160–66. doi:10.1016/j.ijcard.2012.11.072.

Hall, Burr, Vinodh Jeevanantham, Rochelle Simon, John Filippone, Gabriel Vorobiof, and James Daubert. 2006. "Variation in Left Atrial Transmural Wall Thickness at Sites Commonly Targeted for Ablation of Atrial Fibrillation." *Journal of Interventional Cardiac Electrophysiology* 17 (2). Kluwer Academic Publishers-Plenum Publishers: 127–32. doi:10.1007/s10840-006-9052-2.

Harrison, J L, C Sohns, N. W. Linton, R. Karim, S. E. Williams, K. S. Rhode, J. Gill, et al. 2015. "Repeat Left Atrial Catheter Ablation: Cardiac Magnetic Resonance Prediction of Endocardial Voltage and Gaps in Ablation Lesion Sets." *Circulation: Arrhythmia and Electrophysiology* 8 (2): 270–78. doi:10.1161/CIRCEP.114.002066.

Harrison, J L, John Whitaker, Henry Chubb, Steven E. Williams, Matthew Wright, Reza S. Razavi, and Mark D. O'Neill. 2015. "Advances in CMR of Post-Ablation Atrial Injury." *Current Cardiovascular Imaging Reports* 8 (6): 22. doi:10.1007/s12410-015-9336-y.

Harrison, James L. 2014. "Cardiac Magnetic Resonance in Catheter Ablation of Atrial Arrhythmias : Characterisation of Substrate and Guidance of Therapy."

Harrison, James L, Henrik K Jensen, Sarah A Peel, Amedeo Chiribiri, Anne K Grøndal, Lars Ø Bloch, Steen F Pedersen, et al. 2014. "Cardiac Magnetic Resonance and Electroanatomical Mapping of Acute and Chronic Atrial Ablation Injury: A Histological Validation Study." *European Heart Journal* 35 (January): 1486–95. doi:10.1093/eurheartj/eht560.

Hashemi, Ray H., William G. Bradley, and Christopher J. Lisanti. 2010. *MRI: The Basics*. 3rd Revise. Lippincott Williams and Wilkins.

Hauser, Thomas H, Vidal Essebag, Ferdinando Baldessin, Seth McClennen, Susan B Yeon, Warren J Manning, and Mark E Josephson. 2015. "Prognostic Value of Pulmonary Vein Size in Prediction of Atrial Fibrillation Recurrence after Pulmonary Vein Isolation: A Cardiovascular Magnetic Resonance Study." *Journal of Cardiovascular Magnetic Resonance* 17 (1): 49. doi:10.1186/s12968-015-0151-z.

Heinrich, Mattias P., Ivor J A Simpson, BartLomiej W. Papiez, Sir Michael Brady, and Julia A. Schnabel. 2016. "Deformable Image Registration by Combining Uncertainty Estimates from Supervoxel Belief Propagation." *Medical Image Analysis* 27: 57–71. doi:10.1016/j.media.2015.09.005.

Higuchi, Koji, Mehmet Akkaya, Matthias Koopmann, Joshua J E Blauer, Nathan S Burgon, Kavitha Damal, Ravi Ranjan, Eugene Kholmovski, Rob S Macleod, and Nassir F Marrouche. 2013. "The Effect of Fat Pad Modification during Ablation of Atrial Fibrillation: Late Gadolinium Enhancement MRI Analysis." *Pacing and Clinical Electrophysiology : PACE* 36 (4): 467–76. doi:10.1111/pace.12084.

Hilbert, Sebastian, Philipp Sommer, Matthias Gutberlet, Thomas Gaspar, Borek Foldyna, Christopher Piorkowski, Steffen Weiss, et al. 2015. "Real-Time Magnetic Resonance-Guided Ablation of Typical Right Atrial Flutter Using a Combination of Active Catheter Tracking and Passive

Catheter Visualization in Man : Initial Results from a Consecutive Patient Series." *Europace* 18 (4): 572–77. doi:10.1093/europace/euv249.

Hoffmann, B. A., A. Koops, T. Rostock, K. Mullerleile, D. Steven, R. Karst, M. U. Steinke, et al. 2010. "Interactive Real-Time Mapping and Catheter Ablation of the Cavotricuspid Isthmus Guided by Magnetic Resonance Imaging in a Porcine Model." *European Heart Journal* 31 (4): 450–56. doi:10.1093/eurheartj/ehp460.

Huang, Jin Long, Ching Tai Tai, Yenn Jiang Lin, Kwo Chang Ueng, Bien Hsien Huang, Kun Tai Lee, Satoshi Higa, et al. 2008. "Right Atrial Substrate Properties Associated with Age in Patients with Typical Atrial Flutter." *Heart Rhythm* 5 (8): 1144–51. doi:10.1016/j.hrthm.2008.05.009.

Hunter, Ross J, Daniel a Jones, Redha Boubertakh, Louisa C Malcolme-Lawes, Prapa Kanagaratnam, Christoph F Juli, D Wyn Davies, et al. 2013. "Diagnostic Accuracy of Cardiac Magnetic Resonance Imaging in the Detection and Characterization of Left Atrial Catheter Ablation Lesions: A Multicenter Experience." *Journal of Cardiovascular Electrophysiology* 24 (4): 396–403. doi:10.1111/jce.12063.

Ipek, Esra Gucuk, and Saman Nazarian. 2015. "Safety of Implanted Cardiac Devices in an MRI Environment." *Current Cardiology Reports* 17 (7): 1–6. doi:10.1007/s11886-015-0605-9.

Issa, Ziad F., John M. Miller, and Douglas P. Zipes. 2012. *Clinical Arrhythmology and Electrophysiology: A Companion to Braunwald's Heart Disease*. Saunders; 2nd edition.

Issa, Ziad F., John M. Miller, Douglas P. Zipes, Ziad F. Issa, John M. Miller, and Douglas P. Zipes. 2012. "Chapter 12 – Typical Atrial Flutter." In *Clinical Arrhythmology and Electrophysiology: A Companion to Braunwald's Heart Disease*, 239–59. doi:10.1016/B978-1-4557-1274-8.00012-9.

Jacobs, Victoria, Heidi T. May, Tami L. Bair, Brian G. Crandall, Michael Cutler, John D. Day, J. Peter Weiss, et al. 2015. "The Impact of Risk Score (CHADS2 versus CHA2DS2-VASc) on Long-Term Outcomes after Atrial Fibrillation Ablation." *Heart Rhythm* 12 (4): 681–86. doi:10.1016/j.hrthm.2014.12.034.

Jadidi, Amir S., Hubert Cochet, Ashok J. Shah, Steven J. Kim, Edward Duncan, Shinsuke Miyazaki, Maxime Sermesant, et al. 2013. "Inverse Relationship Between Fractionated Electrograms and Atrial Fibrosis in Persistent Atrial Fibrillation." *Journal of the American College of Cardiology* 62 (9): 802–12. doi:10.1016/j.jacc.2013.03.081.

Jaïs, Pierre, Bruno Cauchemez, Laurent Macle, Emile Daoud, Paul Khairy, Rajesh Subbiah, Mélèze Hocini, et al. 2008. "Catheter Ablation Versus Antiarrhythmic Drugs for Atrial Fibrillation: The A4 Study." *Circulation* 118 (24): 2498–2505. doi:10.1161/CIRCULATIONAHA.108.772582.

Jais, Pierre, Méleze Hocini, Li Fern Hsu, Prashanthan Sanders, Christophe Scavee, Rukshen Weerasooriya, Laurent Macle, et al. 2004. "Technique and Results of Linear Ablation at the Mitral Isthmus." *Circulation* 110 (19): 2996–3002. doi:10.1161/01.CIR.0000146917.75041.58.

Jiang, Ru Hong, Sunny S. Po, Roderick Tung, Qiang Liu, Xia Sheng, Zu Wen Zhang, Ya Xun Sun, et al. 2014. "Incidence of Pulmonary Vein Conduction Recovery in Patients without Clinical Recurrence after Ablation of Paroxysmal Atrial Fibrillation: Mechanistic Implications." *Heart Rhythm* 11 (6): 969–76. doi:10.1016/j.hrthm.2014.03.015.

Johnson, Glyn, Youssef Zain Wadghiri, and Daniel H. Turnbull. 1999. "2D Multislice and 3D MRI Sequences Are Often Equally Sensitive." *Magnetic Resonance in Medicine* 41: 824–28.

doi:10.1002/(SICI)1522-2594(199904)41:4<824::AID-MRM23>3.0.CO;2-1.

Josephson, Mark E., and Elad Anter. 2015. "Substrate Mapping for Ventricular Tachycardia Assumptions and Misconceptions." *JACC: Clinical Electrophysiology* 1 (5): 341–52. doi:10.1016/j.jacep.2015.09.001.

Kahn, Thomas, and Harald Busse. 2012. *Interventional Magnetic Resonance Imaging*. Edited by Thomas Kahn and Harald Busse. Medical Radiology. Berlin, Heidelberg: Springer Berlin Heidelberg. doi:10.1007/978-3-642-20706-8.

Karim, Rashed, Henry Chubb, Wieland Staab, Shadman Aziz, R. James Housden, Mark O'Neill, Reza Razavi, and Kawal Rhode. 2015. "Left Atrial Segmentation from 3D Respiratory- and ECG-Gated Magnetic Resonance Angiography." *Functional Imaging and Modeling of the Heart* 9126. Springer International Publishing: 155–63. doi:10.1007/978-3-319-20309-6_18.

Karim, Rashed, R James Housden, Mayuragoban Balasubramaniam, Zhong Chen, Daniel Perry, Ayesha Uddin, Yosra Al-Beyatti, et al. 2013. "Evaluation of Current Algorithms for Segmentation of Scar Tissue from Late Gadolinium Enhancement Cardiovascular Magnetic Resonance of the Left Atrium: An Open-Access Grand Challenge." *Journal of Cardiovascular Magnetic Resonance* 15 (January): 105. doi:10.1186/1532-429X-15-105.

Kautzner, Josef, Petr Neuzil, Hendrik Lambert, Petr Peichl, Jan Petru, Robert Cihak, Jan Skoda, et al. 2015. "EFFICAS II: Optimization of Catheter Contact Force Improves Outcome of Pulmonary Vein Isolation for Paroxysmal Atrial Fibrillation." *Europace* 17 (8): 1229–35. doi:10.1093/europace/euv057.

Kellman, Peter, Andrew E. Arai, Elliot R. McVeigh, and Anthony H. Aletras. 2002. "Phase-Sensitive Inversion Recovery for Detecting Myocardial Infarction Using Gadolinium-Delayed Hyperenhancement." *Magnetic Resonance in Medicine* 47 (2): 372–83. doi:10.1002/mrm.10051.

Khawaja, Aurang Z., Deirdre B. Cassidy, Julien Al Shakarchi, Damian G. McGrogan, Nicholas G. Inston, and Robert G. Jones. 2015. "Revisiting the Risks of MRI with Gadolinium Based Contrast Agents-Review of Literature and Guidelines." *Insights into Imaging* 6 (5): 553–58. doi:10.1007/s13244-015-0420-2.

Khurram, Irfan M., Mohammadali Habibi, Esra Gucuk Ipek, Jonathan Chrispin, Eunice Yang, Kotaro Fukumoto, Jane Dewire, et al. 2015. "Left Atrial LGE and Arrhythmia Recurrence Following Pulmonary Vein Isolation for Paroxysmal and Persistent AF." *JACC: Cardiovascular Imaging* 9 (2). Journal of the American College of Cardiology: 142–48. doi:10.1016/j.jcmg.2015.10.015.

Khurram, Irfan M, Roy Beinart, Vadim Zipunnikov, Jane Dewire, Hirad Yarmohammadi, Takeshi Sasaki, David D Spragg, et al. 2014. "Magnetic Resonance Image Intensity Ratio, a Normalized Measure to Enable Interpatient Comparability of Left Atrial Fibrosis." *Heart Rhythm* 11 (1): 85–92. doi:10.1016/j.hrthm.2013.10.007.

Kimura, Masaomi, Shingo Sasaki, Shingen Owada, Daisuke Horiuchi, Kenichi Sasaki, Taihei Itoh, Yuji Ishida, Takahiko Kinjo, Hirofumi Tomita, and Ken Okumura. 2014. "Comparison of Lesion Formation between Contact Force-Guided and Non-Guided Circumferential Pulmonary Vein Isolation: A Prospective, Randomized Study." *Heart Rhythm* 11 (6): 984–91. doi:10.1016/j.hrthm.2014.03.019.

Kirchhof, Paulus, Stefano Benussi, Dipak Kotecha, Anders Ahlsson, Dan Atar, Barbara Casadei, Manuel Castella, et al. 2016. "2016 ESC Guidelines for the Management of Atrial Fibrillation Developed in Collaboration with EACTS." *European Heart Journal*, ehw210. doi:10.1093/eurheartj/ehw210.

Kirchhof, Paulus, and Hugh Calkins. 2016. "Catheter Ablation in Patients with Persistent Atrial Fibrillation." *European Heart Journal*, ehw260. doi:10.1093/eurheartj/ehw260.

Kirchhof, Paulus, Murat Özgün, Stephan Zellerhoff, Gerold Mönnig, Lars Eckardt, Kristina Wasmer, Walter Heindel, Günter Breithardt, and David Maintz. 2009. "Diastolic Isthmus Length and 'Vertical' Isthmus Angulation Identify Patients with Difficult Catheter Ablation of Typical Atrial Flutter: A Pre-Procedural MRI Study." *Europace* 11 (1): 42–47. doi:10.1093/europace/eun308.

Knowles, Benjamin R, Philip G Batchelor, Victoria Parish, Matthew Ginks, Sven Plein, Reza Razavi, and Tobias Schaeffter. 2008. "Pharmacokinetic Modeling of Delayed Gadolinium Enhancement in the Myocardium." *Magnetic Resonance in Medicine* 60 (6): 1524–30. doi:10.1002/mrm.21767.

Knowles, Benjamin R, Dennis Caulfield, Michael Cooklin, C Aldo Rinaldi, Jaswinder Gill, Julian Bostock, Reza Razavi, Tobias Schaeffter, and Kawal S Rhode. 2010. "3-D Visualization of Acute RF Ablation Lesions Using MRI for the Simultaneous Determination of the Patterns of Necrosis and Edema." *IEEE Transactions on Biomedical Engineering* 57 (6): 1467–75. doi:10.1109/TBME.2009.2038791.

Koken, P, R Holthuizen, J Smink, S Krueger, S Weiss, A J Wiethoff, and T Schaeffter. 2010. "Advanced Scan-Geometry Planning for MR-EP Interventions (Abstract)." *Proceedings of the 8th Interventional MRI Symposium, Leipzig, Germany*, 2–5.

Kolbitsch, Christoph, Claudia Prieto, Jouke Smink, and Tobias Schaeffter. 2011. "Highly Efficient Whole-Heart Imaging Using Radial Phase Encoding-Phase Ordering with Automatic Window Selection." *Magnetic Resonance in Medicine* 66 (4): 1008–18. doi:10.1002/mrm.22888.

Kosiuk, Jedrzej, Borislav Dinov, Jelena Kornej, Willem Jan Acou, Robert Schonbauer, Lukas Fiedler, Piotr Buchta, et al. 2015. "Prospective, Multicenter Validation of a Clinical Risk Score for Left Atrial Arrhythmogenic Substrate Based on Voltage Analysis: DR-FLASH Score." *Heart Rhythm* 12 (11): 2207–12. doi:10.1016/j.hrthm.2015.07.003.

Kowallick, Johannes T., Geraint Morton, Pablo Lamata, Roy Jogiya, Shelby Kutty, Gerd Hasenfuss, Joachim Lotz, et al. 2015. "Quantification of Atrial Dynamics Using Cardiovascular Magnetic Resonance: Inter-Study Reproducibility." *Journal of Cardiovascular Magnetic Resonance* 17 (1): 36. doi:10.1186/s12968-015-0140-2.

Kowalski, Marcin, Margaret M Grimes, Francisco J Perez, David N Kenigsberg, Jayanthi Koneru, Vigneshwar Kasirajan, Mark a Wood, and Kenneth a Ellenbogen. 2012. "Histopathologic Characterization of Chronic Radiofrequency Ablation Lesions for Pulmonary Vein Isolation." *Journal of the American College of Cardiology* 59 (10). Elsevier Inc.: 930–38. doi:10.1016/j.jacc.2011.09.076.

Krueger, Sascha, Oliver Lips, Bernd David, Daniel Wirtz, Steffen Weiss, Steen F Pedersen, Dennis Caulfield, Julian Bostock, Reza Razavi, and Tobias Schaeffter. 2009. "Towards MR-Guided EP Interventions Using an RF-Safe Approach." *Journal of Cardiovascular Magnetic Resonance* 11 (Suppl 1): O84. doi:10.1186/1532-429X-11-S1-O84.

Kuck, Karl-Heinz, Josep Brugada, Alexander Fürnkranz, Andreas Metzner, Feifan Ouyang, K.R. R Julian Chun, Arif Elvan, et al. 2016. "Cryoballoon or Radiofrequency Ablation for Paroxysmal Atrial Fibrillation." *New England Journal of Medicine* 374: 2235–45. doi:10.1056/NEJMoa1602014.

Kuck, Karl-Heinz, Boris A Hoffmann, Sabine Ernst, Karl Wegscheider, Andras Treszl, Andreas Metzner, Lars Eckardt, Thorsten Lewalter, Gunter Breithardt, and Stephan Willems. 2016. "Impact of Complete Versus Incomplete Circumferential Lines Around the Pulmonary Veins During Catheter Ablation of Paroxysmal Atrial Fibrillation: Results From the Gap-Atrial Fibrillation-German Atrial Fibrillation Competence Network 1 Trial." *Circulation. Arrhythmia and Electrophysiology* 9 (1): e003337. doi:10.1161/CIRCEP.115.003337.

Kuck, Karl-Heinz, Vivek Y. Reddy, Boris Schmidt, Andrea Natale, Petr Neuzil, Nadir Saoudi, Josef Kautzner, et al. 2012. "A Novel Radiofrequency Ablation Catheter Using Contact Force Sensing: Toccata Study." *Heart Rhythm* 9 (1): 18–23. doi:10.1016/j.hrthm.2011.08.021.

Kugel, Harald. 2012. "Safety Considerations in Interventional MRI." In *Interventional Magnetic Resonance Imaging*, 77–88. doi:10.1007/174.

Kuppahally, Suman S, Nazem Akoum, Troy J Badger, Nathan S Burgon, Thomas Haslam, Eugene Kholmovski, Rob Macleod, Christopher McGann, and Nassir F Marrouche. 2010. "Echocardiographic Left Atrial Reverse Remodeling after Catheter Ablation of Atrial Fibrillation Is Predicted by Preablation Delayed Enhancement of Left Atrium by Magnetic Resonance Imaging." *American Heart Journal* 160 (5). Mosby, Inc.: 877–84. doi:10.1016/j.ahj.2010.07.003.

Ladd, Mark E., and Harald H. Quick. 2000. "Reduction of Resonant RF Heating in Intravascular Catheters Using Coaxial Chokes." *Magnetic Resonance in Medicine* 43 (4): 615–19. doi:10.1002/(SICI)1522-2594(200004)43:4<615::AID-MRM19>3.0.CO;2-B.

Lancelot, Eric. 2016. "Revisiting the Pharmacokinetic Profiles of Gadolinium-Based Contrast Agents." *Investigative Radiology* 51 (11): 691–700. doi:10.1097/RLI.0000000000000280.

Landis, J Richard, and Gary G Koch. 1977. "The Measurement of Observer Agreement for Categorical Data." *Biometrics* 33 (1): 159–74. doi:10.2307/2529310.

Lankveld, Theo, Cees B. de Vos, Ione Limantoro, Stef Zeemering, Elton Dudink, Harry J. Crijns, and Ulrich Schotten. 2016. "Systematic Analysis of ECG Predictors of Sinus Rhythm Maintenance after Electrical Cardioversion for Persistent Atrial Fibrillation." *Heart Rhythm* 13 (5): 1020–27. doi:10.1016/j.hrthm.2016.01.004.

Lardo, A. C., E. R. McVeigh, P. Jumrussirikul, R. D. Berger, H. Calkins, J. Lima, and H. R. Halperin. 2000. "Visualization and Temporal/Spatial Characterization of Cardiac Radiofrequency Ablation Lesions Using Magnetic Resonance Imaging." *Circulation* 102 (6): 698–705. doi:10.1161/01.CIR.102.6.698.

Leong-Sit, Peter, Jean Francois Roux, Erica Zado, David J. Callans, Fermin Garcia, David Lin, Francis E. Marchlinski, et al. 2011. "Antiarrhythmics after Ablation of Atrial Fibrillation (5A Study) Six-Month Follow-up Study." *Circulation: Arrhythmia and Electrophysiology* 4 (1): 11–14. doi:10.1161/CIRCEP.110.955393.

Liang, Jackson J., Melissa A. Elafros, William W. Chik, Pasquale Santangeli, Erica S. Zado, David S. Frankel, Gregory E. Supple, et al. 2015. "Early Recurrence of Atrial Arrhythmias Following Pulmonary Vein Antral Isolation: Timing and Frequency of Early Recurrences Predicts Long-

Term Ablation Success." *Heart Rhythm* 12 (12): 2461–68. doi:10.1016/j.hrthm.2015.07.015.

Liang, Jackson J., Melissa A. Elafros, Daniele Muser, Rajeev K. Pathak, Pasquale Santangeli, Erica S. Zado, David S. Frankel, et al. 2016. "Pulmonary Vein Antral Isolation and Nonpulmonary Vein Trigger Ablation Are Sufficient to Achieve Favorable Long-Term Outcomes Including Transformation to Paroxysmal Arrhythmias in Patients With Persistent and Long-Standing Persistent Atrial Fibrillation." *Circulation: Arrhythmia and Electrophysiology* 9 (11): e004239. doi:10.1161/CIRCEP.116.004239.

Lin, Tina, Feifan Ouyang, Karl-Heinz Kuck, and Roland Tilz. 2013. "ThermoCool SmartTouch Catheter - The Evidence So Far for Contact Force Technology and the Role of VisiTag Module." *Arrhythmia & Electrophysiology Review* 3 (1): 44–47. doi:10.15420/aer.2011.3.1.44.

Ling, Liang-Han, Alex J A McLellan, Andrew J Taylor, Leah M Iles, Andris H Ellims, Saurabh Kumar, Andrew Teh, et al. 2014. "Magnetic Resonance Post-Contrast T1 Mapping in the Human Atrium: Validation and Impact on Clinical Outcome after Catheter Ablation for Atrial Fibrillation." *Heart Rhythm* 11 (9): 1551–59. doi:10.1016/j.hrthm.2014.06.012.

Link, Mark S., Michel Haïssaguerre, and Andrea Natale. 2016. "Ablation of Atrial Fibrillation." *Circulation* 134 (4): 339–52. doi:10.1161/CIRCULATIONAHA.116.021727.

Macle, Laurent, Paul Khairy, Rukshen Weerasooriya, Paul Novak, Atul Verma, Stephan Willems, Thomas Arentz, et al. 2015. "Adenosine-Guided Pulmonary Vein Isolation for the Treatment of Paroxysmal Atrial Fibrillation: An International, Multicentre, Randomised Superiority Trial." *The Lancet* 386 (9994): 672–79. doi:10.1016/S0140-6736(15)60026-5.

Mahnkopf, Christian, Troy J Badger, Nathan S Burgon, Marcos Daccarett, Thomas S Haslam, Christopher T Badger, Christopher J McGann, et al. 2010. "Evaluation of the Left Atrial Substrate in Patients with Lone Atrial Fibrillation Using Delayed-Enhanced MRI: Implications for Disease Progression and Response to Catheter Ablation." *Heart Rhythm* 7 (10): 1475–81. doi:10.1016/j.hrthm.2010.06.030.

Mahrholdt, Heiko, Anja Wagner, Thomas A. Holly, Michael D. Elliott, Robert O. Bonow, Raymond J. Kim, and Robert M. Judd. 2002. "Reproducibility of Chronic Infarct Size Measurement by Contrast-Enhanced Magnetic Resonance Imaging." *Circulation* 106 (18): 2322–27. doi:10.1161/01.CIR.0000036368.63317.1C.

Malcolme-Lawes, L.C., C. Juli, R. Karim, W. Bai, R. Quest, P.B. Lim, S. Jamil-Copley, et al. 2013. "Automated Analysis of Atrial Late Gadolinium Enhancement Imaging That Correlates with Endocardial Voltage and Clinical Outcomes: A 2-Center Study." *Heart Rhythm* 10 (8): 1184–91. doi:10.1016/j.hrthm.2013.04.030.

Marrouche, N F, R Schweikert, W Saliba, S V Pavia, D O Martin, T Dresing, C Cole, et al. 2003. "Use of Different Catheter Ablation Technologies for Treatment of Typical Atrial Flutter: Acute Results and Long-Term Follow-Up." *PACE - Pacing and Clinical Electrophysiology* 26 (3). Blackwell Publishing Inc: 743–46. doi:10.1046/j.1460-9592.2003.00126.x.

Marrouche, N F, D Wilber, G Hindricks, P Jais, N Akoum, Francis Marchlinski, Eugene Kholmovski, et al. 2014. "Association of Atrial Tissue Fibrosis Identified by Delayed Enhancement MRI and Atrial Fibrillation Catheter Ablation: The DECAAF Study." *JAMA : The Journal of the American Medical Association* 311 (5): 498–506. doi:10.1001/jama.2014.3.

Masuda, Masaharu, Masashi Fujita, Osamu Iida, Shin Okamoto, Takayuki Ishihara, Kiyonori Nanto, Takashi Kanda, et al. 2016. "Influence of Underlying Substrate on Atrial Tachyarrhythmias after Pulmonary Vein Isolation." *Heart Rhythm* 13 (4): 870–78. doi:10.1016/j.hrthm.2015.12.029.

McGann, Christopher, Nazem Akoum, Amit Patel, Eugene Kholmovski, Patricia Revelo, Kavitha Damal, Brent Wilson, et al. 2014. "Atrial Fibrillation Ablation Outcome Is Predicted by Left Atrial Remodeling on MRI." *Circulation. Arrhythmia and Electrophysiology* 7 (1): 23–30. doi:10.1161/CIRCEP.113.000689.

McGann, Christopher J., Eugene G. Kholmovski, Robert S. Oakes, Joshua J.E. E Blauer, Marcos Daccarett, Nathan Segerson, Kelly J. Airey, et al. 2008. "New Magnetic Resonance Imaging-Based Method for Defining the Extent of Left Atrial Wall Injury After the Ablation of Atrial Fibrillation." *Journal of the American College of Cardiology* 52 (15): 1263–71. doi:10.1016/j.jacc.2008.05.062.

McGraw, Kenneth O., and S. P. Wong. 1996. "Forming Inferences about Some Intraclass Correlations Coefficients." *Psychological Methods* 1 (4): 390–390. doi:10.1037/1082-989X.1.4.390.

McLellan, Alex J A, Liang Han Ling, Sonia Azzopardi, Andris H. Ellims, Leah M. Iles, Michael A. Sellenger, Joseph B. Morton, Jonathan M. Kalman, Andrew J. Taylor, and Peter M. Kistler. 2014. "Diffuse Ventricular Fibrosis Measured by T1 Mapping on Cardiac MRI Predicts Success of Catheter Ablation for Atrial Fibrillation." *Circulation: Arrhythmia and Electrophysiology* 7 (5): 834–40. doi:10.1161/CIRCEP.114.001479.

McLellan, Alex J A, Liang Han Ling, Sonia Azzopardi, Geraldine A. Lee, Geoffrey Lee, Saurabh Kumar, Michael C G Wong, et al. 2015. "A Minimal or Maximal Ablation Strategy to Achieve Pulmonary Vein Isolation for Paroxysmal Atrial Fibrillation: A Prospective Multi-Centre Randomized Controlled Trial (the Minimax Study)." *European Heart Journal* 36 (28): 1812–21. doi:10.1093/eurheartj/ehv139.

McLellan, Alex J A, Liang Han Ling, Diego Ruggiero, Michael C G Wong, Tomos E. Walters, Ashley Nisbet, Anoop K. Shetty, et al. 2014. "Pulmonary Vein Isolation: The Impact of Pulmonary Venous Anatomy on Long-Term Outcome of Catheter Ablation for Paroxysmal Atrial Fibrillation." *Heart Rhythm* 11 (4): 549–56. doi:10.1016/j.hrthm.2013.12.025.

McVeigh, E. R., R. M. Henkelman, and M. J. Bronskill. 1985. "Noise and Filtration in Magnetic Resonance Imaging." *Medical Physics* 12 (5). American Association of Physicists in Medicine: 586–91. doi:10.1118/1.595679.

Mines, George Ralph. 1913. "On Dynamic Equilibrium in the Heart." *The Journal of Physiology* 46: 349–83. doi:10.1113/jphysiol.1913.sp001596.

Moe, Gordon K, Werner C Rheinboldt, and J.A Abildskov. 1964. "A Computer Model of Atrial Fibrillation." *American Heart Journal* 67 (2). Mosby: 200–220. doi:10.1016/0002-8703(64)90371-0.

Mont, Lluís, Felipe Bisbal, Antonio Hernández-Madrid, Nicasio Pérez-Castellano, Xavier Viñolas, Angel Arenal, Fernando Arribas, et al. 2014. "Catheter Ablation vs. Antiarrhythmic Drug Treatment of Persistent Atrial Fibrillation: A Multicentre, Randomized, Controlled Trial (SARA Study)." *European Heart Journal* 35 (8): 501–7. doi:10.1093/eurheartj/eht457.

Montserrat, Silvia, Luigi Gabrielli, Bart Bijnens, Roger Borras, Antonio Berruezo, Silvia Poyatos, Josep Brugada, Lluis Mont, and Marta Sitges. 2015. "Left Atrial Deformation Predicts Success of First

and Second Percutaneous Atrial Fibrillation Ablation." *Heart Rhythm* 12 (1): 11–18. doi:10.1016/j.hrthm.2014.08.032.

Morillo, Carlos A, Atul Verma, Stuart J Connolly, Karl H Kuck, Girish M Nair, Jean Champagne, Laurence D Sterns, et al. 2014. "Radiofrequency Ablation vs Antiarrhythmic Drugs as First-Line Treatment of Paroxysmal Atrial Fibrillation (RAAFT-2): A Randomized Trial." *JAMA : The Journal of the American Medical Association* 311 (7): 692–700. doi:10.1001/jama.2014.467.

Morton, Geraint, Roy Jogiya, Sven Plein, Andreas Schuster, Amedeo Chiribiri, and Eike Nagel. 2012. "Quantitative Cardiovascular Magnetic Resonance Perfusion Imaging: Inter-Study Reproducibility." *European Heart Journal Cardiovascular Imaging* 13 (11): 954–60. doi:10.1093/ehjci/jes103.

Narayan, Sanjiv M., Tina Baykaner, Paul Clopton, Amir Schricker, Gautam G. Lalani, David E. Krummen, Kalyanam Shivkumar, and John M Miller. 2014. "Ablation of Rotor and Focal Sources Reduces Late Recurrence of Atrial Fibrillation Compared with Trigger Ablation Alone: Extended Follow-up of the CONFIRM Trial (Conventional Ablation for Atrial Fibrillation with or without Focal Impulse and Rotor Modulat." *Journal of the American College of Cardiology* 63 (17): 1761–68. doi:10.1016/j.jacc.2014.02.543.

Natale, Andrea, Vivek Y. Reddy, George Monir, David J. Wilber, Bruce D. Lindsay, H. Thomas McElderry, Charan Kantipudi, et al. 2014. "Paroxysmal AF Catheter Ablation with a Contact Force Sensing Catheter: Results of the Prospective, Multicenter SMART-AF Trial." *Journal of the American College of Cardiology* 64 (7): 647–56. doi:10.1016/j.jacc.2014.04.072.

Nattel, Stanley, and Dobromir Dobrev. 2016. "Deciphering the Fundamental Mechanisms of Atrial Fibrillation: A Quest for over a Century." *Cardiovascular Research* 109 (4): 465–66. doi:10.1093/cvr/cvw028.

Nazarian, S., A. Kolandaivelu, M. M. Zviman, G. R. Meininger, R. Kato, R. C. Susil, A. Roguin, et al. 2008. "Feasibility of Real-Time Magnetic Resonance Imaging for Catheter Guidance in Electrophysiology Studies." *Circulation* 118 (3): 223–29. doi:10.1161/CIRCULATIONAHA.107.742452.

Nazarian, S, D Bluemke, A C Lardo, Menekhem M Zviman, Stanley P Watkins, Timm L Dickfeld, Glenn R Meininger, et al. 2005. "Magnetic Resonance Assessment of the Substrate for Inducible Ventricular Tachycardia in Nonischemic Cardiomyopathy." *Circulation* 112 (18): 2821–25. doi:10.1161/CIRCULATIONAHA.105.549659.

Neilan, Tomas G., Ravi V. Shah, Siddique A. Abbasi, Hoshang Farhad, John D. Groarke, John A. Dodson, Otavio Coelho-Filho, et al. 2013. "The Incidence, Pattern, and Prognostic Value of Left Ventricular Myocardial Scar by Late Gadolinium Enhancement in Patients with Atrial Fibrillation." *Journal of the American College of Cardiology* 62 (23): 2205–14. doi:10.1016/j.jacc.2013.07.067.

Nery, Pablo B., Daniel Belliveau, Girish M. Nair, Jordan Bernick, Calum J. Redpath, Agnieszka Szczotka, Mouhannad M. Sadek, Martin S. Green, George Wells, and David H. Birnie. 2016. "Relationship Between Pulmonary Vein Reconnection and Atrial Fibrillation Recurrence." *JACC: Clinical Electrophysiology* 2 (4): 474–83. doi:10.1016/j.jacep.2016.02.003.

Neuzil, Petr, Vivek Y. Reddy, Josef Kautzner, Jan Petru, Dan Wichterle, Dipen Shah, Hendrik Lambert,

Aude Yulzari, Erik Wissner, and K.-H. Karl-Heinz Kuck. 2013. “Electrical Reconnection After Pulmonary Vein Isolation Is Contingent on Contact Force During Initial Treatment: Results From the EFFICAS I Study.” *Circulation: Arrhythmia and Electrophysiology* 6 (2): 327–33. doi:10.1161/CIRCEP.113.000374.

Nevo, E. 2003. Method and apparatus to estimate location and orientation of objects during magnetic resonance imaging. US9037213 B2. *U. S. Patent*, issued 2003. doi:10.1074/JBC.274.42.30033.(51).

Niendorf, Thoralf, Lukas Winter, and Tobias Frauenrath. 2012. *Electrocardiogram in an MRI Environment: Clinical Needs, Practical Considerations, Safety Implications, Technical Solutions and Future Directions*. InTech Open Access , Rijeka, Croatia. doi:10.5772/24340.

Nordbeck, Peter, Wolfgang R. Bauer, Florian Fidler, Marcus Warmuth, K.-H. Karl-Heinz Hiller, Matthias Nahrendorf, Michelle Maxfield, et al. 2009. “Feasibility of Real-Time MRI With a Novel Carbon Catheter for Interventional Electrophysiology.” *Circulation: Arrhythmia and Electrophysiology* 2 (3): 258–67. doi:10.1161/CIRCEP.108.778357.

Nordbeck, Peter, Meinrad Beer, Herbert Köstler, Mark E. Ladd, Harald H. Quick, Wolfgang R. Bauer, and Oliver Ritter. 2012. “Cardiac Catheter Ablation under Real-Time Magnetic Resonance Guidance.” *European Heart Journal* 33 (15): 1977. doi:10.1093/eurheartj/ehs139.

Nordbeck, Peter, K.-H. Karl-Heinz Hiller, Florian Fidler, Marcus Warmuth, Natalie Burkard, Matthias Nahrendorf, Peter M. Jakob, et al. 2011. “Feasibility of Contrast-Enhanced and Nonenhanced MRI for Intraprocedural and Postprocedural Lesion Visualization in Interventional Electrophysiology: Animal Studies and Early Delineation of Isthmus Ablation Lesions in Patients With Typical Atrial Flutter.” *Circulation: Cardiovascular Imaging* 4 (3): 282–94. doi:10.1161/CIRCIMAGING.110.957670.

Nuñez Garcia, Marta, Catalina Tobon-Gomez, Kawal Rhode, Bart Bijnens, Oscar Camara, and Constantine Butakoff. 2015. “Quantification of Gaps in Ablation Lesions Around the Pulmonary Veins in Delayed Enhancement MRI.” In , 215–22. Springer International Publishing. doi:10.1007/978-3-319-20309-6_25.

O’Neill, Mark D., and Henry Chubb. 2016. “Look Before You Leap. Optimizing Outcomes of Atrial Fibrillation Ablation.” *JACC: Cardiovascular Imaging* 9 (2): 149–51. doi:10.1016/j.jcmg.2015.10.014.

O’Neill, Mark D., Matthew Wright, Sébastien Knecht, Pierre Jaïs, Mélze Hocini, Yoshihide Takahashi, Anders Jönsson, et al. 2009. “Long-Term Follow-up of Persistent Atrial Fibrillation Ablation Using Termination as a Procedural Endpoint.” *European Heart Journal* 30 (9): 1105–12. doi:10.1093/eurheartj/ehp063.

Oakes, Robert S RS, TJ Troy J Badger, Eugene G EG Kholmovski, Nazem Akoum, Nathan S Burgon, Eric N Fish, Joshua J E Blauer, et al. 2009. “Detection and Quantification of Left Atrial Structural Remodeling with Delayed-Enhancement Magnetic Resonance Imaging in Patients with Atrial Fibrillation.” *Circulation* 119 (13): 1758–67. doi:10.1161/CIRCULATIONAHA.108.811877.

Oduneye, Samuel, L Biswas, and Sudip Ghate. 2012. “The Feasibility of Endocardial Propagation Mapping Using Magnetic Resonance Guidance in a Swine Model, and Comparison With Standard Electroanatomic Mapping.” *IEEE Transactions on Medical Imaging* 31 (4): 977–83.

doi:10.1109/TMI.2011.2174645.

Oduneye, Samuel O, Mihaela Pop, Mohammed Shurrab, Labonny Biswas, Venkat Ramanan, Jennifer Barry, Eugene Crystal, and Graham a Wright. 2015. "Distribution of Abnormal Potentials in Chronic Myocardial Infarction Using a Real Time Magnetic Resonance Guided Electrophysiology System." *Journal of Cardiovascular Magnetic Resonance* 17 (1): 1–9. doi:10.1186/s12968-015-0133-1.

Okumura, Yasuo, Susan B Johnson, T Jared Bunch, Benhur D Henz, Christine J O'Brien, and Douglas L Packer. 2008. "A Systematical Analysis of in Vivo Contact Forces on Virtual Catheter Tip/tissue Surface Contact during Cardiac Mapping and Intervention." *Journal of Cardiovascular Electrophysiology* 19 (6): 632–40. doi:10.1111/j.1540-8167.2008.01135.x.

Okumura, Yasuo, Ichiro Watanabe, Kazuki Iso, Koichi Nagashima, Kazumasa Sonoda, Naoko Sasaki, Rikitake Kogawa, et al. 2016. "Clinical Utility of Automated Ablation Lesion Tagging Based on Catheter Stability Information (VisiTag Module of the CARTO 3 System) with Contact Force-Time Integral during Pulmonary Vein Isolation for Atrial Fibrillation." *Journal of Interventional Cardiac Electrophysiology* 47 (2): 245–52. doi:10.1007/s10840-016-0156-z.

Oral, Hakan, Christian Sticherling, Hiroshi Tada, Steven R Chough, Robert L Baker, Kristina Wasmer, Frank Pelosi, Bradley P Knight, Fred J. Morady, and S Adam Strickberger. 2001. "Role of Transisthmus Conduction Intervals in Predicting Bidirectional Block after Ablation of Typical Atrial Flutter." *Journal of Cardiovascular Electrophysiology* 12 (2): 169–74. doi:10.1046/j.1540-8167.2001.00169.x.

Otsu, Nobuyuki. 1975. "A Threshold Selection Method from Gray-Level Histograms." *Automatica* 11: 23–27.

Ouyang, Feifan, Matthias Antz, Sabine Ernst, Hitoshi Hachiya, Hercules Mavrakis, Florian T. Deger, Anselm Schaumann, et al. 2005. "Recovered Pulmonary Vein Conductiona as a Dominant Factor for Recurrent Atrial Tachyarrhythmias after Complete Circular Isolation of the Pulmonary Veins: Lessons from Double Lasso Technique." *Circulation* 111 (2): 127–35. doi:10.1161/01.CIR.0000151289.73085.36.

Patel, Nileshkumar J, Abhishek Deshmukh, Dhaval Pau, Vishal Goyal, Samir V Patel, Nilay Patel, Kanishk Agnihotri, et al. 2016. "Contemporary Utilization and Safety Outcomes of Catheter Ablation of Atrial Flutter in the United States: Analysis of 89,638 Procedures." *Heart Rhythm* 13 (6): 1317–25. doi:10.1016/j.hrthm.2016.02.005.

Pathak, Rajeev K., Melissa E. Middeldorp, Megan Meredith, Abhinav B. Mehta, Rajiv Mahajan, Christopher X. Wong, Darragh Twomey, et al. 2015. "Long-Term Effect of Goal-Directed Weight Management in an Atrial Fibrillation Cohort: A Long-Term Follow-up Study (LEGACY)." *Journal of the American College of Cardiology* 65 (20): 2159–69. doi:10.1016/j.jacc.2015.03.002.

Perez-David, Esther, Angel Arenal, José L Rubio-Guivernau, Roberto del Castillo, Leonardo Atea, Elena Arbelo, Eduardo Caballero, et al. 2011. "Noninvasive Identification of Ventricular Tachycardia-Related Conducting Channels Using Contrast-Enhanced Magnetic Resonance Imaging in Patients with Chronic Myocardial Infarction: Comparison of Signal Intensity Scar Mapping and Endocardial Voltage Mappin." *Journal of the American College of Cardiology* 57 (2): 184–94. doi:10.1016/j.jacc.2010.07.043.

Pérez, Francisco J., Christine M. Schubert, Babar Parvez, Vishesh Pathak, Kenneth A. Ellenbogen, and Mark A. Wood. 2009. "Long-Term Outcomes after Catheter Ablation of Cavo-Tricuspid Isthmus Dependent Atrial Flutter: A Meta-Analysis." *Circulation: Arrhythmia and Electrophysiology* 2 (4): 393–401. doi:10.1161/CIRCEP.109.871665.

Peters, Dana C., John V. Wylie, Thomas H. Hauser, Kraig V. Kissinger, René M. Botnar, Vidal Essebag, Mark E. Josephson, and Warren J. Manning. 2007. "Detection of Pulmonary Vein and Left Atrial Scar after Catheter Ablation with Three-Dimensional Navigator-Gated Delayed Enhancement MR Imaging: Initial Experience1." *Radiology* 243 (3): 690–695.

Peters, Dana C, and Litten K Bertelsen. 2015. "Simulations for Determining the Optimal Enhancement Ratio Threshold for Segmentation of Left Atrial Fibrosis [Abstr]." *Journal of Cardiovascular Magnetic Resonance* 17 (Suppl 1): P60. doi:10.1186/1532-429X-17-S1-P60.

Peters, Dana C, John V Wylie, Thomas H Hauser, Reza Nezafat, Yuchi Han, Jeong Joo Woo, Jason Taclas, et al. 2009. "Recurrence of Atrial Fibrillation Correlates with the Extent of Post-Procedural Late Gadolinium Enhancement: A Pilot Study." *JACC. Cardiovascular Imaging* 2 (3). Elsevier Inc.: 308–16. doi:10.1016/j.jcmg.2008.10.016.

Platonov, Pyotr G., Vitaly Ivanov, Siew Yen Ho, and Lubov Mitrofanova. 2008. "Left Atrial Posterior Wall Thickness in Patients with and without Atrial Fibrillation: Data from 298 Consecutive Autopsies." *Journal of Cardiovascular Electrophysiology* 19 (7). Blackwell Publishing Inc: 689–692. doi:10.1111/j.1540-8167.2008.01102.x.

Plein, Sven, John Greenwood, and John Phillip Ridgway. 2011. *Cardiovascular MR Manual*. London: Springer London. doi:10.1007/978-1-84996-362-6.

Pop, Mihaela, Nilesh R Ghugre, Venkat Ramanan, Lily Morikawa, Greg Stanisz, Alexander J Dick, and Graham a Wright. 2013. "Quantification of Fibrosis in Infarcted Swine Hearts by Ex Vivo Late Gadolinium-Enhancement and Diffusion-Weighted MRI Methods." *Physics in Medicine and Biology* 58 (15): 5009–28. doi:10.1088/0031-9155/58/15/5009.

Psaty, B M, T A Manolio, L H Kuller, R A Kronmal, M Cushman, L P Fried, R White, C D Furberg, and P M Rautaharju. 1997. "Incidence of and Risk Factors for Atrial Fibrillation in Older Adults." *Circulation* 96 (7): 2455–61.

Ranjan, Ravi, Eugene G Kholmovski, Joshua Blauer, Sathya Vijayakumar, Nelly a Volland, Mohamed E Salama, Dennis L Parker, Rob MacLeod, and Nassir F Marrouche. 2012. "Identification and Acute Targeting of Gaps in Atrial Ablation Lesion Sets Using a Real-Time Magnetic Resonance Imaging System." *Circulation. Arrhythmia and Electrophysiology* 5 (6): 1130–35. doi:10.1161/CIRCEP.112.973164.

Razavi, Reza, Derek LG Hill, Stephen F. Keevil, Marc E. Miquel, Vivek Muthurangu, Sanjeet Hegde, Kawal Rhode, et al. 2003. "Cardiac Catheterisation Guided by MRI in Children and Adults with Congenital Heart Disease." *The Lancet* 362 (9399): 1877–1882.

Reddy, Ugan, Mark J White, and Sally R Wilson. 2012. "Anaesthesia for Magnetic Resonance Imaging." *Continuing Education in Anaesthesia, Critical Care & Pain* 12 (3). Oxford University Press: 140–44. doi:10.1093/bjaceaccp/mks002.

Reddy, Vivek Y., Srinivas R. Dukkipati, Petr Neuzil, Andrea Natale, Jean Paul Albenque, Josef Kautzner, Dipen Shah, et al. 2015. "Randomized, Controlled Trial of the Safety and Effectiveness of a

Contact Force-Sensing Irrigated Catheter for Ablation of Paroxysmal Atrial Fibrillation: Results of the TactiCath Contact Force Ablation Catheter Study for Atrial Fibrillation (TOCCASTAR)." *Circulation* 132 (10): 907–15. doi:10.1161/CIRCULATIONAHA.114.014092.

Reddy, Vivek Y., Zachary J Malchano, Godtfred Holmvang, Ehud J Schmidt, Andre D'Avila, Christopher Houghtaling, Raymond C Chan, and Jeremy N Ruskin. 2004. "Integration of Cardiac Magnetic Resonance Imaging with Three-Dimensional Electroanatomic Mapping to Guide Left Ventricular Catheter Manipulation: Feasibility in a Porcine Model of Healed Myocardial Infarction." *Journal of the American College of Cardiology* 44 (11): 2202–13. doi:10.1016/j.jacc.2004.08.063.

Rieke, Viola. 2011. "MR Thermometry." In , 271–88. doi:10.1007/174_2011_478.

Rizvi, Kamran A., Nathan S. Burgon, Jordan B. King, Nazem Akoum, Gaston Vergara, Paul A. Anderson, Gregory P. Gardner, et al. 2016. "Exercise Capacity Correlates With Left Atrial Structural Remodeling as Detected by Late Gadolinium-Enhanced Cardiac Magnetic Resonance in Patients With Atrial Fibrillation." *JACC: Clinical Electrophysiology* 2 (6): 711–19. doi:10.1016/j.jacep.2016.03.012.

Rogers, Toby, and Robert J. Lederman. 2015. "Interventional CMR: Clinical Applications and Future Directions." *Current Cardiology Reports* 17 (5): 31. doi:10.1007/s11886-015-0580-1.

Rohrer, Martin, Hans Bauer, Jan Mintorovitch, Martin Requardt, and Hanns-Joachim Weinmann. 2005. "Comparison of Magnetic Properties of MRI Contrast Media Solutions at Different Magnetic Field Strengths." *Investigative Radiology* 40 (11): 715–24. doi:10.1097/01.rli.0000184756.66360.d3.

Roujol, Sebastien, Tamer Basha, Alex Tan, Varun Khanna, Raymond H. Chan, Mehdi H. Moghari, Hussein Rayatzadeh, Jaime L. Shaw, Mark E. Josephson, and Reza Nezafat. 2013. "Improved Multimodality Data Fusion of Late Gadolinium Enhancement MRI to Left Ventricular Voltage Maps in Ventricular Tachycardia Ablation." *IEEE Transactions on Biomedical Engineering* 60 (5): 1308–17. doi:10.1109/TBME.2012.2233738.

Rueckert, D, L I Sonoda, C Hayes, D L Hill, M O Leach, and D J Hawkes. 1999. "Nonrigid Registration Using Free-Form Deformations: Application to Breast MR Images." *IEEE Transactions on Medical Imaging* 18 (8): 712–21. doi:10.1109/42.796284.

Russo, Robert J., Heather S. Costa, Patricia D. Silva, Jeffrey L. Anderson, Aysha Arshad, Robert W.W. Biederman, Noel G. Boyle, et al. 2017. "Assessing the Risks Associated with MRI in Patients with a Pacemaker or Defibrillator." *New England Journal of Medicine* 376 (8): 755–64. doi:10.1056/NEJMoa1603265.

Sanders, Prashanthan, Omer Berenfeld, Meleze Hocini, Pierre Jaïs, Ravi Vaidyanathan, Li Fern Hsu, Stephane Garrigue, et al. 2005. "Spectral Analysis Identifies Sites of High-Frequency Activity Maintaining Atrial Fibrillation in Humans." *Circulation* 112 (6): 789–97. doi:10.1161/CIRCULATIONAHA.104.517011.

Schmidt, Ehud J., Charles L. Dumoulin, and Stephan B. Danik. 2014. "Image-Guided Cardiac Electrophysiology Procedures Focusing on MRI Guidance." In *Intraoperative Imaging and Image-Guided Therapy*, 613–28. doi:10.1007/978-1-4614-7657-3.

Schmidt, Ehud J., Zion T. H. Tse, Tobias R. Reichlin, Gregory F. Michaud, Ronald D. Watkins, Kim Butts-

Pauly, Raymond Y. Kwong, et al. 2013. “Voltage-Based Device Tracking in a 1.5 Tesla MRI during Imaging: Initial Validation in Swine Models: MRI-Compatible Voltage-Based Device Tracking.” *Magnetic Resonance in Medicine* 71 (3): 1197–1209. doi:10.1002/mrm.24742.

Schmidt, Ehud J., Ronald D. Watkins, Menekhem M. Zviman, Michael A. Guttman, Wei Wang, and Henry A. Halperin. 2016. “A Magnetic Resonance Imaging–Conditional External Cardiac Defibrillator for Resuscitation Within the Magnetic Resonance Imaging Scanner BoreCLINICAL PERSPECTIVE.” *Circulation: Cardiovascular Imaging* 9 (10): e005091. doi:10.1161/CIRCIMAGING.116.005091.

Schmidt, Ehud J, Richard P Mallozzi, Aravinda Thiagalingam, Godtfred Holmvang, Andre d’Avila, Renee Guhde, Robert Darrow, et al. 2009. “Electroanatomic Mapping and Radiofrequency Ablation of Porcine Left Atria and Atrioventricular Nodes Using Magnetic Resonance Catheter Tracking.” *Circulation. Arrhythmia and Electrophysiology* 2 (6): 695–704. doi:10.1161/CIRCEP.109.882472.

Schoene, Katharina, Sascha Rolf, Denis Schloma, Silke John, Arash Arya, Borislav Dinov, Sergio Richter, Andreas Bollmann, Gerhard Hindricks, and Philipp Sommer. 2015. “Ablation of Typical Atrial Flutter Using a Non-Fluoroscopic Catheter Tracking System vs. Conventional Fluoroscopy—results from a Prospective Randomized Study.” *Europace* 17 (7): 1117–21. doi:10.1093/europace/euu398.

Schotten, Ulrich, Sander Verheule, Paulus Kirchhof, and Andreas Goette. 2011. “Pathophysiological Mechanisms of Atrial Fibrillation: A Translational Appraisal.” *Physiological Reviews* 91: 265–325. doi:10.1152/physrev.00031.2009.

Shurrab, Mohammed, Luigi Di Biase, David F Briceno, Anna Kaoutskaia, Saleem Haj-Yahia, David Newman, Ilan Lashevsky, Hiroshi Nakagawa, and Eugene Crystal. 2015. “Impact of Contact Force Technology on Atrial Fibrillation Ablation: A Meta-Analysis.” *Journal of the American Heart Association* 4 (9): e002476. doi:10.1161/JAHA.115.002476.

Sohns, Christian, Rashed Karim, James L Harrison, Aruna Arujuna, Nick Linton, Richard Sennett, Hendrik Lambert, et al. 2013. “Quantitative Magnetic Resonance Imaging Analysis of the Relationship between Contact Force and Left Atrial Scar Formation after Catheter Ablation of Atrial Fibrillation.” *Journal of Cardiovascular Electrophysiology*, no. July (October): 1–8. doi:10.1111/jce.12298.

Sommer, P., M. Grothoff, C. Eitel, T. Gaspar, C. Piorkowski, M. Gutberlet, and G. Hindricks. 2012. “Feasibility of Real-Time Magnetic Resonance Imaging-Guided Electrophysiology Studies in Humans.” *Europace* 15 (1): 101–8. doi:10.1093/europace/eus230.

Sonka, Milan., Vaclav. Hlavac, and Roger Boyle. 2008. *Image Processing, Analysis, and Machine Vision*. Thompson Learning.

Spector, Peter, Matthew R. Reynolds, Hugh Calkins, Manu Sondhi, Yingxin Xu, Amber Martin, Catherine J. Williams, and Isabella Sledge. 2009. “Meta-Analysis of Ablation of Atrial Flutter and Supraventricular Tachycardia.” *The American Journal of Cardiology* 104 (5): 671–77. doi:10.1016/j.amjcard.2009.04.040.

Spragg, David D., Irfan Khurram, Stefan L. Zimmerman, Hirad Yarmohammadi, Bernie Barcelon, Matthew Needleman, David Edwards, Joseph E. Marine, Hugh Calkins, and Saman Nazarian.

2012. “Initial Experience with Magnetic Resonance Imaging of Atrial Scar and Co-Registration with Electroanatomic Voltage Mapping during Atrial Fibrillation: Success and Limitations.” *Heart Rhythm* 9 (12): 2003–9. doi:10.1016/j.hrthm.2012.08.039.

Steiner, Paul, Rene Botnar, Nahum S Goldberg, Gazell G Scott, and Jorg F Debatin. 1997. “Monitoring of Radio Frequency Tissue Ablation in an Interventional Magnetic Resonance Environment: Preliminary Ex Vivo and In Vivo Results.” *Investigative Radiology* 32 (11): 671–78.

Suksaranjit, Promporn, Nazem Akoum, Eugene G. Kholmovski, Gregory J. Stoddard, Lowell Chang, Kavitha Damal, Krishna Velagapudi, et al. 2015. “Incidental LV LGE on CMR Imaging in Atrial Fibrillation Predicts Recurrence after Ablation Therapy.” *JACC: Cardiovascular Imaging* 8 (7): 793–800. doi:10.1016/j.jcmg.2015.03.008.

Taclas, Jason E, Reza Nezafat, John V Wylie, Mark E Josephson, Jeff Hsing, Warren J Manning, and Dana C Peters. 2010. “Relationship between Intended Sites of RF Ablation and Post-Procedural Scar in AF Patients, Using Late Gadolinium Enhancement Cardiovascular Magnetic Resonance.” *Heart Rhythm* 7 (4): 489–96. doi:10.1016/j.hrthm.2009.12.007.

Thiagalingam, Aravinda, Andre D’Avila, Lori Foley, J. Luis Guerrero, Hendrik Lambert, Giovanni Leo, Jeremy N. Ruskin, and Vivek Y. Reddy. 2010. “Importance of Catheter Contact Force during Irrigated Radiofrequency Ablation: Evaluation in a Porcine Ex Vivo Model Using a Force-Sensing Catheter.” *Journal of Cardiovascular Electrophysiology* 21 (7): 806–11. doi:10.1111/j.1540-8167.2009.01693.x.

Timmermans, C. 2003. “Randomized Study Comparing Radiofrequency Ablation With Cryoablation for the Treatment of Atrial Flutter With Emphasis on Pain Perception.” *Circulation* 107: 1250–52. doi:10.1161/01.CIR.0000061915.06069.93.

Tobon-Gomez, Catalina, Maria A Zuluaga, Henry Chubb, Steven E Williams, Constantine Butakoff, Rashed Karim, Oscar Camara, Sebastien Ourselin, and Kawal Rhode. 2015. “Standardised Unfold Map of the Left Atrium: Regional Definition for Multimodal Image Analysis.” *Journal of Cardiovascular Magnetic Resonance* 17 (Suppl 1): P41. doi:10.1186/1532-429X-17-S1-P41.

Tung, Roderick, Steve Kim, Daigo Yaghisita, Marmar Veschi, Daniel Ennis, Sarah Oudah, Olujimi Ajijola, et al. 2016. “Scar Voltage Threshold Determination Using Ex Vivo MRI Integration in a Porcine Infarct Model: Influence of Inter-Electrode Distances and 3-D Spatial Effects of Scar.” *Heart Rhythm*, no. 3. doi:10.1016/j.hrthm.2016.07.003.

Ullah, W., A. McLean, M. Tayebjee, D. Gupta, MR. Ginks, GA. Haywood, M. O’Neill, PD. Lambiase, M. Earley, and R. Schilling. 2016. “Randomized Trial Comparing Pulmonary Vein Isolation Using the Smarttouch Catheter with or without Real-Time Contact Force Data.” *Heart Rhythm* 13 (9): 1761–67. doi:10.1016/j.hrthm.2016.05.011.

Ullah, Waqas, Ross J Hunter, Victoria Baker, Mehul B Dhinoja, Simon Sporton, Mark J Earley, and Richard J Schilling. 2014. “Target Indices for Clinical Ablation in Atrial Fibrillation: Insights from Contact Force, Electrogram, and Biophysical Parameter Analysis.” *Circulation. Arrhythmia and Electrophysiology* 7 (1): 63–68. doi:10.1161/CIRCEP.113.001137.

Vaziri, S M, M G Larson, E J Benjamin, and D Levy. 1994. “Echocardiographic Predictors of Nonrheumatic Atrial Fibrillation. The Framingham Heart Study.” *Circulation* 89 (2): 724–30. doi:10.1161/01.CIR.89.2.724.

Vergara, Gaston R, and Nassir F Marrouche. 2011. "Tailored Management of Atrial Fibrillation Using a LGE-MRI Based Model: From the Clinic to the Electrophysiology Laboratory." *Journal of Cardiovascular Electrophysiology* 22 (4): 481–87. doi:10.1111/j.1540-8167.2010.01941.x.

Vergara, Gaston R, Sathya Vijayakumar, Eugene G. Kholmovski, Joshua J.E. E Blauer, Mike A. Guttman, Christopher Gloschat, Gene Payne, et al. 2011. "Real Time MRI Guided Radiofrequency Atrial Ablation and Visualization of Lesion Formation at 3-Tesla." *Heart Rhythm* 8 (2): 295–303. doi:10.1016/j.hrthm.2010.10.032.

Verma, Atul, Chen-yang Jiang, Timothy R. Betts, Jian Chen, Isabel Deisenhofer, Roberto Mantovan, Laurent Macle, et al. 2015. "Approaches to Catheter Ablation for Persistent Atrial Fibrillation." *The New England Journal of Medicine* 372 (19): 1812–22. doi:10.1056/NEJMoa1408288.

Vermes, Emmanuelle, Helene Childs, Iacopo Carbone, Philipp Barckow, and Matthias G Friedrich. 2013. "Auto-Threshold Quantification of Late Gadolinium Enhancement in Patients with Acute Heart Disease." *Journal of Magnetic Resonance Imaging* 37 (2): 382–90. doi:10.1002/jmri.23814.

Vernickel, Peter, Volkmar Schulz, Steffen Weiss, and Bernhard Gleich. 2005. "A Safe Transmission Line for MRI." *IEEE Transactions on Biomedical Engineering*.

Vijayakumar, Sathya, Ravi Ranjan, Kyungpyo Hong, Daniel Kim, Nassir F Marrouche, and Eugene G Kholmovski. 2014. "Assessment of Cardiac RF Ablation Lesions by DCE-MRI." *Journal of Cardiovascular Magnetic Resonance* 16 (Suppl 1): P155. doi:10.1186/1532-429X-16-S1-P155.

Vogler, Julia, Stephan Willems, Arian Sultan, Doreen Schreiber, Jakob Lüker, Helge Servatius, Benjamin Schäffer, Julia Moser, Boris A. Hoffmann, and Daniel Steven. 2015. "Pulmonary Vein Isolation Versus Defragmentation the CHASE-AF Clinical Trial." *Journal of the American College of Cardiology* 66 (24). Elsevier Inc: 2743–52. doi:10.1016/j.jacc.2015.09.088.

Voigt, Tobias, Peter Koken, James L. Harrison, Steffen Weiss, Sascha Krueger, and Tobias Schaeffter. 2013. "Atrial Wall Thickness Imaging for Cavotricuspid Isthmus Ablation." *Proceedings of the 21st Annual Meeting of International Society for Magnetic Resonance in Medicine* 21: 470.

Wagoner, David R. Van, Jonathan P. Piccini, Christine M. Albert, Mark E. Anderson, Emelia J. Benjamin, Bianca Brundel, Robert M. Califf, et al. 2015. "Progress toward the Prevention and Treatment of Atrial Fibrillation: A Summary of the Heart Rhythm Society Research Forum on the Treatment and Prevention of Atrial Fibrillation, Washington, DC, December 9-10, 2013." *Heart Rhythm* 12 (1): e5–29. doi:10.1016/j.hrthm.2014.11.011.

Waldo, A L. 1997. "Atrial Flutter: Entrainment Characteristics." *Journal of Cardiovascular Electrophysiology* 8 (3): 337–52.

Walters, Tomos E., and Jonathan M. Kalman. 2015. "Human Persistent Atrial Fibrillation Is Maintained by Rotors: The Jury Is Still Out." *Circulation: Arrhythmia and Electrophysiology* 8 (3): 517–19. doi:10.1161/CIRCEP.115.003089.

Walters, Tomos E., Ashley Nisbet, Gwilym M. Morris, Gabriel Tan, Megan Mearns, Eliza Teo, Nigel Lewis, et al. 2016. "Progression of Atrial Remodeling in Patients with High-Burden Atrial Fibrillation: Implications for Early Ablative Intervention." *Heart Rhythm* 13 (2): 331–39. doi:10.1016/j.hrthm.2015.10.028.

Weiss, S., P. Vernickel, T. Schaeffter, B. Gleich, and V. Schulz. 2005. "Towards an RF-Safe Active

Catheter for MR-Guided Interventions." *Kontraste (Hamburg)* 49 (3): 48–53.

Weiss, S, H Eggers, and T Schaeffter. 2001. "MR-Controlled Fast Optical Switching of a Resonant Circuit Mounted to the Tip of a Clinical Catheter [Abstr]." *Proceedings of the 9th Annual Meeting of ISMRM, Glasgow, Scotland* 816.

Weiss, S, T Schaeffter, K.M. Luedeke, C. Leussler, D. Holz, K. Nehrke, V. Rasche, and R. Sinkus. 1999. "Catheter Localization Using a Resonant Fiducial Marker during Interactive MR Fluoroscopy." *ISMRM* 25.

Weiss, Steffen, Sascha Krueger, Peter Koken, Gregg Stenzel, Lars Bloch, Won Yong Kim, Anne Yoon Krogh Gr?ndal, et al. 2013. "MR-Guided Cardiac Radiofrequency Ablation with Catheter-Tracked Local MR Lesion Monitoring." *Journal of Cardiovascular Magnetic Resonance* 15 (Suppl 1): M10. doi:10.1186/1532-429X-15-S1-M10.

Weiss, Steffen, Titus Kuehne, Florian Brinkert, Gabriele Krombach, Marcus Katoh, Tobias Schaeffter, Rolf W. Guenther, and Arno Buecker. 2004. "In Vivo Safe Catheter Visualization and Slice Tracking Using an Optically Detunable Resonant Marker." *Magnetic Resonance in Medicine* 52 (4): 860–68. doi:10.1002/mrm.20214.

Weiss, Steffen, Peter Vernickel, Tobias Schaeffter, Volkmar Schulz, and Bernhard Gleich. 2005. "Transmission Line for Improved RF Safety of Interventional Devices." *Magnetic Resonance in Medicine* 54 (1): 182–89. doi:10.1002/mrm.20543.

Weiss, Steffen, Daniel Wirtz, Bernd David, Sascha Krueger, Oliver Lips, Dennis Caulfield, Steen Fjord Pedersen, Julian Bostock, Reza Razavi, and Tobias Schaeffter. 2011. "In Vivo Evaluation and Proof of Radiofrequency Safety of a Novel Diagnostic MR-Electrophysiology Catheter." *Magnetic Resonance in Medicine* 65 (3): 770–77. doi:10.1002/mrm.22669.

Whitaker, John, Ronak Rajani, Henry Chubb, Mark Gabrawi, Marta Varela, Matthew Wright, Steven Niederer, and Mark D. O'Neill. 2016. "The Role of Myocardial Wall Thickness in Atrial Arrhythmogenesis." *Europace*, euw014. doi:10.1093/europace/euw014.

Wijffels, M C, C J Kirchhof, Rick Dorland, and Maurits A Allessie. 1995. "Atrial Fibrillation Begets Atrial Fibrillation." *Circulation* 92 (7): 1954–68. doi:10.1161/01.CIR.92.7.1954.

Williams, Steven E., James Harrison, Henry Chubb, Lars Ølgaard Bloch, Niels Peter Andersen, Høgni Dam, Rashed Karim, et al. 2015. "The Effect of Contact Force in Atrial Radiofrequency Ablation." *JACC: Clinical Electrophysiology* 1 (5): 421–31. doi:10.1016/j.jacep.2015.06.003.

Wittkampf, F H, R N Hauer, and E O Robles de Medina. 1989. "Control of Radiofrequency Lesion Size by Power Regulation." *Circulation* 80 (4): 962–68. doi:10.1161/01.CIR.80.4.962.

Wittkampf, Fred H M, and Hiroshi Nakagawa. 2006. "RF Catheter Ablation: Lessons on Lesions." *Pacing and Clinical Electrophysiology* 29: 1285–97.

Wyse, D.G., A.L. Waldo, J.P. DiMarco, M.J. Domanski, Y. Rosenberg, E.B. Schron, J.C. Kellen, et al. 2002. "A Comparison of Rate Control and Rhythm Control in Patients with Atrial Fibrillation." *New England Journal of Medicine* 347 (23): 1825–33.

Yokoyama, Katsuaki, Hiroshi Nakagawa, Dipen C Shah, Hendrik Lambert, Giovanni Leo, Nicolas Aeby, Atsushi Ikeda, et al. 2008. "Novel Contact Force Sensor Incorporated in Irrigated Radiofrequency Ablation Catheter Predicts Lesion Size and Incidence of Steam Pop and Thrombus." *Circulation. Arrhythmia and Electrophysiology* 1 (5): 354–62.

doi:10.1161/CIRCEP.108.803650.

Zahid, Sohail, Kaitlyn N. Whyte, Erica L. Schwarz, Robert C. Blake, Patrick M. Boyle, Jonathan Chrispin, Adityo Prakosa, et al. 2016. "Feasibility of Using Patient-Specific Models and the 'minimum Cut' Algorithm to Predict Optimal Ablation Targets for Left Atrial Flutter." *Heart Rhythm* 13 (8): 1687–98. doi:10.1016/j.hrthm.2016.04.009.

Zhang, Shelley Hua Lei, Zion Tsz Ho Tse, Charles L. Dumoulin, Raymond Y. Kwong, William G. Stevenson, Ronald Watkins, Jay Ward, Wei Wang, and Ehud J. Schmidt. 2016. "Gradient-Induced Voltages on 12-Lead ECGs during High Duty-Cycle MRI Sequences and a Method for Their Removal Considering Linear and Concomitant Gradient Terms." *Magnetic Resonance in Medicine* 75 (5): 2204–16. doi:10.1002/mrm.25810.

APPENDIX A: SINGLE REPRESENTATIVE SLICES OF 3D-LGE IMAGING

1 **Scan type: repro**

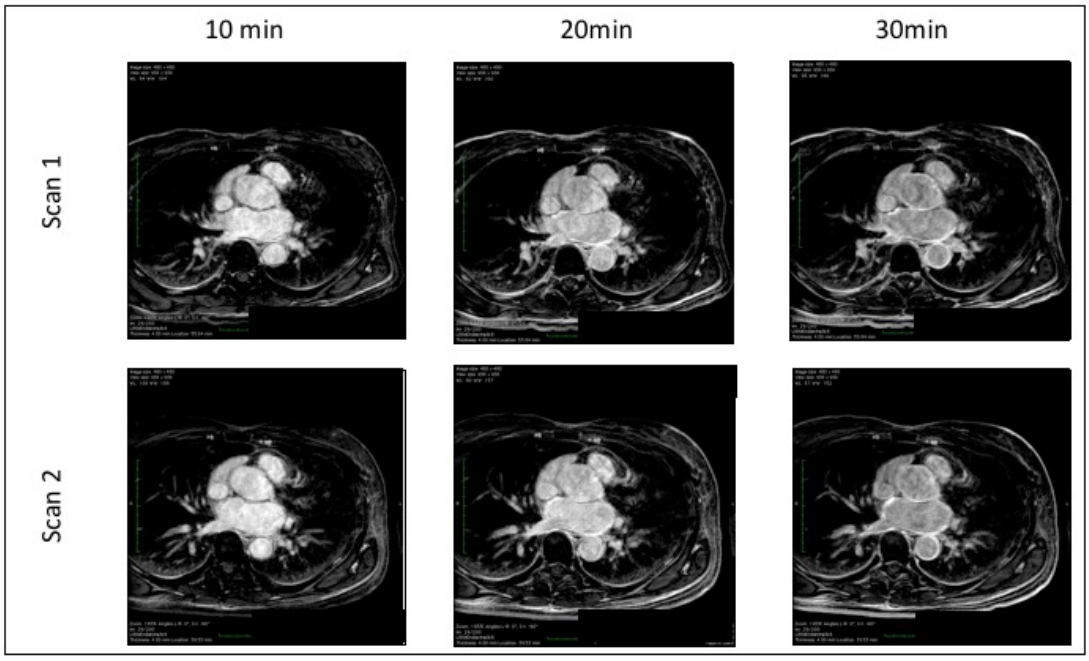

Comments:

2 **Scan type: Repro**

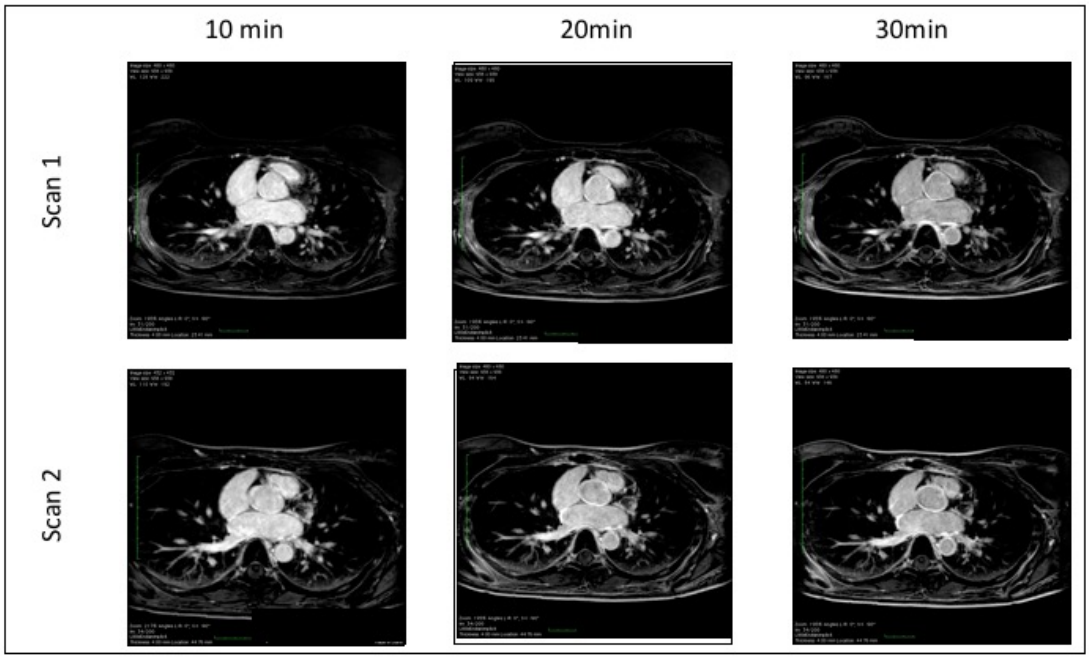

Comments:

3 **Scan type:3T**

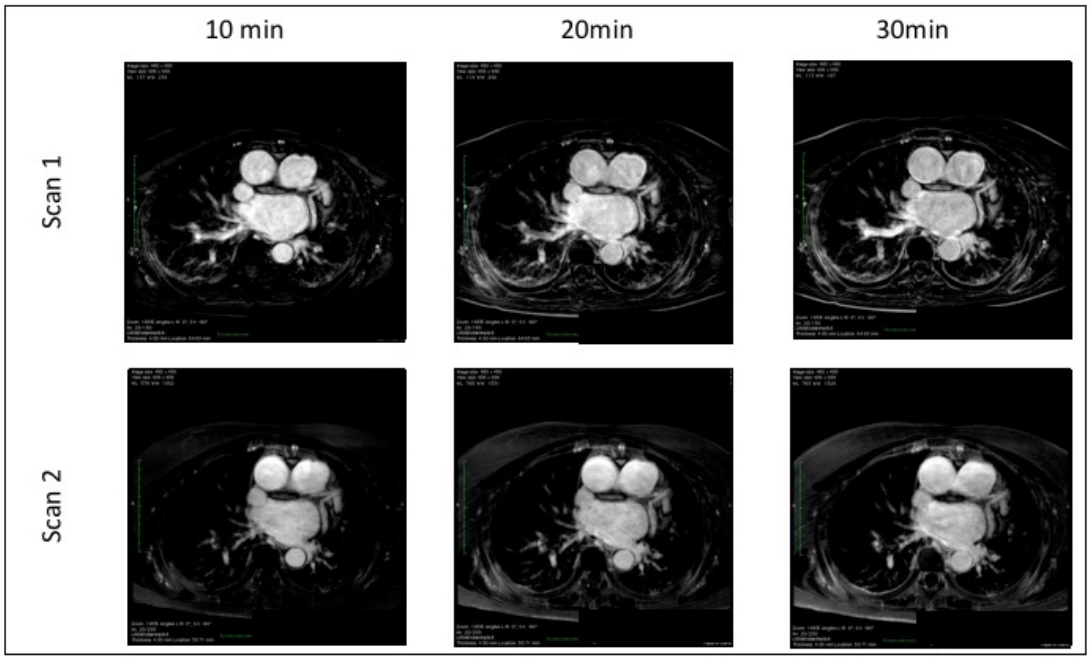

Comments:

4 **Scan type: Allocated to Repro**

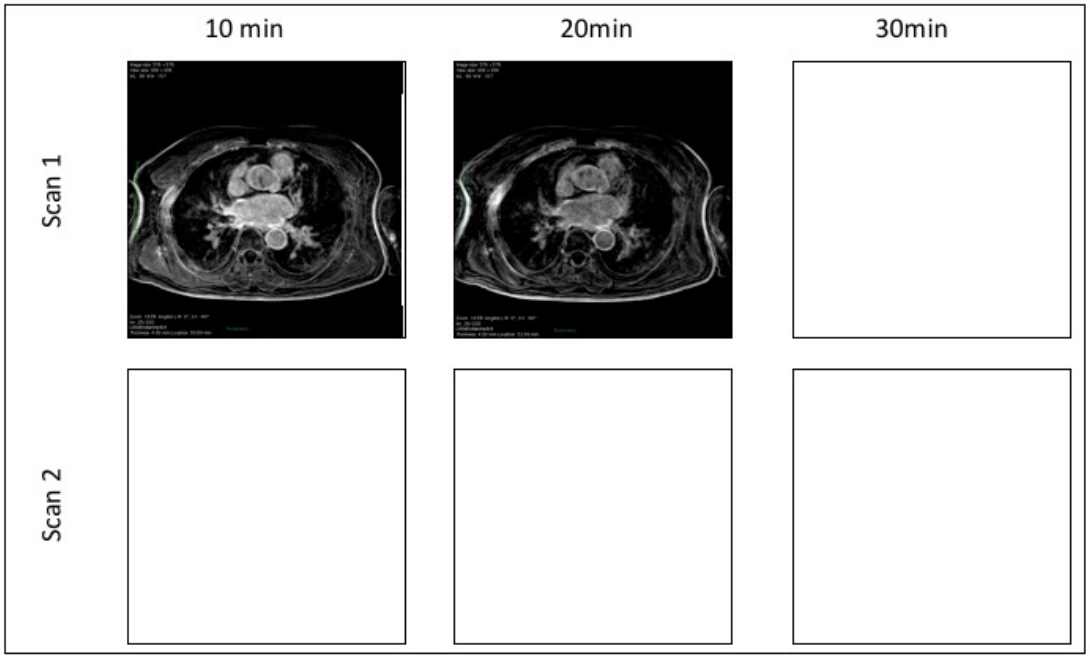

Comments: Viral illness- could not return for Scan 2

5 **3T**

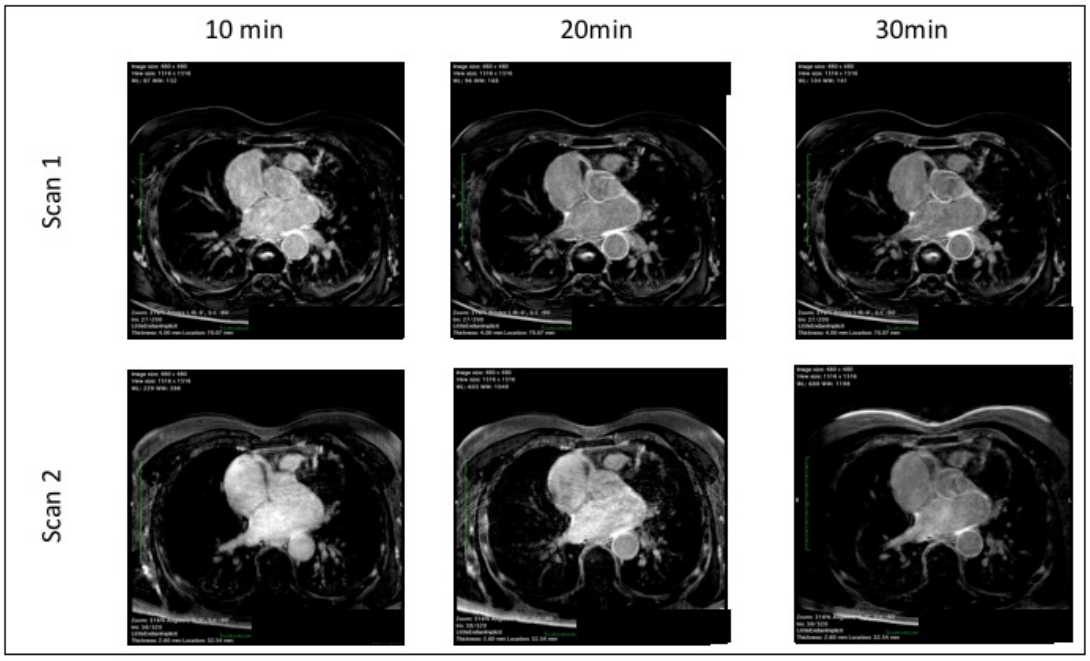

Comments:

6 **Scan type: half gad**

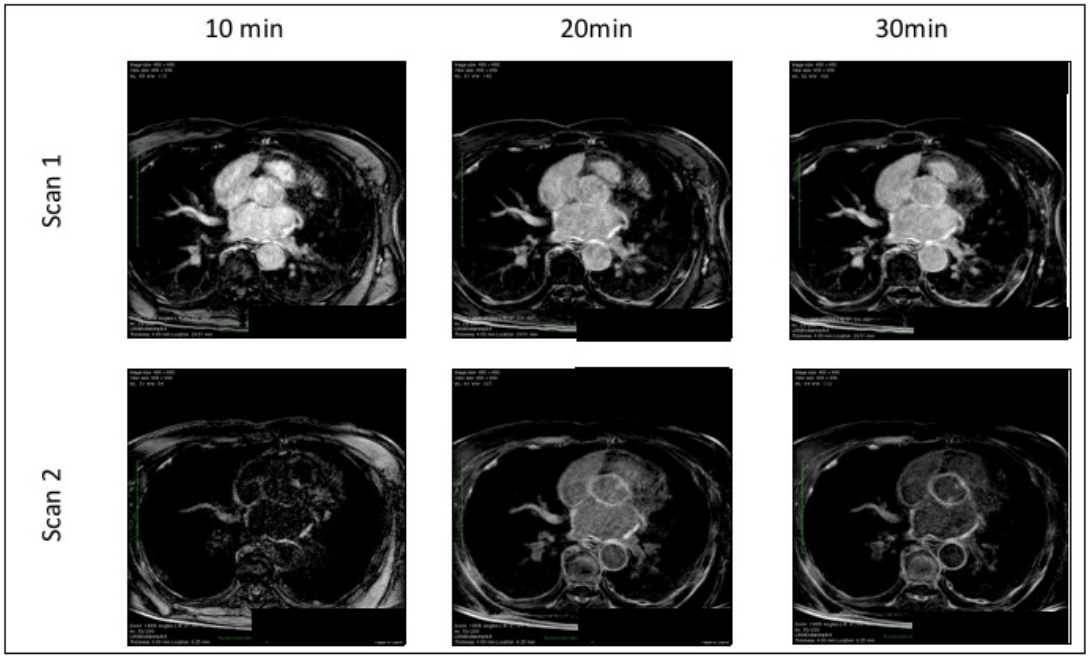

Comments:

7 **Scan type: half slice**

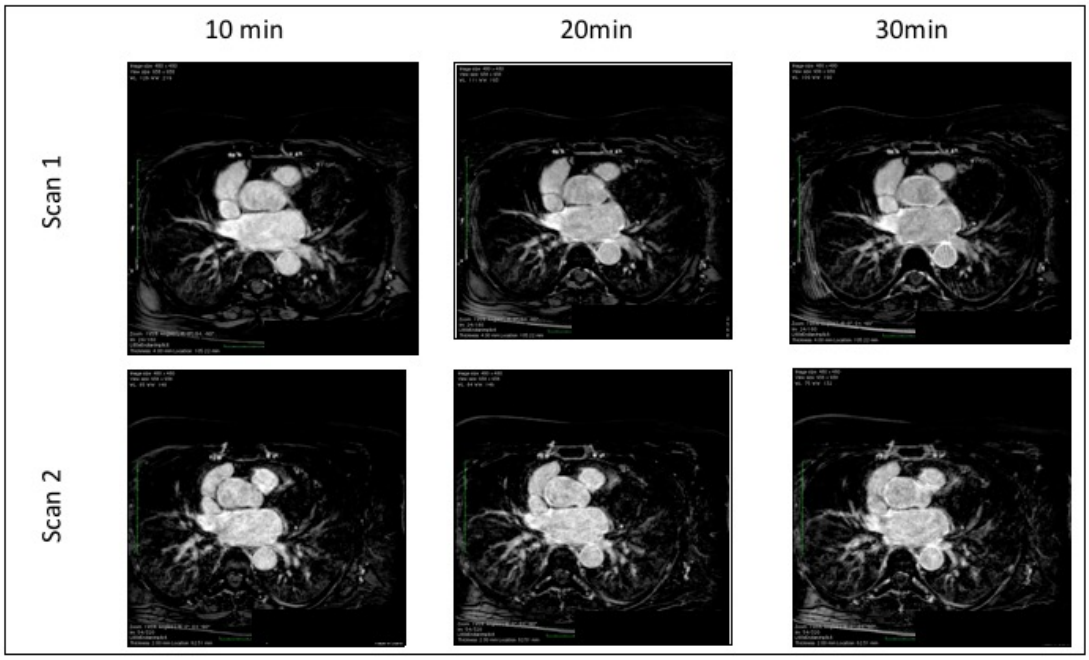

Comments:

8 **Scan type: Repro**

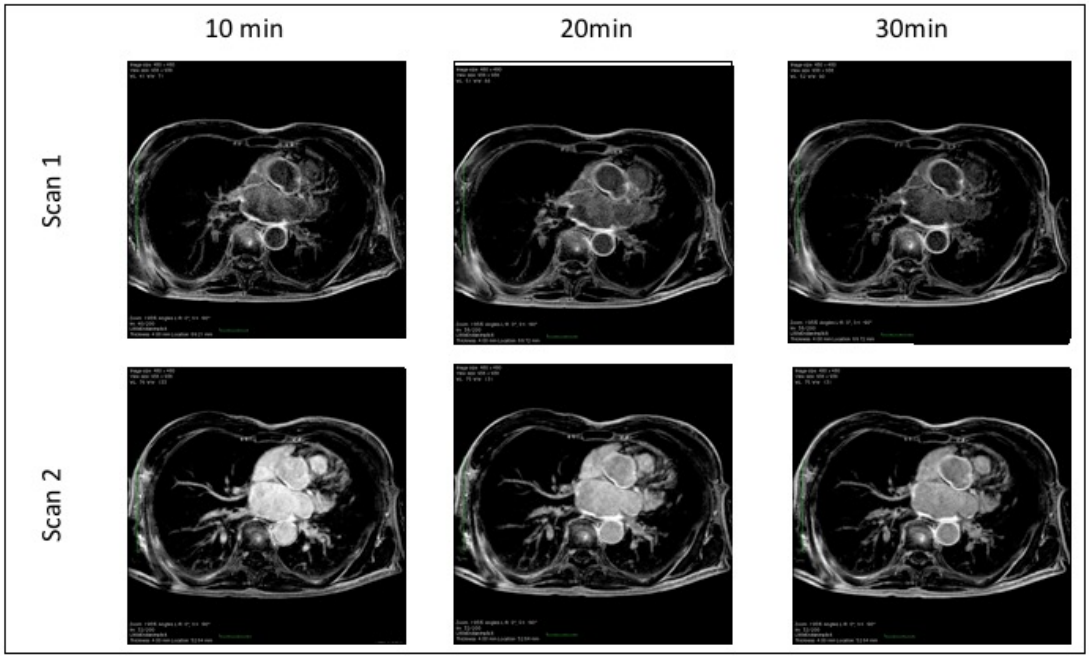

Comments:

9 **Scan type: 3T**

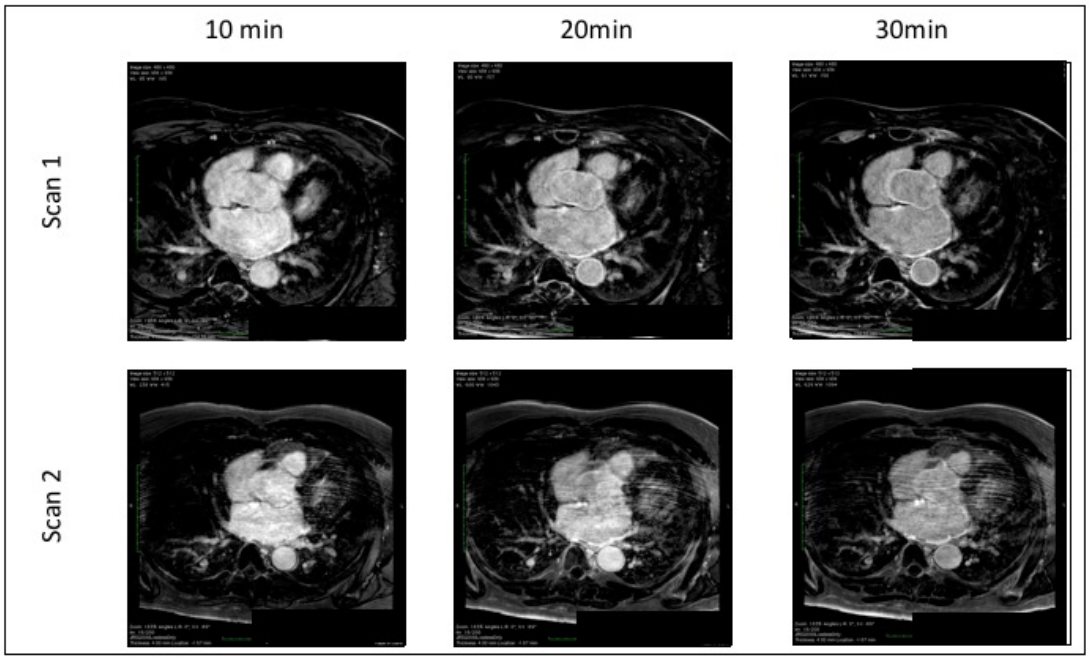

Comments:

10 **Scan type: Repro**

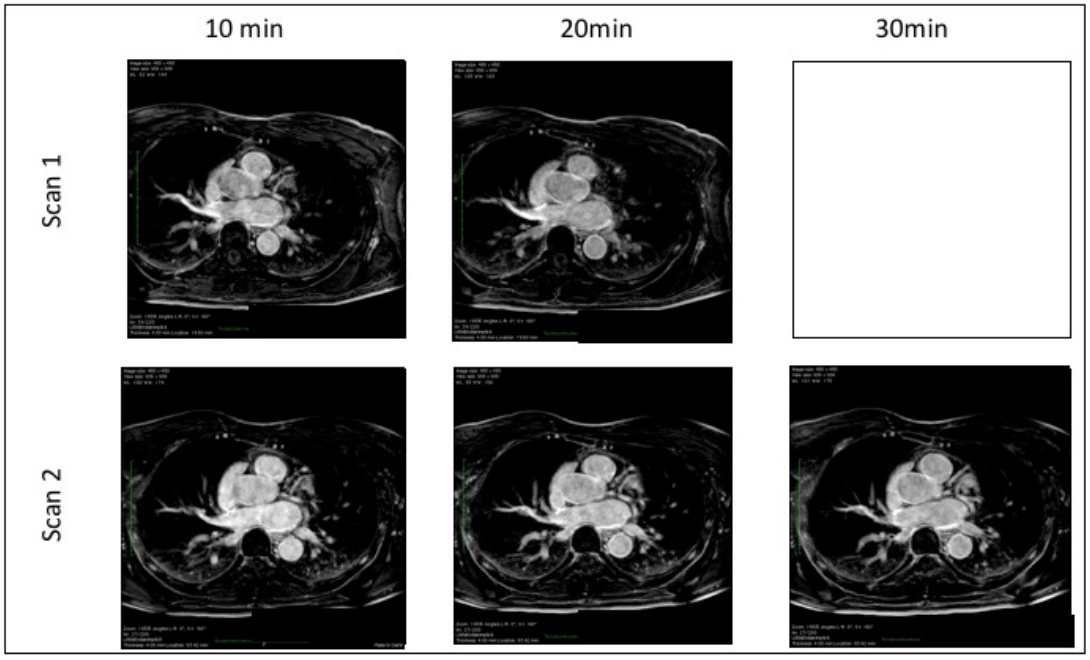

Comments:

11 **Scan type: Half slice**

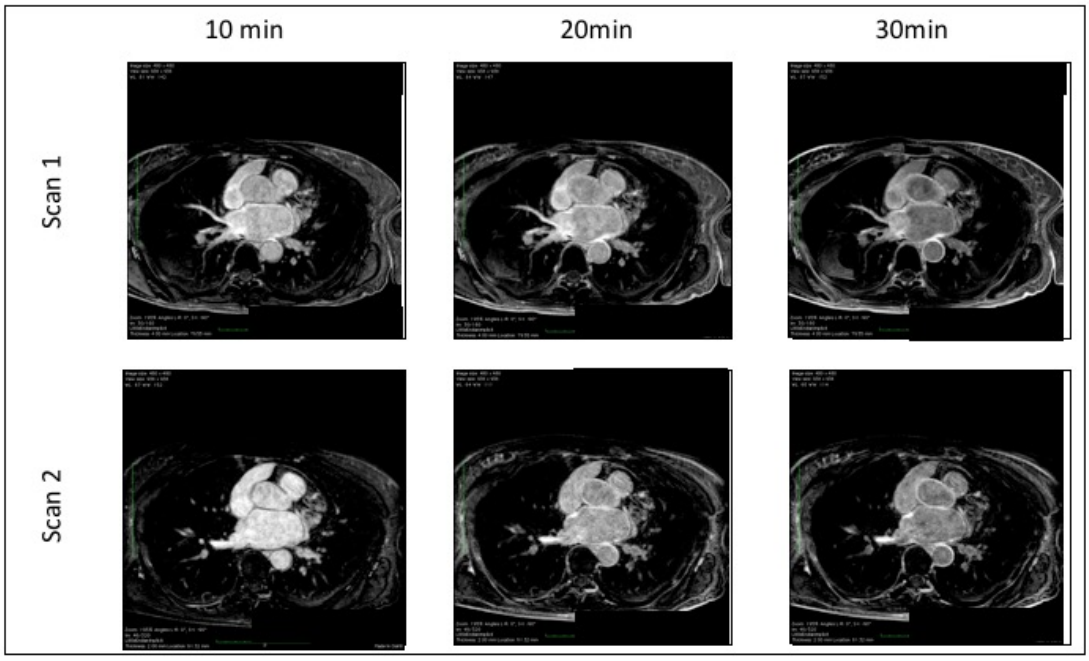

Comments:

12 **Half Gad**

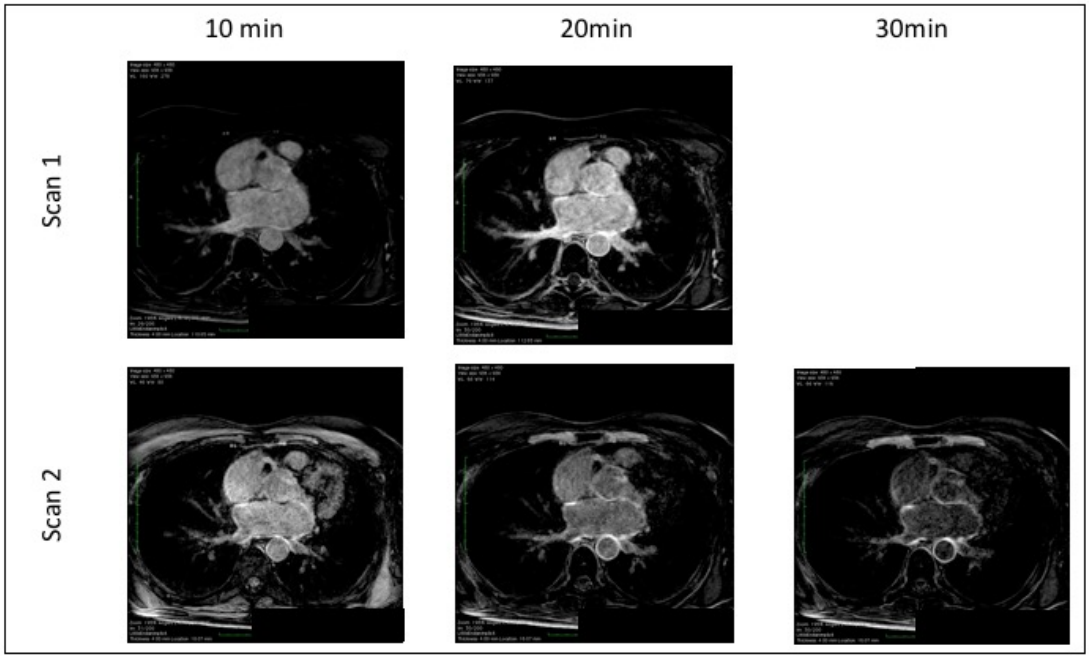

Comments:

13 **Scan type: 3T**

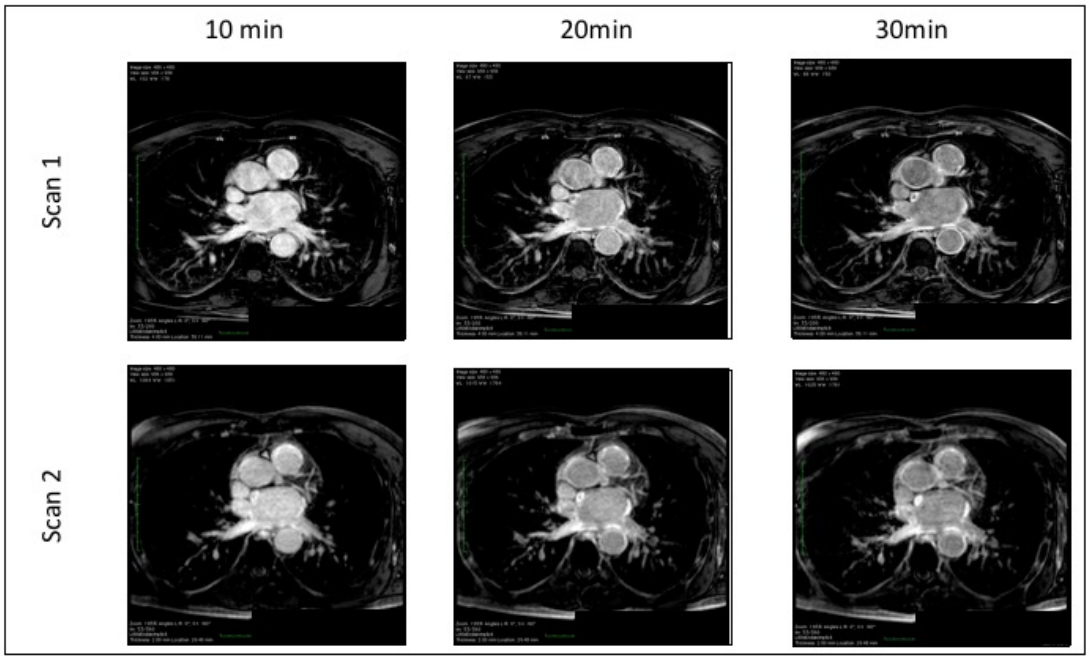

Comments:

14 **Scan type: half slice**

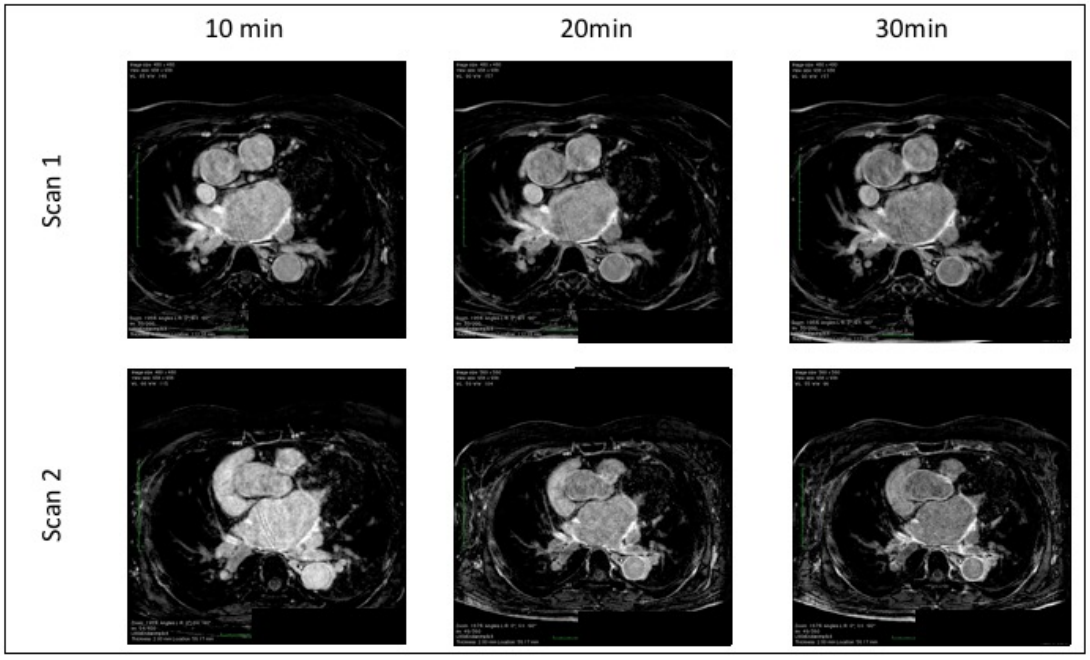

Comments:

15 **Scan type: 3T**

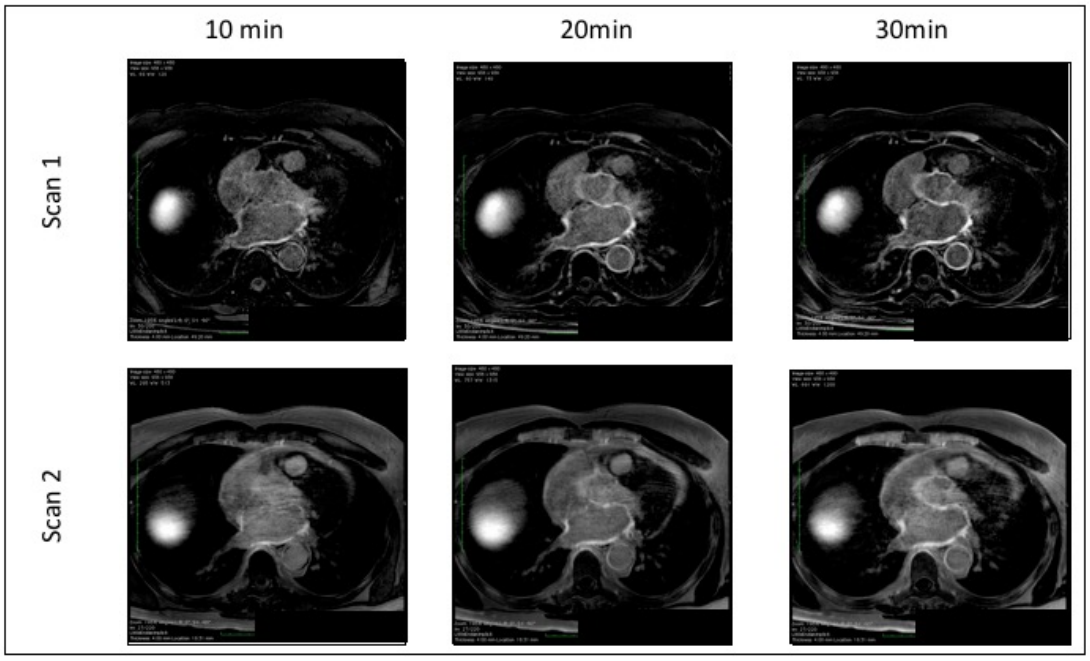

Comments:

16 **Scan type: half slice**

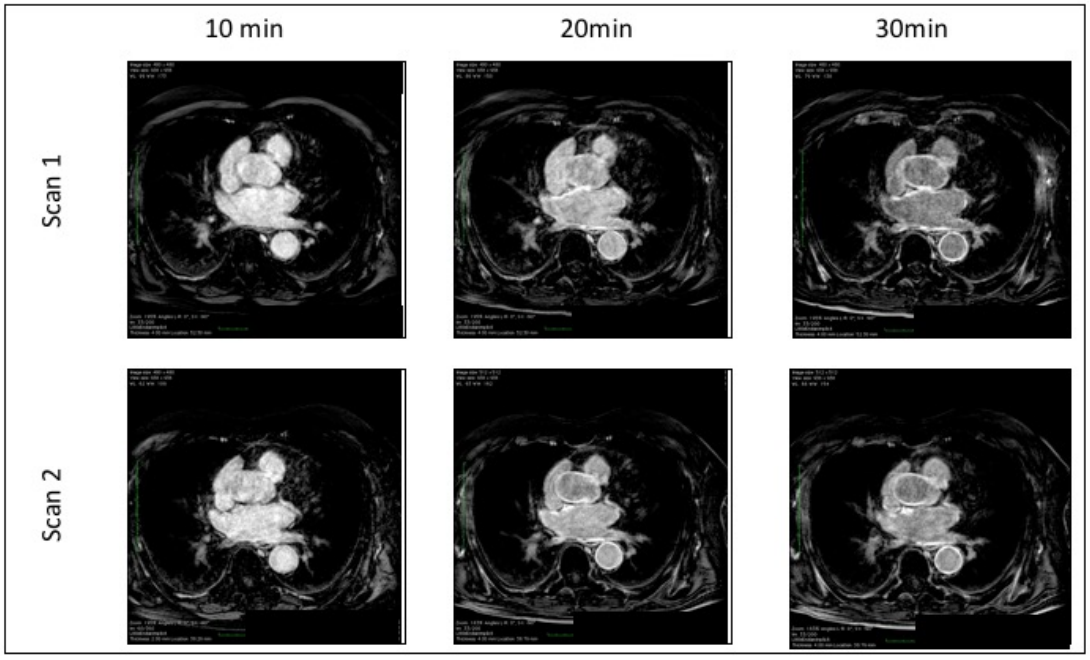

Comments:

17 **Scan type: 3T**

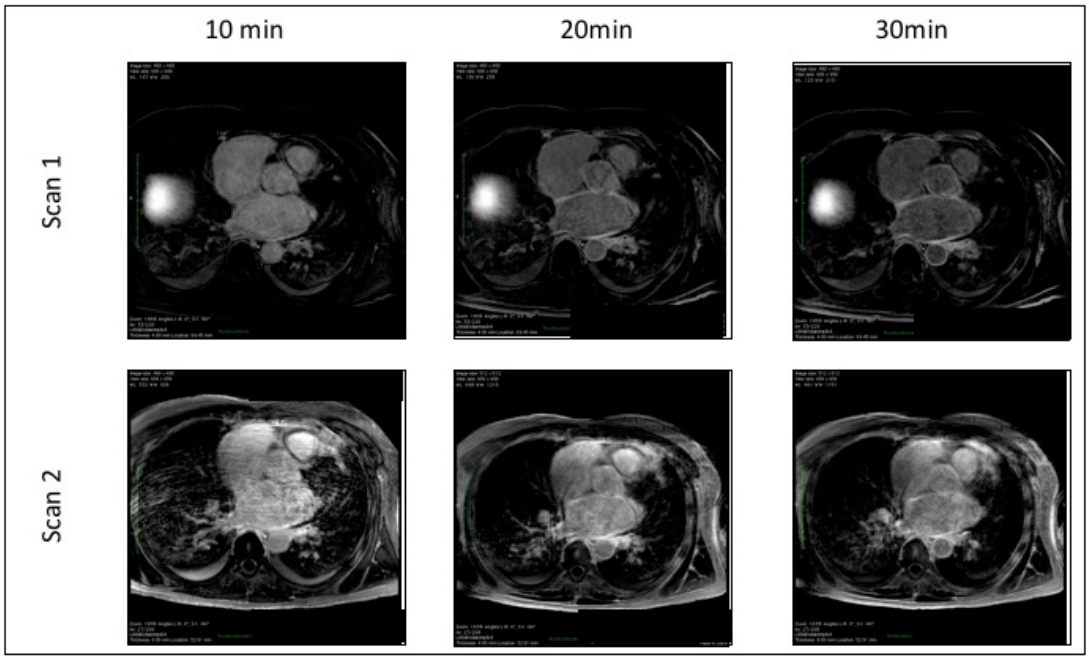

Comments:

18 **Scan type: 3T**

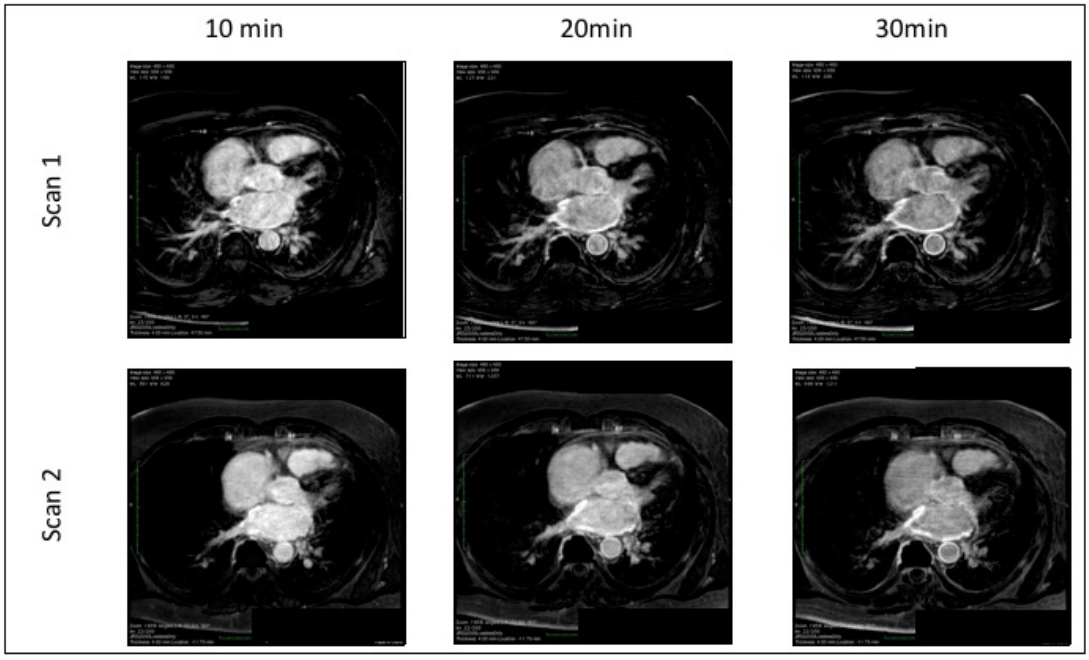

Comments:

19 **Scan type: half slice**

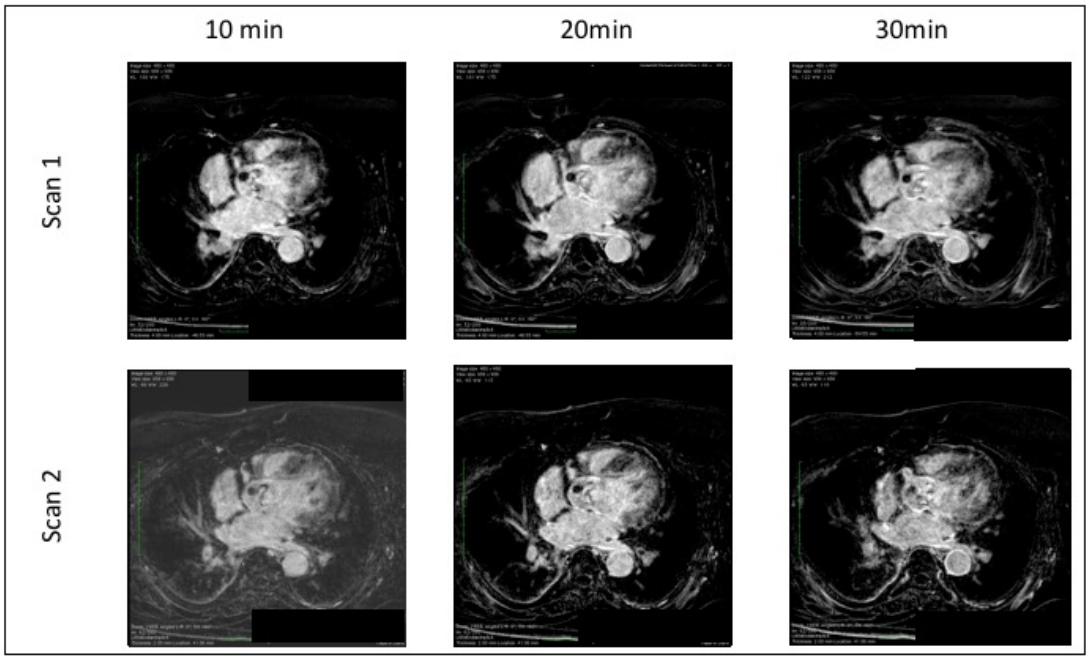

Comments:

20 **Scan type: half slice**

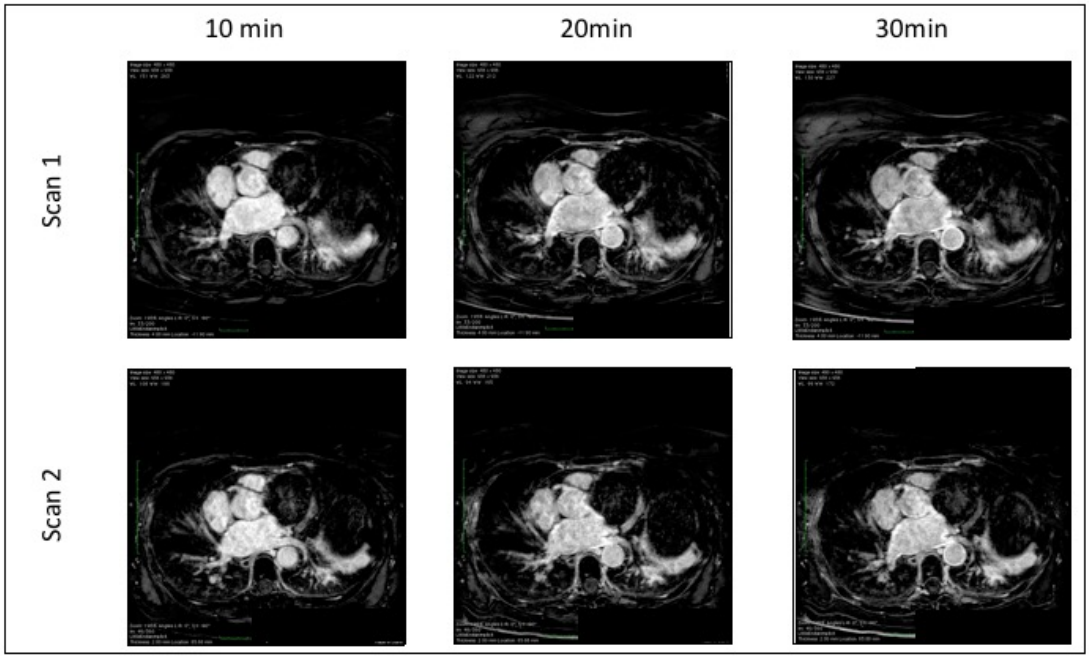

Comments:

21 **Scan type: 3T**

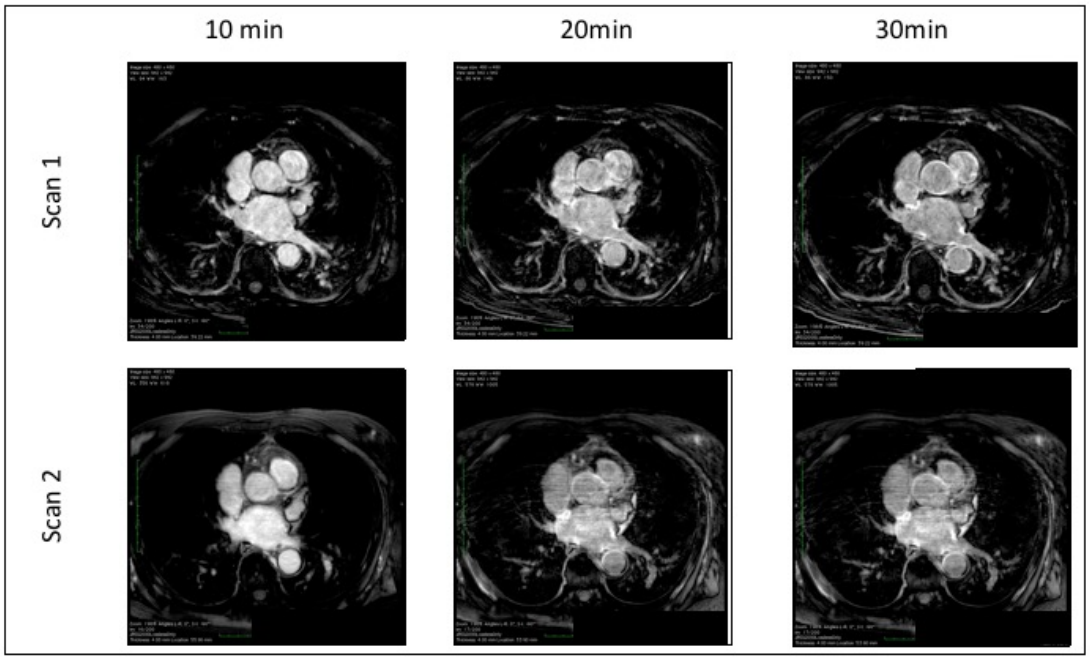

Comments:

22 **Scan type: repro**

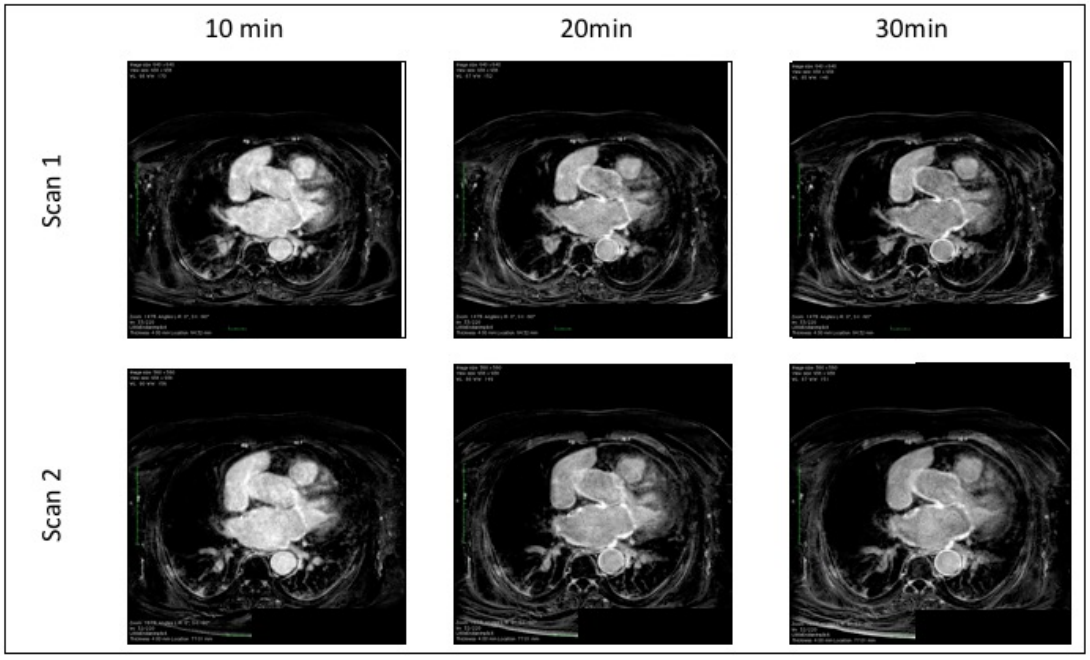

Comments:

23 **Scan type: half slice**

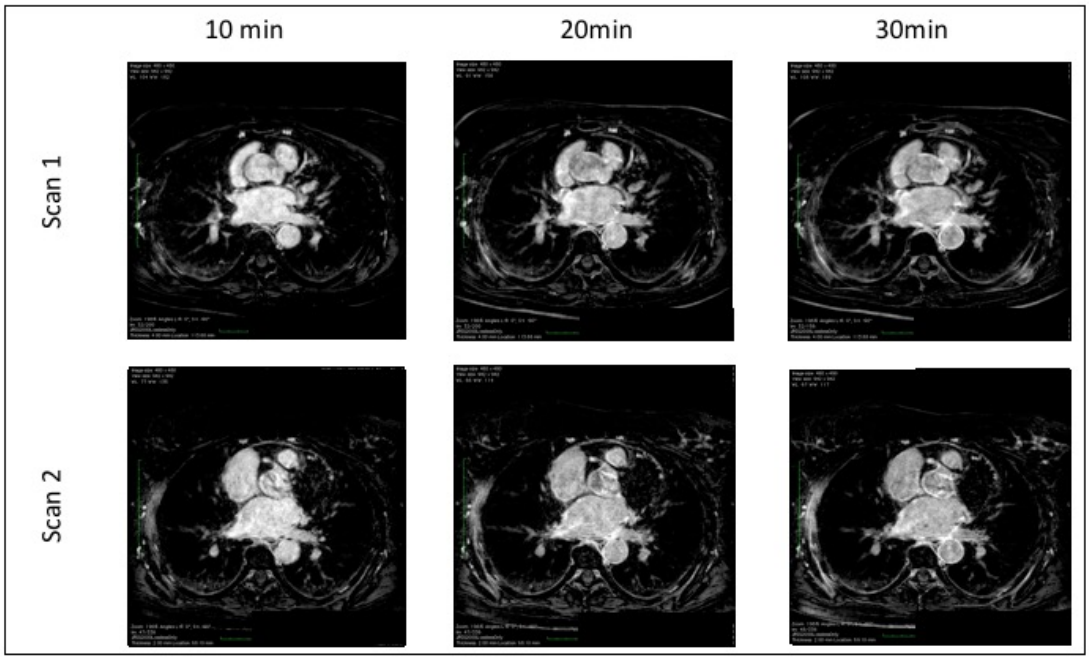

Comments:

24 **Scan type: Repro**

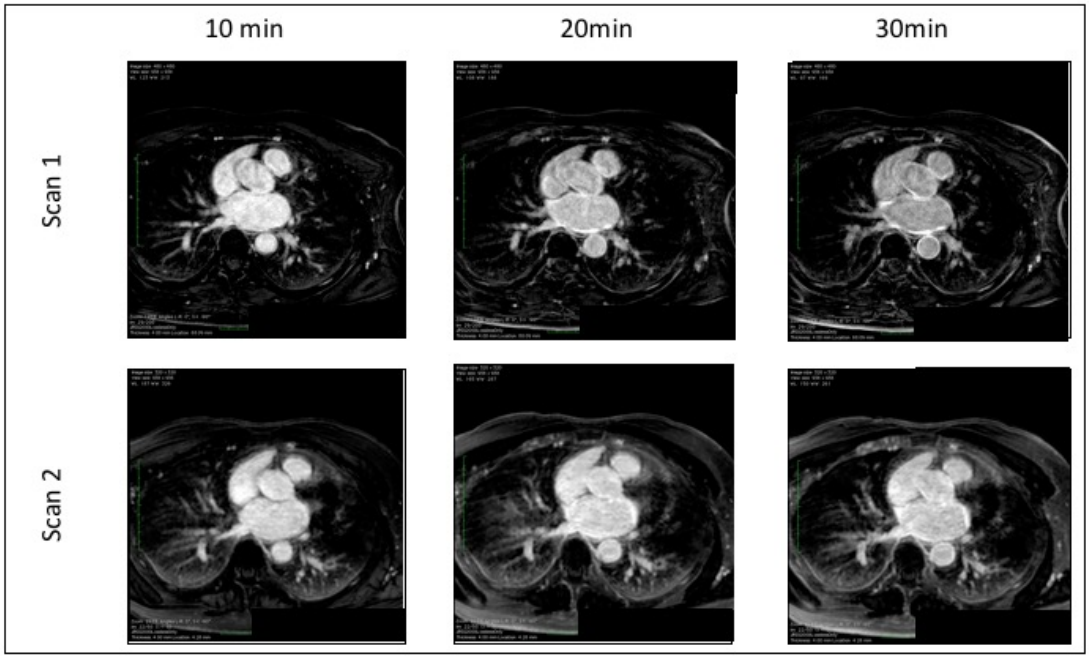

Comments:

25 **Scan type: Repro**

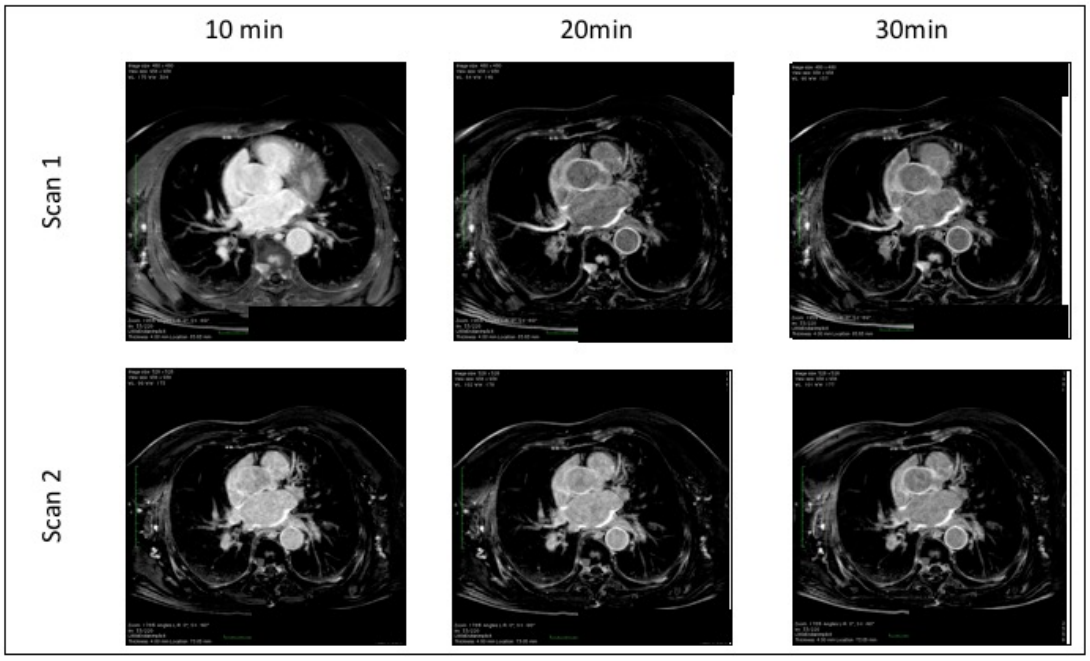

Comments:

26 **Scan type: half gad**

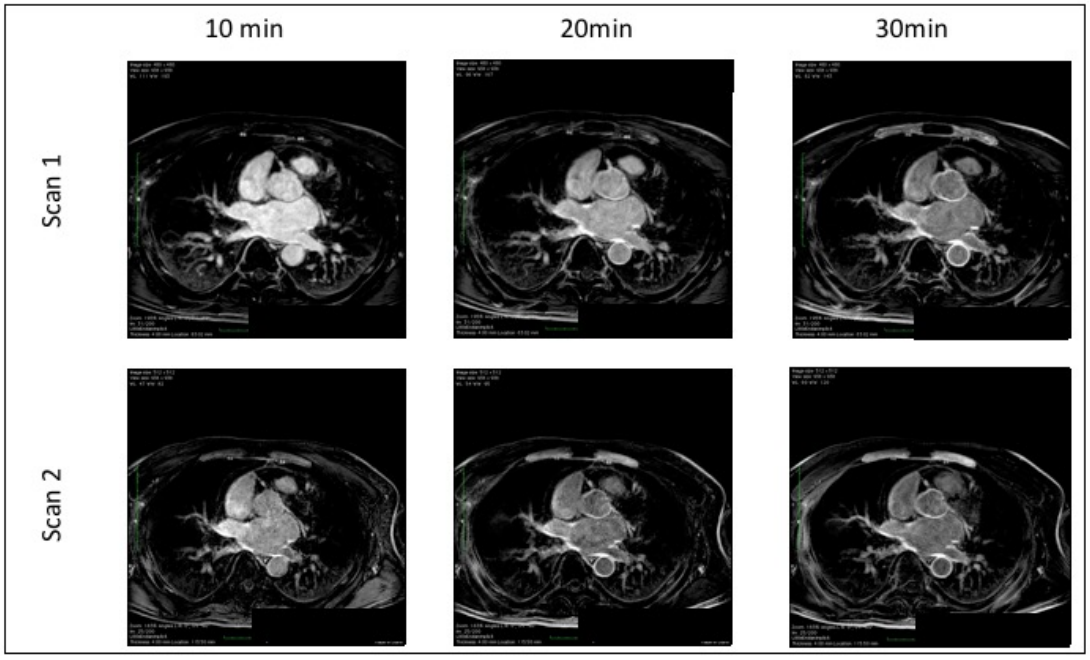

Comments:

27 **Scan type: half gad**

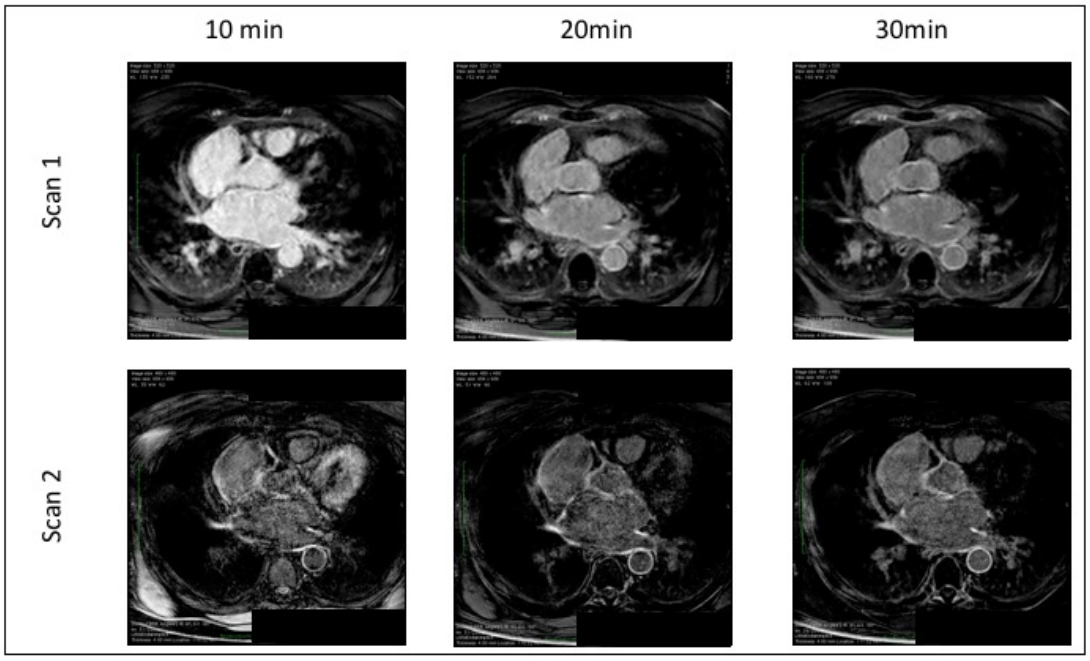

Comments:

28 **Scan type: half gad**

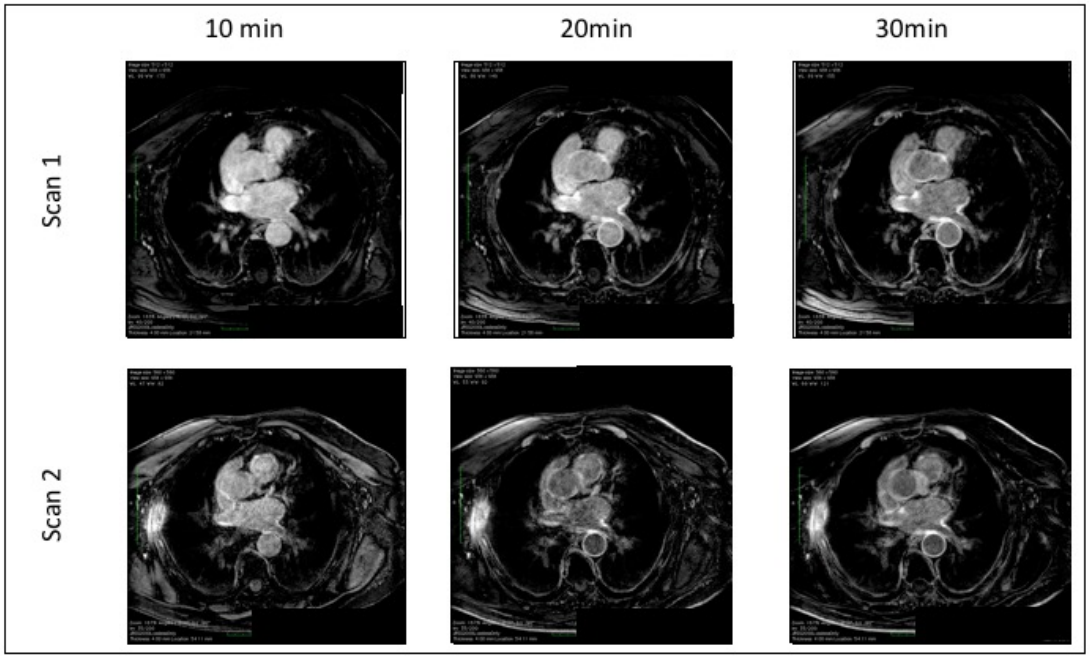

Comments:

29 **Scan type: Half slice**

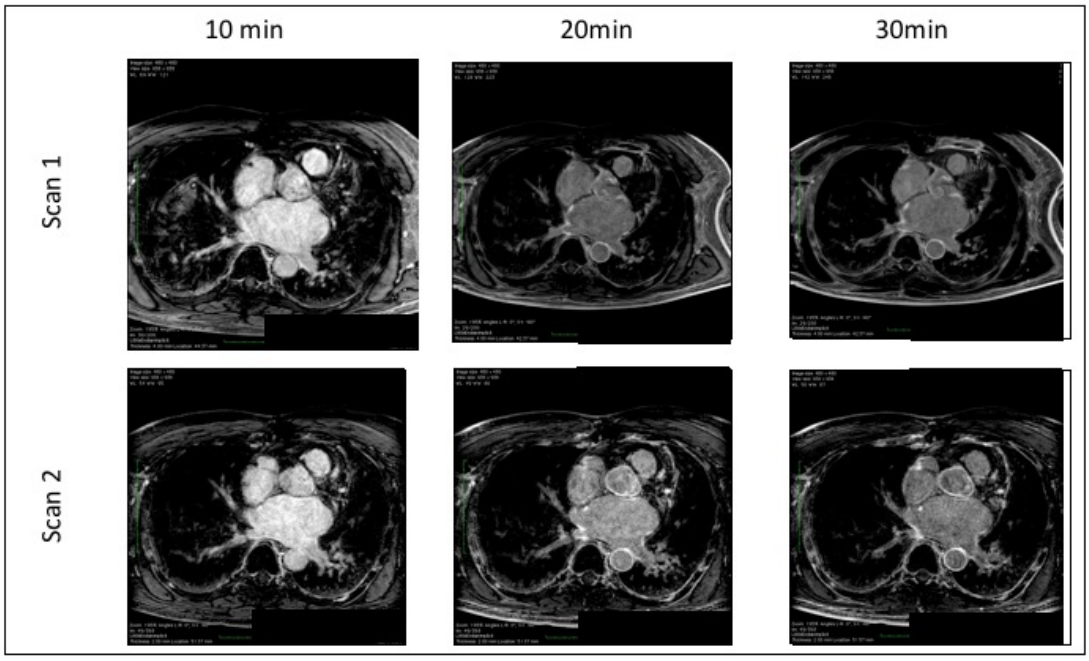

Comments:

30 **Scan type: Repro**

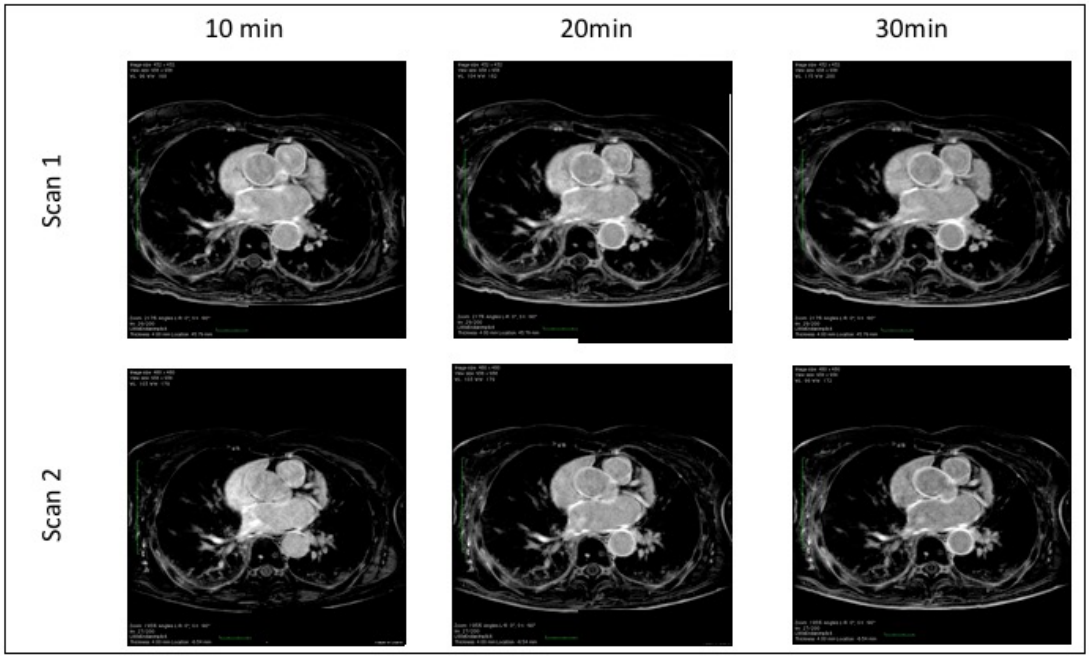

Comments:

31 **Scan type: half gad**

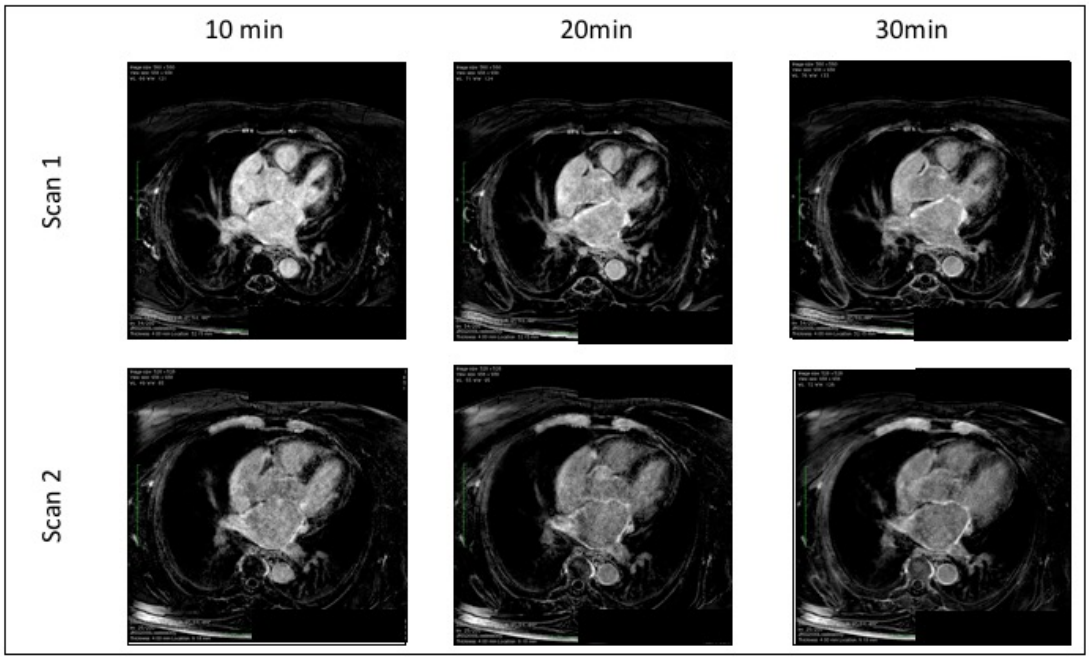

Comments:

32 **3T**

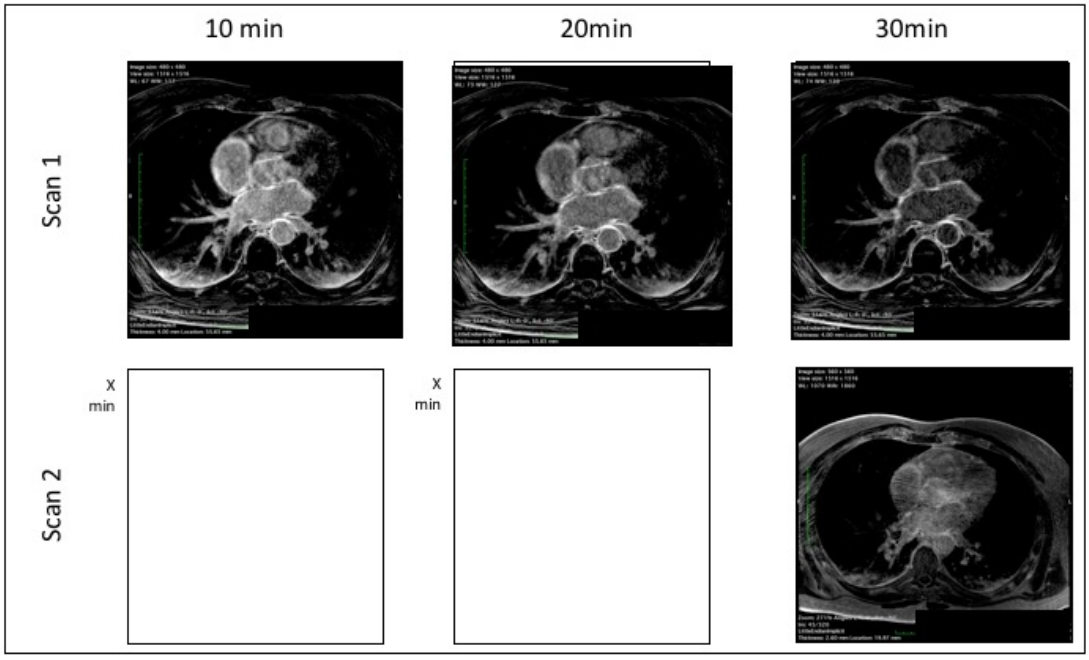

Comments:

33 **Scan type: half slice**

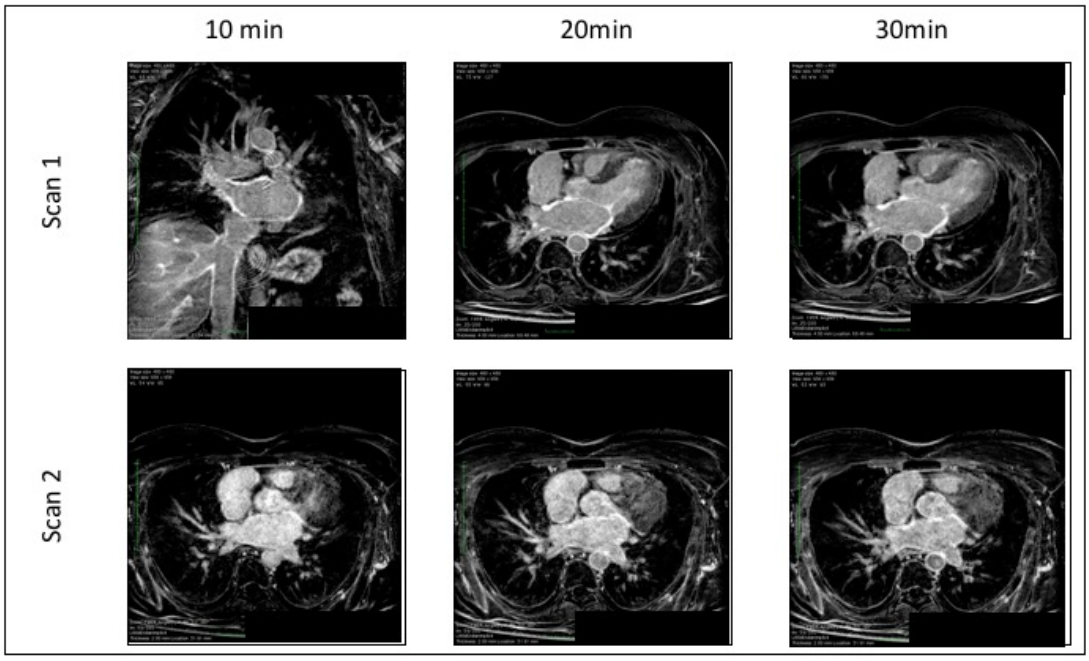

Comments:

34 **Scan type: 3T**

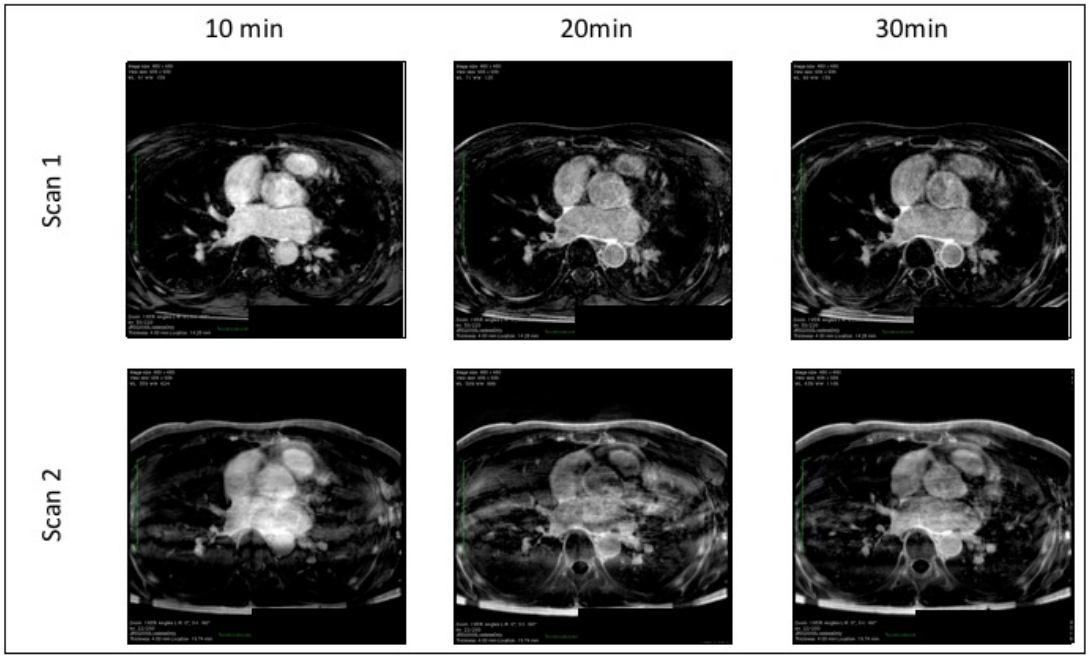

Comments: In AF for both scans

35 **Scan type: half slice**

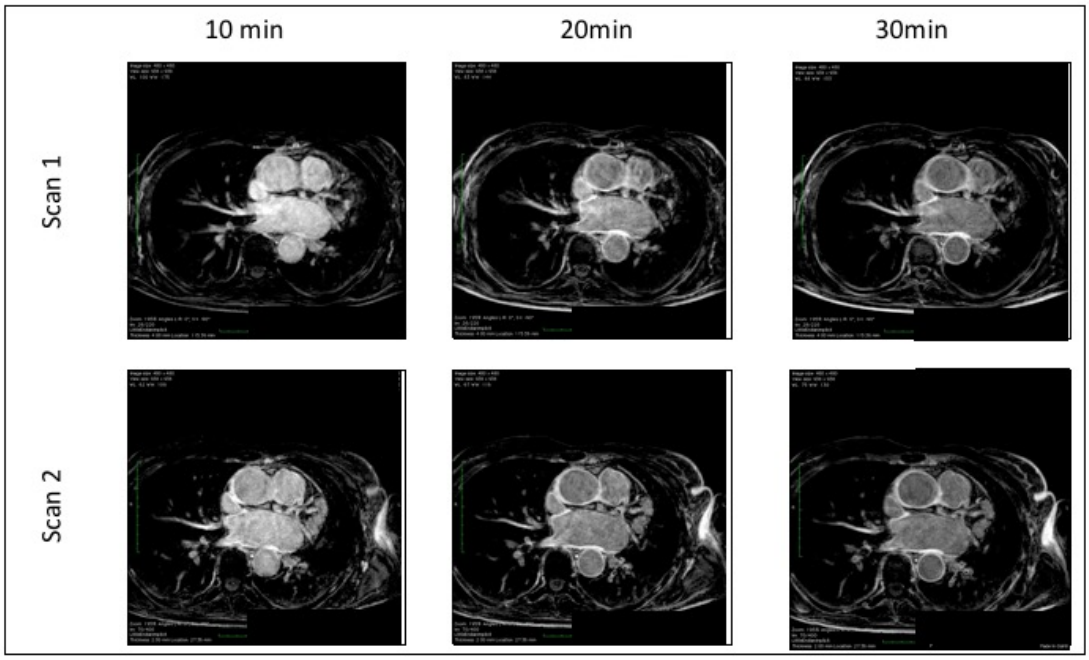

Comments:

36 **Scan type: half dose**

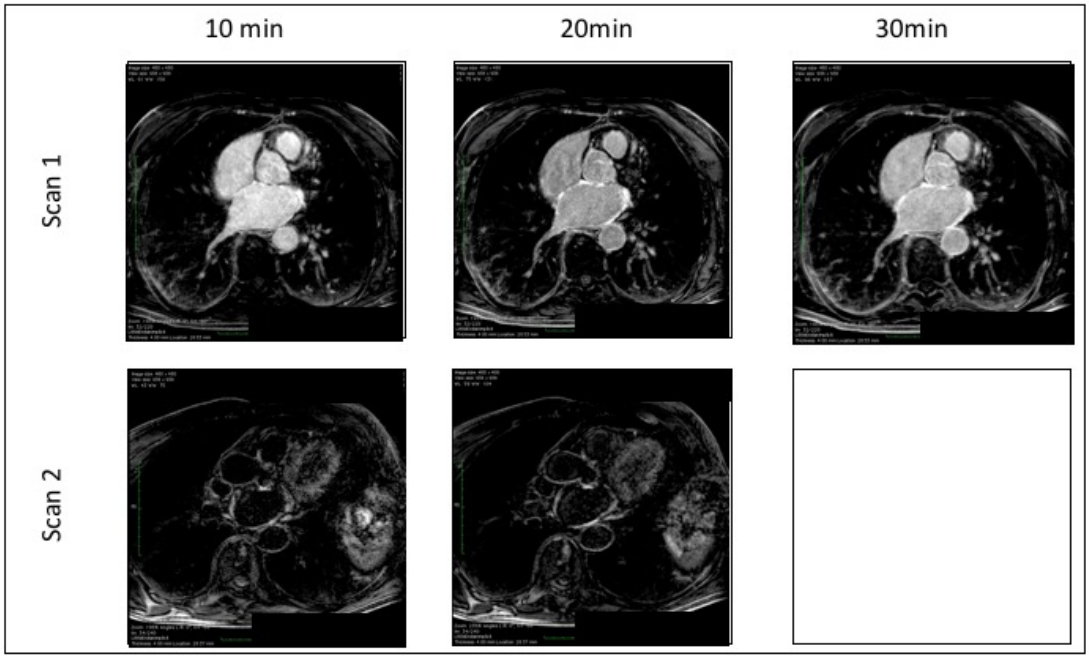

Comments: Scan 2 done by LC

37 **Scan type: half gad**

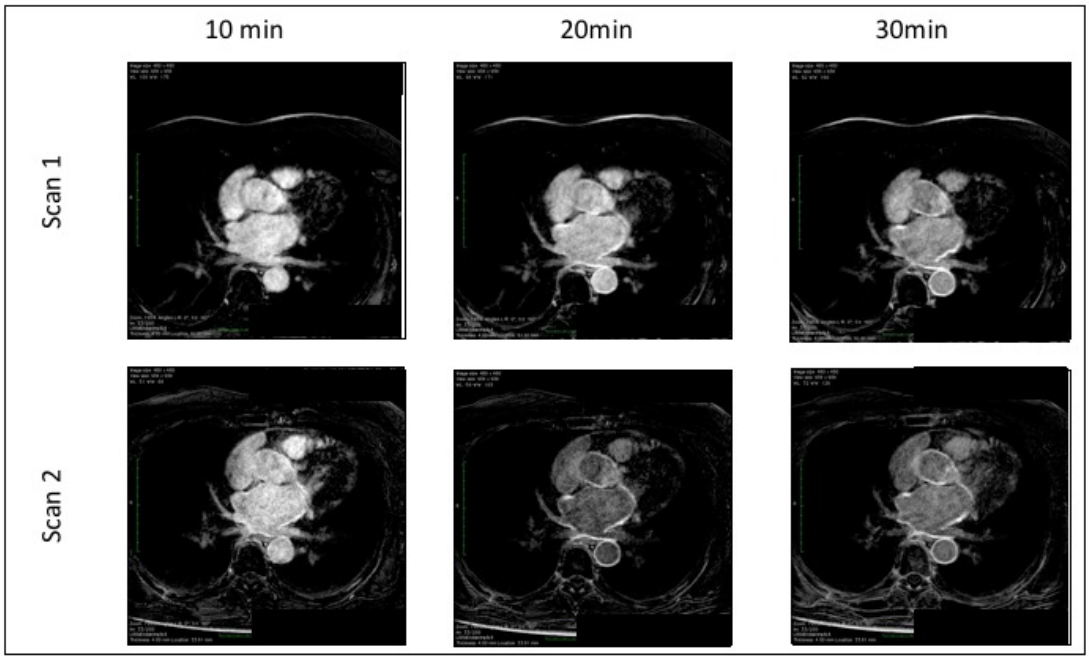

Comments:

38 **Half Gad**

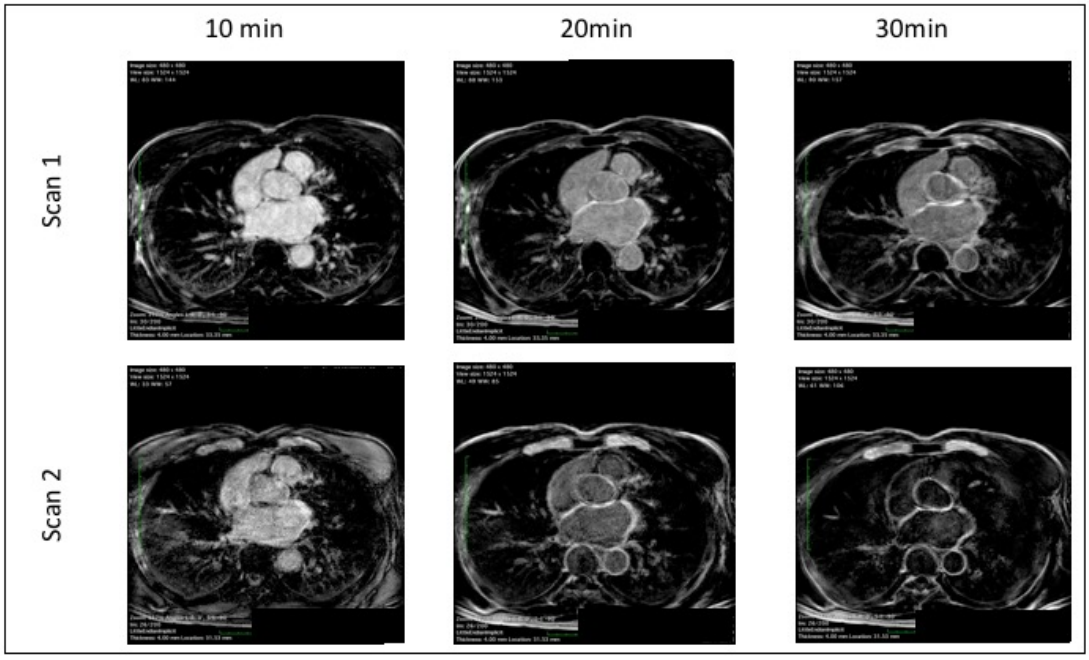

Comments:

39 **Scan type: Repro**

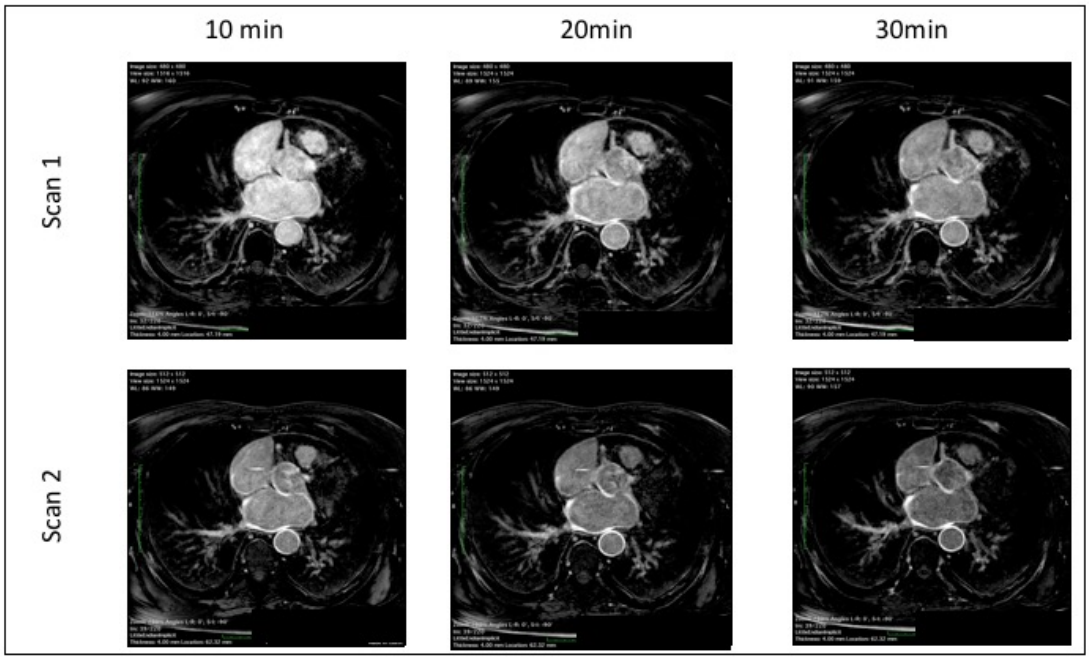

Comments:

40 **Scan type: half Gad**

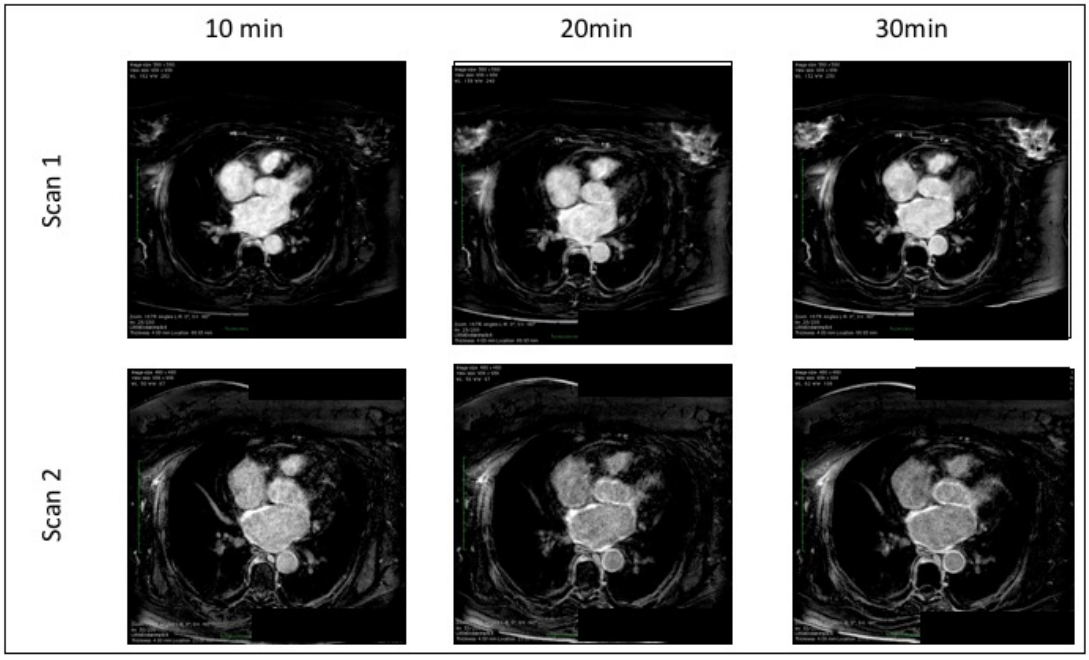

Comments:

APPENDIX B: PULMONARY VEIN ENCIRCLEMENT ANALYSIS TECHNIQUE

The main stages of the method are:

- Left atrial (LA) segmentation and tissue characterisation.
- Semi-automatic labelling of regions within the left atrium
- Gap identification and quantification.

1. Left atrial segmentation and tissue characterisation.

LA segmentation was performed according to the methods described in Chapter 4, and the resulting LA shell was thresholded at 3.3 standard deviations above the blood pool mean in order to define the locations of atrial scar.

2. Semi-automatic labelling of the regions of the LA

In order to determine consistent anatomical regions for each LA, a registration-based method was applied. Anatomical regions were defined on a template atrium that was developed in collaboration with Catalina Tobon-Gomez (Tobon-Gomez et al. 2015). An extra division in the middle of the atrium separating the left from the right side was also added, creating 28 regions in total, with particular attention paid to the regions surrounding the pulmonary veins (PVs) Figure B 1.

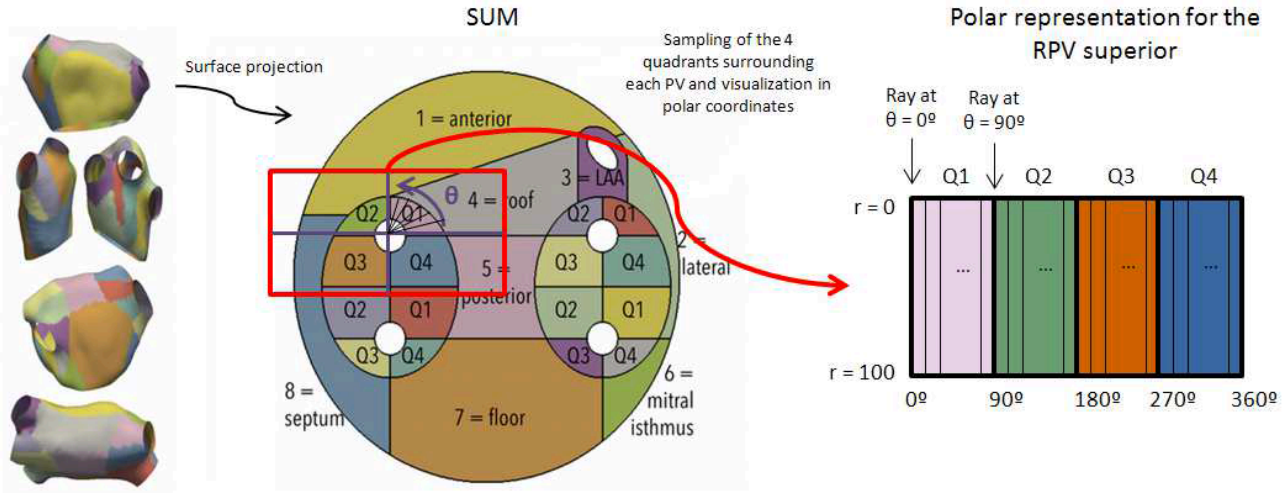

Figure B 1. Labelling of LA regions.

From left to right: LA region definition; surface projection to standardised unfold map (SUM); Radial sampling of the four quadrants around each PV; Representation in polar coordinates (only one vein in this case). Reproduced with permission from Nuñez Garcia et al., 2015.

In order to define the regions of the LA, it required registration to the LA template. However, prior to registration, standardisation of the shell was required, with the semi-automated removal of PVs, left atrial appendage (LAA) and mitral valve (MV) orifice. Five user-defined seeds were placed at the antrum of the PVs and the LAA, and lines connecting each PV (or the LAA) to the 2 PVs on the other side of the LA were calculated to define the lumen of the vein or appendage. The body of the atrium was then defined at the point along the connecting line when the contour of the vein (or the LAA) widened significantly, and an automated clipping was then applied at a user-defined distance from the LA body. For this study the distance was set to 3mm. Other clipping distances were trialled (0 to 10mm), and minimal difference in the final outcome was observed. The MV was then cut automatically using the location of the placed seeds to define a suitable plane representing the MV position.

Registration was then performed using an affine registration technique with iterative closest point fusion. In this way, each vertex on the original (not template) LA shell was labelled according to region.

3. Gap identification and quantification

Gaps in the ablation line were quantified using a technique developed from that described in a previous publication by the Barcelona group (Nuñez Garcia et al. 2015). The detailed labelling of the LA shell enabled the size of the wide area circumferential ablation to be defined accurately, and the veins were assessed in pairs. The ablation line was assessed at a relatively large maximum distance from the PV antrum (up to one quarter of the whole LA diameter) in order not to ignore appropriate ablation locations when a very wide ablation line was performed. The isolating path was defined as the closed path that encircled the PV pair with the minimum gap length between regions of binarised scar along that pathway. A graph was constructed where each node represented a scar patch and the edges are the minimum distance between the corresponding patches. The Dijkstra algorithm was then applied to find the shortest path. Note that according to this method, healthy areas would only be defined as gap if they belonged to the isolating path.

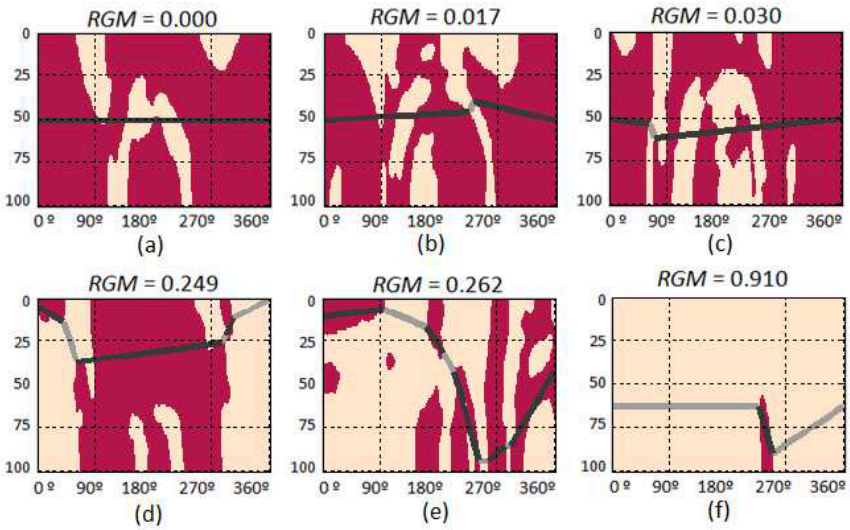

Figure B 2. Results of the gap quantification method.

The peri-antral region is unfolded, and scar regions are shown in red. On top of every subplot the corresponding RGM is shown. Reproduced with permission from Nuñez Garcia et al., 2015.

In this way a Relative Gap Measure (RGM) was defined where:

$$RGM = \frac{Gap\ Length}{Total\ Length}$$

Where where gap length is the sum of the length of all gaps in the isolating path and total length is the total length of the path (gaps + scar patches length).

As a more intuitive measure for clinical application, a Pulmonary Vein Encirclement (PVE) index was also defined where:

$$PVE = 1 - RGM$$